

2

ANNUAL REPORT

University Research Initiative

Contract No.: N00014-92-J-1808

March 1992 - April 1993

AD-A266 397

DTIC
ELECTE
JUN 21 1993
S A D

The Processing and Mechanical Properties of High Temperature/High Performance Composites

by

A.G. Evans & F. Leckie
University of California,
Santa Barbara

University of Pennsylvania
Harvard University

Washington State University
Carnegie Mellon University
University of Virginia

This document has been approved
for public release and sale; its
distribution is unlimited.

93 6 17 03 8

93-13753

||||| ||| ||| ||

Book 4 of 5:

CONSTITUTIVE LAWS AND DESIGN

**SUMMARY
OF
TABLE OF CONTENTS**

EXECUTIVE SUMMARY

BOOK 1: CONSTITUENT PROPERTIES OF COMPOSITES

**BOOK 2: CONSTITUENT PROPERTIES AND MACROSCOPIC
PERFORMANCE: CMCs**

**BOOK 3: CONSTITUENT PROPERTIES AND MACROSCOPIC
PERFORMANCE: MMCs**

BOOK 4: CONSTITUTIVE LAWS AND DESIGN

BOOK 5: PROCESSING AND MISCELLANEOUS PROPERTIES

DTIC QUALITY INSPECTED 8

Accession For	
NTIS GRA&I	✓
DTIC TAB	
Unannounced	
Justification	
By per A216146	
DTIC TAB	
Unannounced	
Justification	
A-1	

BOOK 4

CONSTITUTIVE LAWS AND DESIGN

- | | | |
|-----|--|--|
| 50. | Remarks on Crack-Bridging Concepts | G. Bao
Z. Suo |
| 51. | Notch Ductile-to-Brittle Transition due to Localized Inelastic Band | Z. Suo
S. Ho
X. Gong |
| 52. | On the Tensile Strength of a Fiber-Reinforced Ceramic Composites Containing a Crack-Like Flaw | B. Budiansky
Y.L. Cui |
| 53. | Mechanical Behavior of a Continuous Fiber-Reinforced Aluminum Matrix Composite Subjected to Transverse and Thermal Loading | S. Jansson
F.A. Leckie |
| 54. | Modeling of Anisotropic Behavior of Weakly Bonded Fiber Reinforced MMCs | Gunawardena
S. Jansson
F.A. Leckie |
| 55. | Transverse Ductility of Metal Matrix Composites | Gunawardena
S. Jansson
F.A. Leckie |
| 56. | Localization due to Damage in Two Direction Fiber Reinforced Composites | F. Hild
P.-L. Larsson
F.A. Leckie |
| 57. | On the Notch-Sensitivity and Toughness of a Ceramic Composite | K. Kedward
P. Beaumont |
| 58. | Thermal, Mechanical & Creep Behavior of Metal Matrix Composites | S. Jansson
F.A. Leckie |
| 59. | The Treatment of Fatigue and Damage Accumulation in Composite Design | K. Kedward
P. Beaumont |

- | | | |
|-----|--|---|
| 60. | A Direct Method for the Shakedown Analysis of Structures Under Sustained and Cyclic Loads | W. Jiang
F.A. Leckie |
| 61. | Creep of Fiber-Reinforced Metal-Matrix Composites: Constitutive Equations and Computational Issues | N. Aravas
C. Cheng |
| 62. | On Neutral Holes in Tailored, Layered Sheets | B. Budiansky
J.W. Hutchinson
A.G. Evans |
| 63. | The In-Plane Shear Properties of 2-D Ceramic Matrix Composites | P.A. Brøndsted
F.E. Heredia
A.G. Evans |
| 64. | Transverse Cracking in Fiber-Reinforced Brittle Matrix, Cross-Ply Laminates | Z.C. Xia
R.R. Carr
J.W. Hutchinson |
| 65. | Plane Strain Delamination Growth in Composite Panels | P-L. Larsson
F.A. Leckie |
| 66. | Mixed Mode Delamination Cracking in Brittle Matrix Composites | G. Bao
B. Fan
A.G. Evans |
| 67. | Mixed Mode Cracking in Layered Materials | J.W. Hutchinson
B.-X. Wu |
| 68. | Crazing of Laminates | J. Lemaitre
F.A. Leckie
D. Sherman |

EXECUTIVE SUMMARY

1. GENERAL STRATEGY

The overall program embraces property profiles, manufacturing, design and sensor development (Fig. 1) consistent with a concurrent engineering philosophy. For this purpose, the program has created networks with the other composites activities. *Manufacturing* research on MMCs is strongly coupled with the 3M Model Factory and with the DARPA consolidation team. Major links with Corning and SEP are being established for CMC manufacturing. *Design Team* activities are coordinated by exchange visits, in February/March, to Pratt and Whitney, General Electric, McDonnell Douglas and Corning. Other visits and exchanges are being discussed. These visits serve both as a critique of the research plan and as a means of disseminating the knowledge acquired in 1992.

The program strategy concerned with design attempts to provide a balance of effort between *properties* and *design* by having studies of mechanisms and property profiles, which intersect with a focused activity devoted to design problems (Fig. 2). The latter includes two foci, one on MMCs and one on CMCs. Each focus reflects differences in the property emphases required for design. The intersections with the mechanism studies ensure that commonalities in behavior continue to be identified, and also facilitate the efficient transfer of models between MMCs and CMCs.

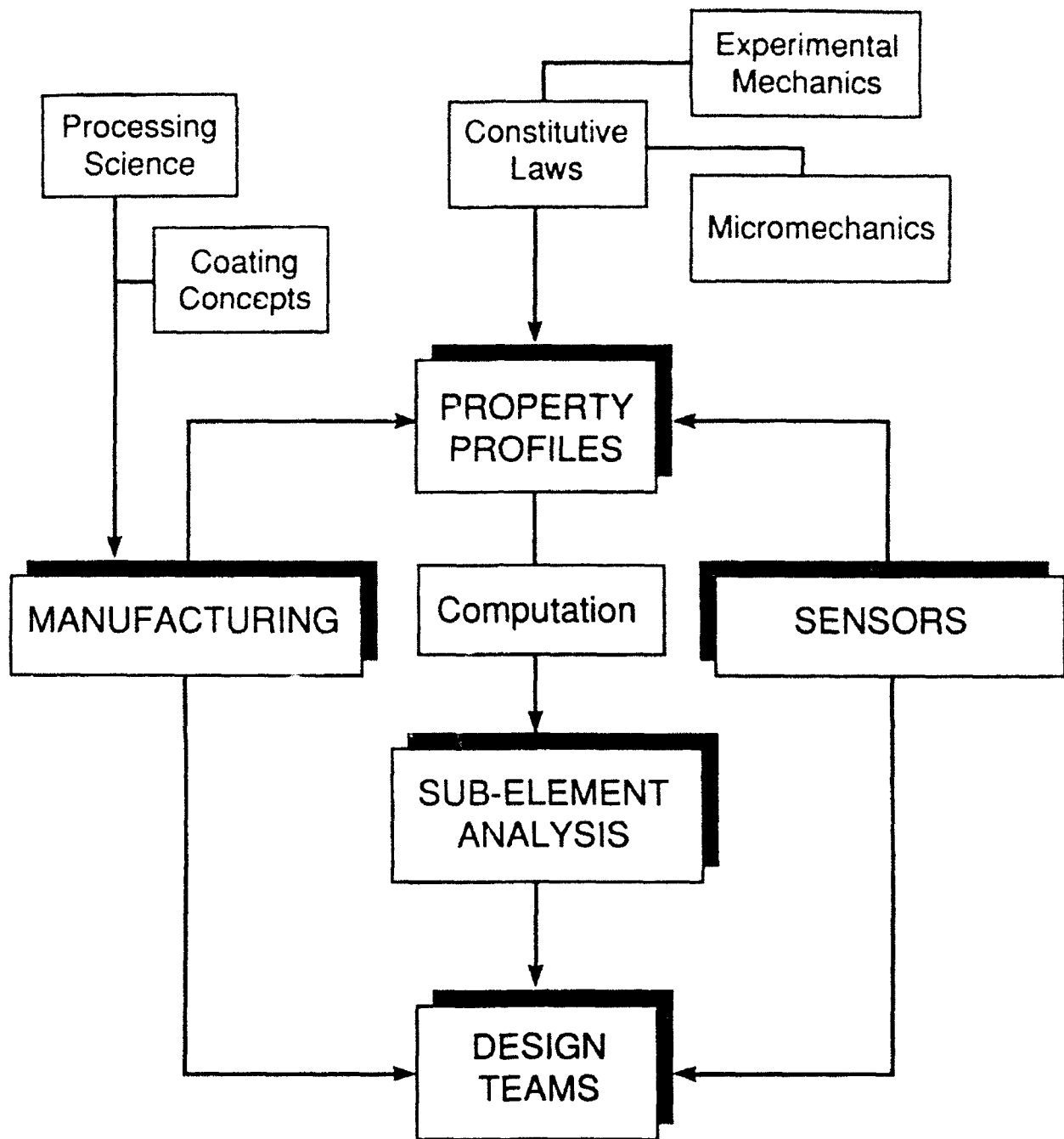


Fig. 1 The Concurrent Engineering Approach

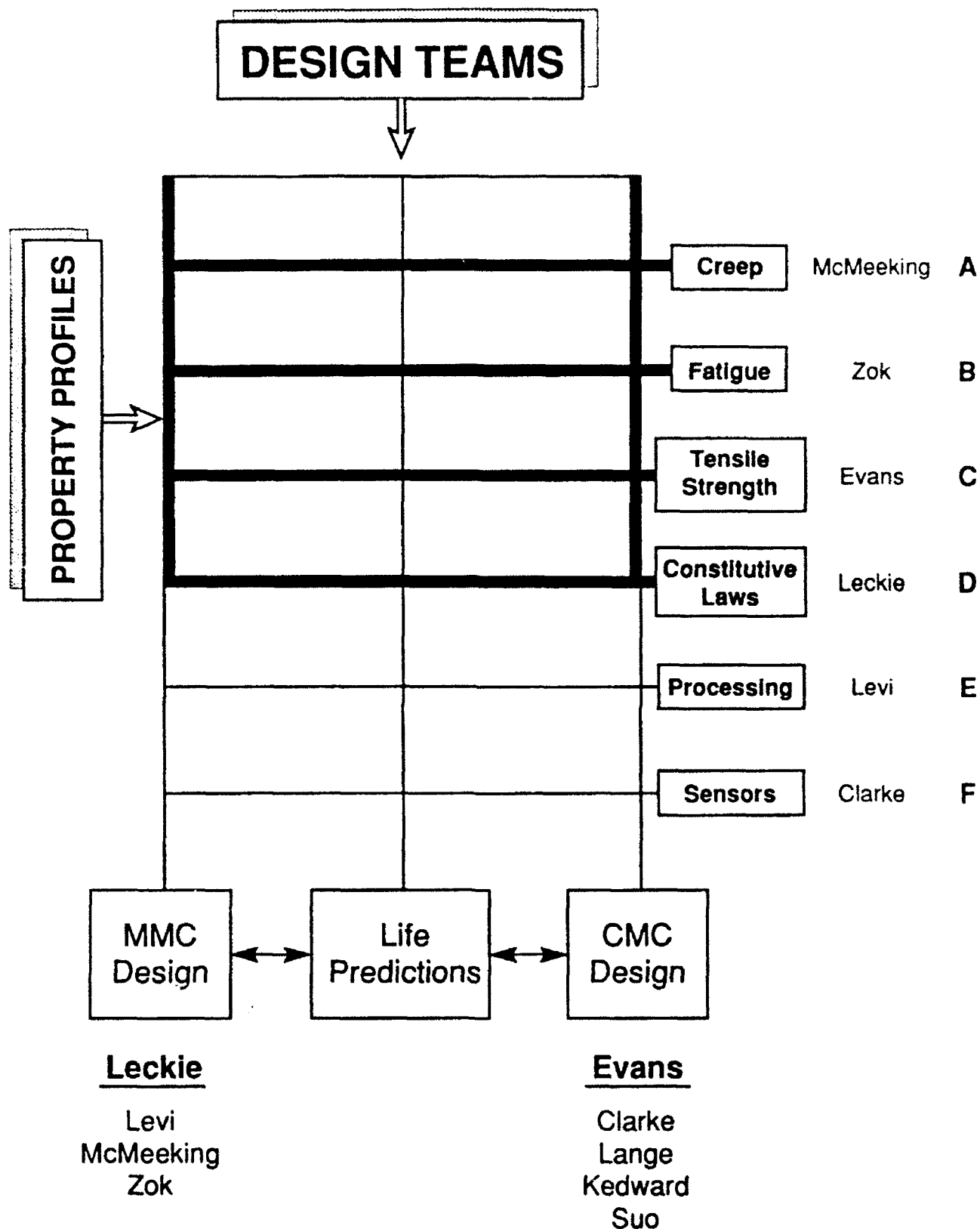


Fig. 2
Matrix Structure of Program

2. PROPERTY PROFILES

Each research activity concerned with properties begins with experiments that identify the principal property-controlling phenomena. Models are then developed that relate the physical response to constituent properties. These models, when validated, provide the constitutive laws required for calculating stress redistribution, failure and damage progression. They also provide a solid physics and mechanics understanding, which can be used to judge the effectiveness of the simplified procedures needed for design purposes.

2.1 Fatigue

Studies of the propagation of dominant mode I fatigue cracks from notches in MMCs, including the role of fiber bridging and fiber failure, have been comprehensively addressed (Zok, McMeeking). Software programs that include these effects have been developed. These are being transferred to Pratt and Whitney and KAMAN Sciences. The effects of thermal cycling on crack growth in MMCs have also been modelled (McMeeking). The results highlight the opposing effects of cycling on matrix crack growth and fiber failure (the fatigue threshold), when thermal cycles are superposed onto load cycles. Notably, matrix crack growth is enhanced by out-of-phase thermomechanical cycling, but fiber failure is suppressed (and vice versa for in-phase cycling). Experimental studies that examine these predictions are planned (Zok).

Studies have also been conducted on systems that exhibit *multiple* matrix cracking (Zok). The tensile stress-strain behavior of composites containing such cracks is analogous to the behavior of unidirectional CMCs

under monotonic tensile loading. As a result, models developed to describe the tensile response of the CMCs have found utility in describing the MMCs. However, two important differences in the two classes of composite have been identified and are presently being addressed. The first deals with the nature of the crack patterns. In the CMCs, the cracks are more or less uniformly spaced and generally span across the entire composite section. In contrast, the MMCs exhibit a broader distribution of crack sizes, many of which are short compared with the specimen dimensions. Methodologies for measurement and interpretation of crack densities in MMCs are being developed. The second problem deals with degradation in the interfacial sliding properties with cyclic sliding in the MMCs. Such degradation is presently being studied using fiber push-out tests in fatigued specimens.

Thermal fatigue studies on MMCs subject to transverse loading have been performed and have established the conditions that allow shakedown (Leckie). The shakedown range is found to be strongly influenced by the extent of matrix creep, which defines a temperature limitation on the use of the material. The eventual outcome of this activity would be the specification of parameters that ensure shakedown and avoid ratcheting.

The next challenge for MMCs concern the quantification of transitions in fatigue behavior, especially those found at higher temperatures. These include multiple matrix cracking and shear band formation. Experimental studies are in progress which will be used to establish a mechanism map. The map, when developed, would explicitly identify the transitions (Zok). The analogous behavior found in CMCs will facilitate this development. Other high temperature phenomena to be explored include changes in the interfacial sliding behavior due to both relaxations in the thermal residual stresses and the growth of reaction products near the fiber-matrix interface.

Fatigue damage studies on 2-D CMCs will focus on interface and fiber degradation phenomena, especially at elevated temperatures (Evans, Zok). Cyclic loading into the stress range at which matrix cracks exist is known to modify the interface sliding stress and may weaken the fibers. These degradation effects can be distinguished, because they change the hysteresis loop and reduce the UTS, respectively. Experiments that probe these material responses are planned. In addition, models that include the influence of cyclic fiber failure and pull-out on fatigue damage will be developed (Suo).

2.2 Matrix Cracking

Models of the plastic strain and modulus changes caused by various modes of matrix cracking have been developed. These solutions have provided a rationale for experimental studies on the tensile and shear behavior of CMCs and on the fatigue of MMCs (Hutchinson, Zok, Evans, Suo, Budiansky, McMeeking). The information has been used in two distinct ways. (i) Test methodologies have been devised that relate stress/displacement measurements to constituent properties (Table I). (ii) Stress/strain curves and matrix crack evolution have been simulated for specific combinations of constituent properties.

The development of the procedures and their implementation are still in progress. Independent solutions have been established for matrix cracks in 0° plies and 90° plies upon tensile loading. The former has been experimentally validated on 1-D materials (SiC/SiC and SiC/CAS). Measurements of plastic strain, hysteresis loops and crack densities have been checked against the models for consistency.

TABLE I

Relevant Constituent Properties and Measurement Methods

CONSTITUENT PROPERTY	MEASUREMENT
Sliding Stress, τ	<ul style="list-style-type: none"> • Pull-Out Length, \bar{h} • Saturation Crack Spacing, \bar{l}_s • Hysteresis Loop, $\delta \epsilon_{1/2}$ • Unloading Modulus, \bar{E}_L
Characteristic Strength, S_c, m	<ul style="list-style-type: none"> • Fracture Mirrors • Ultimate Strength, S
Misfit Strain, $\Omega (q)$	<ul style="list-style-type: none"> • Bilayer Distortion • Permanent Strain, ϵ_p • Residual Crack Opening
Matrix Fracture Energy, Γ_m	<ul style="list-style-type: none"> • Monolithic Material • Saturation Crack Spacing, \bar{l}_s • Matrix Cracking Stress, $\bar{\sigma}_{mc}$
Debond Energy, Γ_l	<ul style="list-style-type: none"> • Permanent Strain, ϵ_p • Residual Crack Opening

The next challenge is to couple the models together in order to simulate the evolution of matrix cracks in 2-D materials, subject to tensile loading (Hutchinson, Budiansky). Related effects on the ultimate tensile strength caused by stress concentrations in the fibers in the presence of matrix cracks, would also be evaluated. Experimental measurements of stress/strain behavior in 2-D CMCs, with concurrent observations of matrix crack evolution, would be used to guide and validate such models (Evans, Kedward).

2.3 Constitutive Equations

Constitutive equations provide the link between material behavior at the meso-scale and the performance of engineering components. The equations can be established from the results of uniaxial and transverse tensile tests together with in-plane shear loading. For a complete formulation, which describes accurately the growth of failure mechanisms and the conditions of failure at the meso-scale, it is also necessary to perform calculations which are valid at the micro-scale.

These procedures have been completed for metal-matrix composites (Jansson, Leckie), and the resulting constitutive equations are operational in the ABAQUS finite element code. The behavior of simple panels penetrated by circular holes have been studied and the results await comparison with experiments which are planned for the coming year. The constitutive equations are formulated in terms of state variables which include the hardening tensors and damage state variables which describe debonding at the interface and void growth in the matrix. The format is sufficiently general to allow the inclusion of failure mechanisms such as environmental attack as the appropriate understanding is available. For

example, the effect of matrix and fiber creep mechanisms (Aravas) have also been introduced into ABAQUS, and it is proposed to extend the creep conditions to include the effects of variable loading and temperature.

A similar approach has been taken towards the modulus of CMCs. In this case, efforts have been made to include the influence of matrix cracking, in-plane shearing and fiber breakage. The latter consideration is based on the global load sharing model (Hayhurst). The equations are also available in ABAQUS. At present, matrix cracking is introduced by assuming a matrix stress accompanied by an increase of strain. However, based on the more recent understanding of the growth of matrix cracks (above) it is intended to introduce these mechanisms into the constitutive equations for CMCs.

2.4 Creep

The emphases of the creep investigations have been on the anisotropic characteristics of unidirectional layers in which the fibers are elastic, but the matrix creeps. Experiments and models of the longitudinal creep properties of such materials have been initiated (McMeeking, Leckie, Evans, Zok, Aravas). The critical issues in this orientation concern the incidence of fiber failure and the subsequent sliding response of the interface. A modelling effort has established an approach that allows the stochastic evolution of fiber failure to occur as stress is transferred onto the fibers by matrix creep (McMeeking). This approach leads to creep rates with a large power law exponent. Various attempts are underway to incorporate the interface sliding initiated by fiber breaks and to introduce sliding into the creep rate formulation. Experiments being performed on unidirectional Ti matrix materials are examining the incidence of fiber failures on the creep

deformation (Evans, Leckie, Zok). These results will guide the modelling effort concerned with interface sliding effects. Insight will also be gained about fiber failure stochastics during creep, especially differences from room temperature behavior.

The transverse creep properties are expected to have direct analogies with composite deformation for a power law hardening matrix (Section 2.3). In particular, the same effects of debonding and matrix damages arise and can be incorporated in an equivalent manner (Leckie, Aravas). Testing is being performed on Ti MMCs and on SiC/CAS to validate the models.

Experiments on Ti-matrix $0^\circ/90^\circ$ cross-ply composites are planned. Creep models appropriate to cross-ply materials will be developed by combining those corresponding to the unidirectional materials in the longitudinal and transverse orientations, using a rule-of-mixtures approach. Such an approach is expected to be adequate for loadings in which the principal stresses coincide with the fiber axes. Alternate approaches will be sought to describe the material response in other orientations.

Some CMCs contain fibers that creep more extensively than the matrix. This creep deformation has been found to elevate the stress in the matrix and cause time dependent evolution of matrix cracks. This coupled process results in continuous creep deformation with relatively low creep ductility. Experiments on such materials are continuing (Evans, Leckie) and a modelling effort will be initiated (Suo). The models would include load transfer into the matrix by creeping fibers, with sliding interfaces, leading to enhanced matrix cracking.

Tensile Strength

The ultimate strength (UTS) of both CMCs and MMCs (as well as fatigue and creep thresholds) is dominated by fiber failure. With the global load sharing (GLS) concept of fiber failure now well established, the recent emphasis has been on defining the constituent properties needed to ensure GLS. The approach has been to perform local load sharing calculations and then compare experimental UTS data with the GLS predictions (Curtin, Evans, Leckie). The situation is unresolved. However, initial calculations on CMCs (Curtin) and MMCs (Evans) have provided some insight. Two key remaining issues concern the magnitude of the stress concentration in intact fibers caused by matrix cracks and the role of fiber pull-out in alleviating those stresses. Calculations of these effects are planned (Budiansky, Suo).

Degradation of the fiber strength upon either high temperature (creep) testing, atmospheric exposure, or fatigue are other topics of interest. Rupture testing performed under these conditions will be assessed in terms of degradation in fiber properties.

3. DESIGN TEAMS

3.1 The Approach

The overall philosophy of the design effort is to eventually combine *material models*, with a *materials selector*, and a *data base*, within a unified software package (Prinz). One example of a composites data base is that developed for MMCs by KAMAN Sciences, which forms the basis for a potential collaboration. The materials selector has already been developed

for monolithic materials (Ashby) and is available for purchase. This selector requires expansion to incorporate phenomena that have special significance for high temperature composites, including creep and thermal fatigue. These new features will be developed and included in the advanced selector software (Ashby).

The modelling approach is illustrated in Table II. Failure mechanisms and their effect on material behavior have been introduced into constitutive equations. The stress, strain and damage fields which develop in components during the cycles of loading and temperature can then be computed. Experiments shall be performed on simple components such as holes in plates, and comparison made with the computational predictions. Since constitutive equations are modeled using the results of coupon tests, it is likely that additional failure modes shall come to light during component testing. These mechanisms shall be studied and the appropriate mechanics developed so that their influence is correctly factored into the constitutive equations. In this way, increased confidence in the reliability of the constitutive equations can be established in a systematic way.

In practice, it is most probable that the constitutive equations are too complex for application at the creative level of the design process. It is then that simple but reliable procedures are of greater use. Some success has been achieved in this regard for MMCs subjected to cyclic mechanical and thermal loading (Jansson, Ponter, Leckie), as well as for strength calculations of CMC panels penetrated by holes (Suo) and the fatigue of MMCs (Zok, McMeeking). In all cases simplifications are introduced after a complete and reliable analysis has been completed which provides a standard against which the effects of simplification can be assessed.

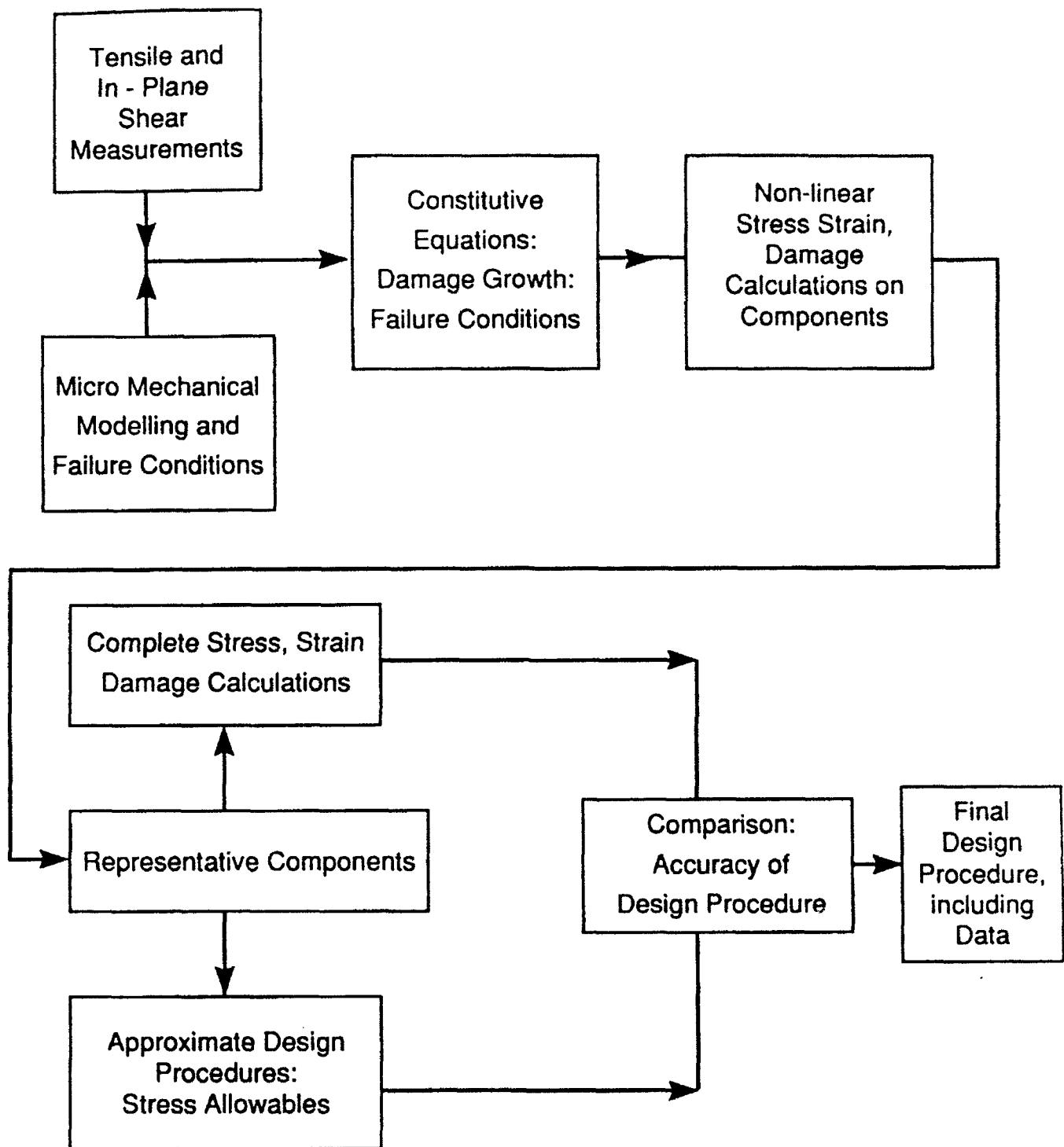


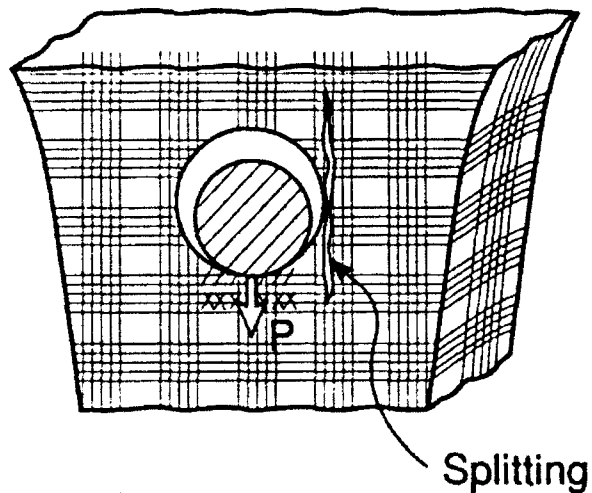
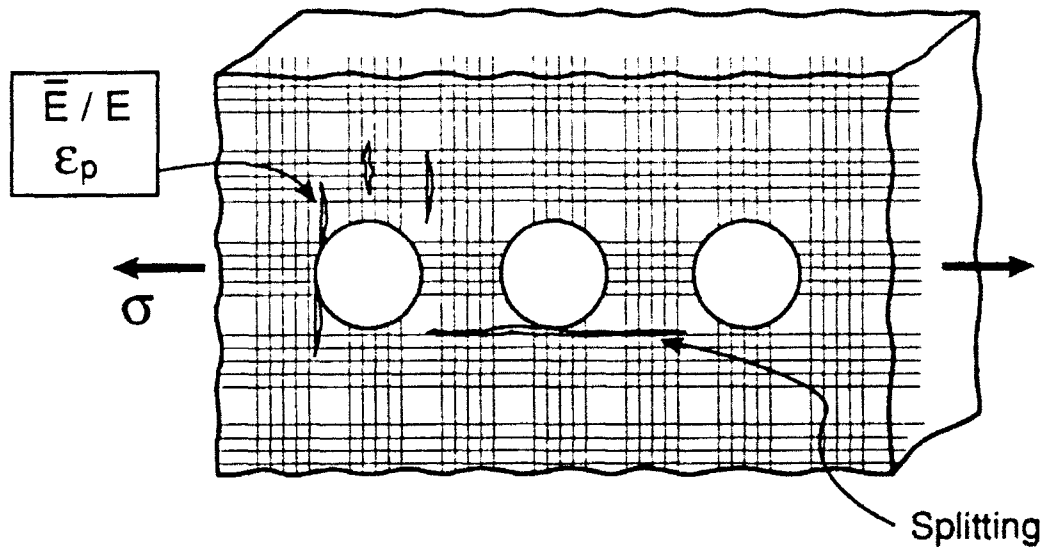
Table II
The Modelling Approach

3.2 Ceramic Matrix Composite Design

The design effort on CMCs will have its major focus on pin-loaded holes used for attachments (Fig. 3). A smaller activity, expected to expand in 1994, will address delamination cracking. The hole design includes several related topics. Each topic is concerned with aspects of constitutive law development (Table III), highlighted during the study group. Combined experimental and modelling efforts on the *tensile properties* of CMCs have established that the plastic strains are dominated by matrix cracks in the 0° plies. The matrix cracking models developed in the program demonstrate that these strains are governed by four independent constituent properties [(Table I) τ , Γ_1 , Ω and Γ_m] which combine and interrelate through five non-dimensional parameters (Table IV). This modelling background suggests a concept for using model-based knowledge to develop constitutive laws. The following steps are involved (Table III). (i) A model-based methodology for inferring the constituent properties of unidirectional CMCs from macroscopic stress/strain behavior has been devised and is being experimentally tested on a range of materials (Evans). (ii) Upon validation, the models would allow stress/strain curves to be simulated (Hutchinson). This capability would facilitate a sensitivity study to be performed, in order to determine the minimum number of independent parameters that adequately represent the constitutive law. A strictly empirical law would require 3 parameters (yield strength, hardening rate and unloading modulus). Consequently, the objective might be to seek 3 combinations of the 4 constituent properties. (iii) Experiments would be performed and models developed that establish the matrix cracking sequence in 2-D materials (Hutchinson, Evans, Kedward). These would be conducted on

DESIGN PROBLEM IN CMC's

Design of Holes in Nozzles / Combustors



Issues

Tensile Rupture
Crushing
Splitting

Design Variables

Hole Size
Hole Spacing
Fiber Architecture
Material Choice
New Concepts

Fig. 3

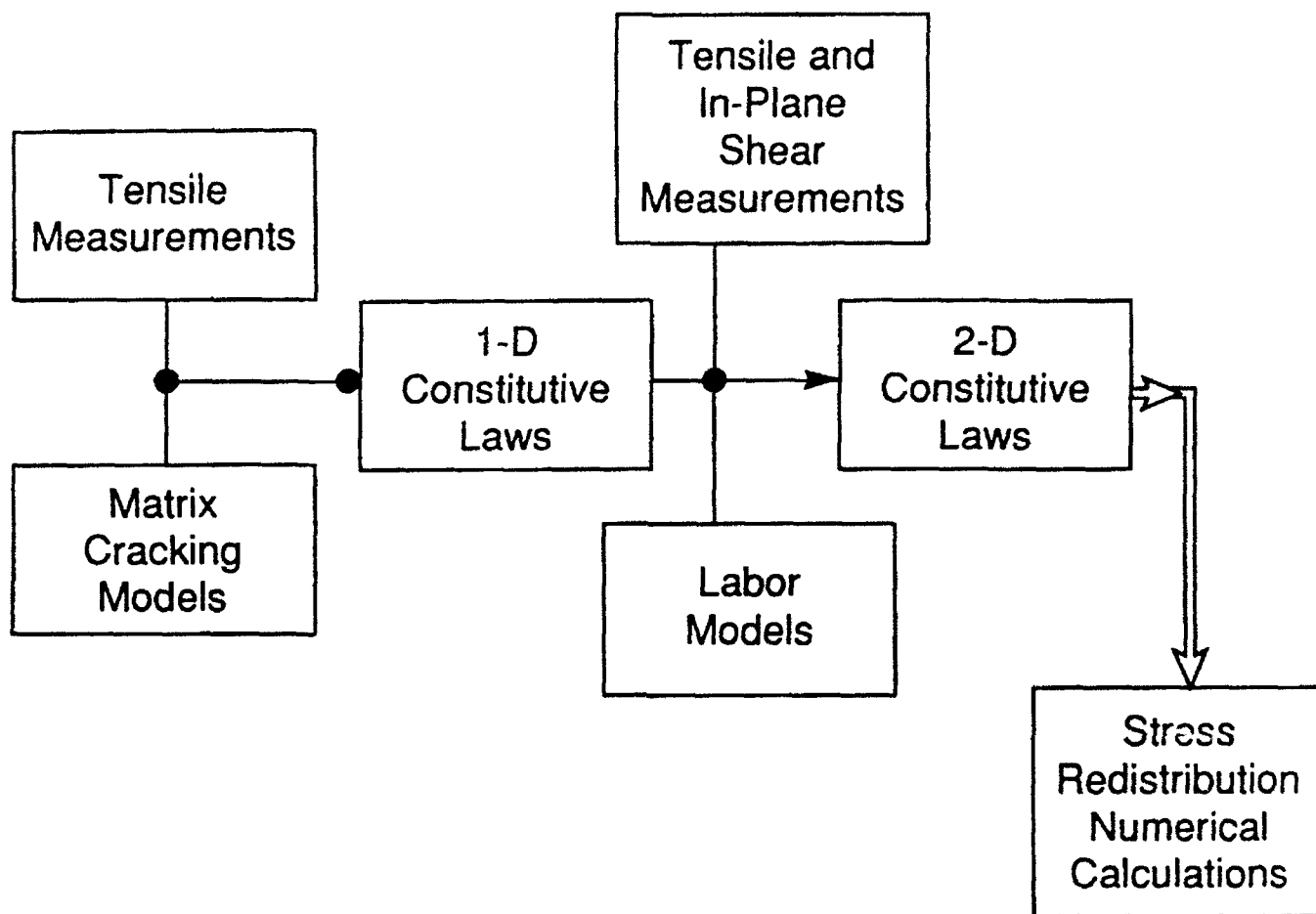


Table III
Design Strategy for CMCs

TABLE IV

Summary of Non-Dimensional Coefficients

$$\mathcal{A}_b = [f/(1-f)]^2 (E_f E_L / E_m^2) (a_o \tau / RS_u), \text{ Flaw Index for Bridging}$$

$$\mathcal{A}_p = (a_o / \bar{h}) (S_p / E_L), \text{ Flaw Index for Pull-Out}$$

$$\mathcal{D} = \Gamma_m (1-f)^2 E_f E_m / f \tau^2 E_L R, \text{ Crack Spacing Index}$$

$$\mathcal{H} = b_2 (1-a_1 f)^2 R \bar{\sigma}_p^2 / 4 \bar{d} \tau E_m f^2, \text{ Hysteresis Index}$$

$$I = \bar{\sigma}_p / E_m \Omega, \text{ Misfit Index}$$

$$\mathcal{M} = 6 \tau \Gamma_m f^2 E_f / (1-f) E_m^2 R E_L, \text{ Matrix Cracking Index}$$

$$Q = E_p f \Omega / E_L (1-\nu), \text{ Residual Stress Index}$$

$$\Delta_i = (1/c_1 \Omega) \sqrt{\Gamma_i / E_m R}, \text{ Debond Index}$$

CMCs with a range of different constituent properties and fiber architectures. The plastic strains would be related to constituent properties by adapting the 1-I models.

The in-plane shear behavior will be characterized by performing experiments and developing models of matrix cracking that govern the plastic *shear strain* in 2-D CMC (Evans, Hutchinson, Bao). The information will be used to establish the constitutive laws for in-plane shear, as well as interlaminar shear. For continuity of interpolation between tension and shear, the shear models will include the same constituent properties as those used to represent the tensile behavior.

The model-based constitutive laws, based on matrix damage, will be built into a CDM (continuum damage mechanics) formulation, compatible with finite element codes (Hayhurst). Computations will be performed to explore *stress redistribution* around holes and other strain concentration sites. The calculations will establish visualizations of stress evolution that can be compared with experimental measurements performed using the SPATE method, as well as by Moiré interferometry (Mackin, Evans). These experiments will be on specimens with notches and holes, loaded in tension. The comparisons between the measured and calculated stress patterns will represent the ultimate validation of the constitutive law. The composite codes, when validated, will be made available to industry.

Some preliminary experimental work will be performed on pin-loaded holes. Damage patterns will be monitored and stress redistribution effects assessed using SPATE (Kedward, Evans, Mackin). These experiments will be conducted on SiC/CAS and SiC/C. The results will provide the focus for future CDM computations, based on the constitutive law for the material.

Smaller scale activities will involve basic aspects of stress redistribution around holes caused by fatigue and creep *damage*, using the experience gained from the matrix cracking studies. Some experimental measurements of these effects will be performed using SPATE (Zok, Evans).

Some delamination crack growth measurements and calculations are also envisaged (Ashby, Kedward, Hutchinson). Cantilever beam and C-specimens will be used for this purpose (Fig. 4). During such tests, crack growth, multiple cracking and stiffness changes will be addressed. Models of bridging by inclined fibers will be developed (Ashby) and used for interpretation.

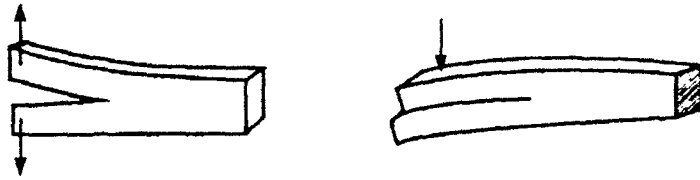
3.3 Metal Matrix Composite Design

The 3D constitutive equations for MMCs are now available for use in the ABAQUS finite element code, and the immediate task is to use these equations to predict the behavior of representative components (Leckie). One such system is a ring-type structure which is being studied together with Pratt and Whitney. Clearly no experimental verification is possible with a component of this scale, but the experience of Pratt and Whitney shall provide invaluable input on the effectiveness of the calculations. A component sufficiently simple to be tested is the panel penetrated by holes. The holes shall be both unloaded and loaded (Jansson), and it is expected to include the effects of cyclic mechanical and thermal loading.

It is proposed to develop simplified procedures which are based on shakedown procedures (Jansson, Leckie). Demonstrations have already been made of the effectiveness of the Gohfeld method (which uses only simple calculations) in representing the behavior of MMCs subjected to cyclic thermal loading.

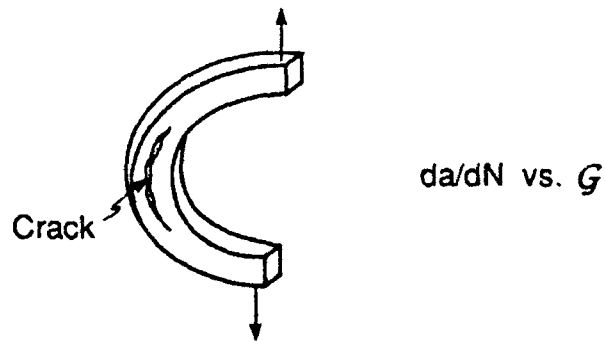
TRANSVERSE CRACKING OF CMC

CONVENTIONAL COUPON TESTS

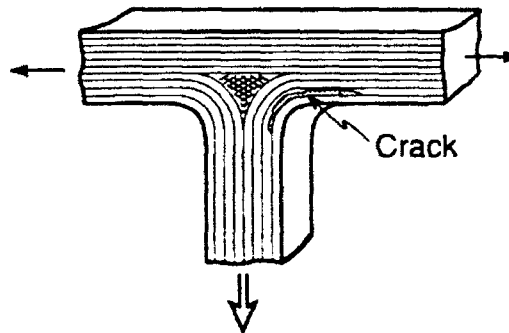


- Fiber Bridging Problem ($G \gg \Gamma_T$)

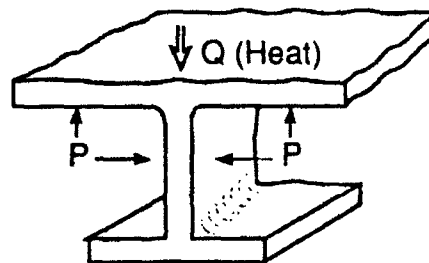
IMPROVED TESTS



SUB - ELEMENT TEST



DESIGN PROBLEM



- Thermal Conductivity
- Fiber Architecture
- Matrix Toughness

Fig. 4

During the complex histories of stress and temperature, it is known that the matrix-fiber interface properties change. Fatigue loading (Zok) is known to decrease the interface sliding stress. Transverse creep appears to cause matrix-fiber debonding (Jansson), which might result in loss of the ability to transfer stress between matrix and fiber. It is intended to study this effect of transverse creep on the integrity of the longitudinal strength of the material by performing tests on panels which shall allow rotation of the stress fields. A good understanding now exists of the fatigue properties of MMCs (Zok). It is intended to extend the ideas developed from earlier theoretical studies (McMeeking, Evans) to include cyclic thermal effects and experimental programs on holes in plates.

4. MANUFACTURING

The activities in processing and manufacturing have had the following foci:

- Matrix development to address specific requirements identified by the design problems, particularly first matrix cracking in CMCs (Lange) and creep strengthening in MMC/IMCs (Levi, Lucas).
- Hybrid architectures which offer possible solutions to environmental degradation and thermal shock problems (Evans, Lange, Leckie, Levi, Yang, Zok).
- Software development that predicts and controls fiber damage and interface properties during densification (Wadley).
- Processing techniques to generate model MMC sub-elements (Leckie, Levi, Yang).

4.1 Metal Matrix Composites

Work on MMC matrix development has focused on dispersion strengthening approaches to increase the *transverse* tensile and creep strength of 1-D and 2-D fiber architectures. The initial work has emphasized a model system, Cu/Al₂O₃, wherein dispersoids are produced by internal oxidation of a dilute Cu-Al alloy deposited by PVD onto sapphire fibers. These are subsequently consolidated by HIP'ing. Specimens with fiber volume fractions of $0.3 \leq f \leq 0.5$ and 2-3% γ -Al₂O₃ dispersoids (~ 20 nm in size) have been produced in this manner and will be tested to assess their transverse creep behavior. The new emphasis will be on higher temperature matrices based on TiB dispersoids in Ti-(Cr/Mo)-B alloys (Levi). Initial solidification studies have demonstrated the potential of these materials as *in-situ* composites. Efforts are underway to develop sputtering capabilities to implement this concept.

Fiber damage during densification of composite prepreps generated by plasma-spray (GE) and PVD (3M) have also been emphasized (Wadley). Interdiffusion studies coupled with push-out tests have been used to study the evolution of reaction layers in Ti/SiC composites and their effect on the relevant interfacial properties as a function of process parameters. Additional efforts under other programs have focused on developing predictive models for fiber breakage during densification. The interdiffusion and breakage models are being incorporated into software that predicts pressure-temperature paths, which simultaneously minimize fiber damage and control the interface properties.

The feasibility of producing MMC sub-elements consisting of fiber reinforced rings (1-D) and tubes (2-D) has been demonstrated by using

liquid metal infiltration of Al alloy matrices (Levi). These are presently undergoing testing in combined tension/torsion modes. Future efforts will be directed toward extending the technique to other shapes (e.g., plates with reinforced holes), as well as devising methods to modify the (currently strong) interfaces. The identification of methods that provide the appropriate interfacial debonding/sliding characteristics should enable the use of these composites as *model systems* for higher temperature MMCs, such as Ti.

4.2 Intermetallic Matrix Composites

The focus of the IMC processing activities has been on the synthesis of $\text{MoSi}_2/\beta\text{-SiC}_p$ composites by solidification processing. These materials are of interest as potential matrices for fiber composites. Significant progress was made in the elucidation of the relevant Mo-Si-C phase equilibria, the growth mechanisms of SiC from the melt and their impact on reinforcement morphology, as well as the orientation relationships between matrix and reinforcements, and the interfacial structure. An amorphous C layer, ≤ 5 nm thick, was found at the MoSi_2/SiC interface in the as cast condition, and persisted after 12 h heat treatments at 1500°C . This interfacial layer has been reproduced in $\alpha\text{-SiC}_p/(\text{MoSi}_2 + \text{C})$ composites produced by powder metallurgy techniques and was found to exhibit promising debonding and pull-out behavior during fracture (Levi). Future efforts are aimed at implementing this *in-situ coating* concept in $\alpha\text{-SiC}$ fiber composites.

4.3 Ceramic Matrix Composites

The processing issues for creating CMCs with high *matrix strength* continue to be explored (Lange, Evans). The basic concept is to create a strong ceramic matrix framework within a fiber preform, by means of slurry

infiltration followed by heat treatment. This strong framework would then be infiltrated by a polymer precursor and pyrolyzed to further densify the matrix. It has been demonstrated that strong matrices of Si_3N_4 can be produced using this approach (Lange). Further work will address relationships between matrix strength and microstructure (Lange, Evans).

4.4 Hybrids

These activities cover materials consisting of thin monolithic ceramic layers alternating with layers containing high strength fibers bonded by a glass or metallic binder. The primary motivation behind this concept is the potential for manufacturing shapes that have a high resistance to environmental degradation and also have good thermal shock resistance. The concept has been demonstrated using alumina plates and graphite reinforced polymer prepregs (Lange). The availability of glass-ceramic bonded SiC_f prepregs and tape-cast SiC plates has facilitated the extension of this technique to high temperature systems (Lange). Future assessment will address new crack control concepts. These concepts would prevent damage from propagating into the fiber reinforced layers, especially upon thermal loading (Zok, Lange). If successful, this concept would allow the development of hybrid CMCs which impart resistance to environmental degradation, as well as high thermal strain tolerance.

Preliminary work has been performed on laminates consisting of alumina plates and sapphire-fiber reinforced Cu monotapes (Levi). The latter are produced by deposition of Cu on individual fibers which are subsequently aligned and bonded by hot pressing between two Cu foils. After suitable surface preparation, the alumina/monotape assemblies are

bonded by hot pressing. Future work is aimed at implementing the concept with Ni based alloys.

5. SENSORS

The principal challenge being addressed is the non-destructive and non-evasive measurement of stresses in composites (Clarke, Wadley). The motivation is to make detailed measurements of stresses in components for incorporation into evolving design models, as well as validation of the stress distributions computed by finite element methods. A major emphasis has been placed on measuring the residual stresses in sapphire fibers in various matrices, using the recently developed technique of optical fluorescence spectroscopy. These measurements have provided data on the distribution of residual thermal stresses in the fiber reinforcement, as a function of depth below the surface. This approach will be extended, in conjunction with finite element modelling (Hutchinson), to measure the stresses during the process of fiber pull-out from a variety of metal and ceramic matrices. Initial experiments indicate that such in-situ measurements are feasible.

The technique will also be applied to the measurement of the stresses in sapphire fibers located in the vicinity of pin-loaded holes in order to understand the manner in which the stresses redistribute during loading. It is anticipated that this measurement will provide information about the detailed fiber loadings and also about the stresses that cause debonding of the fibers from the matrix. Moreover, in support of the activities on thermal ratcheting, the redistribution of stresses with thermal cycling will be established. This will be accomplished by using the fluorescence technique as well as Moiré interferometry, based on lithographically defined features.

Remarks on crack-bridging concepts

G Bao

Mechanical Engineering Department, The Johns Hopkins University, Baltimore MD 21218

Z Suo

*Department of Mechanical and Environmental Engineering, The University of California,
Santa Barbara CA 93106*

The article draws upon recent work by us and our colleagues on metal and ceramic matrix composites for high temperature engines. The central theme here is to deduce mechanical properties, such as toughness, strength and notch-ductility, from bridging laws that characterize inelastic processes associated with fracture. A particular set of normalization is introduced to present the design charts, segregating the roles played by the shape, and the scale, of a bridging law. A single material length, $\delta_0 E / \sigma_0$, emerges, where δ_0 is the limiting-separation, σ_0 the bridging-strength, and E the Young's modulus of the solid. It is the huge variation of this length—from a few nanometers for atomic bond, to a meter for cross-over fibers—that underlies the richness in material behaviors. Under small-scale bridging conditions, $\delta_0 E / \sigma_0$ is the only basic length scale in the mechanics problem and represents, with a pre-factor about 0.4, the bridging zone size. A catalog of small-scale bridging solutions is compiled for idealized bridging laws. Large-scale bridging introduces a dimensionless group, $a / (\delta_0 E / \sigma_0)$, where a is a length characterizing the component (e.g., hole radius). The group plays a major role in all phenomena associated with bridging, and provides a focus of discussion in this article. For example, it quantifies the bridging scale when a is the unbridged crack length, and notch-sensitivity when a is hole radius. The difference and the connection between Irwin's fracture mechanics and crack bridging concepts are discussed. It is demonstrated that fracture toughness and resistance curve are meaningful only when small-scale bridging conditions prevail, and therefore of limited use in design with composites. Many other mechanical properties of composites, such as strength and notch-sensitivity, can be simulated by invoking large-scale bridging concepts.

1. BACKGROUND

Building upon the analyses of Dugdale (1960) and Bilby *et al.* (1963), Cottrell (1963) put forward the concept of crack-bridging as a unifying theory for fracture at various length scales, from atomic cleavage to void growth. Much has happened in the last thirty years in developing this idea for all kinds of materials—metals, ceramics, polymers, cementitious materials, and their composites in various forms. In this article, we try to place the relevant aspects into the perspective of design *with*—and *of*—ceramic matrix composites. In particular, we will emphasize the concept of large-scale bridging, and its implications for strength, notch-sensitivity, and splitting resistance.

This section sets the stage for our remarks on crack bridging concepts. In particular, we briefly discuss bridging laws, the microscopic properties to be transmitted to continuum models. The fundamentals of Irwin's fracture

mechanics are reviewed, motivating the models for toughness, and demonstrating the limitations of small-scale bridging. The section is concluded with comments on current practice of fracture testing, and needs for large-scale bridging concepts.

1.1 Atomic bond vs fiber bridging

A solid will fall apart unless something holds it together. For example, an ionic crystal adheres by electrostatic force between unlike ions. A unifying idea, sufficiently rigorous for our purpose, is to represent atomic bond by a relation between attractive stress, σ , and separation, δ , of two lattice planes. Such a relation is sketched in Fig. 1, and is formally written as

$$\sigma / \sigma_0 = \chi(\delta / \delta_0). \quad (1)$$

The dimensionless function χ describes the *shape* of the relation; the *scale* is set by strength, σ_0 , and limiting-separation, δ_0 . For an inorganic solid, the strength is about

one tenth of its Young's modulus, and the limiting-separation is on the order of lattice spacing (see Table 1).

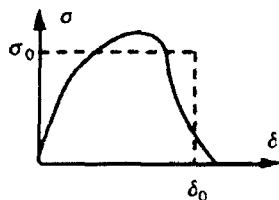


FIG. 1 A stress-separation relation that represents both atomic bond and fiber bridging. The strength and limiting-separation are very different for the two mechanisms; see Table 1.

TABLE 1 Illustrative properties for bridging mechanisms

	atomic bond	fiber pull-out	fiber cross-over
σ_0 (N/m ²)	10^{10}	10^9	10^7
δ_0 (m)	10^{-10}	10^{-5}	10^{-4}
$\sigma_0 \delta_0$ (J/m ²)	1	10^4	10^3
$\delta_0 E / \sigma_0$ (m)	10^{-9}	10^{-3}	1

As pointed out by Needleman (1990), relation (1) introduces a stress level σ_0 and a length scale δ_0 , and provides an intrinsic failure criterion, based on which macroscopic phenomena can be simulated. Table 1 lists the values of $\sigma_0 \delta_0$ and $\delta_0 E / \sigma_0$ (Young's modulus is taken to be $E \sim 10^{11}$ N/m²). As we shall see later, they represent, with pre-factors of order unity, fracture energy and fracture process zone length, respectively, when the process zone is much smaller than flaw size. The significance of the length, $\delta_0 E / \sigma_0$, was first appreciated by Cottrell (1963), and will be further elaborated upon in this article in connection with composite design.

Things other than atomic bonds can also hold a material together. Illustrated in Fig. 2 are strong fibers bridging a ceramic matrix, mimicking atomic bonds holding a solid. By analyzing a fiber-matrix cylinder, one finds an approximate stress-separation relation (Marshall *et al.* 1985; also Hutchinson and Jensen 1990 for a correction):

$$\sigma / \sigma_0 = (\delta / \delta_0)^{1/2}. \quad (2)$$

The closure-strength is

$$\sigma_0 = f S_b, \quad (3)$$

where S_b is the fiber bundle strength, and f the fiber volume fraction. The limiting-separation is

$$\delta_0 = \frac{(1-f)^2 S_b^2}{2E\tau} R, \quad (4)$$

where R is the fiber radius, τ the sliding friction of fiber/matrix interface, and E the Young's modulus, assuming that elastic constants are identical for fiber and matrix. In practice, δ_0 can be varied substantially by varying τ .

Note that (2) is valid before fiber breaking. Fiber pull-out after breaking has also been modeled; see Hutchinson and Jensen (1990) for review. Yet design with ceramic matrix

composites under static loading, and metal matrix composites under cyclic loading usually allows matrix cracking to relieve stress concentration, but requires fibers to remain intact, so that (2) provides a conservative limit in design.

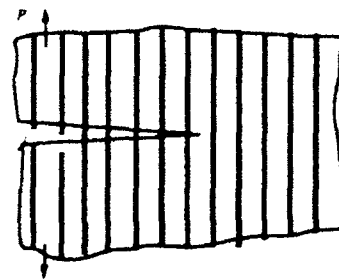


FIG. 2 Fiber pull-out.

Fibers can even bridge transverse cracks if they are not perfectly aligned (Fig. 3). High fracture resistance due to cross-over fibers has been demonstrated for a glass matrix composite (Spearing and Evans 1992). The stress-separation relation has not been modeled in any detail, but the flexible fibers are expected to provide small closure-strength and large limiting-separation. Values listed in Table 1 are inferred from the experimental data of a CAS/SiC composite.

Ductile, crack-bridging particles can substantially toughen a ceramic (e.g., Bannister *et al.* 1992). The closure-strength is a few times the yield stress of the ductile alloy, and the limit separation scales with the product of the size and the ultimate strain of the particles. They are also influenced by debonding of the particle/matrix interface (Mataga 1990, Bao and Hui 1990).

All bridging mechanisms can be represented by stress-separation relations, but there is a significant difference: the scales of σ_0 and δ_0 . It is the large variation in the bridging scales, from a nanometer to a meter, that accounts for the richness in material behaviors. In particular, as indicated in Table 1, the fracture energy and damage extent differ substantially for atomic bond and fiber bridging.

Given a stress-separation relation that tells how a solid is held together, one can analyze any components to determine the load-carrying capacity, which is the approach to be reviewed in this article. However, this was *not* how Irwin established the Linear Elastic Fracture Mechanics. In fact, LEFM makes no reference to microscopic details of fracture process. To place bridging concepts into perspective, it is interesting, then, to first reflect upon the facts underlying the fracture mechanics that is independent of the fracture mechanisms. The classical view outlined below can be found in the textbook by Kanninen and Popelar (1985).

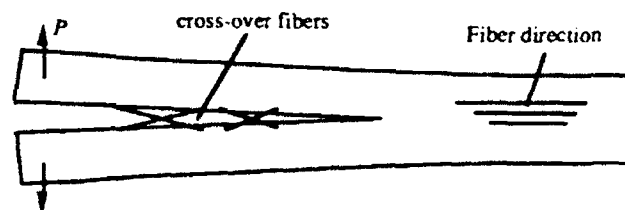


FIG. 3 Fiber cross-over.

1.2 Linear elastic fracture mechanics

Ironically, it is the very irrelevance to microscopic details that gave rise to the great success of fracture mechanics in the early days. LEFM is versatile: it applies, with some justifications, to any solids—metals, ceramics, polymers and composites. LEFM is precise: it relies on macroscopic measurements of toughness and elasticity solutions of stress intensity factors. LEFM is far-reaching: the concepts have been extended to ductile fracture, fatigue cracking, dynamic fracture, and interface debonding.

Irwin's LEFM erects upon a single premise: At the onset of fracture, the material is elastic over the whole component, except for a *damage zone* localized around the crack tip, whose size L_0 is much smaller than crack size a :

$$L_0 \ll a. \quad (5)$$

The condition is satisfied by either a large crack, or a brittle solid suffering little diffused damage upon fracture. This statement will be made more precise later.

Then follows the central corollary: *However complex a fracture process is, a single material property (called toughness) quantifies the resistance to fracture.* That is, for a given material, toughness measured from a laboratory sample can be used to design components.

No microscopic details are mentioned.

The elastic field in a component is analyzed as if the crack tip—or the tiny inelastic zone—were a mathematical point with no physical structure, an idea analogous to the boundary layer approach in fluid mechanics. Such stress field is square root singular:

$$\sigma_{ij} \sim K(2\pi r)^{-1/2} F_{ij}(\theta), \quad (6)$$

where r and θ form polar coordinates centered at the crack tip, $F_{ij}(\theta)$ are functions listed in elasticity textbooks, and K is *stress intensity factor*. The external boundary conditions of the component do not change the structure of the singular field—the square root and functions $F_{ij}(\theta)$, but do change the magnitude of K .

The physical significance of K can be appreciated from Fig. 4. The actual stress distribution is modified in two ways from the elastic solution (6). Within the damage zone, the inelastic deformation redistributes stress, bounding the stress by the closure-strength, σ_0 . Close to the component boundary, the stress merges to the boundary conditions. Despite the modifications, provided condition (5) is satisfied, the stress field within the annulus, $L_0 < r < a$, is well approximated by elastic solution (6).

Consequently, K is the *only parameter* through which the applied load can influence the damaging process at the crack tip. The resistance to fracture can therefore be defined as the maximum stress intensity factor that a material can sustain. That is, for a given cracked specimen made of a certain material, denoting K as the stress intensity factor of the *geometry and loading*, and K_c the toughness of the *material*, the crack will not grow if

$$K < K_c. \quad (7)$$

In contrast to other measures of toughness such as impact energy, K_c is both macroscopically measurable and

quantitatively relevant to design. Two handbooks are thus sufficient: one contains stress intensity factors of various *geometries*, computed from elasticity problems; and the other contains toughness values for various *materials*, measured from laboratory samples.

No microscopic details are mentioned.

Another useful concept is energy release rate \bar{G} , the decrease of elastic strain energy of the body, for a unit area of crack growth, when the deflection at the external loading point is held fixed. Irwin (1957) showed that \bar{G} and K are related by

$$\bar{G} = K^2 / E', \quad (8)$$

where $E' = E$ for plane stress, and $E' = E/(1 - \nu^2)$ for plane strain, E and ν being the Young's modulus and Poisson's ratio. Fracture energy Γ is related to K_c by a similar relation

$$\Gamma = K_c^2 / E'. \quad (9)$$

In summary, K and \bar{G} are equivalent *loading parameters*; K_c and Γ are equivalent *material properties*. All these are valid concepts when small-scale damage condition (5) prevails.

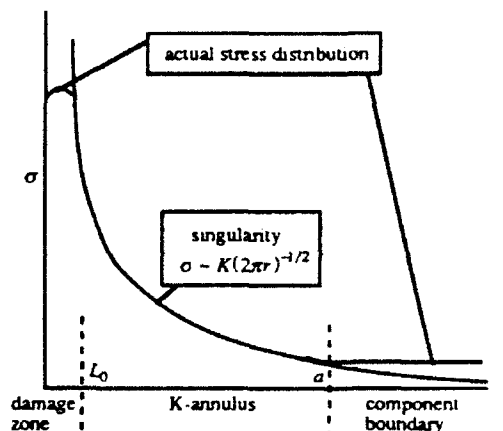


FIG. 4 Elastic solution and actual stress distribution.

1.3 Mechanics of toughness

Powerful as it is, LEFM uncovers little of what happens *within* the damage zone. There is a number of disadvantages of this black-box approach. For one, toughness can be enhanced by controlling microstructure: it is of great significance to have a theory for toughness, so that the controllable quantities can be optimized. This theme has been vigorously pursued for the past twenty years, culminating in an understanding of toughness—to various degrees of sophistication—for almost all engineering materials. For example, the microstructural basis of toughness has been reviewed by Evans (1990) for ceramics, by Ritchie and Thompson (1985) for ductile alloys, and by Li (1990) for cementitious materials.

Here we focus on toughness mechanisms that can be described by stress-separation relations. The standard small-scale bridging model is as follows (Fig. 5). If condition (5) is

satisfied, the crack can be taken to be semi-infinite compared to the damage zone size L , and the external boundary conditions condensed to stress intensity factor K , or energy release rate G , by handbook solutions. The bridging law (1) is applied in the damage zone, coupled with the elastic solid.

A fiber-reinforced ceramic is characterized in a mechanical test by a resistance curve (R -curve), such as that in Fig. 6. A pre-cut is made prior to a fracture test and, upon loading, a driving force, Γ_0 , about the matrix fracture energy, starts matrix crack. As the crack length L increases and more fibers bridge the crack, higher driving force is needed to maintain the growth. The separation at the pre-cut root finally reaches the limiting-separation, $\delta_l = \delta_0$, after which, the damage strip is in a *steady-state*, translating in the body, cracking the matrix in the front, and breaking the fibers in the wake. Quantities of significance on an R -curve are the plateau fracture energy, Γ , and the crack extension to attain the plateau, L_0 , which is the length referred to in (5).

Neglecting Γ_0 and assuming a rectilinear bridging law (the rectangle in Fig. 1), Bilby *et al.* (1963) showed that the plateau fracture energy is

$$\Gamma = \sigma_0 \delta_0, \quad (10)$$

and the steady-state damage zone size is

$$L_0 = \frac{\pi}{8} E' \delta_0 / \sigma_0. \quad (11)$$

Observe that L_0 scales with the material length $\delta_0 E' / \sigma_0$. As will be shown later, a different bridging law shape χ only modifies the pre-factors in (10) and (11) within order unity. The estimates based on these formulas are listed in Table 1, and discussed below.

Atomic bonds break at a small limiting-separation, amounting to both a small fracture energy and a small damage zone. In practice, condition (5) is always justified, so that LEFM is valid for inherently brittle solids containing cracks longer than a few nanometers.

In contrast, large limiting-separations in fiber bridging lead to both large fracture energies and large damage zones. As indicated in Table 1, the bridging zone size for *fiber pull-out* may violate condition (5), depending on specimen size. The bridging zone size for *fiber cross-over* will certainly violate (5) for most applications.

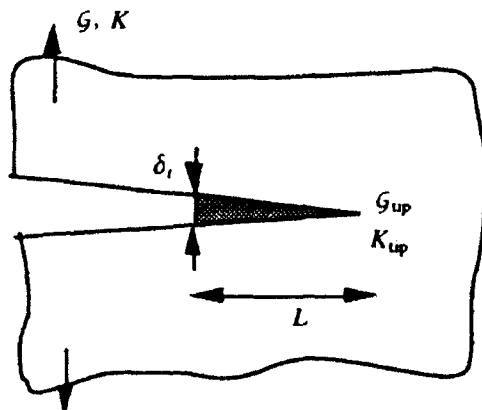


FIG. 5 Small-scale bridging model: the damage is embedded in a K field, decoupled from the actual component geometry.

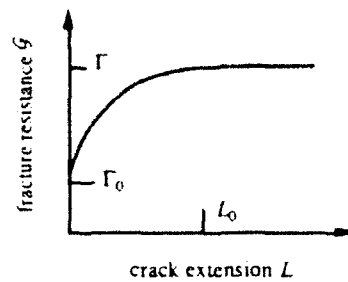


Fig. 6 An R -curve under small-scale bridging conditions

Given σ_0 and δ_0 , (10) and (11) provide estimates for fracture energy and bridging zone size. For example, using (3) and (4) for a fiber-reinforced ceramic, one finds that the fracture energy scales with

$$\Gamma \sim \frac{f(1-f)^2 S_b^2 R}{2E\tau}, \quad (12)$$

and the steady-state bridging zone size scales with

$$L_0 \sim \frac{\pi}{16} \frac{(1-f)^2 S_b R}{f\tau}. \quad (13)$$

Relations of this sort are easy to obtain for other bridging mechanisms, and can serve as a guide for microstructure design. For example, it is clear from (12) that a composite gains high fracture energy from a large fiber strength and radius, but a small sliding friction.

Yet these same quantities also cause a long damage zone. The small-scale damage condition (5) can be combined with (11) to give

$$a / (\delta_0 E' / \sigma_0) \gg 1. \quad (14)$$

The above dimensionless group will appear many times in this article, and provide a focus for discussions. In this context, it measures the *unbridged crack length*, a , in units of material length, $\delta_0 E' / \sigma_0$. Condition (14) is rarely satisfied in practice for a component made of a composite, so toughness is of limited use in design.

1.4 Large-scale bridging

In the recent literature, there is a tendency to report "effective" R -curves, converted from either numerical simulation or experimental record. As demonstrated by Zok and Hom (1990), under large-scale bridging conditions, the R -curves so constructed depend sensitively on specimen geometry and size: they are ineffective and misleading. The practice must be stopped.

Retrospectively, this tendency stems from the success of the concepts related to stress intensity factor in design with metals and ceramics. However, as we will see later in this article, since large-scale bridging is prevalent in composites, many significant concepts in design with, and of, composites, such as strength and notch-brittleness, cannot be deduced from fracture toughness. An all-embracing statement, when large-scale bridging conditions prevail, is that Irwin's one-parameter framework, the classical LEFM, is invalid. To determine load-carrying capacity, a stress analysis is required for *coupled* specimen and bridging law. Consequences of

this statement will be reviewed in Section 3.

2. SMALL-SCALE BRIDGING SOLUTIONS

Small- and large-scale bridging solutions are discussed in detail in this and next section, respectively. The two topics can be read independently, in any order.

2.1 General problem

Now the small-scale bridging model (Fig. 5) is taken up to compute R -curves (Fig. 6). Stress analysis is unnecessary to compute the plateau fracture energy, Γ . An application of Rice's J -integral shows that

$$\mathcal{G} = \mathcal{G}_{up} + \sigma_0 \delta_0 \int_0^{\delta_i/\delta_0} \chi(\epsilon) d\epsilon, \quad (15)$$

This equation gives plateau fracture energy Γ when $\delta_i/\delta_0 = 1$ and $\mathcal{G}_{up} = \Gamma_0$.

A stress analysis is necessary to compute the full R -curve. On dimensional grounds, the separation at the root of the pre-cut takes the form

$$\frac{\delta_i}{\delta_0} = f\left(\frac{L\sigma_0}{\delta_0 E'}, \frac{K}{\sigma_0 \sqrt{L}}\right), \quad (16)$$

and the stress intensity factor at the crack tip

$$\frac{K_{up}}{\sigma_0 \sqrt{L}} = g\left(\frac{L\sigma_0}{\delta_0 E'}, \frac{K}{\sigma_0 \sqrt{L}}\right). \quad (17)$$

Functions f and g will also depend on bridging law shape χ , but nothing else. Integral equations are efficient to solve this class of problems (e.g., Budiansky *et al.* 1988). Observe that K and \mathcal{G} , and K_{up} and \mathcal{G}_{up} are both related by Irwin's relation (8), so that only two among (15), (16) and (17) are independent.

After f and g are computed, the rising part of the R -curve is given by (17) by letting $K_{up} = K_0$ and the steady-state bridging zone size L_0 is solved from (16) by letting $\delta_i/\delta_0 = 1$ and $K = K_c = (\Gamma E')^{1/2}$. Explicit solutions are collected in the following sections to assist practitioners in the field.

2.2 Rectilinear bridging law

First consider the rectilinear bridging law (the rectangle in Fig. 1). Specialized from (15), the plateau fracture energy is

$$\Gamma = \Gamma_0 + \sigma_0 \delta_0. \quad (18)$$

The stress analysis gives (Tada *et al.* 1985)

$$K = (8/\pi)^{1/2} \sigma_0 \sqrt{L} + K_0. \quad (19)$$

This equation defines the rising part of the R -curve. The bridging zone size, L_0 , is obtained by substituting (18) into (19), giving

$$L_0 = \frac{\pi}{8} E' \frac{\delta_0}{\sigma_0} \left[\left(1 + \frac{\Gamma_0}{\sigma_0 \delta_0} \right)^{1/2} + \left(\frac{\Gamma_0}{\sigma_0 \delta_0} \right)^{1/2} \right]^2. \quad (20)$$

For the same bridging mechanism, i.e., σ_0 and δ_0 being held constant, the tougher the matrix, the smaller the bridging

zone size. When $\Gamma_0/\sigma_0 \delta_0 \ll 1$, which is typically the case for fiber-reinforced ceramics, (18) and (20) recover (10) and (11), respectively.

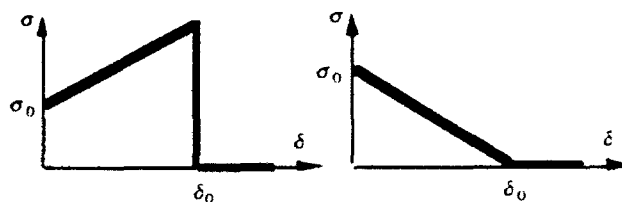


FIG. 7 Bridging laws with hardening and softening.

2.3 Hardening and softening

Consider the stress-separation relation sketched in Fig. 7, having an analytic form

$$\sigma = \begin{cases} \sigma_0 + s\delta, & \delta < \delta_0 \\ 0, & \delta > \delta_0 \end{cases} \quad (21)$$

where s is the slope: $s > 0$ for hardening, and $s < 0$ for softening. The shapes are versatile enough to fit many bridging mechanisms, and yet the solutions are simple enough to be tabulated completely. Equation (15) is specialized to

$$\mathcal{G} = \Gamma_0 + \sigma_0 \delta_i + \frac{1}{2} s \delta_i^2. \quad (22)$$

The driving force attains the plateau Γ when $\delta_i/\delta_0 = 1$.

TABLE 2 Hardening Bridging

$8\beta\pi$	c_2	c_1
0.25	1.244	1.670
0.5	1.478	1.737
1	1.91	1.836
2	2.68	1.984
5	4.44	2.184
10	6.54	2.307
15	8.15	2.356
20	9.51	2.386
25	10.70	2.404
30	11.76	2.414

Once σ_0 is treated as a residual stress, the problem becomes purely linear (e.g., Suo *et al.* 1992a). Linearity and dimensionality dictate that

$$K = c_1 \sigma_0 \sqrt{L} + c_2 K_0, \quad (23)$$

and that

$$\delta_i = c_3 \sigma_0 L / E' + c_4 K_0 \sqrt{L} / E'. \quad (24)$$

The pre-factors, c_i , depend only on dimensionless parameter

$$\beta = sL / E'. \quad (25)$$

Substituting (23) and (24) into (22) gives a quadratic in K_0 and σ_0 being identically zero. This in turn implies that the coefficient of each term in the quadratic vanishes, leading to

$$c_2 = (1 + 2\beta c_1^2)^{1/2}, \quad c_3 = (c_2 - 1) / \beta, \quad c_4 = 2c_1. \quad (26)$$

That is, all c s are determined if any one of them is.

The hardening spring with $\sigma_0 = 0$ has been solved by Budiansky *et al.* (1988). In present notation, their paper

gives c_2 reproduced in Table 2. Also listed are values of c_1 inferred according to (26).

For many bridging mechanisms, stress rises sharply with a small separation and then decays with a long tail, well fitted by the linear softening triangle in Fig. 7. Bao and Hui (1990) solved the problem when $K_0 = 0$, and their results are listed in Table 3. The solution is now interpreted for the general case with $K_0 \neq 0$, with c_2 , c_3 and c_4 obtained from (26).

When $\Gamma/\sigma_0\delta_0 \ll 1$, the plateau fracture energy is

$$\Gamma = \frac{1}{2} \sigma_0 \delta_0, \quad (27)$$

and the damage zone size upon fracture is

$$L_0 = 0.366 E' \delta_0 / \sigma_0 \quad (28)$$

These can be compared to (10) and (11) for rectilinear bridging.

TABLE 3 Softening bridging

$-4\beta\pi$	$2K^2/E\sigma_0\delta_0$	c_1
0.05	0.192	1.564
0.1	0.366	1.526
0.15	0.521	1.487
0.2	0.657	1.446
0.25	0.771	1.401
0.3	0.864	1.354
0.35	0.933	1.303
0.4	0.978	1.248
0.45	0.998	1.189
0.466	1.000	1.169

To demonstrate the effect of bridging law shape, R -curves calculated using rectilinear and softening laws are contrasted in Fig. 8, both with $\Gamma_0/\sigma_0\delta_0 = 0$. The plateau fracture energy Γ and the strength σ_0 can be measured macroscopically, so they are used to normalize the R -curves. As shown in Fig. 8, given the same Γ and σ_0 , the damage zone sizes differ by approximately a factor of 2. R -curves derived from most other bridging laws are expected to be bounded between the two curves in Fig. 8.

2.4 Power-law bridging

Power-law

$$\sigma/\sigma_0 = (\delta/\delta_0)^m \quad (29)$$

embodies fiber pull-out as a special case ($m = 1/2$), and linear and rectilinear relations as limiting cases ($m = 1$ and $m = 0$, respectively). The general solution takes the form

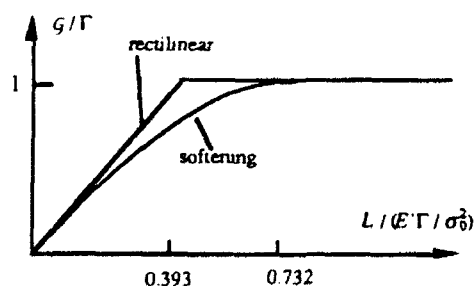


FIG. 8 R -curves due to rectilinear and softening bridging.

$$\delta_i/\delta_0 = \lambda^{1/(1-m)} \Delta(\lambda^{-m/(1-m)} K/\sigma_0\sqrt{L}, m), \quad (30)$$

and

$$K_{up}/\sigma_0\sqrt{L} = \lambda^{m/(1-m)} k(\lambda^{-m/(1-m)} K/\sigma_0\sqrt{L}, m), \quad (31)$$

where

$$\lambda = L/(\delta_0 E'/\sigma_0). \quad (32)$$

A scaling relation noted by McMeeking and Evans (1990) and Cox (1992) is used to obtain the above functional forms. Dimensionless functions Δ and k depend on two variables as indicated; they will be tabulated elsewhere (Gu *et al.* 1992).

3. CONSEQUENCES OF LARGE-SCALE BRIDGING

When large-scale bridging prevails, K_c , Γ and R -curve are irrelevant concepts, and load-carrying capacity must be computed by analyzing the component geometry coupled with the bridging law. A large-scale bridging model consists of two elements: derive the bridging law for a candidate material from either micromechanics models or mechanical tests; and compute the load-carrying capacity by analyzing a projected component coupled with the bridging law. Attention here is focused on the latter in a special context: how various mechanical properties, such as strength, notch-ductility and splitting-resistance, can be deduced from bridging laws.

3.1 Dimensionless groups

A dimensionless group appears in *all* large-scale bridging models (see Appendix):

$$\alpha = \frac{a}{\delta_0 E'/\sigma_0}. \quad (33)$$

Note that α is the same in (14), but a should be interpreted as a characteristic length of the component. As we shall see, various size effects stem from this dimensionless group.

Design charts can be organized in a nondimensional form. Figure 9 illustrates a panel containing a notch of size a loaded by stress $\bar{\sigma}$. The load-carrying capacity is written

$$\bar{\sigma}_{max}/\sigma_0 = F(\alpha, \Gamma_0/\sigma_0\delta_0). \quad (34)$$

Parameter $\Gamma_0/\sigma_0\delta_0$ measures the relative amount of energy dissipation at the crack tip (e.g., matrix toughness). Also entering (34) are ratios of a to other lengths specifying the component geometry, such as notch root radius and panel width. A different bridging law shape χ only modifies the design curves within order unity, which usually does not affect qualitative conclusions (e.g., notch-brittle or -ductile).

Segregation of the *shape* from the *scale* of a bridging law is of practical significance. Once charts are constructed for idealized bridging laws with important design features (e.g., holes), components with actual bridging laws can be designed, with the charts, by fitting to one of the idealized laws. This approach is equally valuable in design of composites. In this phase, the detailed bridging law shape may be unknown, but the scale of the bridging, σ_0 and δ_0 , can be related to microstructural variables. Whether a

material is viable for a particular application can be assessed, before the material is made, by consulting the charts.

The general mechanics problem is stated as follows (Fig. 9). In a body of characteristic length a loaded by stress $\bar{\sigma}$, a matrix crack trajectory of length L is identified, experimentally or hypothetically, emanating from a stress concentrator, bridged according to stress-separation relation (1). The separation at the end of the crack takes the form

$$\delta_1 / \delta_0 = f(\bar{\sigma} / \sigma_0, \alpha, L / a), \quad (35)$$

and the energy release rate at the tip

$$\mathcal{G}_{up} / \sigma_0 \delta_0 = g(\bar{\sigma} / \sigma_0, \alpha, L / a). \quad (36)$$

Functions f and g will also depend on bridging law shape χ , and ratios of a to other lengths characterizing the component geometry. The coupled problem, either linear or nonlinear depending on χ , can be solved by both integral equation and finite element methods. An integral equation using dislocation kernels is derived in Appendix, from which (35) and (36) can be inferred.

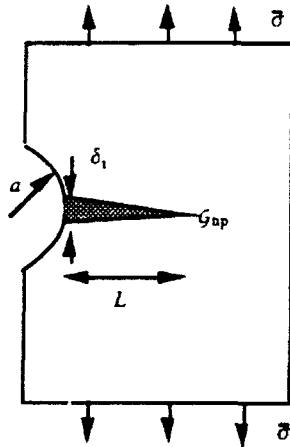


FIG. 9 Large-scale bridging model: the bridging zone is coupled with component geometry.

For rectilinear bridging, linearity dictates that

$$\delta \mathcal{E}' / a = f_1 \bar{\sigma} - f_2 \sigma_0, \quad (37)$$

and that

$$K_{up} / \sqrt{a} = f_3 \bar{\sigma} - f_4 \sigma_0, \quad (38)$$

where f_s depend on damage extent L/a , and ratios of a over lengths specifying the geometry, but not on α . In particular, when $K_0 = 0$, the above lead to

$$\bar{\sigma}_{max} / \sigma_0 = f_4 / f_3, \quad (39)$$

and

$$\frac{a}{\delta_0 \mathcal{E}' / \sigma_0} = \frac{1}{(f_1 f_4 / f_3) - f_2}. \quad (40)$$

This pair gives the function (34), damage extent L/a being regarded as a parameter. Solution for linear softening is still of form (37) and (38), but f_s in addition depend on α .

For power-law bridging (29), the solution takes the form

$$\delta_1 / \delta_0 = \alpha^{1/(1-m)} \Delta(\alpha^{-m/(1-m)} \bar{\sigma} / \sigma_0, L/a), \quad (41)$$

and

$$K_{up} / \sigma_0 \sqrt{a} = \alpha^{m/(1-m)} k(\alpha^{-m/(1-m)} \bar{\sigma} / \sigma_0, L/a). \quad (42)$$

The dimensionless functions Δ and k also depend on m , and

the ratios of a over lengths specifying the geometry, but nothing else (see Appendix). Many solutions of this type have been given by the group at Rockwell International (Marshall *et al.* 1987, Cox and Lo 1992, and Cox 1992).

In obtaining (39) and (40), $\bar{\sigma} / \sigma_0$ is assumed to monotonically increase with L/a , so that the maximum load $\bar{\sigma}_{max} / \sigma_0$ happens at $\delta_1 = \delta_0$. This in general is incorrect when $\mathcal{G}_{up} \neq 0$ (Marshall *et al.* 1987), or the bridging softens (Carpinteri 1990, Bao and Zok 1992). If this seems to be the case, a formal procedure is as follows. After f and g are computed, $\bar{\sigma}_{max}$ is searched as a function of damage extent L/a , subjected to $\mathcal{G}_{up} = \Gamma_0$ in (35), and $\delta_1 \leq \delta_0$ in (36).

Consequences of large-scale bridging are discussed in the following sections. To focus on issues of qualitative significance, the bridging law is assumed to be rectilinear, and the crack tip energy dissipation is negligible, $\Gamma_0 / \sigma_0 \delta_0 = 0$, unless otherwise stated.

3.2 Strength: monolithic solids vs composites

A comparison of the strength of a monolithic ceramic and the strength of a composite is particularly illuminating. Similar comparison has been made by Cottrell (1963) in connection with notch-brittleness.

The strength of a monolithic ceramic measured by a mechanical test, S , is known to be only about a hundredth of the atomic bond strength, σ_0 . Griffith (1921) put forth an explanation on a basis of two postulates: 1) atomic debond is the only inelastic process during fracture and, 2) the solid contains traction-free, crack-like flaws comparable to the size of microstructure (e.g., grain diameter). The small-scale damage condition is satisfied: the microstructure is typically on the order of microns, and the atomic debond process is confined within a few nanometers. Crack tips are therefore idealized to be mathematical points in calculating elastic field in the solid. In particular, the energy release rate for a plane strain crack of size $2a$ is (Tada *et al.* 1985)

$$\mathcal{G} = \pi a \bar{\sigma}^2 / E'. \quad (43)$$

Atomic debond absorbs energy $\Gamma = \sigma_0 \delta_0$, as given by (10).

The applied stress $\bar{\sigma}$ reaches strength S when $\mathcal{G} = \Gamma$, so that

$$\frac{S}{\sigma_0} = \frac{1}{\sqrt{\pi}} \left(\frac{a}{\delta_0 \mathcal{E}' / \sigma_0} \right)^{-1/2}. \quad (44)$$

This curve is indicated by SSB in Fig. 10. Griffith's small-scale bridging model explained the small values of S / σ_0 when $a / (\delta_0 \mathcal{E}' / \sigma_0) \gg 1$. However, as clearly indicated in Fig. 10, the model fails when $a / (\delta_0 \mathcal{E}' / \sigma_0) \sim 1$, for the strength of a solid should never exceed the atomic bond strength.

For a fiber-reinforced ceramic, the dominant inelastic process is frictional sliding of fiber/matrix interface. Using the illustrative properties in Table 1, assuming that the unbridged flaw size, a , is of a few fiber diameters, one finds that $a / (\delta_0 \mathcal{E}' / \sigma_0) < 1$. Consequently, the bridging zone length is comparable to the flaw size, so that the damage zone and the flaw must be analyzed as coupled. The

pertinent results are (Tada *et al.* 1985)

$$\frac{\delta F'}{\sigma_0 a} = 4(\eta^2 - 1)^{1/2} \left[\frac{\bar{\sigma}}{\sigma_0} - \frac{2}{\pi} \cos^{-1}(1/\eta) \right] + \frac{8}{\pi} \ln \eta, \quad (45)$$

and

$$\frac{K_{up}}{\sigma_0 \sqrt{\pi a}} = \eta^{1/2} \left[\frac{\bar{\sigma}}{\sigma_0} - \frac{2}{\pi} \cos^{-1}(1/\eta) \right], \quad (46)$$

where $\eta = 1 + L/a$.

The strength $\bar{\sigma} = S$ is obtained by setting $\delta_i = \delta_0$ and $K_{up} = 0$:

$$\frac{8}{\pi} \left(\frac{a}{\delta_0 E' / \sigma_0} \right) \ln \left[\sec \left(\frac{\pi S}{2 \sigma_0} \right) \right] = 1. \quad (47)$$

This equation is indicated by LSB in Fig. 10. A comparison of the two curves gives a quantitative feel for the regime where the small-scale bridging assumption is valid. Indeed, the LSB model predicts that S/σ_0 approaches unity when the unbridged flaw size a is small, as anticipated. Since typically $a/(\delta_0 E' / \sigma_0) \sim 1$ for a composite, the strength of a composite is insensitive to processing defects, as compared to the strength of a monolithic ceramic.

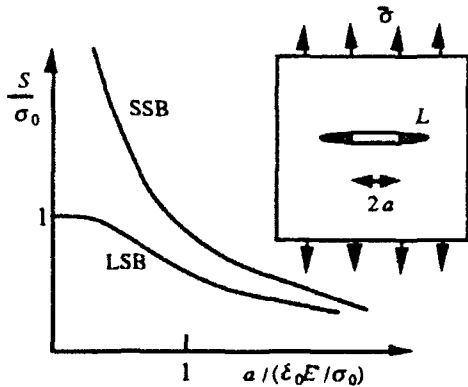


Fig. 10 Strength predicted by small- and large-scale bridging. The former is correct only when a is large.

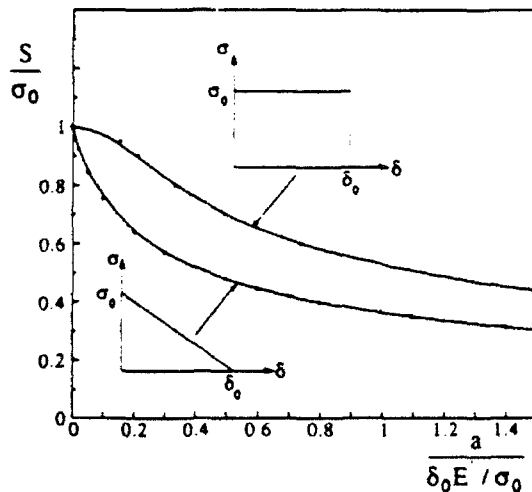


Fig. 11 Strength of a material computed from rectilinear and softening bridging laws.

To demonstrate the effect of bridging law shape, Fig. 11 plots strength computed from rectilinear and softening bridging laws (Bao and Zok 1992). The difference is appreciable, but of order unity. When a proper selection of σ_0 and δ_0 is made, bridging laws of other shapes would give rise to strength bounded between the two curves in Fig. 11.

3.3 Notch-sensitivity

Holes are often drilled in a panel for fastening or cooling. Neither toughness nor strength can be directly used to determine the maximum static load. However, a designer knows to ignore a small hole in a ductile metal panel, but not a hole in a ceramic. What about a fiber-reinforced ceramic? To fix the idea, Fig. 12 illustrates a panel with a hole, and the question is how much load the panel can carry.

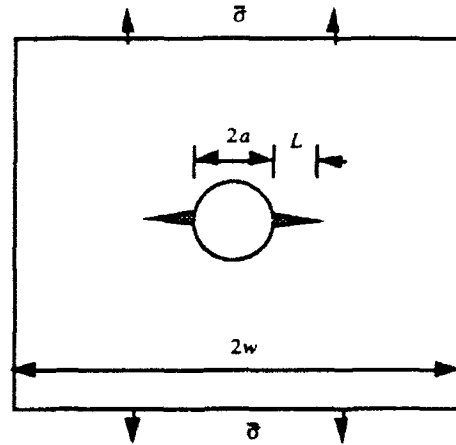


FIG. 12 A panel containing a hole.

The answer depends on materials. For a monolithic ceramic panel, the load should be such that the stress at the hole is below the "strength" of the ceramic. Let σ_0 be a reference value of strength (ignoring statistical distribution), and C be the stress concentration factor at the hole. The maximum load that can be carried by the panel is given by

$$\bar{\sigma}_{max} / \sigma_0 = 1 / C. \quad (48)$$

The stress concentration factor depends on a/w (Peterson 1971); Equation (48) is plotted in Fig. 13. Notice that even a small hole ($a/w = 0$) reduces the load-carrying capacity by a factor of 3: ceramics are *notch-sensitive*.

The design criterion is different for a ductile metal panel under static load. Plasticity relieves stress concentration near the hole, so that the maximum load should be such that the net section fully yields:

$$\bar{\sigma}_{max} / \sigma_0 = 1 - a/w, \quad (49)$$

where σ_0 is the yield strength of the metal. Equation (49) is plotted in Fig. 13. A small hole does not reduce much load-carrying capacity: ductile metals are *notch-insensitive*.

What about a panel made of a fiber-reinforced ceramic? The answer depends on material and hole size. Matrix cracking near the hole, allowing fibers to slide, provides a mechanism for ductility δ_0 and stress redistribution. The

composite behaves according to the dimensionless group

$$\frac{a}{\delta_0 E' / \sigma_0} = \begin{cases} 0, & \text{notch - ductile} \\ \infty, & \text{notch - brittle} \end{cases} \quad (50)$$

That is, notch-sensitivity is a property of both material *and* notch size: for a given composite, a large hole tends to be ceramic-like, but a small hole metal-like. In practice, δ_0 can be changed, by orders of magnitude, by varying the sliding friction. Such experiments would verify the model.

Classification (50) emerges directly from the dimensional analysis of the large-scale bridging model (see Appendix). Another dimensionless group, $a / (\Gamma E' / \sigma_0^2)$, has long been used to correlate transition behaviors for metals (see Kanninen and Popelar 1985). The two groups are equivalent since $\Gamma \sim \delta_0 \sigma_0$. Large-scale bridging concepts provide a framework to simulate notch brittle-to-ductile transition behaviors for composites. As we shall see, some behaviors have close analogues in metals, others do not.

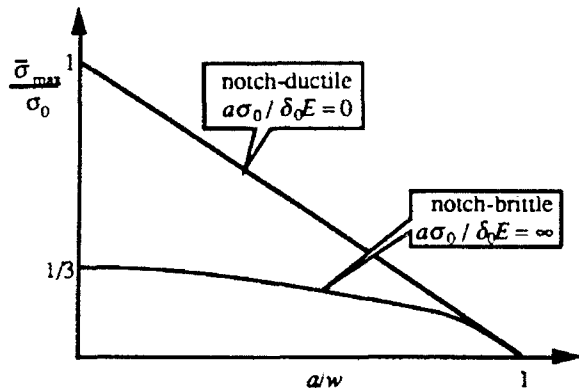


FIG. 13 The maximum load for a panel containing a hole.

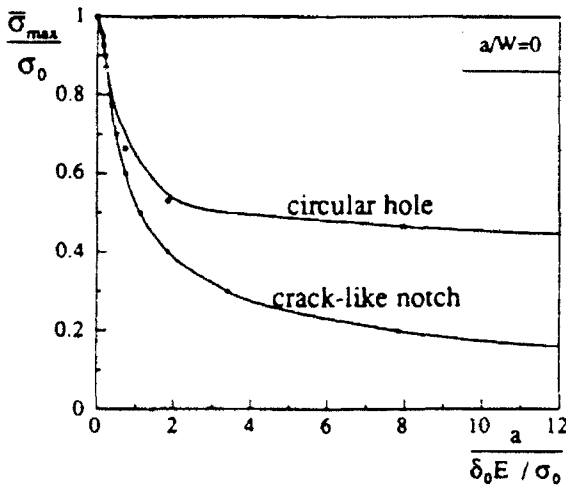


Fig. 14 Notch ductile-to-brittle transition (Ho and Suo 1992).

The maximum loads for intermediate values of $(a\sigma_0)/(\delta_0 E)$ fall in between the two limiting curves in Fig. 13, which can be computed by invoking large-scale bridging concepts. Figure 14 plots the results of such a computation

for a hole in a large panel ($a/w = 0$). Specifically, the hole becomes notch-brittle when $a / (\delta_0 E' / \sigma_0) > 10$. For example, for a composite with $\delta_0 E' / \sigma_0 \sim 1$ mm, a hole of a centimeter radius will be notch-brittle. The mechanics model to construct Fig. 14 is similar to that in Section 3.2, except that finite elements are used to compute f_s in (37) and (38).

Also included in Fig. 14 is the maximum load for a panel containing a crack-like notch (Eq. 47). The two are expected to bound the curves for notches of various root radii. Computations on the effects of notch radius and elastic orthotropy are in progress (Gu *et al.* 1992).

Notch-ductility can be enhanced by various damage modes, notably, multiple cracking and matrix splitting along the fiber direction. To illustrate, consider a hole with splits (Fig. 15). The extent of the splits, h/a , is determined by the shear resistance $\hat{\tau}$, resulting from either friction in unidirectional composites, or bending of 90 degree fibers in woven composites. The anticipated results are sketched in Fig. 16. When $\hat{\tau} / \sigma_0 \sim 0$, the splits are long and the matrix crack becomes an edge crack, so that the full load-carrying capacity can be reached. When $\hat{\tau} / \sigma_0 \sim \infty$, the splits are small, so that the curve in Fig. 14 is reached. Detailed results will be reported elsewhere (He and Suo 1992).

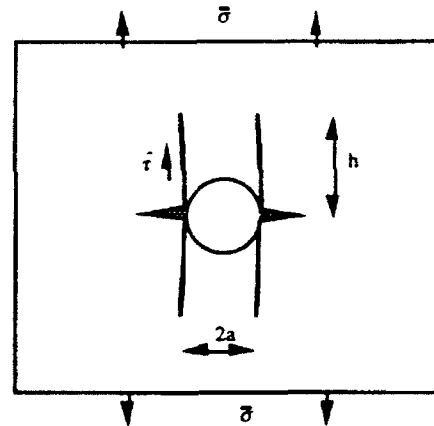


FIG. 15 A stress concentrator (the hole) relaxed by splits.

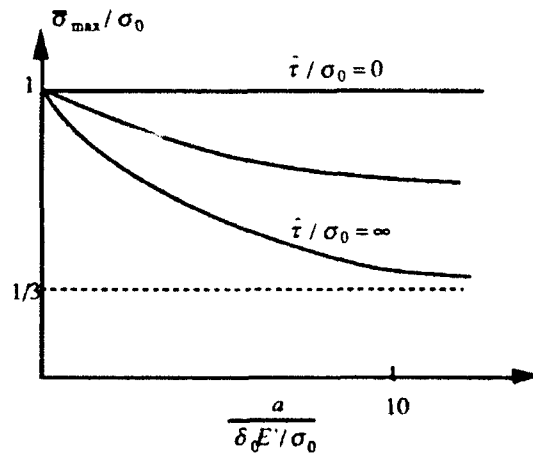


FIG. 16 Notch-ductility due to splitting.

3.4 Transverse cracks: Splitting vs tunneling

Two types of transverse cracks, splitting and tunneling, are illustrated in Figs. 17 and 18. They take the same fracture path in the matrix, along the fiber direction, with fibers crossing over the crack plane. For splitting, the cross-over fibers supply substantial fracture resistance *in addition to* matrix fracture energy (Spearing and Evans 1992). In contrast, the cross-over fibers provide little resistance to tunneling cracks (Beyerle *et al.* 1992). As we shall show, this is a large-scale bridging effect.

To understand the difference, first consider a splitting beam of thickness $2h$, bridged over length L , and loaded by moment M (Fig. 17). Typically L is comparable to $2h$, but smaller than the total crack length. The problem has been analyzed by Suo *et al.* (1992a); the results pertinent to the present discussion are outlined below.

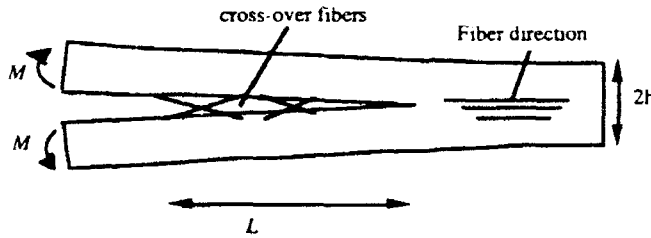


FIG. 17 A splitting beam interacting with cross-over fibers.

An application of the J -integral shows that

$$12M^2/E'h^3 = \sigma_0\delta_i + \Gamma_0, \quad (51)$$

where the left-hand side is the integral computed over the external boundary of the beam, and the right-hand side over the bridging zone. The crack tip energy dissipation, Γ_0 , is also included for the sake of discussion. The maximum moment is reached when $\delta_i = \delta_0$:

$$12M_{\max}^2/E'h^3 = \sigma_0\delta_0 + \Gamma_0. \quad (52)$$

Using the illustrative numbers in Table 1 and the typical value for a glass matrix, $\Gamma_0 \sim 10 \text{ J/m}^2$, one finds that the cross-over fibers substantially increases M_{\max} . Since it is small, Γ_0 is to be ignored in the following estimate of the bridging zone size.

The disturbing number in Table 1, $L_0 = 1 \text{ m}$, is predicted from the small-scale bridging model. It is incorrect: L of a few beam thickness, about several centimeters, is observed in experiments. The flexibility of a beam can substantially reduce the critical bridging zone length. This is a large-scale bridging effect, as shown below.

Dimensional considerations lead to

$$M = \frac{1}{2} a_1 L^2 \sigma_0, \quad (53)$$

where a_1 depends only on L/h , and is of order unity when $L/h > 1$ (Suo *et al.* 1992a). Combination of (52) and (53) gives the critical bridging zone length when $\delta_i = \delta_0$:

$$L_0 = a_1^{-1/2} (E'\delta_0/3\sigma_0)^{1/4} h^{3/4}. \quad (54)$$

For example, with $h = 1 \text{ cm}$, one finds $L_0 = 3 \text{ cm}$, suggesting that the potential fracture resistance can be

realized in beams with practical size.

The J -integral over the external boundary of the beam can be interpreted as the driving force for splitting. Figure 19 plots J as a function of matrix crack extension, L , where (53) is the rising part, and (52) the plateau. In contrast to the R -curves under small-scale bridging conditions, the J - L curves depend on beam thickness. The latter are therefore *not* material properties.

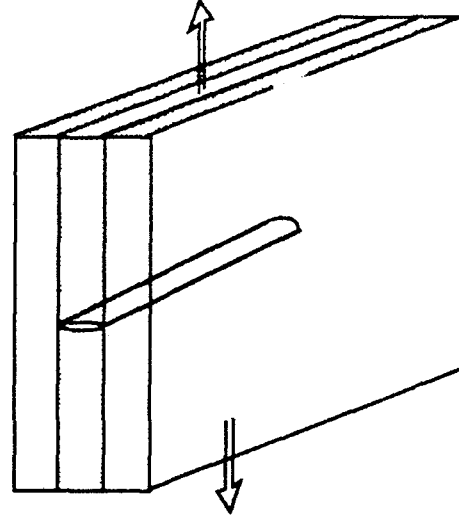


FIG. 18 A crack tunneling in a 90°-ply.

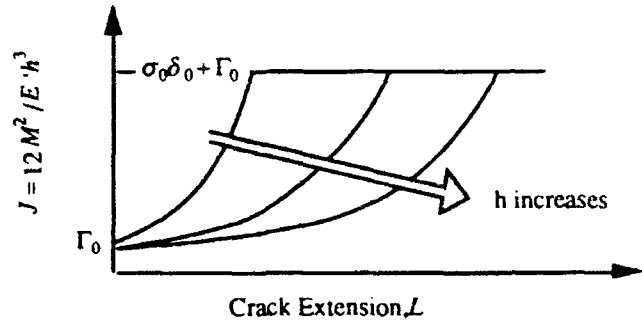


FIG. 19 J -integral as a function of crack extension, L , and beam thickness, h .

Cross-over fibers do not provide much resistance to tunneling cracks (Beyerle *et al.* 1992). A large crack separation is a prerequisite for using the large limiting separation δ_0 ($\sim 100 \mu\text{m}$), which cannot be realized in a tunnel constrained by the surrounding material. Consequently, tunneling cracks are only resisted by matrix fracture energy Γ_0 . A mechanics model for tunneling cracks is given by Ho and Suo (1991)

3.5 A note on measuring bridging law

Various methods have been considered to determine the bridging law from either experiments, models, or combinations (Cox 1991). One such method is described as follows (Li *et al.* 1987).

Write a bridging law as

$$\sigma = \sigma(\delta). \quad (55)$$

Rice (1968) showed that

$$J = J_{up} + \int_0^{\delta_i} \sigma(\delta) d\delta, \quad (56)$$

where J is the J -integral computed over a contour outside the bridging zone, J_{up} over a contour close to the crack tip, and δ_i the separation at the pre-cut root (Fig. 20). Upon loading, $J_{up} = \Gamma_0$ is maintained as the matrix crack extends. Differentiating (56) with respect to δ_i gives

$$\sigma(\delta_i) = dJ / d\delta_i. \quad (57)$$

Consequently, the bridging law can be determined if both J and δ_i can be determined as a function of applied load P . Since the limiting-separation for various bridging mechanisms in composites is in the range 10 ~ 100 μm , many experimental techniques may be used to measure δ_i , *in situ*.

Difficulty arises to relate J to the applied load P . There has been a misconception that J is related to P through handbook solutions for K . This is wrong since Irwin's relation (8) is valid only under small-scale bridging conditions. Under large-scale bridging conditions, J usually depends on the bridging law, which is yet to be determined from the very experiment. A procedure has been proposed by Li *et al.* (1987) to determine J experimentally. In general, the method suggested by (57) will be difficult to use under large-scale bridging conditions.

There are exceptions. For example, the J -integral over the external boundary of a splitting beam (Fig. 17) is independent of the bridging law (Rice 1968):

$$J = 12M^2 / E'h^3. \quad (58)$$

Thus, splitting beam can be used to determine the bridging law under large-scale bridging conditions. Specimens having the same attribute are reviewed by Suo *et al.* (1992a).

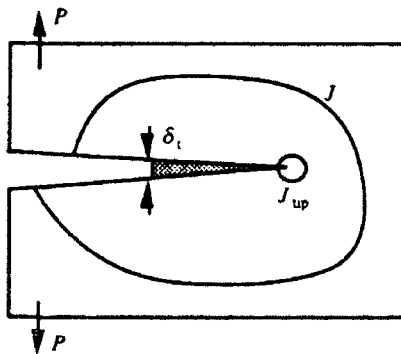


FIG. 20 Contours over which J -integrals are computed.

4. SUMMARY

Figure 21 summarizes the main theme of crack-bridging concepts. At the center is the bridging law, derived from micromechanics models and experiments, which, combined with continuum stress analysis, gives rise to mechanical properties such as toughness, strength, notch-ductility. Consequently, bridging law (1) replaces toughness or

strength as the basic material property. Together with an elastic component, the bridging law provides a length, $\delta_i E' / \sigma_0$, varying from a nanometer to a meter for different bridging mechanisms (Table 1), which is responsible for the vast differences in failure behaviors. Large-scale bridging introduces a dimensionless group, $a / (\delta_i E' / \sigma_0)$, where a is the length characterizing a component, having different meanings in various contexts: unbridged crack size for toughness, unbridged flaw size for strength, and hole radius for notch-sensitivity. It is demonstrated that the set of normalization introduced in this article separates the roles played by the shape and the scale of a bridging law, so that a design chart can be presented in a nondimensional form (34), and a different bridging law only modifies the chart within order unity. A collection of small-scale bridging solutions is given in Section 2 for several idealized bridging laws. Large-scale bridging effects are illustrated in Section 3 by examples of practical significance.

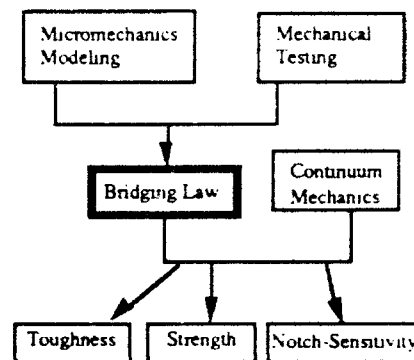


FIG. 21 The main theme of crack-bridging concepts.

ACKNOWLEDGEMENTS

ZS is grateful for the financial support of NSF grant MSS-9011571, and of DARPA University Research Initiative, ONR Contract N00014-86-k-0753.

REFERENCES

- Bannister M, Shercliff H, Bao G, Zok FW and Ashby MF (1992) Toughening in brittle systems by ductile bridging ligaments, *Acta Metall Mater*, in press.
- Bao G and Hu CY (1990) Effects of interface debonding on the toughness of ductile particle reinforced ceramics. *Int J Solids Structure*, 26, 631-642.
- Bao G and Zok FW (1992) On the strength of particle reinforced brittle matrix composites. Manuscript in preparation.
- Beyerle DS, Spearling SM and Evans AG (1992) Damage mechanisms and the mechanical properties of laminated 0/90 ceramic-matrix composites. Submitted to *J Am Ceram Soc*.
- Bilby BA, Cottrell AH and Swinden KH (1963) The Spread of Plastic Yield from a Notch, *Proc Roy Soc Lond A272*, 304-314.
- Budiansky B, Amazigo JC and Evans AG (1988) Small-scale crack bridging and the fracture toughness of particulate reinforced ceramics. *J*

- Carpinen A (1990) A catastrophe theory approach to fracture mechanics, *Int J Fracture*, 44, 17-69.
- Cottrell AH (1963) Mechanics of fracture, *Tewksbury Symposium on Fracture*, 1-27, University of Melbourne (1975) *Fracture, in The Physics of Metals, 2: Defects*, Ed P B Hirsch, Cambridge University Press, New York.
- Cox BN (1991) The determination of crack bridging forces, *Int J Fracture*, In press.
- Cox BN (1992) Scaling for bridged cracks. Submitted to *J Appl Mech*.
- Cox BN and Lo CS (1992) Load ratio and notch effects for bridged fatigue cracks in fibrous composites, *Acta Met Mater*, 40, 69-80.
- Dugdale DS (1960) Yielding of steel sheets containing slits, *J Appl Mech*, 8, 100-104.
- Dundurs J (1968) Elastic interaction of dislocations with inhomogeneities, in *Mathematical Theory of Dislocations*, 70-115, ASME, New York.
- Evans AG (1990) Perspective on the development of high-toughness ceramics, *J Am Ceram Soc*, 73, 187-206.
- Griffith AA (1921) The phenomena of rupture and flow in solids, *Phil Trans Roy Soc Lond*, A221, 163-197.
- Gu P, Shih CF and Suo Z (1992) Toughness and notch sensitivity of composites having power-law bridging. Work in progress.
- He MY and Suo Z (1992) Notch sensitivity and splitting. Work in progress.
- Ho S and Suo Z (1991) Tunneling cracks in constrained layers. Submitted for publication.
- Ho S and Suo Z (1992) Notch brittle-to-ductile transition in metal and ceramic matrix composites. Work in progress.
- Hutchinson JW and Jensen HM (1990) Models of fiber debonding and pullout in brittle composites with friction, *Mech Mater*, 9, 139-163.
- Irwin GR (1957) Analysis of stresses and strains near the end of a crack traversing a plate, *J Appl Mech*, 24, 361-364.
- Kanninen MF and Popelar CH (1985) *Advanced Fracture Mechanics*, Oxford University Press, New York.
- Li VC (1990) Non-linear fracture mechanics of inhomogeneous quasi-brittle materials, in *Nonlinear Fracture Mechanics*, ed. MP Wnuk, Springer-Verlag, New York.
- Li VC, Chan CM and Leung KY (1987) Experimental determination of the tension-softening relations for cementitious composites, *Cement and Concrete Research*, 17, 441-452.
- Marshall DB, Cox BN and Evans AG (1985) The mechanics of matrix cracking in brittle matrix composites, *Acta Metall*, 33, 2013-2021.
- Marshall DB and Cox BN (1987) Tensile fracture of brittle matrix composites: influence of fiber strength, *Acta Metall*, 35, 2607-2619.
- Malaga PA (1989) Deformation of crack-bridging ductile reinforcements in toughened brittle materials, *Acta Metall*, 37, 3349-3359.
- McMeeking RM and Evans AG (1990) Matrix fatigue cracking in fiber composites, *Mech Mater*, 9, 217-227.
- Needleman A (1990) An analysis of tensile decohesion along an interface, *J Mech Phys Solids*, 38, 389-324.
- Peterson RE (1974) *Stress Concentration Factors*, John Wiley, New York.
- Rice JR (1968) A path independent integral and the approximate analysis of strain concentrations by notches and cracks, *J Appl Mech*, 35, 379-386.
- Ritchie RO and Thompson AW (1985) On macroscopic and microscopic analysis for crack initiation and crack growth toughness in ductile al. vs. *Met Trans*, 16A, 233-247.
- Spearin, SM and Evans AG (1992) The role of fiber bridging in the delamination resistance of fiber reinforced composites, *Acta Metall Mater*, In press.
- Suo Z, Bao G and Fan B (1992a) Delamination R-curves due to damage, *J Mech Phys Solids*, 40, 1-16.

- Suo Z, Ortiz M and Needleman A (1992b) Stability of solids with interfaces, *J Mech Phys Solids*, In press.
- Tada H, Paris PC and Irwin GR (1985) *The Stress Analysis of Cracks Handbook*, Del Research, St Louis, MO.
- Zok FW and Horn CL (1990) Large scale bridging in brittle matrix composites, *Acta Metall Mater*, 38, 1895-1904.

APPENDIX

A crack, traction-free or bridged, is equivalent to an array of continuously distributed dislocations (Bilby *et al.* 1963). The dislocation per unit length, b , is related to crack separation δ , by

$$b(x) = -\partial\delta / \partial x. \quad (A1)$$

Resulting from geometric considerations, this has nothing to do with pile-up dislocations in a real crystal. Solutions to a single dislocation interacting with a hole, a free surface, or a crack are available in the literature, which can be used as kernels to formulate integral equations for notch-sensitivity problems (Gu *et al.* 1992).

To illustrate, consider a hole in an infinite composite (Fig. 12, $a/w = 0$). The stress prior to matrix cracking is given by the standard elasticity solution of a hole in an infinite plate:

$$\sigma(x) = \bar{\sigma}F(x/a), \quad (A2)$$

where $\bar{\sigma}$ is the applied stress, and dimensionless function F is given in elasticity textbooks. The stress induced by a pair of edge dislocations, symmetrically located at $x = \pm \xi$, is given by

$$\sigma(x) = \frac{E'}{a} H(x/a, \xi/a) b(\xi), \quad (A3)$$

where H is a known function (Dundurs 1968).

Superimposing the stress due to the dislocations and the remote stress leads to

$$\sigma(x)(\delta/\delta_0) = \bar{\sigma}F - \frac{E'}{a} \int_a^{a+L} H \frac{\partial\delta}{\partial\xi} d\xi \quad (A4)$$

The bridging law (1) is also incorporated in the above. Equation (A4) is the integral equation governing crack separation $\delta(x)$, to be solved numerically. Normalizing (A4) according to

$$\bar{\sigma}/\sigma_0, \delta/\delta_0, x/a, L/a, \quad (A5)$$

one can confirm (35) and (36) for any bridging law, and (41) and (42) for power-law.

NOTCH DUCTILE-TO-BRITTLE TRANSITION DUE TO LOCALIZED INELASTIC BAND

Z. Suo, S. Ho and X. Gong

Mechanical and Environmental Engineering Department
University of California
Santa Barbara, CA 93106-5070, USA

Revised in October 1992
for Publication in *ASME J. Engng. Mater. Tech.*

ABSTRACT

Holes are often drilled in a panel for cooling or fastening. For a panel made of a monolithic ceramic, such a hole concentrates stress, reducing load-carrying capacity of the panel by a factor of 3. By contrast, for a ductile alloy panel, plastic flow relieves stress concentration so that the small hole does not reduce load-carrying capacity. A panel made of ceramic-matrix composite behaves in the middle: matrix cracks permit unbroken fibers to slide against friction, leading to inelastic deformation which partially relieves stress concentration. Load-carrying capacity is studied in this paper as an outcome of the competition between stress concentration due to the notch, and stress relaxation due to inelastic deformation. The inelastic deformation is assumed to be localized as a planar band normal to the applied load, extending like a bridged crack. The basic model is large-scale bridging. A material length, $\delta_0 E / \sigma_0$, scales the size of the inelastic band, where σ_0 is the unnotched strength, δ_0 the inelastic stretch at the onset of rupture, and E Young's modulus. Load-carrying capacity is shown to depend on notch size a , measured in units of $\delta_0 E / \sigma_0$. Calculations presented here define the regime of notch ductile-to-brittle transition, where ceramic-matrix composites with typical notch sizes would lie. Both sharp notches and circular holes are considered. The shape of the bridging law, as well as matrix toughness, is shown to be unimportant to load-carrying capacity.

1. INTRODUCTION

Cottrell (1963) was among the first to recognize the full capacity of the work of Dugdale (1960), Barenblatt (1962) and Bilby *et al.* (1963), and put forth crack-bridging as a unifying process at all scales—from atomic debond to metal voiding. Instead of being viewed as a singularity, fracture, or any localized damage band, is now a gradual stretching of nonlinear springs. He also drew the analogy with the Peierls model, where a crystalline dislocation is a nonsingular, solitary solution of a spring-substrate system.

The crack-bridging concept integrates physical mechanisms of damage and macroscopic

performance of materials in two steps. First, a sufficiently localized damage process is represented by nonlinear springs—be it electron cloud or metal ligament—with essential physical variables retained. Second, at a coarse scale, the interaction between the springs and the undamaged elastic substrate is viewed as a continuum problem. A common thread is that the spring law introduces a reference stress σ_0 and a reference length δ_0 , and that together with Young's modulus E of the substrate, they form a material length, $\delta_0 E / \sigma_0$, varying from a few nanometers for atomic decohesion, to a few centimeters for metal voiding. This material length determines the size of the inelastic deformation region. Cottrell was able to correlate notch-brittleness by the ratio of this material length to notch size.

Much has since been developed in vastly different contexts. A few recent examples are cited here. Metal-ceramic debonding is studied by Needleman (1990) on a basis of phenomenological spring laws mimicking atomic decohesion, and inelastic substrates representing background dislocation motion. Using springs with atomic periodicity, Rice (1992) reconsidered dislocation emission from a crack tip; instead of a full dislocation and a sharp crack (two singularities!), a dislocation now emerges incrementally from a crack tip, in a way analogous to Barenblatt's cleavage process. On a coarser scale, Huang and Hutchinson (1989) modeled shear localization by using springs representing void interaction. Suo (1991) examined domain band propagation in ferroelectric crystals under combined electric field and stress. Compressive kink band emanating from a hole is studied by Soutis *et al.* (1991) with springs representing fiber buckling. Using an earlier model of Aveston *et al.* (1971), Marshall *et al.* (1985) derived a bridging law representing frictional sliding, which set the basis for much of the subsequent work on composites.

Rice (1976) suggested two approaches to localization. In one approach, localization is due to loss of uniqueness, the entire band setting in simultaneously from a homogeneous field. In the second approach, a localization band nucleates at a material defect or a stress concentrator, spreading like a bridged crack. They are not equivalent, physically or mathematically. The second approach has the advantage that a physical length scale is introduced through bridging law, which

links material performance with processing variables, such as fiber strength and fiber/matrix interface friction. The first approach seems to be irrelevant to ceramic-matrix composites, where the band consisting of the matrix crack and sliding fibers nucleates from a processing flaw.

This paper is out of a more practical concern. We have been trying to reconcile design practices for ductile alloys and monolithic ceramics, and thereby provide a theoretical link between design *with* and design *of* ceramic-matrix composites. A representative design problem, notch sensitivity, is as follows. Holes are often drilled in a panel for fastening or cooling. In determining maximum load, a designer knows to ignore a small hole in a ductile metal panel, but not in a monolithic ceramic. What about a fiber-reinforced ceramic?

To focus the idea, Fig. 1 illustrates a panel with a hole, and the question is how much load the panel can carry. For a monolithic ceramic panel, the load should be such that the stress near the hole is below the strength of the ceramic. The latter is the Griffith stress associated with a crack-like flaw in the vicinity of the hole surface, of size close to grain diameter. Because of stress concentration, even a tiny hole reduces the load-carrying capacity by a factor of 3: ceramics are *notch-sensitive*. By contrast, a ductile alloy panel is designed with much tolerance. Plasticity relieves stress concentration, so that the maximum load should be such that the net-section fully yields. A small hole does not reduce the load-carrying capacity much: ductile alloys are *notch-insensitive*.

What about a fiber-reinforced ceramic? Without a hole, a composite sustains stress up to the fiber strength times the fiber volume fraction. The presence of a hole knocks down load-carrying capacity, but not necessarily by a factor of 3. Matrix cracks, allowing unbroken fibers to slide, partially relieve stress concentration. Elastic stress concentrates over a region that scales with the hole radius, a . On the other hand, sliding fibers provide extra deformation to redistribute stress over a region that scales with $\delta_0 E / \sigma_0$. Here δ_0 is the extra displacement due to frictional sliding at the onset of fiber breaking, σ_0 the fiber strength times the fiber volume fraction, and E Young's modulus of the composite. Consequently, the ultimate load, $\bar{\sigma}_{\max}$, is determined by the

competition between elastic concentration and inelastic relaxation:

$$\frac{a}{\delta_0 E / \sigma_0} = \begin{cases} 0, & \text{notch - ductile, } \bar{\sigma}_{\max} / \sigma_0 = 1 \\ \infty, & \text{notch - brittle, } \bar{\sigma}_{\max} / \sigma_0 = 1/3 \end{cases} \quad (1)$$

Both material *and* notch size are important: for a given composite, a large hole reduces load-carrying capacity by a factor close to 3, but a small hole does not reduce it as much. Large or small, hole radius a is measured in units of material length $\delta_0 E / \sigma_0$.

This concept places design practices into perspective. Take $a = 1 \sim 10$ mm in usual engineering practice and take, for ceramic-matrix composites, $\delta_0 E / \sigma_0 = 0.1 \sim 10$ mm. As our calculation will show, these put a notched composite into the ductile-to-brittle transition regime. Criterion (1) also prompts the notion of designing materials for a given application. For ceramic-matrix composites, the limiting-separation δ_0 can be varied, by orders of magnitude, by varying fiber radius, fiber strength and fiber-matrix interface friction. Thus, a composite may be *engineered* to make a hole ductile for a required hole size.

In a broader context, $\delta_0 E / \sigma_0$ serves as a figure of merit of ductility. The ultimate strain of an unnotched bar in tension is not a good measure of ductility; it depends on gauge length and the number of deformation bands. Cross-section reduction is a valid measure of ductility for metals, but is not transferable to a notched component, nor does it have any counterpart in composites.

The basic ideas outlined above and a few preliminary results have been discussed in a review article by Bao and Suo (1992). The present paper is to supply mechanics calculations that define the ductile-to-brittle transition regime, where ceramic-matrix composites—with holes of useful sizes—would lie. A more general theme pursued here, as well as in the previous article, is to search for commonality in large-scale bridging models, where Irwin's linear fracture mechanics breaks down. A dilemma which has become evident over the last few years is this. While crack-bridging concepts are versatile to explain many phenomena, the mechanics analyses—and interpretations—are complicated enough to be author-dependent, particularly in the large-scale bridging regime. At this stage, any simplification or integration would help.

2. THE MODEL

2.1 Dimensionless Groups

Figure 1 defines the general mechanics problem: a band of inelastic deformation emanates from a notch in a component monotonically loaded by $\bar{\sigma}$. The band is *localized* in that its thickness is much smaller than any other lengths characterizing the component. The load $\bar{\sigma}$ can be regarded as a function of the stretch at the band-tail, δ_{tail} ; the band length L is an internal variable to be determined by the model. The model will predict the ultimate stress, or *load-carrying capacity*, $\bar{\sigma}_{\text{max}}$, of the notched component. The answer takes the functional form

$$\bar{\sigma}_{\text{max}} / \sigma_0 = \mathcal{F}(\alpha, \gamma). \quad (2)$$

Also entering the right-hand side are the bridging law shape, and the ratios of a to other lengths of geometry, such as notch root radius and panel width. The rest of this subsection explains these dimensionless groups.

The inelasticity may be divided into that localized in the band, and that further localized at the band tip. The inelasticity in the band is modeled as an array of springs with a nonlinear stress-stretch relation:

$$\sigma / \sigma_0 = \chi(\delta / \delta_0). \quad (3)$$

The dimensionless function χ describes the *shape* of the relation; the *scale* is set by a reference stress, σ_0 , and a reference stretch, δ_0 . Figure 2 shows several bridging laws to be used in numerical calculations. The second mechanism is represented by a critical energy release rate at the tip, Γ_0 . For a ceramic-matrix composite with debonded fibers, the inelastic stretch is due to sliding between fibers and matrix, and $\Gamma_0 = (1 - f)\Gamma_m$, where f is fiber volume fraction and Γ_m matrix fracture energy. For a void band in a ductile alloy, the band stretches at the expense of enlarging voids, and Γ_0 dissipates in creating new voids by inclusion/matrix debonding.

The relative magnitude of the two inelastic mechanisms is described by the dimensionless number

$$\gamma = \Gamma_0 / \sigma_0 \delta_0. \quad (4)$$

It enters (2) to determine load-carrying capacity. Two limiting cases are of particular significance.

When $\gamma \rightarrow \infty$, the energy dissipation in the band is insignificant compared to that at the tip, so that Linear Fracture Mechanics applies. However, for composites and ductile alloys, inelastic dissipation of the band dominates, say $\gamma < 0.1$. This paper focuses on the latter case.

Outside the band, the material is taken to be isotropic and linearly elastic, E being Young's modulus, ν Poisson's ratio, and $E' = E$ for plane stress and $E' = E/(1 - \nu^2)$ for plane strain. The coupled substrate-spring defines a material length

$$\delta_0 E' / \sigma_0. \quad (5)$$

This length serves as a figure of merit for the ductility of a bridging mechanism. The dimensionless group

$$\alpha = a / (\delta_0 E' / \sigma_0) \quad (6)$$

measures the size of the notch, a , in units of the material length. Observe that α enters (2) as a *size effect*.

2.2 Mathematical Description

The basic model is large-scale bridging; see Bao and Suo (1992) for references. An inelastic band can be viewed as either a bridged crack, or an array of continuously distributed dislocations. An inelastic band and a traction-free crack behave the same at their tips. The stress a short distance r ahead of the band-tip is square root singular:

$$\sigma_y = K_{\text{tip}} (2\pi r)^{-1/2}, \quad r / L \rightarrow 0. \quad (7)$$

Here K_{tip} is Irwin's stress intensity factor. The stretch a short distance r behind the band-tip is parabolic:

$$\delta = 8(K_{\text{tip}} / E')(r / 2\pi)^{1/2}, \quad r / L \rightarrow 0. \quad (8)$$

This may be verified by superimposing the result for a pair of concentrated force, on crack faces that are otherwise free of traction. Irwin's relation connects the stress intensity factor and the energy release rate at the band-tip:

$$\mathcal{G}_{\text{tip}} = K_{\text{tip}}^2 / E'. \quad (9)$$

We will use G_{tip} and K_{tip} interchangeably.

An inelastic band is also equivalent to an array of continuously distributed dislocations (e.g., Cottrell 1963). The stress in the spring, at position x , is due both to the applied stress $\bar{\sigma}$, and to the dislocation array:

$$\sigma_0 \chi(\delta / \delta_0) = \bar{\sigma} F(x/a) + \frac{E'}{a} \int_a^{a+L} H(x/a, \xi/a) \frac{\partial \delta}{\partial \xi} d\xi. \quad (10)$$

Here F and H are known functions; this integral equation governs the stretch $\delta(x)$, which can be solved numerically (Gu *et al.* 1992).

Of direct bearing on load-carrying capacity are the tail-stretch δ_{tail} , and the band-tip energy release rate G_{tip} (Fig. 1). Normalizing (10) by

$$\bar{\sigma} / \sigma_0, \delta / \delta_0, x/a, \xi/a, L/a, \quad (11)$$

one finds that the answers take the forms

$$\bar{\sigma} / \sigma_0 = f(\delta_{tail} / \delta_0, \alpha, L/a), \quad (12)$$

and

$$G_{tip} / \sigma_0 \delta_0 = g(\delta_{tail} / \delta_0, \alpha, L/a). \quad (13)$$

The functions f and g will also depend on the bridging law shape χ , and the ratios of a to other lengths of geometry, but nothing else. Note that G_{tip} may be obtained from $\delta(x)$ according to (8) and (9).

For hardening bridging, at fixed α and L/a , $\bar{\sigma}$ monotonically increases with δ_{tail} , so that either one can be prescribed in solving (10). This is not so for softening bridging; $\bar{\sigma}$ may first increase with δ_{tail} , reaching a peak, and then drop. Thus, in general, δ_{tail} should be prescribed in a calculation. Given a notched component, α and γ are fixed; upon loading, the applied stress $\bar{\sigma}$ is a function of tail-stretch δ_{tail} . The band length L , being regarded as an internal variable, is to be determined from (13) by maintaining $G_{tip} = \Gamma_0$. Load-carrying capacity $\bar{\sigma}_{max} / \sigma_0$ is the maximum as δ_{tail} varies within the range allowed by the bridging law. We therefore confirm (2).

2.3 A Simplification

For well-toughened materials, band-tip dissipation is negligible, $\gamma = \Gamma_0 / \sigma_0 \delta_0 \ll 1$. A drastic simplification is suggested by *steady-state banding*. When the band is long compared to the notch size, \mathcal{G}_{tip} becomes independent of L/a and notch shape, being equal to the complementary energy of the spring law (Budiansky *et al.* 1986, Rose 1987). For example,

$$\mathcal{G}_{up}^{ss} = \frac{1}{3} \sigma_0 \delta_0 (\bar{\sigma} / \sigma_0)^3 \quad (14)$$

for the square-root law $\chi(\varepsilon) = \sqrt{\varepsilon}$. Consequently, if $\gamma = \Gamma_0 / \sigma_0 \delta_0$ is small, the band runs across the entire component at a low load $\bar{\sigma} / \sigma_0$, leaving springs intact.

The cross-component band is nonuniformly stretched, $\delta_{tail} > \bar{\delta}$, where $\bar{\delta}$ is related to $\bar{\sigma}$ by the spring law. The dimensional argument similar to that leading to (12) now gives

$$\bar{\sigma} / \sigma_0 = \mathcal{S}(\delta_{tail} / \delta_0, \alpha). \quad (15)$$

Obviously, no equation analogous to (13) exists in this case. The maximum $\bar{\sigma}_{max}$ can thus be determined as δ_{tail} varies within the range allowed by the bridging law. The rest of the article will focus on presenting results for the special case $\gamma = 0$, with occasional excursion to the case of small γ , only to show the insignificance of the latter as far as load-carrying capacity is concerned.

Figure 2 shows bridging laws representative of a wide range of behaviors; their solutions are summarized in the Appendix. A few general observations are made here. Rectilinear and linear-softening laws cause a peculiarity; they have no complementary energy, $\mathcal{G}_{up}^{ss} = 0$. Thus, the band length L is finite even if $\gamma = 0$, and should be determined from (13).

The exponential law

$$\sigma / \sigma_0 = (\delta / \delta_0) \exp(1 - \delta / \delta_0) \quad (16)$$

is taken by Needleman (1990) to represent atomic decohesion. The two reference quantities, σ_0 and δ_0 , can be inferred in the usual way from measurable cohesive properties—lattice spacing, Young's modulus and surface energy. This law is used here to illustrate all laws of this type. First, the law has no limiting-stretch; δ_0 is assigned, arbitrarily, as the stretch where the stress reaches the maximum, σ_0 . Nonetheless, δ_0 still conveys the idea of interaction range ($\delta_0 \sim 1 \text{ \AA}$ for atomic debond). Second, due to softening in the springs, for fixed α in (15), $\bar{\sigma}$ first

increases with δ_{tail} , reaching a maximum, and then drops. Third, uniqueness is not guaranteed for systems with softening. In fact, for the defect-free case ($\alpha = 0$), multiple solutions are found, ranging from periodic to solitary (Suo *et al.* 1992b). However, uniqueness seems to prevail when a defect is present.

3. DAMAGE PROGRESSION IN CERAMIC COMPOSITES

To be definite, the model is now interpreted in the context of ceramic-matrix composites, even though conclusions may be applicable to other inelastic mechanisms. Figure 3 is a schematic of damage progression in a notched component under monotonic loading $\bar{\sigma}$. A matrix crack initiates at $\bar{\sigma} = \bar{\sigma}_i$; prior to this, $\delta_{\text{tail}} = 0$. For a crack-like notch, $\bar{\sigma}_i$ is governed by notch size a , according to Griffith's formula

$$\bar{\sigma}_i = (E' \Gamma_0 / \pi a)^{1/2}. \quad (17)$$

This stress is insensitive to processing flaws in the matrix, so long as the flaws are much smaller than the notch size.

For a circular hole, an initial flaw must be assumed in the vicinity of the hole, of size, say, on the order of the fiber diameter. Take the flaw to be a traction-free, penny-shaped crack of diameter d , so that

$$\bar{\sigma}_i = \frac{1}{3} (\pi E' \Gamma_0 / 2d)^{1/2}. \quad (18)$$

This has been reduced by the stress concentration factor 3, and assumes that the fibers and matrix have similar elastic constants. In practice, $\bar{\sigma}_i$ may also depend on the hole radius a , for a larger hole concentrates stress in a wider region, increasing the chance to trigger a bigger defect. Since $a \gg d$, the cracking initiation stress is larger for a hole than for a crack-like notch. In either case, further loading may be sustained without fiber breaking. Consequently, $\bar{\sigma}_i$ is unimportant as far as the ultimate strength is concerned.

After extending into the component, the crack is bridged by the fibers sliding against friction. This inelastic deformation can be represented by a bridging law (Marshall *et al.* 1985)

$$\sigma / \sigma_0 = (\delta / \delta_0)^{1/2}. \quad (19)$$

Upon assuming a deterministic fiber strength S , one has

$$\sigma_0 = fS, \quad (20)$$

and

$$\delta_0 = \frac{R}{2} \left(\frac{E_m}{E} \right)^2 \frac{(1-f)^2 S^2}{\tau E_f}. \quad (21)$$

Here f is the fiber volume fraction, R the fiber radius, τ the sliding friction of fiber/matrix interface, and E , E_m and E_f are Young's moduli for the composite, matrix and fiber, respectively. In terms of primary processing variables, the material length identified in Section 2 now scales as

$$\delta_0 E / \sigma_0 \propto RS / \tau. \quad (22)$$

Thus, the "ductility" of a composite increases with increasing fiber radius and fiber strength, but decreases with increasing friction of the fiber-matrix interface.

In practice, the fiber strength is statistical; S is taken to be some average value, since the ultimate stress of a composite corresponds to the breaking of many fibers. It is wrong to take δ as physical separation of the matrix crack. As pointed out by Hutchinson and Jensen (1990), δ should be inelastic deformation associated with frictional sliding—that is, total elongation of the composite with a matrix crack minus the elastic deformation of the composite without the matrix crack. The inelastic band consists of both the matrix crack and the frictional dissipation off the crack plane. The above equations were derived from an approximate analysis of fibers frictionally constrained in a matrix, and are valid when the slip length

$$l = \frac{R}{2} \frac{E_m (1-f)}{E f} \frac{\sigma}{\tau} \quad (23)$$

is several times fiber radius, which is typically the case in ceramic-matrix composites. Also note that the square-root law is only valid prior to fiber breaking. Yet design with ceramic-matrix composites may allow matrix cracking to relieve stress concentration, but require fibers to remain unbroken, so that the square-root law is adequate for this purpose.

An important feature is multiple cracks. Broadly, multiple cracks provide additional frictional dissipation sites or, equivalently, larger inelastic deformation to relieve stress

concentration. As an illustration, consider multiple cracks emanating from a long, blunt notch in Fig. 4. The matrix is assumed to be sufficiently brittle so that these cracks run across the component at a low load without fibers breaking. If the slip lengths do not overlap with one another and each spring is described by (19), the fracture energy is given by

$$\Gamma = \frac{2}{3} \sigma_0 \delta_0 \mathcal{N}, \quad (24)$$

where \mathcal{N} is the number of cracks, presumably related to the ratio of notch root radius over slip length. More detailed modeling is needed to take into account overlapping slip, analogous to models for unnotched panels by Aveston *et al.* (1971) and Zok and Spearing (1992). Nonetheless, to a first approximation, the effect of multiple cracks on load-carrying capacity may be captured by a single inelastic band with a larger equivalent δ_0 .

4. NOTCH SIZE AND MATRIX TOUGHNESS: α AND γ

Now the calculated load-carrying capacity is presented in form (2). The strength of a monolithic ceramic is only a fraction of its bridging strength (the atomic bond), and is sensitive to processing flaws. By contrast, the strength of a composite is close to its bridging strength (the fiber strength times fiber volume fraction), and is insensitive to processing flaws. To understand this difference, consider an unbridged crack of length $2a$, as in Fig. 5. The inelasticity—either atomic separation or fiber sliding—is approximated by a rectilinear law in the band, and by $\Gamma_0 = 0$ at the band tip. The standard solution is reproduced in the Appendix. Under monotonic loading $\bar{\sigma}$, the band length L is determined from (A4) by maintaining $K_{\text{tip}} = 0$. The ultimate stress $\bar{\sigma}_{\text{max}}$ is reached when $\delta_{\text{tail}} = \delta_0$. Eliminating the internal variable L from (A3) and (A4), Cottrell (1963) obtained that

$$\frac{8}{\pi} \left(\frac{a}{\delta_0 E' / \sigma_0} \right) \ln \left[\sec \left(\frac{\pi \bar{\sigma}_{\text{max}}}{2 \sigma_0} \right) \right] = 1. \quad (25)$$

This curve is labeled in Fig. 5 by $\Gamma_0 / \sigma_0 \delta_0 = 0$, to show load-carrying capacity as a function of notch size.

For a fine grain ceramic, energy dissipates to separate a few atoms at the crack tip, so that

$\delta_0 E' / \sigma_0 \sim 1$ nm; the flaw size is about the grain diameter, say $a \sim 1$ μ m. Consequently, $\alpha \sim 10^3$ so that $\bar{\sigma}_{\max} / \sigma_0 \ll 1$, confirming that the strength of a monolithic ceramic is much smaller than that of the atomic bond. By contrast, for a ceramic-matrix composite, energy dissipates over many atoms by interface sliding, say $\delta_0 E' / \sigma_0 \sim 1$ mm; material processing is unlikely to break many fibers on the same location, so that $\alpha < 1$. Consequently, the strength is close to the limiting stress $\bar{\sigma}_{\max} \sim \sigma_0 = fS$, and is insensitive to processing defects. This comparison reveals the central concept of making strong materials: the limiting-strength for a composite is very low compared with atomic bond strength, but amply compensated by a large inelastic stretch δ_0 , which retains this strength in the presence of flaws or small notches.

Next consider the case $\Gamma_0 / \sigma_0 \delta_0 = 0.1$, which is perhaps the largest value any well-toughened ceramic-matrix composite may assume. The left-hand side of (A3) equals $\delta_{\text{tail}} / \delta_0 \alpha$, and the left-hand side of (A4) equals $(\gamma / \pi \alpha)^{1/2}$. Thus, for fixed α and γ , (A3) and (A4) prescribe the applied stress $\bar{\sigma} / \sigma_0$ as a function of $\delta_{\text{tail}} / \delta_0$, the band length L/a being viewed as an internal variable. This $\bar{\sigma} - \delta_{\text{tail}}$ relation is plotted in Fig. 6 for $\gamma = 0.1$ and various α . Depending on α , the maximum, $\bar{\sigma}_{\max} / \sigma_0$, is reached at either $\delta_{\text{tail}} / \delta_0 = 1$ or $\delta_{\text{tail}} / \delta_0 < 1$. The maxima so obtained are plotted in Fig. 5. Except for very small α , the difference between the two curves is small. The curve for $\gamma = 0.1$ tends to infinity for small α , which is consistent with Griffith theory. However, this difference is practically inconsequential, for it only happens for a notch smaller than fiber diameter. Corresponding plots have been made for the linear bridging law and for a circular hole (not shown here); the trend is similar to Fig. 5. In the rest of the paper, we shall focus on the case $\Gamma_0 / \sigma_0 \delta_0 = 0$.

5. BRIDGING LAW SHAPE

The shape of the bridging law is uncertain in practice. Fortunately, load-carrying capacity is a robust quantity: a different χ only modifies it slightly, not to affect the judgement of a designer (e.g., notch-brittle or -ductile). Figure 7 demonstrates this for a sharp notch in an infinite

panel, and Fig. 8 for a circular hole. On the basis of the preceding discussion, it is sufficient to consider the case $\Gamma_0 / \sigma_0 \delta_0 = 0$, so that the inelastic band has extended across the component for bridging laws with nonvanishing complementary energy. The curves in Figs. 7 and 8 may shift somewhat as more accurate calculations become available, but the small difference in load-carrying capacity for the various bridging laws may be inconsequential in practice. An explanation for such small differences follows.

Instead of α , a modified dimensionless group, $a / (E' \Gamma / \sigma_0^2)$, is used in Fig. 7, where Γ is the energy to separate a unit area of the inelastic band:

$$\Gamma = \sigma_0 \delta_0 \int_0^\infty \chi(\epsilon) d\epsilon. \quad (26)$$

As discussed in Section 3, the inelastic band may consist of several matrix cracks, each permitting fibers to slide, so that δ_0 should be regarded as the sum of all inelastic deformation.

Two limiting cases can be solved analytically; both are independent of bridging law shape. As $\alpha \rightarrow 0$, stress concentration is fully relieved—that is, $\bar{\sigma}_{\max} / \sigma_0 = 1$. As $\alpha \rightarrow \infty$, the unbridged crack is long so that Griffith's formula applies:

$$\bar{\sigma}_{\max} / \sigma_0 = \left[\pi a / (E' \Gamma / \sigma_0^2) \right]^{-1/2}. \quad (27)$$

This curve is indicated in Fig. 7, which is only valid for large α . The mechanics problem involved here, which consists of two elastic substrates joined by springs (inset of Fig. 7), is different from that in Griffith's original paper. Nonetheless (27) can be confirmed by an energy argument. A simple interpolation of the two limiting cases is

$$\bar{\sigma}_{\max} / \sigma_0 = \left[1 + \pi a / (E' \Gamma / \sigma_0^2) \right]^{-1/2}. \quad (28)$$

This is a close approximation of the computed result for the linear law, and a fair representation of the curves for other laws. One can use this equation for arbitrary α , as an extrapolation of the Griffith formula (27).

Equation (28) can also be derived from an energy consideration. Under the applied load $\bar{\sigma}$, the springs are nonuniformly stretched: $\delta_{\text{tail}} > \bar{\delta}$, where $\bar{\delta}$ and $\bar{\sigma}$ are related by the spring law. In equilibrium, the increment of the combined strain energy in the substrates and springs

must vanish for any small increment of the notch size. Thus,

$$\sigma_0 \delta_0 \int_{\bar{\delta}/\delta_0}^{\delta_{tail}/\delta_0} \chi(\varepsilon) d\varepsilon \approx \pi a \bar{\sigma}^2 / E'. \quad (29)$$

The left-hand side is the energy decrease in the springs, and the right-hand side the energy increase in the substrates, for a unit enlargement of the notch under fixed load. The latter is approximate, with relaxation due to the springs ignored. Equation (29) becomes exact as $\alpha \rightarrow \infty$, which reduces to (27); and is also correct as $\alpha \rightarrow 0$, since $\delta_{tail} = \bar{\delta}$ in this case. Specializing (29) for the linear law $\chi(\varepsilon) = \varepsilon$, one obtains (28).

Plotted in Fig. 8 is the load-carrying capacity reduced by a circular hole, which is constructed by using finite element solutions, discussed in the Appendix. Note that the difference for various bridging laws is still small, and that the two limiting cases are given by (1).

Normalized as such, it appears from Figs. 7 and 8 that load-carrying capacity is insensitive to bridging law shape. We have not carried out comparisons other than for notches in an infinite panel. Nonetheless the normalization scheme used here separates the *rules of the shape* and the *scale* of a bridging law. This is of practical significance. Once charts are constructed for idealized bridging laws with important design features (e.g., fasteners), a new material can be used by fitting its bridging law to one of the idealized laws. This approach is equally valuable in design of composites. In this phase, the detailed bridging law shape may be unknown, but the scale of the bridging, σ_0 and δ_0 , can be related to microstructural variables. Whether a material is viable for a particular application can be assessed, before the material is made, by consulting the charts.

6. EFFECT OF a/w

The effect of finite panel width is studied with $\Gamma_0 / \sigma_0 \delta_0 = 0$. The model consists of halves joined by springs, with an unbridged sharp notch (Fig. 9) and a circular hole (Fig. 10). Independent of bridging law, full notch-ductility is reached when $a / (\Gamma E' / \sigma_0^2) = 0$. Stress concentration is completely relieved, so the load-carrying capacity is governed by the net-section:

$$\bar{\sigma}_{max} / \sigma_0 = 1 - a / w. \quad (30)$$

This is the straight line in Figs. 9 and 10.

Notch-brittleness prevails for large $a / (\Gamma E' / \sigma_0^2)$. In this limit, Linear Elastic Fracture Mechanics applies for a sharp notch, regardless of the bridging law shape. Thus,

$$\frac{\bar{\sigma}_{\max}}{\sigma_0} = \left[\pi F^2 \frac{a}{\Gamma E' / \sigma_0^2} \right]^{-1/2} \quad (31)$$

where F is a dimensionless number in the stress intensity factor for a crack in an elastic strip, approximated by (Tada *et al.* 1985)

$$F(a/w) = \left[1 - 0.5(a/w) + 0.326(a/w)^2 \right] \left[1 - (a/w) \right]^{-1/2} \quad (32)$$

An interpolation similar to (28) is

$$\frac{\bar{\sigma}_{\max}}{\sigma_0} = \left[\left(1 - \frac{a}{w} \right)^{-2} + \pi F^2 \frac{a}{\Gamma E' / \sigma_0^2} \right]^{-1/2} \quad (33)$$

This equation is plotted in Fig. 9, and expected to be a fair approximation for the entire parameter range and arbitrary bridging law, and highly accurate when $a / (\Gamma E' / \sigma_0^2) > 2$, as inferred from Fig. 7.

For a circular hole, when $a / (\Gamma E' / \sigma_0^2)$ is large, load-carrying capacity is reduced by the stress concentration factor k , namely

$$\bar{\sigma}_{\max} / \sigma_0 = 1 / k \quad (34)$$

The handbook solution (e.g. Peterson 1974) of the stress concentration factor for a circular hole in an elastic strip, k , is indicated in Fig. 10, as the boundary of notch-brittleness. A finite element calculation using linear springs is carried out for intermediate $a / (\Gamma E' / \sigma_0^2)$. Linearity suggests that the stress at the band-tail takes the form

$$\sigma_{\text{tail}} = \bar{\sigma} f(\alpha, a/w) \quad (35)$$

The applied load $\bar{\sigma} \rightarrow \bar{\sigma}_{\max}$ when $\sigma_{\text{tail}} = \sigma_0$, so that $\bar{\sigma}_{\max} / \sigma_0 = 1 / f$. The calculated coefficient f is plotted in Fig. 10. Judged from Fig. 8, the curves in Fig. 10 should be fair approximations for other bridging laws.

7. CONCLUDING REMARKS

Notch-sensitivity can be substantially reduced by inelastic deformation. In a ceramic-matrix composite, the inelastic deformation is due to one or several matrix cracks bridged by frictionally

sliding fibers. The strength of notched ceramic-matrix composites is found to depend on notch size, as governed by a dimensionless group $a / (\delta_0 E' / \sigma_0)$. Notch-insensitivity is attained if the composite is made such that $a / (\delta_0 E' / \sigma_0) \leq 1$. It is found that the shape of the bridging law is unimportant as far as notch strength is concerned. Although the results are interpreted for ceramic-matrix composites, they may be applicable for other materials or inelastic mechanisms. For example, the notch strength presented here is the same as the residual strength of a metal-matrix composite with a fatigue-cracked matrix.

Acknowledgement—We are grateful to Professor B. Budiansky for a stimulating conversation, and to Professors A.G. Evans, F.A. Leckie and F.W. Zok for inspiration. Financial support is provided by ONR/URI contract N00014-86-K-0753. Finite element analyses are carried out using ABAQUS.

REFERENCE

- Aveston, J., Cooper, G.A., and Kelly, A., 1971, "Single and Multiple Fracture," in *The Properties of Fiber Composites*, IPC Science and Technology Press, UK.
- Bao, G. and McMeeking, R.M., 1992, "Fatigue Crack Growth in Fiber-Reinforced Metal-Matrix Composites," *J. Mech. Phys. Solids*. In press.
- Bao, G. and Suo, Z., 1992, "Remarks of Crack-Bridging Concepts," *Appl. Mech. Rev.* Vol. 24, pp. 355-366.
- Barenblatt, G.I., 1962, "The Mathematical Theory of Equilibrium Cracks in Brittle Fracture," *Adv. Appl. Mech.* Vol 7, pp. 55-129.
- Bilby, B.A., Cottrell, A.H., and Swinden, K.H., 1963, "The Spread of Plastic Yielding from a Notch," *Proc. Roy. Soc. Lond.* Vol. A272, pp. 304-314.
- Budiansky, B., Hutchinson, J.W., and Evans, A.G., 1986, "Matrix Fracture in Fiber-Reinforced Ceramics," *J. Mech. Phys. Solids* Vol. 34, pp. 167-189.

- Cottrell, A.H., 1963, "Mechanics of Fracture," in *Tewksbury Symposium on Fracture*, pp. 1-27.
University of Melbourne, Australia.
- Cui, L. and Budiansky, B., 1992, private communication.
- Dugdale, D.S., 1960, "Yielding of Steel Sheets Containing Slits," *J. Mech. Phys. Solids* Vol. 8, pp. 100-104.
- Gu, P., Shih, C.F. and Suo, Z., 1992, manuscript in preparation.
- Huang, Y. and Hutchinson, J.W., 1989, "A Model Study of the Role of Nonuniform Defect Distribution on Plastic Shear Localization," in *Role of Modeling in Materials Design*, ed. J.D. Embury, AIME.
- Hutchinson, J.W. and Jensen, H.M., 1990, "Models of Fiber Debonding and Pullout in Brittle Composites with Friction," *Mech. Mater.* Vol. 9, pp. 139-163.
- Marshall, D.B., Cox, B.N., and Evans, A.G., 1985, "The Mechanics of Matrix Cracking in Brittle Matrix Composites," *Acta Metall.* Vol. 33, pp. 2013-2021.
- Marshall, D.B. and Cox, B.N., 1987, "Tensile Fracture of Brittle Matrix Composites: Influence of Fiber Strength," *Acta Metall.* Vol. 35, pp. 2607-2619.
- Needleman, A., 1990, "An Analysis of Tensile Decohesion along an Interface," *J. Mech. Phys. Solids* Vol. 38, pp. 289-324.
- Peterson, R.E., 1974, *Stress Concentration Factors*, John Wiley, New York.
- Rice, J.R., 1976, "The Localization of Plastic Deformation," *Proc. 14th IUTAM Congress.* pp. 207-220.
- Rice, J.R., 1992, "Dislocation Nucleation from a Crack Tip: an Analysis based on the Peierls Concept," *J. Mech. Phys. Solids* Vol. 40, pp. 239-271.
- Rose, L.R.F., 1987, "Crack Reinforcement by Distributed Springs," *J. Mech. Phys. Solids* Vol. 35, pp. 383-405.
- Soutis, C. Fleck, N.A., and Smith, P.A., 1991, "Failure Prediction Technique for Compression Loaded Carbon Fiber-Epoxy Laminate with Open Hole," *J. Composite Materials*, Vol. 25,

pp. 1476-.

- Suo, Z., 1991, "Mechanics Concepts for Failure in Ferroelectric Ceramics," in *Smart Structures and Materials*, ed. A.V. Srinivasan. p. 1-6. ASME, New York.
- Suo, Z., Bao, G. and Fan, B., 1992a, "Delamination R-Curve Phenomena due to Damage." *J. Mech. Phys. Solids* Vol. 40, pp. 1-16.
- Suo, Z., Ortiz, M., and Needleman, A., 1992b, "Stability of Solids with Interfaces," *J. Mech. Phys. Solids* Vol. 40, pp. 613-640.
- Tada, H., Paris, P.C., and Irwin, G.R., 1985, *The Stress Analysis of Cracks Handbook*, Del Research, St. Louis, MO.
- Zok, F.W. and Spearing, S.M., 1992, "Matrix Crack Spacing in Brittle Matrix Composites," *Acta Met. Mater.* Vol. 40, pp. 2033-2043.

APPENDIX

Representative bridging laws are drawn in Fig. 2. Solutions for a hole/crack in an infinite body are reviewed here. For the *rectilinear law*, the solution is linear in both the applied stress and the closure-stress, so that

$$\delta_{\text{tail}} E' / a = f_1 \bar{\sigma} - f_2 \sigma_0, \quad (\text{A1})$$

and

$$K_{\text{tip}} / \sqrt{a} = f_3 \bar{\sigma} - f_4 \sigma_0, \quad (\text{A2})$$

with coefficients f_s depending on L/a only. For a crack-like notch the solution is (Tada *et al.* 1985)

$$\frac{\delta_{\text{tail}} E'}{\sigma_0 a} = 4(\eta^2 - 1)^{1/2} \left[\frac{\bar{\sigma}}{\sigma_0} - \frac{2}{\pi} \cos^{-1}(1/\eta) \right] + \frac{8}{\pi} \ln \eta, \quad (\text{A3})$$

and

$$\frac{K_{\text{tip}}}{\sigma_0 \sqrt{\pi a}} = \eta^{1/2} \left[\frac{\bar{\sigma}}{\sigma_0} - \frac{2}{\pi} \cos^{-1}(1/\eta) \right], \quad (\text{A4})$$

where $\eta = 1 + L/a$. Coefficients for a circular hole are obtained by using finite elements (Ho 1992).

The *square-root law* is written

$$\sigma / \sigma_0 = (\delta / \delta_0)^{1/2}. \quad (\text{A5})$$

The solutions take the forms (e.g., Gu *et al.* 1992)

$$\sigma_{\text{tail}} / \alpha \sigma_0 = \Sigma(\bar{\sigma} / \alpha \sigma_0, L/a), \quad (\text{A6})$$

with σ_{tail} being connected to δ_{tail} by the bridging law, and

$$K_{\text{tip}} / \alpha \sigma_0 \sqrt{a} = \kappa(\bar{\sigma} / \alpha \sigma_0, L/a). \quad (\text{A7})$$

Solutions for a crack-like notch are given by Marshall and Cox (1987), Bao and McMeeking (1992), and Cui and Budiansky (1992). Solutions for elliptic holes are given by Gu *et al.* (1992).

The *linear law* is written

$$\sigma / \sigma_0 = \delta / \delta_0, \quad (\text{A8})$$

The coupled spring-substrate is linear, so that

$$\sigma_{\text{tail}} / \bar{\sigma} = g_1(\alpha, L/a), \quad (\text{A9})$$

and

$$K_{up} / \bar{\sigma} \sqrt{\pi a} = g_2(\alpha, L/a). \quad (A10)$$

Solutions for a crack-like notch are given by Rose (1987), and for elliptical holes by Gu *et al.* (1992).

The *linear softening* is an idealization of the following situation. Some bridging mechanisms, notably ductile reinforcement, attain the limiting stress at a very small stretch, and the stress then drops with a long tail. The initial rising portion may be conveniently lumped into Γ_0 , leaving the post-limit tail idealized to be linear softening. The bridging law is thus

$$\sigma / \sigma_0 = 1 - \delta / \delta_0. \quad (A11)$$

The reward for such a simplification is that the limiting-stress, σ_0 , can be treated as a residual stress, so that the coupled substrate-spring becomes linear, which can be solved by using commercial finite element codes (e.g. Suo *et al.* 1992a). The solution is still of form (A1) and (A2), but now the coefficients depend on both α and L/a .

FIGURE CAPTIONS

- Fig. 1 An inelastic band is viewed as either a bridged crack or an array of continuously distributed dislocations.
- Fig. 2 Idealized bridging laws.
- Fig. 3 Damage progression in ceramic-matrix composites.
- Fig. 4 Multiple cracks modeled as an inelastic band.
- Fig. 5 Effect of the two primary dimensionless groups.
- Fig. 6 Relation between load and tail-separation (rectilinear bridging).
- Fig. 7 Notch ductile-to-brittle transition (sharp notch).
- Fig. 8 Notch ductile-to-brittle transition (circular hole).
- Fig. 9 Effect of a/w (sharp notch).
- Fig. 10 Effect of a/w (circular hole).

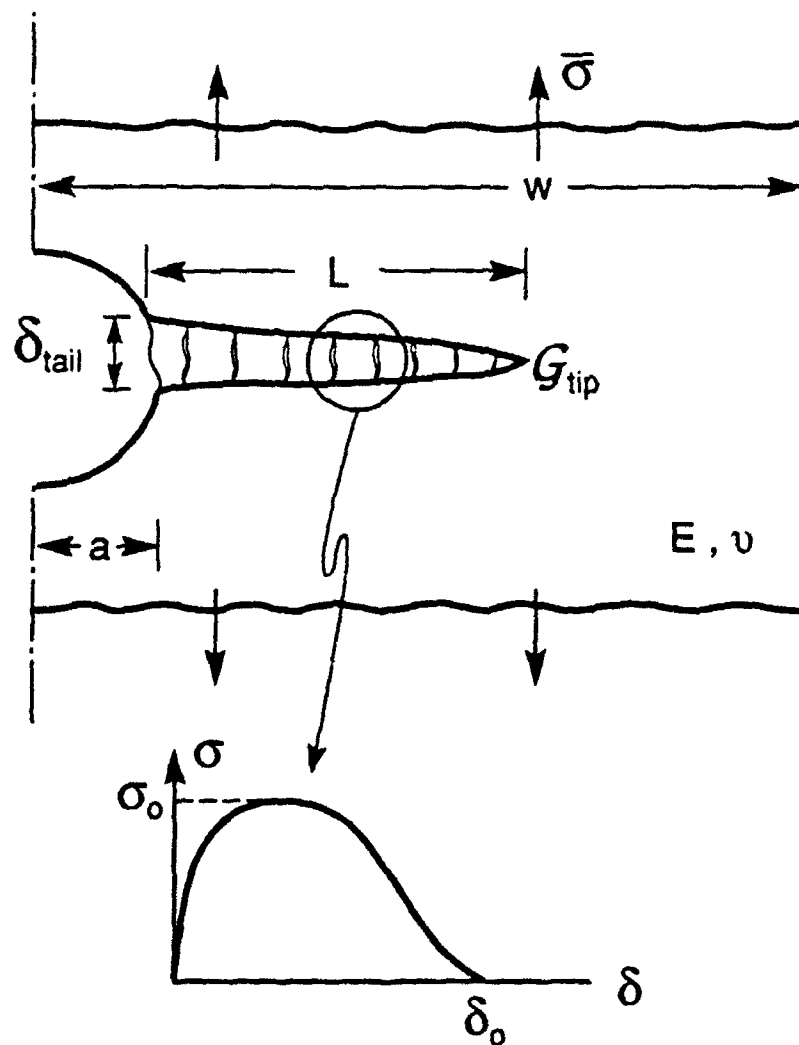


Fig. 1

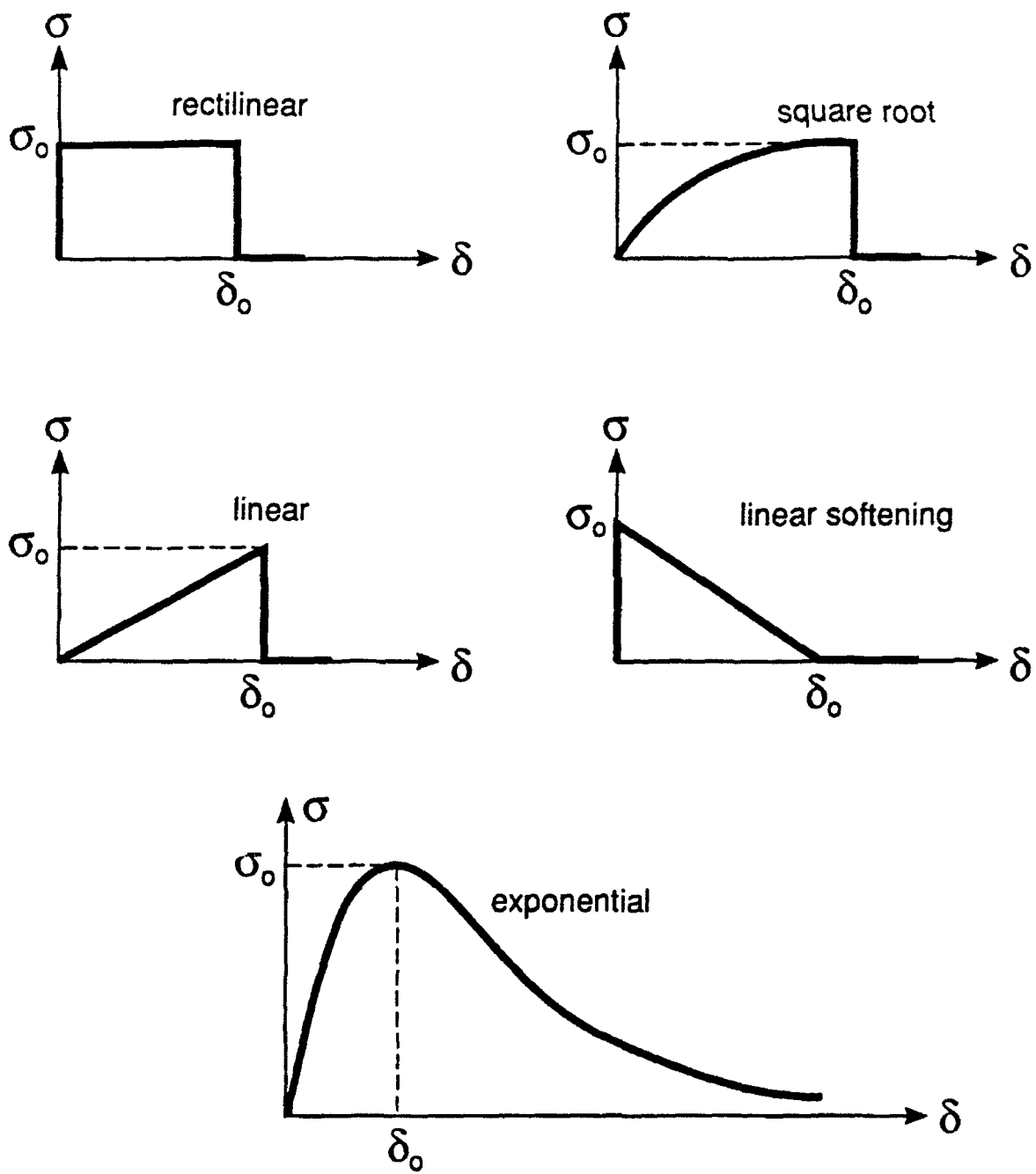


Fig. 2

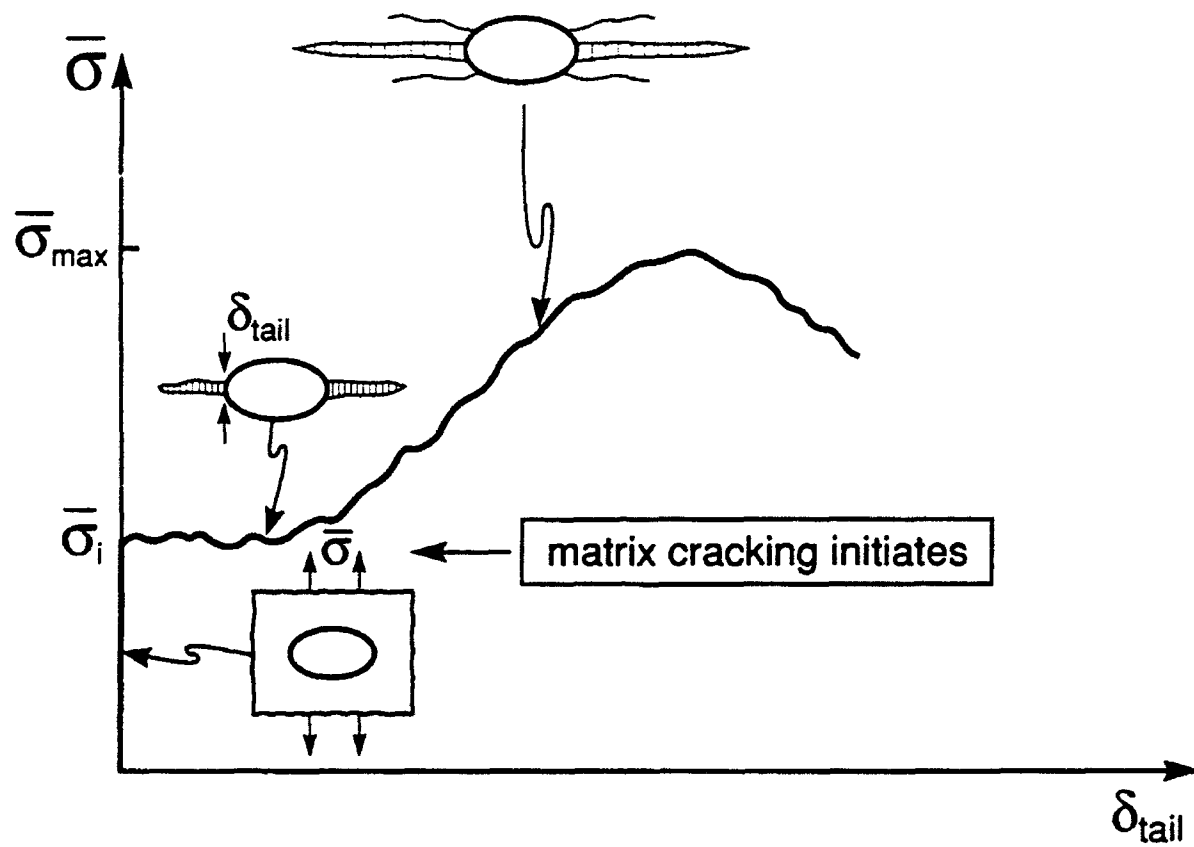


Fig. 3

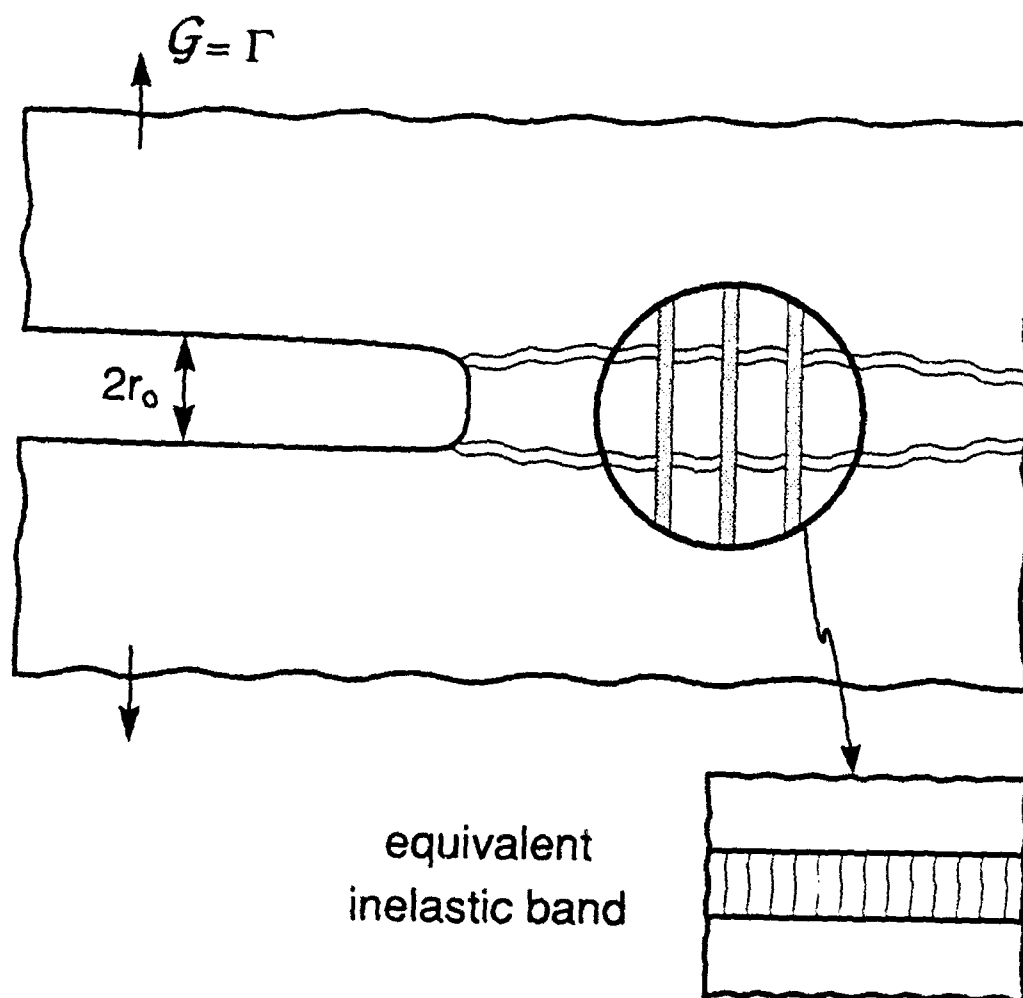


Fig. 4

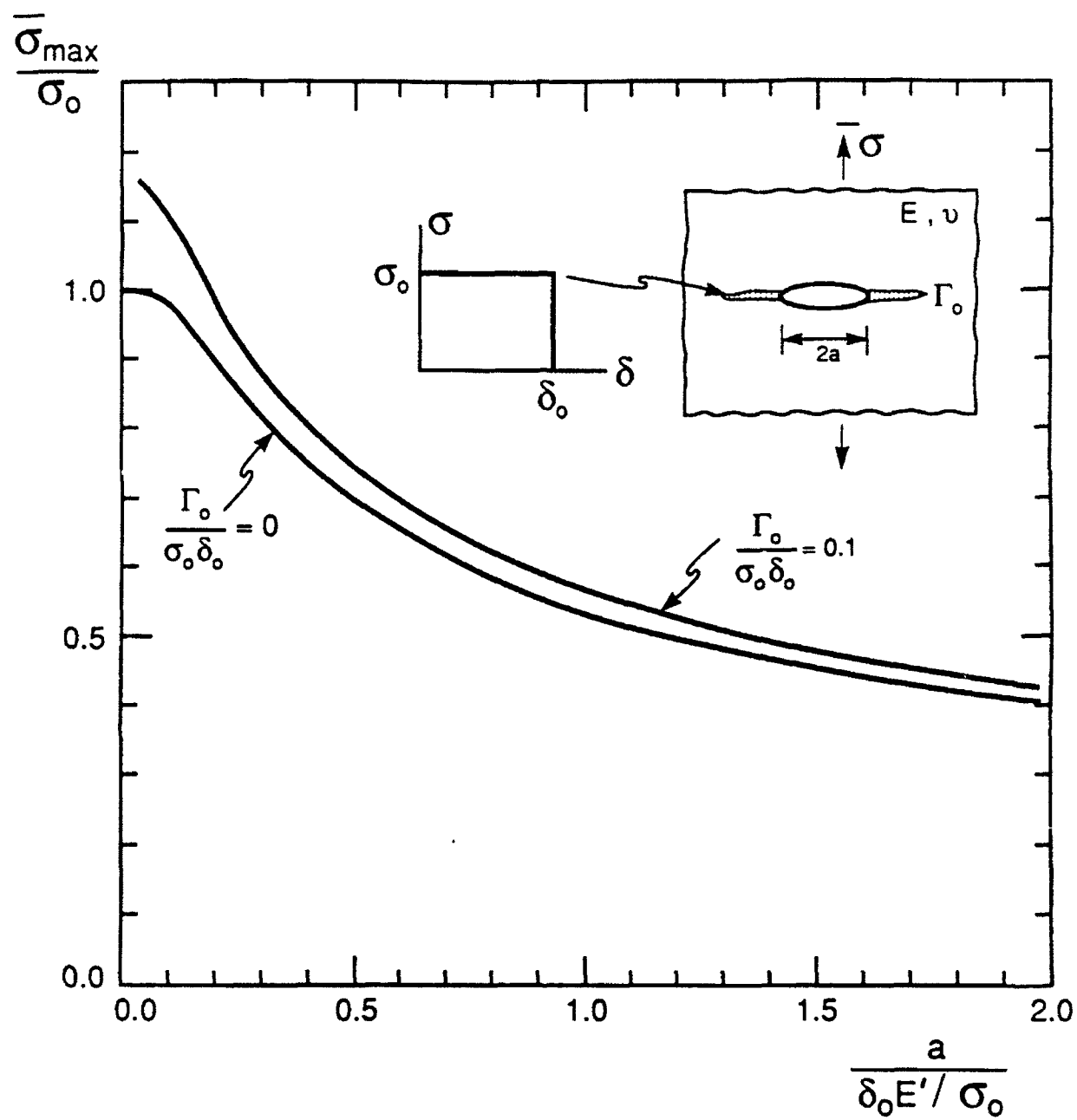


Fig. 5

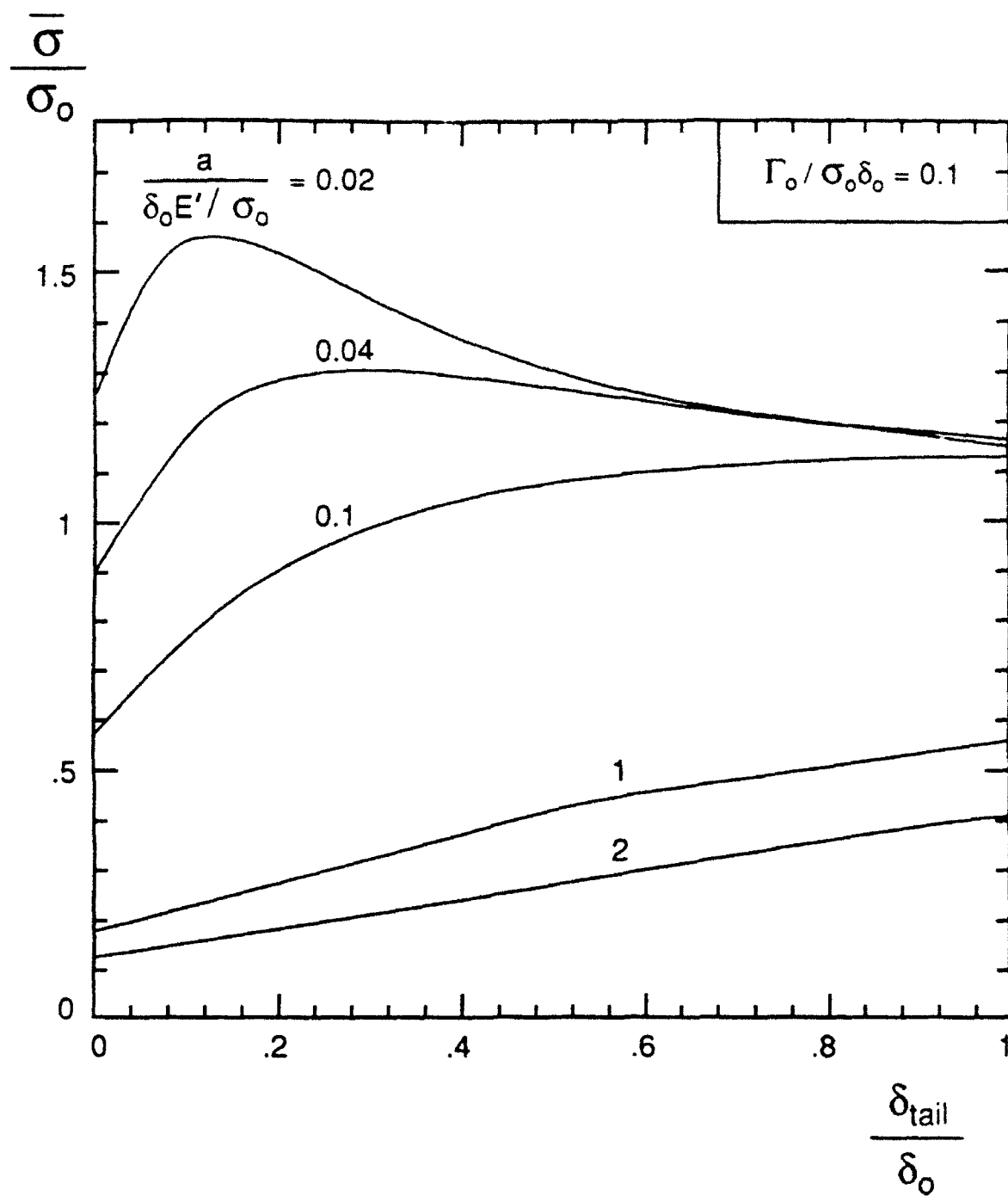


Fig. 6

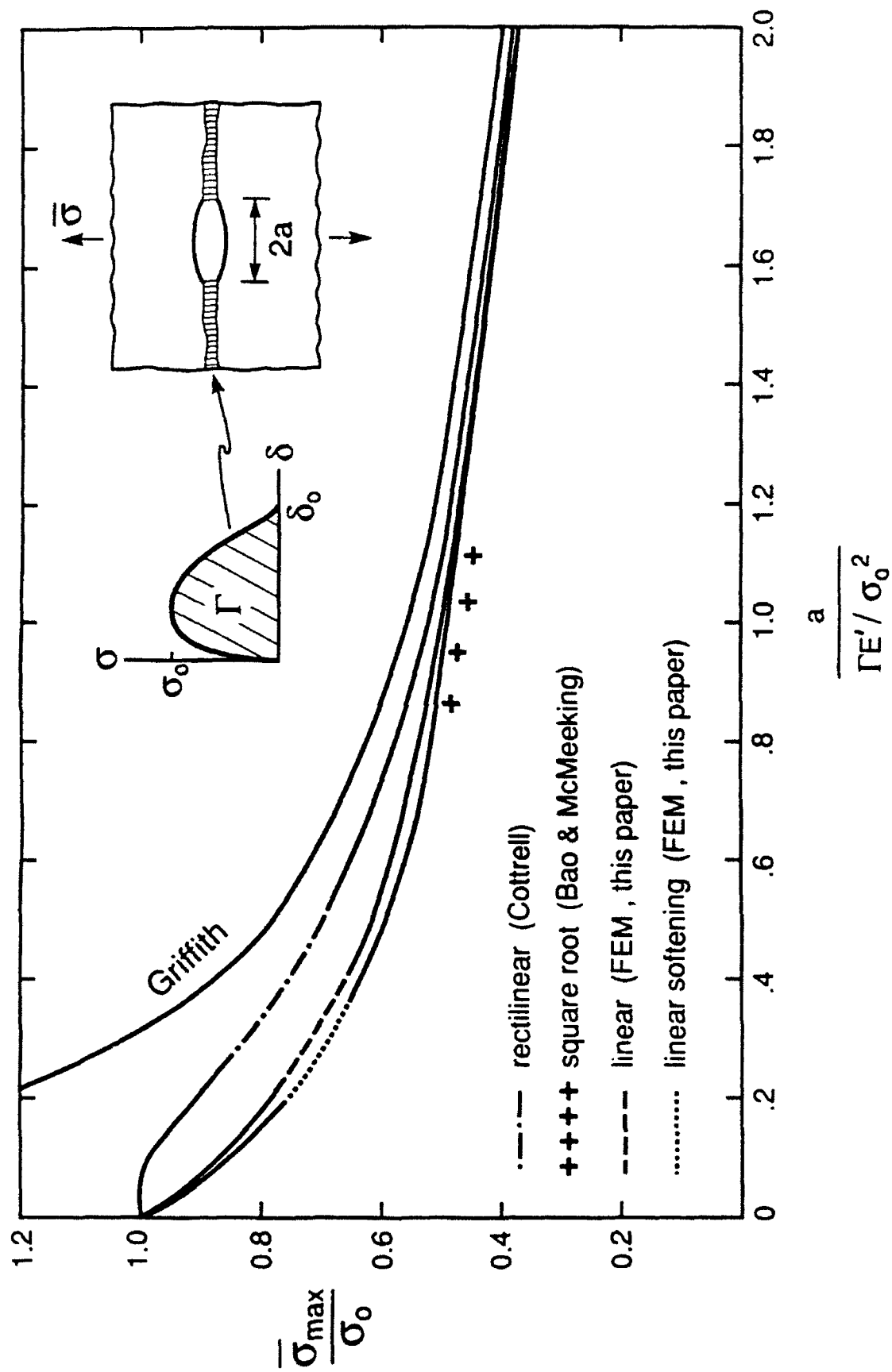


Fig. 7

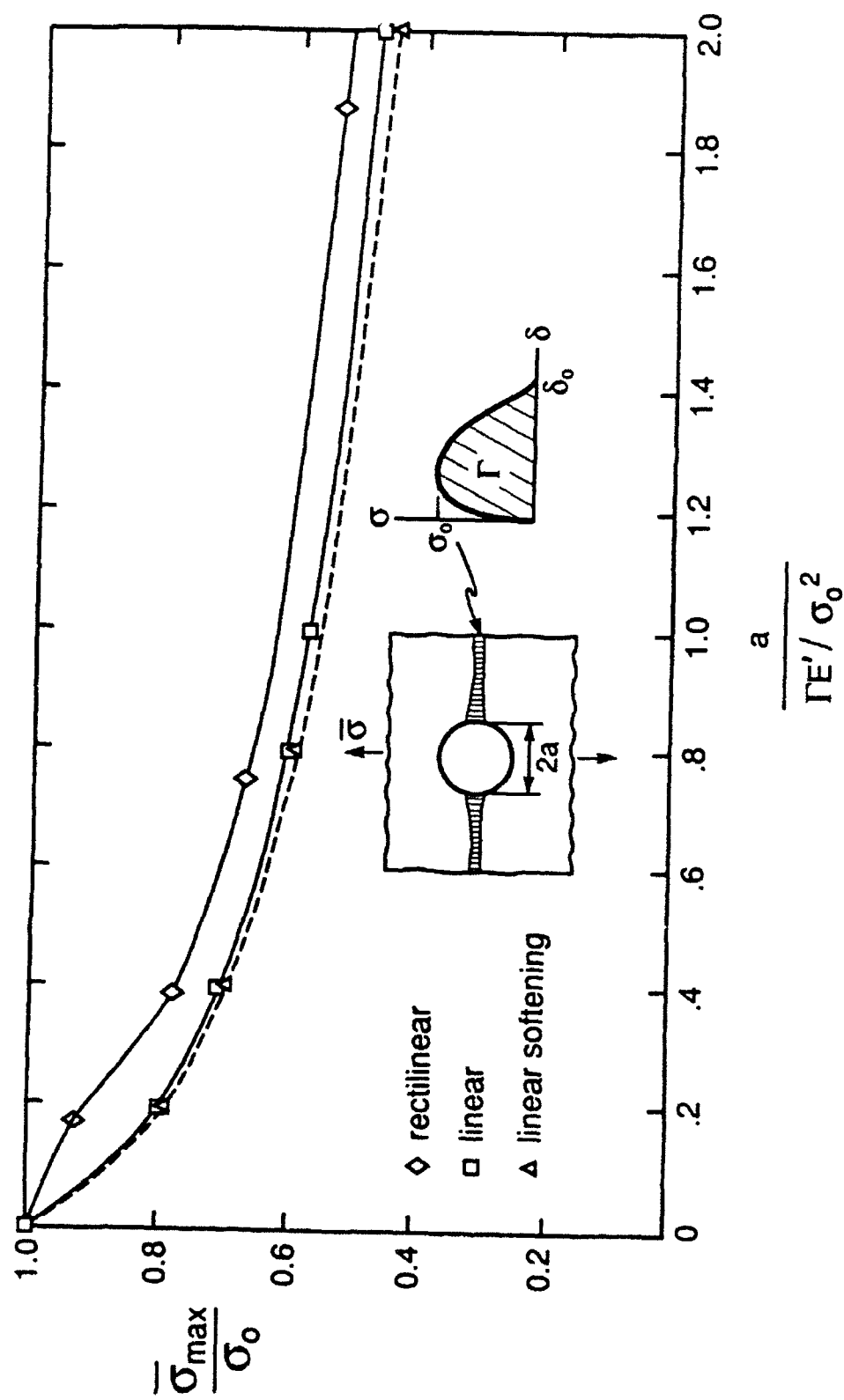


Fig. 8

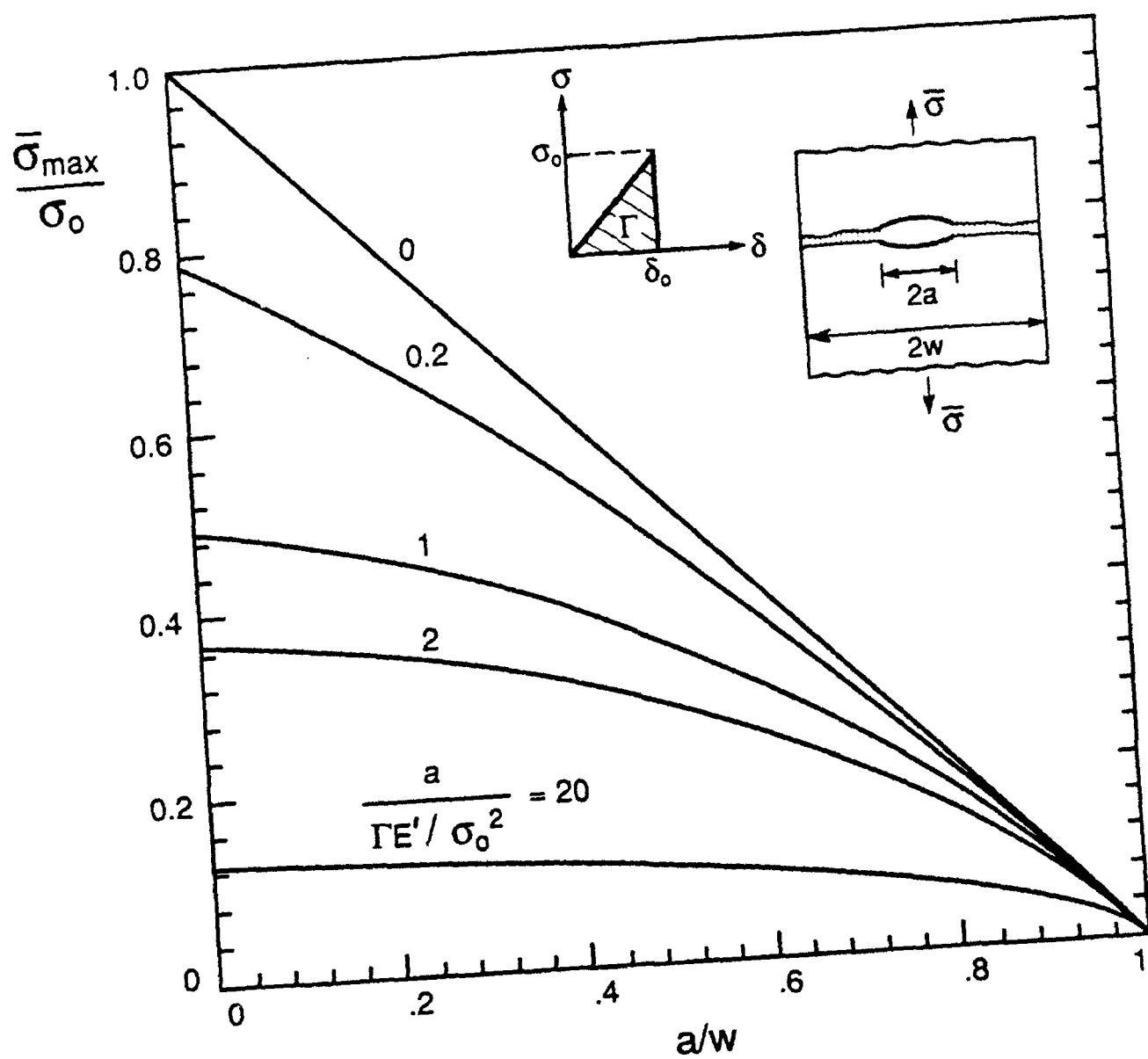


Figure 9

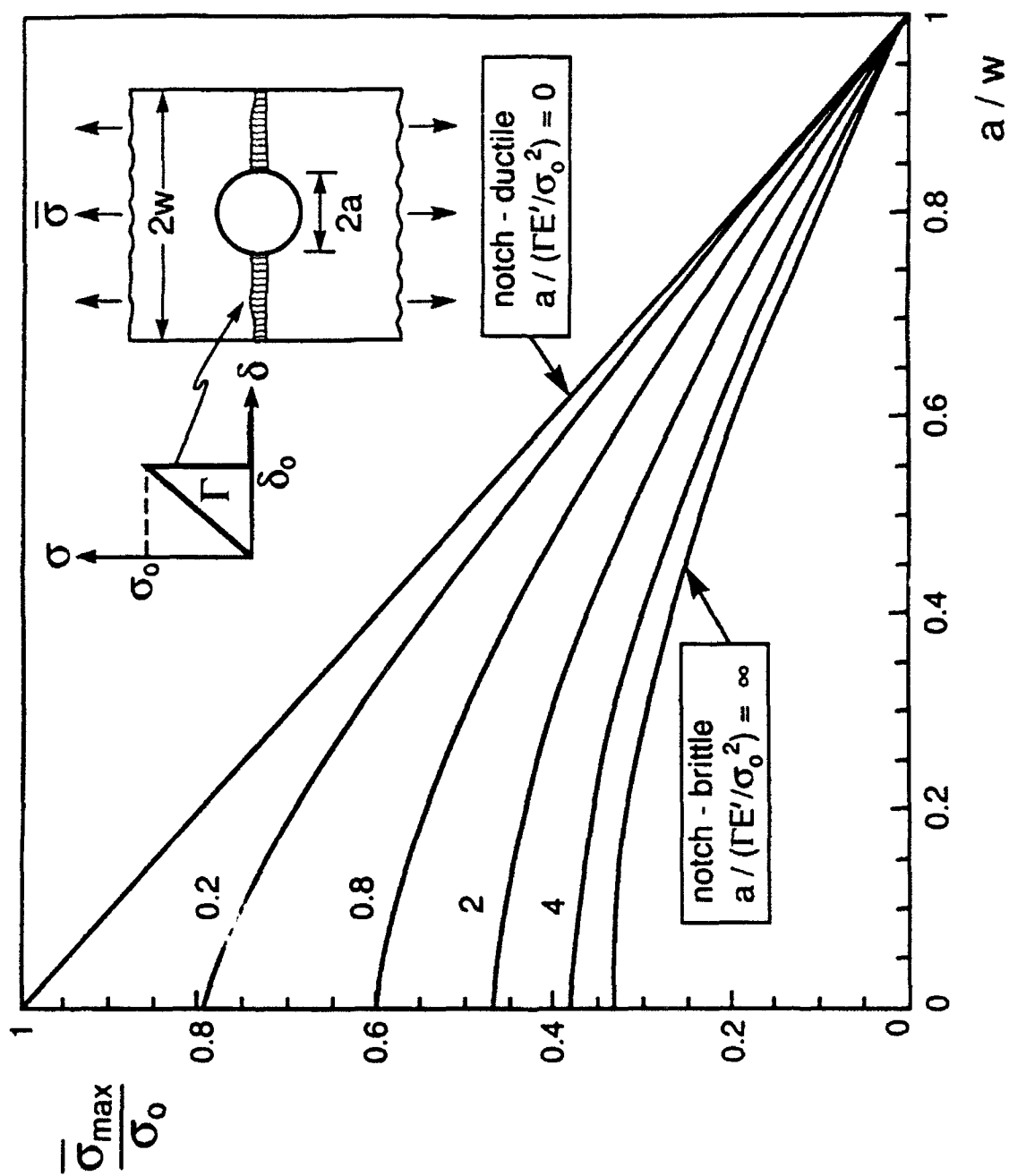


Fig. 10



MECH-209

ON THE TENSILE STRENGTH OF A FIBER-REINFORCED CERAMIC COMPOSITE
CONTAINING A CRACK-LIKE FLAW

Bernard Budiansky and Yingqing Lawrence Cui

Division of Applied Sciences
HARVARD UNIVERSITY
Cambridge, Massachusetts 02138

April 1993

ON THE TENSILE STRENGTH OF A FIBER-REINFORCED CERAMIC COMPOSITE CONTAINING A CRACK-LIKE FLAW

Bernard Budiansky and Yingqing Lawrence Cui

Division of Applied Sciences

Harvard University

Cambridge, MA 02138

ABSTRACT

The tensile strength of a fiber reinforced ceramic composite containing a through-the-fiber flaw in the form of a sharp crack is studied. The strength of a brittle unreinforced ceramic containing a sharp crack of length $2a_0$, subjected to uniaxial load in the direction normal to the crack plane, is given by linear elastic fracture mechanics as $\sigma_s = K_m / \sqrt{\pi a_0}$, where K_m is the fracture toughness of the material. However, for a fiber reinforced ceramic, the strength can only be determined on the basis of a full analysis of crack growth in the matrix and the failure of crack bridging fibers. The tensile strength of a flawed ceramic material that is reinforced by fibers aligned in the direction perpendicular to the flaw surfaces is studied in this paper. Crack bridging fibers are assumed to slip relative to the matrix when a critical interface shear stress is reached. The orthotropy of the composite produced by the presence of aligned fibers is rigorously accounted for in the analysis. The dependence of the composite tensile strength on fiber tensile strength, matrix toughness, flaw-size, and frictional shear stress at the fiber-matrix interface is determined and described in terms of a universal set of non-dimensional parameters.

NOMENCLATURE

$2a_0$	initial crack size
c_f	fiber volume concentration
A	orthotropy factor (see Eq. (1))
K_m	matrix toughness
E, E_f, E_m	Young's moduli (composite, fiber, matrix)
R	fiber radius
S	fiber strength
ν, ν_f, ν_m	Poisson's ratio (composite, fiber, matrix)
τ	fiber-matrix sliding shear resistance
σ_0	matrix cracking-initiation stress
σ_{mc}	steady-state matrix cracking stress
$c_f S$	base fibers-only strength

Λ	modified toughening ratio (see Eq. (14))
σ_s	tensile strength of flawed composite

INTRODUCTION

This paper is concerned with the tensile strength of flawed, fiber-reinforced ceramics. On the basis of linear elastic fracture mechanics, an unreinforced brittle ceramic containing a sharp, two-dimensional flaw of length $2a_0$, loaded in the direction perpendicular to the faces of the flaw, has a tensile strength given by $\sigma_s = K_m / \sqrt{\pi a_0}$, where K_m is the fracture toughness of the material. However, the tensile strength of a fiber reinforced ceramic can only be determined by a full analysis of a process involving matrix crack growth, frictional sliding along the fiber-matrix interfaces, and failure of crack bridging fibers. We shall study the configuration shown in Fig. 1, in which a large, aligned-fiber reinforced ceramic body containing an isolated center flaw of length $2a_0$ that cuts through the fibers is subjected to uniform remote tension in the fiber direction. We define the tensile strength as the maximum applied stress the composite can carry, and seek to determine this stress theoretically.

As in most previous studies the fibers are assumed to be held in the matrix by friction; that is, sliding between the fibers and the matrix is suppressed only if the interface frictional shear is less than some limiting stress τ . The brittle ceramic matrix is assumed to have a fracture toughness K_m , and, except near the tip of the matrix crack, the composite is treated as a homogeneous orthotropic elastic medium. The effects of crack bridging fibers are taken into account by means of a spring model that embodies the additional assumption that the frictional resistance is low enough to permit long slip lengths relative to the fiber diameter. Failure of the composite is assumed to be associated with the fracture of crack-bridging fibers in the matrix crack plane and we assume that there is no statistical variation in fiber strength. It is further assumed that during the course of matrix crack extension leading to the final failure of the composite, no longitudinal splitting or shear banding takes place in the vicinity of the flaw tip. Both splitting and statistical variation in fiber strength may often be important, but we neglect them in the present study.

The mechanical behavior of both flawed and unflawed unidirectional fibrous composites has been a subject of research efforts for the past two decades. Matrix cracking without associated fiber failure is a distinctive tensile damage mechanism often observed in unidirectional fibrous ceramic composites. The tensile stress required for the steady-state propagation of a single, long matrix crack, known as the matrix cracking stress, was first evaluated by Aveston et al. (1971) for the limits of large and small frictional shear resistance at the fiber-matrix interfaces. More recently, Budiansky et al. (1986) extended these results to intermediate friction values. For the limiting case of very long, initial flaws, the solution for tensile strength has been obtained by Budiansky and Amazigo (1989) on the basis of the *small scale bridging* condition, wherein (see Fig. 2) the bridge

length Δa prior to fiber failure is very small relative to original flaw length $2a_0$. Although Marshall and Cox (1987) have done extensive calculations for a composite with a flaw of arbitrary length, their presentation is quite complicated and it is difficult to extract the desired general, comprehensive results for the composite tensile strength from their paper.

There are many parameters governing the tensile failure of unidirectional composites, such as fiber tensile strength, matrix toughness, flaw-size, fiber and matrix elastic properties, and fiber-matrix frictional shear stress. We shall, however, be able to determine the composite strength σ_c in terms of just the following three basic stress quantities that suffice to characterize the flawed composite:

- σ_0 , the critical applied stress for the initiation of matrix cracking;
- σ_{mc} , the steady-state matrix-cracking stress; and
- $\sigma_{fs} = c_f S$, the base fibers-only strength,

where S is the fiber fracture stress and c_f is the fiber volume concentration. More precisely, the ratio of σ_c to any one of these stresses depends on only *two* ratios of the three parameters. We start with a qualitative description of the matrix crack growth process that leads to failure of a flawed, unidirectional fiber composite.

DESCRIPTION OF FAILURE PROCESS

When a tensile stress σ is applied to the composite in the fiber direction (Fig. 1), failure due to a preexisting, through-the-fibers flaw that is normal to the fibers always begins with growth of the crack in the matrix (Fig. 2), and ends with the fracture of bridging fibers. Consider a typical curve of applied stress σ vs. matrix crack growth Δa , shown schematically in Fig. 3. Such a curve would be governed by the requirement that the average energy release rate along the matrix crack front must remain equal to the critical value for matrix crack extension. In the absence of fiber failure, a typical $\sigma - \Delta a$ curve has the following qualitative features. Crack growth starts when the applied stress σ reaches the initiation stress σ_0 , which is essentially a crack-size parameter. Due to the constraining effects of crack-bridging fibers, matrix crack growth requires increasing applied stress σ until a peak value σ_p is reached at $\Delta a = \Delta a_p$. Then the crack growth continues under decreasing applied σ , which approaches the steady-state matrix cracking stress σ_{mc} asymptotically for $\Delta a \rightarrow \infty$. (It is also conceivable that for sufficiently small values of the initiation stress σ_0 , the applied stress σ may never reach a peak value at a finite Δa , but simply increases monotonically as it approaches the steady-state matrix-cracking stress σ_{mc} asymptotically.) After the matrix crack extends to infinity, the applied loading is supported entirely by the crack-bridging fibers, and the vertical line at $\Delta a = \infty$ indicates that further increase in σ is then possible.

Now consider fiber failure. Corresponding to each point on the $\sigma - \Delta a$ curve, there is a smeared-out bridging stress distribution $p(x)$ that has its maximum value $p(a_0)$ at the *original* flaw tip. Let Δa_f denote the amount of matrix crack growth corresponding to the first-fiber-failure criterion $p(a_0) = c_f S$, and, if $\Delta a_f < \infty$, let σ_f be the value of the associated applied load. Similarly, for the composite containing a matrix crack that has grown to infinity from each edge of the original flaw (Fig. 4), let σ_{fmc} denote the value of the applied stress σ that gives $p(a_0) = c_f S$. In both cases, we find that maintaining the applied load σ at the value that produces the first fiber failure results in the failure on the matrix crack plane of all the fibers. Accordingly, the strength σ_s of the composite is set by one of the following three conditions:

- (i) the flaw-tip fibers fail during *increasing* applied stress at a value of applied stress $\sigma_f < \sigma_p$ and $\Delta a_f < \Delta a_p$; then $\sigma_s = \sigma_f$;
- (ii) the applied stress reaches the peak value σ_p without the occurrence of fiber failure, and σ_p exceeds the value of the stress σ_{fmc} needed to produce flaw-tip fiber failure when the crack is infinitely long; then $\sigma_s = \sigma_p$;
- (iii) the matrix crack extends to infinity without fiber failure, and σ_p is less than σ_{fmc} ; then $\sigma_s = \sigma_{fmc}$.

A complete determination of the strength of flawed composites will therefore require consideration of both the transient crack-growth problem of Fig. 2 and the auxiliary problem of the fully cracked composite shown in Fig. 4.

MATRIX CRACKING: INITIATION, GROWTH, AND STEADY-STATE

Crack growth criterion

We shall now discuss an appropriate criterion for matrix crack growth in an aligned-fiber composite (Fig 1). What we seek is a criterion based on the stress-intensity factor of a crack, bridged or unbridged, in an equivalent, uniform, orthotropic (but transversely isotropic) material (Fig. 2). Consider the plane-strain energy release rate \mathcal{G} for a Mode-I crack lying in the plane of transverse isotropy. We can write

$$\mathcal{G} = \frac{1 - \nu^2}{AE} K_I^2 \quad (1)$$

where K_I is the conventional stress-intensity factor, E is the Young's modulus for longitudinal tension normal to the crack plane, ν is the associated Poisson's ratio (for the ratio of transverse contraction to longitudinal extension), and A is a factor that characterizes the orthotropy. We will assume that matrix crack growth occurs when the orthotropic energy release rate \mathcal{G} , given by (1), satisfies the condition

$$\mathcal{G} = (1 - c_f) \mathcal{G}_m \quad (2)$$

where \mathcal{G}_m is the critical energy release rate for fracture in the *matrix*, given by

$$G_m = \frac{1 - \nu_m^2}{E_m} K_m^2 \quad (3)$$

in terms of the elastic constants of the matrix and its fracture toughness K_m . The factor $(1 - c_f)$ accounts for the reduction in length of the edge of the matrix crack due to the presence of the aligned fibers. It follows that the critical orthotropic stress intensity factor K_{IC} for matrix cracking in the direction perpendicular to the direction of fibers in unidirectional fibrous ceramic composites is

$$K_{IC} = \sqrt{\frac{AE(1 - \nu_m^2)}{E_m(1 - \nu^2)}} (1 - c_f) K_m \quad (4)$$

The magnitude of A as a function of the plane-strain compliances of an orthotropic material follows from the formula given by Tada et al (1985) for the energy release rate (see Appendix A). If we let E , E_f , and E_m be the Young's moduli of the composite, fiber, and matrix, respectively, and if we assume, for the sake of simplicity, that fibers and matrix have the same Poisson's ratio $\nu_f = \nu_m = \nu$, then E is given by the rule of mixtures formula $E = c_f E_f + (1 - c_f) E_m$. The dependence of A on E_f/E_m and c_f for $\nu_f = \nu_m = 1/4$ has been calculated on the basis of the Hill (1965) self-consistent estimates for the effective compliances of an aligned-fiber composite having isotropic constituents, and the results for A vs. c_f are plotted in Fig. 5a for various values of $E_f/E_m > 1$. (These curves, and the associated formulas shown in Appendix A, correct errors in the earlier work by Budiansky and Amazigo (1989)). Fig. 5b shows A for several values of $E_f/E_m < 1$.

It is important to note that the parameter K_{IC} is a material property of the composite which encompasses information about matrix toughness, fiber volume concentration, the orthotropy induced by unidirectional fiber reinforcement, and the moduli of the matrix and composites. In order to analyze the matrix cracking problem illustrated in Fig. 2, we will be calculating the orthotropic stress intensity factor K_I in the presence of both external loading and crack bridging fibers, and then using $K_I = K_{IC}$ as the criterion for matrix crack growth.

Matrix cracking initiation

For the special case of matrix cracking *initiation* in the configuration of Fig. 1, we can use the familiar formula $K_I = \sigma_0 \sqrt{\pi a_0}$, which is valid for any anisotropic as well as isotropic 2D elastic body (Sih et al., 1965). Setting $K_I = K_{IC}$ gives the matrix crack-growth initiation stress of the composite -- one of our three basic stress parameters -- as

$$\sigma_0 = K_{IC} / \sqrt{\pi a_0} \quad (5)$$

Thus σ_0 may be regarded as a crack-length parameter, decreasing like $a_0^{-1/2}$. Note too, that for $\nu_f = \nu_m = \nu$, the initiation stress σ_0 is related to the corresponding strength σ_{s0} of a unreinforced, cracked monolithic ceramic of the same crack geometry by

$$\sigma_0 = \sqrt{\frac{A(1-c_f)E}{E_m}} \sigma_{s0} \quad (6)$$

Matrix crack growth

Equations connecting the applied stress, the bridging-fiber stress distribution, and the matrix crack extension in the absence of fiber failure (Fig. 2) are presented in Appendix B. In this formulation the orthotropic stress-intensity factor is kept equal to K_{IC} , and the smeared-out bridging fiber stress $p(x)$ is related to the displacement $v(x)$ of the upper crack face (Fig. 2) by

$$p(x) = \beta \sqrt{v(x)} \quad (7)$$

where the equivalent spring constant β is given by

$$\beta = \left\{ \frac{4c_f^2 E_f E^2 \tau}{R(1-c_f)^2 E_m^2} \right\}^{\frac{1}{2}} \quad (8)$$

This relation follows from the assumption of "large" slip lengths adjacent to the crack faces and neglect of initial stresses (Aveston et al 1971; Budiansky et al 1986; Budiansky and Amazigo 1989; Hutchinson and Jensen 1991). Various non-dimensional forms of the governing equations and their numerical solution are discussed in detail in Appendix B.

Steady-state matrix cracking

As already mentioned, when the matrix crack extension becomes large, the applied stress σ approaches the steady-state matrix cracking stress of Aveston et al (1971). Under the assumptions adopted, the steady-state matrix cracking stress σ_{mc} is given by

$$\sigma_{mc} = \left[\frac{6c_f^2 (1-v_m^2) K_m^2 \tau E_f}{(1-c_f) R E} \right]^{\frac{1}{3}} \frac{E}{E_m} \quad (9)$$

where R is the fiber radius and τ is the interface slipping shear resistance stress. This is the second of the three basic stress parameters that define the composite; the third one, we remind the reader, is just $\sigma_{fs} = c_f S$.

MATRIX CRACK GROWTH AND PEAK STRESS

The analysis and calculations described in Appendix B provide the connections between the applied stress σ and the matrix crack extension Δa (Figs. 2-3) shown nondimensionally in Fig. 6. (These relations assume no fiber fracture, and so the basic stress parameters $c_f S$ is not involved.) The abscissa σ_0/σ_{mc} is a measure of the original flaw size. Note that for $\Delta a/a_0 > .5$ the curves giving σ/σ_{mc} vs. σ_0/σ_{mc} cross each other in the vicinity of $\sigma_0/\sigma_{mc} = .95$. It follows that the peak

stress σ_p during crack growth (see Fig. 3) must occur for $\Delta a_p/a_0 > 5$ whenever the flaw size corresponds to $\sigma/\sigma_{mc} < .94$; but for $\sigma_0/\sigma_{mc} > 1$, $\Delta a_p/a_0$ must be less than 0.5!

As discussed earlier, the strength σ_s of the flawed composite will, for some parametric ranges, be equal to the peak stress σ_p attained during matrix crack growth (Fig. 3). The results for σ_p obtained from the solution of the crack-growth equations are completely described by the curve in Fig. 7, which shows σ_p/σ_{mc} as a function of σ_0/σ_{mc} . (This curve is actually the upper envelope of the family of curves in Fig. 6). Note that σ_p is almost always very close to either σ_0 or σ_{mc} . The accuracy to which we could calculate σ_p was much better than that of the associated values of Δa_p . It may be that for sufficiently small values of σ_0/σ_{mc} , σ_p becomes equal to σ_{mc} , corresponding to a monotonic increase in the value of the applied stress as the matrix crack grows to infinity (see Fig. 3); but the numerical calculations do not resolve this point. In any case, this is not important, and, as we shall see, parametric ranges for which the strength σ_s is given by σ_p turn out to be small.

FULLY CRACKED MATRIX: AN AUXILIARY PROBLEM FOR σ_{fmc}

We will find that there are significant ranges of the ratios of the three basic stress parameters for which failure of the flawed composite occurs only after the matrix crack has become infinite, and then σ_s equals the strength σ_{fmc} of the fully cracked configuration sketched in Fig. 4. Clearly, σ_{fmc} is independent of the fracture toughness K_m of the matrix. But because of the bridging-fiber stress concentration induced at the edge of the original through-the-fibers crack, σ_{fmc} suffers a reduction from the base fibers-only strength $c_f S$ it would have if the flaw were absent. An integral-equation formulation for the calculation of σ_{fmc} is given in Appendix C in terms of the non-dimensional combination

$$\bar{a}_0 \equiv \frac{\sigma_{mc}^3}{c_f S \sigma_0^2} = \alpha \left[\frac{a_0 \tau}{RS} \right] \quad (10)$$

of the basic stress parameters, where

$$\alpha = \left[\frac{6\pi(1-\nu^2)c_f E E_f}{A(1-c_f)^2 E_m^2} \right] \quad (11)$$

The parameter \bar{a}_0 , independent of K_m , may be regarded as a measure of the original flaw size. The solution found numerically for $\sigma_{fmc}/(c_f S)$ as a function of this parameter is shown by the solid curve in Fig. 8*. A remarkably accurate approximation to this result is given by

* See Suo et al (1992) as well as Bao and Suo (1992) for the results of similar calculations based on other bridging laws, and suggestions concerning the possibility of unifying these results over a wide range of bridging laws via energy concepts.

$$\bar{a}_0 \equiv \frac{\sigma_{mc}^3}{c_f S \sigma_0^2} = 2 \left[\left(\frac{\sigma_{fmc}}{c_f S} \right)^{-4/3} - \left(\frac{\sigma_{fmc}}{c_f S} \right)^{2/3} \right]^{3/2} \quad (12)$$

which provides the dot-dash curve in Fig. 7. This formula was discovered fortuitously, and we have not found a persuasive way to derive it.

STRENGTH σ_s : RESULTS AND DISCUSSION

We can now put together the final results for the strength σ_s of the composite in terms of the basic stress parameters σ_0 , σ_{mc} , and $c_f S$, and we will display these results in several different forms to bring out various trends. By monitoring the magnitude of the bridging-fiber stress at the original flaw tip during the matrix crack growth, as calculated from the analysis of Appendix B, the magnitude of the load σ_f corresponding to fiber failure during this growth has been determined, and, on the basis of the discussion given in the earlier description of the failure process, the appropriate choices have been made for the assignment of σ_f , σ_p , or σ_{fmc} to the strength σ_s . This has been done on the basis of various non-dimensional forms of the governing equations, described in detail in Appendix B.

One nondimensional form of the results for σ_s is

$$\frac{\sigma_s}{\sigma_0} = F_1 \left(\frac{c_f S}{\sigma_{mc}}; \frac{\sigma_0}{\sigma_{mc}} \right) \quad (13)$$

where σ_s/σ_0 may be regarded as a *modified strengthening ratio* provided to a flawed ceramic by aligned-fiber reinforcement. (The *actual* strengthening ratio is σ_s/σ_{s0} , to which σ_s/σ_0 (see Eq. (6)) is a fair approximation.) We prefer, however, to introduce the parameter

$$\Lambda = \sqrt{1 + 2 \left(\frac{c_f S}{\sigma_{mc}} \right)^3} \quad (14)$$

in lieu of $c_f S/\sigma_{mc}$ in exhibiting the results for the strength of the composite, and we have done so in Fig. 9, where we show curves of σ_s/σ_0 vs. Λ for various values of σ_0/σ_{mc} . The quantity Λ is the *modified toughening ratio* K/K_{IC} found by Budiansky and Amazigo (1989) for the case of *small-scale bridging*. The significance of Λ is that it provides the modified strengthening ratio of a composite containing a very long initial crack, which corresponds to a very small value of σ_0/σ_{mc} . Thus, $\sigma_s/\sigma_0 = \Lambda$ for $\sigma_0/\sigma_{mc} = 0$, and this is an upper bound to σ_s/σ_0 for all finite values of σ_0/σ_{mc} . In effect, the sequence of curves in Fig. 9 shows quantitatively how much the small-scale-bridging strengthening due to aligned-fiber reinforcement is reduced for flaws of decreasing size.

As indicated by the key to the line types in Fig. 9, the strength σ_s , at each fixed value of σ_0/σ_{mc} , always starts out equal to σ_f at low values of Λ ; for a sufficiently large value of Λ , this first range, associated with fiber failure during matrix crack growth (Fig. 3), merges into a generally small interval in Λ for which σ_s is given by the "peak" stress σ_p ; and then, beyond

another critical value of Λ , failure at $\sigma_s = \sigma_{fmc}$ in the fully cracked matrix becomes the rule. Note that because σ_0/σ_{mc} does not depend on S , each of the curves of Fig. 9 can be interpreted as showing the influence of fiber strength on the composite strength.

The results for σ_s have also been computed in the form

$$\frac{\sigma_s}{\sigma_0} = F_2 \left(\frac{c_f S}{\sigma_{mc}}, \frac{c_f S}{\sigma_0} \right) \quad (15)$$

and Fig. 10 shows σ_s/σ_0 vs. Λ for various fixed values of $c_f S/\sigma_0$, which may be regarded as a crack length parameter that is an increasing function of the initial flaw size. Since $c_f S/\sigma_0$ is independent of the shear stress τ , each curve in Fig. 10 shows how the fiber-matrix interface friction affects the strength. The matrix cracking stress σ_{mc} is an increasing function of τ (Eq. (9)), and therefore the small-scale-bridging toughening ratio Λ gets larger as τ goes down. The curves in Fig. 10 show that for flaws of finite size the strengthening generally remains an *increasing* function of $1/\tau$, except for some insignificant isolated parametric ranges.

In both Fig. 9 and Fig. 10, displaying the ratio σ_s/σ_0 as the dependent variable provides the answer to the question: how much has the flawed matrix been *strengthened* by aligned fibers? An alternative viewpoint is to contemplate the base fibers-only strength $\sigma_{fs} = c_f S$ as a starting point of reference, and study what happens to the ratio $\sigma_s/c_f S$ under the degrading influence of a flaw *and* the reinforcing presence of the matrix. A useful representation of the results is in the form

$$\frac{\sigma_s}{c_f S} = F_3 \left(\frac{\sigma_{mc}^3}{c_f S \sigma_0^2}, \frac{\sigma_{mc}}{c_f S} \right) \quad (16)$$

as shown in Fig. 11. The abscissa \bar{a}_0 is a flaw-size parameter that is independent of the matrix toughness K_m , and the increasing values of $\sigma_{mc}/c_f S$ labeling each curve reflect increasing values of K_m . The curve for $\sigma_{mc}/c_f S = 0$ reproduces the one in Fig. 7; for $K_m = 0$, the matrix will crack out to infinity as soon as load is applied, and then the strength will be given by σ_{fmc} . The curves in Fig. 11 show that σ_{fmc} constitutes a lower bound to the strength, and that for reasonable finite values of $\sigma_{mc}/(c_f S)$ only modest increases above this value are obtained. In terms of the parameters of Eq. (16) and Fig. 11, the identity of the failure mode can exhibit a curious progression. Thus, for $\sigma_{mc}/c_f S = .75$, σ_s is given by σ_f for large flaw size; then, as \bar{a}_0 decreases, $\sigma_s = \sigma_p$ over for a tiny interval of the abscissa; this is followed by $\sigma_s = \sigma_{fmc}$ along the bottom curve; and finally, below a critical value of flaw size, $\sigma_s = \sigma_p$ again. Actually, values of the abscissa much below unity are unlikely to be in a practical range of interest.

The formula (12) suggests that the results of Fig. 11 might usefully be replotted as shown in Fig. 12, wherein $\sigma_s/(c_f S)$ is shown over the full practical range of $(\bar{a}_0)^{-1/2}$. Note that for $\sigma_{mc}/c_f S$ greater than some critical value between .75 and .85, failure always occurs during finite extension of the matrix crack.

NUMERICAL EXAMPLES

To provide some quantitative feel for the theoretical results of Figs. 9-12, we present a set of numerical examples for a well-documented ceramic composite system that was used in matrix cracking experiments by Marshall et al (1985), consisting of silicon-carbide fibers in a lithium-alumino-silicate glass matrix. The nominal values of pertinent parameters were

$$\left. \begin{array}{l} c_f = 0.5 \\ v_m = v_f = 0.25 \\ E_m = 85 \text{ GPa} \\ E_f = 200 \text{ GPa} \end{array} \right\} \Rightarrow E = 142.5 \text{ GPa}$$

$$\begin{array}{l} R = 8 \mu\text{m} \\ K_m = 2 \text{ MPa} \cdot \text{m}^{1/2} \\ S = 1 \text{ GPa} \\ \tau = 2 \text{ MPa} \end{array}$$

On the basis of this data, we get

$$A = 0.95 \quad \sigma_{mc} = 265 \text{ MPa} \quad \Lambda = 3.8$$

Table I shows the strength predictions of the present analysis, for several values of flaw length $2a_0$ and the corresponding values of σ_0 , $c_f S/\sigma_0$, and \bar{a}_0 . Numerical results for σ_s are given, as well as the ratios σ_s/σ_0 and $\sigma_s/(c_f S)$; the failure type (i.e., σ_f , σ_p , or σ_{fmc}) is listed.

TABLE I

$2a_0 (\mu\text{m})$	$\sigma_0 (\text{MPa})$	$c_f S/\sigma_0$	\bar{a}_0	$\sigma_s (\text{MPa})$	σ_s/σ_0	$\sigma_s/(c_f S)$	type
32.5	250	2	0.60	415	1.7	0.83	σ_{fmc}
130	125	4	2.38	319	2.6	0.64	σ_{fmc}
290	83.3	6	5.36	257	3.1	0.51	σ_f
520	62.5	8	9.53	213	3.4	0.43	σ_f

In these examples the strength σ_{s0} of the unreinforced ceramic is about 10% higher than σ_0 (Eq. (6)). Thus, the composite containing a flaw (or sharp notch) about 1/2 mm in length is strengthened considerably (by about a factor of three) by the presence of aligned fibers that do not bridge the initial flaw. But the failure mode, of the σ_f type, remains catastrophic, occurring before the onset of widespread matrix cracking at σ_{mc} . In contrast, the strength of the matrix with the smallest of the flaws considered above is increased by only about 50%, but this is enough to raise σ_s above σ_{mc} .

CONCLUDING REMARKS

Our study has produced theoretical results for the tensile strength of a flawed, aligned-fiber ceramic composite in succinct non-dimensional forms that encompass the effects of a large number of geometrical and physical variables. The results for the strength σ_s , displayed in

terms of three basic characterizing reference stresses σ_0 , σ_{mc} , and $c_f S$ in Figs. 9-12, may provide a basis for the micromechanical design and analysis of such materials, as well as for the formulation of design criteria. A useful lower bound to the strength σ_c is given by the post-matrix-cracking failure stress σ_{fmc} provided by Fig. 8.

The present study provides a sound foundation from which to proceed to elaborations that include the effects of initial stress and statistical variations in the fiber strength. The latter, in particular, can lead to intra-matrix fiber failures at locations off the crack faces, and the consequent higher fiber-pullout lengths during failure can produce substantial increases in predicted composite strengths (Thouless and Evans 1988). However, the extent to which design should rely on beneficial effects of statistical dispersions in fiber strength remains an open question. Finally, it should be emphasized that the possible intervention of failure modes not considered here, such as longitudinal splitting or shear localization, requires investigation.

ACKNOWLEDGMENTS

We are grateful to Professor A.G. Evans for his comments on this work and to Professor Z. Suo for an illuminating discussion. This work was partially supported by the DARPA University Research Initiative (Subagreement P.O. #VB38639-0 with the University of California, Santa Barbara, ONR Prime Contract N00014-86-K-0753 and Subagreement P.O. #KK3007 with the University of California, Santa Barbara, ONR Prime Contract N00014-92-J-1808), the Office of Naval Research (Contract N00014-90-J-1377), and by the Division of Applied Sciences, Harvard University.

REFERENCES

- | | | |
|---|------|---|
| AVESTON, J., COOPER, G.A
and KELLY, A. | 1971 | <i>The properties of fiber composites</i> , pp. 15-26. Conference proceedings, National Physical Laboratory, Guildford. IPC Science and Technology Press Ltd. |
| BAO, G. and SUO, Z. | 1992 | <i>Appl. Mech. Rev.</i> 45 , 355. |
| BUDIANSKY, B. and AMAZIGO, J.C. | 1989 | <i>J. Mech. Phys. Solids</i> 37 , 93. |
| BUDIANSKY, B., HUTCHINSON, J.W
and EVANS, A.G. | 1986 | <i>J. Mech. Phys. Solids</i> 34 , 167. |
| ERDOGAN, F. and GUPTA, G.D. | 1972 | <i>Quart. Appl. Math.</i> 29 , 525. |
| EVANS, A.G. | 1991 | <i>Mat. Sci. Eng.</i> A143 , 63. |
| HILL, R. | 1965 | <i>J. Mech. Phys. Solids</i> 13 , 189. |

- HUTCHINSON, J.W. 1990 *Mech. Mater.* **9**, 139.
 and JENSEN, H.M.
 MARSHALL, D.B., COX, B.N. 1985 *Acta. Metall.* **33**, 2013.
 and EVANS, A.G.
 MARSHALL, D.B. and COX, B.N. 1987 *Acta. Metall.* **35**, 2607.
 SIH, G. C., PARIS, P. C. 1965 *Int. J. Fracture Mech.* **1**, 189.
 and IRWIN, G. R..
 SUO, Z., HO, S. and GONG, X. 1992 *ASME J. Engr. Mat. Tech.*, *in press*
 TADA, H., PARIS, P., 1985 *The Stress Analysis of Cracks Handbook*, Del
 and IRWIN, G. R. Research, St. Louis.
 THOULESS, M.D., 1988 *Acta. metall.* **36**, 517.
 and EVANS, A.G.

APPENDIX A ORTHOTROPY FACTOR A

This Appendix corrects the one with the same title in the paper by Budiansky and Amazigo (1989), in which several blunders occur.

We consider a transversely isotropic, orthotropic elastic material satisfying the stress-strain relations

$$\begin{cases} \epsilon_x = \sigma_x / \bar{E} - \nu \sigma_y / E - \bar{\nu} \sigma_z / \bar{E} \\ \epsilon_y = -\nu \sigma_x / E + \sigma_y / E - \nu \sigma_z / E \\ \epsilon_z = -\bar{\nu} \sigma_x / \bar{E} - \nu \sigma_y / E + \sigma_z / \bar{E} \\ \gamma_{xy} = \tau_{xy} / G \end{cases} \quad (A1)$$

According to Tada et al (1985), quoting results of Sih et al (1965), the plane-strain energy release rate at the edge of a mode-I crack lying in the transversely isotropic x-z plane is

$$\mathcal{G} = CK_I^2 \quad (A2)$$

where

$$C = \sqrt{\frac{A_{11}A_{22}}{2}} \left[\sqrt{\frac{A_{22}}{A_{11}}} + \frac{2A_{12} + A_{66}}{2A_{11}} \right]^{1/2} \quad (A3)$$

and the A_{ij} are defined by the plane-strain constitutive relations

$$\begin{cases} \epsilon_x = A_{11}\sigma_x + A_{12}\sigma_y \\ \epsilon_y = A_{12}\sigma_x + A_{22}\sigma_y \\ \gamma_{xy} = A_{66}\tau_{xy} \end{cases} \quad (A4)$$

The A_{ij} are given by

$$A_{11} = \frac{1 - \bar{\nu}^2}{\bar{E}}, \quad A_{12} = -\frac{\nu(1 + \bar{\nu})}{E}, \quad A_{22} = \frac{1 - \nu^2 \bar{E}/E}{E}, \quad A_{66} = \frac{1}{G} \quad (A5)$$

Hence, in the representation

$$G = \frac{(1 - \nu^2)K_I^2}{AE} \quad (A6)$$

we have

$$A = \frac{1 - \nu^2}{CE} \quad (A7)$$

For the aligned fiber composite, the elastic constants E , \bar{E} , G , $\bar{\nu}$ have been calculated for the case $\nu = \nu_f = \nu_m$ in terms of c_f , E_m , and E_f , and the resulting dependence of A on c_f is plotted in Figs. 5(ab) for various values of E_f/E_m .

APPENDIX B

FORMULATION AND NUMERICAL SOLUTION FOR MATRIX CRACKING INITIATED FROM A CRACK-LIKE FLAW

Formulation

This section details the formulation of an integral equation and an associated scalar equation for matrix cracking that is initiated from a preexisting flaw. The matrix crack together with the original flaw is modeled as a crack of length $2(a_0 + \Delta a)$ (see Fig. 2) with a cohesive, bridged zone of length Δa at both ends. The upper crack face displacement is

$$v(x) = \frac{2(1 - \nu^2)}{AE} \sigma \sqrt{(a_0 + \Delta a)^2 - x^2} - \frac{2(1 - \nu^2)}{\pi AE} \int_{a_0}^{a_0 + \Delta a} p(\xi) \log \left| \frac{\sqrt{(a_0 + \Delta a)^2 - x^2} + \sqrt{(a_0 + \Delta a)^2 - \xi^2}}{\sqrt{(a_0 + \Delta a)^2 - x^2} - \sqrt{(a_0 + \Delta a)^2 - \xi^2}} \right| d\xi \quad (B1)$$

Except for the factor A , the first term is the standard crack face displacement due to remote uniform loading of an isotropic material. The second term is the crack face closure displacement due to the bridging stresses, and, again except for A , is obtained by superposition of the crack face displacements due to concentrated loading on crack surfaces given by Tada et al. (1985). The orthotropy factor A , defined by Eq. (1) in terms of energy release rate, correctly takes orthotropy into account in this expression for displacement. (This can most easily be shown by weight-function considerations.) An integral equation for $p(x)$ may be obtained by equating $v(x)$ in (B1)

to $[p(x)/\beta]^2$ in accordance with the bridging law (7), and then differentiation with respect to x gives

$$p(x) \frac{dp(x)}{dx} = - \frac{2\beta^2(1-\nu^2)x}{\pi AE \sqrt{(a_0 + \Delta a)^2 - x^2}} \left[\int_{a_0}^{a_0 + \Delta a} \frac{\sqrt{(a_0 + \Delta a)^2 - \xi^2}}{\xi^2 - x^2} p(\xi) d\xi + \frac{\pi\sigma}{2} \right] \quad \text{for } a_0 \leq x \leq a_0 + a \quad (B2)$$

A scalar equation that must be satisfied simultaneously with (B2) is obtained by asserting that the orthotropic stress intensity factor K_I (which depends on σ and $p(x)$ in the same way as for isotropy) must remain equal to K_{IC} . Hence (Tada et al, 1985)

$$K_I = \sigma \sqrt{\pi(a_0 + \Delta a)} - 2 \sqrt{\frac{a_0 + \Delta a}{\pi}} \int_{a_0}^{a_0 + \Delta a} \frac{p(x)}{\sqrt{(a_0 + \Delta a)^2 - x^2}} dx = K_{IC} \quad (B3)$$

By making the substitutions

$$\begin{cases} x = (a_0 + \Delta a)s & p(x) = \sigma_{mc} q(s) \\ \alpha = \frac{1}{1 + \Delta a/a_0} & \sigma = \Sigma \sigma_{mc} \quad \sigma_0 = \Sigma_0 \sigma_{mc} \end{cases} \quad (B4)$$

one may express the governing equations (B2) and (B3) in the normalized forms

$$\sqrt{1-s} q(s) \frac{dq(s)}{ds} = - \frac{4f_1(s)}{3\pi^2 \alpha \Sigma_0^2} \left[\int_{\alpha}^1 f_2(t,s) q(t) dt + \frac{\pi}{2} \Sigma \right] \quad \text{for } \alpha \leq s \leq 1 \quad (B5)$$

$$\Sigma - \frac{2}{\pi} \int_{\alpha}^1 f_3(s) q(s) ds = \sqrt{\alpha} \Sigma_0 \quad (B6)$$

where

$$f_1(y) = \frac{y}{\sqrt{1+y}}, \quad f_2(t,s) = \frac{\sqrt{1-t^2}}{t^2 - s^2} \quad \text{and} \quad f_3(s) = \frac{1}{\sqrt{1-s^2}}. \quad (B7)$$

For assigned values of α , Eqs. (B5) and (B6) can be solved for Σ and $q(s)$ versus Σ_0 , and thereby provide the results of Fig. 6, and the curve for σ_f/σ_{mc} in Fig. 7. The condition of fiber fracture at $x=a_0$ is $q(1)=c_f S/\sigma_{mc}$. Hence, for given values of Σ_0 and $c_f S/\sigma_{mc}$, Eqs. (B5) and (B6) can be solved (by a Newton-Raphson technique) for the corresponding distributions $p(s)$ and magnitudes of α and $\Sigma_f = \sigma_f/\sigma_{mc}$ at fracture, and then the points for $\sigma_f/\sigma_0 = \sigma_f/\sigma_0 = \Sigma_f/\Sigma_0$ on the dot-dash curves of Fig. 9 can be plotted.

To get points on the dot-dash curves of Fig. 10, we assign values of $c_f S / \sigma_0$ as well as $c_f S / \sigma_{mc}$, replace Σ_0 in Eqs. (B5) and (B6) by the ratio of these quantities, and similarly solve for Σ_f .

Finally, to plot the curves for $\sigma_s = \sigma_f$ in Figs. 11 and 12, it is convenient to renormalize the governing equations by letting

$$\bar{a}_0 = \frac{\sigma_{mc}^3}{c_f S \sigma_0^2}, \quad \bar{q}(s) = \frac{p(s)}{c_f S}, \quad \bar{\Sigma} = \frac{\sigma}{c_f S} \quad (B8)$$

to get

$$\sqrt{1-s} \bar{q}(s) \frac{d\bar{q}(s)}{ds} = -\frac{4f_1(s)\bar{a}_0}{3\pi^2\alpha} \left[\int_{\alpha}^1 f_2(t,s) \bar{q}(t) dt + \frac{\pi}{2} \bar{\Sigma} \right] \quad \text{for } \alpha \leq s \leq 1 \quad (B9)$$

$$\bar{\Sigma} - \frac{2}{\pi} \int_{\alpha}^1 f_3(s) \bar{q}(s) ds = \left(\frac{\sigma_{mc}}{c_f S} \right)^{3/2} \sqrt{\alpha / \bar{a}_0} \quad (B10)$$

The fracture criterion is now $\bar{q}(1)=1$, and so, for assigned values of \bar{a}_0 and $\sigma_{mc}/(c_f S)$ the magnitude of $\bar{\Sigma}_s = \bar{\Sigma}_f$ corresponding to this condition can be found from Eqs. (B9) and (B10).

We omit a detailed description of the fairly straightforward procedures used to plot the curves in Figs. (9-12) corresponding to the results in Figs. 7 and 8 for σ_p and σ_{fmc} .

Numerical procedure

This section describes the numerical procedure used to solve Eqs. (B5) and (B6) for $q(s)$ and Σ ; the method is equally applicable to Eqs. (B9) and (B10). Make the substitutions

$$s = \frac{1}{2}[(1+\alpha) + (1-\alpha)z], \quad t = \frac{1}{2}[(1+\alpha) + (1-\alpha)\zeta], \quad q(s(z)) \equiv Q(z) \quad (B11)$$

in Eqs. (B9-B10) to get

$$\sqrt{1-z} Q(z) \frac{dQ(z)}{dz} = -\frac{4f_1[s(z)]}{3\pi^2\alpha\Sigma_0^2} \sqrt{\frac{1-\alpha}{2}} \left\{ \frac{1-\alpha}{2} \int_{-1}^1 f_2[t(\zeta), s(z)] Q(\zeta) d\zeta + \frac{\pi}{2} \Sigma \right\} \quad (B12)$$

for $-1 \leq z \leq 1$, and

$$\Sigma - \frac{1-\alpha}{\pi} \int_{-1}^1 f_3[s(z)] Q(z) dz = \sqrt{\alpha} \Sigma_0 \quad (B13)$$

Note that the displacement $v \propto \sqrt{1-z}$ near $z=1$, and since $Q \propto \sqrt{v}$ it is appropriate to write

$$Q(z) = (1-z)^{1/2} \sum_{k=1}^M a_k T_{k-1}(z) \quad (B14)$$

where $T_k(z)$ is the Chebyshev polynomial of the first kind of degree k . For given values of α , and Σ_0 , the M coefficients a_k , together with the additional unknown Σ , were determined by collocation of Eq. (B12) at the M points

$$z_r = \cos\left(\frac{\pi r}{M+1}\right) \quad (r = 1, 2, \dots, M) \quad (B15)$$

and enforcement of Eq. (B13). The definite integrals with respect to z in (B12) and (B13) were evaluated by means of the general Cauchy-Chebyshev formula (Erdogan and Gupta 1972)

$$\int_{-1}^1 \frac{F(\zeta) d\zeta}{(z_r - \zeta) \sqrt{1 - \zeta^2}} = \frac{\pi}{M+1} \sum_{p=1}^{M+1} \frac{F(\zeta_p)}{z_r - \zeta_p} \quad (r = 1, 2, \dots, M) \quad (B16)$$

and the standard Gaussian integration formula

$$\int_{-1}^1 \frac{F(z) dz}{\sqrt{1 - z^2}} = \frac{\pi}{M+1} \sum_{p=1}^{M+1} F(z_p) \quad (B17)$$

where

$$z_p = \zeta_p = \cos \left[\frac{(2p-1)\pi}{2(M+1)} \right] \quad (p = 1, 2, \dots, M+1) \quad (B18)$$

A Newton-Raphson iterative scheme was used to find solutions for the a_n 's and Σ , with convergence specified by a relative change of less than .01% in the values of each of the unknowns in successive iterations. The physical argument that for a long matrix crack the applied stress σ should approach the steady-state matrix cracking stress σ_{mc} provides a consistency check on the accuracy of the numerical solution. It was found that with M between 40 and 60, the consistency check was always satisfied to within about 0.1%.

APPENDIX C

AUXILIARY PROBLEM FOR σ_{fmc}

We can obtain an integral equation for the auxiliary problem of Fig. 4 by letting $\Delta a \rightarrow \infty$ in Eq. (B2). The result is

$$p(x) \frac{dp(x)}{dx} = - \frac{2\beta^2(1-\nu^2)}{\pi AE} \int_{a_0}^{\infty} \frac{x}{\xi^2 - x^2} p(\xi) d\xi \quad \text{for } a_0 \leq x < \infty \quad (C1)$$

By making the substitutions shown in Eq. (B7), together with

$$x = a_0 y \quad (C2)$$

we obtain

$$\bar{q}(y) \frac{d\bar{q}(y)}{dy} = - \frac{4\bar{a}_0}{3\pi^2} \int_1^{\infty} \frac{y}{\eta^2 - y^2} \bar{q}(\eta) d\eta \quad \text{for } 1 \leq y < \infty \quad (C3)$$

Note (Fig. 4) that under the applied stress σ , $\bar{q}(\infty) = \sigma/(c_f S) = \bar{\Sigma}$, and the condition for fiber fracture at the original flaw tip is given by

$$\bar{q}(1) = 1 \quad (C4)$$

Accordingly, for assigned values of $\bar{a}_0 \equiv \frac{\sigma_{mc}^3}{c_f S \sigma_0^2}$, the solutions $\bar{q}(y)$ of (C3) that satisfy (C4) provide the associated values of $\bar{q}(\infty) = \bar{\Sigma}_f = \sigma_{fmc} / (c_f S)$ needed to plot the solid curve of Fig. 8. The transformation

$$y = 1 + \frac{1 + \omega}{1 - \omega} \quad (C5)$$

may be introduced into (C3) to map the infinite domain into the interval $(-1, 1)$. The subsequent numerical procedure used to calculate $\bar{\Sigma}_f$ versus \bar{a}_0 , involving expansion of \bar{q} in Chebyshev polynomials and Newton-Raphson iteration, was basically similar to that outlined in Appendix B.

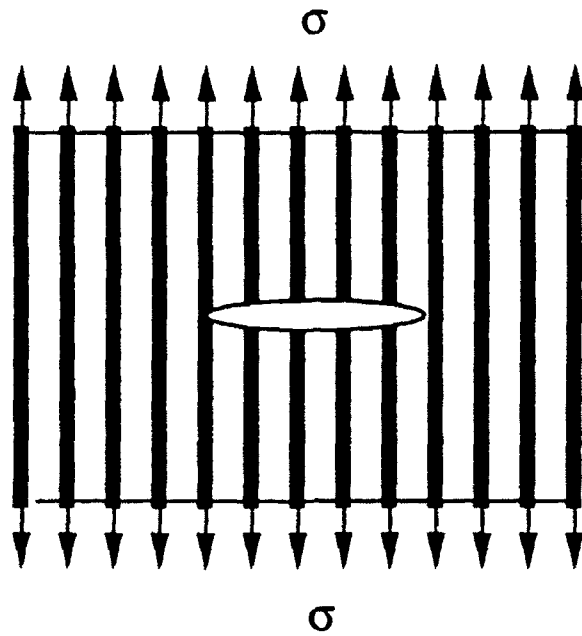


Fig. 1. Initial through-the-fibers crack-like flaw.

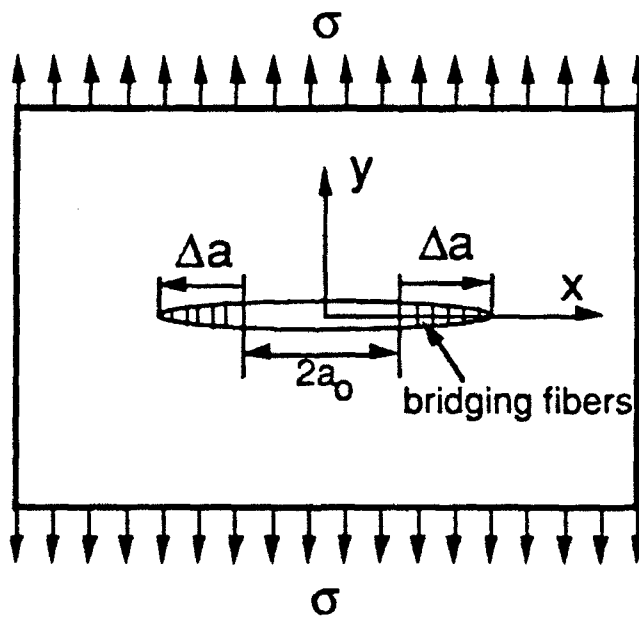


Fig. 2. Matrix cracking initiated from flaw tips.

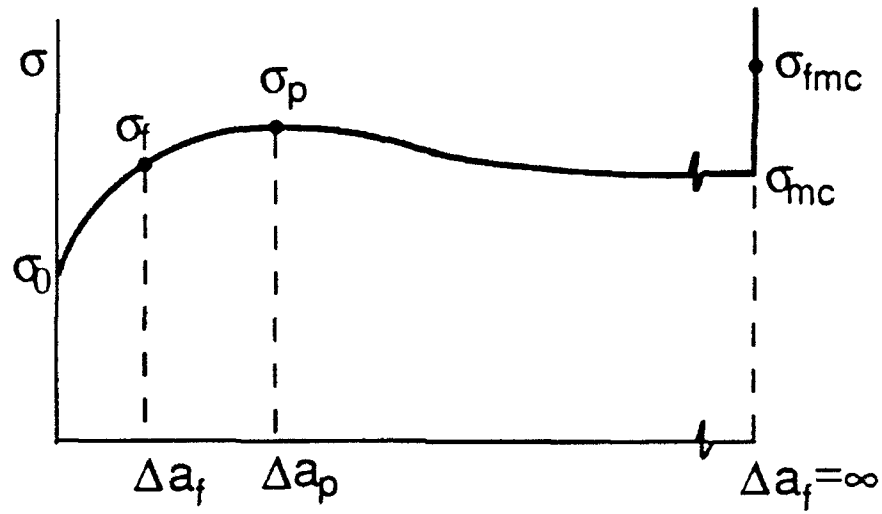


Fig. 3. Applied stress vs. matrix crack growth.

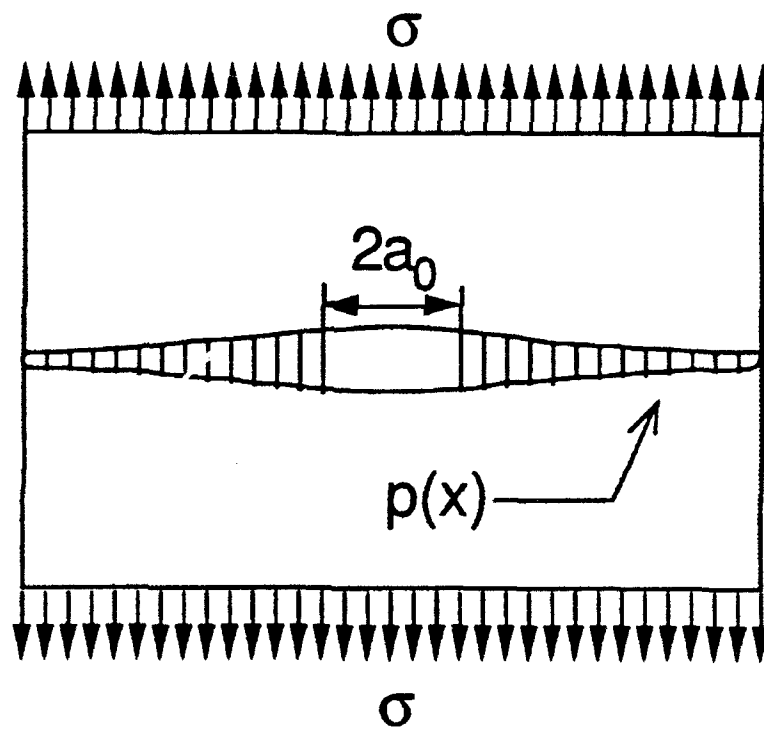
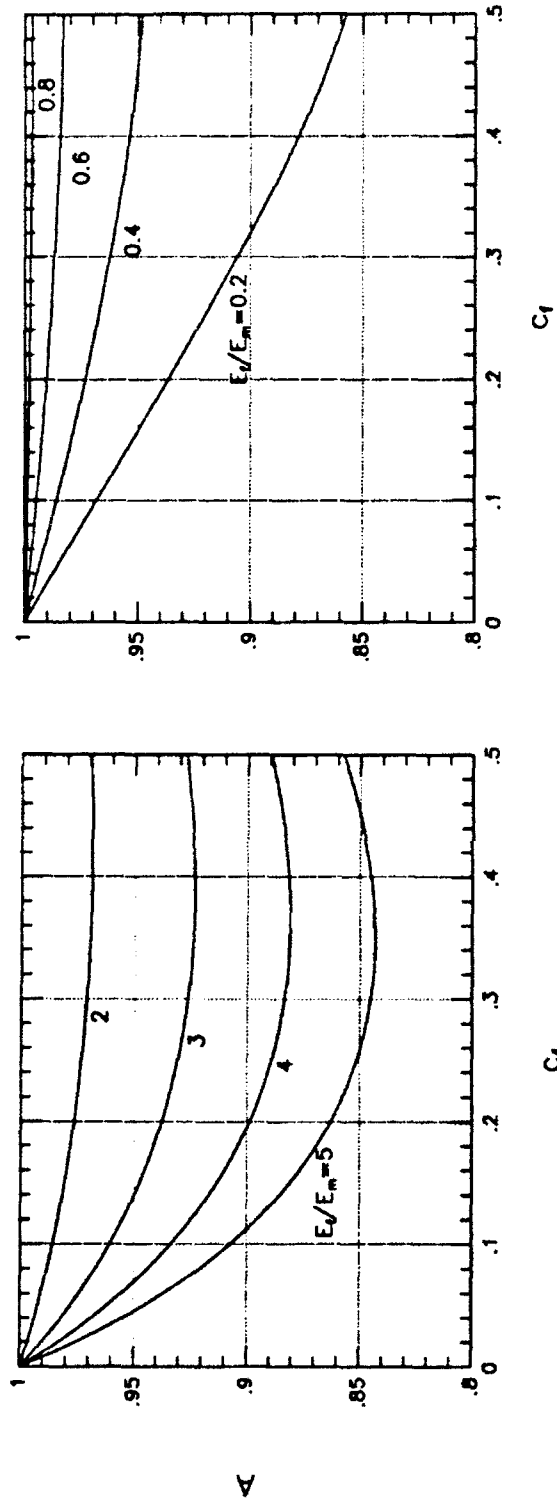


Fig. 4. Auxiliary problem: fully cracked matrix.



(a)

(b)

Fig. 5. Orthotropy factor A vs. fiber concentration c_f : (a) $E_f/E_m \geq 1$ (b) $E_f/E_m \leq 1$

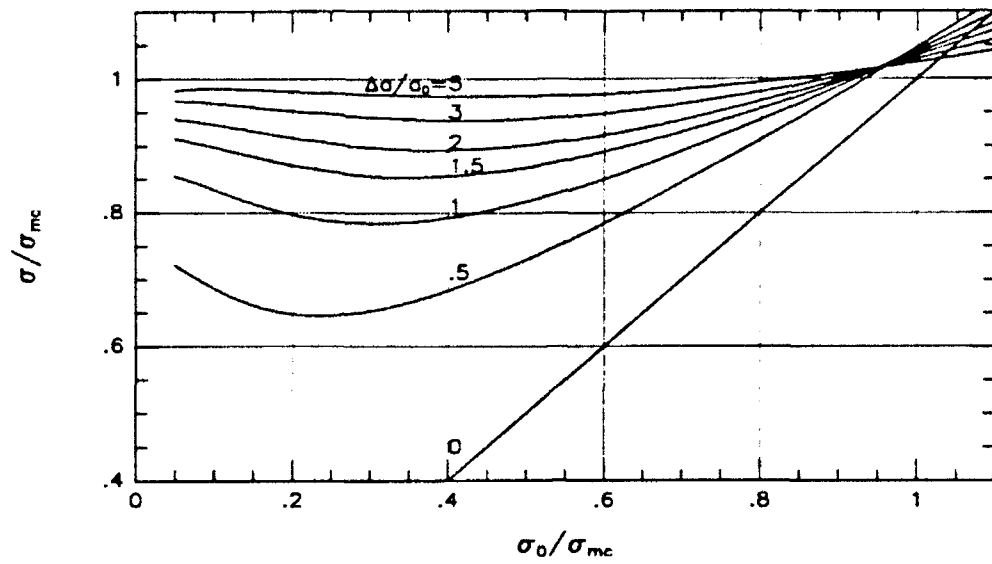


Fig. 6. Applied stress for various amounts of matrix crack growth.

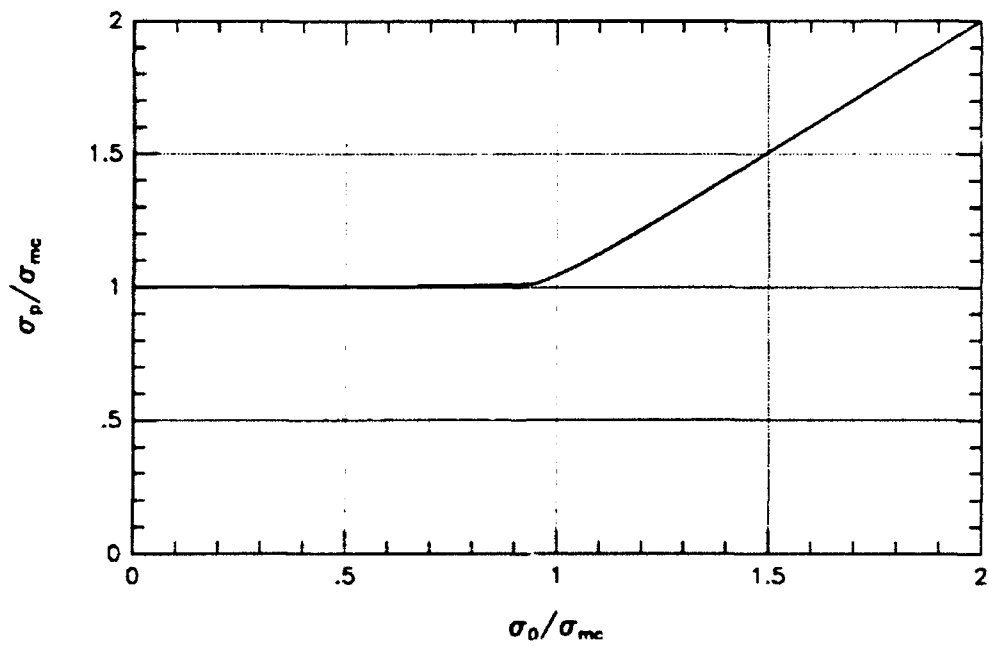


Fig. 7. Peak stress during matrix crack growth.

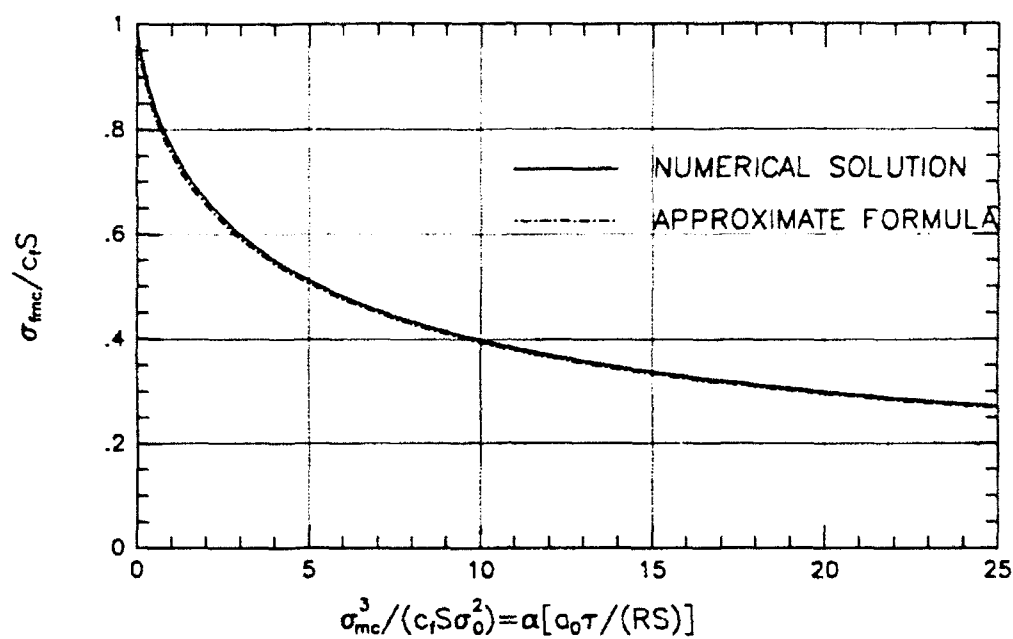


Fig. 8. Results for σ_{fmc} , fully cracked matrix.

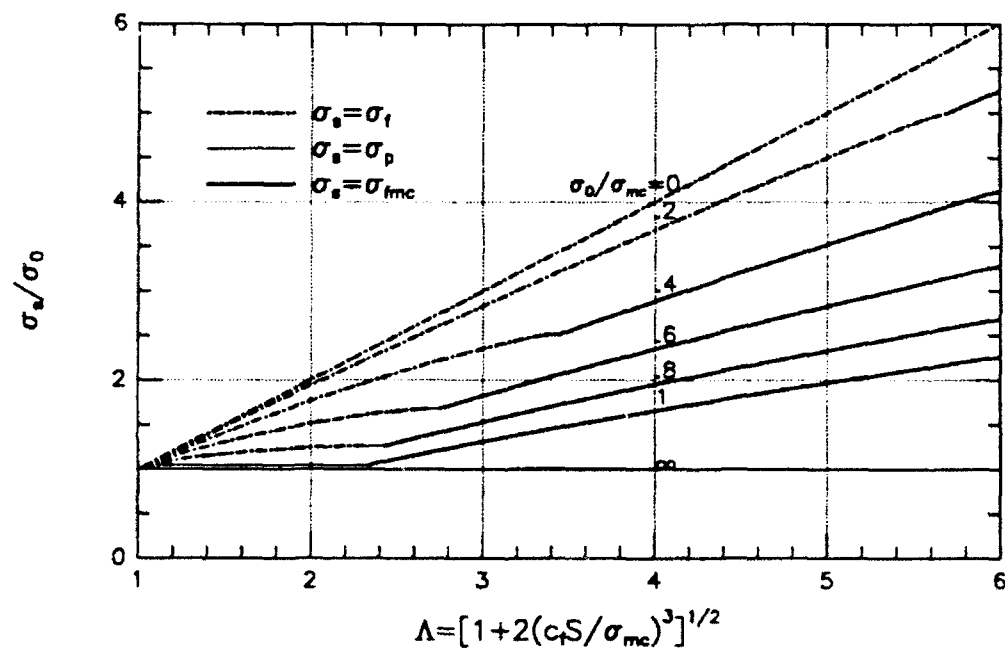


Fig. 9. Modified strengthening ratio σ_s/σ_0 for various values of σ_0/σ_{mc} . The parameter Λ is the modified toughening ratio for small-scale bridging.

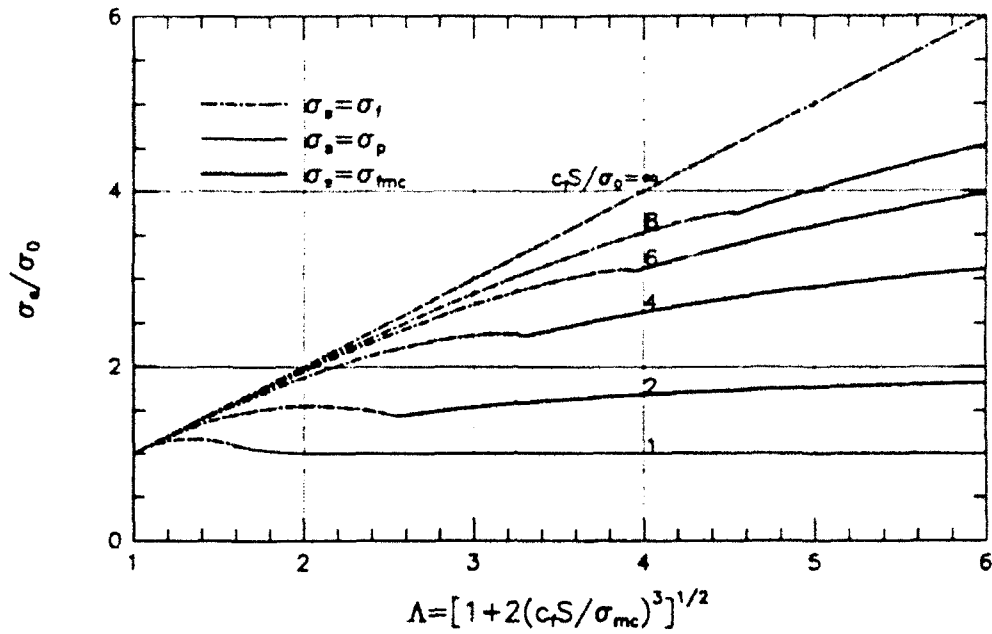


Fig. 10. Modified strengthening ratio σ_s/σ_0 for various values of $c_f S/\sigma_0$. The parameter Λ is the modified toughening ratio for small-scale bridging.

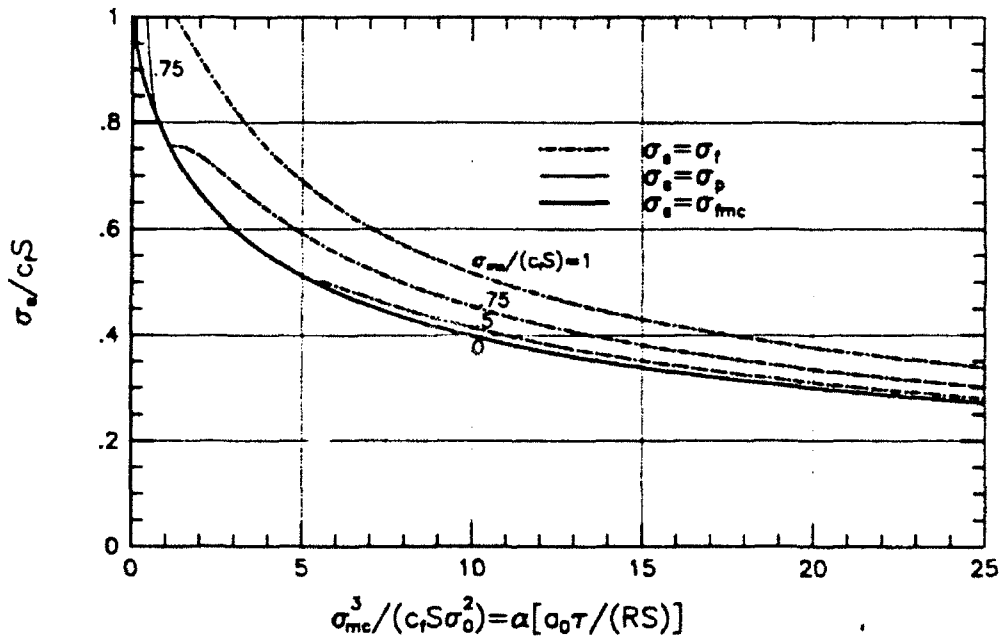


Fig. 11. Strength ratio $\sigma_s/(c_f S)$ vs. $\bar{a}_0^3 \equiv \frac{\sigma_{mc}^3}{c_f S \sigma_0^2}$ for various values of $\sigma_{mc}/(c_f S)$. The constant α is defined in Eq. (11)

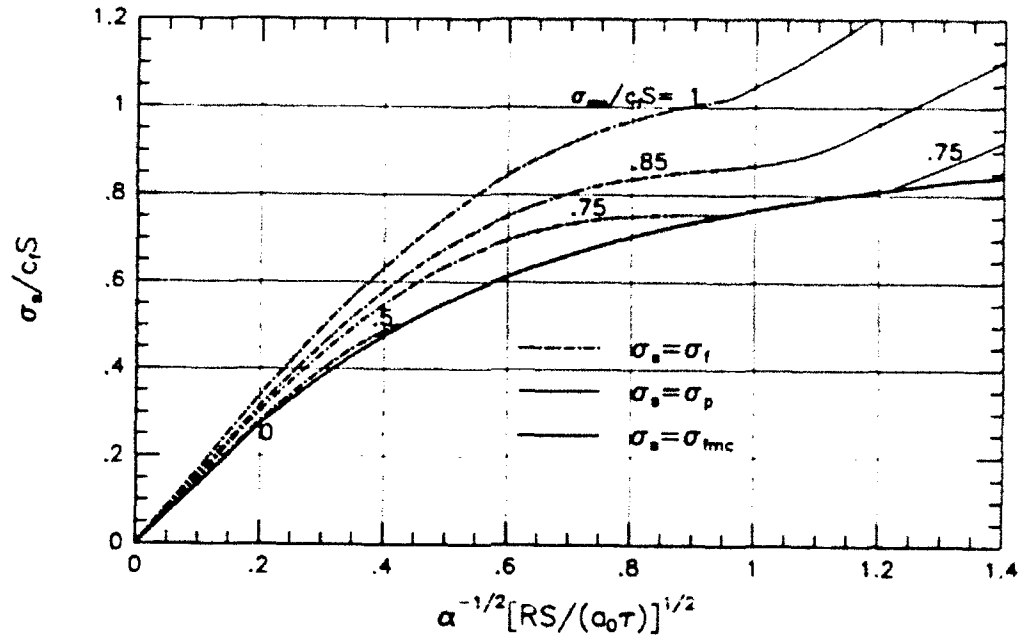


Fig. 12. Strength ratio $\sigma_s / (c_f S)$ vs. $(\bar{a}_0)^{-1/2} \equiv \left(\frac{\sigma_{mc}^3}{c_f S \sigma_0^2} \right)^{-1/2}$ for various values of $\sigma_{mc} / (c_f S)$. The constant α is defined in Eq. (11)

MECHANICAL BEHAVIOR OF A CONTINUOUS FIBER-REINFORCED ALUMINUM MATRIX COMPOSITE SUBJECTED TO TRANSVERSE AND THERMAL LOADING

S. JANSSON and F. A. LECKIE

Department of Mechanical and Environmental Engineering, University of California,
Santa Barbara, CA 93106, U.S.A.

(Received 2 November 1990; in revised form 9 May 1991)

ABSTRACT

THE TRANSVERSE properties of an aluminum alloy metal matrix composite reinforced by continuous alumina fibers have been investigated. The composite is subjected to both mechanical and cyclic thermal loading. The results of an experimental program indicate that the shakedown concept of structural mechanics provides a means of describing the material behavior. When the loading conditions are within the shakedown region the material finally responds in an elastic manner after initial plastic response, and for loading conditions outside the shakedown region the material exhibits a rapid incremental plastic strain accumulation. The failure strain varies by an order of magnitude according to the operating conditions. Hence for high mechanical and low thermal loading the failure strain is small, while for low mechanical and high thermal loading the failure strain is large.

1. INTRODUCTION

THE POTENTIAL for weight and strength advantages of components made of metal matrix composites is the consequence of the anisotropic properties of the composite. That advantage is diminished, or is even lost, for laminates with a less marked anisotropy. Consequently, if full advantage is to be taken of the dominant strength characteristics then the fibers should be oriented in the direction of maximum stress transmission. In this circumstance the transverse properties of the composite are critical since there must be sufficient strength in the matrix to carry the secondary stresses applied in the transverse direction.

The transverse properties of a metal matrix composite consisting of an Al-Li alloy matrix reinforced with continuous alumina fibers are investigated in this study. An important characteristic of this material is the combination of a strong bond at the fiber-matrix interface and a ductile matrix. There is also a large mismatch in the coefficient of thermal expansion of the fiber and matrix so that fluctuations in operating temperature induce thermal stresses in the composite. It is the goal of this study to determine the behavior of the composite when subjected to mechanical and thermal loading with special attention given to the transverse properties. The properties in the

fiber direction are the subject of another study. As a result of this study it is possible to describe the behavior of the composite in terms of the shakedown concept used in structural mechanics, and it is also possible to develop a rather simple method for establishing the constitutive equations for use in structural calculations.

2 EXPERIMENTAL PROGRAM

The composite studied is Du Pont's FP Al (CHAMPION *et al.*, 1978), with continuous fibers in a unidirectional lay-up. The fiber volume fraction was determined to be 55%. The FP fiber consists of 99% polycrystalline α -alumina (Al_2O_3) coated with silica that improves the strength of the fiber and aids the wetting by the molten metal. The fibers have a diameter of approximately 20 μm , a modulus of 345–380 GPa, a tensile strength of 1.9–2.1 GPa for 6.4 mm gauge length, and a fracture strain of 0.5–0.4%. The matrix material is a 2 wt% Li–Al binary alloy. The lithium promotes the wetting of the alumina fibers that forms a strong matrix–fiber interface and it also raises the modulus and decreases the density of the aluminum. The composite is fabricated by preparing the FP fibers into tapes by using a fugitive binder and the tapes are subsequently laid up in a metal mold in the desired orientation. The binder is burned away and the mold is vacuum-infiltrated with the molten matrix. The composite was available in the form of a plate 150 \times 150 \times 12.5 mm thick.

The specimen used in the test is shown in Fig. 1(a). It has a relatively large radius at the transition from the gripping section to the reduced-gauge section to provide a low stress concentration and a short gauge length for efficient use of the material. The specimen was loaded in a servo hydraulic machine and heated by means of induction coils [Fig. 1(b)], and the strain was measured with an extensometer with 3.8" gauge length. The temperature was measured by using three type K thermocouples mounted at the center and at the ends of the gauge section. The center thermocouple controlled the temperature while the top and bottom thermocouples were used to measure the

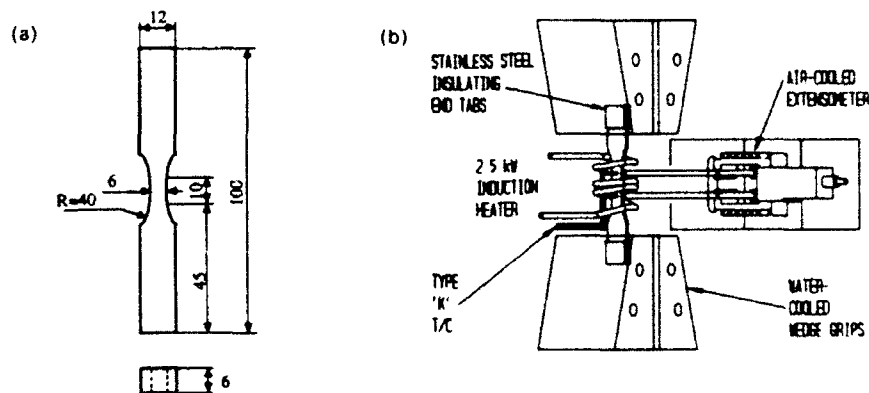


FIG. 1. (a) Specimen geometry. (b) Experimental setup.

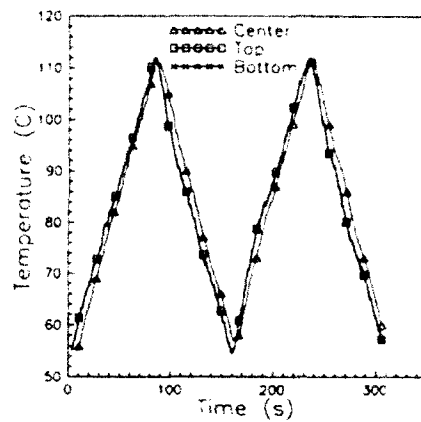


FIG. 2 Temperature distribution in specimen

variation of temperature along the length of the specimen. The variation of temperature with time and space is shown in Fig. 2. The spatial temperature distribution is slightly different for the heating and cooling parts of the cycle. It was not possible to adjust the coil to have a uniform temperature distribution over the whole cycle. It was therefore adjusted to have a minimal spatial variation over the cycle. A computer was used to control the tests by generating command signals for load and temperature, and to perform data acquisition.

The tests reported in this study involved a constant transverse stress in combination with cycles of temperature with heating rates of 0.7 C/s that give cycle times of approximately 150 s. Because of the limited availability of the composite only one specimen was used for each transverse stress level. The specimen was loaded and subjected to cyclic temperature and the ratcheting rate was measured when the steady-state condition was reached. The cyclic temperature range was then increased and the next rate was measured on reaching the next steady-state condition. The temperature and strain variations were continuously recorded. Examples of recorded strain in the direction of the applied stress are shown in Fig. 3.

3. EXPERIMENTAL OBSERVATIONS

Transverse stress-strain curves at room temperature are shown in Fig. 4, from which a deviation from linearity is observed to occur at 75 MPa. The ultimate strength is 200 MPa and the strain to fracture is 0.8%. The ultimate strength is about 50% higher than the ultimate matrix strength while the failure strain of 0.8% is only 3% of the 30% failure strain of the matrix (SAKUI and TAMURA, 1969).

Representative results for operating conditions in excess of shakedown are given in Fig. 3(a) for a low transverse stress and in Fig. 3(b) for a high transverse stress. In both cases transient behavior is followed by a cyclic response for which there is an increment of strain after each cycle, i.e. ratcheting occurs in both examples. For the

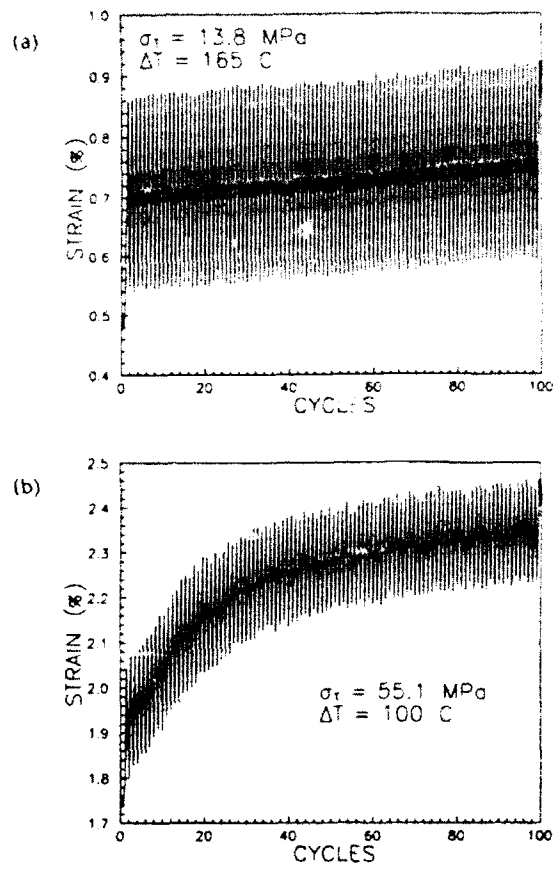


FIG. 3. Accumulation of plastic strain: (a) low transverse loading, (b) high transverse loading.

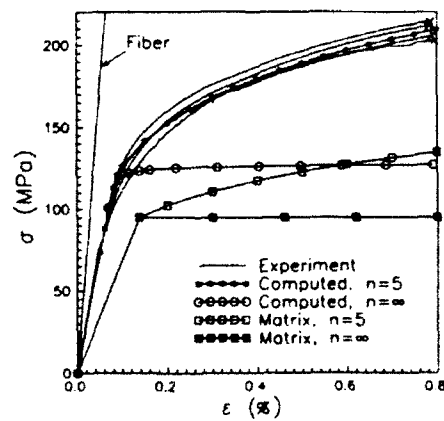


FIG. 4. Transverse stress strain curves for different matrix behavior.

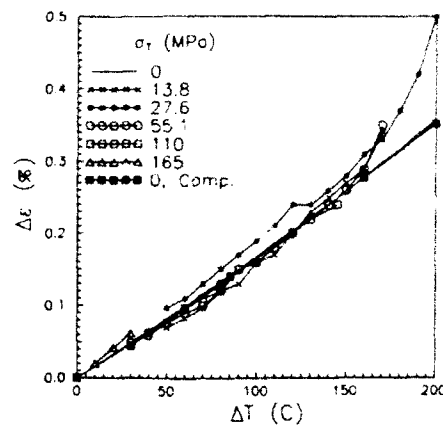


FIG. 5. Average cyclic strain as a function of transverse loading and temperature range

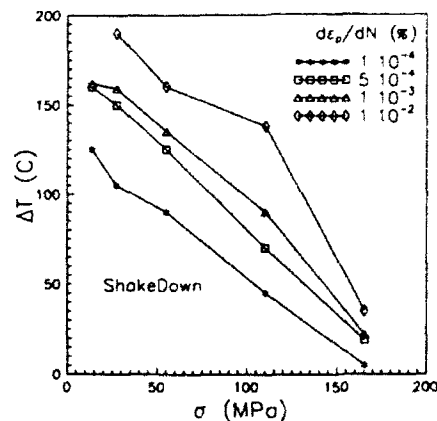


FIG. 6. Ratcheting rate as a function of transverse stress and temperature range. The rate of 10^{-4} is very close to the shakedown limit.

low transverse stress the transient portion is completed after one cycle [Fig. 3(a)] whereas in the case of the high load the transient behavior continues for 40 cycles before a steady-state condition is reached [Fig. 3(b)].

Similar tests were performed at different values of constant transverse stress and temperature cycles. In Fig. 5, the steady-state strain range $\Delta\epsilon$ recorded over a cycle of temperature is plotted as a function of the temperature range ΔT for different values of the transverse stress σ_T . It may be inferred from this plot that the cyclic strain is independent of the level of the transverse stress and is linearly dependent on the temperature range ΔT . Some of the samples have a higher strain range close to fracture.

Contours of constant values of steady-state accumulation rate of $\partial\epsilon_p/\partial N$, where ϵ_p is the plastic ratchet strain and N the cycle number, are plotted in Fig. 6 as a function of the thermal and mechanical loading. There are combinations of σ_T and ΔT for

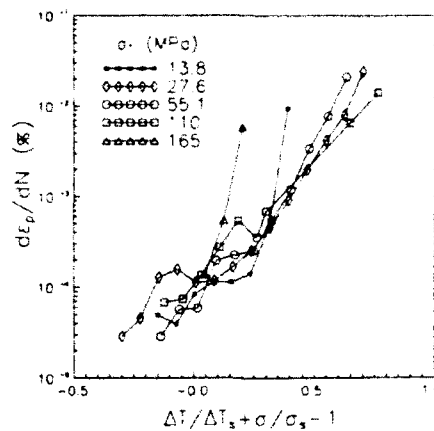


Fig. 7. Steady-state ratcheting rate as a function of the distance from the shakedown surface

which no ratcheting occurs and after an initial (transient) response the cyclic material behavior is elastic. This condition is indicated in Fig. 6 as the shakedown condition ($\partial \epsilon_p / \partial N < 10^{-4}$). When the operating conditions exceed the shakedown condition ratcheting occurs at rates indicated in Figs 6 and 7.

The contours of constant ratchet strain rate plotted in Fig. 6 are generally parallel to the shakedown surface. This observation suggests that the force β which drives the ratchet strain rate is given by

$$\beta = \frac{\Delta T}{T_s} + \frac{\sigma_T}{\sigma_s} - 1, \quad (1)$$

where T_s and σ_s are the ordinates defining the shakedown condition. The relationship of $d\epsilon_p/dN$ has the form

$$\frac{d\epsilon_p}{dN} = f(\beta), \quad (2)$$

where $f(\beta)$ has the form given in Fig. 7. The relationship is exponentially dependent on β for the present range of β and can be written as

$$f(\beta) = \exp(9.5 \times 10^2 \beta) - 1$$

The failure strain is dependent on the operating condition as indicated in Fig. 8. The failure strain was 0.8% for high stress and low thermal load whereas for a low transverse stress of 30 MPa the failure strain reaches 12%. Microscopic observations of specimens subjected to low transverse loading and with large failure strains [Fig. 9(a)] showed distributed damage in the form of small cracks over the whole gauge section. The cracks are initiated from areas with poor matrix infiltration and locations with closely spaced fibers. The macroscopic fracture surface is wavy. A high-magnification view [Fig. 9(b)] indicates a ductile fracture in the matrix with extremely oblong voids. It appears that the initial fracture is close to the fiber-matrix interface



FIG. 9. Typical fracture surface for low transverse loading: (a) a low-magnification view showing the distributed cracking in the sample, (b) a close up indicating initial fracture close to the fiber-matrix interface.



FIG. 10 Typical fracture surface for high transverse loading: (a) a low-magnification view showing that the fracture is localized to one plane, (b) a close up showing a ductile fracture in the matrix with no traces of fiber on the fracture surface

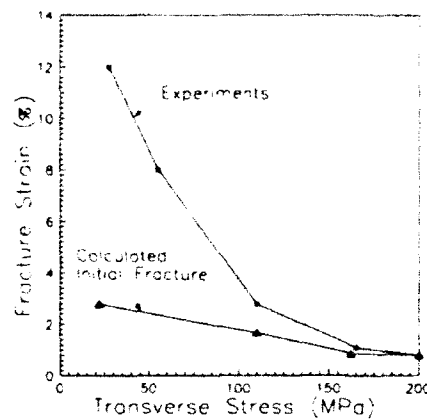


FIG. 8 Fracture strain

on planes perpendicular to the loading direction and that the final fracture consists of a ductile fracture in the remaining matrix ligaments between the fibers.

The fracture for high transverse loading and small failure strain [Fig. 10(a)] is localized to one narrow band oriented approximately 45° to the loading direction. The fracture surface [Fig. 10(b)] also indicates that the fracture is governed by a ductile matrix failure. However, the fracture does not approach the fiber-matrix interface as for the low transverse loading and it appears as if the whole load carrying capacity of the matrix has been lost at the same time. These observations suggest that the failure mechanism in the matrix is associated with void growth.

4. COMPUTATIONAL STUDIES

By using the theory of homogenization in conjunction with finite-element procedures an attempt is made to determine the mechanics that governs the behavior of the composite in terms of the properties of the fiber and the matrix.

The present composite consists of long fibers in a unidirectional lay up that are randomly distributed in the transverse plane. In the model to be analyzed the fibers are assumed to be long parallel cylinders arranged in a hexagonal array [Fig. 11(a)]. This periodical array has the mechanical properties with the closest symmetries to a composite with randomly distributed fibers. Both systems are transversely isotropic when the constituents are linear elastic but the hexagonal array has a weak deviation from transverse isotropy when the matrix exhibits a nonlinear stress strain relation (JANSSON, 1990a). The deviation is most pronounced for a perfectly-plastic matrix. However, reasonable results can be expected if effective properties are calculated for loadings that do not permit slip planes unconstrained by the fibers.

The governing boundary value problem for the effective properties of the unit cell is two-dimensional and has been solved with the finite element method by using ABACUS (1988). A 10-node biquadratic quadrilateral generalized plane strain

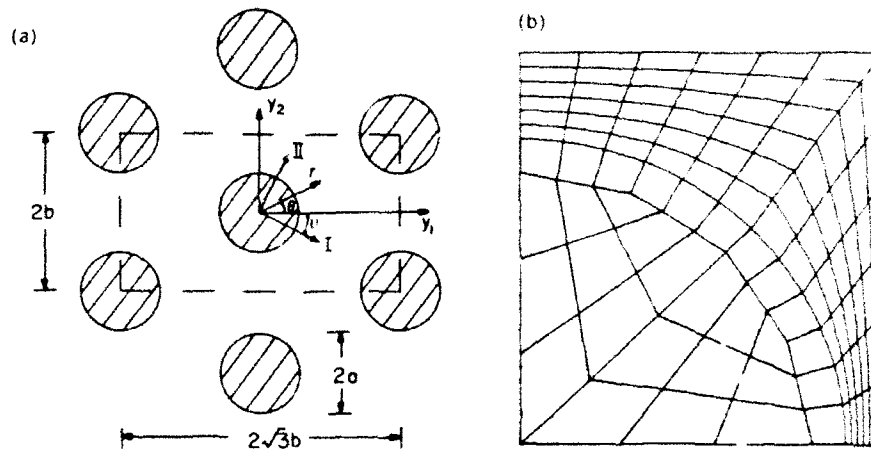


FIG. 11. (a) Hexagonal array with unit cell indicated. (b) Finite element mesh.

element with reduced integration was used to avoid locking. The considered loading of the unit cell [Fig. 11(a)] is symmetric with respect to the y_1 - and y_2 -axes. This implies that only an eighth of the indicated unit cell in Fig. 11(a) need be analyzed. The mesh shown in Fig. 11(b) is subject to the following in-plane boundary conditions for the tractions T_i and displacements u_i on the boundary S :

$$T_i \left(\frac{\sqrt{3}}{2} b, \frac{b}{2} + c \right) = T_i \left(\frac{\sqrt{3}}{2} b, \frac{b}{2} - c \right), \quad 0 \leq c \leq \frac{b}{2},$$

$$u_2(y_2 = 0) = -u_2(y_2 = b) = \text{constant} \quad \text{so} \quad \int_{y_2=0} T_2 \, dS - \int_{y_2=b} T_2 \, dS = 0,$$

$$u_1(y_1 = 0) = -\frac{\sqrt{3}}{2} b \langle \epsilon_1 \rangle, \quad \frac{1}{b} \int_{y_2=0} T_1 \, dS = -\langle \sigma_1 \rangle,$$

where $\langle \sigma_1 \rangle$ is the average stress and $\langle \epsilon_1 \rangle$ is the average strain in the 1-direction. The generalized plane strain condition gives

$$\epsilon_3 = \text{constant} \quad \text{so} \quad \int_{y_1=0} T_3 \, dS = 0.$$

A detailed description of the derivation of the boundary conditions for different loadings is given in JANSSON (1990a).

The elastic properties of fiber and matrix are not greatly affected by the history of processing and heat treatment of the composite so that it is possible to use data from the literature. However, the flow properties of the Al-Li matrix alloy are strongly dependent on the histories of heat treatment and cold-working (STARKE *et al.*, 1981; SAKUI and TAMURA, 1969). Details of the processing of the composite and of any post-heat treatments are not available. Hence, the exact state of the matrix is not

known and it is not possible to determine the flow properties of the matrix from the literature. The only means of estimating the flow properties of the matrix of the composite is to select matrix properties so that the calculated response fits the experimental stress-strain curve for the composite. This procedure has been performed by JÄNSSON (1990b), who demonstrated that the matrix properties obtained from one stress state could be used to predict accurately stress-strain relationships for other loading states. The initial yield stress of the matrix was determined to be 94 MPa with a hardening exponent $n = 5$ (Fig. 4) for isotropic hardening. The isotropic hardening cannot describe the matrix behavior when it is subjected to cyclic loading conditions and nonlinear kinematic hardening would be more appropriate. The tests required to determine the cyclic properties of the matrix have not been performed due to lack of material. However, observations indicate that the initial yield stress is close to the cyclic yield stress of the composite. The matrix was therefore modeled as an elastic-perfectly-plastic material. In the calculations the fibers are assumed to be linear elastic and the matrix behavior is modelled with a small-strain J_2 perfectly-plastic theory using the properties given in Table 1. It is therefore not expected that the calculations can be used to provide accurate predictions but should be sufficiently reliable to provide insight into the material behavior.

The calculated transverse stress-strain curve (Fig. 4) for an elastic-perfectly-plastic matrix agrees well with the experimental curve up to $\epsilon = 0.1\%$. The calculated limit load is much lower than the observed load because the matrix hardening has not been included. It can be noted that the increase in limit load is 30% for the perfectly-plastic matrix. A substantial portion of the increase comes from the plane strain condition for the matrix in the fiber direction which is $2\sqrt{3}$ and the remainder represents constraint. The calculated strain ranges agree well with the measured values (Fig. 5).

The calculated response for constant stress and cyclic temperature [Fig. 12(a) and (b)] exhibit the same features as the experiments [Fig. 3(a) and (b)] with a short transition period for low transverse stress and a long transition period for high transverse stress.

In performing the elastic-plastic calculation it was possible to determine initial yield surface for the case of no residual stresses and shakedown boundary given in Fig. 13. These have been expressed in terms of the dimensionless loadings $E\Delta\alpha/\Delta T$, σ_i/σ_0 , and σ_T/σ_0 . It was found for an exponentially temperature-dependent yield stress that the shakedown boundary is given by the result for a temperature-independent yield stress to a good approximation by replacing the yield stress with the average yield stress for the temperature-dependent case. The initial yield surface is dependent on the residual stress state induced during fabrication and cannot be determined without knowing

TABLE 1. *Material constants used in computations*
($c_f = 55\%$)

	E (GPa)	ν	α ($^{\circ}\text{C}$)	σ_i (MPa)
Fiber	345	0.26	8.6×10^{-6}	
Matrix	70	0.32	24×10^{-6}	95

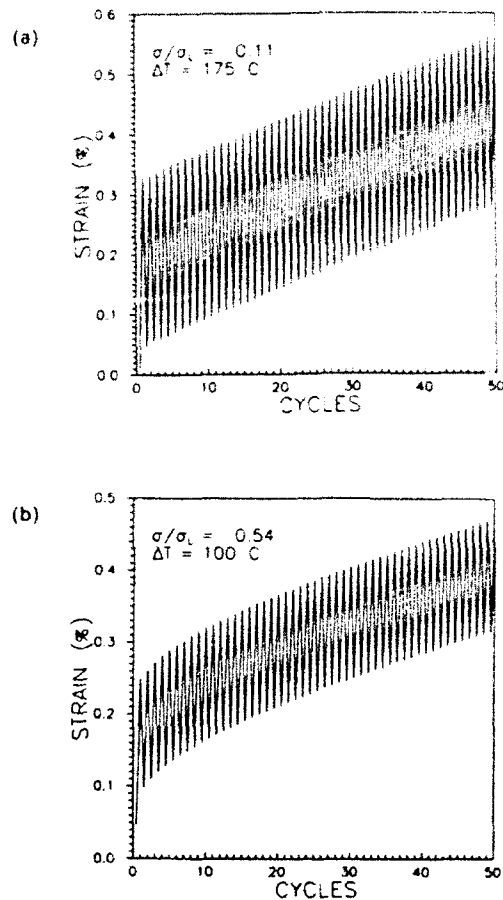


FIG. 12. Calculated strain accumulation: (a) low transverse loading, (b) high transverse loading.

the history of the composite. The shakedown boundary is not dependent on the history. The ratchet rates for different loading conditions fall on the master curve (Fig. 14) when plotted as a function of $\Delta\epsilon_T \sigma/\sigma_L$, where $\Delta\epsilon_T$ is the thermal strain increment in excess of the shakedown condition and σ/σ_L is the current transverse stress over the limit stress.

It was observed earlier that the failure strain was found to be strongly dependent on the transverse stress (Fig. 8). It is known that ductility is usually strongly dependent on the void growth factor $\sigma_{kk}/\bar{\sigma}$ for a ductile fracture, where σ_{kk} is the sum of the principal stresses and $\bar{\sigma}$ represents the effective stress. The void growth factor in the matrix attains its highest value close to the fiber-matrix interface (JANSSON, 1990b). The evolution of the void growth factor with the highest peak value is plotted in Fig. 15 as a function of accumulated transverse strain for different loadings. For transverse tension it increases from 3 at the initial linear elastic response to 6 at the observed fracture strain. Pure heating causes a hydrostatic pressure in the matrix. For transverse

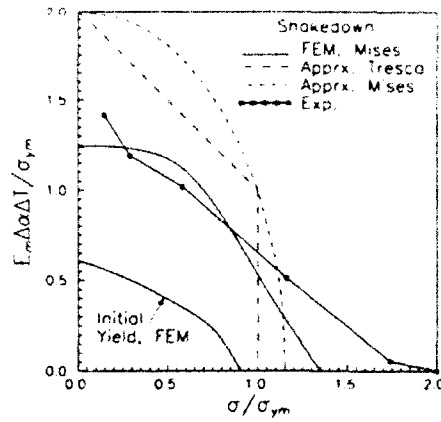


FIG. 13. Initial yield surface and shakedown region

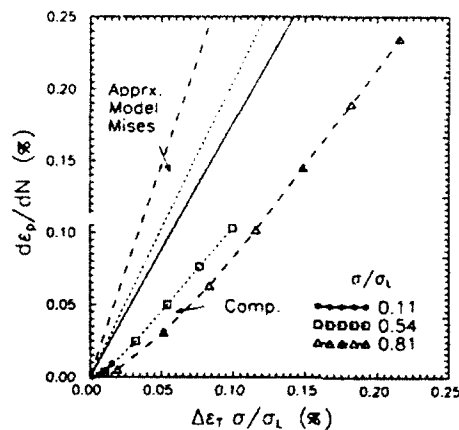


FIG. 14. Calculated steady-state plastic strain accumulation as a function of strain range and transverse loading.

loading combined with thermal cycling $\sigma_{kk}/\bar{\sigma}$ decreases during the heating period after the initial transverse loading and increases during the subsequent cooling period. The calculations indicate that the peak value of $\sigma_{kk}/\bar{\sigma}$ decreases initially for low values of transverse stress (Fig. 16). However, as strain is accumulated $\sigma_{kk}/\bar{\sigma}$ increases and reaches a steady-state condition with an increase of $\sigma_{kk}/\bar{\sigma}$ for each cycle.

The computations indicate that the peak value in a cycle of $\sigma_{kk}/\bar{\sigma}$ for a given accumulated transverse strain is strongly dependent on the magnitude of the transverse stress (Fig. 16). A low transverse stress requires more strain than a high transverse stress to build up the same constraint.

In Fig. 17 the equivalent plastic strain at the location with the highest value of $\sigma_{kk}/\bar{\sigma}$ is plotted against the accumulated transverse strain for different loadings. From Fig.

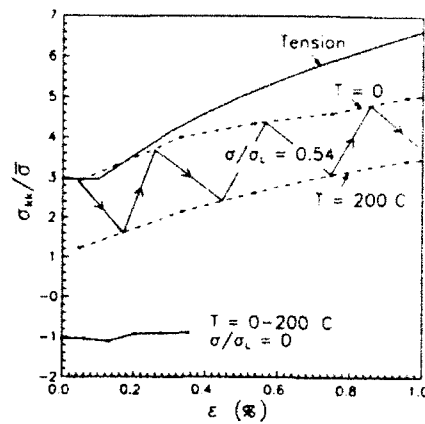


FIG. 15. History of void growth factor at location in matrix with highest peak value

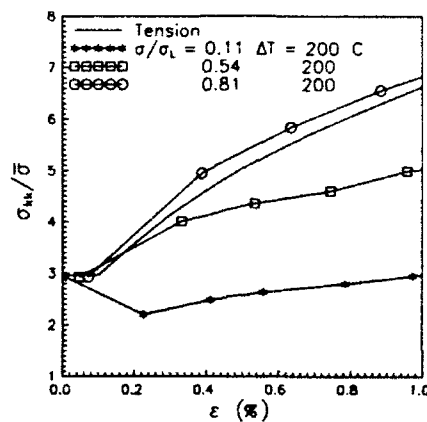


FIG. 16. Peak value of void growth factor in each cycle as a function of transverse strain.

17 it can be deduced that the equivalent strain is linearly related to the transverse strain and is relatively independent of the transverse loading.

5. ANALYSIS OF THE EXPERIMENTAL AND COMPUTATIONAL STUDIES

The experiments and computations indicate that after a transient response the material reaches a steady-state condition. If the operating point lies within the shakedown condition the final behavior of the composite is elastic. When the shakedown condition is exceeded steady-state ratcheting occurs. The experimental contours of constant ratcheting rates are found to be parallel to the surface defining the shakedown surface (Fig. 6). Computational studies based on the assumption that the matrix is

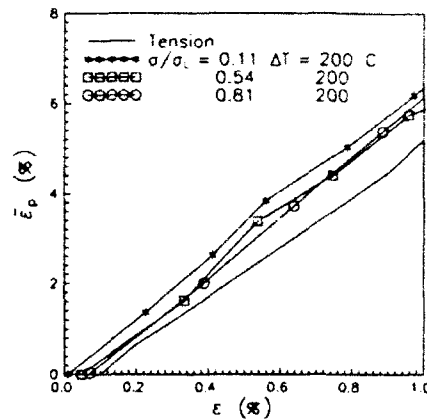


FIG. 17. Relation between effective strain at the location of the highest void growth factor and transverse strain.

elastic-perfectly-plastic also predict shakedown behavior but the shape of the predicted shakedown surface is slightly convex while the experimental results fall on a straight line (Fig. 13). The computations give a close prediction of the shakedown condition for low to intermediate transverse loading. The elastic-perfectly-plastic matrix model underestimates the limit strength of the composite and the shakedown region for high transverse loadings. Results for an approximate model that provides insight to the shakedown mechanisms in the composite are also given in Fig. 13. The model is based on constant stress fields in fiber and matrix, and is given in the Appendix. It underestimates the stress concentration for thermal loading and the limit load of the composite. The stress concentration for thermal loading can be determined accurately by using the elastic solution for a concentric cylinder model.

The calculations and general results for shakedown conditions [cf. PONTER and COCKS (1982)], indicate that the shakedown condition should intercept the stress axis at the limit stress. However, the experimental values intercept at a slightly lower stress (170 MPa) compared to the measured limit stress of 200 MPa. This discrepancy may be caused by the simple constitutive equations used in the calculations. The experiments intercept the temperature axis at 130°C and the calculations predict 110°C. This is close in view of the uncertainty of CTEs of fiber and matrix and yield stress. This indicates that the transverse strength is weakened when the composite is subjected to cyclic loading conditions.

It is observed experimentally that the ratchet strain rate has the form

$$\frac{d\epsilon_p}{dN} = f(\beta), \quad (3)$$

where β is proportional to the distance outside the shakedown surface and $f(\beta)$ is defined in Fig. 7. The simplified analysis performed in the Appendix for the Tresca yield condition gives similar results and predicts the same relative change in ratcheting rate for operating points far in excess of the shakedown condition. However, the

computer calculations predict a more complex structure of the expression for the ratcheting rate with the form

$$\frac{d\epsilon_r}{dN} = \frac{\sigma}{\sigma_i} f(\beta), \quad (4)$$

where β is the thermal strain in excess of the shakedown condition and is then also proportional to the distance outside the shakedown surface in the temperature direction.

It can be deduced from Fig. 14 that $f(\beta)$ is a nonlinear function of β for operating conditions close to the shakedown condition that is consistent with the experimental observations. For operating conditions far in excess of the shakedown condition it is linearly dependent on β and is consistent with the model in the Appendix for the Mises yield condition.

The approximate model and the calculations give the same trend when the cyclic plastic region extends over the whole unit cell.

A lower bound on the ratchet strain per cycle has been determined by PONTÉ and COCKS (1982) for Bree-like problems where the ratchet strain is uniform through the body. The lower bound applies for loading conditions which just exceed the shakedown condition. The lower bound is given by

$$\frac{\Delta\epsilon_r}{\Delta N} \geq 4\Delta\epsilon_e + \Delta\epsilon_T, \quad (5)$$

where the increment of elastic strain is given as

$$\Delta\epsilon_e = \frac{\Delta\sigma_T}{E}, \quad (6)$$

where $\Delta\sigma$ is the stress increment between the current state and the shakedown condition (Fig. 13) and E is the modulus in the transverse direction. The thermal strain can be identified for the present problem as

$$\Delta\epsilon_T = \Delta\alpha\Delta T, \quad (7)$$

where $\Delta\alpha$ is the difference in coefficient of thermal expansion between fiber and matrix and ΔT is the temperature increment in excess of the shakedown condition. The experiments exhibit ratcheting rates that are lower than the lower bound (5). For operating conditions close to shakedown the cyclic plastic zones do not extend over a large portion of the matrix and the bound is not applicable. For operating conditions far in excess of shakedown the cyclic zone extends over a large portion of the matrix and the bound gives a better estimate for these conditions.

The failure strain can differ by over an order of magnitude depending on the operating condition. This behavior which is illustrated in Fig. 8 has been observed previously by COTTRELL (1964). It is known for Al-Li (PILLING and RIDLEY, 1986) that ductile failure is the result of void nucleation and growth from small particles. In the studies of HANCOCK and MACKENZIE (1976) it is suggested that, when failure is the result of void nucleation and growth, the effective strain ϵ_f at failure for multiaxial state of stress has the form

$$\epsilon_r = 1.65\epsilon_0 \exp\left(-\frac{1}{2} \frac{\sigma_{xx}}{\bar{\sigma}}\right), \quad (8)$$

where ϵ_0 is the uniaxial failure strain. The failure strain for this matrix in uniaxial tension is reported to be approximately 0.3 (SAKUI and TAMURA, 1969) and JANSSON (1990a) has reported in tests on the composite under consideration that the strain for in-plane shear parallel to the fibers is 0.2. From the computer studies it has been determined that transverse loading alone introduces a multiaxial stress state for which $\sigma_{xx}/\bar{\sigma} = 6.0$ over a large region of the matrix at fracture. This is not greatly different from the values present in the classical Prandtl punch problem. For a history-dependent stress state the damage equation of (8) is equivalent to

$$\int_0^{\epsilon_r} \exp\left(\frac{\sigma_{xx}}{2\bar{\sigma}}\right) d\bar{\epsilon} = 1.65\epsilon_0. \quad (9)$$

Applying formula (9) for the failure strain and using the data in Figs 16 and 17 gives the failure strain for transverse loading:

$$\epsilon'_{11} = 0.9\%.$$

which compares quite well with the observed failure strain of 0.8% in the transverse direction. Applying (9) for the thermomechanical loading histories gives the predicted failure strain is shown in Fig. 8. The observed failure strain is higher than that predicted by the model for low transverse stress. However, the model gives the right trend but clearly requires modification.

In the model it is assumed that catastrophic failure coincides with the condition when local failure occurs. This gives an accurate prediction when the transverse load is close to the limit load, when a small defect is sufficient to trigger failure.

In the case of low transverse loading the loss of load carrying capacity occurs in a small volume of matrix material and may not be sufficient to cause global fracture. The damage has to be extended over a larger volume and the calculations give the strain for the first matrix failure and not the strain for which the damage causes global instability. This may explain the observed difference in failure strains for low and high transverse loading. The analysis required to illustrate this failure mechanism would require calculations which follow the growth of damage throughout the matrix and it has not yet been attempted.

6. CONCLUSIONS

When the metal matrix composite was subjected to a constant transverse stress and cyclic temperature it is found that after an initial transient response the material reaches a steady-state condition.

For loading conditions which fall within a shakedown condition the increment of strain over a cycle is zero. However, if the shakedown condition is exceeded there is an increment of irreversible strain after each cycle of temperature. The shakedown condition is defined by the relation

$$g(\sigma_T, \Delta T) = \frac{\sigma_T}{\sigma_1} + \frac{\Delta T}{\Delta T_1} - 1 = 0.$$

where $\sigma_1 = 1.3\sigma_0$ and ΔT_1 is defined by

$$\frac{E_m \Delta \alpha \Delta T_1}{\sigma_1} = 1.4.$$

Predictions of finite element computations agree reasonable well with the experimental observations of the shakedown surface. The differences exist presumably because of the deficiencies in the constitutive equations of the matrix which in the calculations are assumed to be of a very simple form.

The increment of strain per cycle is also found to depend on the function which defines the shakedown surface so that

$$\frac{d\epsilon_1}{dN} = \exp(9.5 \times 10^{-2} \beta) - 1.$$

where β is defined as

$$\beta = g(\sigma_T, \Delta T).$$

The transverse failure strain varies substantially with operating conditions. The failure strain is 0.08% when transverse stress is the only loading, and it increases to 12% when the transverse stress is 30 MPa and the thermal loading is sufficiently high to cause ratcheting.

ACKNOWLEDGEMENTS

This work was supported by a grant from the NASA Lewis Research Center. The authors wish to express their gratitude to Dr Peter Sotkovszki for his help with the metallurgical studies and to Chrysler Corporation for supplying the composite material.

REFERENCES

- | | | |
|---|------|--|
| CHAMPION, A. R.,
KRUEGER, A. R.,
HARTMAN, H. S. and
DHINGRA, A. K. | 1978 | <i>Proceedings of 2nd International Conference on Composite Materials</i> , p. 883. Metallurgical Society of the AIME. |
| COTTRELL, A. H. | 1964 | <i>The Mechanical Properties of Matter</i> . John Wiley, New York. |
| HANCOCK, J. W. and
MACKENZIE, A. C. | 1976 | <i>J. Mech. Phys. Solids</i> 24 , 141. |
| HIBBITT, H. D., KARLSSON, B. I.
and SORENSEN, E. P. | 1988 | <i>ABAQUS Users Manual</i> , Version 4.7. Hibbitt, Karlsson & Sorensen, Providence, RI. |

- JANSSON, S. 1990a *Homogenized Nonlinear Constitutive Properties and Local Stress Concentrations for Composites with Periodical Internal Structure*. Mechanical Engineering Department, UC Santa Barbara, CA.
- JANSSON, S. 1990b To appear in *Mech. Mater.*
- PILLING, J. and RIDLEY, N. 1986 *Al-Li Alloys* III, p. 184. Inst. Metals, London.
- PONTER, A. R. S. and COCKS, A. C. F. 1982 *The Incremental Strain Growth of an Elastic-Plastic Body Loaded in Excess of the Shakedown Limit*. Department of Engineering, Leicester University, Leicester.
- SAKUI, S. and TAMURA, M. 1969 *Trans. Japan Inst. Metals* 10, 343.
- STARKE, E. A., SANDERS, T. H. and PALMER, J. G. 1981 *J. Metals* 33, 24.

APPENDIX:

DETERMINATION OF SHAKEDOWN SURFACE AND RATCHET STRAINS

A simple calculation has been performed which provides physical insight and some limited quantitative information.

The composite consists of an elastic-perfectly-plastic metal matrix with modulus E_m and yield stress σ_y . The fiber with modulus E_f is assumed to remain elastic. It is also assumed that the stresses are constant in the matrix and fiber, and that the fiber is so stiff that the longitudinal strain is given by the thermal expansion of the fiber. This is an approximation which satisfies equilibrium and consequently will tend to give lower bounds on stiffness, limit load and shakedown conditions.

Since the fiber modulus E_f is 5 times higher than the matrix modulus E_m , the elastic matrix response is readily calculated using the condition

$$\epsilon_3 = \frac{\sigma_3}{E_m} - \frac{\nu_m \sigma_1}{E_m} + \Delta \alpha \Delta T = 0, \quad (A1)$$

where σ_1 is the stress corresponding to the transverse loading and σ_3 is the stress in the fiber direction acting on the matrix. Hence, for heating

$$\sigma_3 = -E_m \Delta \alpha \Delta T_1 + \nu_m \sigma_1. \quad (A2)$$

Using the Tresca yield condition plastic yielding occurs when

$$\sigma_3 - \sigma_1 = -\sigma_y \quad (A3)$$

if $\sigma_3 < \sigma_2$. Eliminating σ_3 gives

$$\sigma_1(1 - \nu_m) = \sigma_y - E \Delta \alpha \Delta T_1. \quad (A4)$$

Plastic deformation occurs if temperature is increased by a further amount, ΔT_2 . Since $\Delta \epsilon_3 = 0$,

$$\Delta \epsilon_3^p + \Delta \alpha \Delta T_2 = 0 \quad (A5)$$

and from the normality rule $\Delta \epsilon_3^p = -\Delta \epsilon_1^p$ the plastic strain ϵ_1^p is given by

$$\Delta \epsilon_1^p = \Delta \alpha \Delta T_2. \quad (A6)$$

Now when the temperature is decreased by an amount ΔT_3 , elastic unloading takes place until the yield condition $\sigma_3 - \sigma_2 = \sigma_y$ is reached. Since $\sigma_2 = 0$,

$$\sigma_3 = -\sigma_y + \sigma_1 + E_m \Delta \alpha \Delta T_3 = \sigma_y, \quad (A7)$$

from which the shakedown condition

$$E_m \Delta \alpha \Delta T_1 \leq 2\sigma_1 - \sigma_1 \quad (\text{A8})$$

can be deduced. The transverse load is also restricted by the limit load condition

$$\sigma_1 \leq \sigma_1 \quad (\text{A9})$$

If the shakedown condition is exceeded by applying an additional temperature decrease ΔT_4 then plastic increments of deformation occur:

$$\Delta \epsilon_1^p = \Delta \alpha \Delta T_4 \quad (\text{A10})$$

and normality gives

$$\Delta \epsilon_1^p = -\Delta \epsilon_2^p \quad (\text{A11})$$

In continued cycling no incremental accumulation of strain can occur in the third direction because the fiber is elastic. For steady-state conditions

$$\Delta T_2 = -\Delta T_4 \quad (\text{A12})$$

Let the total temperature difference be ΔT for steady-state conditions. Hence,

$$\Delta T = \Delta T_2 + \Delta T_1 \quad (\text{A13})$$

where ΔT_1 is the value for shakedown. The expression for the ratchet strain increment in the 1-direction is then

$$\frac{\Delta \epsilon_1^p}{\sigma_1 E_m} = \frac{E_m \Delta \alpha \Delta T}{\sigma_1} + \frac{\sigma_1}{\sigma_1} - 2 \quad (\text{A14})$$

This increment can also be expressed in terms of the shakedown condition. Defining the function g by

$$g_1(\Delta T, \sigma_1) = \frac{E_m \Delta \alpha \Delta T}{\sigma_1} + \frac{\sigma_1}{\sigma_1} - 2 \quad (\text{A15})$$

gives the condition for shakedown

$$g_1(\Delta T, \sigma_1) \leq 0 \quad (\text{A16})$$

The ratchet increment of strain when the shakedown condition is exceeded is given by

$$\Delta \epsilon_1^p = \frac{\sigma_1}{E_m} g_1(\Delta T, \sigma_1) = \Delta \alpha \Delta T' \quad (\text{A17a, b})$$

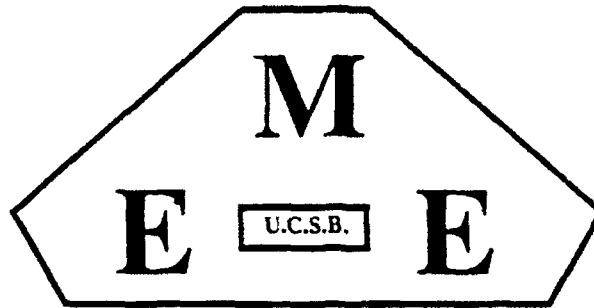
where $\Delta T'$ is the temperature change in excess of the shakedown condition. The same model for a Mises yield condition gives the shakedown boundary

$$g_2(\Delta T, \sigma_1) = \frac{E_m \Delta \alpha \Delta T}{\sigma_1} - \sqrt{4 - 3 \left(\frac{\sigma_1}{\sigma_1} \right)^2} \quad (\text{A18})$$

with the ratchet increment of strain

$$\Delta \epsilon_1^p = \frac{3}{4} \frac{\sigma_1}{E_m} \frac{1}{\sqrt{\left(\frac{\sigma_1}{\sigma_1} \right)^2 - \frac{3}{4}}} g_2(\Delta T, \sigma_1) = \sqrt{\frac{3}{1 - \left(\frac{\sigma_1}{\sigma_1} \right)^2}} \frac{\sigma_1}{\sigma_1} \Delta \alpha \Delta T' \quad (\text{A19a, b})$$

where $\sigma_1 = (2/\sqrt{3})\sigma_1$.



MECHANICAL AND ENVIRONMENTAL
ENGINEERING DEPARTMENT

Modeling of Anisotropic Behavior of Weakly Bonded Fiber Reinforced MMC's

S. R. Gunawardena, S. Jansson, F. A. Leckie

Department of Mechanical and Environmental Engineering

University of California at Santa Barbara

Santa Barbara, CA 93106

February, 1993

ABSTRACT

The anisotropic mechanical behavior of a continuous fiber reinforced Ti alloy matrix composite which possesses a weak fiber matrix interface is modeled numerically. Effects of interface properties and residual stresses incurred during the fabrication are addressed in detail. The computational modeling is guided by comparison with experimental data. The study provides an understanding which will be used to model the multiaxial behavior of weakly bonded composites and to provide a tool for predicting the failure of composite structures.

1. INTRODUCTION

Continuous fiber reinforced metal matrix composites (MMC's) are attractive because of excellent longitudinal properties and relatively high transverse strength and stiffness. The MMC's can be utilized effectively when the loading is predominantly uniaxial with primary stresses in the longitudinal direction and only secondary stresses in transverse directions. However, many structural components and joints are subjected to complex multiaxial stress states. The efficient use of composite materials in such situations requires an understanding of the overall anisotropic mechanical behavior of the MMC systems. MMC's are presently available in restricted quantities and shapes which limit the data that can be produced experimentally. This implies that for the present, numerical models are useful supplements and provide estimates of mechanical responses that cannot be determined experimentally. The models also provide insight which helps establish the failure conditions of the composite.

Experimental and numerical procedures have been applied in a previous study (Jansson,

1991) to establish the anisotropic behavior of an FP/Al system which features a strong interface. The present study focuses on the anisotropic mechanical behavior of SCS6/Ti 15-3 which is a candidate for moderately high temperature application. The composite features a weak interface designed to maintain the fiber strength in the fabricated composite.

Single deformation modes such as the transverse tensile behavior of the similar system SCS6/Ti-6V-4Al has been studied by Nimmer et al (1990, 1991). Experiments (Jansson et al, 1991) established that the fiber matrix interface plays a major role on the transverse and in-plane shear behavior of the composite. For a system featuring a perfect bond, the constraints induced by the fibers cause the transverse strength to be higher than the matrix strength. The use of a weak interface in the SCS6/ Ti 15-3 system results in a transverse strength that is substantially lower than the matrix strength.

A detailed micro-mechanical model is developed that determines the influence of weak interface, residual stresses from fabrication and the matrix plasticity. The model is verified by comparing the computations with experimental data obtained from longitudinal tension, transverse tension and in-plane shear tests performed on specimens manufactured from the composite plate. The different failure modes are also investigated so that failure criteria can be established.

2.COMPOSITE MATERIAL

The material used in this study is SCS6/Ti 15-3 made by Textron. It consists of SiC fibers

with a carbon and a SiC coating in a uniaxial lay-up. The fiber volume fraction is 35% and the average fiber diameter 140 μ m. The matrix is a β -Ti alloy, Ti-15V-3Cr-3Al-3Sn. The composite is fabricated by vacuum hot pressing a fiber-matrix foil lay-up. Detailed information of the processing is not available, but the composite is consolidated at approximately 900 C. In the subsequent cool down, the mismatch in coefficients of thermal expansion of fibers and the matrix causes residual stresses.

Tensile properties of the matrix were obtained from tests on matrix foil extracted from the composite. The fiber modulus was determined from the average of 50 bend tests (Jansson et al, 1991). The remaining properties have been extracted from the literature and the elastic properties are summarized in Table 1. The matrix and fiber stress-strain curves are shown in Fig. 1.

The longitudinal and transverse behavior (Jansson et al, 1991) were determined using dog-bone specimens for longitudinal and transverse tension. Specimens of the Iosipescu type were used to determine the in-plane shear response.

3. MICRO MECHANICAL STUDY

Numerical simulations were performed using homogenization techniques in conjunction with the general purpose finite element package ABAQUS (1988). In the computations the fibers are assumed to be long parallel cylinders arranged in a hexagonal array (Fig. 3). This is the

simplest periodic array for which the linear elastic properties are transversely isotropic. The nonlinear response of the array has a slight deviation from transverse isotropy. It was demonstrated by Jansson (1991) that the array can be used to predict the properties of a transversely isotropic system with randomly distributed fibers, if care is exercised when selecting the loading directions. For a system with randomly distributed fibers the matrix area fraction on any plane cut through the composite is equal to the matrix volume fraction, cf Underwood (1970). However the matrix area fraction is strongly dependent on the orientation and location for a periodic array. The present system has some form of arrangement resulting from the fiber-foil consolidation process, but is difficult to identify any definite simple array type, since the distribution pattern differs from point to point. However it was found that an important feature of the weakly bonded systems for transverse tension is the matrix area fraction on the weakest planes. It was determined to be 40 %, which is substantially lower than the value of 65 % for randomly distributed fibers. The corresponding value for the hexagonal array is 38 % when loaded in the 1-direction, Fig. 2. The hexagonal array was selected in this case because it models the correct volume fraction and matrix area fraction on the weak planes that dictates the transverse strength.

In the homogenization technique, cf (Jansson, 1992), the displacement field is assumed to have the form

$$u_i = u_i^0 + \langle \epsilon_{ij} \rangle x_j + u_i^p \quad (1)$$

where u_i^0 is an arbitrary constant displacement, $\langle \epsilon_{ij} \rangle$ is the average strain in the composite and u_i^p is an unknown displacement field which is periodic on the unit cell. The average stress $\langle \sigma_{ij} \rangle$

can be determined from the traction T_i on surface S on the unit cell by use of the mean stress theorem as

$$\langle \sigma_{ij} \rangle = \frac{1}{V} \int_V T_i x_j ds \quad (2)$$

All the loading cases considered are symmetric with respect to the x_1 and x_2 axes in Fig. 2 and the displacement field has an inversion symmetry about the point $(x_1=a\sqrt{3}/2, x_2=a/2)$. This implies that only the unit cell A-B-C-D in Fig. 2 need be analyzed. Ten node quadratic generalized plane strain elements with reduced integration were used to model the longitudinal and transverse behavior. The boundary conditions at the interface were selected to satisfy the interface bond characteristics. A fully bonded interface was modeled by enforcement of displacement continuity across the interface. The weak interface was modeled by a 3-node sliding interface element available in ABAQUS. The interface is assumed to debond when the normal stresses become tensile and the interface is thereafter traction free. Normal compressive stresses can be accompanied by shear stresses given by Coulomb's law of friction. Restrictions of the code meant that the modeling of the in-plane shear response required a 3-dimensional analysis using a 20 node brick element. Boundary conditions which ensured generalized plane strain behavior and the symmetries on the unit cell were imposed. These conditions reduce the degrees of freedom in the model substantially and results in reasonable solution times. Numerical difficulties were encountered when calculating residual stresses using available 3-dimensional interface elements. This difficulty was overcome by modeling the interface as a thin elastic-perfectly plastic solid layer whose yield strength was selected to be equal to the sliding

resistance of the interface.

The fibers were assumed to be isotropic and linear elastic and the matrix is assumed to be elastic-plastic with isotropic hardening. The influence of different temperature dependence of moduli and matrix yield strength were studied. It was found that the simplified temperature dependence of the yield stress given in Fig. 3 together with temperature independent moduli gave the same residual stress distribution as more refined models. The elastic properties of fiber and matrix given in Table 1 and the temperature dependence of the matrix yield strength given in Fig. 3 were used in the computations.

3.1 Residual Stresses After Fabrication

The residual stresses following fabrication are likely to influence the mechanical behavior of weakly bonded composites. When calculating the residual stress fields the composite is assumed to be stress free at the consolidation temperature before it is subsequently cooled down to room temperature. The exact details of the processing are unknown and consequently no time-dependent viscous behavior was included in the analysis. The residual stress distribution in the matrix is shown in Fig. 4 for the consolidation temperature 900 C. The residual stress in the fiber consists of a compressive axial stress of 720 MPa and almost uniform compressive radial and hoop stresses of 220 MPa. The residual hoop and radial stresses in the matrix vary substantially. The highest magnitudes are found near the interface with a compressive radial stress of 200 MPa and a tensile hoop stress of 500 MPa. The axial stress is tensile and is almost constant, varying between 390 and 420 MPa. No matrix cracking was observed in the as received composite

(Jansson et al, 1990) which suggests that the matrix toughness and ductility are sufficiently high to sustain the tensile stresses induced during processing.

3.2 Longitudinal Tension

The computed stress-strain curves following the different assumed consolidation temperatures of 0, 600 and 900 C are shown in Fig. 5. The difference in response for different consolidation temperatures is modest which indicates that the magnitude of residual stress has only a weak effect on the longitudinal behavior. The calculated longitudinal modulus E_{33} and Poisson's ratio ν_{31} are close to the experimental values given in Table 2. A slight sample to sample variation in the longitudinal tensile response was observed in experiments, as shown in Fig. 5. The variation is equivalent to a variation in the consolidation temperatures of 600 C. This is unlikely and the observed variation is most likely caused by handling of the panels after fabrication.

Since the longitudinal response is only weakly affected by the constraint in the transverse direction the longitudinal stress strain relationship can be estimated closely using the simple parallel bar model to give

$$\sigma_{33} = fE_f \epsilon_{33} + (1-f) \left[\sigma_m \left(\epsilon_{33} + \frac{\sigma_{rm}}{E_m} \right) - \sigma_{rm} \right] \quad (3)$$

where, f is the volume fraction, E_f is the fiber modulus, E_m is the matrix modulus, σ_{rm} is the longitudinal residual stress in the matrix after consolidation and σ_m is the longitudinal stress in

the matrix. This relation agrees well with the corresponding numerical calculations when the longitudinal residual stress used is that determined by computation.

The calculated transverse contractions following consolidation temperatures of 0 and 900 C are compared with the experimental data in Fig. 6. The experimental and calculated curves exhibit the same behavior with an initial linear response followed by increased contraction after matrix yielding. The difference in the calculated responses for the two consolidation temperatures is modest and is of the same order as the sample to sample variation.

3.3 Transverse Tension

The effect of interface bond conditions on the transverse tensile behavior was first investigated by computing responses for an initially stress free state. Calculations were performed for a fully bonded and for a weak frictionless interface. As illustrated in Fig. 7a, the stress strain curve for the fully bonded interface has an initial transverse elastic modulus of 167 GPa and a limit strength of 1195 MPa. These values are higher than the experimentally observed values of 129 GPa and 420 MPa respectively. For a weak frictionless interface the calculated elastic modulus is 48 GPa and the limit strength 380 MPa. For this case the predicted elastic modulus is much lower than the experimental value, while the limit strength is in close agreement with experiment.

When a residual stress state corresponding to the consolidation temperature of 900 C is included in the analysis for the weakly bonded interface, it was found that the elastic properties,

Table 2, and the strength agree very well with experiment. The influence of the coefficient of friction at the interface on the stress-strain relationship is negligible as is shown in Fig. 7b for the values of $\mu = 0$ and 0.8 . The calculations predict that debond initiates when $\sigma_{11}=140$ MPa at the pole of the fiber and the angle of debond increases rapidly with applied stress until it subtends an angle of 90° . Matrix yielding was predicted to occur in a small confined region on first loading but the effect of plasticity on the transverse stress-strain behavior is not noticeable until after debond. This is illustrated in Fig. 7b where the stress strain curve for a linear elastic matrix shows the same response up to debond and the non-linearity caused by plasticity is only evident after the initiation of debond.

The presence of the weak interface reduces the transverse strength of the composite to approximately 40% of the matrix strength. A limit load calculation, based on a constant tensile stress in the ligament, gives the limit strength (Jansson et al, 1991) as

$$\sigma_{TL} = \frac{2}{\sqrt{3}} A_{fm} \sigma_{um} \quad (4)$$

where A_{fm} is the matrix area fraction and σ_{um} is the matrix strength. The limit load calculated using eqn. (4) is 420 MPa which agrees well with experimental and computational values.

The measured contraction in the unloaded transverse direction for transverse loading is shown in Fig. 8. The initial linear response is closely given by a linear elastic calculation based on a value of $\mu = 0.8$ at the interface and a residual stress state sufficiently high to maintain

continuity at the interface. Following the initial linear response, when debond occurs there is substantial strain increment in the loaded direction. The total strain just after debond is closely given by a calculation for a fully debonded interface with a linear elastic matrix. For higher stress the contraction increases as the region of plastic deformation increases in the matrix. The slope then follows the calculation for a fully plastic matrix and a debonded interface. The full simulation following consolidation temperature of 900 C has all the features of the observed deformation but slightly overestimates the contraction.

The longitudinal contraction resulting from the transverse loading is shown in Fig. 9. The initial linear response and the limit behavior are closely modelled using a consolidation temperature of 900 C and a sliding interface. While a coefficient of friction $\mu = 0.8$ fits the experiments most closely the sliding resistance has modest influence on the response

3.4 In Plane Shear

Experimental results are available for the Iosipescu specimen for two fiber orientations (Jansson et al, 1991). In one set of experiments the fibers are orientated in the direction of the notches, Fig. 10a, and is referred to as longitudinal loading. The other case when the fibers are orientated perpendicular to the notches, Fig. 10b is referred to as transverse loading. It was observed experimentally that the initial elastic moduli are close for the two orientations but the limit strength for transverse loading at 400 MPa was approximately 40% higher than the value of 280 MPa observed for longitudinal loading. In longitudinal loading the fibers are orientated such that the global stress field is constant over a long segment of the matrix orientated in the

fibers direction. This condition permits highly concentrated bands of shear to develop in the matrix along the fibers at the weakest plane. In the case of transverse loading only a short segment of the matrix along the fiber directions is subjected to the higher stress in the gauge section. This effect suppresses the development of bands of concentrated shear since the stresses decrease with increasing distance from the gauge section. Consequently the limit strength is higher for transverse loading compared to longitudinal loading. No such dependence on fiber orientation was observed (Jansson, 1991) for a system that has a strong interface and a smaller fiber diameter.

The computed and experimental shear stress-strain curves for longitudinal loading are shown in Figs. 10a. The computations for a fully bonded interface predict an initial elastic response which agrees with experiment, but the final limit strength is substantially higher than the experimental value. A calculation based on an interface yield strength of 185 MPa exhibits an initial non-linear response that agrees with experiment but the predicted limit strength is higher than the experimental value. The correct limit strength is given by a computation for which the interface yield strength is 115 MPa. Hence, it might be inferred that the interface is initially in full contact. Sliding first develops when the shear stress at the interface is 185 MPa and the sliding stress is subsequently reduced during the slip to a saturation value of 115 MPa.

The initial linear elastic response for transverse loading, Fig. 10b, is identical to the response for longitudinal loading. This suggests that the calculations based on the assumption that the local displacement field consists of linear and periodic components, eqn. (1), also predict the

correct linear elastic response for transverse loading. However the limit strength is higher for transverse loading, Fig. 10b, than the longitudinal loading, Fig. 10a. This implies that the calculations based on eqn. (1) underestimate the limit strength for transverse loading. As mentioned earlier, the plastic deformation in the matrix is very constrained for this loading and the assumption of a displacement field with linear and periodic, eqn. 1, components fails to pick up this feature.

To simulate this constraint the deformation field in the elastic fiber was still assumed to have linear and periodical components. However the deformation field in the matrix was assumed to have only linear components, to be given by,

$$u_3 = u_3^0 + \langle \gamma_{13} \rangle x_1 \quad (5)$$

This formulation suppresses the development of regions with high concentrations of shear. The calculated responses assuming the same interface characteristics as those assumed for longitudinal loading are shown in Fig. 10b. It can be observed that use of the same interfacial shear strength as that for longitudinal loading predicts the correct limit behavior for transverse loading. The initial shear modulus before debond and limit strengths for calculations based on an interface shear stress of 115 MPa are listed in Table 2 for the two loading cases.

A simple estimate of the limit strength for longitudinal loading is given by considering a deformation that is given by a slip in the matrix on the surface $x_1 = 0$ and at the fiber matrix interfaces. This gives

$$\tau_L = \tau_y^i \frac{\pi}{2} (1 - A_{fm}) + \frac{1}{\sqrt{3}} \sigma_{Lm} A_{fm} \quad (6)$$

where τ_L is the limiting strength of τ_{13} , τ_y^i is the shear strength of the interface, σ_{Lm} is the limit stress of the matrix under uniaxial tension and A_{fm} is the matrix area fraction of the weakest plane. For the system under consideration $A_{fm} = 0.4$ and use of eqn. (6) with the experimental limit strength $\tau_L = 300$ MPa gives an interface shear strength $\tau_y^i = 95$ MPa, which is close to the computed value of 115 MPa.

The limit strength for the transverse loading can be estimated by assuming that the deformation in the matrix is linear and as given by eqn. (5). This deformation causes a plastic deformation throughout the matrix with slip at the interface. A work balance gives

$$\tau_L = \frac{1}{\sqrt{3}} \sigma_{Lm} (1 - f) + \frac{4}{\pi} \tau_y^i f \quad (7)$$

where f is the fiber volume fraction. This expression is a modified version of the upper bound given by Majumdar and McLaughlin (1973) for a strong interface. Using the experimental strength $\tau_L = 400$ MPa in this relation gives an interfacial shear strength of $\tau_y^i = 100$ MPa, which is consistent with the value of 115 MPa determined from the computations.

3.5 Transverse Shear

While no experimental results are available for this form of loading, the calculations were performed to provide a more complete understanding of the anisotropic behavior of the material. Shear loading τ in the transverse plane is represented by the principal stress state shown in Fig. 11. Two loading conditions have been investigated: one loading defined by $\sigma_{11} = -\sigma_{22} = \tau$ and the other by $\sigma_{11} = \sigma_{22} = \tau$, where $\tau > 0$. Computed shear stress strain curves for a fully bonded and a frictionless interface following a consolidation temperature of 900 C are shown in the Figs. 11a and 11b. For the fully bonded interface the two loading cases, $\sigma_{11} > 0$ and $\sigma_{22} > 0$ exhibit very similar behavior with a limit strength of 600 MPa. However in the case of a weak interface, the strength for $\sigma_{11} > 0$ is 310 MPa while the strength for $\sigma_{22} > 0$ is 270 MPa. This difference indicates that a system with a debonded interface does not exhibit the transverse isotropy commonly assumed for fiber reinforced composites. It was observed in the calculations that the debond always initiated close the point of the interface whose normal coincides with the direction global maximum principal stress.

Pure transverse shear loading results in global strains that have both shear and normal components. For a fully bonded interface the normal strain component exists only when one of the constituents has a non-linear response. However for this case, as shown in Fig. 11c, the normal component is very small compared to the shear strain. For a weak interface the normal strain is small before debond and grows to 30 % of the shear strain after debond, Fig. 11c. For a initially stress free state the debond occurs earlier and the normal strain component is greater.

4. FAILURE MECHANISMS

The computational procedures described previously provide the local stress and strain distributions in the composite which can be used to determine local failure conditions of the constituents. Macroscopic failure condition for the composite can then be predicted for different loadings.

4.1 Longitudinal Tension

The fracture in the longitudinal tension is dominated by fiber failure. The observed failure strain of the composite is of the same magnitude as the fiber failure strain ϵ_f . The stress at failure can be written as

$$\sigma_{UTS} = f\sigma_F + (1-f)\sigma_{ym}\left(\epsilon_f + \frac{\sigma_{rm}}{E_m}\right) \quad (8)$$

where σ_{ym} is yield stress of the matrix at fiber failure and σ_F is the stress in the fibers at failure.

For the present residual stress state $\sigma_{ym} = 900$ MPa at failure.

The exact nature of the fiber failure is still an open question. Failure occurs when a defect of critical size has formed in the composite. One extreme estimate of the strength is to assume that fracture occurring in two adjacent fibers within a stress transfer length causes a critical defect. The average stress in the fibers when this occurs is give by

$$\sigma_F = f \frac{\overline{\sigma_F}}{\Gamma(1+1/m)} \left[\frac{\tau d^2 l_0^2 (m+1)(k-1)}{16fv\delta_t k^{m+1}-1} \right]^{\frac{1}{2m}} \quad (9)$$

where v is the loaded volume, k the stress concentration in a fiber next to a broken fiber, d is the fiber diameter, δ_t is the stress transfer length and Γ is the gamma function. This is the model by Zweben and Rosen (1970) modified to account for a linearly varying fiber stress within the transfer length of the fiber. Based on data for the SCS6 fiber given by Bair et al (1985) it was deduced that the average fiber strength is $\sigma_F = 4.3$ GPa for a gauge length $l_0 = 6.25$ mm and the Weibull modulus is $m = 6.5$. For the present specimen the loaded volume $v = 125$ mm³ and the transfer length is estimated to be $\delta_t = \tau_y/\sigma_F d/4$, where the sliding resistance of the interface $\tau_y = 115$ MPa. An upper bound on k for fibers arranged in an hexagonal array is $k = 1.17$. Use of these values in eqn. (9) gives a failure strength $\sigma_{UTS} = 1890$ MPa.

The other extreme is to assume that fiber fractures do not introduce local stress concentrations in adjacent fibers and that global load sharing occurs. The fiber contribution at the load maximum for the global load sharing model has been estimated in an approximate way by Curtin (1989) and Neumeister (1991) as

$$\sigma_F = \frac{\overline{\sigma_F}}{\Gamma(1+1/m)} \frac{m+1}{m+2} \left[\frac{4}{m+2} \frac{l_0 \tau_y \Gamma(1+1/m)}{d \overline{\sigma_F}} \right]^{\frac{1}{m+1}} \quad (10)$$

This model predicts a strength $\sigma_{UTS} = 2080$ MPa. Both models predict the strength within 10% and are in good agreement with the experimental result. Tests of specimens of different

volumes and with stress gradients are required to reveal the exact nature of the failure process and to discriminate between the models.

4.2 Transverse Tension and Shear

The observed failure strain in transverse tension is 1.2% which is approximately 40% of the uniaxial matrix failure strain (Fig. 1). The computations for transverse tension and shear indicate that the stiff fibers cause multiaxial stress fields to develop in the matrix. When a ductile material is subjected to stress states with a high hydrostatic tension component the failure ductility is reduced. Hancock and Mackenzie (1976) suggested that failure is the result of void nucleation and growth. They estimated that the effective plastic strain at failure, ϵ_f^* , for multiaxial stress states is related to the uniaxial failure strain by

$$\epsilon_f^* = 1.65 \epsilon_0 \exp \left[-\frac{1}{2} \frac{\sigma_{kk}}{\sigma^*} \right] \quad (11)$$

where ϵ_0 is the plastic component of the uniaxial failure strain of the matrix, σ_{kk} is the hydrostatic stress and σ^* is the von Mises equivalent stress. From the uniaxial stress-strain curve for the Ti alloy in Fig. 1. it can be deduced that $\epsilon_0 = 3\%$. This value for the matrix foil is substantially lower than what is normally observed for β -Ti alloys. The low matrix ductility implies that large strain effects can be neglected in the analysis. For a time dependent stress state, the void growth rate has to be integrated over the history and the used portion of the matrix ductility is given by

$$D = \frac{\int_0^{\bar{\epsilon}} \exp\left[\frac{\sigma_{kk}}{2\sigma^e}\right] d\bar{\epsilon}}{1.65\epsilon_0} \quad (12)$$

where the variable D is used as a damage variable with $D=0$ for a virgin material and $D=1$ when the material has lost its load carrying capacity and $\epsilon^e = \epsilon_f^e$. The evolution of the damage D has been calculated by integrating eqn. (12) numerically using the stresses and strain increments from the computations.

The distribution of the damage parameter D in transverse tension is shown in Fig. 12 for a global strain of 1%, which is close to the observed failure strain of 1.2%. The computations indicate that most of the load carrying capacity is lost. A region of high damage is localized in the matrix ligament between the fibers and stimulates fracture on a plane approximately at 45° to the loading direction. Microscopic observations (Jansson et al, 1991) showed the failure surface consists of plastically deformed matrix ligaments and debonded matrix fiber interfaces.

The damage distribution for transverse shear with $\tau > 0$ is shown in Fig. 13 for a global shear strain of 1.6% . The trend is similar to transverse tension with a region of high damage in the matrix ligament between the fibers, orientated in the direction of the global tensile principal direction. The damage starts to exceed unity in some regions of the matrix when the global stress is 272 MPa, which is 13% lower than the predicted limit strength of 310 MPa. This suggests that the available matrix ductility may be exceeded in portions of the matrix before the limit condition is reached.

4.3 In-Plane Shear

The only non-vanishing stress components in-plane shear, except for the residual thermal stresses, are the shear stresses τ_{13} and τ_{23} . This implies that this type of loading does not cause high hydrostatic stresses to build up in the matrix. The effect of the initial residual stress is small and the failure criterion described previously then simplifies to

$$D = \frac{1}{1.65} \left[\frac{\epsilon'}{\epsilon_0} \right] \quad (13)$$

The computed damage distribution for longitudinal loading corresponding to the observed failure strain $\gamma_{13} = 3\%$ is shown in Fig. 14. The damage exceeds unity across the whole matrix ligament between the fibers indicating that the model predicts a failure strain slightly lower than the experimental value.

5. CONCLUSIONS

The longitudinal and transverse tensile properties can be predicted by a computational model which makes use of fiber and matrix properties, fiber distribution and an interface which debonds when the interface is subjected to normal tension. In addition to predicting the elastic properties and limit strength the calculations also predict the failure strains. The residual stresses following the fabrication strongly affect the mechanical behavior. The compressive normal residual stress at the interface dictates that the initial elastic properties are consistent with normal

continuity at the interface. In transverse tension the applied stress can overcome the residual stress and interface debonding occurs which gives rise to a loss of stiffness. The presence of the debond also decreases greatly the transverse limit strength, with the composite strength being dictated by a matrix perforated by un-reinforced holes.

The in-plane shear properties cannot be predicted by a frictionless interface. It is necessary to assume an initial sliding stress of 185 MPa that subsequently reduces to 115 MPa when the sliding is fully developed. However the interface characteristics determined from the shear test with longitudinal loading predict the substantially different strength for the shear test with transverse loading. The different limit behavior for transverse and longitudinal shear loading indicates that the in-plane shear response is strongly dependent on the extent of the plastic zone along the fiber direction. This feature has to be addressed in the formulation of macroscopic constitutive equations.

The analysis of the transverse tension test indicates that the sliding resistance at the interface can be modeled by Columb friction with a coefficient of friction $\mu = 0.8$. Use of this value and the residual stress state following a consolidation temperature of 900 C predicts an initial sliding resistance of 160 MPa for in-plane shear. This is close to the value determined from the inplane shear test of 185 MPa. However, during the in-plane shear loading after matrix yielding the normal pressure at the interface relaxes and the steady state sliding resistance vanishes for a Columbs friction model. Microscopic observations of the fibers showed that the fibers have a surface texture with ridges oriented in the hoop direction. For in-plane shear loading

the sliding direction is normal to the ridges while it is parallel to the ridges for transverse tension and this could cause the observed steady state sliding resistance for in-plane shear.

Using the mechanisms of interface debonding and a void growth model for matrix failure it was possible to predict with accuracy the macroscopic failure strains for matrix dominated failure modes. The exact nature of the longitudinal failure is still an open question. However, models of two extreme failure conditions give approximately the same predictions of the failure stress.

It has been demonstrated that the composite properties can be predicted from the matrix, fiber and interface properties by using established computational procedures. In this case the interfacial properties have not been measured but have been inferred from the longitudinal shear test of the composite. Independent push-through tests (Warren et al, 1992) show sliding resistances that are close to the saturation value used here. The push-through test may therefore be used as a means of providing some information on the sliding characteristics for the analysis.

5. ACKNOWLEDGMENTS

Funding for this work has been provided by NASA-Lewis Research Center (NAG3-834), Pratt and Whitney (F432052) and the DARPA URI at UCSB (ONR N442-2494-23100).

6. REFERENCES

ABAQUS Finite Element Program, 1988, Hibbitt, Karlson and Sorensen, Inc., (Version 4.7).

Bain, K. R., Byrnes, M. L. and Jain, S. K., 1985, "Fatigue and Fracture of Titanium Aluminides," Allison Gas Turbine, Indianapolis, Indiana, EDR 13084.

Curtin, 1991, "Theory of Mechanical Properties of ceramic-matrix composites," Journal of American Ceramics Society, vol. 75 , pp. 2837-2845.

Jansson, S., 1991, "Mechanical Characterization and Modeling of Non Linear Deformation and Fracture of a Fiber Reinforced Metal Matrix Composite," Journal of Mechanics of Materials, Vol.12, pp. 47-62

Jansson, S. 1992, "Homogenized Nonlinear Constitutive properties and Local Stress Concentration for Composites with Periodic Internal Structure," International Journal of Solids and Structures, vol. 29, pp. 2181-2200.

Jansson, S., Deve, H. E. and Evans, A. G., 1991, "The Anisotropic Mechanical Properties of a Ti-Matrix Composite Reinforced with SiC Fibers," Metallurgical Transactions A, Vol. 22A, pp. 2975-2983.

Hancock, J.W. and Mackenzie, A. C., 1976, "On the Mechanisms of Ductile Fracture in High Strength Steels Subject to Multiaxial States of Stress," *Journal of the Mechanics and Physics of Solids*, Vol. 24, pp. 141-169.

Warren, P. D., Mackin, A. G. and Evans, A. G., 1992 "Design Analysis and application of an Improved Push-Through Test for the Measurement of Interface Properties in Composites," to appear in *Acta Metallurgica*.

Majumdar, S. and McLaughlin JR., P. V., 1973, "Upper Bounds to In-Plane Shear Strength of Unidirectional Fiber-Reinforced Composites," *Journal of Applied Mechanics*, vol.95, pp. 824-825.

Nimmer, R. P., Bankert, R. J., Russell, E. S., Smith, G. S., Wright, P. K., 1991, "Micromechanical Modeling of Fiber/Matrix Interface Effects in Transversely Loaded SiC/Ti-6-4 Metal Matrix Composites," *Journal of composites Technology & Research, JCTRER*, Vol. 13, No. 1, pp. 3-13.

Nimmer, R. P., 1990, "Fiber/Matrix Interface Effects in the Presence of Thermally Induced Residual Stresses," *Journal of composites Technology & Research, JCTRER*, Vol. 12, No. 2, pp. 65-75.

Neumesitrer, J., 1992, "A Constitutive Law for Longitudinally Reinforced Brittle Matrix Composites with Fiber Fragmentation and Stress Recovery," Department of Solid Mechanics, Chalmers University, Sweden.

Underwood, E. E., 1970, Quantitative Stereology, Addison-Wesley, Massachusetts, pp. 25-27.

Zweben, C. and Rosen, B. W., 1970, "A Statistical Theory of Material Strength with Application to Composite Materials," Journal of the Mechanics and Physics of Solids, vol. 18, pp. 189-206.

Table 1. Matrix and fiber properties at ambient temperature

	Matrix	Fiber
Young's Modulus (GPa)	115	360
Poisson's Ratio	0.33	0.17
Tensile Strength (MPa)	950	4300
Strain to failure in tension (%)	3	1.2
Coeff. of thermal expansion (1/C)	$9.7 \cdot 10^{-6}$	$4.5 \cdot 10^{-6}$

Table 2 Comparison of computed and experimental elastic properties

	E_{33}	ν_{33}	E_{11}	ν_{12}	ν_{13}	σ_{11L}	G_{13}^*	τ_{13L}^*	G_{13}^*	τ_{13L}^{**}
	GPa		GPa			MPa	GPa	MPa	GPa	MPa
Experimental	196	0.25	129	0.34	0.2	420	62	300	62	400
Computed	202	0.27	133	0.48	0.17	420	64	300	73	400

* Longitudinal loading

** Transverse loading

FIGURE CAPTIONS

Fig. 1 Uniaxial Stress-Strain behaviors of Ti 15-3 matrix and SCS6 fibers.

Fig. 2 Hexagonal array with unit cell indicated.

Fig. 3 Temperature dependence of matrix the yield strength and highest calculate equivalent matrix stress for a consolidation temperature of 900 C.

Fig. 4 Calculated residual stress distribution after consolidation at 900 C.

Fig. 5 Longitudinal stress-strain behavior for different consolidation temperatures.

Fig. 6 Transverse contraction for longitudinal loading.

Fig. 7 Transverse tensile stress-strain behavior for different interface characteristics.

(a) Effect of interface bond condition.

(b) Effect of friction at the interface.

Fig. 8 Contraction in unloaded transverse direction for transverse loading. $\Delta T = 0$ indicates an initially open interface and $\Delta T = \infty$ indicates an interface that remains closed.

Fig. 9 Contraction in longitudinal direction for transverse loading.

Fig. 10 In-plane shear stress-strain curves for different sliding conditions at the interface.

(a) Longitudinal loading

(b) Transverse loading

Fig. 11 Calculated transverse shear stress-strain curves for different consolidation temperatures and interface bound conditions

(a) Stress-Strain curve for $\sigma_{11} = -\sigma_{22} = \tau$

(b) Stress-Strain curve for $\sigma_{22} = -\sigma_{11} = \tau$

(c) Normal strain components for the two loadings.

Fig. 12 Distribution of damage parameter D for transverse tension, at $\epsilon_{11} = 1\%$.

Fig. 13 Distribution of damage parameter D for transverse shear at $\gamma = 1.6\%$.

Fig. 14 Distribution of damage parameter D for in-plane shear, at $\gamma_{13} = 3\%$

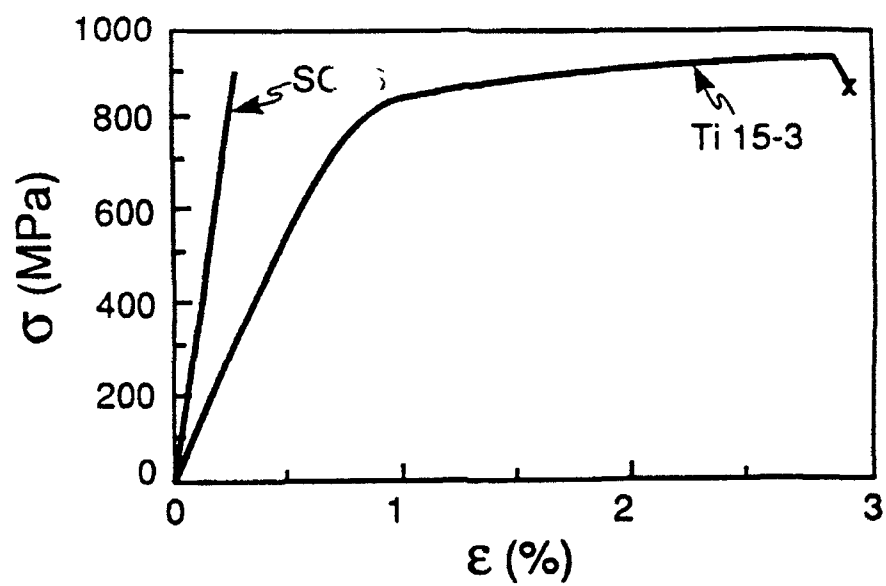


Fig. 1

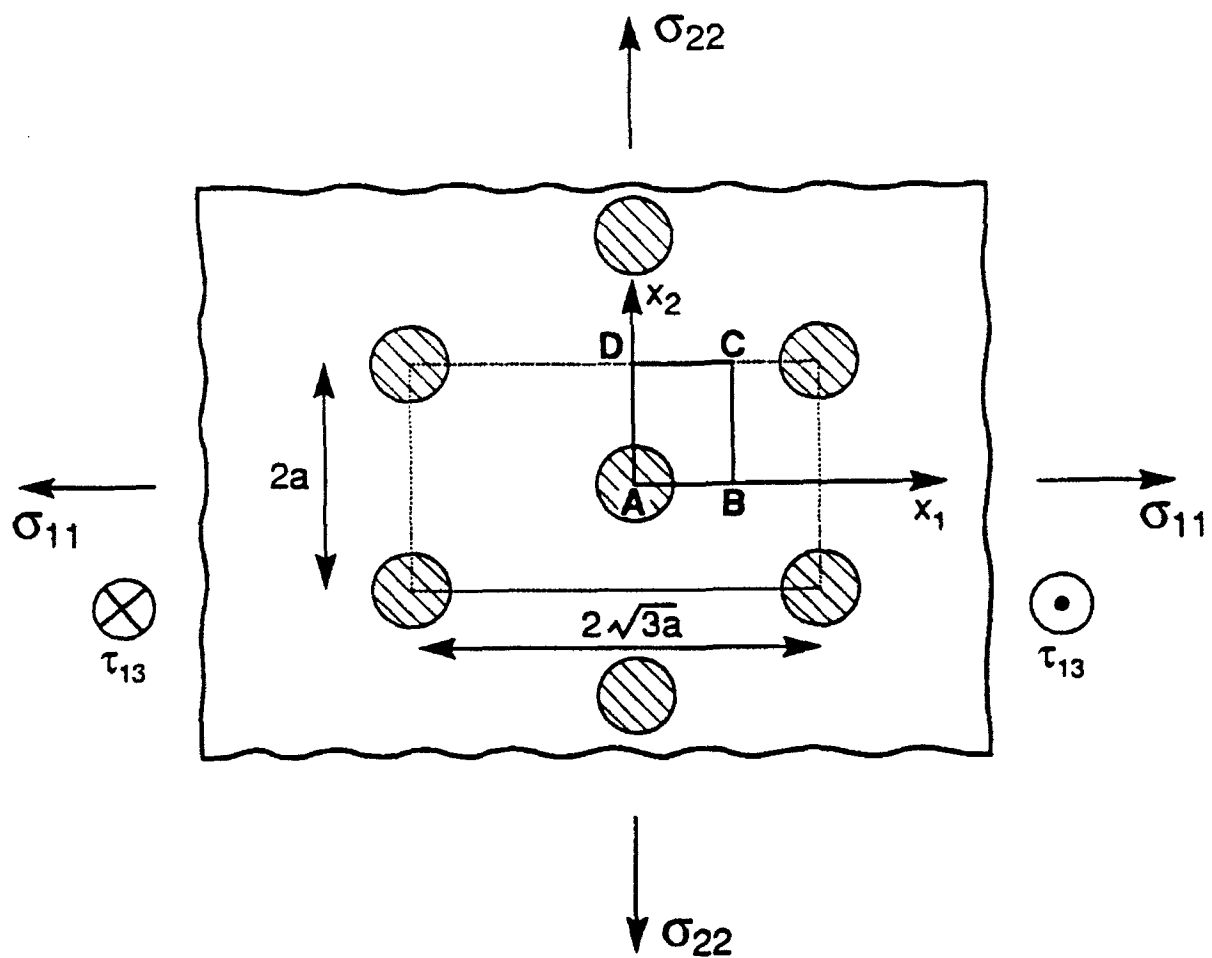


Fig. 2

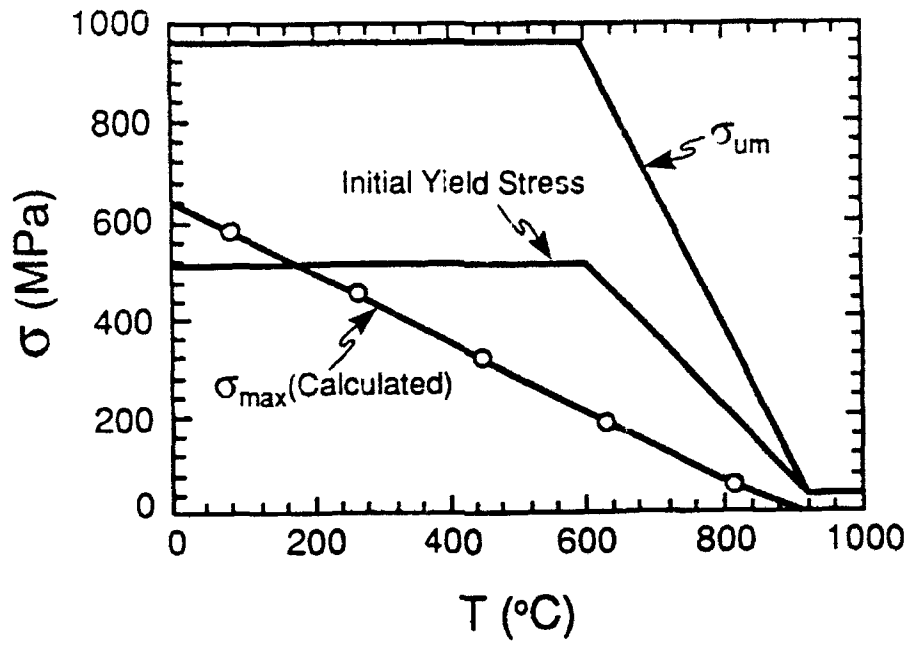
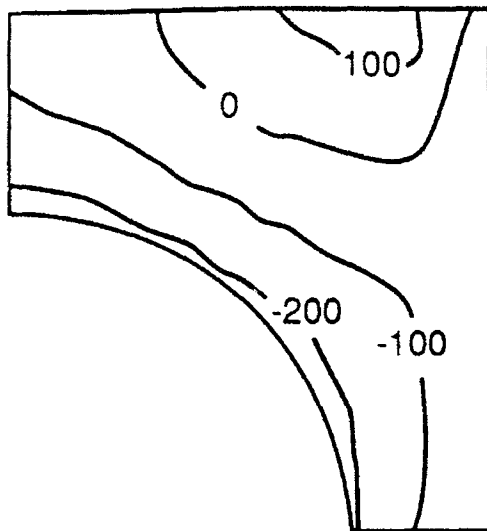
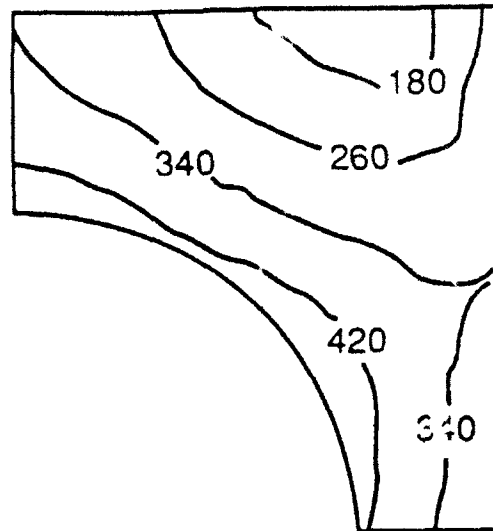


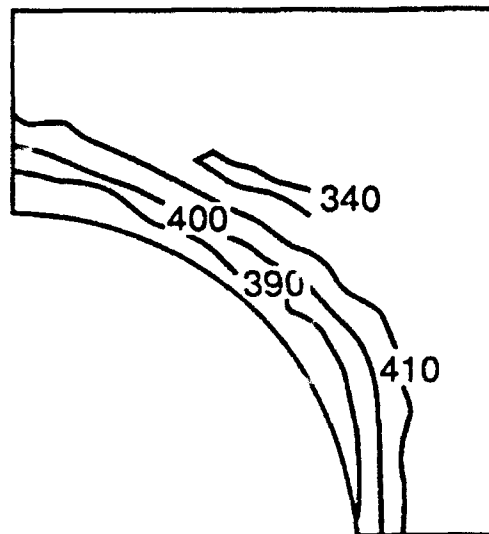
Fig. 3



Radial Stress



Hoop Stress



Axial Stress

Fig. 4

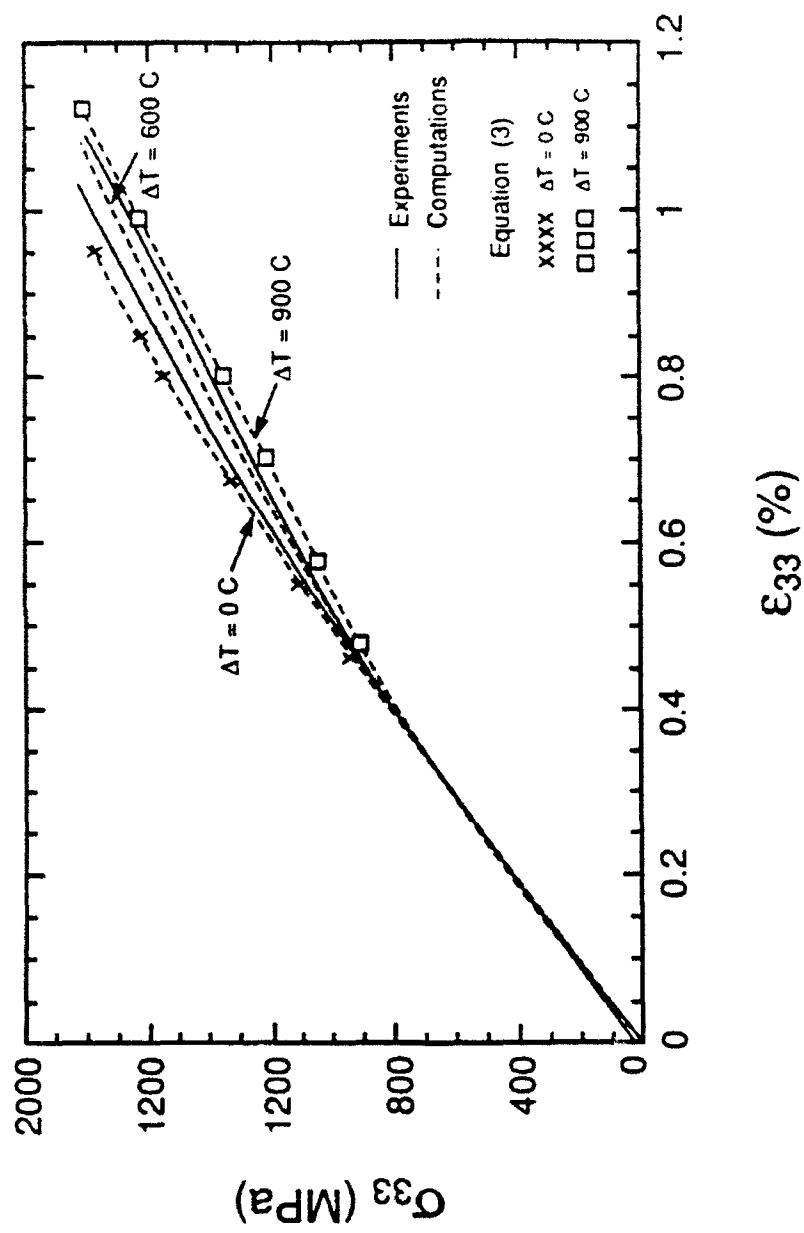


Fig. 5

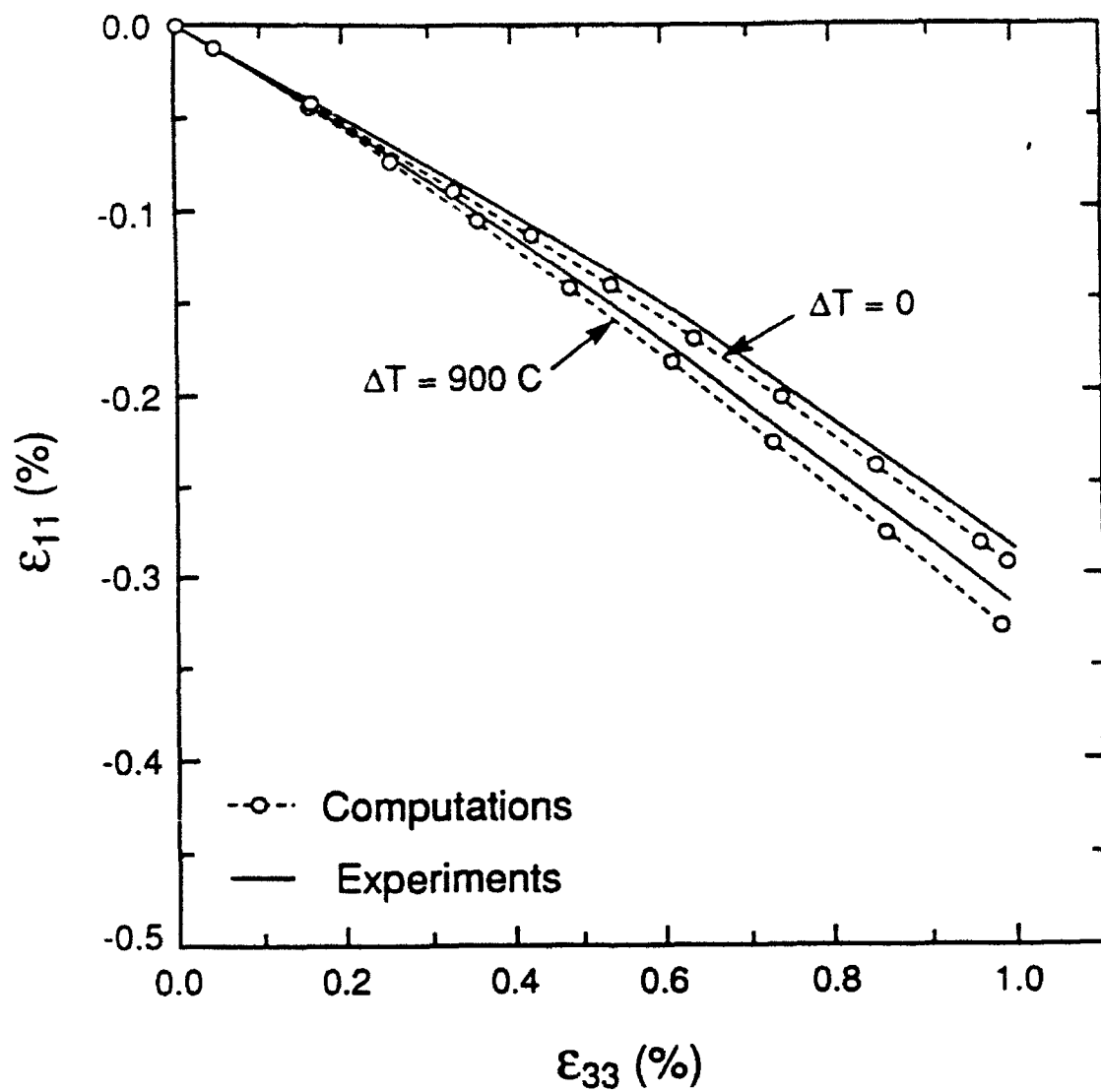


Fig. 6

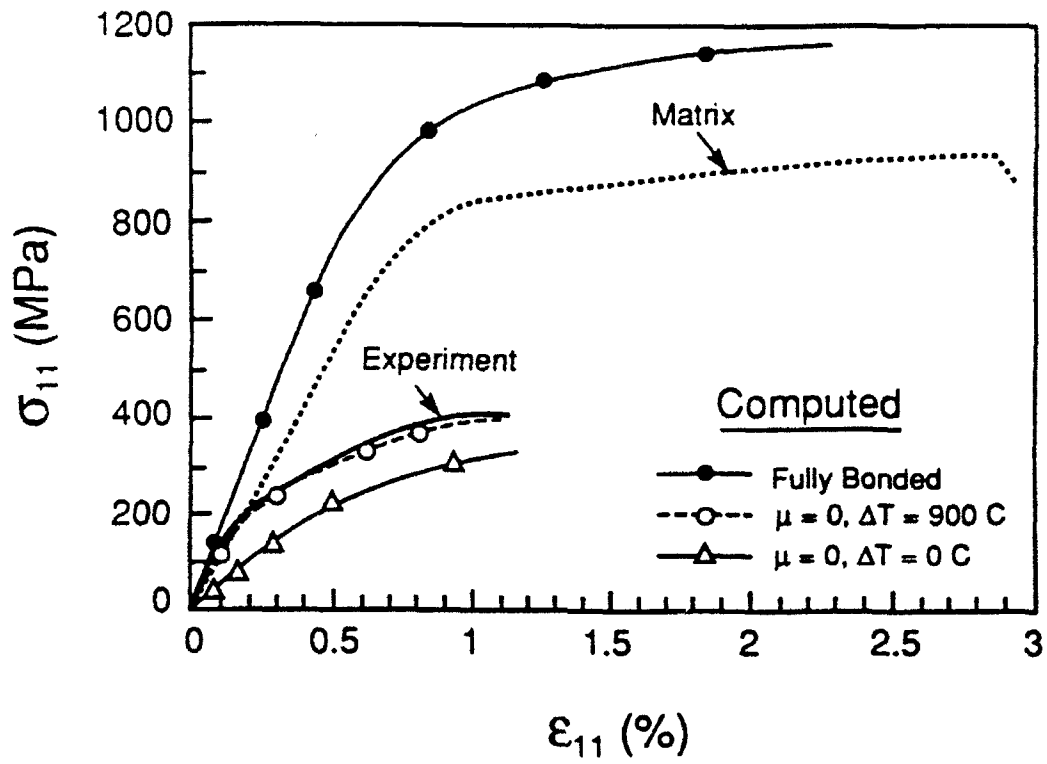


Fig. 7a

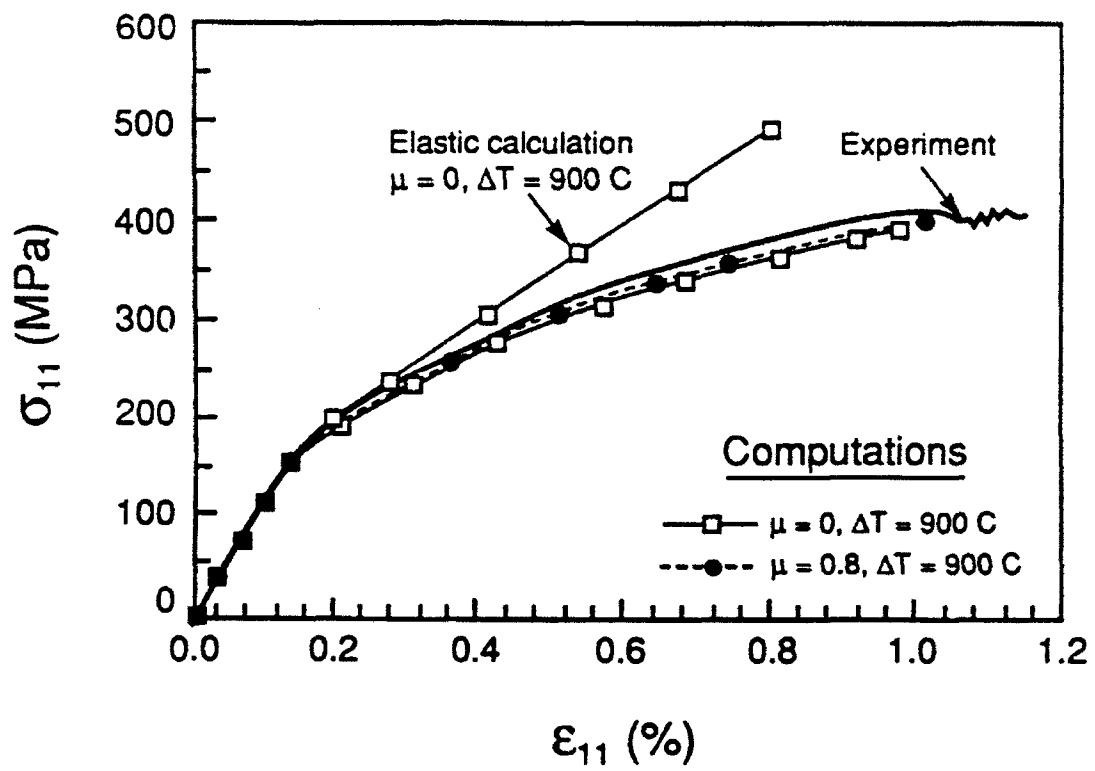


Fig. 7b

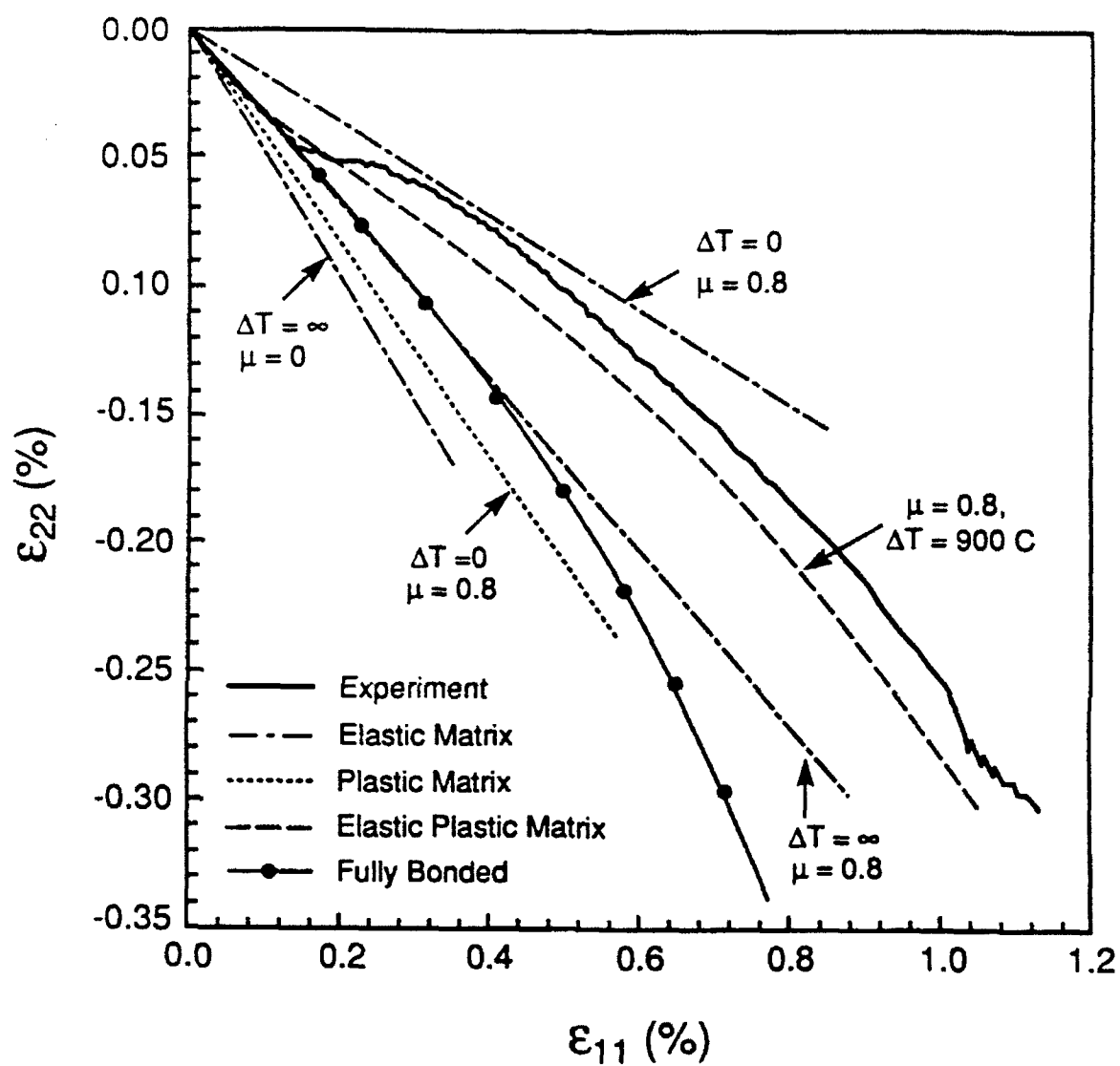


Fig. 8

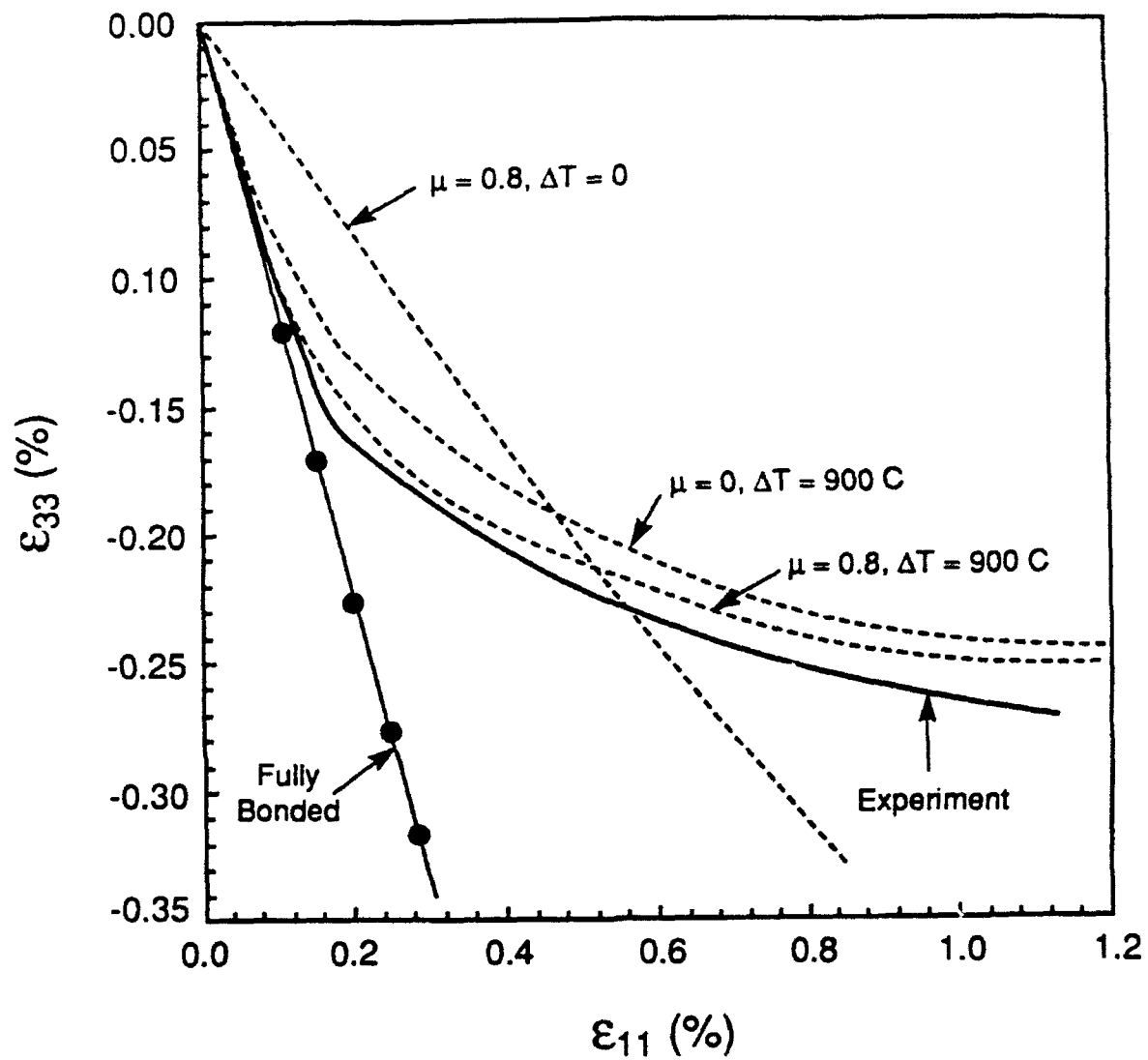


Fig. 9

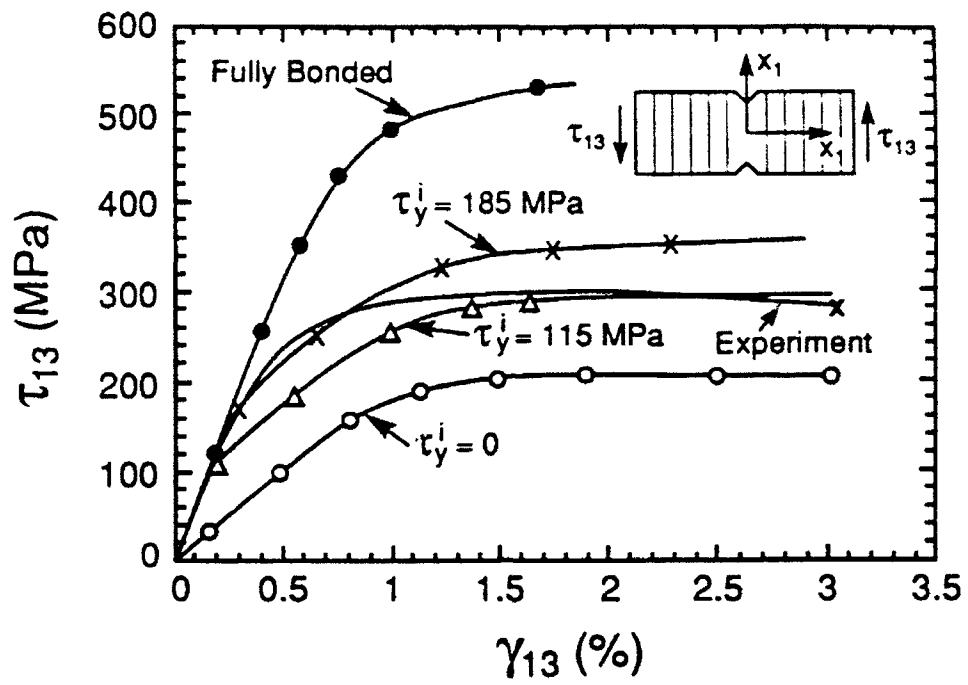


Fig. 10a

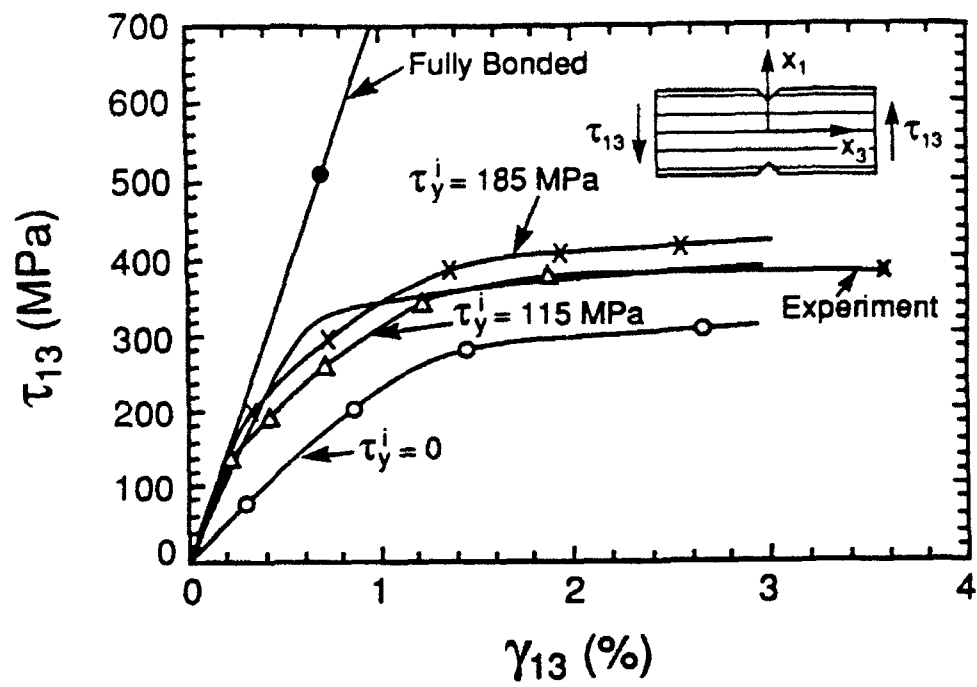


Fig. 10b

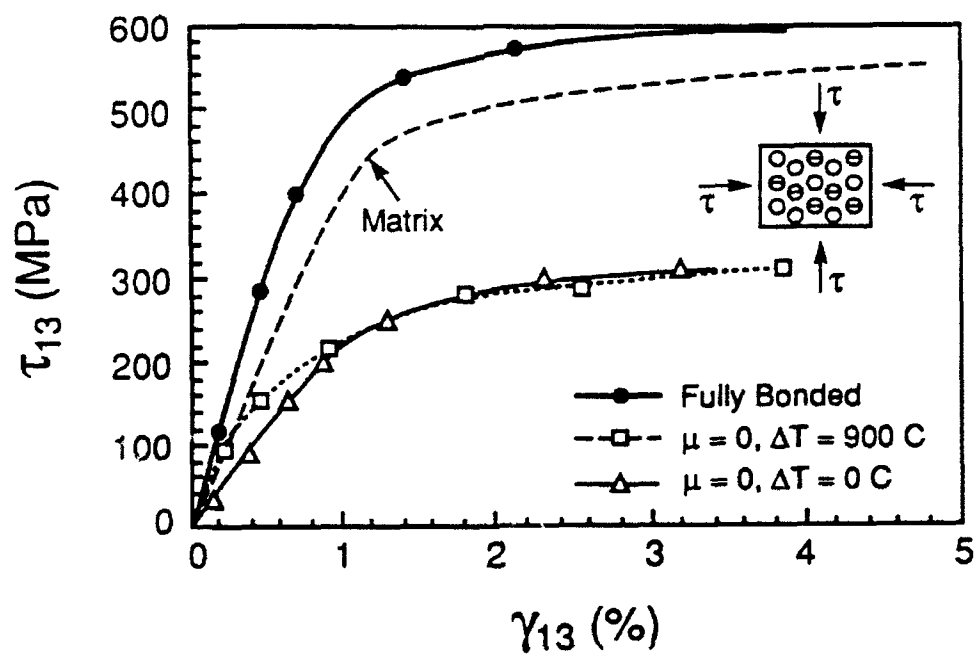


Fig. 11a

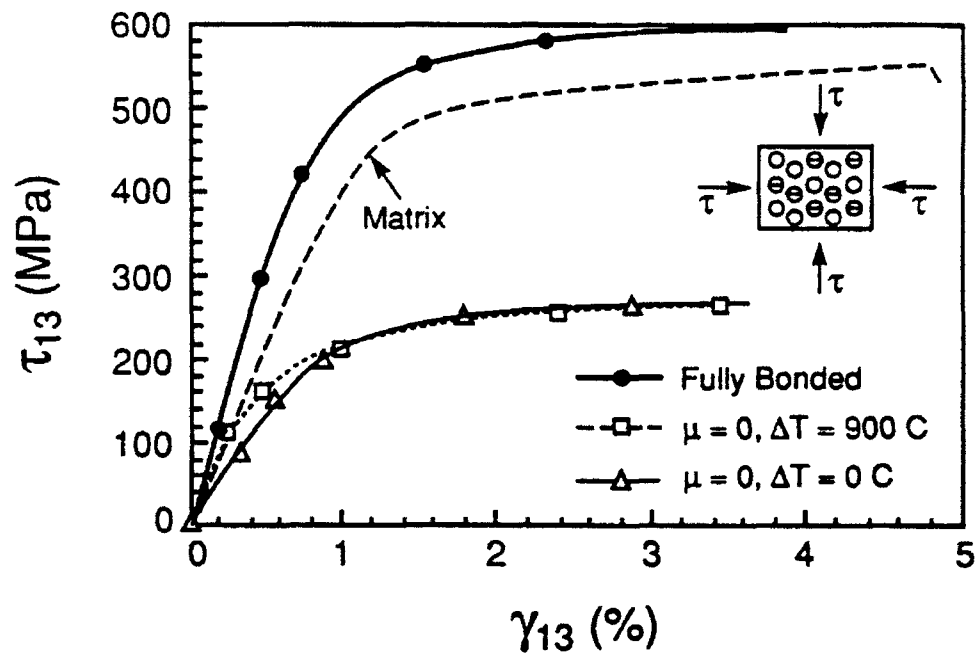


Fig. 11b

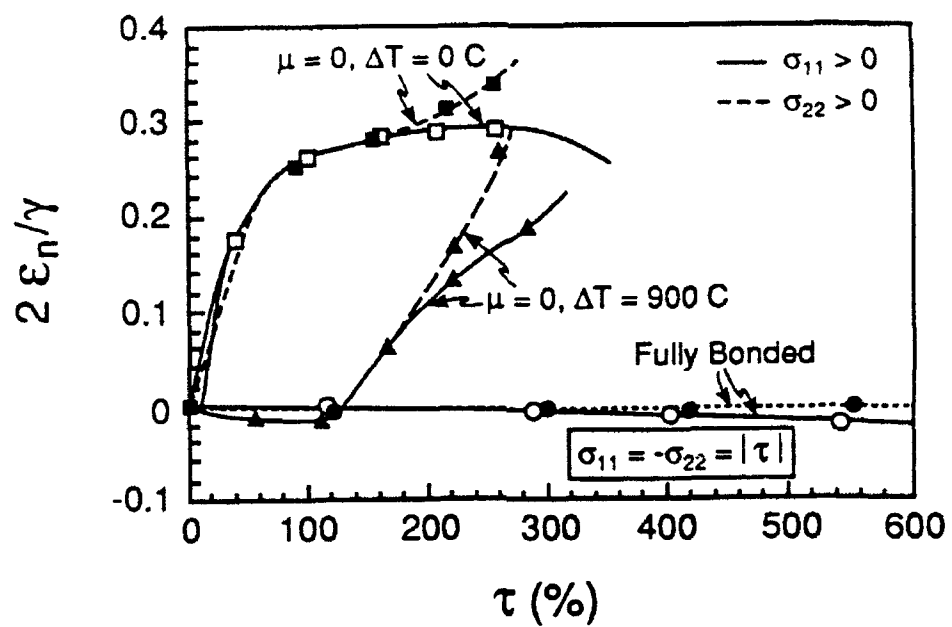


Fig. 11c

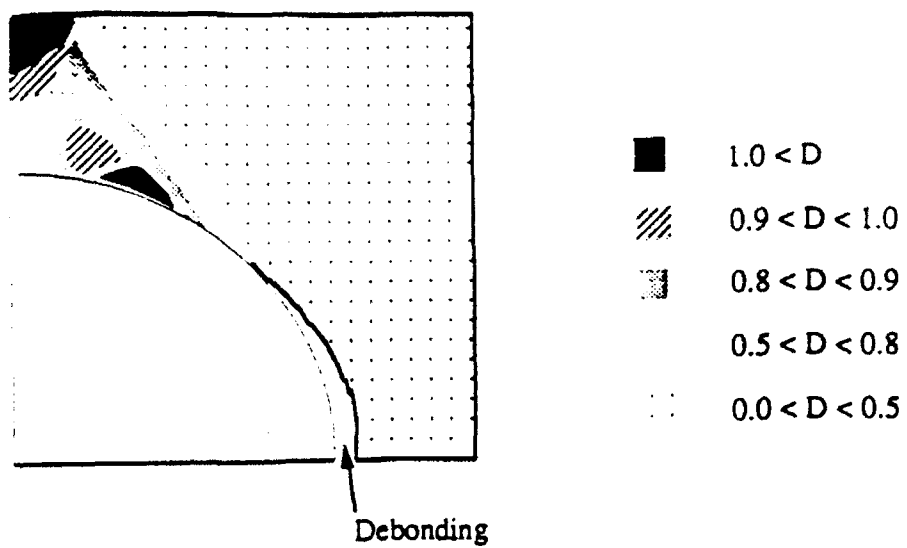


Fig. 12

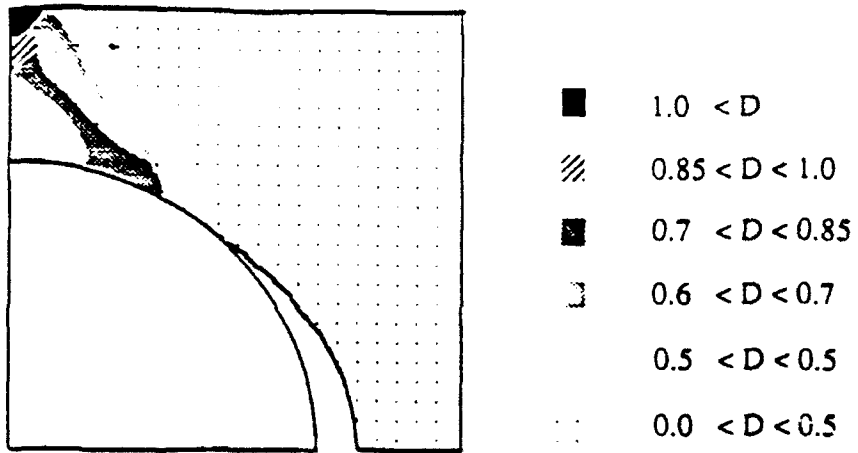
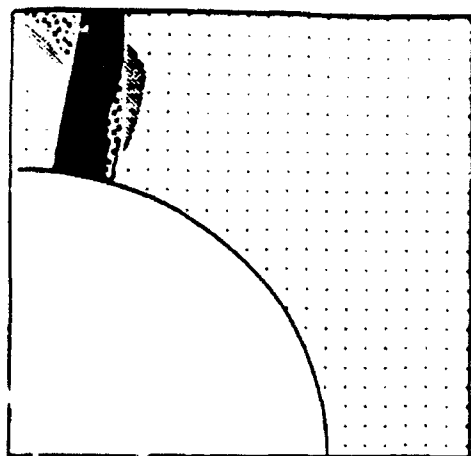


Fig. 13



- $1.0 < D$
- ▨ $0.7 < D < 1.0$
- ▤ $0.5 < D < 0.7$
- $0.0 < D < 0.5$

Fig. 14

TRANSVERSE DUCTILITY OF METAL MATRIX COMPOSITES

S. R. Gunawardena, S. Jansson and F. A. Leckie

Department of Mechanical and Environmental Engineering

University of California

Santa Barbara, CA 93106

ABSTRACT

The role of the fiber matrix interface bond on the transverse ductility of continuous fiber reinforced composites has been investigated. Two specific systems have been considered: an Aluminum alloy matrix reinforced by Alumina fibers, characterized by a strong interface and a Titanium alloy reinforced by coated Silicon Carbide fibers, characterized by a weak interface. A micro-mechanical study indicates that the bond condition has a significant effect on the state of stress in the matrix which in turn dictates the available matrix ductility. The micro-mechanical predictions are in good agreement with the experimental results for the two systems.

fiber strength and in this circumstance the transverse strength and modulus of the composite are lower than those of the matrix. The interface strength also affects the ductility of the composites.

To clarify the effect of the bond condition on the transverse ductility, two different continuous fiber reinforced composite systems are investigated in this study. One composite consists of an Aluminum alloy reinforced with Alumina(Al_2O_3) fibers. An important characteristic of this material is the combination of a strong bond at the fiber-matrix interface and a matrix with a large ductility of 30%. The other composite consists of a Titanium alloy reinforced with coated Silicon Carbide(SiC) fibers. This system features a weak bond between the fiber and matrix and a matrix ductility of 3%. A micro-mechanical study has been performed to understand the mechanics that governs the behavior of these composites. The computed results are compared with the experimentally determined mechanical behavior in sections 2 and 3. A matrix failure criterion based on void nucleation and growth is suggested in Chapter 4 and verified with the aid of the computations and experiments. As a result of this study it is possible to predict the transverse ductility of the composite in terms of the matrix ductility and the interface bond strength.

1. INTRODUCTION

Metal matrix composites reinforced with continuous fibers have attractive strength and stiffness properties. They have the advantage of providing superior transverse properties compared to polymeric matrix composites. Transverse properties are strongly dependent on the fiber matrix interface and systems with strong interface are expected to have a higher transverse strength and stiffness than the matrix. Some systems have a weak interface in order to maintain the

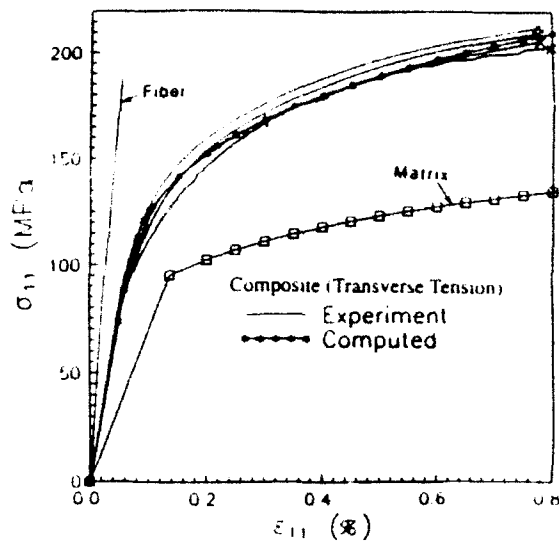


Fig. 1 Stress-strain curves for FP/Al and Al alloy matrix (Experimental and computed)

2. EXPERIMENTAL PROGRAM

The composite with strong interface bond is DuPont's FP/Al reinforced with continuous α -alumina fibers in a unidirectional lay-up [Champion et al, 1978]. The fiber volume fraction was determined to be 55%. The fibers have a diameter of approximately 20 μm , a modulus of 345 to 380 GPa, a tensile strength of 1.9 to 2.1 GPa for 6.4 mm gauge length, and a fracture strain of 0.3-0.4%. The matrix material is a 2 wt% Li-Al binary alloy and its tensile properties are shown in Fig. 1. The composite is fabricated by vacuum-infiltration of the molten matrix and was available in the form of a plate of 150 x 150 x 12.5 mm thick.

The composite with the weak interface bond consists of a Titanium alloy (Ti-15V-3Cr-3Nb-3Al) matrix reinforced by continuous SiC fibers (SCS6). The mechanical properties are reported in [Jansson et al, 1991a]. The fiber volume fraction was determined to be 35%. The fiber diameter is 150 μm and the elastic modulus is 360 GPa. The matrix properties, determined from a delaminated matrix foil, are given in Fig. 2. The composite is made by hot-pressing alloy foils between the fiber tapes. The composite was available in plates of 150 x 150 x 2 mm thick.

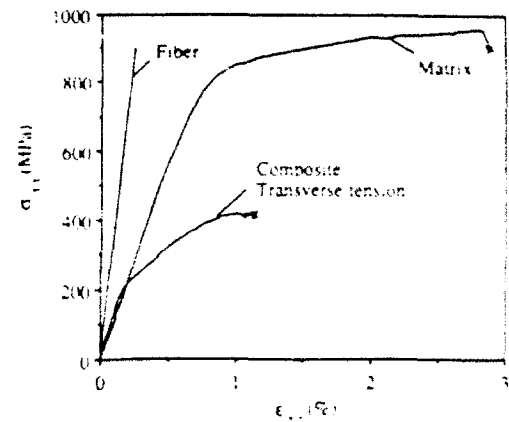


Fig. 2 Transverse stress-strain curve for SCS6/Ti-15V-3 and curves for matrix and fiber materials for comparison (Experimental)

Transverse stress-strain curves for the FP/Al composite are shown in Fig. 1, from which a deviation from linearity is observed to occur at 75 MPa. The ultimate strength is 200 MPa and the strain to fracture is 0.8%. The ultimate strength is about 50% higher than the ultimate matrix strength while the failure strain of 0.8% is only 3% of the 30% failure strain of the matrix [Sakui and Tamura, 1969].

The fracture is observed to be localized to one narrow band oriented approximately 45° to the loading direction. The fracture surface is confined to the matrix and no bare fibers were visible on the fracture surface. The matrix fracture is ductile with the appearance of voidage.

The transverse stress strain curve for the SCS6/Ti composite is shown in Fig. 2. A slight deviation from the initial elastic response occurs at a stress of 150 MPa (as illustrated in Fig. 4) and the ultimate strength is 420 MPa, which is less than 50% of the matrix strength of 950 MPa. The composite failure strain is 1.2% compared to the observed matrix failure strain of 3%.

The macroscopic fracture surface is perpendicular to the tensile direction. The failure surface is irregular with debonding that is a combination of debond at the fiber matrix

interface and fracture in the carbon layer of the fiber. The matrix ligaments between the fibers exhibit a ductile fracture [Jansson et al., 1991a].

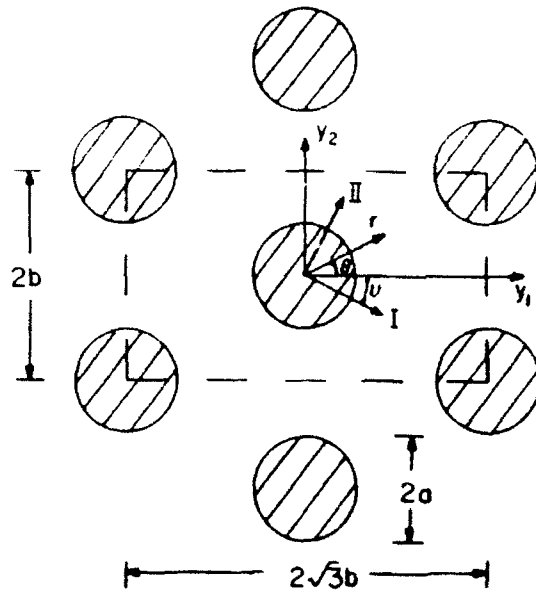


Fig. 3 Hexagonal array with unit cell indicated.

3. MICRO-MECHANICAL STUDIES

By using the theory of homogenization in conjunction with finite element procedures, the mechanics that governs the behavior of the composite in terms of the properties of the fiber and the matrix have been studied.

The composites both consist of long fibers in a unidirectional layout. The fibers in the FP/Al composite are randomly distributed in the transverse plane while the fibers in the SCS6/Ti 15-3 composite are more arranged. In the model to be analyzed the fibers are assumed to be long parallel cylinders arranged in a hexagonal array, Fig. 3. This is the periodical array which has the mechanical properties with the closest symmetries to a composite with randomly distributed fibers. Both systems are transversely isotropic when the constituents are linear elastic but the hexagonal array has a weak deviation from transverse isotropy when the matrix exhibits a nonlinear stress strain relation [Jansson, 1990]. The deviation is most pronounced for a perfectly-plastic

matrix. The transverse loading have been simulated by loading the array in the 1-direction. This loading does not activate slip on planes that are unconstrained by the fibers and gives reasonable results. It also gives the correct limit stress for the SCS6/Ti composite because the matrix area fraction on the fracture surface and the weakest cross-section of the array are close. A loading in the 2-direction gives a lower limit stress.

The governing boundary value problem for the effective properties of the unit cell is two dimensional and has been solved with the Finite Element method by using ABAQUS finite element program [1988]. A 10 node biquadratic quadrilate generalized plane strain element with reduced integration was used to avoid locking. The considered loading of the unit cell, Fig. 3, is symmetric with respect to y_1 and y_2 axis. This implies that only an eighth of the indicated unit cell in Fig. 3 needs to be analyzed. The boundary conditions for different loadings are given in the reference [Jansson, 1990]. In the calculations, the fibers are assumed to be linear elastic and the matrix behavior is modelled by a small strain J_2 plastic theory. The interface of the FP/Al is sufficiently strong to assume displacement continuity across the interface, whereas the interface of SCS6/Ti matrix is weak and interface displacement continuity can not be assumed. The interface was modelled by assuming that it is frictionless and can just transfer normal compressive tractions.

The elastic properties of the FP fiber and aluminum matrix are readily available from the literature. However, the flow properties of the Al-Li matrix alloy are strongly dependent on histories of heat treatment and cold-working [Stark et al., 1981, and Sakui and Tamura, 1969]. Details of the processing of the composite and of any post heat treatments are not available and the flow properties of the Al matrix could not be determined from the literature. Those were determined by fitting the calculated response to the inplane shear stress-strain curve [Jansson and Leckie, 1991b]. The matrix properties obtained could be used to predict accurate stress-strain relationships for the other loading states. The matrix

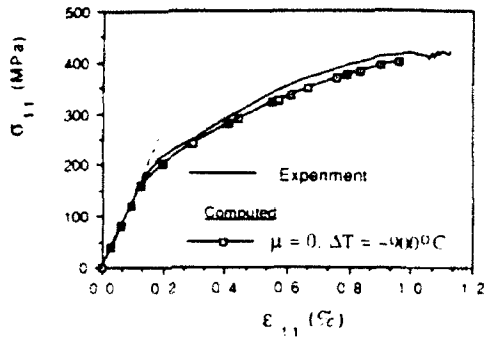


Fig. 4 Transverse stress-strain curve for SCS6/Ti 15-3 computed vs Experimental results.

properties of the SCS6/Ti composite were determined by performing tests on a foil extracted from the composite.

The residual stresses induced during processing strongly affect the stress strain characteristics of the SCS6/Ti composite and have to be included in the analysis. The stress field has a compressive component across the fiber matrix interface which inhibits the onset of debond when the composite is subjected to transverse tensile loading. The residual stresses induced during the fabrication was modelled by letting the composite be stress free at the consolidation temperature. The residual stresses build up during subsequent cooldown and are dominated by the thermal mismatch and the temperature dependent yield stress. Although the consolidation was done at approximately 900°C the strength of the Ti alloy is considerably smaller at temperatures higher than 600°C and the major portion of the residual stress is built up below 600°C. For the purpose of computation, it was found to be sufficient to use the temperature dependence of the matrix as shown in Fig. 5 and the properties of the SCS6 fiber and Ti matrix are given earlier.

The calculated transverse stress strain relationship, using the interface conditions and the residual stress state given above, is shown in Fig. 4. The calculations predict that debonding occurs when the stress is about 160 MPa. The maximum attainable transverse stress is about 410 MPa and this is 43% of the matrix strength. This reduction is a

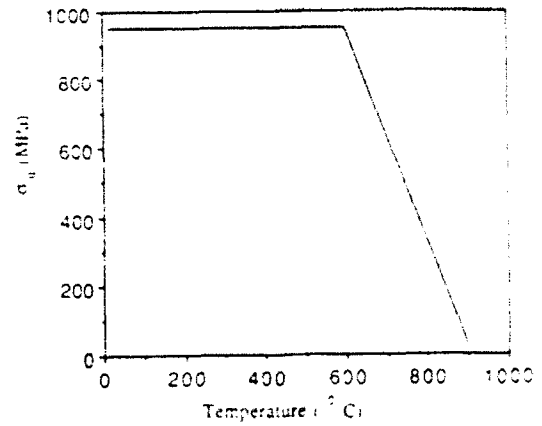


Fig. 5 Assumed variation of strength of Ti 15-3 with temperature.

consequence of debonding that reduces the effective load carrying area of the composite. The stress strain predictions using the fiber and matrix properties described above agree well with the experimental observations which gives confidence in the use of the calculation results for the interpretation of micro-mechanical phenomena.

4. FAILURE DUCTILITY

Micrographic observations [Jansson et al. 1991a, Jansson and Leckie, 1991b] suggests that failure is due to ductile fracture accompanied by void growth in both the aluminum and titanium matrices. It is known for Al-Li [Pilling and Ridley, 1986] that the ductile failure is the result of void nucleation and growth from small particles.

The computations show that the stiff fibers cause constrained multiaxial stress fields to build up in the matrix. In the studies of Hancock and Mackenzie [1976] it is suggested that when the failure is the result of void nucleation and growth the effective plastic strain at failure for multiaxial stress states has the form

$$\bar{\epsilon}_f = 1.65\epsilon_0 \exp\left[-\frac{1}{2} \frac{\sigma_{kk}}{\bar{\sigma}}\right] \quad (1)$$

where ϵ_0 is the plastic component of uniaxial failure strain of the matrix, σ_{kk} is the sum of the principal stresses and $\bar{\sigma}$ is

the effective stress. The result is based on the void growth mechanism suggested by Rice and Tracey [1969]. The plastic component of uniaxial failure strain for Al-Li was reported to be approximately 0.3 [Sakui and Tamura, 1969] and that for a foil of Ti alloy was found from Fig.2 to be 0.02.

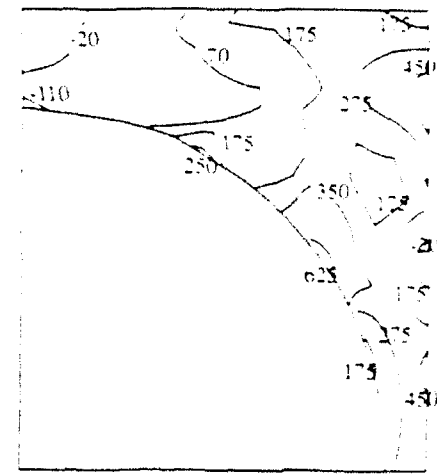
For a time dependent stress state the void growth rate has to be integrated over the history and the failure strain is then given by the condition

$$D = \frac{\int_0^{\bar{\epsilon}} \exp\left(\frac{\sigma_{kk}}{2\bar{\sigma}}\right) d\bar{\epsilon}}{1.65\epsilon_0} \quad (2)$$

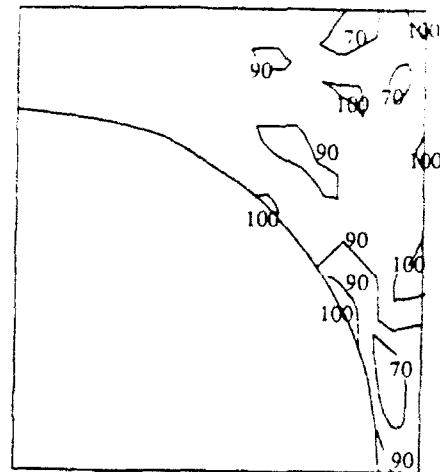
where $D=1$ at $\bar{\epsilon} = \bar{\epsilon}_f$. The variable D here will be used as a damage variable since it is equal to zero for a virgin material and approaches unity when the material has lost its load carrying capacity.

The spatial stress and strain distributions in the matrix for the FP/Al system are shown in Figures 6a-c for a global transverse strain of 1%. The plastic zones are fully developed at this strain. High hydrostatic stresses, Fig. 6a, develop near the fiber matrix interface at approximately 30° to the direction of tensile stress (y_1 direction in Fig.3). A relatively high hydrostatic stress is also present between the fibers, away from the interface and close to the axis of stress. The distribution of the effective stress, Fig. 6b, is more uniform and has a high value at the location of the high hydrostatic stress component. The effective plastic strain, Fig. 6c, attains its highest value at the interface approximately 50° to the y_1 axis. It is relatively low at the location of the highest hydrostatic stress.

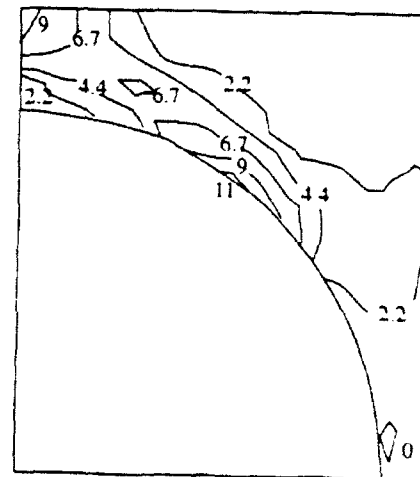
The stress and strain distributions for SCS6/Ti system are shown in Figs. 7a-c for a global strain of 1%. In contrast to the FP/Al system the highest hydrostatic stress here is in the matrix ligament between the fibers at 90° to the y_1 axis. During the loading, the interface debonds and opens up at the



a) Hydrostatic stress σ_{kk} (MPa)

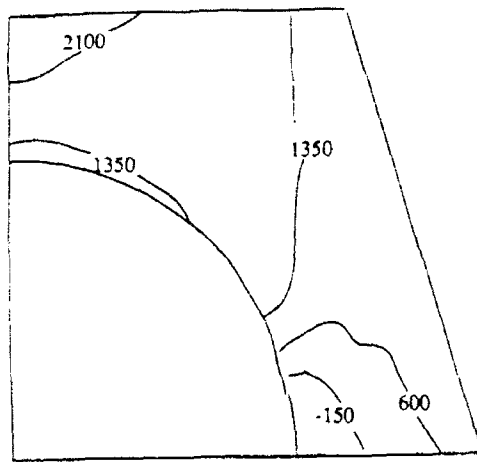


b) Effective stress $\bar{\sigma}$ (MPa)

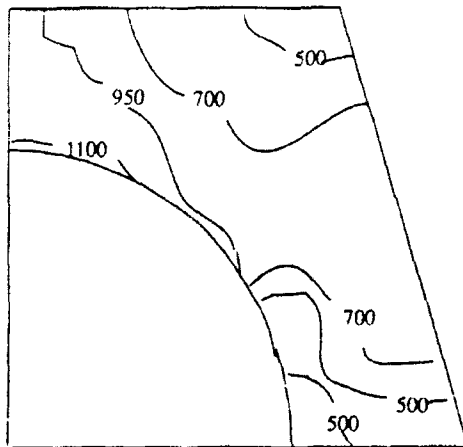


c) Effective plastic strain $\bar{\epsilon}_p$ (%)

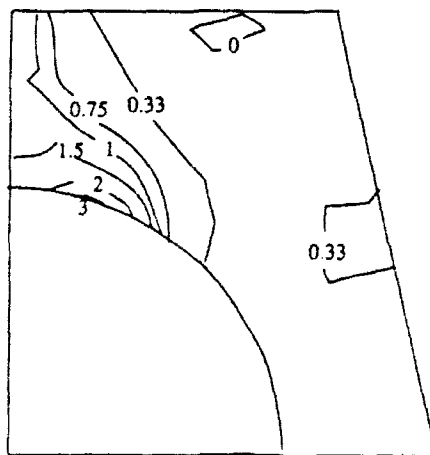
Fig. 6 Stress and Strain distributions in the matrix for FP/Al at $\epsilon_{11} = 1\%$



a) Hydrostatic stress σ_{kk} (MPa).



b) Effective stress $\bar{\sigma}$ (MPa).



c) Effective plastic strain: ϵ_{11} (%) a)

Fig. 7 Stress and Strain distributions in the matrix for SCS6/Ti at $\epsilon_{11} = 1\%$

y_1 axis and the ligaments between the fibers carry the load. The fibers remain in contact with the matrix ligament since the transverse contraction of the matrix is higher than that of the fibers, and this reduces the hydrostatic stresses close to the interface. The effective stress, Fig. 7b, varies more than for the FP/Al system and has the highest value in the ligament close to the slipping interface. However, the high concentration is confined to a very small region. It has been observed that slip-bands are initiated at this location (Jansson et al., 1991a).

The distribution of the damage parameter D , defined by equation (2), is shown in Fig. 8a for the FP/Al system and in Fig. 8b for the SCS6/Ti system for a global strain of 1%. This strain is close to the observed failure strains of 0.8% and 1.2% for the two systems respectively. The region with a high damage is relatively small for the FP/Al system and is confined to a band in the middle between the fibers away from the interface. This explains why the fracture surface observed is covered with the matrix and no bare fibers are visible. During the loading, the load carrying capacity of the matrix is first lost at the small region with the high damage. This local loss of load carrying capacity is sufficient to trigger a global instability with a shear fracture in the orientation indicated by the damage zone.

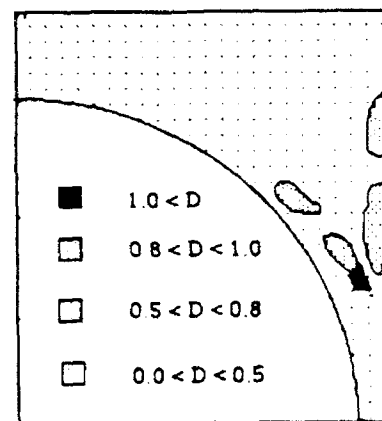
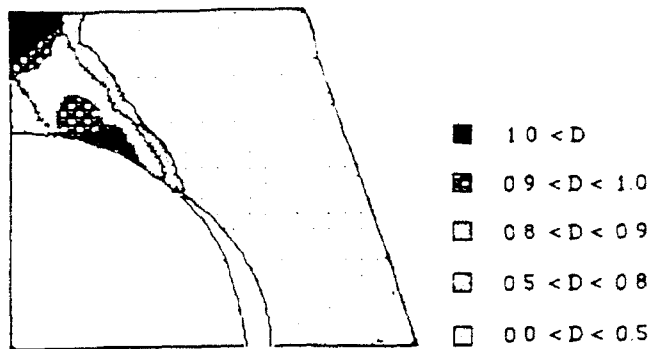


Fig. 8a) Distribution of Damage variable D in the matrix for FP/Al at $\epsilon_{11} = 1\%$



Magnification factor for displacement is 6.5

Fig. 8 b) Distribution of Damage variable D in the matrix for SCS6/Ti at $\epsilon_{11} = 1\%$.

For the SCS6/Ti system the region with a high damage is localized to the matrix ligament between the fibers. Fractographical observations [Jansson et al. 1991a] also supports the result that the ductile fracture is localized to planes in the ligaments within the portion that has a sliding contact with the fiber.

CONCLUSIONS

The strength of the matrix-fiber interface has a pronounced effect on the transverse properties of metal-matrix composites. In the case of a strong bond with FP aluminum as an example, the transverse strength is 30% greater than the matrix strength. This increase of stress is the consequence of the hydrostatic stresses developed in the matrix. However, the beneficial influence of the hydrostatic stress in increasing the strength of the matrix also has the dramatic effect in reducing the 30% ductility of the matrix by a factor of 40 to the 0.8% failure strain observed in the composite.

The weak interface of the SCS6/Ti-15-3 composite results in a transverse composite strength which is less than half of the matrix strength. However, the effect of the smaller hydrostatic stress in the matrix means that the 2.8% failure

strain of the matrix is reduced only to 1.2% failure strain of the composite.

The proposed failure criterion of equation (1) in conjunction with finite element calculations performed gives an estimate of transverse strain to failure of the composite in terms of the matrix failure strain and the fiber/matrix interface condition.

ACKNOWLEDGEMENTS

The work was supported by a grant from the NASA-Lewis Research Center. The authors wish to express their gratitude to Pratt and Whitney and the Chrysler Corporation for supplying the composite materials.

REFERENCES

- ABAQUS Finite Element Program, Hibbitt, Karlson and Sorensen, Inc., 1988 (Version 4.7).
- Champion, A. R., Krueger, W. H., Hartman, H. S. and Dhingra, A. K., 1978 "Fiber/F.P. Reinforced Metal Matrix Composites", Proc. 2nd International Conference on Composite Materials, Toronto, Metallurgical Soc. AIME, pp. 883-904.
- Hancock, J.W. and Mackenzie, A. C., 1976, "On the Mechanisms of Ductile Fracture in High Strength Steels Subject to Multiaxial States of Stress", Journal of the Mechanics and Physics of Solids, Vol. 24, pp. 141-169.
- Jansson, S., 1990, "Homogenized Non linear Constitutive Properties and Local Stress Concentrations for Composites With Periodical Internal Structure", Department of Mechanical Engineering, UC Santa Barbara.
- Jansson, S., Deve, H. E. and Evans, A. G., 1991a, "The Anisotropic Mechanical Properties of a Ti-Matrix Composite Reinforced with SiC Fibers", to be published in Met. Trans.
- Jansson, S. and Leckie, F. A., 1991b, "Mechanical Behavior of a Continuous Fiber Reinforced Aluminum Matrix

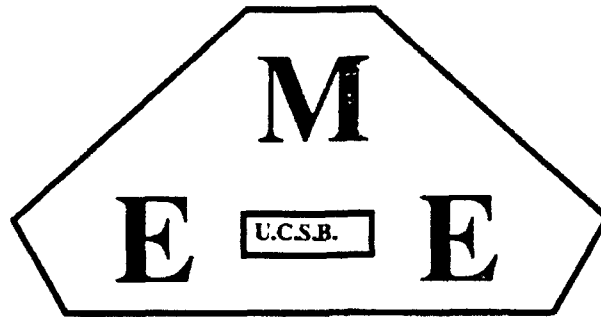
Composite Subjected to Transverse and Thermal Loading, to be published in 1991, Journal of the Mechanics and Physics of Solids.

Pilling, J. and Ridley, N., 1986, "Role of Hydrostatic Pressure on Cavitation During Superplastic Flow of Al-Li Alloy", Aluminum-Lithium Alloys III, The Institute of Metals, London, pp. 184-190.

Rice, J.R. and Tracey, D.M., 1969, "On the Ductile Enlargement of Voids in Triaxial Stress Fields", J. Mech. Phys. Solids, Vol. 17, pp. 201-217.

Sakui, S. and Tamura, M., 1969, "Yielding Phenomena of an Al-3% Li Alloy", Transaction of the Japan Institute of Metals, Vol. 10, pp. 343-356.

Stark, E. A., Sanders, T. H. and Palmer, J. G., 1981, "New Approaches to Alloy Development in Al-Li Systems", Journal of Metals, Vol. 33, pp. 24-32.



MECHANICAL AND ENVIRONMENTAL
ENGINEERING DEPARTMENT

LOCALIZATION DUE TO DAMAGE IN TWO DIRECTION FIBER REINFORCED COMPOSITES

François HILD¹
Per-Lennart LARSSON²
Frederick A. LECKIE

Department of Mechanical and Environmental Engineering
University of California, Santa Barbara, CA 93106-5070, U.S.A.

¹Visiting postgraduate researcher, also at Laboratoire de Mécanique et Technologie,
E.N.S. de Cachan/C.N.R.S./Université Paris 6
61 avenue du Président Wilson, F-94235 Cachan Cedex, France.

²Department of Solid Mechanics, Royal Institute of Technology,
S-100 44 Stockholm, Sweden.

LOCALIZATION DUE TO DAMAGE IN TWO DIRECTION FIBER REINFORCED COMPOSITES

François HILD
Per-Lennart LARSSON
Frederick A. LECKIE

Abstract: Fiber pull-out is one of the fracture features of fiber reinforced ceramic matrix composites. The onset of this mechanism is predicted by using Continuum Damage Mechanics, and corresponds to a localization of the deformations. After deriving two damage models from a uniaxial bundle approach, different configurations are analyzed through numerical methods. For one model some very simple criteria can be derived, whereas for the second one none of these criteria can be derived and the general criterion of localization must be used.

1. Introduction

Ceramic Matrix Composites (CMC's) can either be reinforced by fibers in one direction or by fibers in two directions. The aim of this paper is to study composites reinforced with fibers in two perpendicular directions by extending a previous study on CMC's with fibers in one direction (Hild et al., 1992).

The rupture of most of the CMC's involves two separate failure mechanisms. The first mechanism is matrix cracking. The matrix cracks develop and their density saturates as the load level increases. The second mechanism is fiber breakage accompanied with fiber pull-out. Eventually, the final rupture will take place around one of the matrix cracks: it corresponds to *localized* fiber pull-out due to fiber breakage. The occurrence of this mechanism corresponds to the appearance of a macro-crack and will be described by a localization of the deformations. The initiation of macro-cracks in a structure during service often constitutes the early stage of the final failure of the structure. Starting from a material that is assumed free from any initial defect, the initiation of macro-cracks can be predicted using Continuum Damage Mechanics. The driving force is fiber breakage, which is accompanied by *distributed* pull-out. The approach using localization has successfully been used for ductile materials (Billardon and Doghri, 1989a,b; Doghri, 1989). The initiation stage is considered as the onset of a surface across which the velocity gradient is discontinuous. Under small deformation assumptions, this phenomenon is mainly driven by the damage mechanism that causes strain-softening. For CMC's, the damage mechanism is related to fiber breakage, and the damage variable describes the percentage of broken fibers (Hild et al., 1992).

Although localization can be studied at the scale of fibers bonded to a matrix through an interface (Benallal et al., 1991a), i.e. at a micro-level, localization also can be analyzed at a meso-level, when the material is assumed to be homogeneous. Continuum Damage Mechanics, which represents a local approach to fracture (Benallal et al., 1991b), constitutes an efficient tool for this purpose. The progressive deterioration of the material is modeled by internal variables defined at

the meso-level. These variables are called *damage* variables. The damage state and the evolution of these variables is obtained through a uniaxial study based on fiber breakage (Coleman, 1958; Curtin 1991). A 2-D plane stress analysis is performed based on an extended model. The loss of uniqueness and the localization are studied for shear free states. A criterion referring to a critical value of the damage or to a maximum normal stress can describe the localization, which constitutes an objective criterion, from a design point of view.

2. Localization and Loss of Uniqueness

The failure at a meso-level, with the initiation of a macro-crack, is defined as the bifurcation of the rate problem in certain modes, viz. the appearance of a surface across which the velocity gradient is discontinuous (Billardon and Doghri., 1989a). This phenomenon is referred to as *localization*, and corresponds to the failure of the ellipticity condition. The condition of localization can also be compared to the loss of uniqueness of the rate problem.

Stationary waves were studied by Hadamard (1903) in elasticity, by Hill (1962) and Mandel (1962) in elasto-plasticity. Rice (1976) related the localization of plastic shear bands to jumps of the velocity gradient. Borré and Maier (1989) have given necessary and sufficient conditions for the onset of modes inside the body, who extended the results given by Rice (1976) and Rice and Rudnicki (1975, 1980).

Under small strain assumption and in elasticity coupled with damage, the behavior of a material is assumed to be described by the following piece-wise linear rate constitutive law

$$\dot{\sigma}_i = \begin{cases} E : \dot{\epsilon} & \text{if } \dot{D} = 0 \\ H : \dot{\epsilon} & \text{if } \dot{D} \neq 0 \end{cases} \quad (1)$$

where $\dot{\sigma}$ and $\dot{\epsilon}$ respectively denote the stress and strain rates, Ξ and \mathbb{H} are fourth rank tensors, Ξ is assumed to be positive definite, and D is either a single damage variable or a set of damage variables.

Localization occurs *inside* the body, *if and only if* (Rudnicki and Rice, 1975; Borré and Maier, 1989; Benallal et al., 1991a)

$$\text{Det}(\mathbf{n} \cdot \mathbb{H} \cdot \mathbf{n}) = 0 \quad \text{for a vector } \mathbf{n} \neq 0 \text{ and at a point inside a structure } \Omega \quad (2)$$

This criterion corresponds to the failure of the ellipticity condition of the rate equilibrium equation; it also can be used as an indicator of the local failure of the material, at a meso-scale (Billardon and Doghri, 1989a).

Furthermore, any loss of uniqueness, considered as bifurcation of the rate boundary value problem, is excluded provided

$$\dot{\sigma} : \dot{\epsilon} > 0 \quad (3)$$

In this study, the quantity that defines loss of uniqueness and localization is the linear tangent modulus \mathbb{H} . In the following, we analyze loss of uniqueness and loss of ellipticity (i.e. localization) for states when

$$\begin{cases} \epsilon_{11} = \alpha \epsilon_{22} \\ \epsilon_{12} = 0 \end{cases} \quad (4)$$

The parameter α is referred to as the strain ratio and its inverse is denoted by β . These particular states only are considered. When the hypothesis of Eqn. (4) is satisfied, the non-vanishing components of the vector \mathbf{n} are n_1 and n_2 , and the matrix $A = \mathbf{n} \cdot \mathbb{H} \cdot \mathbf{n}$ reduces to (Ortiz et al., 1987)

$$A = \begin{bmatrix} n_1^2 H_{1111} + n_2^2 H_{1212} & n_1 n_2 (H_{1212} + H_{1122}) \\ n_1 n_2 (H_{1212} + H_{2211}) & n_1^2 H_{1212} + n_2^2 H_{2222} \end{bmatrix} \quad (5)$$

If we rewrite $(n_1, n_2) = (\cos\theta, \sin\theta)$, $X = \tan^2\theta$, then the localization condition is equivalent to finding real positive roots of the following equation

$$a X^2 + b X + c = 0 \quad (6)$$

with

$$\begin{aligned} a &= H_{1212} H_{2222} \\ b &= H_{1111} H_{2222} - H_{1122} H_{2211} - H_{1122} H_{1212} - H_{2211} H_{1212} \\ c &= H_{1212} H_{1111} \end{aligned} \quad (7)$$

If real positive roots are found, then the localization direction is perpendicular to the vector $(n_1, n_2, 0) = (\cos\theta, \sin\theta, 0)$, characterized by the angle θ (Fig. 1). The values of H_{1111} , H_{2222} , H_{1122} , H_{2211} and H_{1212} are model dependent and specific models are now developed.

3. Constitutive Laws

This section is concerned with the development of two constitutive laws in the case of CMC's reinforced in two perpendicular directions. At constant temperature, the behavior of a CMC reinforced by unidirectional fibers in the x_2 -direction (see Fig. 1) can be characterized by the Helmholtz free energy density ψ_2 , which is a function of the state variables ϵ_{11} , ϵ_{22} , ϵ_{12} , and the damage variable D_2 in the x_2 -direction

$$\rho\psi_2 = \rho\psi(\epsilon_{11}, \epsilon_{22}, \epsilon_{12}, D_2, f, k_2) \quad (8)$$

where D_2 represents the fiber degradation in the x_2 -direction, E_2 the Young's modulus in the x_2 -direction, ν_{12} the Poisson's ratio, k_2 the ratio of the Young's modulus in the fiber direction (E_2) to the Young's modulus in the transverse direction (E_1), and G_{12} the shear modulus. It is worth noting that the elastic quantities depend on the volume fraction of fibers. The expression for the general Helmholtz free energy density ψ is given by

$$\rho\psi(x, y, z, d, f, k) = \frac{E_2(f)}{2} \left[\frac{x^2 + 2\nu_{12}k(1-d)xy + ky^2}{k \left\{ 1 - \nu_{12}^2 k(1-d) \right\}} \right] + 2G_{12}z^2 \quad (9)$$

where ρ is the material density, x, y, z are dummy variables representing strains, d damage, f volume fraction, and k Young's moduli ratio. The stresses and the thermodynamic force Y_2 associated to the damage variable D_2 are derived from the Helmholtz free energy density ψ_2 as follows

$$\begin{aligned} \sigma_{11} &= \rho \frac{\partial \psi_2}{\partial \epsilon_{11}} & \sigma_{22} &= \rho \frac{\partial \psi_2}{\partial \epsilon_{22}} & 2\sigma_{12} &= \rho \frac{\partial \psi_2}{\partial \epsilon_{12}} \\ Y_2 &= \rho \frac{\partial \psi_2}{\partial D_2} \end{aligned} \quad (10)$$

The explicit expressions for the stresses related to the strains and the damage variable modeling the fiber degradation in the x_2 -direction are given by

$$\begin{aligned} \sigma_{11} &= \frac{E_2}{k_2[1 - \nu_{12}^2(1 - D_2)k_2]} [\epsilon_{11} + \nu_{12}(1 - D_2)k_2\epsilon_{22}] \\ \sigma_{22} &= \frac{E_2(1 - D_2)}{1 - \nu_{12}^2(1 - D_2)k_2} (\epsilon_{22} + \nu_{12}\epsilon_{11}) \\ \sigma_{12} &= 2G_{12}\epsilon_{12} \end{aligned} \quad (11)$$

The damage state of fibers in the x_2 -direction, D_2 can be related to the stress (and is denoted by $D_2^{(1)}$) or strain state (and is denoted by $D_2^{(2)}$). The relationship is either implicit in terms of the normal stress in the x_2 -direction (model #1)

$$D_2^{(1)} = 1 - \exp \left[- \left\{ \frac{\sigma_{22}}{(1-D_2^{(1)})f_2\sigma_c} \right\}^{m+1} \right] \quad \text{if } \epsilon_{22} > 0 \text{ and } \dot{\epsilon}_{22} > 0 \quad (12)$$

where m is the shape parameter of a Weibull law (Weibull, 1939), σ_c the characteristic strength (Henstenburg and Phoenix, 1989), and f_2 is the volume fraction of fibers in the x_2 -direction; or explicit in terms of the normal strain in the x_2 -direction (model #2)

$$D_2^{(2)} = 1 - \exp \left[- \left(\frac{\epsilon_{22}}{\epsilon_c} \right)^{m+1} \right] \quad \text{if } \epsilon_{22} > 0 \text{ and } \dot{\epsilon}_{22} > 0 \quad (13)$$

where ϵ_c is related to the characteristic strength σ_c by $\sigma_c = E_F \epsilon_c$ (E_F is the Young's modulus of the fibers). Both models describe the same material behavior when subjected to uniaxial tension. However the models give different predictions for multiaxial loading states (Hild et al., 1992). It is worth noting that the damage evolution laws are *a priori* independent of the volume, since we assume that the local behavior of the fiber degradation is not dependent on the total length of the fiber (Curtin, 1991). This type of behavior is observed when *distributed* pull-out happens in conjunction with fiber breakage, and it can be shown that in most practical cases, the statistics driving the fiber breakage is independent of the total length of the composite. On the other hand, if the composite length becomes very small, a length dependence is found again, and in this case the evolution of the damage variable is mainly given by a fiber-bundle-type of behavior, which leads to replacing $m+1$ by m , the characteristic strength σ_c by $\sigma_0 (L/L_0)^{1/m}$, where σ_0 is the scale parameter of a Weibull law, and the scale strain ϵ_c by $\epsilon_0 (L/L_0)^{1/m}$, where L_0 is the gauge length at which the

scale parameter has been identified, and $\sigma_0 = E_F \epsilon_0$. Since the results are the same for both damage evolution laws when the previous permutation is used, we will just express them in the case when the model is length independent, which is the most relevant in practice.

If the fibers are in the x_1 -direction then the breakage can be modeled by a damage variable denoted by D_1 . Using Eqn. (9), the Helmholtz free energy density $\rho\psi_1$ is given by

$$\rho\psi_1 = \rho\psi(\epsilon_{22}, \epsilon_{11}, \epsilon_{12}, D_1, f_1, k_1) \quad (14)$$

If the fibers are in both x_1 - and x_2 -directions, then we assume as a first approximation that the total specific Helmholtz free energy $\rho\psi_{12}$ is given by a law of mixture of the Helmholtz free energy densities in the x_1 - and in the x_2 -directions

$$\rho\psi_{12} = (1-f)\rho\psi_1 + f\rho\psi_2 \quad (15)$$

where f is the fraction of fibers in the x_2 -direction ($f=f_2/(f_1+f_2)$, and where f_1 and f_2 are the volume fraction of fibers in the x_1 - and x_2 -direction, respectively). This assumption also corresponds to a Lin-Taylor Hypothesis. The evolution of the stresses is given by

$$\begin{aligned} \sigma_{11} &= \rho \frac{\partial \psi_{12}}{\partial \epsilon_{11}} = (1-f)S_{11} + fS_{12} \\ \sigma_{22} &= \rho \frac{\partial \psi_{12}}{\partial \epsilon_{22}} = (1-f)S_{21} + fS_{22} \\ \sigma_{12} &= \rho \frac{\partial \psi_{12}}{\partial \epsilon_{12}} = 2G_{12}\epsilon_{12} \end{aligned} \quad (16)$$

where the explicit expression for S_{ij} is given in appendix 1, and the corresponding thermodynamic forces associated to the two *independent* damage variables D_1 and D_2 are

$$\begin{aligned}
Y_1 &= \rho \frac{\partial \psi_{12}}{\partial D_1} = (1-f)\rho \frac{\partial \psi_1}{\partial D_1} \\
Y_2 &= \rho \frac{\partial \psi_{12}}{\partial D_2} = f\rho \frac{\partial \psi_2}{\partial D_2}
\end{aligned} \tag{17}$$

Again, the evolution of the damage variables can either be implicit in terms of the respective normal stresses (model #1)

$$\begin{aligned}
D_1^{(1)} &= 1 - \exp \left[- \left\{ \frac{\sigma_{11}}{(1-D_1^{(1)})f_1\sigma_c} \right\}^{m+1} \right] & \text{if } \epsilon_{11} > 0 \text{ and } \dot{\epsilon}_{11} > 0 \\
D_2^{(1)} &= 1 - \exp \left[- \left\{ \frac{\sigma_{22}}{(1-D_2^{(1)})f_2\sigma_c} \right\}^{m+1} \right] & \text{if } \epsilon_{22} > 0 \text{ and } \dot{\epsilon}_{22} > 0
\end{aligned} \tag{18}$$

or explicit in terms of the respective normal strains (model #2)

$$\begin{aligned}
D_1^{(2)} &= 1 - \exp \left[- \left(\frac{\epsilon_{11}}{\epsilon_c} \right)^{m+1} \right] & \text{if } \epsilon_{11} > 0 \text{ and } \dot{\epsilon}_{11} > 0 \\
D_2^{(2)} &= 1 - \exp \left[- \left(\frac{\epsilon_{22}}{\epsilon_c} \right)^{m+1} \right] & \text{if } \epsilon_{22} > 0 \text{ and } \dot{\epsilon}_{22} > 0
\end{aligned} \tag{19}$$

It is worth noting that we assume that the statistical properties of the fibers are supposed to be identical in both directions. This hypothesis will be maintained throughout the paper since generalization would be straightforward. Both models are studied for shear free states when the strain ratio α (see Eqn. (4)), and thus its inverse β are given.

3.1. Failure Criteria for Model #1

For model #1, the evolution of the damage variables is implicit in the sense that $D_1^{(1)}$ (respectively $D_2^{(1)}$) is a function of the normal stress σ_{11} (respectively σ_{22}) and the damage variable

$D_1^{(1)}$ (respectively $D_2^{(1)}$) itself. The evolution is therefore computed by a numerical scheme based upon a Newton method. To study localization and loss of uniqueness, we need to compute the tangent operator, which takes the following form

$$\begin{aligned}
H_{1111} &= \frac{[(1-f)F_{11} + fF_{12}] (1 + fF_{52}F_{72}) - fF_{22}F_{72} [(1-f)F_{41} + fF_{42}]}{[1 + fF_{21}F_{72}] (1 + fF_{52}F_{72}) - f(1-f)F_{22}F_{72}F_{51}F_{71}} \\
H_{2222} &= \frac{[(1-f)F_{61} + fF_{62}] [1 + (1-f)F_{21}F_{71}] - (1-f)F_{51}F_{71} [(1-f)F_{41} + fF_{42}]}{[1 + fF_{21}F_{72}] (1 + fF_{52}F_{72}) - f(1-f)F_{22}F_{72}F_{51}F_{71}} \\
H_{1122} &= \frac{[(1-f)F_{41} + fF_{42}] (1 + fF_{52}F_{72}) - fF_{22}F_{72} [(1-f)F_{61} + fF_{62}]}{[1 + fF_{21}F_{72}] (1 + fF_{52}F_{72}) - f(1-f)F_{22}F_{72}F_{51}F_{71}} \\
H_{2211} &= \frac{[(1-f)F_{41} + fF_{42}] [1 + (1-f)F_{21}F_{71}] - (1-f)F_{51}F_{71} [(1-f)F_{11} + fF_{12}]}{[1 + fF_{21}F_{72}] (1 + fF_{52}F_{72}) - f(1-f)F_{22}F_{72}F_{51}F_{71}} \\
H_{1212} &= 2G_{12}
\end{aligned} \tag{20}$$

where the explicit expressions for F_{ij} are given in appendix 2.

The loss of uniqueness and localization are investigated when the fiber fraction f and the strain ratio α vary. Although analytical results cannot be derived from criterion (2) in the general case, some simple results can be found when f is equal to 0 or 1. In these cases, the criteria derived by Hild et al. (1992) apply. If f is equal to 0 (fibers only in the x_1 -direction), then localization and loss of uniqueness occur at the same load level when

$$\begin{aligned}
D_1^{(1)} &= D_c = 1 - \exp\left(\frac{-1}{m+1}\right) \\
\sigma_{11} &= \sigma_{u1} = f_1 \sigma_c \left(\frac{1}{(m+1)e}\right)^{1/(m+1)} \\
Y_1 &= Y_c = \frac{\sigma_{u1}^2}{2E_1(1-D_c)^2}
\end{aligned} \tag{21}$$

where the stress σ_{u1} corresponds to the ultimate tensile strength in the x_1 -direction. It is worth noting that the three previous criteria are easier to compute than the general criterion (2). The

direction of localization is $\theta = 0^\circ$, i.e., a localization surface perpendicular to the fiber direction . If f is equal to 1, the same kind of result apply and the direction of localization is $\theta = 90^\circ$, i.e., a localization surface again perpendicular to the fiber direction . When $f \neq 0$ and $f \neq 1$, these results cannot be proved. However the computations show that loss of uniqueness and localization can be described very accurately by the two following criteria

$$\text{Max}(D_1^{(1)}, D_2^{(1)}) = D_c = 1 - \exp\left(\frac{-1}{m+1}\right) \quad (22)$$

$$\sigma_{11} = \sigma_{u1} \quad \text{or} \quad \sigma_{22} = \sigma_{u2} \quad (23)$$

when the fiber properties are the same in the two directions. The maximum error is .5% in terms of criteria (22), and (23).

Criterion (22) shows that for model #1, maximum damage at localization depends only on the Weibull exponent of the fibers. Furthermore, criterion (23) shows that the maximum normal stress σ_{11} (respectively σ_{22}) depends only on the volume fraction of fibers in the x_1 - (respectively x_2 -) direction and on the fiber characteristics. This result is consistent with some experimental observations on woven carbon matrix composites reinforced with SiC (Nicalon) fibers (Heredia et al., 1992). On the other hand, the localization angle is dependent on the fiber percentage f (see Fig. 2). When the fiber percentage f and the sign of the strains ϵ_{11} and ϵ_{22} are constant, the variation of the localization angle is due to the fact that the maximum tensile stress is either reached in the x_1 - or in the x_2 -direction.

Moreover, if the strain ratio α is different from 0 and 1 then there is a complete symmetry of the results. If the strain ratio α , the strains ϵ_{11} and ϵ_{22} are positive, changing α into β , f_2 into f_1 , changes f into $1-f$, and alters the absolute value of the localization angle $|\theta|$ into $\pi/2 - |\theta|$ and keeps the maximum stresses and damage levels constant. These two properties are referred to as *symmetry properties*, and are mainly due to the features of Eqns. (4), (8), (14) and (15).

When the strain ratio α is equal to 1 and the fiber percentage f is equal to .5, the localization

angle is undetermined. This is due to the vanishing of the three constants a , b , and c in Eqn. (6), for $H_{1111} = H_{1122} = H_{2211} = H_{2222} = 0$. Any value of the angle θ satisfies Eqn (6). This phenomenon can be observed when the fiber percentage f is different from 1: if $\sigma_{11} = \sigma_{u1}$ and $\sigma_{22} = \sigma_{u2}$ simultaneously, then $D_1^{(1)} = D_2^{(1)} = D_c$, and $H_{1111} = H_{1122} = H_{2211} = H_{2222} = 0$. This particular result shows that in terms of this model, for a given strain ratio α , it is possible to optimize locally a CMC reinforced by fibers in two perpendicular directions. Indeed, in terms of fiber breakage, a condition $\sigma_{11} = \sigma_{u1}$ and $\sigma_{22} = \sigma_{u2}$ leads to an optimum of the fiber behavior in both directions.

Model #1 constitutes a straightforward generalization of the fiber bundle models studied by Krajcinovic and Silva (1982), and Hult and Travnicek (1983). Finally, a shear stress has no influence on all the previous results since we assumed no coupling between the damage variables and the shear strain or stress for both model #1 and #2.

3.2. Study of Localization with Model #2

For model #2, the evolution of the damage variables is explicit and therefore is easier to compute. The tangent operator takes the form

$$\begin{aligned}
 H_{1111} &= (1-f)(F_{11} - F_{21} F_{31}) + fF_{12} \\
 H_{2222} &= (1-f)F_{62} + f(F_{42} - F_{52} F_{32}) \\
 H_{1122} &= (1-f)F_{41} + f(F_{42} - F_{22} F_{32}) \\
 H_{2211} &= (1-f)(F_{41} - F_{21} F_{31}) + fF_{42} \\
 H_{1212} &= 2G_{12}
 \end{aligned} \tag{24}$$

where the explicit expressions for F_i are given in appendix 2. As shown in the case of fibers in only one direction (Hild et al., 1992), the localization criterion cannot be described by some simple

criteria as those given by model #1. When fibers are in both directions the latter results are confirmed. A first consequence is that an optimization procedure can be performed since the maximum stress at localization, and the maximum damage at localization are dependent on both the strain ratio α and on the fiber percentage f .

Since the elastic law given in Eqns. (16) is identical for both models, the symmetry properties apply also for model #2 (see Figs. 3, 4, and 5). It can also be noticed that the maximum stress at localization varies with the fiber fraction f and with the strain ratio α .

In the experiments reported by Heredia et al. (1992) the stress at localization was given by the ultimate tensile strength corresponding to the volume fraction of fibers in the same direction. This is not found by using model #2. Indeed, in a tensile test, when $f_1 = f_2 = .5$ the maximum stress σ_{22} normalized by the ultimate tensile strength σ_{u2} is given by .63, whereas the same tensile test when $f_1 = .0$ and $f_2 = .5$ would give a normalized tensile strength σ_{22}/σ_{u2} equal to 1. On the other hand, the damage at localization D_2 normalized by the critical damage D_c is equal to 1.04 when $f_1 = .5$ and $f_2 = .5$ and is equal to 1. when $f_1 = .0$ and $f_2 = .5$.

It is too early to draw a final conclusion, but it seems that the predictions of model #1 correspond more to reality than those of model #2. On the other hand, model #2 turned out to give results very close to model #1 when applied to structures with fibers in one direction (Hild et al., 1992). This will be addressed in the case of structures with fibers in two perpendicular directions such as spinning discs.

4. Conclusions

Using a one-dimensional study of fiber breakage modeled by a single damage variable, two models are derived. Both of them are then generalized to a 2-D plane stress analysis, with fibers in two perpendicular directions. Whereas model #1 constitutes a straightforward generalization of the elementary study, model #2 exhibits different features. Indeed, loss of uniqueness and localization can be described by some very simple criteria referring to Continuum Damage Mechanics for

model #1. Conversely, these simple criteria do not apply for model #2. Physically, model #1 gives a better description of some experimental trends observed in the case of a carbon matrix reinforced with silicon carbide (Nicalon) fibers in two perpendicular directions. On the other hand, model #2 is easier to compute, and when applied to the study of spinning disc with fibers in one direction, it leads to load levels at localization of the same order of magnitude as model #1 (Hild et al, 1992).

Lastly, this study shows that the localization for model #1 can be described by using criterion (23) derived from the general criterion of localization (2). This criterion can also be used for a computation in elasticity and may turn out to be sufficient in first approximation to predict load levels at which a macro-crack initiates, instead of using a computation in elasticity coupled with damage. This work is still in progress and will be presented in a subsequent publication.

5. Acknowledgments

The authors gratefully acknowledge the financial support of the U.S. Air Force through contract AFOSR-90-0132 with the Department of Mechanical and Environmental Engineering, University of California at Santa Barbara, and the DARPA University Research Initiative at the University of California at Santa Barbara (ONR contract N00014-86-K0753).

References

- Benallal, A., Billardon, R. and Geymonat, G. (1991a). Localization Phenomena at the Boundaries and Interfaces of Solids. 3rd Conference on Constitutive Laws for Engineering Materials: Theory and Applications, Tucson, AZ, January 1991.
- Benallal, A., Billardon, R. and Lemaitre J. (1991b). Continuum damage mechanics and local approach to fracture: Numerical procedures. *Comp. Meth. in Appl. Mech. and Eng.*, **92**, 141-155.
- Billardon, R. and Doghri, I. (1989a). Pr vision de l'amor age d'une macro-fissure par la localisation de l'endommagement. *C. R. Acad. Sci. Paris* **308** [II], 347-352.
- Billardon, R. and Doghri, I. (1989b). Localization Bifurcation Analysis for Damage Softening Elasto-Plastic Materials. *Strain Localization and Size Effect due to Cracking and Damage*. J. Mazars and Z.P. Baz. eds. Elsevier, 295-307.
- Borr , G. and Maier, G. (1989). On Linear versus Nonlinear Flaw Rules in Strain Localization Analysis. *Meccanica* **24**, 36-41.
- Coleman, B.D. (1958). On the Strength of Classical Fibers and Fiber Bundles. *J. Mech. Phys. Solids* **7**, 60-70.
- Curtin, W.A., (1991). Theory of Mechanical Properties of Ceramic-Matrix Composites. *J. Am. Ceram. Soc.*, **74** [11], 2837-2845.
- Doghri, I. (1989). Etude de la localisation de l'endommagement. Th se de l'Universit  Paris 6, May 1989.
- Hadamard, J. (1903). *Le on sur la propagation des ondes et les  quations de l'hydrodynamique*. Paris.
- Heredia, F.E., Spearing, S.M., Evans, A.G., Mosher, P., and Curtin, W.A. (1992). Mechanical Properties of Carbon Matrix Composites Reinforced with Nicalon Fibers. *J. Am. Ceram. Soc.*, **75** [11], 3017-3025.
- Henstenburg, R.B. and Phoenix, S.L. (1989). Interfacial Shear Strength Using Single-Filament-Composite Test. Part II: A Probability Model and Monte-Carlo Simulations. *Polym. Comp.*, **10** [5], 389-406.
- Hild, F., Larsson, P.-L., and F.A. Leckie (1992). Localization due to Damage in Fiber Reinforced Composites. *Int. J. Solids Struct.*, **29** [24], 3221-3238.
- Hill, R. (1962). Acceleration Waves in Solids. *J. Mech. Phys. Solids* **10**, 1-16.
- Hult, J. and Travnicek, L. (1983). Carrying Capacity of Fiber Bundles with Varying Strength and Stiffness. *Journal de M canique Th orique et Appliqu e* **2** [2], 643-657.
- Krajcinovic, D. and Silva, M.A.G. (1982). Statistical Aspects of the Continuous Damage Theory.

- Int. J. Solids Structures 18 [7], 551-562.
- Mandel, J. (1962). Ondes plastiques dans un milieu indéfini à trois dimensions. *J. de Mécanique* 1, 3-30.
- Ortiz, M., Leroy, Y. and Needelman, A. (1987). A Finite Element Method for Localized Failure Analysis. *Comput. Meths Appl. Engrg.* 61, 189-214.
- Rice, J.R. and Rudnicki, J.W. (1980). A Note on Some Features of the Theory of Localization of Deformation. *Int. J. Solids Struct.* 16, 597-605.
- Rice, J.R. (1976). The Localization of Plastic Deformations. *Theoretical and Applied Mechanics*, edited by W.T. Koiter (North-Holland), 207-220.
- Rudnicki, J.W. and Rice, J.R. (1975). Conditions for Localization of Deformation in Pressure-Sensitive Dilatant Materials. *J. Mech. Phys. Solids* 23, 371-394.
- Weibull, W., (1939). A Statistical Theory of the Strength of Materials. *Ingeniörsvetenskapakademiens, Handlingar* Nr 151.

Appendix 1

$$k_1 = \frac{E_2(f_1)}{E_1}$$
$$k_2 = \frac{E_2(f_2)}{E_1}$$

$$S_{11} = \frac{E_2(f_1)(1-D_1)}{1-v_{12}^2(1-D_1)k_1} (\epsilon_{11} + v_{12}\epsilon_{22})$$

$$S_{12} = \frac{E_2(f_2)}{k_2[1-v_{12}^2(1-D_2)k_2]} [\epsilon_{11} + v_{12}(1-D_2)k_2\epsilon_{22}]$$

$$S_{21} = \frac{E_2(f_1)}{k_1[1-v_{12}^2(1-D_1)k_1]} [\epsilon_{22} + v_{12}(1-D_1)k_1\epsilon_{11}]$$

$$S_{22} = \frac{E_2(f_2)(1-D_2)}{1-v_{12}^2(1-D_2)k_2} (\epsilon_{22} + v_{12}\epsilon_{11})$$

Appendix 2

$$F_{11} = \frac{E_2(f_1)(1-D_1)}{1-v_{12}^2(1-D_1)k_1}$$

$$F_{21} = \frac{E_2(f_1)(v_{12}\epsilon_{11}+\epsilon_{22})}{(1-v_{12}^2(1-D_1)k_1)^2}$$

$$F_{41} = \frac{E_2(f_1)v_{12}(1-D_1)}{1-v_{12}^2(1-D_1)k_1}$$

$$F_{51} = \frac{E_2(f_1)v_{12}(v_{12}\epsilon_{11}+\epsilon_{22})}{(1-v_{12}^2(1-D_1)k_1)^2}$$

$$F_{61} = \frac{E_2(f_1)}{k_1(1-v_{12}^2(1-D_1)k_1)}$$

$$F_{12} = \frac{E_2(f_2)}{k_2(1-v_{12}^2(1-D_2)k_2)}$$

$$F_{22} = \frac{E_2(f_2)v_{12}(v_{12}\epsilon_{11}+\epsilon_{22})}{(1-v_{12}^2(1-D_2)k_2)^2}$$

$$F_{42} = \frac{E_2(f_2)v_{12}(1-D_2)}{1-v_{12}^2(1-D_2)k_2}$$

$$F_{52} = \frac{E_2(f_2)(v_{12}\epsilon_{11}+\epsilon_{22})}{(1-v_{12}^2(1-D_2)k_2)^2}$$

$$F_{62} = \frac{E_2(f_2)(1-D_2)}{1-v_{12}^2(1-D_2)k_2}$$

$$F_{31} = \frac{m+1}{\epsilon_c} \left(\frac{\epsilon_{11}}{\epsilon_m} \right)^m \exp \left[- \left(\frac{\epsilon_{11}}{\epsilon_c} \right)^{m+1} \right]$$

$$F_{32} = \frac{m+1}{\epsilon_c} \left(\frac{\epsilon_{22}}{\epsilon_m} \right)^m \exp \left[- \left(\frac{\epsilon_{22}}{\epsilon_c} \right)^{m+1} \right]$$

$$F_{71} = \frac{\frac{m+1}{f_1\sigma_c} \left[\frac{\sigma_{11}}{(1-D_1)f_1\sigma_c} \right]^m}{1 - (m+1) \left[\frac{\sigma_{11}}{(1-D_1)f_1\sigma_c} \right]^{m+1}}$$

$$F_{72} = \frac{\frac{m+1}{f_2\sigma_c} \left[\frac{\sigma_{22}}{(1-D_2)f_2\sigma_c} \right]^m}{1 - (m+1) \left[\frac{\sigma_{22}}{(1-D_2)f_2\sigma_c} \right]^{m+1}}$$

Figure Caption

Figure 1: Localization mode.

Figure 2: Absolute value of the localization angle in degrees at localization for model #1, the main caption of the axes corresponds to the case where $f_2 = .5$, $f_1 = .0, .125, .333, .5$, and the captions in brackets correspond to the cases where $f_1 = .5$, $f_2 = .0, .125, .333, .5$.

Figure 3: Normalized maximum stress at localization for model #2, the main caption of the axes corresponds to the case where $f_2 = .5$, $f_1 = .0, .125, .333, .5$, and the captions in brackets correspond to the cases where $f_1 = .5$, $f_2 = .0, .125, .333, .5$.

Figure 4: Absolute value of the localization angle in degrees for model #2, the main caption of the axes corresponds to the case where $f_2 = .5$, $f_1 = .0, .125, .333, .5$, and the captions in brackets correspond to the cases where $f_1 = .5$, $f_2 = .0, .125, .333, .5$.

Figure 5: Maximum normalized damage value at localization ($m=4$.) for model #2, the main caption of the axes corresponds to the case where $f_2 = .5$, $f_1 = .0, .125, .333, .5$, and the captions in brackets correspond to the cases where $f_1 = .5$, $f_2 = .0, .125, .333, .5$.

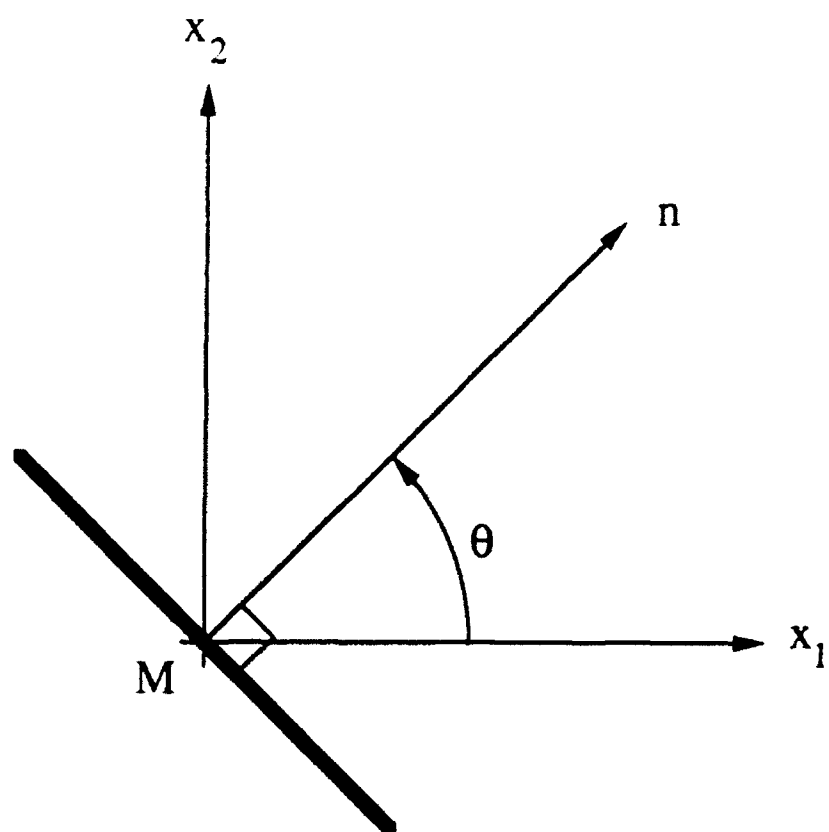


Fig. 1

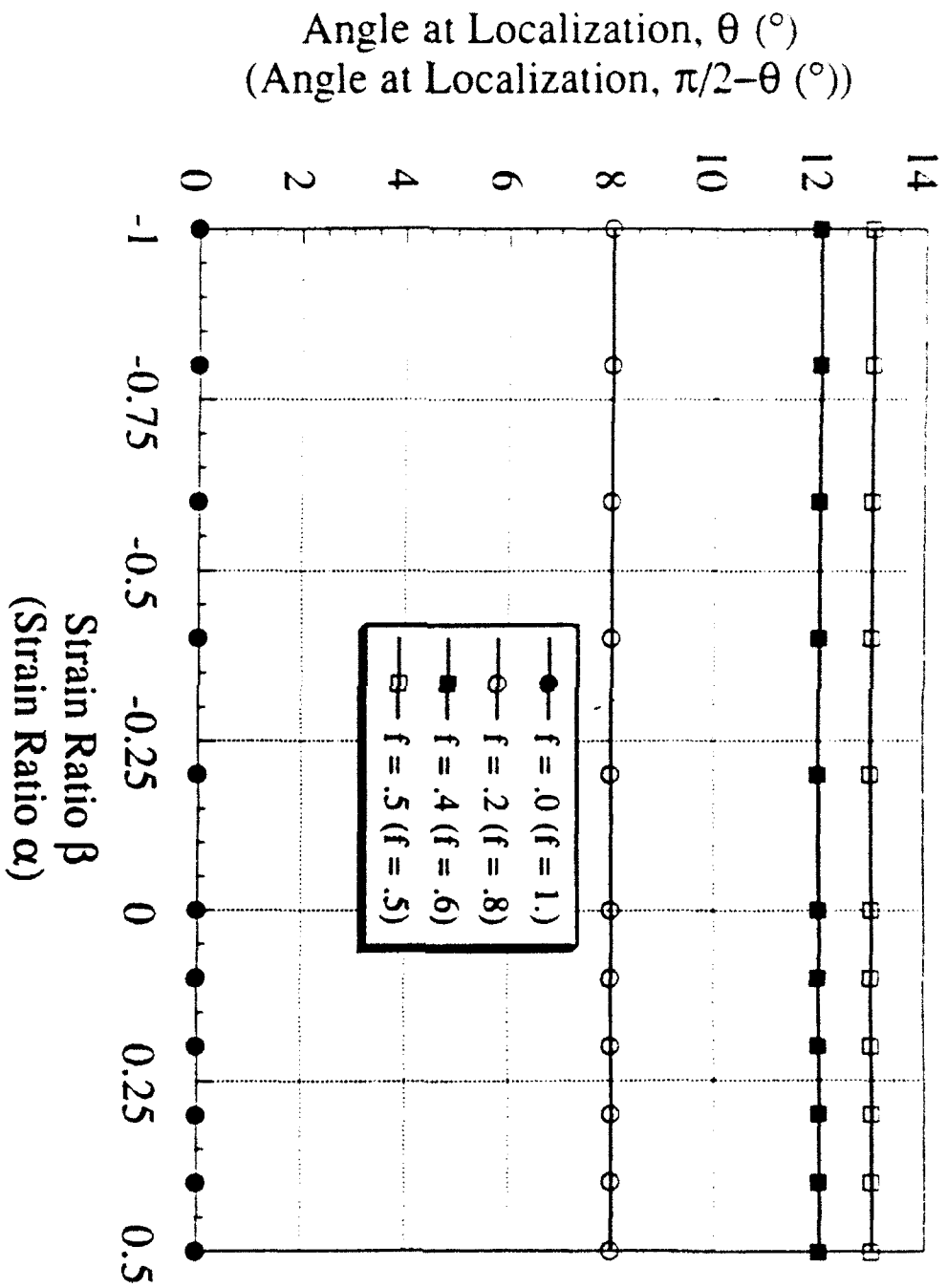


Fig. 2

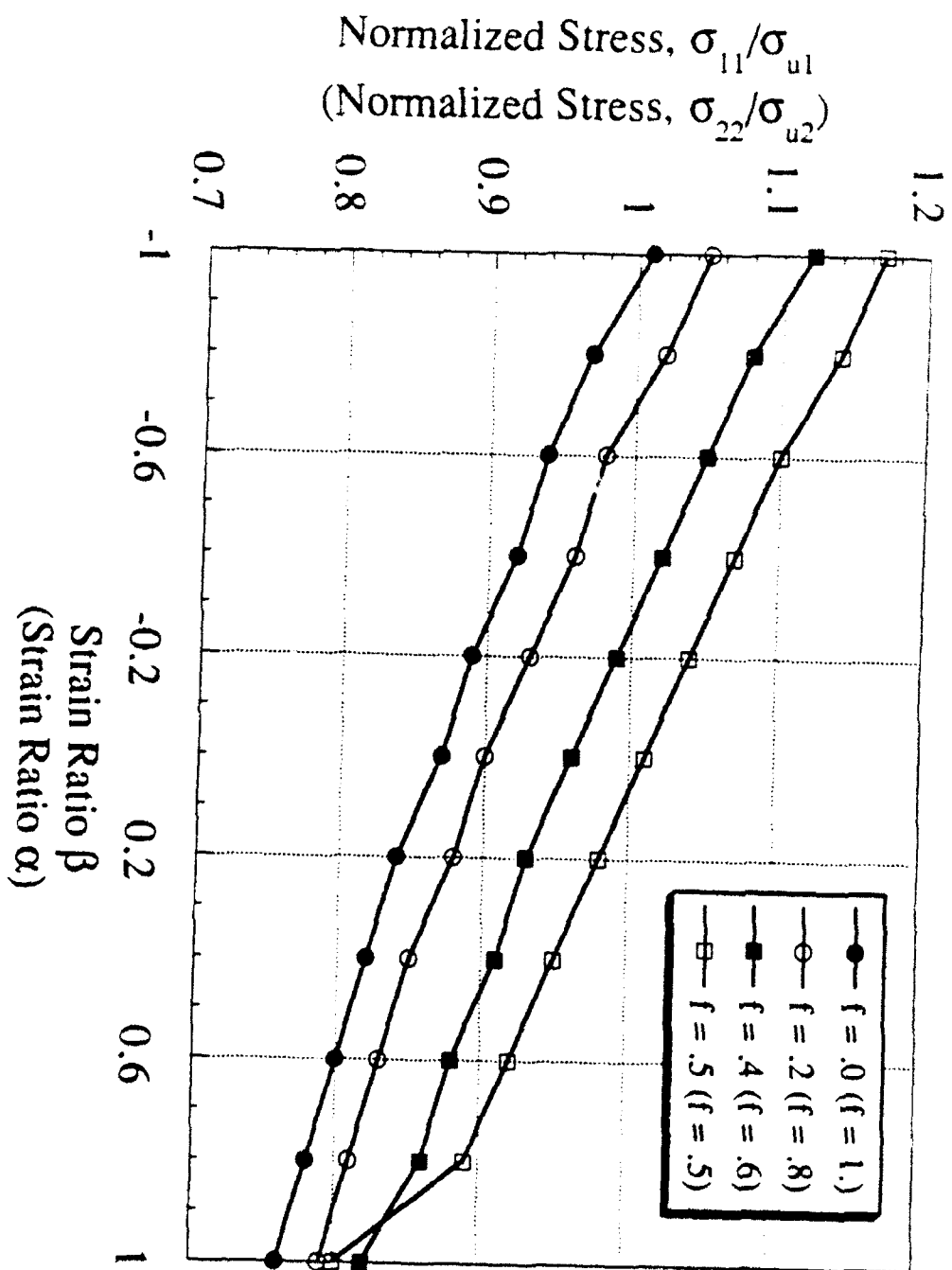


Fig. 3

Angle at Localization, θ ($^{\circ}$)
 (Angle at Localization, $\pi/2 - \theta$ ($^{\circ}$))

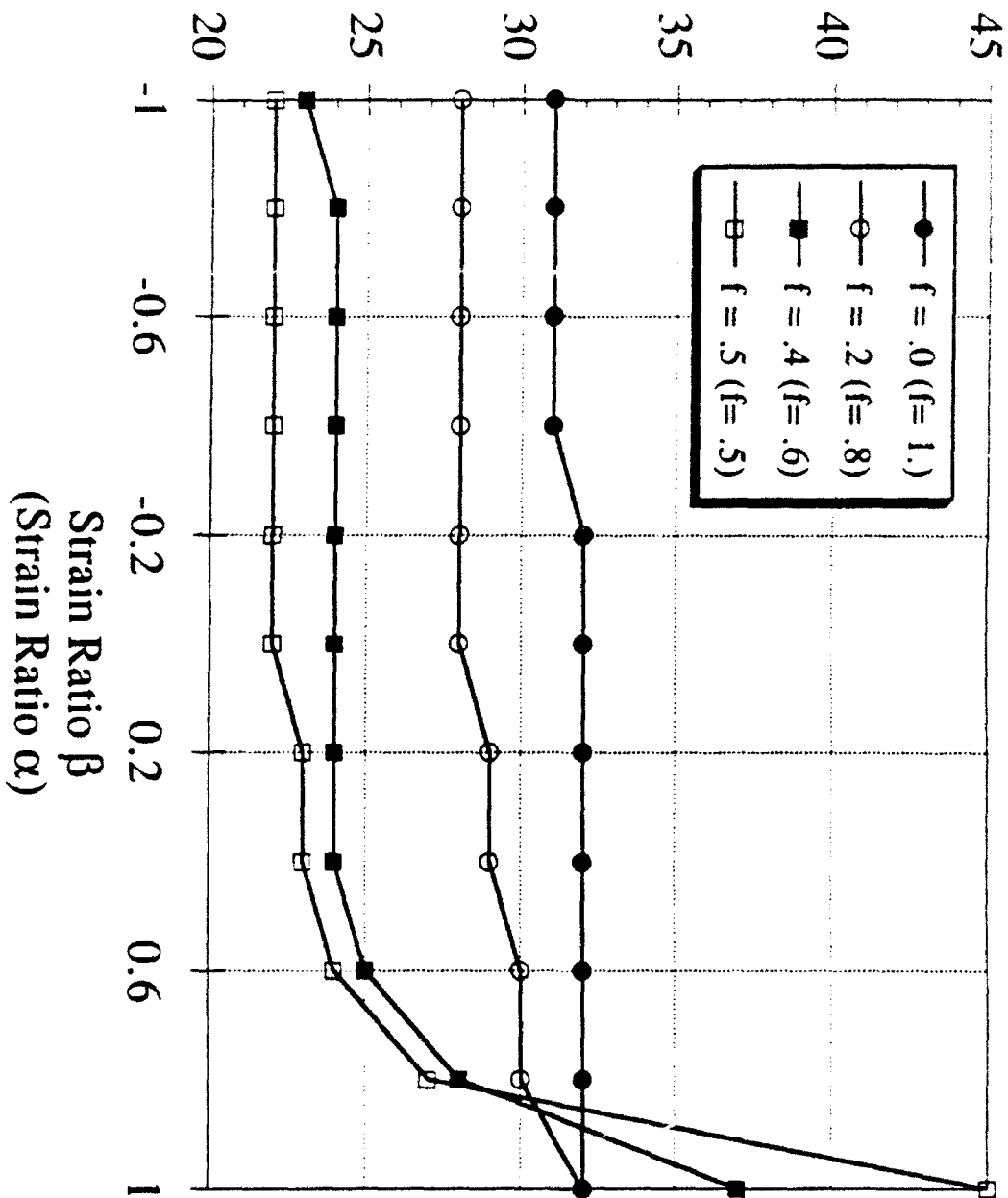


Fig. 4

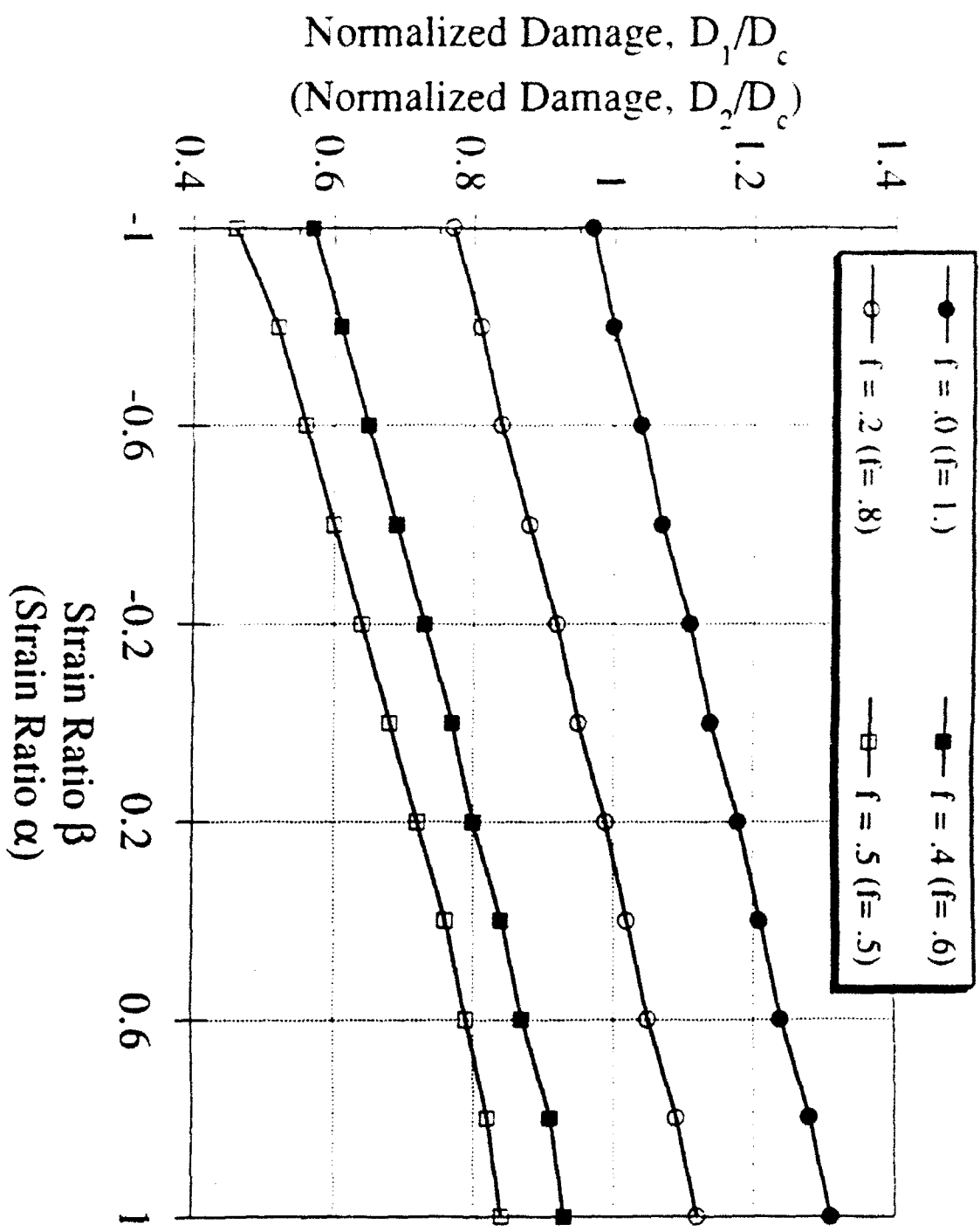


Fig. 5

ON THE NOTCH-SENSITIVITY AND TOUGHNESS OF A CERAMIC COMPOSITE

Keith T Kedward
Department of Mechanical Engineering
University of California
Santa Barbara, U S A

Peter W R Beaumont
Department of Engineering
University of Cambridge
Cambridge, U K

ABSTRACT

A Nicalon TM/SiC fabric (8-harness satin) reinforced alumina matrix (CMC) was loaded in tension to fracture. A coating on the surface of the fibre reduced the strength of the fibre-matrix bond, increased the fibre pull-out length and toughness of the CMC by more than 3 times, and raised the unnotched strength by more than 2 times.

1. INTRODUCTION

The development of ceramic-matrix composites (CMC) for general engineering usage must address the inherent notch-sensitive characteristics for which most unreinforced ceramic materials are notorious. For most polymeric matrix composites (PMC) the subject of notch sensitivity is quite well understood and characterized (1). With the more rigid matrix of CMC's the general design approaches must not be too strongly influenced by PMC experience and the possibility of closer attention to the microstructural characteristics, and particularly the fibre/matrix interface, is required. One example of a potential CMC-specific design criterion is the importance placed on limiting the tensile stress or strain to a level below which matrix cracking will be precluded, particularly when the ambient service environment degrades the reinforcing fibres.

2. MATERIALS

For a preliminary experimental evaluation specimens of a Nicalon TM/SiC fabric (8-harness satin) reinforced alumina matrix CMC was obtained. The CMC was produced by an aluminium oxide-based slurry process wherein the ceramic fibre fabric is drawn through a matrix bath to form preimpregnated layers. These layers are stacked and heated under pressure to establish a well-bonded laminate before firing to the finished CMC condition. The final CMC comprises typically 45% fibre volume fraction with 15-20% void fraction (porosity). In some samples, the Nicalon fibres were coated with boron nitride (BN). Specimens were cut from four plates of 1.5 mm nominal thickness using a conventional water-jet system.

Specimen configurations of unnotched and notched type illustrated in fig. 1 included a standard "dogbone" and two double edge notched (DEN) geometries. For comparative purposes, a tensile specimen containing a central hole was tested.

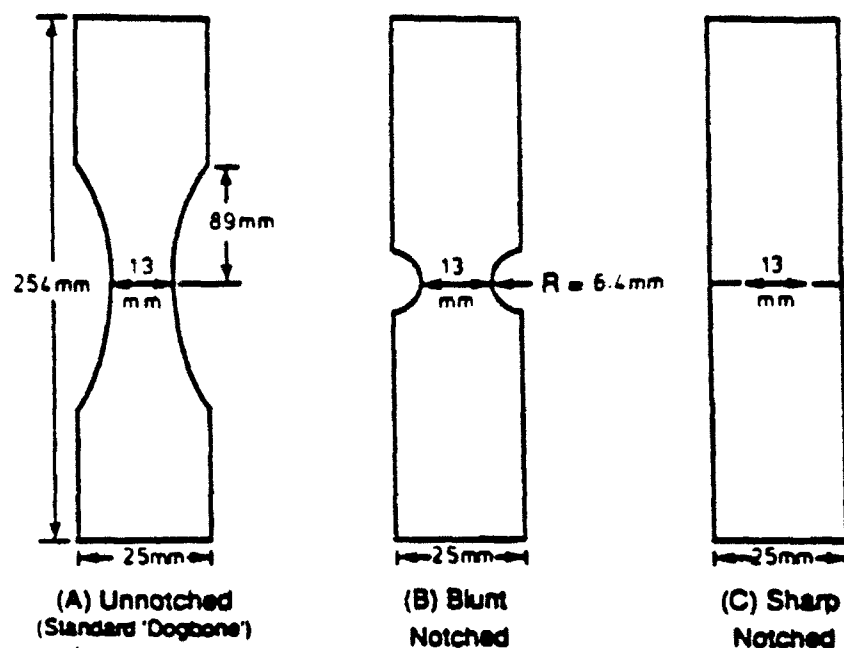


Fig.1 Specimen Configurations

In the experiments tensile loading was introduced using adhesively bonded aluminium end tabs and an MTS servohydraulic universal testing machine or an Instron servomechanical machine. Displacement control was adopted in both cases using an unclamped gauge length of 150 mm and an actuator velocity of 0.05 mm/min. Strain/displacement measurement was recorded by centrally mounted 10 mm clip gauges. Three replicates were used for both the notched and unnotched specimen configurations.

3. RESULTS

Results of the CMC testing are presented in Table 1 and Figure 2 and, despite the limited data, clearly indicate the superior performance of the coated fibre system relative to the uncoated system. The coating essentially provides a reduced fibre/matrix bond strength shown by longer fibre pull-out lengths (fig. 3). A similar ratio of unnotched to notched strength for the semicircular notch configuration of both strengths are much higher for the coated fibre condition. Furthermore, the sharp slit notched DEN specimen results indicate no significant effect of notch acuity for the coated fibre condition (see Table 1). The data point on the fig. 2 representing a ratio of flaw size-to-specimen width of 0.2 was for the configuration of a centrally located open hole. Of interest here is the location of the data points relative to the notch-insensitive and ideally notch-sensitive curves. Observe that the uncoated CMC specimens with the slit DEN configuration exhibit classical notch-sensitivity.

	σ_0 , MPa Unnotched Configuration (A)	σ_n / σ_0 Blunt Notched $R = 6.4$ mm Configuration (B)	σ_n / σ_0 Sharp Notched $R = 0.15$ mm Configuration (C)
CMC / Uncoated Filaments	61	0.35	0.24
CMC / Coated Filaments	143	0.34	0.33

Table 1 Results of exploratory investigation of the notch sensitivity of bi-directionally reinforced CMC.

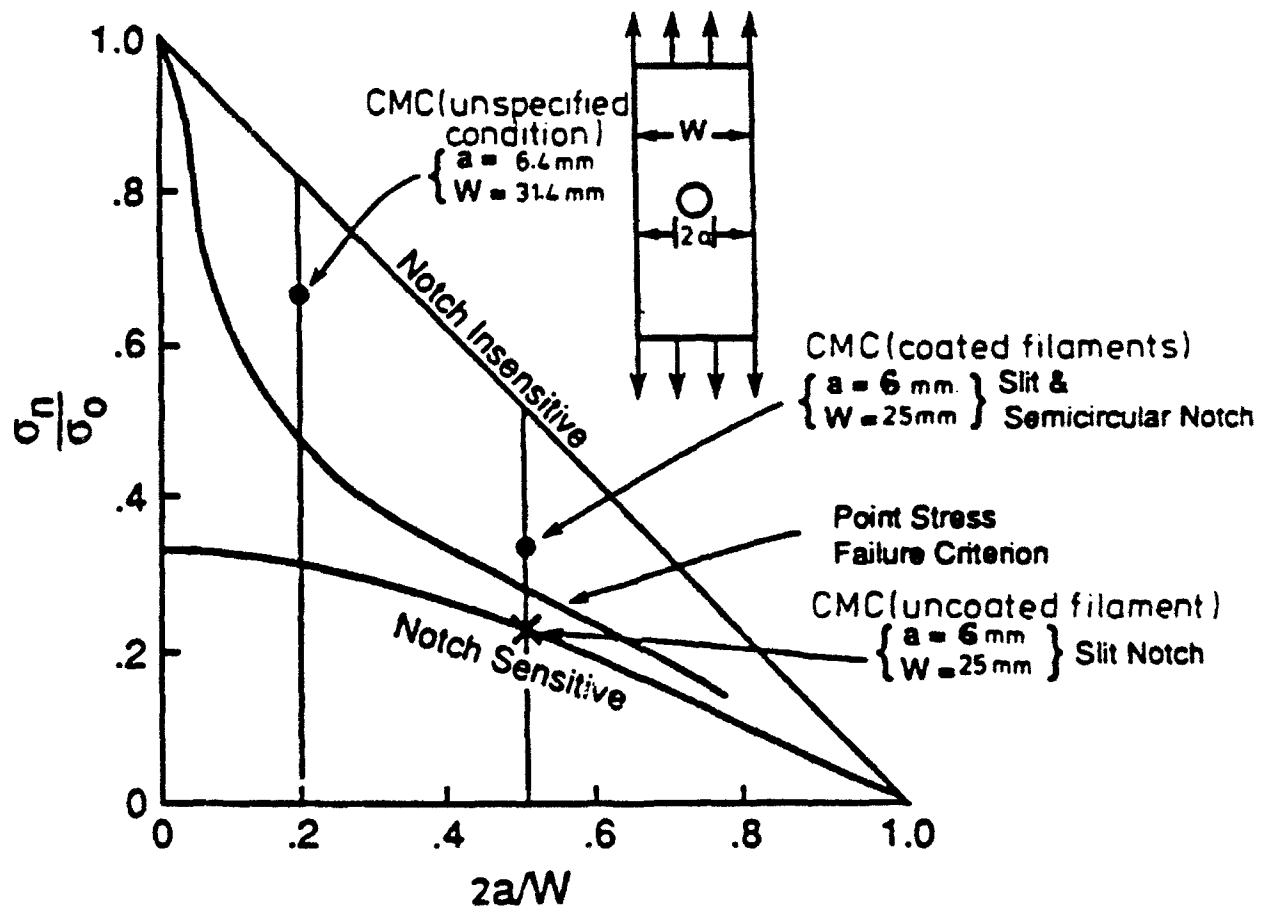
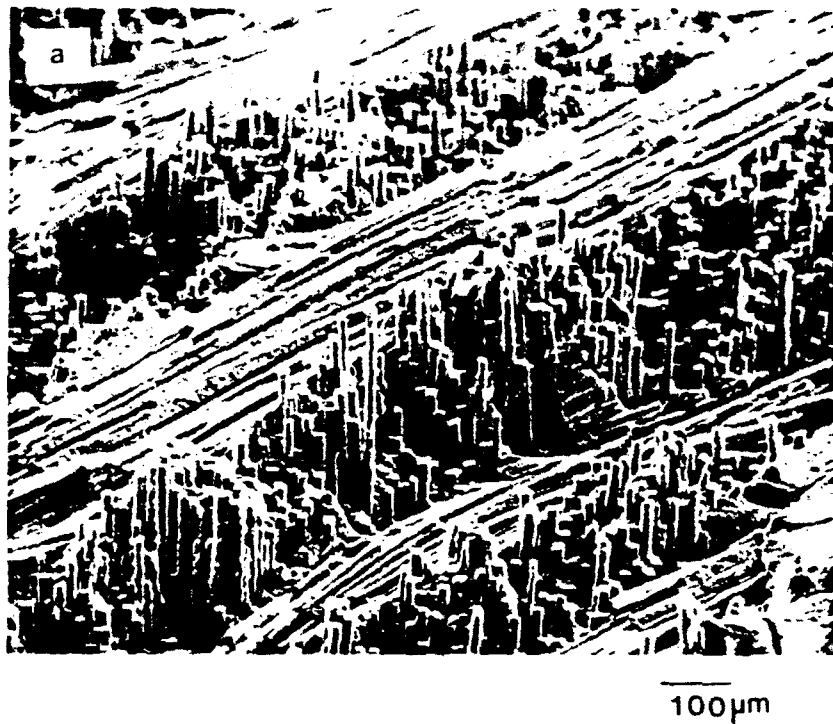


Figure 2 Results for preliminary notch sensitivity assessment of CMC.

All specimens tested displayed substantial nonlinearity in stress/strain (for the unnotched condition) and stress/displacement (for the notched condition) but post-failure examination by scanning electron microscopy revealed surface roughness with extensive fibre pullout for the coated specimens (fig. 3). Failure surfaces for the uncoated samples were considerably smoother (fig. 3).



"Strong" bond



"Weak" bond

4. DAMAGE MECHANICS AND FRACTURE TOUGHNESS

A further point of interest concerns the notch tensile strength which, for the DEN configuration with a slit (sharp) notch of length a , is given by the equation (assuming isotropy):

$$\sigma_n = \frac{K_C}{Y\sqrt{a}} \quad (1)$$

where the finite specimen width correction factor $Y_{DEN} = 1.98 + 0.36 \left(\frac{2a}{W}\right) - 2.12 \left(\frac{2a}{W}\right)^2 + 3.42 \left(\frac{2a}{W}\right)^3$ and K_C = Fracture Toughness.

For the center cracked plate (OCP), $Y_{OCP} = 1.77 \left[1 - 0.1 \left(\frac{2a}{W}\right) + \left(\frac{2a}{W}\right)^2 \right]$

By substituting the nominal dimensions of the DEN specimens, i.e. $\frac{2a}{W} = 0.5$, we obtain:

$$Y_{DEN} = 2.06 \quad \text{and} \quad Y_{OCP} = 2.12$$

Finally, by adopting the simple notch tip damage zone concept of macroscopic fracture mechanics introduced by Waddoups, Eisenmann, and Kaminski (2) and utilizing the preliminary notched, σ_n , and unnotched strength, σ_o , data from Table 1:

$$\sigma_o = \frac{K_C}{\sqrt{\pi a_o}} \quad , \quad \sigma_n = \frac{K_C}{Y_{DEN} \sqrt{a+a_o}} \quad (2)$$

where a_o represents the dimension related to the size of the notch tip damage zone which for an unnotched sample can be thought of as equivalent to the "inherent" flaw size. Next, we obtain

$$\frac{\sigma_n}{\sigma_o} = \frac{\sqrt{\pi a_o}}{Y_{DEN} \sqrt{a+a_o}} = 0.86 \sqrt{\frac{a_o}{a+a_o}} \quad (3)$$

Hence, a value of $a_o = 1.17 \text{ mm}$ is implied.

Using equation (2) a fracture toughness for the coated CMC material is estimated as:

$$K_C = 8.66 \text{ MPa } \sqrt{\text{m}} \quad \text{COATED CMC}$$

Following a similar procedure the fracture toughness for the uncoated CMC material is estimated as:

$$K_C = 2.50 \text{ MPa } \sqrt{\text{m}} \quad \text{UNCOATED CMC}$$

with a value of $a_o = 0.54 \text{ mm}$.

Clearly, further research is required to substantiate the above and extend the correlations for a range of notch sizes and configurations. More extensive microscopy is required to establish reasons for the shortfall in strength of the "uncoated" fibre laminate which is suspected to be due to fibre damage incurred during processing. Thus, an opportunity exists here for material enhancements through improved processing techniques and to further investigate fibre/matrix interface phenomena.

Some of our exploratory fatigue testing on notched specimens with coated fibres at cyclic loads corresponding to 50% and 80% of static notched strength suggested that residual strengths after 10^6 cycles were negligibly different from the initial static strength. More extensive research is required before any general and definitive conclusions can be drawn on this subject however.

5. REFERENCES

- (1) M.T. Kortschot and P.W.R. Beaumont, "Damage Mechanics of Composites", Parts 1-4, Composites Science and Technology, 39 pp. 289 (1990) and 40, pp. 147 (1991).
- (2) M.E. Waddoups, J.R. Eisenmann and B.E. Kaminski, "Macroscopic Fracture Mechanics of Advanced Composite Materials", J. Comp. Materials, Vol 5, pp. 446-454 (1971).

Thermal, Mechanical & Creep Behavior of Metal Matrix Composites

Stefan Jansson

Frederick A. Leckie

Department of Mechanical and Environmental Engineering

University of California

Santa Barbara, CA 93106

1. INTRODUCTION

The high strength/weight ratio and thermal conductivities of metal matrix composites are properties which make them attractive for application in modern components for which low weight and good thermal efficiency are essential. An intrinsic difficulty in establishing the mechanics of these materials is that they are at a very early stage of their development when changes in their manufacture are frequent and many. As a consequence the amount of material available for comprehensive testing is limited. Furthermore, the test specimens tend to be small and have high strength so that problems associated with gripping are considerable. Consequently, the mechanics describing the behavior of metal matrix composites must be achieved with only very little information. However, the recent advances in computational techniques combined with established mechanics principles are helpful in establishing the material properties and their effect on component performance.

This paper shall describe some of the advances with special reference to the properties of a composite consisting of an aluminum-lithium matrix reinforced with continuous alumina fibers. This material combination is distinguished by the strong bond which exists between matrix and fiber so that stress and displacement continuity conditions may be assumed. Attempts shall be made to describe the general approach which is being developed. It should be emphasized that the procedures are not fully developed but sufficient progress has been made to believe that the prospects of success are high.

diminished or even lost if multi-laminate systems are adopted. Consequently, if full advantage is to be taken of the dominant strength characteristics then the fibers should be aligned in the direction of maximum stress transmission. In this circumstance the transverse properties of the material are also important since there must be sufficient strength in the matrix to support the secondary stresses applied in the transverse direction. In addition to the strong bond existing between the fiber and the matrix another important feature of the composite is the large mismatch in the coefficients of thermal expansion so that fluctuations in operating temperature induce substantial thermal stresses. It is the goal of this study to establish the behavior of the composite when subjected to transverse stress and cycles of temperature. This study shall be used to illustrate how the shakedown concept can be used to describe the material behavior when subjected to the described loading conditions and when creep effects are also important.

2. EXPERIMENTAL PROGRAM

The composite studied is Du Pont's FP/AL with continuous fibers in a unidirectional lay-up. The fiber volume fraction was determined to be 55%. The FP fiber consists of 99% pure crystalline α -alumina (Al_2O_3) coated with silica that improves the strength of the fiber and aids the wetting by the molten metal. The fibers have a diameter of approximately 12 μm , a modulus of 345 to 380 GPa, a tensile strength of 1.9 to 2.1 GPa for 6.4 mm gauge length, and a fracture strain of 0.3-0.4%. The matrix material is a 2 wt% Li-Al binary alloy. The modulus is 68.9 GPa and Poisson's ratio is 0.32. The lithium promotes the wetting of the alumina fibers that forms a strong matrix-fiber interface. The composite is fabricated by preparing the FP fibers into tapes by using a fugitive binder and the tapes subsequently laid up in a metal mold in the desired orientation. The binder is burned away and the mold is vacuum-infiltrated with the molten matrix. The composite was available in the form of a plate 150 x 150 x 12.5 mm thick.

The specimen used for transverse tests is shown in Fig. 1. It has a relatively large radius at the transition from the gripping section to the reduced gauge section to provide a low stress concentration and a short specimen to prevent specimen buckling during

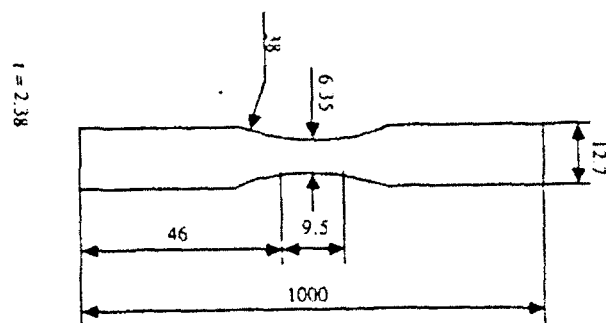


Fig. 1

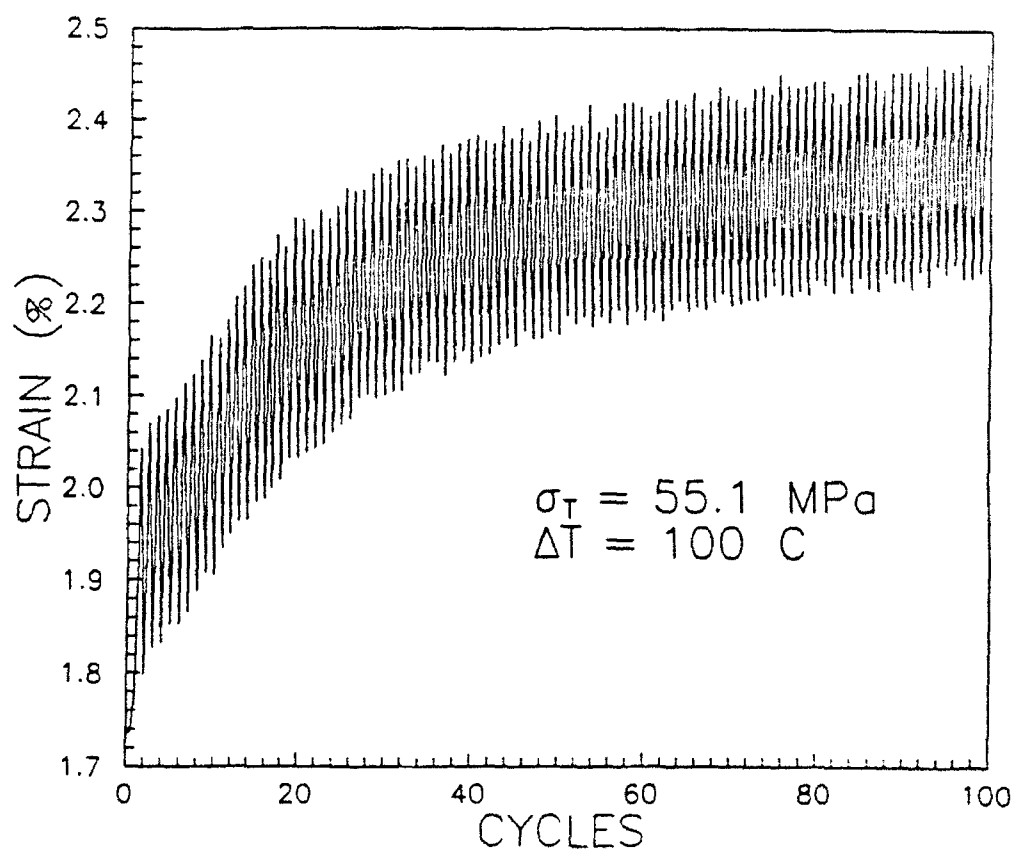


Fig. 2

compressive loading. The gauge section is 10 mm long and 6 mm wide and 2.4 mm thick. The strains were measured with 3.2 mm strain gauges. Specimen was loaded by an M. T. S. hydraulic machine and it was heated by means of induction coils. The control of the temperature was achieved by using thermocouple measurements..

The tests reported in this study involved a constant transverse stress in combination with cycles of temperature with cycle time 150 s. The temperature and strain variations were continuously recorded, and a typical example of the accumulation of strain is illustrated in Fig. 2.

The transverse stress strain curve at room temperature is shown in Fig. 3, from which a deviation from linearity is observed to occur at 75 MPa. The ultimate strength is 200 MPa and the strain to fracture is 0.8%. The ultimate strength is about 50% higher than the ultimate matrix strength while the failure strain of 0.8% is only 4% of the failure strain of the matrix [Sakui and Tamura, 1969]. A representative test for the constant transverse stress and cyclic temperature is given in Fig. 2 which indicates that transient behavior is followed by a cyclic response for which there is an increment of strain after each cycle, i.e., ratcheting occurs in both examples. Similar tests were performed at different values of constant transverse stress and temperature cycle. In Fig. 4 contours of constant values of $d\epsilon_p/dN$ are plotted, where ϵ_p is the plastic ratchet strain and N is the cycle number.

There are combinations of σ_T and ΔT for which no ratcheting occurs when the initial transient response is followed by elastic cycle response. This condition is indicated in Fig. 4 as the shakedown condition. When the operating conditions exceed the shakedown condition ratcheting occurs at rates indicated in Fig. 4. The failure strain was observed to vary according to the operating condition as indicated in Fig. 5. The failure strain is 0.08% for high stress and low thermal load whereas for low transverse stress of 30 MPa the failure strain reaches 12%. Microscopic examination of the failure surface indicates the presence of voids in the matrix, with no evidence of damage in either the fiber or fiber-matrix interface. This observation suggests that the failure mechanism in the matrix is associated with void growth.

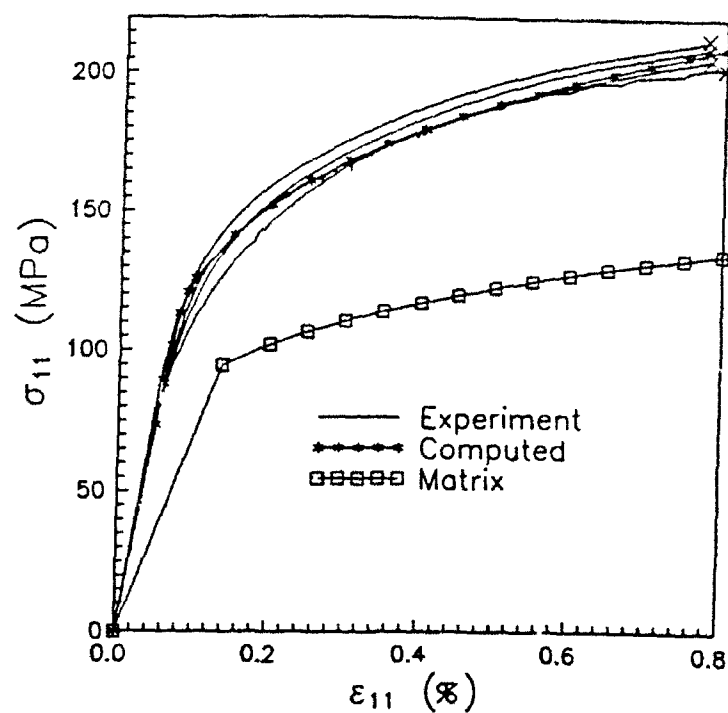


Fig. 3

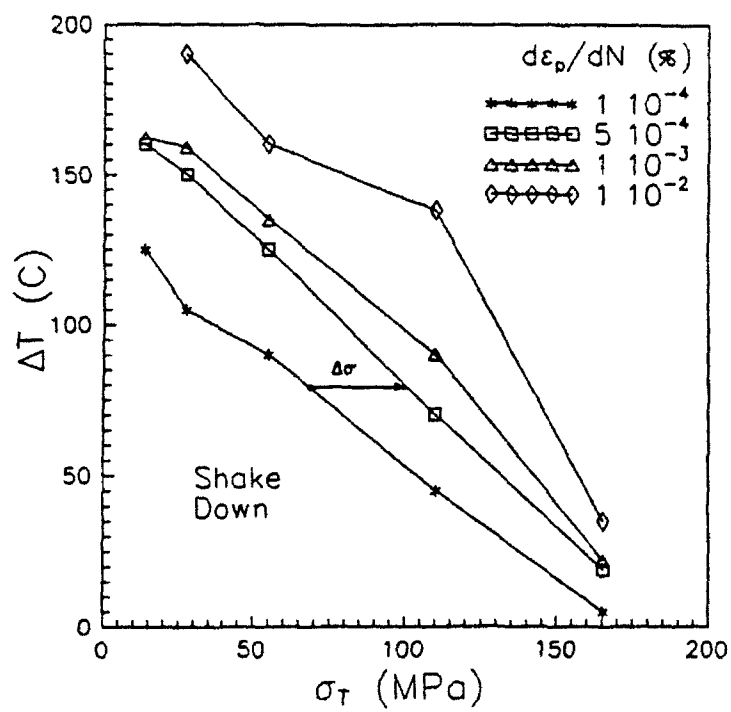


Fig. 4

The contours of constant ratchet strain rate plotted in Fig. 4 are generally parallel to the shakedown surface. This observation suggests that the driving force which drives the ratchet strain rate is given by

$$\alpha = \left[\frac{T}{T_s} + \frac{\sigma_T}{\sigma_s} - 1 \right]$$

where T_s and σ_s are the ordinates defining the shakedown condition. The relationship of $d\epsilon_p/dN$ has the form

$$\frac{d\epsilon_p}{dN} = f(\alpha)$$

where $f(\alpha)$ is linear for small values of α and increases exponentially as α approaches the value 1 - Fig.6.

3. COMPUTATIONAL STUDIES AND THEIR IMPLICATIONS

The homogenization technique has been widely developed and can be used to predict the composite stress-strain response. The procedure can then be used to determine the response to the different loading which form the basis of developing constitutive equations Jansson [1990a]. A difficulty with the approach is the lack of properties of the constituents of the composite when they are subject to a complex history of time and temperature during the manufacturing process.

The elastic properties of fiber and matrix are not greatly affected by the history of processing and heat treatment of the composite and this makes it possible to use data from the literature. However, the flow properties of the Al-Li matrix alloy are strongly dependent on heat treatment and cold-working [Stark et al., 1981 and Sikui and Tamura, 1969]. Details of the processing and post heat treatments of the composite are not available. Hence, the exact state of the matrix is not known and the information is insufficient to extract the flow properties of the matrix from the literature. This leaves as the only option

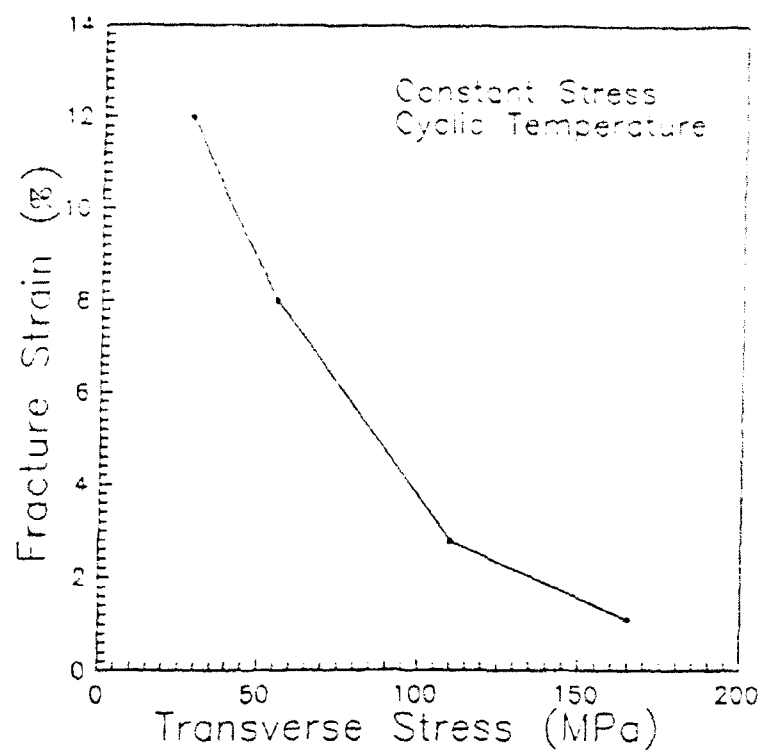


Fig. 5

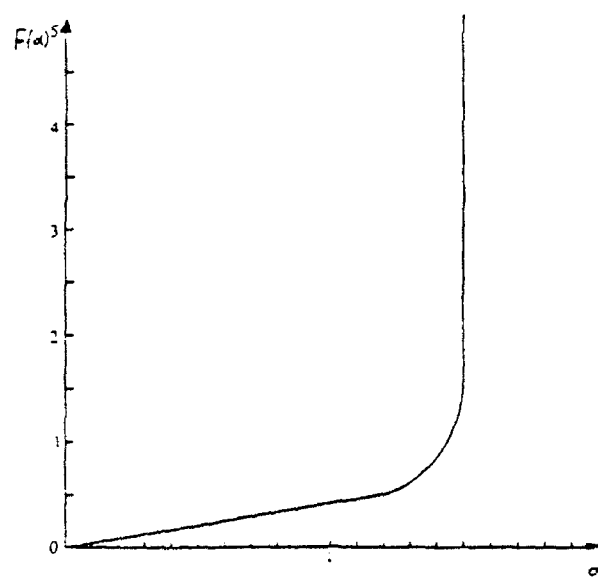


Fig. 6

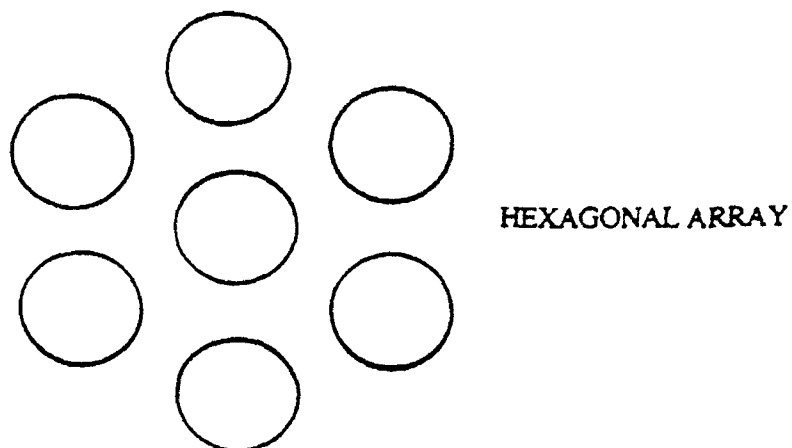
to determine the flow properties of the matrix in the composite is to fit a calculated response, by varying the flow properties of the matrix, to an experimentally determined matrix dominated stress strain curve for the composite. This procedure has been performed by Jansson [1990b] who determined that the initial yield stress of the matrix is 94 MPa with a hardening exponent $n = 5$ (Fig. 3). The matrix properties were then used to predict the performance of the composite when subjected to shear and multiaxial stress loadings. The predictions of the computations agreed well with the experimental observations and provided confidence that predictions of the computations using the material data from one experiment could be applied to different loadings. In practice this could lead to significant savings since complex testing programs may be avoided.

The present composite consists of long fibers in a unidirectional lay up that are randomly distributed in the transverse plane. In the model to be analyzed the fibers are assumed to be long parallel cylinders arranged in a hexagonal array, Fig. 7. This periodical array has the mechanical properties with the closest symmetries to randomly distributed fibers that are transversely isotropic. Both systems are transversely isotropic when the constituents are linear elastic but the hexagonal array has a weak deviation from transverse isotropy when the matrix exhibits a nonlinear stress strain relation Jansson [1990b]. The deviation is most pronounced for a perfectly plastic matrix. However, reasonable results can be expected if effective properties are calculated for loadings that do not permit slip planes unconstrained by the fibers. This resembles the closest condition to a composite with randomly distributed fibers.

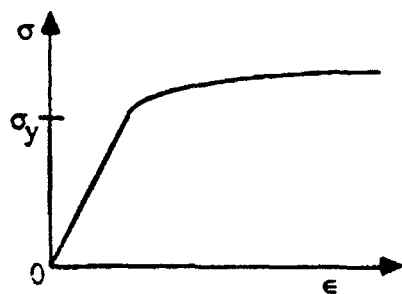
In the present calculations the fibers are assumed to be linear elastic and the matrix behavior is modelled with a small strain J_2 perfectly plastic theory using the properties given in Fig. 7.

The governing boundary value problem for the effective properties of the unit cell is two dimensional and has been solved with the Finite Element method. The displacement field is interpolated with nine nodes isoparametric elements and reduced integration is used to avoid locking, 2×2 for the hydrostatic component and 3×3 for the deviatoric component of the stress tensor. The nonlinear system of equations is solved with a

FIBROUS COMPOSITE



PROPERTIES OF MATRIX (aluminum-lithium)



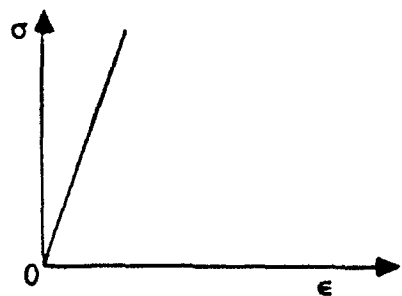
$$E = 69.0 \text{ GPa}$$

$$\sigma_y = 95 \text{ MPa}$$

$$\nu = 0.32$$

$$\alpha = 23.6 \times 10^{-6}/^{\circ}\text{C}$$

PROPERTIES OF FIBER (alumina)



$$E = 345 \text{ MPa}$$

$$\nu = 0.26$$

$$\alpha = 8.6 \times 10^{-6}/^{\circ}\text{C}$$

$$V_f = 55\%$$

Fig. 7

Newton-Raphson scheme. The loading of the unit cell, Fig. 7, is symmetric with respect to the y_1 and y_2 axis. This implies that only an eighth of the indicated unit cell need be analyzed. A detailed description of the finite element mesh of the implementation of the method and deviations of the boundary conditions for different loadings are given in Jackson [1990a].

In performing the elastic-plastic calculation it was possible to determine the shakedown boundary defined in Fig. 4. This has been expressed in terms of the dimensionless loadings $E\alpha\Delta T/\sigma_y$ and σ_T/σ_y . In terms of the material parameters for the present system the experimental determination of the shakedown surface is also shown in Fig. 4. The agreement is reasonably good but it is noted that the experimental results indicate a straight line relationship exists between ΔT and σ_T whereas the computed boundary is somewhat convex. The differences in the experimental and computational predictions is likely to be related to deficiencies in the constitutive model for the matrix. The computational procedures involved very heavy computation since more than 100 cycles are often required before a steady state condition was reached. For this reason no attempt was made to determine the behavior for operating points outside the shakedown condition, and this is left to a bound method developed by Ponter and Cox [1983].

The upper bound applies for loading conditions which exceed the shakedown condition by a modest amount. The upper bound is given by

$$\frac{\Delta\epsilon}{\Delta N} \geq 4\Delta e$$

where $\Delta\epsilon$ is the increment of elastic strain given by

$$\Delta e = \frac{\Delta\sigma_1}{E_T}$$

$\Delta\sigma_1$ being the stress increment in excess of the shakedown condition and E_T is the elastic modulus in the transverse direction.

For the optional point shown in Fig. 4 $\Delta\sigma = 35$ MPa and with $E_T = 150$ GPa [Jansson, 1990] the upper bound as ratchet strain is

$$\Delta\varepsilon = \frac{4 \times 35}{150} = 0.93 \times 10^{-3} / \text{cycle}$$

which compares with the experimental value of $0.5 \times 10^{-3} / \text{cycle}$.

The failure strain can differ by over an order of magnitude depending on the operating condition. It is known for Al-Li [Pilling and Rindly, 1986] that ductile failure is the result of void nucleation and growth from small particles. In the studies of Hancock and Mackenzie [1976] it is suggested that when failure is the result of void nucleation and growth the failure strain ε_f for multiaxial states of stress has the form

$$\varepsilon_f = 1.65\varepsilon_0 \exp\left\{-\frac{3}{2} \frac{\sigma_M}{\bar{\sigma}}\right\} \quad (3)$$

where ε_0 is the uniaxial failure strain, σ_M is the mean stress and $\bar{\sigma}$ the effective stress. The failure strain for the present matrix in uniaxial tension is reported to be approximately 0.2 [Sakui and Tamura, 1969]. Jansson [1990b] has reported in tests on the composite under consideration that the strain for in-plane shear parallel to the fibers is also 0.2. From

the computer studies it has been determined that transverse loading alone introduces a multiaxial stress state for which $\frac{\sigma_M}{\bar{\sigma}} = 2.5$ over a large region of the matrix.

Applying the formula for the failure strain gives the failure strain for transverse loading

$$\epsilon_{11}^f = 0.008$$

which compares well with the observed failure. As the transverse stress decreases the degree of triaxiality decreases and the failure strain is expected to increase.

4. EXTENSION TO CREEP CONDITIONS

Creep experiments have not yet been performed on the composite but these are now in hand. However, it is possible to gain some insight into the creep behavior using bounding

theorems for components subjected to cyclic loading conditions. Based on the Bailey Orowan theory, constitutive equations which describe the creep strains for variable stress histories can be expressed by the potential developed by Ponter and Leckie [1976]. The potential form is given by

$$\Omega = F(\phi - s) + G(s)$$

from which the strain and internal variable rates can be determined to be,

$$\begin{aligned} \dot{\epsilon}_{ij}^c &= f(\phi - p) \frac{\partial \phi}{\partial \sigma_{ij}} & [F' = f] \\ \dot{s} &= h(s)f(\phi - p) - r(p) & \left[G' = \frac{r(p)}{h(p)} \right] \end{aligned}$$

where $\phi^2 = \frac{3}{2} s_{ij} s_{ij}$ and p the internal variable is a scalar

The function $f(\phi - p)$ is defined by

$$\begin{aligned} f(\phi - p) &> 0 && \text{when } \phi = p \\ &= 0 && \text{when } \phi \leq p \end{aligned}$$

Following the expression for $f(\phi - p)$ strains only occur when $\phi = p$.

For fast loading $\dot{\phi} = \dot{p}$ and

$$\dot{\epsilon}_{ij}^p = \frac{\dot{p}}{h(p)} \frac{\partial \phi}{\partial \sigma_{ij}}$$

so that $h(p)$ can be determined from the short time stress-strain curve.

At steady state conditions $\dot{p} = 0$ and

$$\dot{\epsilon}_{ij} = \frac{r(p)}{h(p)} \frac{\partial \phi}{\partial \sigma_{ij}} = \dot{\epsilon}_0 \left(\frac{\sigma}{\sigma_0} \right)^n \frac{\partial \phi}{\partial \sigma_{ij}}$$

where σ_0 is the reference stress and $\dot{\epsilon}_0$ is the corresponding strain rate. The above relation can then be used to establish the function $r(p)$. Following the procedure developed by Ponter [1976], Cocks and Leckie [1988] found an optimized bound for the creep deformations when the component is subjected to cyclic loading. The bound applied to the current problem when the composite is subjected to transverse stress σ_1 and cyclic thermal loading gives the result

$$\dot{\epsilon}_1 \leq \frac{\sigma_y}{\sigma_u} \dot{\epsilon}_0$$

where σ_u is the maximum transverse stress corresponding to a matrix yield stress σ_y matrix. Reference to Fig. 3 shows the value

$$\frac{\sigma_u}{\sigma_y} = 1.5$$

Consequently

$$\dot{\epsilon}_1 \leq \frac{\dot{\epsilon}_0}{1.5}$$

The result only applies when the loading condition does not exceed the shakedown condition for a yield stress corresponding to the reference stress σ_0 . However the shakedown condition is known for σ_y and a simple scaling produces the shakedown for the reference stress σ_0 . A proviso for the application of the result is that the continuity conditions between fiber and matrix be maintained. Diffusion mechanisms have been reported which reduce the shear stress which can be supported at the interface. In these circumstances the result developed above could be seriously non-conservative.

CONCLUSIONS

It has been demonstrated that the shakedown concept provides useful insight into the behavior of a metal matrix composite when loaded with transverse stress and cyclic thermal loading. It is also shown that a slight modification in which the reference stress is used in conjunction with the shakedown condition is sufficient to give estimates on the creep behavior.

ACKNOWLEDGEMENTS

The authors acknowledge the support of a grant from NASA-Lewis.

REFERENCES

- Campion, A.R., Krueger, W.H., Hartman, H.S. and Dhingra, A. K., [1978], "Fiber F.P. Reinforced Metal Matrix Composites," Proc. 2nd International Conference on Composite Materials, Toronto, 1978, Metallurgical Soc. AIME, pp. 883-904.

Cocks, A.C.F. and Leckie, F.A., [1988] "Deformation Bounds for Cyclically Loaded Shell Structures Operating Under Creep Conditions," *J. Appl. Mech.*, p. 56, 1988.

Hancock, J.W., and Mackenzie, A.C., [1976] "On the Mechanisms of Ductile Fracture in High Strength Steels Subject to Multiaxial States of Stress," *J. Mech Physics of Solids*, 24, pp. 141-169, 1976.

Jansson, S., [1990a] "Homogenized Nonlinear Constitutive Properties and Local Stress Concentrations for Composites with Periodical Internal Structure," Department of Mechanical Engineering, UC Santa Barbara, 1990.

Jansson, S., [1990b] "Mechanical Characterization and Numerical Modeling of Non-Linear Deformation and Fracture of a Continuous Fiber Reinforced Metal Matrix Composite," Department of Mechanical Engineering, UC Santa Barbara, 1990.

Pilling, J. and Ridley, N., [1986] "Role of Hydrostatic Pressure on Cavitation During Superplastic Flow of Al-Li Alloy," *Aluminum-Lithium Alloys III*, The Institute of Metal, London, pp. 184-190, 1986.

Ponter, A.R.S. and Leckie, F.A., [1976] "Constitutive Relationships for Time-Dependent Deformation of Metals," *J. Eng. Mat. Tec., ASME*, 47, 1976.

Ponter, A.R.S., [1976] "Deformation Bounds for the Bailey-Orowan Theory of Creep," *J. Appl. Mech.*, 42, p. 619, 1976.

Ponter, A.R.S. and Cocks, A.C.F., [1983] "The Incremental Strain Growth of an Elastic-Plastic Body Loaded in Excess of the Shakedown Limit," Department of Engineering, Leicester University, 1983.

Sakui, S. and Tamura, M., [1969] "Yielding Phenomena of an Al-3% Li Alloy," *Transactions of the Japan Institute of Metals*, Vol. 10, pp. 343-350, 1969.

Starke, E.A., Sanders, T.H. and Palmer, J.G., [1981], "New Approaches to Alloy Development in Al-Li Systems," *Journal of Metals*, Vol. 33, pp. 24-32, 1981.

The treatment of fatigue and damage accumulation in composite design

K.T. Kedward and P.W.R. Beaumont

Differences between the treatment of damage, damage accumulation and fatigue for various types of advanced composite systems, for example, polymer matrix composites (PMCs), ceramic matrix composites (CMCs) and metal matrix composites (MMCs) are discussed in general. The approach for PMCs from the aspect of damage mechanics is reviewed next and extended to a discussion of various aerospace certification approaches adopted for PMC structures. Following this is an explanation of the theoretical foundations for the 'wearout philosophy' in conjunction with related damage-fracture mechanics relationships is provided. This concludes with a survey of flaw, or more precisely, damage growth rate exponents for various matrix and/or interface-dominated failure mechanisms for PMCs and adhesively bonded joints.

Key words: composites; damage mechanics; wearout

The process of design has traditionally involved a specialized treatment of damage accumulation and the associated fatigue phenomena, for example, Miner's rule. The treatment of such phenomena for the case of advanced composites tends to be complicated by the existence of a multiplicity of competing failure modes. The subject assumes an even greater importance when more types of composite systems are considered, for example, polymer matrix composites (PMCs), ceramic matrix composites (CMCs) and metal matrix composites (MMCs) to name the broader categories. All composite systems are considered herein to comprise continuous fibre reinforcements.

Despite wide recognition of the vital importance of fatigue degradation and the variety of potential damage accumulation mechanisms existing in complex composite designs, so-called experienced composite technologists frequently state that fatigue is not a problem in PMCs. Such statements may arise from the general observation that the reinforcing filaments are not, in themselves, susceptible to fatigue damage and consequently fatigue-dominated laminate designs subjected to pure tensile membrane loadings may similarly be relatively insensitive to high-cycle fatigue environments. However, the industry is frequently experiencing composite hardware development problems owing to design oversights that result in matrix-dominated load paths; a number of these problems will be cited below to illustrate the subtle manner in which fatigue damage may accumulate.

We shall consider PMCs, since these are the most 'mature' composite systems, and an extensive literature base and background experience exists for them. Currently, it may confidently be stated that the composites industry is able to design PMC laminates of uniform thickness in a reliable manner. Extensive experience with PMCs has taught us to use fibre-dominated laminate designs, which are most often specified in the $[0^\circ/\pm 45^\circ/90^\circ]_k$ or pseudo-isotropic form with respect to the in-plane directions. In-plane compression failure is somewhat of an exception since the matrix and the

degradation thereof can influence premature failure. However, by far the largest number of development and in-service problems with composite hardware is associated with matrix-dominated phenomena; that is interlaminar shear and out-of-plane tension. This is a major concern in that failure contributed by either one or a combination of these matrix-dominated phenomena are susceptible to the following:

- (i) high variability contributed by sensitivity to processing and environmental conditions, see Fig. 1;
- (ii) 'brittle' behaviour, particularly for early epoxy matrix systems;
- (iii) inspectability of local details where flaws or defects may exist;
- (iv) low reliability associated with the lack of acceptable or representative test methods and complex, highly localized stress states (The use of the transverse tensile strength of a unidirectional laminate for out-of-plane or through-thickness tensile strength is generally unconservative.);
- (v) potential degradation of residual static strength after fatigue-cyclic load exposure.

The development of stress components that induce interlaminar shear/out-of-plane tension failures is illustrated in Fig. 2 wherein commonplace generic features of composite hardware designs that frequently experience delaminations are shown. It is at such details that PMC structures are particularly vulnerable both under static and fatigue loading. It is of interest to observe, here, that it is the propensity for delamination and localized matrix-dominated failures that provides the character of many PMCs in that the notch sensitivity may be reduced after fatigue load cycling for local through-thickness penetrations. On the other hand, this demands that a fatigue life methodology should be available to deal with composite structures that are subjected to out-of-plane load components. Naturally, the capability of predicting the fatigue life is an essential element of the process

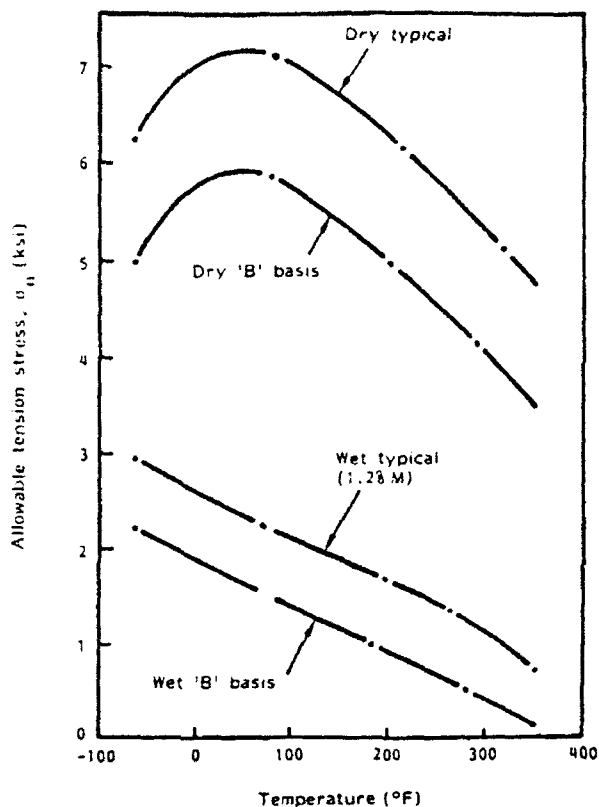


Fig. 1 Effect of moisture and temperature on the transverse tensile strength of unidirectional graphite/epoxy T300/520 f

of certifying aerospace composite hardware. We shall return to this subject in the next section.

Review of damage mechanics

Whereas the inherent anisotropy of composites reinforced by continuous fibres can provide an exceptional performance in the directions of the fibres in the way of unsurpassed specific strength and stiffness, they also pose a challenge for the structural designer who has to allow for deficiencies in the transverse and matrix-dominated directions. The situation is most acute for PMCs where the ratios of elastic strength and fracture toughness, thermal and electrical properties are most extreme. Consequently, the damage accumulation characteristics are very different from the near-isotropic metallic materials because of the multiplicity of potential failure modes. Delamination, for example, is one failure mechanism that is of particular concern in laminated PMCs and the high rates of propagation characteristic of this failure mode can often have catastrophic consequences. In a typical graphite or carbon epoxy composite even the transverse (in-plane) tensile strength amounts to no more than a few percent of the longitudinal (fibre direction) tensile strength; the out-of-plane tensile strength across a typical multidirectional laminate is generally significantly lower.¹ In most advanced composites the early damage process comprises of an increase in the crack growth, for example, transverse cracking of individual plies within a multidirectional laminate, often referred to as first-ply failure. Following initial transverse ply cracking, delaminations may eventually develop and can be precipitated by the transverse ply cracks. Actually, transverse cracking may exist in the initial state, the cracks being caused during processing due to the mismatch in

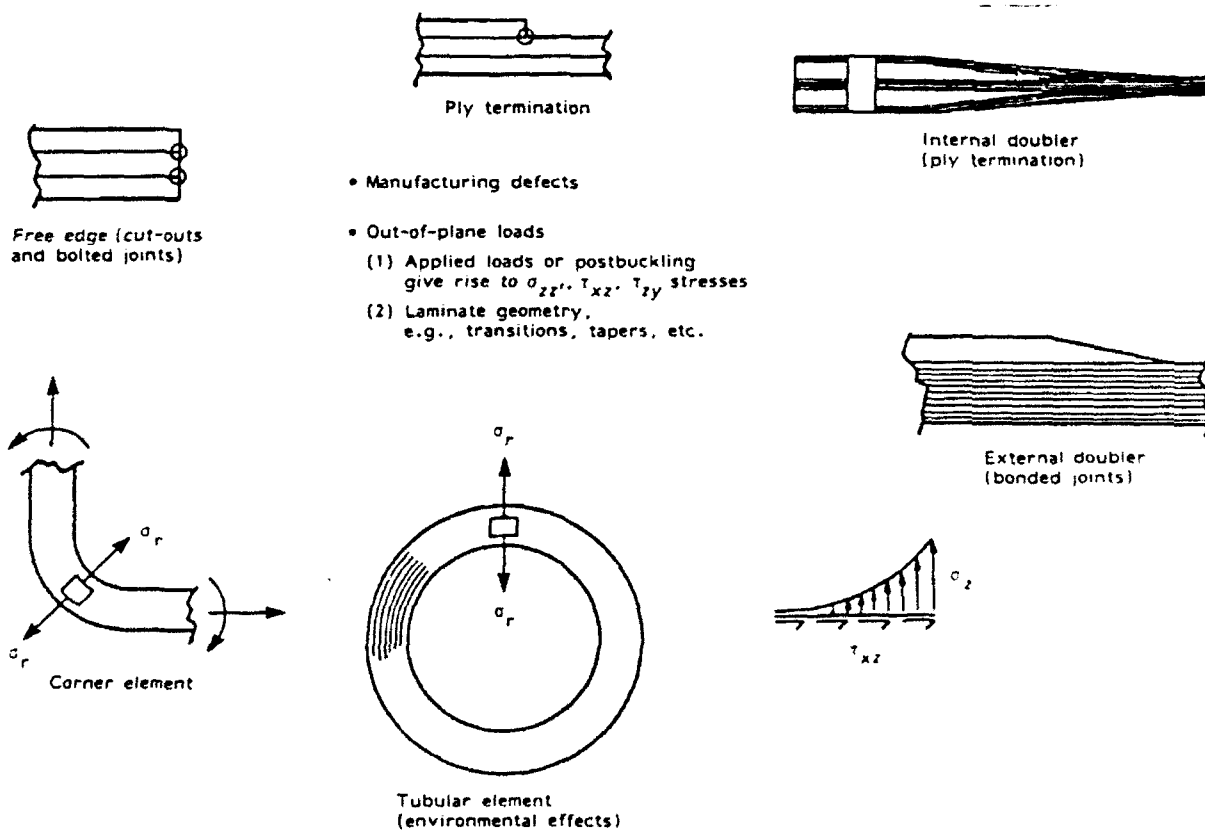


Fig. 2 Delamination sources

thermomechanical properties between adjacent plies. It is fortunate that although composites can be considered to often be a highly flawed structure, they are also a highly redundant structure when in the form of fibre-dominated laminates of the $[0^\circ/\pm 45^\circ/90^\circ]$ family with at least 10% of the fibres in each of the referenced directions.

Very few systematic attempts have been made to apply damage mechanics to advanced composites, for example, Poursartip, Ashby and Beaumont.⁴ In Ref. 4 a fatigue damage mechanics approach is developed for composites based on the assumption of a relationship between fatigue damage and changes in moduli of the composite laminate. The damage growth rate is assumed to depend on the cyclic stress amplitude ' $\Delta\sigma$ ' and on the current damage state ' D ', hence:

$$dD/dN = f(\Delta\sigma, D) \quad (1)$$

In more recent work, the same authors include the load ratio ' R '.⁵ Then

$$dD/dN = f(\Delta\sigma, R, D) \quad (2)$$

For both situations the relationship between the fatigue damage state ' D ' and the change of stiffness is utilised in the form:

$$E = E_0 g(D) \quad (3)$$

which permits

$$D = g^{-1}(E/E_0) \quad (4)$$

Integration of Equations (1) and (2) provides an estimate of life ' N_f ' once the damage accumulation function $f(\Delta\sigma, R, D)$ has been determined. This function can be most directly obtained experimentally using

$$f(\Delta\sigma, R, D) = \frac{1}{g'[g^{-1}(E/E_0)]} \frac{1}{E_0} \frac{dE}{dN} \quad (5)$$

By varying each of $\Delta\sigma$, R and D in turn and holding the other two variables constant, the results may be plotted and the function $f(\Delta\sigma, R, D)$ determined. Both Refs 4 and 5 include examples demonstrating the application to glass/epoxy and carbon/epoxy composite laminates and showing an acceptable correlation with experiments.

Poursartip and Beaumont⁴ extend the damage mechanics approach developed in Ref. 5 to predict the fatigue life for variable-load cycling. Although these predictions are less satisfactory than for the constant-amplitude cases, they are shown to be far superior to Miner's rule predictions. It is noteworthy that in all the work reported in Refs 5 and 6 delaminations originating at the specimen edges, induced by in-plane tension loading, is the principle damage mechanism, and the trans laminar cracking/debonding etc that occurs behind the delamination front becomes more extensive after delamination. This observation raises the question of the effects of finite specimen width, which is briefly anticipated in Ref. 5 as a simple size effect:

$$\left(\frac{dD}{dN}\right)_{w=w_2} = \frac{w_1}{w_2} \left(\frac{dD}{dN}\right)_{w=w_1} \quad (6)$$

where w_1 and w_2 represent different widths of a given laminate configuration.

This feature is vitally important to the composite hardware designer and deserves closer attention in future studies.

Turning now to a related and also a key aspect of design, that is the manner in which a material reacts to the presence of stress concentrators such as holes or notches, we cite the

origins of a research effort alerting the industry to this interesting phenomenon. At General Dynamics, during 1970, the effect of stress concentration in boron epoxy and graphite epoxy laminates was evaluated for both static and cyclic load conditions. Waddoups *et al.*⁷ subsequently published this work proposing the application of macroscopic fracture mechanics to advanced composite laminates containing small holes or through-thickness narrow slits. Numerous adaptations and variations embracing similar concepts have appeared since that time, one notable example being the work of Whitney and Nuismer.⁸ Whilst these approaches have served the industry well they do not provide a great insight into the mechanisms of damage; such approaches also impose a heavy burden on testing and data collection.

A quantitative methodology addressing the effect of notches on composite laminate performance in tension was developed by Kortschot and Beaumont⁹ for the $[90^\circ/0^\circ]$ laminate family. Selecting a double-edge-notched (DEN) specimen, a two dimensional finite element idealisation of a quarter-symmetric region of the specimen (with two coupled layers of elements representing the 0° and 90° layers) was used to demonstrate the significance of the longitudinal splitting failure mechanism within the 0° layers. The split length and delamination zone were hence predicted and compared with the experimental results from the x-ray examination of the damaged region. Later, Spearing, *et al.*¹⁰ extended this work, using a similar approach, to a centre-notched specimen initially confining their attention to the $[90/0]_s$ laminate type. They similarly found a reasonable correlation between theory and experiment, and further extended the work to a limited evaluation of $[0^\circ/\pm 45^\circ/90^\circ]_s$ laminates and to the tensile fatigue loading case. Predictions of the extent of cyclic-load-induced damage and of the resulting residual strength were also achieved and correlated with experimental observations reasonably well.

It is of particular interest to recognise that, since all the work reported in Refs 9 and 10 was confined to monotonic static tension and fatigue loading, the 0° layers will consistently experience transverse tensile stresses because of a mismatch in the Poisson ratio between the 0° and 90° layers as well as the residual time-dependent tensile stresses caused by the reduction in temperature from the cure state in conjunction with the large mismatch in coefficient of thermal expansion (CTE) between the 0° and 90° orientation. Consequently, locally elevated axial stresses in the vicinity of notches and holes will promote a splitting of the 0° layers and this will be exacerbated by the transverse tension and in-plane shear created by the discontinuity. Also noteworthy is the fact that such a reasonable agreement with the experimental data was attained with a two-dimensional finite-element modelling technique. One presumes that the three-dimensional stress state existing in the vicinity of notches and specimen edges results in a condition wherein the out-of-plane stress components have a small effect relative to the in-plane splitting mechanism, at least for the laminate configurations studied.

In other research conducted at Cambridge, Soutis and Fleck¹¹ studied compression failure and damage mechanisms in PMC laminates with and without holes. They demonstrated that microbuckling of fibres in the 0° layers was the dominant failure mechanism based on both theory and experimental observations including x-ray evaluations. Using a fracture toughness modelling technique, a quantitative and qualitative correlation was successfully obtained. Some compression fatigue testing was also conducted and for laminates with holes and notches indicated the development of a similar type of splitting and delamination damage mechanism to that found

with the static tension and fatigue testing of notched laminates.^{9,12} A threshold value of 85% of the notched static compression failure load was found for compression fatigue. For load levels below this threshold, there appeared to be no strong fatigue effects. Here again though, only a limited laminate configuration was studied, that is [$\pm 45^\circ, 0^\circ$], and it is of interest to compare the similarity of the initial loaded stress state for compression on this laminate with that experienced by the [$90^\circ, 0^\circ$] laminate under tensile load. Note that both the residual-stress state and the compression load will develop transverse tensile stresses in the 0° layers because of CTE and Poisson ratio mismatches, respectively, between the $\pm 45^\circ$ and 0° layers.

Review of certification methodologies

Certification procedures for composite structures generally include static strength, fatigue/durability and damage tolerance, all of which rely on a comprehensive appreciation of failure modes, the effect of variability, environment and discontinuities caused by notches, holes with or without fasteners, and damage induced by impact, machining or assembly phenomena. The current state of the art lacks a definitive approach for certifying or qualifying composite structures and an absence of a consensus by the various agencies, civilian or military.

A basic element of any certification or qualification procedure is design development/verification testing which assesses and validates the design of critical hardware features. For composite structures this development testing effort is a particularly crucial part of the certification because of the sensitivity of laminated composites to out-of-plane loading and the consequent multiplicity of potential failure modes. Recently, the process has been termed the 'building block approach' (Ref. 12) and is initiated during the design and analysis phase wherein critical areas of the structure are selected for test verification. The critical features of the strength are therefore isolated in the form of small test articles of progressively increasing complexity. The effect of environment on these localized regions or 'hot spots' are also assessed using these economical subscale test articles. The nature of design development/verification testing is illustrated in Fig. 3 for typical aircraft structural hardware. Obviously, the process of certification poses especially challenging problems in the case of structural hardware that contain design details that are susceptible to significant interlaminar or out-of-plane stresses such as the details illustrated in Fig. 2. All too frequently, the effect of such local details are identified very late in the design cycle and this experience contributes in large part to the fading of early optimism for new materials. Furthermore, the structural analysis performed has rarely been made in sufficient detail to evaluate adequately the effect of these interlaminar stresses on potential failure modes and margins of safety. Being influenced by matrix properties with a strong dependence on processing conditions and the environment, they are also susceptible to a large statistical scatter and to cyclic loading effects. Non-destructive evaluation of these regions can also prove difficult with respect to the detection and evaluation of defects.

Three candidate certification approaches are now considered with a view to defining technological gaps:

- 1) damage tolerance,
- 2) safe life/reliability,
- 3) wearout model.

Damage tolerance methodology

The damage tolerance philosophy assumes that the largest undetectable flaw exists at the most critical location in the structure and that the structural integrity is maintained throughout the flaw growth until detected by periodic inspection.¹³

In this approach the damage tolerance capability covering both the flaw growth potential and the residual strength is verified by both analysis and test. Analyses would assume the presence of flaw damage placed at the most unfavourable location and orientation with respect to applied loads and material properties. The assessment of each component should include areas of high strain, strain concentrations, a minimum margin of safety details, a major load path, damage-prone areas, and special inspection areas. The structure selected as critical by this review should be considered for inclusion in the experimental and test validation of the damage tolerance substantiation procedures. Those structural areas identified as critical after the analytical and experimental screening should form the basis for the subcomponent and full-scale component validation test program. Test data on the coupon, element, detail subcomponent, and full-scale component level, whichever is applicable, should be developed or be available to:

- 1) verify the capability of the analysis procedure to predict damage growth/no growth, and residual strength,
- 2) determine the effects of environmental factors;
- 3) determine the effects of repeated loads.

Flaws and damage will be assumed to exist initially in the structure as a result of the manufacturing process or to occur at the most adverse time after entry into service.

A decision to employ proof testing must take the following factors into consideration.

- (A) The loading that is applied must accurately simulate the peak stresses and stress distributions in the area being evaluated.
- (B) The effect of the proof loading on other areas of the structure must be thoroughly evaluated.
- (C) Local effects must be taken into account in determining the maximum possible initial flaw/damage size after testing and in determining the subsequent flaw/damage growth.

The most probable life-limiting failure experienced in composite structure, and particularly in non-planar structures where interlaminar stresses are present, is delamination growth. Potential initiation sites are free edges, bolt holes, and ply terminations (Fig. 2) in addition to existing manufacturing defects and subsequent impact damage. Hence, an analysis technique for the evaluation of growth/no growth of delaminations is an essential tool for the evaluation of the damage tolerance of composite structures. A numerical method is available through the use of finite-element analysis and the crack closure integral technique from fracture mechanics.¹⁴ Prerequisites for an evaluation are:

- 1) a structural analysis made in sufficient detail to indicate the locations where the critical interlaminar stresses exist,
- 2) experimentally based critical interlaminar strain energy release rates G_{II} , G_{III} , and a subcritical growth law, that is da/dN against ΔG for each mode, and
- 3) a mixed mode I/mode II fracture criteria.

The application of the damage tolerance methodology to

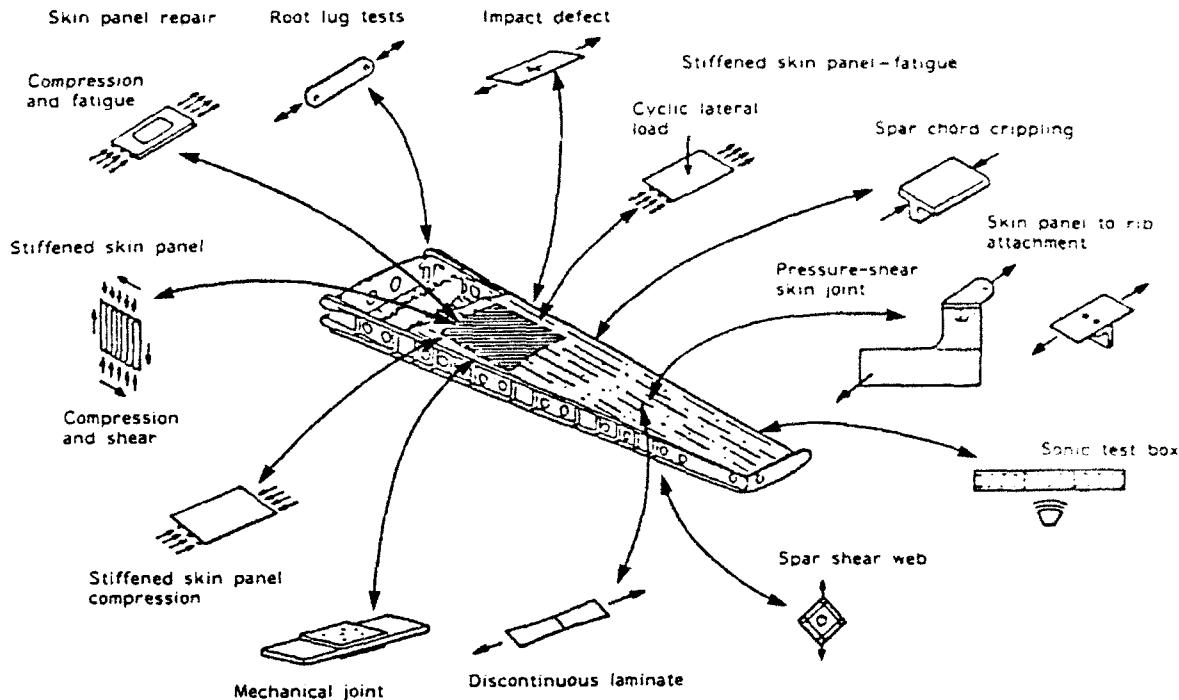


Fig. 3 Building block approach

the F-16 production fleet management program is described in Ref. 15. The test specimens used to generate the required mode-I and mode-II fracture toughness parameters are also described. The application of this approach requires a significant analysis and test effort to evaluate 'hot spots' within the structure and to generate the necessary fracture toughness data. The delamination growth assessment also requires a considerable 3D finite-element modelling and analysis effort. In addition, no reliable mixed-mode fracture criteria has been reported. Hence, this approach is not considered sufficiently mature to warrant a recommendation for a general application to the certification of developmental composite hardware.

Safe life/reliability methodology

Statistically based certification methodologies, as exemplified by Ref. 17, provide a means for determining the strength, life, and reliability of composite structures. Such methods rely on the correct choice of population models and the generation of a sufficient behavioural database. Of the available models, the most commonly accepted for both static and fatigue testing is the two-parameter Weibull distribution. It is attractive for a number of reasons:

- 1) its simple functional form is easily manipulated;
- 2) censoring and pooling techniques are available;
- 3) statistical significance tests have been verified.

The cumulative probability of the survival function is given by

$$P_S(x) = \exp\{(-x/\beta)^{\alpha_S}\} \quad (7)$$

where α_S is the shape parameter and β is the scale parameter.

For composite materials α and β are typically determined using the maximum-likelihood method. In addition, the availability of pooling techniques is especially useful in

composite structure test programs where tests conducted in different environments may be combined. Statistical significance tests are used in these cases to check data sets for similarity.

The following paragraphs present a review of the statistical certification method of Ref. 17. The development tests required to generate the behavioural database are outlined, followed by a discussion of the specific requirements for static strength and fatigue life testing. Special attention is given to the effect that matrix and fibre-dominated failure modes have on test requirements.

A key to the successful application of a statistical certification methodology is the generation of a sufficiently complete database. The tests must range from the level of coupons and elements to full-scale test articles in a 'building block' approach. Additionally, the test program must examine the effects of the operating environment (temperature, moisture, etc) on static and fatigue behaviour. The coupon and subelement tests are used to establish the variability of the material properties. Although they typically focus on the in-plane behaviour it is also important to include the transverse properties. This is especially important in the case of research and development programs. The resulting data can be pooled as required and estimates of the Weibull parameters made.

Thus, the level and scatter of the possible failure modes can be established. The transverse data are characterized by the highest degree of scatter. Element and subcomponent tests can be used to identify the structural failure modes. They may also be used to detect the presence of competing failure modes. Higher level tests, such as tests of components, can be used to investigate the variability of the structural response resulting from fabrication techniques. The resulting database should describe, to the desired level of confidence, the failure mode, the data scatter, and the response variability of a composite structure. This data along with full-scale test articles can be used in the argument to justify certification.

Out-of-plane failure modes can complicate generation of the database. Well proven and reliable transverse test methods are few. The typically high data scatter makes higher numbers of tests desirable. Also, the increased environmental sensitivity in the thickness direction can cause failure mode changes, negating the ability to pool data and possibly resulting in competing failure modes. Thus, a design whose structural capability is limited by transverse strength can lead to increased testing requirements and certification difficulties.

The static strength of a composite structure is typically demonstrated by a test to design the ultimate load (DUL), which is 1.5 times the maximum operating load; that is the design limit load (DLL). Figure 4 shows the reliability achieved for a single static ultimate test to 150% of the DLL for values of the static strength shape parameter from 0 to 25. For fibre-dominated failure with α_s values near 20, such a test would demonstrate an A-basis. However, for matrix-dominated failure modes, with ranging from five to ten, a test to 150% of the DLL would not demonstrate the A-basis. In fact, for values of α_s below seven, reliability in the B-basis could not be demonstrated. Two options are available to increase the demonstrated reliability: (1) increase the number of test specimens, or (2) increase the load level. The most effective choice is to increase the load level beyond 150% of the DLL, whereas increasing the number of test specimens yields little benefit and is expensive.

The two most applicable methods of statistical certification approaches for fatigue are the life factor (also known as the scatter factor) and the load enhancement factor. The life factor approach relies on knowledge of the fatigue life scatter factor from the development test program and a full-scale test or tests. The factor gives the number of lives that must be demonstrated in tests to yield a given level of reliability at the end of one life.

A plot of life factor N_F against the fatigue life shape parameter α_L is given in Fig. 5 for a typical scenario. A single full-scale test to demonstrate the reliability of the B basis ($p = 0.90$, $\gamma = 0.95$) at the end of one life is to be conducted. The curve shows that as the shape parameter approaches 1.0, the number of lives rapidly becomes excessive. Such is the

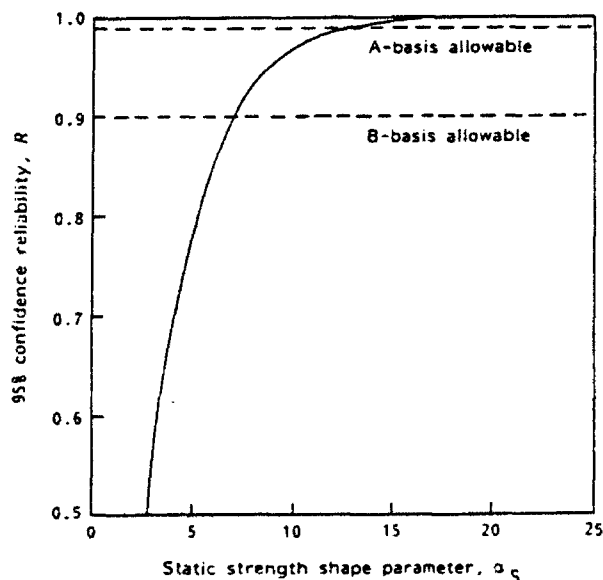


Fig. 4 Plot of the 95% confidence reliability against the static strength shape parameter for a single full-scale static test to 150% of the design limit load

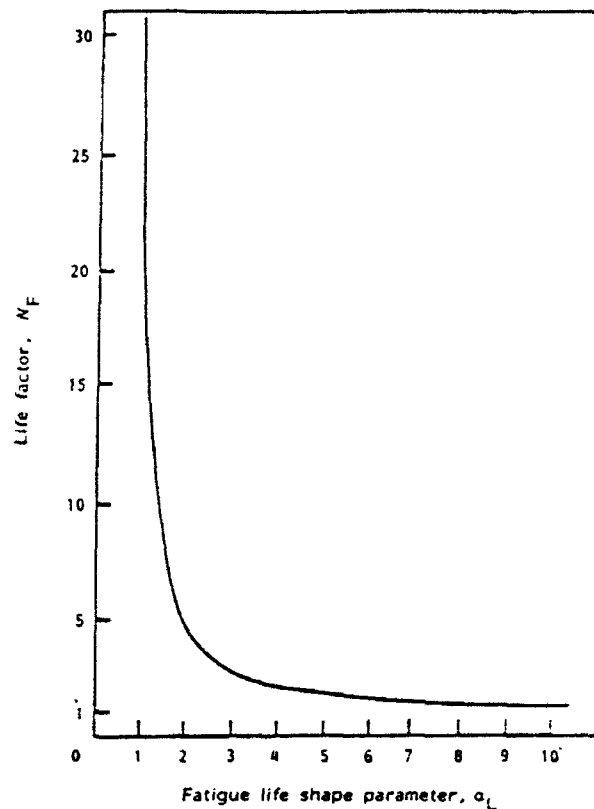


Fig. 5 Plot of the life factor required to demonstrate the reliability of the B-basis results at the end of one life against the fatigue life shape parameter using a single full-scale test article

case of in-plane fatigue failure ($\alpha_L = 1.25$). Although few data for transverse fatigue are available, other than perhaps for bonded parts, it is reasonable to assume that the value of the shape parameter will be the same or less. Hence, it is apparent that the life factor approach is not acceptable for the certification of composites, especially where out-of-plane failure modes are dominant.

An alternate approach to life certification is the load enhancement factor, wherein the loads are increased during the fatigue test to demonstrate the desired level of reliability. Figure 6 illustrates the effect of the fatigue life shape parameter α_L and the residual-strength shape parameter α_R on the load enhancement factor F required to demonstrate B-basis reliability for one life using a single full-scale fatigue test to one lifetime. It is obvious that the required factor does not change significantly for fatigue life shape parameters in the range of five to ten. However, as the shape parameter approaches 1.0, as is the case for composites, the required load enhancement factor increases noticeably, especially for small values of the residual-strength shape parameter. This curve illustrates well the potential problems that may arise from dominant out-of-plane failure modes. Such failure modes tend to have low values of α_L (near 1.0) and also low values of α_R (in the range from 5.0 to 10.0). These values would make the required load enhancement factors prohibitively large. It is evident that for failure modes that exhibit a high degree of static and fatigue scatter, the life factor and load enhancement factor approaches can result in impossible test requirements. A combined approach can be achieved through the manipulation of the functional expressions. The resulting

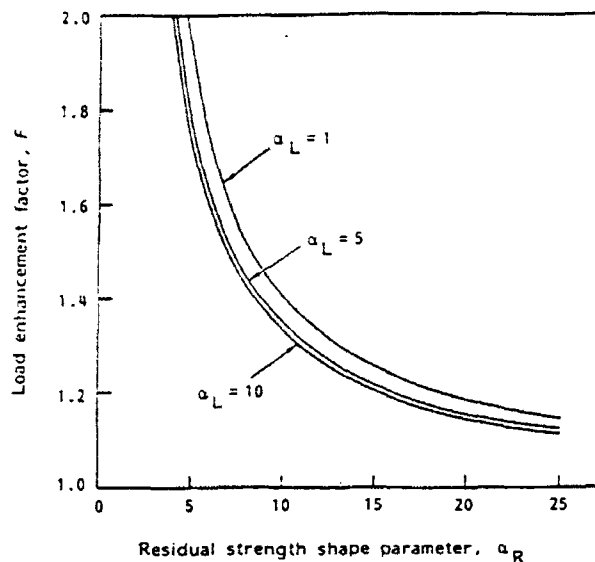


Fig. 6 Plot of the load enhancement factor required to demonstrate the reliability of the B-basis results at the end of one life against the residual strength shape parameter for three values of fatigue life shape parameter α_L using a single fatigue test to one lifetime

method allows some latitude in balancing the test duration and the load enhancement factor to demonstrate a desired level of reliability.

Figure 7 gives the curves of load enhancement factor against life factor for the cases of fibre- and matrix-dominated failure. Typical values for the fatigue life and residual strength shape parameter were employed. The curves show the possible combinations of life factor (or test duration) and load enhancement factor to demonstrate the B-basis reliability at the end of one lifetime using a single full-scale fatigue test article. The curve for fibre-dominated failure modes exhibits quite reasonable values of life factor and load enhancement factor. For test durations ranging from one to five lifetimes, the load enhancement factor ranges from 1.18 down to 1.06.

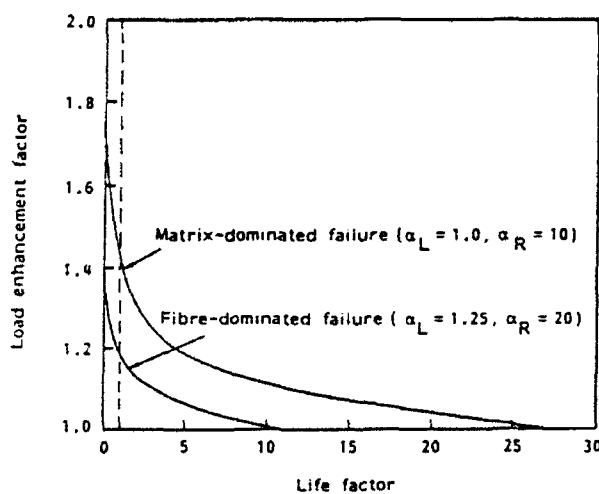


Fig. 7 Plot of possible combinations of load enhancement factor and life factor necessary to demonstrate the reliability of the B-basis results at the end of one lifetime using a single full-scale test article for matrix- and fibre-dominated failure modes

However, the test requirements for matrix-dominated failure are more severe. Over the range of life factor from one to five the load enhancement factor ranges from 1.4 down to 1.19. An environmental knockdown factor would further complicate the test of a matrix-dominated failure. Such a factor must be combined with the load enhancement factor to yield the required test load level. As is well known in composites, the adverse effects of environment on matrix properties is much more severe than on fibre-dominated properties and the resulting factor may be significant.

Further illustration of the problems induced by matrix-dominated failure is possible by assuming a limit exists on the load enhancement factor. Such limits may exist because of failure mode transitions at higher load levels. For instance, assuming a load enhancement factor of 1.2 is the maximum allowable value, it is obvious that a successful one-lifetime test for a fibre-dominated failure will demonstrate the reliability better than a B-basis test. For matrix-dominated failure, the same reliability would require a test duration of about 4.5 lives.

Two key aspects to the statistical certification methodology are the generation of an adequate database and the proper execution of a full-scale demonstration test. The development test program must be conducted in a 'building block' approach that produces confident knowledge of the material shape parameters, environmental effects, failure modes and response variability. Perhaps the most important result should be the ability to predict the failure mode and know the scatter associated with it. Structures that exhibit transverse failures, which can result in competing modes and a high degree of scatter, may render the application of this fatigue methodology impractical. This result has been illustrated by the effect of shape parameters on both the static and fatigue test requirements. The requirements clearly show that a well designed structure that exhibits fibre-dominated failure modes will be more easily certified than one constrained by matrix-dominated effects.

Wearout methodology

The wearout methodology was developed in the early 1970s and is comprehensively summarized in Ref. 19 by Halpin, Jerina and Johnson. This methodology was previously used in the certification of the following composite aircraft components:

- 1) the A-7 outer wing,
- 2) the F-16 empennage,
- 3) the B-1A horizontal tail.

In essence, the wearout approach recognizes the probability of progressive structural deterioration of a composite structure. The approach utilizes the development test data on the static strength and the residual strength, after a specified period of use, in conjunction with proof testing of all flight hardware items to characterize this deterioration and protect the structure against premature failures. It has become evident that the residual stiffness is an indicator of the extent of the structural deterioration and can be an important performance parameter with regard to the natural frequencies of oscillation of the aerodynamic surfaces. Thus, in some instances, it may be prudent to incorporate a residual-stiffness requirement in an adopted methodology to evaluate the tolerance of the structure to component stiffness degradation.

The difficulties in the implementation of the methodology include the determination of the critical load conditions to be applied for static and residual strength and stiffness testing

and for the proof load specification. Similar difficulties would arise in the case of all candidate methodologies considered here and indeed emphasize the importance of a representative structural analysis. However, the advantage of the wearout approach for advanced composite hardware development projects resides in the ability to assign 'gates' for safe flight testing as the flight envelope is progressively expanded.

Proof test philosophy

The truncation in static and residual strength, and life capacity, resulting from proof testing is intended to develop confidence that the structure is unlikely to fail within a specified time under a specified usage. Most of the essential features of the wearout process are illustrated in Fig. 8. Mathematically, the structural deterioration can be represented by the equation from Ref. 19:

$$F(t)^{2(r-1)} = F(0)^{2(r-1)} - (r-1)A_*(F_{max})^{2r}[t - t(0)] \quad (8)$$

where $F(t)$ is the residual strength after time ' t ', $F(0)$ is the initial static strength, F_{max} is the maximum fatigue spectrum stress (failure occurs when $F(t) = F_{max}$) and A_* is a constant.

The key wearout parameter ' r ' is defined as the slope of the da/dN curve or may be derived from the $S-N$ fatigue curve for the failure mode in question. Based on this model, the proof load level required to protect the structure for the desired operating period t_{op} can be deduced as follows:

Setting $F(0) = F_{PL}$, and using $F(t) = F(xx)$, we obtain:

$$F_{PL}^{2(r-1)} = F(xx)^{2(r-1)} + R t_{op} \quad (9)$$

where

$$R = (r-1)A_*(F_{max})^{2r} \quad (10)$$

and is termed the 'damage accumulation rate' or 'wearout rate'.

A minimum of two tests is required to determine the wearout rate R :

- 1) a static test to failure,
- 2) a fatigue test followed by a residual strength test to failure.

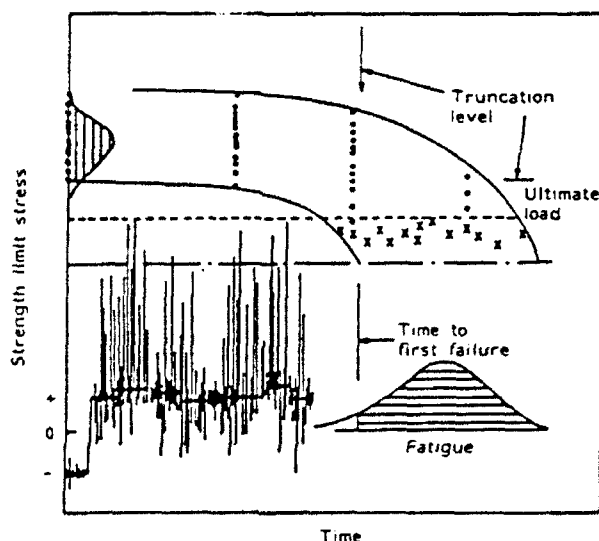


Fig. 8 Essential features of the 'wearout model' relating static failure, load history and fatigue failure

A residual stiffness test should also be incorporated in (2) for the reasons noted earlier.

It is apparent from the above discussion that a reliable estimation of the damage accumulation rate R is the key to the appropriate application of the wearout methodology. Since R depends on the parameter r , data pertaining to the detailed configurations and failure modes of the hardware components in question must be obtained. Now, it has been mentioned previously that a distinct likelihood of matrix-controlled failure modes exists in complex developmental composite hardware and we therefore consider that the failure modes encountered in bonded joints under fatigue loading should exhibit similar characteristics to that of the delamination of advanced composite structures. Understandably, then, a wearout model database exists and other data are available that may be recast into wearout model parameters. We shall return to this subject in the experimental survey analysis section.

Implementation of the wearout methodology

The application of the 'wearout' philosophy to developmental composite hardware projects seems to be feasible. The key tasks necessary to implement the methodology are depicted in Fig. 8 and can be summarized as follows.

- 1) Prescribe a best estimate of the usage spectrum, including the duration ' t_{op} ', or various multiples thereof, to represent phases of the flight test program.
- 2) Based on an adequate structural analysis of the critical loading conditions specify a static strength requirement and conduct a static strength test to failure for the condition deemed to be most critical.
- 3) Incorporating damage tolerance criteria supported by non-destructive inspection (NDI), conduct a fatigue test based on the usage spectrum.
- 4) Conduct a residual strength, and stiffness, test to failure of the fatigued component, drawing again on the static strength requirement defined above.
- 5) Estimate an 'damage accumulation' rate through a series of tests of critical subelements (identified by the structural evaluation) and/or coupons. These tests should provide estimates of the wearout parameter ' r '.
- 6) Conduct a proof test of each flight hardware component to a level deduced from items 1 to 5.

Experimental survey/analysis

In our previous discussion on wearout methodology, we referred to the existence of a wearout model database that can be extracted from the large body of literature on PMCs. These data appear in a directly relatable format¹⁹ or can be recast in a common form from recent sources such as Poursartip *et al.*⁶ or from contemporary composite fracture mechanics parameters used to define damage or damage growth, such as delamination.^{15,16} By observing that the matrix-dominated failure mechanisms of delamination and compression represent phenomena that closely resemble the failure mechanisms exhibited by adhesively bonded joints^{20,21} we may draw on an even larger database.

Review of theoretical foundations of wearout concepts

Before studying the overall database it is first appropriate to review the physical and theoretical basis for the wearout concepts. As previously stated the probability of progressive

structural deterioration of a composite structure is recognized and forms the essential ingredient of the wearout philosophy.

By combining several basic assumptions regarding the behaviour of a composite structure under load with basic Weibull statistics the 'kinetic fracture model' can be derived. This model serves to assist us in predicting the 'fatigue wearout behaviour' of composite structures.

The first assumption concerns the growth of an inherent or real material flaw, da/dt , which is deemed to be proportional to the strain energy release rate G of the material system raised to some power r , where r is to be determined experimentally; thus

$$da/dt \propto G^r \quad (11)$$

where a is the flaw length.

As the cyclic load, $F(t)$, is applied to the flawed body, the internally stored strain energy will occasionally exceed the critical level required to overcome the local resistance of the material to flaw growth, or damage accumulation, and flaw growth will occur. Then, according to the basic theory of Griffith the strain energy release rate for the material is proportional to the stored strain energy U and the flaw length a .

Then, since $G \propto aU$ we obtain

$$da/dt \propto U^r a^r \quad (12)$$

We note that the foregoing applies to the ideal situation of a cracked solid containing a crack that extends in a self-similar manner, typically a mode-I condition. Clearly, the more complex conditions existing in a highly orthotropic, heterogeneous body may give rise to different forms of the relationship.

However, for our present purpose we shall retain the above and also assume that the spectrum load levels and frequencies are selected based on a given aircraft spectrum loading. The same random sequence is taken to be applicable to each specimen.

The only variable regarding the applied load history then, is the spectrum intensity parameter, A_1 , which relates to the reference aircraft spectrum, $F_{ref}(t)$, and the experimentally applied load history, $F(t)$. Hence

$$F(t) = A_1 F_{ref}(t) \quad (13)$$

where A_1 is a constant. By substituting Equation (13) into Equation (12):

$$da/dt \propto A_1^r F_{ref}^r(t) a^r \quad (14)$$

or

$$da/dt = A_2 A_1^r F_{ref}^r(t) a^r \quad (15)$$

where A_2 represents a constant that accounts for the constants of proportionality and the prior history.

By integrating Equation (15) from some initial time t_0 to some later time t , we can keep track of the flaw length $a(t)$, where $a(t_0) = a_0$. Thus:

$$\int_{a_0}^a a^{-r} da = \int_{t_0}^t A_2 A_1^r F_{ref}^r(t) dt = A_3 A_1^r \int_{t_0}^t dt$$

since $F_{ref}(t)$ is assumed to be a stationary random process. For a stationary random process the amount of crack growth or damage accumulation is not a function of the details of the load history. Damage accumulation is merely proportional to the exposure time Δt . Thus, $F_{ref}(t)$ can be treated as a constant for the purposes of integration and can be absorbed

into A_3 . The spectrum intensity parameter, A_1 , must and does appear explicitly, however, to account for variations in spectrum intensity.

Completing the integration:

$$\frac{a^{1-r}}{1-r} \Big|_{a_0}^a = A_3 A_1^r \frac{t-t_0}{r}$$

Therefore

$$a(t)^{-(r-1)} - a(t_0)^{-(r-1)} = -(r-1) A_3 A_1^r (t-t_0) \quad (16)$$

Finally, assuming that linear fracture mechanics theory applies to composite structures we write

$$K = \sigma_i \sqrt{\pi a}$$

and

$$a = (K^2/\pi) \sigma_i^{-2} \quad (17)$$

Substituting Equation (17) into Equation (16):

$$\sigma_{i(t)}^{2(r-1)} - \sigma_{i(t_0)}^{2(r-1)} = -(r-1) A_3 A_1^r (t-t_0) \quad (18)$$

Note here that the constants K and π have been absorbed into the constant A_3 . Equation (18) describes mathematically the strength of the i th specimen, $\sigma_i(t)$, as a function of time and its initial strength at time t_0 , σ_{i0} . The right-hand side of Equation (18) represents the wearout or strength degradation that occurs during the time interval $t_0 \rightarrow t$. The flaw growth exponent r and the history constant A_3 must all be determined from the experimental data.

To describe how the distribution of strengths for a number of tests changes with time we consider a series of specimens that has the distribution of static strengths $\sigma(0)$ at time $t = 0$, see Fig. 9(a). Assuming that each specimen is subjected to a fatigue loading described as $A_1 F_{ref}(t)$ over a time duration t the change in the above distribution may be obtained as a function of time. The resulting time-dependent strength trajectory of specimen i is also illustrated in Fig. 9(a). The equation of the residual-strength wearout trajectory $\sigma_{i0} \rightarrow \sigma_{in}$ is given by the equation:

$$\sigma_i(t) = [\sigma_{i0}^{2(r-1)} - (r-1) A_3 A_1^r (t-t_0)]^{\frac{1}{2(r-1)}} \quad (19)$$

Note that whilst the strength trajectories of each of the i specimens ($1 \leq i \leq n$) are not necessarily parallel, the relative position of their static strengths does not change. As a result, the percentage of specimens with static strengths greater than that of the i th specimen at $t = 0$, σ_{i0} , is the same as the percentage of specimens with static strengths greater than that of the i th specimen at time t , σ_{in} , that is the shaded regions shown in Fig. 9(a) both have the same area.

If we now consider the prediction of the percentage of specimens, at time t , which have a static strength greater than some arbitrary value σ^1 , given the distribution of static strengths at time $t = 0$ in terms of the Weibull parameters, α_0 , β_0 , refer to Fig. 9(b).

Recall that the percentage of specimens having static strengths greater than σ^1 at time t_0 is given by

$$P[\sigma(0) > \sigma^1] = \exp(-\sigma^1/\beta_0)^{\alpha_0} \quad (20)$$

Since the relative position of the specimens in the two distributions does not change in going from $\sigma(0)$ to $\sigma(t)$, it follows that

$$P[\sigma(t) > \sigma^1] = P[\sigma(0) > \sigma^1] \quad (21)$$

by tracing the path of σ backwards in time. Then, by combining Equations (20) and (21):

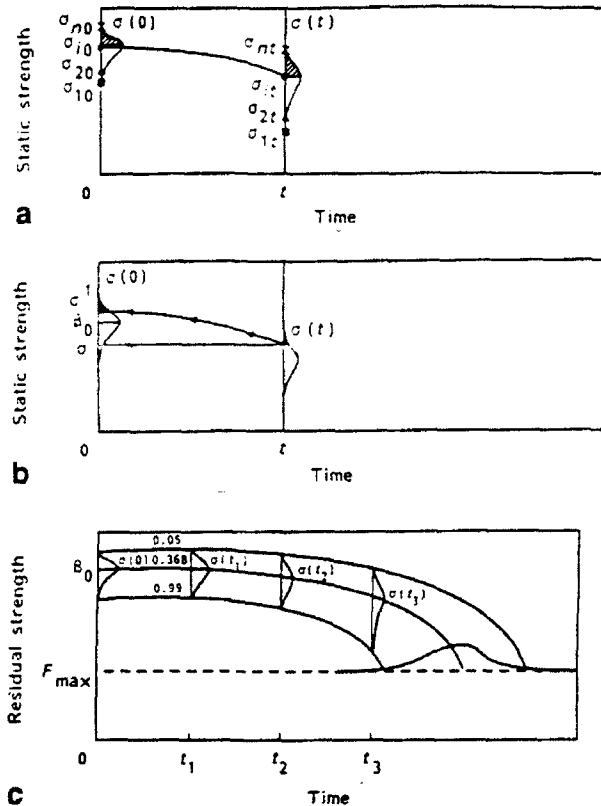


Fig. 9 Features of residual strength and life comprising the wearout model: (a), residual strength as a function of fatigue exposure; (b), trace of residual strength of specimen σ^1 back to time $t = 0$; (c), overall wearout model

$$P[\sigma(t) > \sigma^1] = \exp(-\sigma/\beta_0)^{\alpha_0} \quad (22)$$

The trajectory of the specimen having a static strength equal to σ at time $t = 0$ and strength σ^1 at time t can be expressed as

$$(\sigma^1)^{2(r-1)} - \sigma^{2(r-1)} = -(r-1) A_1^r A_4 (t-t_0) \quad (23)$$

from Equation (18). Rearranging this we obtain that

$$\sigma = [(\sigma^1)^{2(r-1)} + (r-1) A_1^r A_4 t]^{1/2(r-1)} \quad (24)$$

Therefore, by combining Equations (22) and (24) the percentage of specimens that have a static strength $\sigma(t) > \sigma^1$ can be expressed as

$$P[\sigma(t) > \sigma^1] = \exp\left(-\frac{[(\sigma^1)^{2(r-1)} + (r-1) A_1^r A_4 t]^{1/2(r-1)}}{\beta_0}\right)^{\alpha_0} \quad (25)$$

or

$$P[\sigma(t) > \sigma^1] = \exp\left(-\frac{[(\sigma^1)^{2(r-1)} + (r-1) A_1^r A_4 t]^{1/2(r-1)}}{\beta_0^{2(r-1)}}\right)^{\alpha_0 2(r-1)} \quad (26)$$

$P[\sigma(t) > \sigma^1]$ represents the probability of survival for an applied load of magnitude σ^1 at time t . Based on Equation (26) a complete family of trajectories and residual-strength distributions can be generated for any time t . A series of such distributions for times $t = 0, t_1, t_2$ and t_3 are illustrated in Fig. 9(c).

To determine the time required at a given spectrum intensity A_1 , before the probability of survival is reduced to some value P we can assume a value for the latter and solve for t_R from Equation (26). Hence,

$$\ln P = -\left[\frac{(\sigma^1)^{2(r-1)} + (r-1) A_1^r A_4 t_R}{\beta_0^{2(r-1)}}\right]^{\alpha_0 2(r-1)}$$

$$[-\ln P]^{1/2(r-1)} \beta_0^{2(r-1)} = (\sigma^1)^{2(r-1)} + (r-1) A_1^r A_4 t_R \quad (27)$$

and

$$t_R = \frac{\beta_0^{2(r-1)} (-\ln P)^{1/2(r-1)} \alpha_0 - (\sigma^1)^{2(r-1)}}{A_1^r A_4 (r-1)} \quad (28)$$

Now the distribution of fatigue failures can be represented on the same graph as the static residual strengths, along a horizontal line drawn at the maximum load level produced during the fatigue spectrum F_{max} (see Fig. 9(c)). As the residual strength of a specimen falls below the F_{max} level, failure is likely to occur at any time, so that all trajectories end at this point.

Application of the wearout model requires a minimum of four sets of statistical data:

- data describing the static strength distributions at both time $t = 0$ and at some later time t ,
- two sets of fatigue failure data,

which would be sufficient to define the constants α_0 , β_0 , r and A_4 that appear in Equations (26) and (28). The spectrum intensity parameter, A_1 , would be held constant for the two residual-strength tests and one of the fatigue tests. The other fatigue test would be run at two other intensity levels, resulting in a σ against N plot, from which the exponent could be calculated. The method of solution for calculating these various constants is an iterative procedure for which many standard routines are available to facilitate rapid data reduction. Such routines are capable of automatically generating diagrams similar to that illustrated in Fig. 9(c).

Other relationships have been proposed¹⁹ relating the initial static strength shape parameter α_0 and the fatigue life shape parameter α_f . It is of particular interest to observe that these shape parameters, which can also be applied to the study of creep phenomena, are shown to be a function of the flaw size exponent alone.

$$\alpha_0 = 2r + 1 \quad (29a)$$

$$\alpha_f = \alpha_0 / 2(r-1) \quad (29b)$$

However, the relationship that will be of specific interest to this subject is the experimental survey result from the postulate¹⁹ that a material may lose strength at a uniform rate with respect to a logarithmic (or number of cycles) scale.

Thus, from

$$t F_\gamma^\gamma = B \text{ or } N F_\gamma^\gamma = B_1 \quad (30)$$

where $\gamma = -1/2r$ defines the slope of the fatigue curve.

Review of composites and bonded joint data

Various expressions have been proposed for the application to fatigue degradation and damage accumulation predictions of composites. In the previous section we reviewed the wearout approach that is based on the relationship:

$$\partial \sigma / \partial t = A_\omega G^* \quad (31)$$

Subsequently, assumptions were introduced regarding the relationship between the strain energy release rate G and the flaw size a in order to derive the basic wearout equation.

The fracture mechanics approaches that appear to have been introduced initially to address the structural integrity and reliability of adhesively bonded joints are founded on a similar relationship:

$$da/dN = B(\Delta K)^{2r} = A_F(\Delta G)^r \quad (32)$$

where ΔK and ΔG are the cyclic range of stress intensity and strain energy release rate, respectively.

More recently the damage-based fatigue model devised by Poursartip *et al.*⁴⁻⁶ has been applied to composite laminates resulting in the expression:

$$dD/dN = A_D(\Delta\sigma)^{2r} = A_{DF}(\Delta G)^r \quad (33)$$

where D the extent of the accumulated damage is clearly related to the flaw size (length) represented by Equations (31) and (32). $\Delta\sigma$ is the stress range that can be related to stress intensity and hence strain energy release rate via the familiar equation for brittle fracture:

$$\sigma_c = \sqrt{\frac{EG_c}{\pi a}} = \frac{K_c}{\sqrt{\pi a}} \quad (34)$$

To assist our efforts to draw on the data from each of the above approaches we have used a common symbol r for the flaw (or damage) growth rate exponent. Consequently, in view of the relationship of Equation (34) the expression for the damage growth rate dD/dN has been modified in Equation (33).

The comparisons drawn from a very broad range of literature are provided in Table 1.

Final remarks

The subject of damage sources and damage accumulation in composite systems has been discussed herein and various approaches to the certification of composite structures and

the associated fatigue life prediction techniques have been reviewed.

Although fundamental differences between the structural behaviour of PMCs and CMCs exist the prospects of some similar approaches to damage state prediction are considered to be worthy of future evaluation. To this end, the damage mechanics approaches developed at Cambridge by Beaumont, Ashby, and co-workers, appear to be potentially attractive approaches for CMC damage accumulation and fatigue life prediction.

Returning to the subject of PMCs, the general overlap between damage mechanics and fracture mechanics suggests that interrelationships exist wherein the microdamage assessment of discrete interlaminar defects might be performed. Indeed such strategies may also be appropriate for CMCs. One specific area that is of considerable interest to the design community is associated with the finite-width effect that was very briefly addressed by Poursartip *et al.*⁵ A systematic scientific evaluation of this effect is strongly recommended in future considerations.

A striking similarity between the flaw or, more precisely, damage growth rate exponents for matrix-dominated mechanisms is evident from the review of experimental surveys and analyses; see Table 1. In most of the widely ranging damage phenomena interlaminar separation represented the generically similar feature for composite delaminations and adhesively bonded attachments between composite and/or metallic adherends. Since, future reductions in composite manufacturing costs will depend on the reliability of cocured subassemblies, the structural integrity of this category of interfacial damage mechanism will become a critical issue that is well worthy of further research. This research area should be extended to the design features that are commonplace in composite hardware such as tapers and transitions^{23,24} and local curvatures as well as through-thickness penetrations, discontinuities and bolted connections.

Finally, there is also merit in re-evaluating the utility of the wearout model in light of recent developments and where the likelihood of a change of failure mode exists owing to

Table 1. Comparison between damage growth rate exponents from various sources and configurations

Author, reference	Configuration	Damage growth rate exponent r
Halpin <i>et al.</i> ¹⁹	Matrix-dominated failure, ± 450 boron/epoxy	5.05
Waddoups ²⁵	Graphite/epoxy-to-titanium double-lap bonded joint	4.70
Poursartip <i>et al.</i> ⁴⁻⁶	Carbon/epoxy [$\pm 45^\circ/90^\circ/0^\circ$] _s laminates, cyclic tension	6.3-6.6*
Johnson and Mall ²²	Graphite/epoxy bonded lap joints	4.34-4.55
Murri <i>et al.</i> ^{23,24}	Glass/epoxy and graphite epoxy tapered laminates, cyclic tension	5.0-5.6*
Brussat <i>et al.</i> ²⁶	Adhesively bonded joints with metallic adherends	5.03-5.57
Knauss ²⁷	Adhesively bonded joints with metallic/composite adherends	5.75
O'Brien ¹⁶	Glass/epoxy edge delamination specimen, [$\pm 45^\circ/0^\circ/90^\circ$] _s	6.24*

*Value determined from $S-N$ curve, based on Equation (30)

load cycling and/or environmental effects. The damage mechanics concepts introduced by the recent Cambridge research efforts may serve to supplement the wearout philosophy by contributing a quantitative prediction capability for degradation (or change) of residual strength owing to cyclic loading.

Acknowledgement

We wish to acknowledge the financial support of the Science and Engineering Research Council that provided the opportunity for Dr Keith T. Kedward to assume a Research Fellowship at Cambridge.

References

1. Lagace, P. A. and Weems, D. B. 'A through-the-thickness strength specimen for composites' *Proc of 2nd ASTM Symp on Test Methods and Design Allowables*, Phoenix, USA, 1986 (American Society for Testing and Materials, 1986).
2. Kachanov, L. M. 'Time to failure under creep conditions' *Ak Nauk SSR Otd Tekh Nauk* 8 (1958) pp 26-31.
3. Sidoroff, F. 'Damage mechanics and its application to composite materials', in Cardon and Verchery, (Eds) *Mechanical Characterisation of Load Bearing Fibre Composite Laminates* (Elsevier, Amsterdam, 1985).
4. Poursartip, A., Ashby, M. F. and Beaumont, P. W. R. 'Damage accumulation during fatigue of composites', *Scr Metall* 16 (1982) pp 601-606.
5. Poursartip, A., Ashby, M. F. and Beaumont, P. W. R. 'The fatigue damage mechanics of a carbon fibre composite laminate: I—development of the model' *Composite Sci Technol* 25 (1986) pp 193-217.
6. Poursartip, A. and Beaumont, P. W. R. 'The fatigue damage mechanics of a carbon fibre composite laminate: II—life prediction' *Composite Sci Technol* 25 (1986) pp 283-299.
7. Waddoups, M. E., Eisenrath, J. R. and Kaminski, B. E. 'Macroscopic fracture mechanics of advanced composite materials' *J Composite Mater* 5 (1971) pp 446-454.
8. Whitney, J. M. and Nuismer, R. J. 'Stress fracture criteria for laminated composites containing stress concentrations' *J Composite Mater* 8 (1974) pp 253-265.
9. Kortschot, M. T. and Beaumont, P. W. R. 'Damage-based notched strength modeling: a summary' *Proc ASTM Conf on Fracture and Fatigue of Composites*, Orlando, USA, 1989 (American Society for Testing and Materials, 1989).
10. Spearing, S. M., Beaumont, P. W. R. and Ashby, M. F. 'Fatigue damage mechanics of notched graphite epoxy laminates' *ibid*.
11. Soutis, C. and Fleck, N. A. 'Static compression failure of carbon-fibre T800/924C composite plate with a single hole' *J Composite Mater* 24 (1989) pp 536-558.
12. Whitehead, R. S. and Deo, R. B. 'A building block approach to design verification testing of primary aircraft structure', *Proc 24th AIAA/ASME/ASCE AHS Structures, Structural Dynamics and Materials Conference*, Lake Tahoe, USA, 1983.
13. MIL-A-PRIME (Proposed) United States Airforce damage tolerance specification for organic matrix composite aircraft structures', in *Damage Tolerance of Composites* AFVAL-TR-87-3030 Vol 1 (USAF July 1988).
14. Rybicki, E. F. and Kanninen, M. F. 'A finite element calculation of stress intensity factors by a modified crack closure integral' *Eng Mech* 9 (1977) pp 931-938.
15. Wilkins, D. J. 'A preliminary damage tolerance methodology for composite structures', *Proc Workshop on Failure Analysis and Mechanisms of Failure of Fibrous Composite Structures*, NASA-L-2278 (NASA, 1982).
16. O'Brien, T. K. 'Towards a damage tolerance philosophy for composite materials and structures' *NASA-TM-100548* (NASA, March 1988).
17. Whitehead, R. S., Kan, H. P., Cordero, R. and Saether, E. S. 'Certification testing methodology for composite structure' *Report No NADC-87042* (October 1986).
18. Sanger, K. B. 'Certification testing methodology for composite structures' *Report No NADC-86132-60* (January 1986).
19. Halpin, J. C., Jerina, K. L. and Johnson, T. A. 'Characterization of composites for the purpose of reliability evaluation' *Analysis of Test Methods for High Modulus Fibers and Composites*, ASTM STP 521 (American Society for Testing and Materials, 1973) pp 5-64.
20. Wolff, R. V. and Lemon, G. H. 'Reliability predictions for adhesive bonds' *AFML-TR-72-121* (March 1972).
21. Berens, A. P. and West, B. S. 'Evaluation of an accelerated characterization technique for reliability assessment of adhesive joints' *Composite Reliability*, ASTM STP 580 (1975) pp 90-101.
22. Johnson, W. S. and Mall, S. 'A fracture mechanics approach for designing adhesively bonded joints' *Delamination and Debonding of Materials*, ASTM STP 876 (American Society for Testing and Materials 1985) p 189.
23. Murri, G. B., O'Brien, T. K. and Salpekar, S. A. 'Tension fatigue of glass/epoxy and graphite/epoxy tapered laminates' *NASA TM 102628* (NASA, April 1990).
24. Murri, G. B., Salpekar, S. A. and O'Brien, T. K. 'Fatigue delamination on set prediction in tapered composite laminates' *NASA TM 101673* (December 1989).
25. Waddoups, M. E. 'Characterization of advanced composite materials for structural design' *Polymer Eng Sci* 15 3 (March 1975).
26. Brussat, T. R., Chiu, S. T. and Mostovoy, S. 'Fracture mechanics for structural adhesive bonds' *AFML-TR-77-163* (October 1977).
27. Knauss, J. F. 'Fatigue life prediction for bonded primary joints' *NASA-CR-159049* (September 1979).

Authors

K. T. Kedward is with the Department of Mechanical Engineering, University of California, Santa Barbara, USA. P. W. R. Beaumont is with the Department of Engineering, University of Cambridge, Cambridge, UK. Received 22 December 1991; accepted 18 March 1992.



The Society shall not be responsible for statements or opinions advanced in papers or in discussion at meetings of the Society or of its Divisions or Sections, or printed in its publications. Discussion is printed only if the paper is published in an ASME Journal. Papers are available from ASME for three months after the meeting.
Printed in USA

W. Jiang

Asst. Professor
Mechanical Engineering Department
Florida International University
Miami, FL 33199

F. A. Leckie

Professor
Department of Mechanical and
Environmental Engineering
University of California
Santa Barbara, CA 93106

A Direct Method for the Shakedown Analysis of Structures Under Sustained and Cyclic Loads

This paper presents a straightforward method for the direct determination of the steady solutions in shakedown analysis. The direct method was first proposed by Zarka et al. This paper simplifies this method by showing that the modified hardening parameter field can be directly found from the yield condition and the incremental residual stress. Thus, only two elastic analyses are required to obtain the shakedown solutions without the need of performing a full-scale analysis. The two-bar structure and the tube problem are solved as examples to show the feasibility and efficiency of this approach.

1 Introduction

The response of structures subjected to cyclic loads and temperatures is often very complicated. The structure may elastically shake down, or it may incur reversed plasticity or ratchetting. Several fundamental questions can be raised; the existence of a steady state is usually of first concern. We then need to know when the shakedown will occur and what the final steady stress-strain state will be. The theoretical investigation of all the possible responses and the evaluation of the life of a comparatively complex structure can be very difficult, even if the creep effect is neglected in a first step analysis. The computer, based on the finite element can help, but the numerical approach often turns out to be very expensive and cannot yield a definite and accurate answer except for a small number of cycles because of accumulated computational error. On the other hand, in practice the design is primarily based on the maximum possible stress and strain attainable under sustained and periodic loads, and thus a large amount of incremental inelastic calculations approaching the steady state is often inevitable. Note that Ainsworth (1977) has proposed a method to determine an upper bound on creep deformation based on the complete steady state, cyclic stress distributions of a similar structure that does not creep. Therefore, for practical purposes and as a way of getting out of the difficulty involved in detailed shakedown analysis for answering all shakedown questions, the transient state of the structure can be regarded as of less importance, and attention can be focused on the final steady solutions.

In 1978, Zarka et al. first proposed a direct method which

permits a straightforward evaluation of the limit state of the structure on the basis of the elastic solution and the first cycle of the elastic-plastic calculation. Zarka's method takes advantage of the fact that, in the case of elastic shakedown, the plastic strain is constant. Whenever reversed plasticity occurs, however, the plastic strain varies with time and Zarka's method becomes complex. This paper presents a simple method for the direct evaluation of the steady solutions for all shakedown cases. The two-bar assembly and the tube problem are solved as examples. The feasibility and the efficiency of the approach are obvious as compared to the conventional incremental method.

This paper concerns only kinematic hardening materials, since for such materials, a steady state can always be reached

2 Problem Formulation

The total strain ϵ is considered to be composed of three parts, the elastic strain ϵ^e , the thermal strain ϵ^T and the plastic strain ϵ^p :

$$\epsilon = \epsilon^e + \epsilon^T + \epsilon^p \quad (1)$$

The elastic strain ϵ^e relates to the current stress σ through an elastic matrix D :

$$\epsilon^e = D\sigma \quad (2)$$

while the plastic strain ϵ^p is assumed to obey the associated plastic flow law:

$$\dot{\epsilon}^p = \lambda \frac{\partial f}{\partial \sigma} \quad (3)$$

where f is the yield function, and λ is an infinitesimal scalar factor. The creep strain is not considered here. An upper bound of the creep deformation can be estimated after the shakedown solutions are obtained using Ainsworth's method, for example.

Suppose that the material considered follows the kinematic hardening rule. The yield condition is then given by a function in the form of

Contributed by the Applied Mechanics Division of THE AMERICAN SOCIETY OF MECHANICAL ENGINEERS for presentation at the 1992 ASME Summer Mechanics and Materials Meeting, Tempe, AZ, Apr. 28-May 1, 1992.

Discussion on this paper should be addressed to the Technical Editor, Prof. Leon M. Keer, The Technological Institute, Northwestern University, Evanston, IL 60208, and will be accepted until four months after final publication of the paper itself in the JOURNAL OF APPLIED MECHANICS. Manuscript received by the ASME Applied Mechanics Division, June 29, 1990; final revision, June 26, 1991.

Paper No. 92-APM-25

Copies of this paper will be available until July 1993.

$$f(\sigma - \alpha) = 0 \quad (4)$$

where α is the back stress, also called the hardening parameter, which indicates the current center of the yield surface. Some differential relations have been proposed for the determination of the rate $\dot{\alpha}$ of the back stress. In this paper, we will use the simplest, but rather extensively used variant

$$\dot{\alpha} = B\dot{\epsilon}^p \quad (5)$$

where B is a constant symmetric positive matrix. We can thus write

$$\dot{\epsilon}^e = B^{-1}\dot{\alpha} \quad (6)$$

To formulate a direct approach, Zarka et al. (1978) separated the stress and strain into two parts:

$$\begin{cases} \sigma = \sigma^e + \rho \\ \epsilon = \epsilon^e + e \end{cases} \quad (7)$$

where (σ^e, ϵ^e) represents the purely elastic solution to the current boundary value problem, and (ρ, e) represents the residual stress and strain. The residual stress should be statically admissible with zero applied forces, and the residual strain should be kinematically admissible with zero applied displacements. Generally, they all vary with time.

Zarka et al. next introduced a modified hardening parameter $\hat{\alpha}$

$$\hat{\alpha} = \alpha - \rho \quad (8)$$

This new tensor has no physical meaning, but with it we can rewrite the yield condition, Eq. (4), as

$$f(\sigma^e - \hat{\alpha}) = 0 \quad (9)$$

and obtain a residual stress-strain relationship

$$e = (B^{-1} + D)\rho + B^{-1}\hat{\alpha} \quad (10)$$

Zarka's method is that, instead of solving a difficult plasticity problem, he tried to find an $\hat{\alpha}$ field such that at any time the yield condition is satisfied. Then the residual solution (ρ, e) can be obtained by solving an elastic problem with homogeneous equilibrium equations and boundary conditions but with nonhomogeneous stress-strain relationships. After that, the actual solution can be found, according to Eq. (7), by superpositions. Thus, the key point of Zarka's method is how to find the $\hat{\alpha}$ field.

In the case of elastic shakedown, the $\hat{\alpha}$ field is constant, that is, it is independent of time. This fact makes Zarka's method rather simple. However, whenever reversed plasticity occurs, the $\hat{\alpha}$ field varies with time and Zarka's method loses its simplicity. Another difficulty is that many $\hat{\alpha}$ fields can be chosen that meet the requirement and there will be considerable differences in the final shakedown solution, depending on the choice of $\hat{\alpha}$ fields. To single out the correct solution, Zarka et al. calculated the first cycle and deduced, through a complex procedure, the right $\hat{\alpha}$ field.

We now present a simple and straightforward method to directly derive the $\hat{\alpha}$ field and then the shakedown solution.

It is known that under periodic loading, the stress state will always shake down due to the kinematic hardening. As a result, when shakedown is reached, the structure considered can be composed of three kinds of regions: S_1 , S_2 , and S_3 , where S_1 is the reversed plasticity zone, S_2 yields only in the heating half cycles, and S_3 yields only in the cooling half cycles (Fig. 1). In the stress space, it means that stresses in region S_1 hit the yield surface twice in a complete cycle, whereas stresses in regions S_2 and S_3 hit the yield surface only once and remain somewhere inside the yield surface during the other half cycles (Fig. 2). In other words, the above division says that during a complete cycle when the shakedown is reached, the yield condition will be met twice in region S_1 :

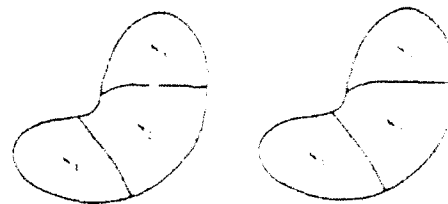


Fig. 1 Possible division of the region. Region S_1 incurs alternating plasticity; region S_2 yields only during the heating; and region S_3 yields only during the cooling.

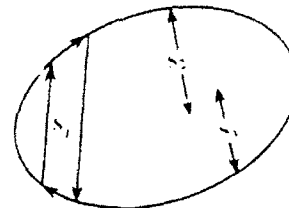


Fig. 2 Yield surface. Stresses in region S_1 hit the yield surface twice in a complete cycle. Stresses in regions S_2 and S_3 hit the yield surface only once and remain somewhere inside the yield surface during the other half cycles.

$$\begin{cases} f(\sigma_H^e - \hat{\alpha}_H) = 0 \\ f(\sigma_C^e - \hat{\alpha}_C) = 0 \end{cases} \quad (11)$$

and will be met only once in region S_2 :

$$\begin{cases} f(\sigma_H^e - \hat{\alpha}_H) = 0 \\ f(\sigma_C^e - \hat{\alpha}_C) < 0 \end{cases} \quad (12)$$

and once in region S_3 :

$$\begin{cases} f(\sigma_H^e - \hat{\alpha}_H) < 0 \\ f(\sigma_C^e - \hat{\alpha}_C) = 0 \end{cases} \quad (13)$$

In Eqs. (11)–(13), the subscripts H and C are used to refer to the values for the heating and cooling half cycles, respectively.

Now suppose that the yield condition, Eq. (9), permits the solution of $\hat{\alpha}$ in terms of the stress σ^e . Then from Eqs. (11)–(13), $\hat{\alpha}_H$ and $\hat{\alpha}_C$ can both be found in S_1 ; $\hat{\alpha}_H$ can be found while $\hat{\alpha}_C$ is unknown in S_2 ; and $\hat{\alpha}_C$ can be found while $\hat{\alpha}_H$ is unknown in S_3 . Since one of the modified hardening parameters is always known, the problem thus becomes that of finding the increment

$$\Delta\hat{\alpha} = \hat{\alpha}_C - \hat{\alpha}_H \quad (14)$$

Once the increment $\Delta\hat{\alpha}$ is found, the $\hat{\alpha}_C$ in S_2 and $\hat{\alpha}_H$ in S_3 , and consequently the entire $\hat{\alpha}$ field in the whole region, are fully determined.

From Eq. (8), we have an incremental relation:

$$\Delta\hat{\alpha} = \Delta\alpha - \Delta\rho \quad (15)$$

Since from Eq. (5) the back stress α depends uniquely on the plastic strain, whereas the regions S_2 and S_3 yield only once in a complete cycle, the plastic strain and consequently the back stress should be constant there. In other words, in these two regions, the incremental back stress $\Delta\alpha$ is zero, and the incremental modified hardening parameter $\Delta\hat{\alpha}$ equals the negative incremental residual stress $\Delta\rho$:

$$\begin{cases} \Delta\sigma = 0 \\ \Delta\hat{\alpha} = -\Delta\rho \end{cases} \quad \text{in } S_2 \text{ and } S_3 \quad (16)$$

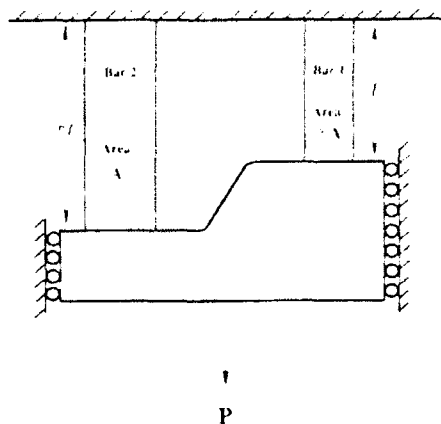


Fig. 3 Two-bar assembly. Two bars are made of the same kinematic hardening material, but of different lengths (l and ηl , respectively) and different cross-section areas (γA and A , respectively). In addition to a constant axial force P , bar 2 is subjected to a temperature change of amplitude T , while the temperature of bar 2 always stays at zero.

Hence, we only need to calculate the increment $\Delta\rho$ to find the increment $\Delta\hat{\alpha}$ and then the $\hat{\alpha}$ field.

It should be noted that for the reversed plasticity region, S_1 , the plastic strain, and hence the back stress, vary with time so that the incremental back stress $\Delta\hat{\alpha}$ does exist. However, for this region, $\hat{\alpha}_H$ and $\hat{\alpha}_C$ are both known and therefore the increment $\Delta\hat{\alpha}$ can be found directly.

From Eq. (7)

$$\Delta\rho = \Delta\sigma - \Delta\sigma^{el} \quad (17)$$

Elastic shakedown is characterized by the fact that the incremental stress is elastic. Hence, in such a case, the residual stress ρ and, as a result, the modified hardening parameter $\hat{\alpha}$ are independent of time and thus can directly be found from the yield condition. On the other hand, whenever reversed plasticity occurs in any part of the structure, an evaluation of the incremental residual stress is necessary for the determination of the modified hardening parameter field.

In using this approach, the key point is that the yield condition should permit the solution of $\hat{\alpha}$ in terms of elastic stress σ^{el} . Also, we should know the shakedown mode, and this can be done by performing some pre-analysis. The solution procedure can best be shown by some examples.

3 Examples

Two-Bar Structure. Two-bar and three-bar structures have been studied by several authors (Zarka, et al., 1978; Megahed, 1978; Leckie and Ranaweera, 1980; etc.) to illustrate the various shakedown analysis. To begin, we will also use a two-bar structure to exemplify the direct method.

The structure considered (Fig. 3) consists of two bars made of the same kinematic hardening material, but of different lengths (l and ηl , respectively) and different cross-section areas (γA and A , respectively). The upper end of this system is fixed, and the lower end, where a constant axial force P is applied, can move only in one direction. In addition to the mechanical load, bar 2 is subjected to a temperature change of amplitude T , while the temperature of bar 1 always stays at zero.

It can be found that eight different modes of behavior are possible for such a two-bar assembly when shakedown is reached. They are the purely elastic behavior—mode E , the elastic shakedown—modes E_1 and E_2 , the reversed plasticity—modes P_1 , P_2 , P_3 , and P_4 , and the ratchetting—mode R . The characteristics of these modes are shown in the following table and Fig. 4 gives the interaction diagram for a particular set of

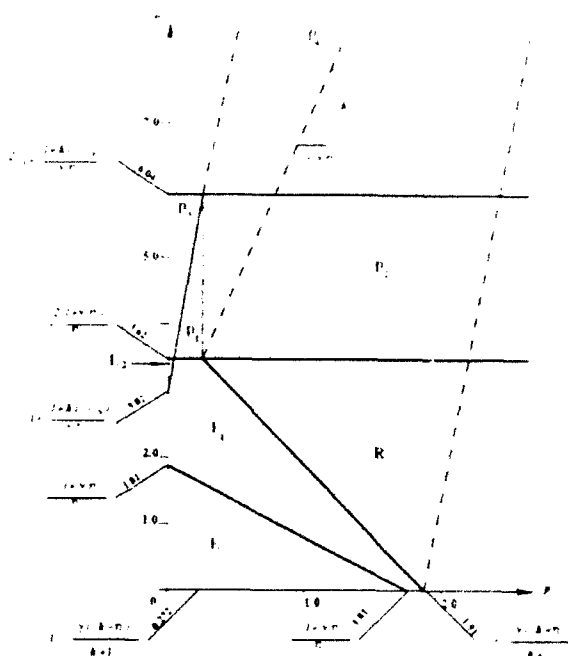


Fig. 4 Interaction diagram, two-bar assembly ($k = 10$, $\gamma = 0.9$, $\eta = 1.1$). Eight different kinds of behavior are possible for a two bar assembly: the purely elastic behavior E , the elastic shakedown E_1 and E_2 , the reversed plasticity responses P_1 , P_2 , P_3 , and P_4 , and the ratchetting R .

Table 1 The possible responses of the two-bar assembly

Mode			E	E1	E2	P1	P2	P3	P4	R
Bar 1	Heating	Elastic Behavior	x							
		Yield in Tension		x	x	x	x	x	x	x
		Yield in Compression								
	Cooling	Elastic Behavior	x	x	x					x
		Yield in Tension								
		Yield in Compression				x	x	x	x	
Bar 2	Heating	Elastic Behavior	x	x		x	x			x
		Yield in Tension								
		Yield in Compression			x			x	x	
	Cooling	Elastic Behavior	x	x	x	x		x		
		Yield in Tension					x		x	x
		Yield in Compression								

parameters. Note that if the transient states are considered, the reversed plasticity regions P_2 and P_4 and the ratchetting region R can be further divided into several subregions as shown by the dotted lines in Fig. 4. Since this paper concerns only the final shakedown solutions, we will not examine the transient behavior.

Now we will use the direct method to derive shakedown solutions. For convenience, the following normalized stress, strain, force, and temperature will be used in the forthcoming:

$$\begin{cases} \sigma = \frac{\text{stress}}{\sigma_1} \\ \epsilon = \frac{E \text{ strain}}{\sigma_1} \end{cases} \quad (18)$$

$$\begin{cases} p = \frac{P}{A\sigma_1} \\ \theta = \frac{E\beta T}{\sigma_1} \end{cases} \quad (19)$$

where E is Young's modulus, β is the coefficient of thermal expansion, and σ_1 is the initial yield stress. They are all considered as temperature-independent material properties.

The basic relationships for the two-bar assembly are as follows.

Equilibrium equation:

$$\gamma\sigma_1 + \sigma_2 = p. \quad (20)$$

Compatibility condition:

$$\epsilon_1 = \eta\epsilon_2. \quad (21)$$

Stress-strain relationship:

$$\begin{cases} \epsilon_1 = \sigma_1 + \epsilon_1^p \\ \epsilon_2 = \sigma_2 + \theta + \epsilon_2^p. \end{cases} \quad (22)$$

Plastic strain-back stress relationship:

$$\begin{cases} \epsilon_1^p = k\alpha_1 \\ \epsilon_2^p = k\alpha_2 \end{cases} \quad (23)$$

where k is a material constant.

Yield condition:

$$\begin{cases} |\sigma_1 - \alpha_1| = 1 \\ |\sigma_2 - \alpha_2| = 1. \end{cases} \quad (24)$$

Now if the stresses and strains are expressed as the sum of two terms as shown in Eq. (7), the residual stresses and strains should satisfy the following equations.

Equilibrium equation:

$$\gamma\rho_1 + \rho_2 = 0. \quad (25)$$

Compatibility condition:

$$\epsilon_1 = \eta\epsilon_2. \quad (26)$$

Stress-strain relationship:

$$\begin{cases} \epsilon_1 = (k+1)\rho_1 + k\hat{\alpha}_1 \\ \epsilon_2 = (k+1)\rho_2 + k\hat{\alpha}_2. \end{cases} \quad (27)$$

Yield condition:

$$\begin{cases} |\sigma_1^e - \hat{\alpha}_1| = 1 \\ |\sigma_2^e - \hat{\alpha}_2| = 1. \end{cases} \quad (28)$$

Based on the above governing equations, the purely elastic solution can be found for the heating half cycles as

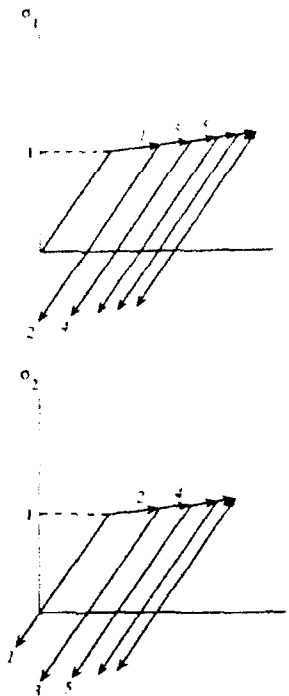


Fig. 5 Ratchetting mode *R*, two-bar assembly. Bar 1 and bar 2 yield in tension alternatively and plastic strains build-up. The kinematic hardening finally stops the ratchetting and the shakedown occurs.

$$\begin{cases} \sigma_1^e = \frac{\eta(p + \theta)}{1 + \gamma\eta} \\ \sigma_2^e = \frac{p - \gamma\eta\theta}{1 + \gamma\eta} \end{cases} \quad (29)$$

and for the cooling half cycles as

$$\begin{cases} \sigma_1^e = \frac{\eta p}{1 + \gamma\eta} \\ \sigma_2^e = \frac{p}{1 + \gamma\eta} \end{cases} \quad (30)$$

and the residual stresses can be expressed in terms of the modified hardening parameters as

$$\begin{cases} \rho_1 = \frac{k(\eta\hat{\alpha}_2 - \hat{\alpha}_1)}{(k+1)(1 + \gamma\eta)} \\ \rho_2 = -\frac{k\gamma(\eta\hat{\alpha}_2 - \hat{\alpha}_1)}{(k+1)(1 + \gamma\eta)}. \end{cases} \quad (31)$$

Therefore, once the modified hardening parameters are found, the residual stresses can be determined directly and the shakedown solution can be obtained by a superposition based on Eq. (7).

As an example, let us first consider the ratchetting mode *R*. In this case, bar 1 yields in tension during the heating and remains elastic during the cooling, while bar 2 behaves elastically during the heating, but yields, also in tension, during the cooling (Fig. 5). Since both bars yield in tension alternatively, the plastic strain will build up and ratchetting occurs. However, the kinematic hardening will finally stop the ratchetting so that the structure will incur large but still finite deformations when the steady state is reached.

According to our general description, Fig. 1, there will be

only two regions S_2 and S_1 in this ratchetting mode. Since it is the case of elastic shakedown, the modified hardening parameter $\hat{\alpha}$ fields are constant and can be determined from the yield conditions, Eq. (28), directly

$$\begin{cases} \hat{\alpha}_1 = \frac{\eta(\rho + \theta)}{1 + \gamma\eta} - 1 \\ \hat{\alpha}_2 = \frac{\rho}{1 + \gamma\eta} - 1. \end{cases} \quad (32)$$

Now from Eq. (31) the residual stresses, which are also constant during the cycles, can be determined

$$\begin{cases} \rho_1 = -\frac{k[\eta\theta - (1 - \eta)(1 + \gamma\eta)]}{(k + 1)(1 + \gamma\eta)^2} \\ \rho_2 = \frac{k\gamma[\eta\theta - (1 - \eta)(1 + \gamma\eta)]}{(k + 1)(1 + \gamma\eta)^2} \end{cases} \quad (33)$$

and finally a superposition gives the shakedown solutions. For the heating, we have

$$\begin{cases} \sigma_1 = \frac{1}{(k + 1)(1 + \gamma\eta)^2} \{ (k + 1)(1 + \gamma\eta)\eta\rho \\ \quad + [(k + 1)\gamma\eta + 1]\eta\theta + k(1 - \eta)(1 + \gamma\eta) \} \\ \sigma_2 = \frac{1}{(k + 1)(1 + \gamma\eta)^2} \{ (k + 1)(1 + \gamma\eta)\rho \\ \quad - [(k + 1)\gamma\eta + 1]\gamma\eta\theta - k\gamma(1 - \eta)(1 + \gamma\eta) \} \end{cases} \quad (34)$$

and for the cooling,

$$\begin{cases} \sigma_1 = \frac{1}{(k + 1)(1 + \gamma\eta)^2} \{ (k + 1)(1 + \gamma\eta)\eta\rho \\ \quad - k\eta\theta + k(1 - \eta)(1 + \gamma\eta) \} \\ \sigma_2 = \frac{1}{(k + 1)(1 + \gamma\eta)^2} \{ (k + 1)(1 + \gamma\eta)\rho \\ \quad + k\gamma\eta\theta - k\gamma(1 - \eta)(1 + \gamma\eta) \}. \end{cases} \quad (35)$$

It is seen from the development that, in the case of elastic shakedown, the steady solution can be found using a very simple, straightforward approach. The derivation of this steady solution based on the conventional incremental calculation is considerably more complex.

We next consider the reversed plasticity mode P_2 . In this case, bar 1 incurs reversed plasticity during the cycles, while bar 2 yields in tension during the cooling and remains elastic during the heating (Fig. 6). Referring to Fig. 1, we now have two regions S_1 and S_2 , and therefore, an incremental solution is necessary in the present situation.

Using the yield condition, we can only find the modified hardening parameter for bar 1 during the heating:

$$\hat{\alpha}_1 = \frac{\eta(\rho + \theta)}{1 + \gamma\eta} - 1 \quad (36)$$

while during the cooling, the modified hardening parameters for both bars are known:

$$\begin{cases} \hat{\alpha}_1 = \frac{\eta\rho}{1 + \gamma\eta} + 1 \\ \hat{\alpha}_2 = \frac{\rho}{1 + \gamma\eta} - 1. \end{cases} \quad (37)$$

Thus, we need to find the increment

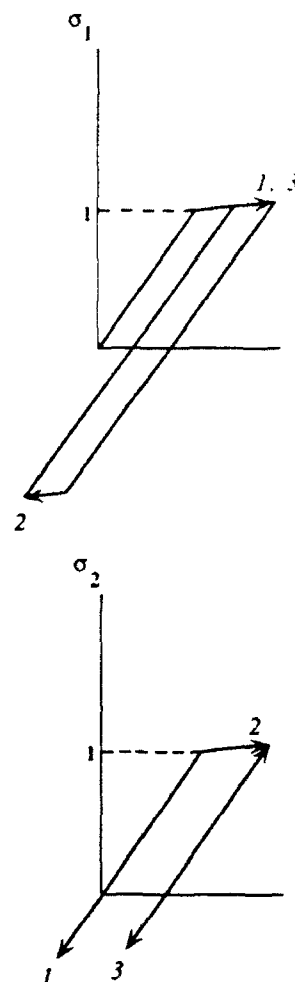


Fig. 6 Reversed plasticity mode P_2 , two-bar assembly. Bar 1 incurs reversed plasticity during the cycles, while bar 2 yields in tension during the cooling and remains elastic during the heating.

$$\Delta\hat{\alpha}_2 = -\Delta\rho_2 \quad (38)$$

for bar 2.

The incremental residual stresses should satisfy the equilibrium equation

$$\gamma\Delta\rho_1 + \Delta\rho_2 = 0 \quad (39)$$

and the compatibility condition

$$\Delta e_1 = \eta\Delta e_2 \quad (40)$$

where, by Eqs. (27) and (36)-(38),

$$\begin{cases} \Delta e_1 = (k + 1)\Delta\rho_1 - k\left(\frac{\eta\theta}{1 + \gamma\eta} - 2\right) \\ \Delta e_2 = \Delta\rho_2. \end{cases} \quad (41)$$

The solution to Eqs. (39) and (40) is

$$\begin{cases} \Delta\rho_1 = \frac{k[\eta\theta - 2(1 + \gamma\eta)]}{(k + 1 + \gamma\eta)(1 + \gamma\eta)} \\ \Delta\rho_2 = -\frac{k\gamma[\eta\theta - 2(1 + \gamma\eta)]}{(k + 1 + \gamma\eta)(1 + \gamma\eta)}. \end{cases} \quad (42)$$

Then, the modified hardening parameter for bar 2 during the heating can be found:

$$\hat{\sigma}_2 = \frac{1}{(k+1-\gamma\eta)(1+\gamma\eta)} \{ (k+1+\gamma\eta)p - k\gamma\eta\theta - (1+\gamma\eta)[k(1-2\gamma) - (1+\gamma\eta)] \} \quad (43)$$

and the residual stresses can be determined from Eq. (31). Finally, a superposition yields the shakedown solution:

For the heating half cycles,

$$\sigma_1 = \frac{1}{(k+1)(k+1+\gamma\eta)(1+\gamma\eta)} \{ (k+1)\eta[(k+1+\gamma\eta)p + (1+\gamma\eta)\theta] + k[k(1-\eta+2\gamma\eta) + (1-\eta)(1+\gamma\eta)] \} \quad (44)$$

$$\sigma_2 = \frac{1}{(k+1)(k+1+\gamma\eta)(1+\gamma\eta)} \{ (k+1)[(k+1+\gamma\eta)p - (1+\gamma\eta)\gamma\eta\theta] - k\gamma[k(1-\eta+2\gamma\eta) + (1-\eta)(1+\gamma\eta)] \}$$

and for the cooling half cycles,

$$\begin{cases} \sigma_1 = \frac{1}{(k+1)(1+\gamma\eta)} \{ (k+1)\eta p - k(1+\eta) \} \\ \sigma_2 = \frac{1}{(k+1)(1+\gamma\eta)} \{ (k+1)p + k\gamma(1+\eta) \} \end{cases} \quad (45)$$

The shakedown solutions for all possible modes can be derived using the direct method. We will not give these solutions in this paper due to the space limitation.

Tube Problem. The tube problem has received great attention in the literature. The ratchetting behavior was first analyzed for nuclear reactor pressure vessels by Miller (1959) and later by Edmunds and Beer (1961), Burgreen (1968), and Bree (1967, 1968).

Bree studied the response of a cylindrical tube subjected to a sustained internal pressure and a cyclic temperature drop across its wall. Using a very simple one-dimensional model, assuming a linear temperature distribution across the tube wall and considering primarily an elastic-perfectly plastic material behavior, he studied various responses of the tube. Later, Mulcahy (1976) analyzed the same problem using a linear kinematic hardening model. Megahed (1978) adopted a bilinear temperature distribution and considered the effects due to cyclic hardening and creep. Leckie and Ranaweera (1980) reanalyzed this problem using a more realistic parabolic temperature distribution, and a bound on the creep deformation was found. A number of these researches, however, were based on Bree's simplified model. As this model is very simple, it is natural to doubt whether it can model the actual situation and yield acceptable results.

Our previous research (Jiang, 1985) discarded all the assumptions and simplifications made by Bree and achieved closed-form shakedown solutions for all possible responses using the conventional incremental method. While the incremental method worked, the derivation turned out to be complex and time consuming. Now we will use the direct method to reanalyze this problem to illustrate the simplicity and efficiency of the approach suggested.

For convenience, some of the basic relationships are cited in the following. The details can be found from the previous research.

Consider a long cylindrical tube that is subjected to an internal pressure p , an external pressure q , a centrifugal force caused by the rotation of an angular velocity ω , and an arbitrarily distributed temperature field T across the tube wall (Fig. 7). All the loads and temperature can be either sustained or cyclic in the analysis.

Due to the symmetry, σ_r and σ_θ are the only stresses, and ϵ_r

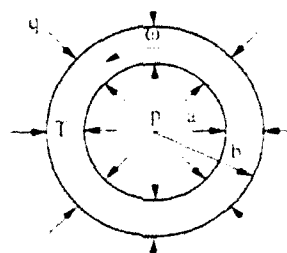


Fig. 7 Loading situation, tube problem. The tube is subjected to an internal pressure p , an external pressure q , a centrifugal force caused by the rotation of an angular velocity ω , and a distributed temperature field T across the tube wall.

and ϵ_θ are the only strains we must deal with. For simplification, the loads, stresses, and strains are normalized as follows:

$$\begin{cases} P = \frac{p}{\tau_y} \\ Q = \frac{q}{\tau_y} \\ \theta = \frac{E\beta T}{2\tau_y} = t_\theta(r) \\ f = \frac{\rho\omega^2}{\tau_y} \end{cases} \quad (46)$$

$$\begin{cases} \sigma = \frac{\sigma}{\tau_y} \\ \tau = \frac{\sigma_\theta - \sigma_r}{2\tau_y} \end{cases} \quad (47)$$

$$\begin{cases} e_r = \frac{G\epsilon_r}{\tau_y} \\ e_\theta = \frac{G\epsilon_\theta}{\tau_y} \end{cases} \quad (48)$$

where E is Young's modulus, G is the shear modulus, β is the thermal expansion coefficient, ρ is the mass density, t_θ is the normalized temperature at the inner wall, $t_\theta(r)$ characterizes the temperature distribution, and τ_y is the yield stress in shear.

There is only one equilibrium equation, namely

$$\frac{d\sigma}{dr} - \frac{2\tau}{r} + fr = 0 \quad (49)$$

one compatibility condition, namely

$$\frac{de_r}{dr} + \frac{e_\theta - e_r}{r} = 0 \quad (50)$$

and two boundary conditions

$$\begin{cases} \sigma|_{r=a} = -P \\ \sigma|_{r=b} = -Q \end{cases} \quad (51)$$

that need to be satisfied. For the kinematic hardening material, the stress-strain relationships are

$$\begin{cases} e_r = \frac{1}{2} [(1-2\nu)\sigma - 2\nu\tau] + \theta - e_p \\ e_\theta = \frac{1}{2} [(1-2\nu)\sigma + 2(1-\nu)\tau] + \theta + e_p \end{cases} \quad (52)$$

where e_p is the normalized plastic strain:

$$e_p = \frac{G}{m} (\tau - \tau_0) \quad (53)$$

in which

$$\tau_0 = \text{sign}(\tau) \quad (54)$$

indicates the yield direction, and m is the hardening constant.

The yield condition is given by

$$\tau - \alpha = \tau_0 \quad (55)$$

where

$$\alpha = \frac{m e_p}{G} \quad (56)$$

is the back stress or the hardening parameter.

Now divide the stresses and strains into two parts according to the general procedure:

$$\begin{cases} \sigma = \sigma^{el} + \bar{\sigma} \\ \tau = \tau^{el} + \bar{\tau} \end{cases} \quad (57)$$

$$\begin{cases} e_r = e_r^{el} + \bar{e}_r \\ e_\theta = e_\theta^{el} + \bar{e}_\theta \end{cases} \quad (58)$$

where (σ^{el}, τ^{el}) and $(e_r^{el}, e_\theta^{el})$ represent the purely elastic solution, whereas $(\bar{\sigma}, \bar{\tau})$ and $(\bar{e}_r, \bar{e}_\theta)$ are the residual stresses and strains. The residual stresses should satisfy the homogeneous equilibrium equation

$$\frac{d\bar{\sigma}}{dr} - \frac{2\bar{\tau}}{r} = 0 \quad (59)$$

and the residual strains should satisfy the compatibility condition

$$\frac{d\bar{e}_\theta}{dr} + \frac{\bar{e}_r - \bar{e}_\theta}{r} = 0. \quad (60)$$

The residual stress-strain relationships can be found as

$$\begin{cases} \bar{e}_r = \frac{1-2\nu}{2} \bar{\sigma} - \frac{G+m\nu}{m} \bar{\tau} - \frac{G}{m} \hat{\alpha} \\ \bar{e}_\theta = \frac{1-2\nu}{2} \bar{\sigma} + \frac{G+m(1-\nu)}{m} \bar{\tau} + \frac{G}{m} \hat{\alpha} \end{cases} \quad (61)$$

and the yield condition, Eq. (55), becomes

$$\tau^{el} - \hat{\alpha} = \tau_0 \quad (62)$$

where, in Eqs. (61) and (62), $\hat{\alpha}$ is the modified hardening parameter

$$\hat{\alpha} = \alpha - \bar{\tau}. \quad (63)$$

Based on the above basic equations, the purely elastic solution can be found as

$$\begin{aligned} \sigma^{el} &= \frac{1}{b^2 - a^2} \left[P a^2 \left(1 - \frac{b^2}{r^2} \right) - Q b^2 \left(1 - \frac{a^2}{r^2} \right) \right] \\ &\quad + \frac{f(3-2\nu)}{8(1-\nu)} \left(1 - \frac{a^2}{r^2} \right) (b^2 - r^2) + \frac{t_a}{1-\nu} S(a, b) \\ \tau^{el} &= \frac{(P-Q)a^2 b^2}{(b^2 - a^2)r^2} + \frac{f}{8(1-\nu)} \left[(1-2\nu)r^2 + (3-2\nu)\frac{a^2 b^2}{r^2} \right] \\ &\quad + \frac{t_a}{1-\nu} Z(a, b) \end{aligned} \quad (64)$$

where

$$\begin{cases} S(a, b) = 2 \left[\frac{1}{b^2 - a^2} \left(1 - \frac{a^2}{r^2} \right) \int_a^r r dr - \frac{1}{r} \int_a^r r dr \right] \\ Z(a, b) = -1 - \frac{2a^2}{(b^2 - a^2)r^2} \int_a^r r dr + \frac{2}{r} \int_a^r r dr \end{cases} \quad (65)$$

and the general residual solution can be found as

$$\begin{cases} \bar{\sigma} = -\frac{2G}{G+m(1-\nu)} \int \frac{\hat{\alpha}}{r} dr - C_1 - \frac{C_2}{r} \\ \bar{\tau} = -\frac{G}{G+m(1-\nu)} \hat{\alpha} + \frac{C_2}{r} \end{cases} \quad (66)$$

where C_1 and C_2 are constants to be determined from the boundary and continuity conditions.

It is seen that if we can find the modified hardening parameter $\hat{\alpha}$ field, the residual stresses can be found by some integrations, and the shakedown solution can be obtained through a simple superposition.

To illustrate the direct method, we consider a case, which was classified as ratchetting mode R_2 in our previous research (Jiang, 1985).

In the case of ratchetting mode R_2 , the inner tube wall yields and the outer tube wall remains in elasticity during the odd half cycles, while both walls yield during the even half cycles. As a result, there exists a reversed plasticity zone near the inner tube surface, and a ratchetting zone in some middle part of the tube wall (Fig. 8(a)). During the cycles, the ratchetting zone will gradually shrink and finally tend to zero when shakedown is attained, because of the kinematic hardening. Fig. 8(b) shows the shakedown pattern of this mode, where three different kinds of regions exist: the reversed plasticity zone S_1 ($a \leq r \leq c$), and the elastic shakedown zones S_2 ($c \leq r \leq d$) and S_3 ($d \leq r \leq b$).

As previously mentioned, due to the occurrence of the reversed plasticity, the increment $\Delta\hat{\alpha}$ should be found in order to determine the $\hat{\alpha}$ field.

Since the stresses in region S_1 hit the yield surface twice during the cycles, the modified hardening parameter $\hat{\alpha}$ can be found from the yield condition, Eq. (62), for both the heating and cooling, the increment $\Delta\hat{\alpha}$ being known there:

$$\Delta\hat{\alpha} = \Delta\tau^{el} + 2 \quad a \leq r \leq c \quad (67)$$

On the other hand, the stresses in regions S_2 and S_3 hit the yield surface only once during the cycles so that we need to find the increment $\Delta\hat{\alpha}$ in these two regions to determine the $\hat{\alpha}$ field. Due to the fact that the back stress does not vary in the elastic shakedown zones, Eq. (63) yields

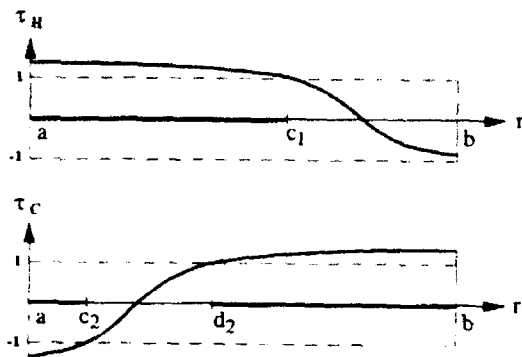
$$\Delta\hat{\alpha} = -\Delta\bar{\tau} \quad c \leq r \leq b \quad (68)$$

Therefore, the problem becomes that of finding the incremental residual stress $\Delta\bar{\tau}$.

The incremental residual stresses ($\Delta\bar{\sigma}$, $\Delta\bar{\tau}$) and the incremental residual strains ($\Delta\bar{e}_r$, $\Delta\bar{e}_\theta$) should satisfy the equilibrium equation, Eq. (59), and the compatibility condition, Eq. (60). The incremental residual stress-strain relationships can be found from Eqs. (61), (67), and (68):

$$\begin{cases} \Delta\bar{e}_r = \frac{1-2\nu}{2} \Delta\bar{\sigma} - \frac{G+m\nu}{m} \Delta\bar{\tau} - \frac{G}{m} (\Delta\tau^{el} + 2) \\ \Delta\bar{e}_\theta = \frac{1-2\nu}{2} \Delta\bar{\sigma} + \frac{G+m(1-\nu)}{m} \Delta\bar{\tau} + \frac{G}{m} (\Delta\tau^{el} + 2) \end{cases} \quad a \leq r \leq c \quad (69)$$

(a) First Cycle



(b) Steady State

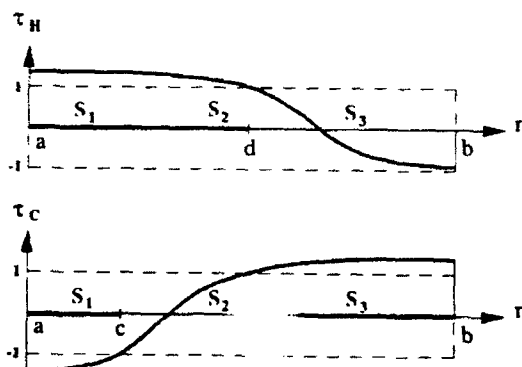


Fig. 8 Ratchetting mode R_2 tube problem. A ratchetting zone exists in some middle part of the tube wall. The ratchetting zone gradually shrinks and finally disappears when the shakedown is attained as a result of the kinematic hardening.

$$\begin{cases} \Delta \bar{\sigma}_r = \frac{1-2\nu}{2} \Delta \bar{\sigma} - \nu \Delta \bar{\tau} \\ \Delta \bar{\sigma}_\theta = \frac{1-2\nu}{2} \Delta \bar{\sigma} + (1-\nu) \Delta \bar{\tau} \end{cases} \quad c \leq r \leq b. \quad (70)$$

Based on these equations, the incremental residual stress $\Delta \bar{\tau}$ can be determined. Assuming that the pressures are sustained loads, while the centrifugal force and the temperature are cyclic, we find

$$\Delta \bar{\tau} = \frac{G a^2 b^2}{[G + m(1-\nu)](b^2 - a^2)r^2} \left[2 \left(1 - \frac{c^2}{a^2} + 2 \ln \frac{c}{a} \right) + \frac{f(1-2\nu)}{8(1-\nu)} \left(\frac{c^2 - a^2}{a} \right)^2 - \frac{I_0}{1-\nu} S_d^T(a, c) \right] \quad c \leq r \leq b \quad (71)$$

where

$$S_d^T(a, c) = -I_0 \left(1 - \frac{c^2}{a^2} \right) - \frac{2}{a^2} \int_a^c r dr. \quad (72)$$

Then, by the yield condition, Eq. (62), the elastic solution,

Eq. (64), and Eqs. (68) and (71), the modified hardening parameter can be obtained as follows. For the heating half cycles:

$$\hat{\alpha} = \begin{cases} \frac{(P-Q)a^2b^2}{(b^2-a^2)r^2} - \frac{f}{8(1-\nu)} \left[(1-2\nu)r^2 + (3-2\nu)\frac{a^2b^2}{r} \right] + \frac{I_0}{1-\nu} Z(a, b) - 1 & a \leq r \leq d \\ \frac{(P-Q)a^2b^2}{(b^2-a^2)r^2} - \frac{G a^2 b^2}{[G + m(1-\nu)](b^2-a^2)r^2} + \left[2 \left(1 - \frac{c^2}{a^2} + 2 \ln \frac{c}{a} \right) + \frac{f(1-2\nu)}{8(1-\nu)} \left(\frac{c^2 - a^2}{a} \right)^2 - \frac{I_0}{1-\nu} S_d^T(a, c) \right] - 1 & d \leq r \leq b \end{cases} \quad (73)$$

For the cooling half cycles:

$$\hat{\alpha} = \begin{cases} \frac{(P-Q)a^2b^2}{(b^2-a^2)r^2} + 1 & a \leq r \leq c \\ \frac{(P-Q)a^2b^2}{(b^2-a^2)r^2} + \frac{f}{8(1-\nu)} \left[(1-2\nu)r^2 + (3-2\nu)\frac{a^2b^2}{r} \right] + \frac{I_0}{1-\nu} Z(a, b) - 1 - \frac{G a^2 b^2}{[G + m(1-\nu)](b^2-a^2)r^2} \\ \times \left[2 \left(1 - \frac{c^2}{a^2} + 2 \ln \frac{c}{a} \right) + \frac{f(1-2\nu)}{8(1-\nu)} \left(\frac{c^2 - a^2}{a} \right)^2 - \frac{I_0}{1-\nu} S_d^T(a, c) \right] & c \leq r \leq d \\ \frac{(P-Q)a^2b^2}{(b^2-a^2)r^2} - 1 & d \leq r \leq b \end{cases} \quad (74)$$

Now the residual stresses can be found from the general solution, Eq. (66), and a superposition with the purely elastic solution finally yields the shakedown solution. For the heating half cycles,

$$\begin{cases} \sigma = -P + \frac{1}{G + m(1-\nu)} \left\{ 2G \ln \frac{r}{a} + \frac{R}{a^2} \left(1 - \frac{a^2}{r^2} \right) + \frac{f}{8} (a^2 - r^2) \left[4G + m(3-2\nu) + m(1-2\nu) \frac{d^4}{a^2 r^2} \right] + m I_0 S_d^T(a, d) \right\} \\ \tau = \frac{1}{G + m(1-\nu)} \left[G + \frac{R}{r^2} + \frac{m(1-2\nu)f}{8} \left(r^2 - \frac{d^4}{r^2} \right) + m I_0 Z^T(a, d) \right] & a \leq r \leq d \end{cases} \quad (75)$$

$$\left\{ \begin{aligned} \sigma &= -Q + \frac{1}{G+m(1-\nu)} \left[2G \ln \frac{r}{b} + \frac{R}{b^2} \left(1 - \frac{b^2}{r^2} \right) \right] \\ &\quad + \frac{f}{8(1-\nu)} (b^2 - r^2) \left[(3-2\nu) + (1-2\nu) \frac{d^4}{b^2 r^2} \right] \\ &\quad + \frac{t_0}{1-\nu} S^T(b, d) \\ \tau &= \frac{1}{G+m(1-\nu)} \left(G + \frac{R}{r^2} \right) + \frac{f(1-2\nu)}{8(1-\nu)} \left(r^2 - \frac{d^4}{r^2} \right) \\ &\quad + \frac{t_0}{1-\nu} Z^T(a, d) \quad d \leq r \leq b. \end{aligned} \right. \quad (76)$$

For the cooling half cycles,

$$\left\{ \begin{aligned} \sigma &= -P - \frac{1}{G+m(1-\nu)} \left[2G \ln \frac{r}{a} + \frac{R}{a^2} \left(1 - \frac{a^2}{r^2} \right) \right] \\ \tau &= -\frac{1}{G+m(1-\nu)} \left(G - \frac{R}{r^2} \right) \quad a \leq r \leq c \\ \sigma &= -P + \frac{1}{G+m(1-\nu)} \left[2G \ln \frac{ar}{c^2} + \frac{R}{a^2} \left(1 - \frac{a^2}{r^2} \right) \right. \\ &\quad \left. + \frac{G(1-2\nu)f}{8(1-\nu)} (c^2 - r^2) \left(1 - \frac{d^4}{c^2 r^2} \right) - \frac{Gt_0}{1-\nu} S^T(c, d) \right] \\ \tau &= \frac{1}{G+m(1-\nu)} \left[G + \frac{R}{r^2} - \frac{G(1-2\nu)f}{8(1-\nu)} \left(r^2 - \frac{d^4}{r^2} \right) \right. \\ &\quad \left. - \frac{Gt_0}{1-\nu} Z^T(c, d) \right] \quad c \leq r \leq d \\ \sigma &= -Q + \frac{1}{G+m(1-\nu)} \left(2G \ln \frac{r}{b} + \frac{R}{b^2} \left(1 - \frac{b^2}{r^2} \right) \right) \\ \tau &= \frac{1}{G+m(1-\nu)} \left(G + \frac{R}{r^2} \right) \quad d \leq r \leq b \end{aligned} \right. \quad (77)$$

where

$$R = \frac{a^2 b^2}{b^2 - a^2} \left\{ [G+m(1-\nu)](P-Q) - 2G \ln \frac{ab}{c^2} - \frac{G(1-2\nu)f}{8(1-\nu)} \left(\frac{c^2 - d^2}{c} \right)^2 + \frac{Gt_0}{1-\nu} S_d^T(c, d) \right\} \quad (80)$$

and

$$\left\{ \begin{aligned} S^T(c, d) &= \frac{d^2}{c^2} \left(t_0 - \frac{2}{d^2} \int_c^d r dr \right) - \frac{d^2}{r^2} \left(t_0 - \frac{2}{d^2} \int_r^d r dr \right) \\ Z^T(c, d) &= -t + \frac{d^2}{r^2} \left(t_0 - \frac{2}{d^2} \int_r^d r dr \right). \end{aligned} \right. \quad (81)$$

It is seen that due to the different responses in different regions, the shakedown solution consists of several local solutions. The problem remaining is how to find the boundaries c and d of the different regions. Figure 8(b) shows that the point c is the boundary where the response of the tube changes from reversed plasticity to elastic shakedown, so that the incremental normalized shear stress at this point equals just -2 .

On the other hand, point d borders two elastic shakedown zones, one yielding during the heating and the other yielding during the cooling, so that the shear stress remains constant at this point. As a result, two conditions are available for the determination of these two boundaries.

$$\begin{cases} \Delta \tau|_{r=c} = -2 \\ \Delta \tau|_{r=d} = 0 \end{cases} \quad (82)$$

or,

$$\begin{cases} 2 - \frac{f(1-2\nu)}{8(1-\nu)} \left(c^2 - \frac{d^4}{c^2} \right) - \frac{t_0}{1-\nu} Z_c^T(c, d) = 0 \\ \frac{4G}{G+m(1-\nu)} \ln \frac{a}{c} \end{cases} \quad (83)$$

$$\begin{aligned} &+ \frac{f}{8(1-\nu)} \left\{ (b^2 - a^2) \left[(3-2\nu) + (1-2\nu) \frac{d^4}{a^2 b^2} \right] \right. \\ &\quad \left. - \frac{G(1-2\nu)}{G+m(1-\nu)} (a^2 - c^2) \left(1 - \frac{d^4}{a^2 c^2} \right) \right\} \\ &+ \frac{t_0}{1-\nu} \left\{ S_d^T(b, d) - \frac{1}{G+m(1-\nu)} [GS_d^T(c, d) \right. \\ &\quad \left. + m(1-\nu)S_d^T(a, d)] \right\} = 0 \end{aligned}$$

where

$$Z_c^T(c, d) = -t_c + t_0 \frac{d^2}{c^2} - \frac{2}{c^2} \int_c^d r dr \quad (84)$$

The shakedown solution, Eqs. (75)–(79), is identical to the one we derived using the traditional incremental method, and agrees very well with the experiment performed by Corum et al. (Jiang, 1985), which justifies the direct method we developed.

4 Conclusions

This paper presents a simple direct method for the straightforward determination of the shakedown solutions of structures subjected to various sustained and cyclic loadings. The advantage of the direct method is that the well-established theory of elasticity can be used to solve difficult plasticity problems which traditionally have to be attacked using complex, step-by-step, and time-consuming incremental analysis. The direct method was first proposed by Zarka, et al. The most important point in their framework is the introduction and the use of the modified hardening parameter field. However, the determination of this field turned out to be very complex in their original work. This paper greatly simplifies Zarka's method by showing that the modified hardening parameter field can be directly found from the yield condition and the incremental residual stress. Thus, only two elastic analyses are required in the determination of shakedown solutions without the need of performing a full-scale elastic-plastic analysis.

It can be seen that Zarka's formulation, for example, a residual stress-strain relationship like Eq. (10), requires a unique mapping between plastic stress and back stress. Thus, Zarka's approach is limited to linear kinematic hardening. On the other hand, for high-temperature problems and nonisothermal problems, the back stress evolution is actually temperature and rate dependent, and an accurate representation of cyclic plasticity requires, in general, a nonlinear kinematic hardening rule. However, the elastic-plastic response of the structure under

sustained and cyclic loadings is usually very complicated, and consequently, any complex constitutive laws would make the problem intractable. Since the purpose of this research is to find directly the steady-state solutions to avoid the time-consuming and expensive transient-state calculations, the linear kinematic hardening rule becomes an ideal one that can be dealt with and render at the same time satisfactory results. The technique developed in this paper obviously is a very useful one under such idealization.

The key point of the present method is that the yield condition should permit the solving of the modified hardening parameter in terms of the purely elastic stresses. A question may be raised as to the conditions which would make this requirement possible. We have succeeded in solving several interesting problems using the direct method. Such general conditions, however, are still under investigation. We hope we can address this problem in the near future.

Several examples have been given in this paper to illustrate the feasibility and the efficiency of the approach. It is believed that this version of the direct method is very promising.

References

- Ainsworth, R. A., 1977, "Application of Bounds for Creeping Structures Subjected to Load Variations above the Shakedown Limit," *International Journal of Solids and Structures*, Vol. 13, pp. 981-993.
- Bree, J., 1967, "Elastic Plastic Behavior of Thin Tubes Subjected to Internal Pressure and Intermittent High Heat Fluxes," *J. Strain Analysis*, Vol. 2, pp. 226-238.
- Bree, J., 1968, "Incremental Growth Due To Creep and Plastic Yielding of Thin Tubes Subjected to Internal Pressure and Cyclic Thermal Stresses," *J. Strain Analysis*, Vol. 3, pp. 122-127.
- Burgreen, D., 1968, "The Thermal Ratchet Mechanism," *ASME, J. Basic Eng.*, Vol. 90, pp. 319-324.
- Burgreen, D., 1968, "Structural Growth Induced by Thermal Cycling," *ASME, J. Basic Eng.*, Vol. 90, pp. 469-475.
- Corum, T. M., Young, H. C., and Grondin, A. C., 1975, "Thermal Ratcheting in Pipes Subjected to Intermittent Thermal Downstrokes at Elevated Temperatures," *Pressure Vessels and Piping: Verification and Qualification of Inelastic Computer Programs*, ASME, New York, pp. 79-85.
- Drabble, E., and Johnson, W., 1963-1964, "The Development of the Zone of Yielding in Thick-Walled Spherical Shells of Non-Work-Hardening Material Subjected to a Steady-State Radial Temperature Gradient and an Internal or External Pressure," *Proc. Instn. Mech. Engrs.*, Vol. 178, Pt. 3B, pp. 267-278.
- Edmunds, H. C., and Beer, E. J., 1961, "Notes on Incremental Analysis of Pressure Vessels," *J. Mech. Eng. Sci.*, Vol. 3, pp. 187-194.
- Gatewood, B. E., 1960, "The Problem of Strain Accumulation Under Thermal Cycling," *J. Aerospace Sci.*, Vol. 27, p. 461.
- Hane, W., 1985, "The Elastic Plastic and Shakedown Analysis of Tubes Subjected to Sustained and Cyclic Loads," Ph.D. Thesis, University of Illinois at Urbana-Champaign.
- Leckie, F. A., and Ranaweera, M. P., 1980, "The Theoretical Assessment of Deformation and Damage of a High Temperature Component," Oak Ridge National Laboratory, Subcontract No. 7689.
- Megahed, M. M., 1978, "On the Inelastic Deformation of Structures Subjected to Variable Loading," *Eng. Trans. Electric.*
- Megahed, M. M., 1978, "Kinematic Hardening Analysis of the Modes of Deformation of Thin Tubes," unpublished report.
- Miller, D. R., 1959, "Thermal Stress Ratchet Mechanism in Pressure Vessels," *ASME, J. Basic Eng.*, Vol. 81, pp. 190-196.
- Mulkahn, T. M., 1976, "Thermal Ratcheting of a Beam Element Having an Idealized Bauschinger Effect," *ASME, J. Eng. Materials and Technology*, pp. 264-271.
- Tribout, J., Inglebert, G., and Casier, J., 1983, "A Simplified Method for the Inelastic Analysis of Structures under Cyclic Loadings," *ASME Journal of Pressure Vessel Technology*, Vol. 105.
- Zarka, J., 1976, "Principe des Methodes Actuelles de Resolution Numerique des Problemes Classiques en Mecanique des Solides," Cours a l'E.N.S.T.A., Paris.
- Zarka, J., Arnaudau, F. C., Casier, J., and Baviac, G., 1978, "A Practical Method to Determine Elastic or Plastic Shakedown of Structures," *Simplified Methods in Pressure Vessel Analysis*, presented at 1978 ASME-CSM Pressure Vessel and Piping Conference, Montreal.

CREEP OF FIBER-REINFORCED METAL-MATRIX COMPOSITES: CONSTITUTIVE EQUATIONS AND COMPUTATIONAL ISSUES

N. Aravas and Cao Cheng
Department of Mechanical Engineering
and Applied Mechanics
University of Pennsylvania
Philadelphia, PA 19104
USA

Abstract

The general form of the constitutive equations that describe transient and steady-state creep of fiber reinforced metal matrix composites is developed. The physical meaning of the constitutive functions involved is discussed in detail. A method for the numerical integration of the constitutive equations is developed. The 'linearization moduli' associated with the integration algorithm are computed, and the constitutive model is implemented in a general purpose finite element program. A constitutive model for steady-state creep of fiber reinforced that has been developed recently by De Botton and Ponte Castañeda (1992) is also considered. A number of 'unit cell' problems with periodic boundary conditions, consistent with the requirements of homogenization theory, are solved using the finite element method, and the results are compared with the predictions of the analytical model of De Botton and Ponte Castañeda.

1 Introduction

Fiber reinforced metal matrix composites are being considered for use in gas turbine engines because of their creep resistance at high temperatures. In view of their high strength and stiffness to weight ratio, they are also considered in automotive industry for replacing steel and aluminum components.

An attempt to derive three-dimensional constitutive equations for creeping transversely isotropic metallic materials was first made by Johnson (1977), who proposed a constitutive equation for modelling steady-state creep in directionally-solidified eutectic alloys. More recently, Jansson (1991, 1992) used homogenization techniques to study the effective mechanical properties and the local stress concentrations for composites with periodic microstructures and nonlinear constituents. De Botton and Ponte Castañeda (1992) have developed estimates as well as rigorous bounds for the dissipation functions of multiple-phase fiber composites, in which the constituent phases are non-linear isotropic materials. A review of the existing models for the effect of fibers on the creep characteristics of unidirectional composites has been presented by McMeeking (1992). However, there have been only few experimental studies on fiber-reinforced composite systems having practical utility at elevated temperatures (Weber et al., 1992a, b).

In this paper, we develop the general form of the constitutive equations that describe transient and steady-state creep of fiber-reinforced metal-matrix composites. The physical meaning of the constitutive functions involved is discussed in detail. A method for the numerical integration of the constitutive equations is developed. The 'linearization moduli' associated with the integration algorithm are computed, and the constitutive model is implemented in a general purpose finite element program. A constitutive model for steady-state creep of fiber reinforced that has been developed recently by De Botton and Ponte Castañeda (1992) is also considered. A number of 'unit cell' problems with periodic boundary conditions, consistent with the requirements of homogenization theory, are solved using the finite element method, and the results are compared with the predictions of the analytical model of De Botton and Ponte Castañeda.

Standard notation is used throughout. Boldface symbols denote tensors the order of which are indicated by the context. All tensor components are written with respect to a fixed Cartesian coordinate system, and the summation convention is used for repeated indices, unless otherwise indicated. The prefixes *tr* and *det* indicate the trace and the determinant respectively, a superscript *T* the transpose of a second order tensor, a superposed dot the material time derivative, and the subscripts *s* and *a* the symmetric and anti-symmetric parts of a second order tensor. Let **a** and **b** be vectors, **A** and **B** second order tensors, and **C** and **D** fourth order tensors; the following products are used in the text $(\mathbf{ab})_{ij} = a_i b_j$, $(\mathbf{A} \cdot \mathbf{a})_i = A_{ij} a_j$, $(\mathbf{a} \cdot \mathbf{A})_i = a_j A_{ji}$, $(\mathbf{A} \cdot \mathbf{B})_{ij} = A_{ik} B_{kj}$, $(\mathbf{AB})_{ijkl} = A_{ij} B_{kl}$, $(\mathbf{C} : \mathbf{A})_{ij} = C_{ijkl} A_{kl}$, and $(\mathbf{C} : \mathbf{D})_{ijkl} = C_{ijmn} D_{mnkl}$.

2 Creep constitutive equations for fiber-reinforced composites

We consider a material reinforced by aligned fibers. The unit vector in the direction of the fibers is denoted by \mathbf{n} and is used to define the axis of transverse isotropy.

The infinitesimal strain tensor ϵ is written as the sum of the elastic and the creep strains, i.e.

$$\epsilon = \epsilon^e + \epsilon^c. \quad (1)$$

The elastic strain is written in terms of the stress tensor σ as

$$\epsilon^e = \mathbf{C}^{-1} : \sigma \quad (2)$$

where \mathbf{C} is the fourth-order elasticity tensor for a linear transversely isotropic material. The elasticity tensor is of the form (Aravas, 1992)

$$\mathbf{C} = 2a \mathbf{II} + 2b \mathbf{J} + 2c \mathbf{a} \mathbf{a} + d \mathbf{P} + e (\mathbf{I} \mathbf{a} + \mathbf{a} \mathbf{I}), \quad (3)$$

where \mathbf{I} is the second order identity tensor, \mathbf{J} is the fourth-order identity tensor with cartesian components $J_{ijkl} = (\delta_{ik}\delta_{jl} + \delta_{il}\delta_{jk})/2$, \mathbf{a} is the orientation tensor $\mathbf{a} = \mathbf{n} \mathbf{n}$,

$$P_{ijkl} = \frac{1}{2}(a_{ik}\delta_{jl} + a_{il}\delta_{jk} + \delta_{ik}a_{jl} + \delta_{il}a_{jk}), \quad (4)$$

and the constants (a, b, c, d, e) are related to the standard elastic moduli $(E_{11}, \mu_{12}, \mu_{23}, K_{23}, \nu_{12})$, as defined for example in Christensen's (1979) book, by

$$a = \frac{1}{2}(K_{23} - \mu_{23}), \quad b = \mu_{23}, \quad c = \frac{1}{2}E_{11} + \frac{1}{2}\mu_{23} - 2\mu_{12} + \frac{1}{2}(1 - 2\nu_{12})^2 K_{23}, \quad (5)$$

$$d = 2(\mu_{12} - \mu_{23}), \quad e = \mu_{23} - (1 - 2\nu_{12})K_{23}. \quad (6)$$

The constitutive equation for the creep strain rate is of the form

$$\dot{\epsilon}^c = \mathbf{f}(\sigma, t) \quad (7)$$

where t is time. Time is explicitly included in the argument of \mathbf{f} so that non-steady-state response can be described. Using the representation theorems for isotropic functions, we can readily show that the most general form the last equation is (Liu, 1982; Wang, 1970a,b; Smith, 1971)

$$\dot{\epsilon}^c = a_1 \mathbf{I} + 2a_2 \sigma + 3a_3 \sigma^2 + a_4 \mathbf{a} + a_5 (\sigma \cdot \mathbf{a} + \mathbf{a} \cdot \sigma) + a_6 (\sigma^2 \cdot \mathbf{a} + \mathbf{a} \cdot \sigma^2) \equiv \mathbf{f}(\sigma, t). \quad (8)$$

where the a_i 's are functions of t , and the following five transversely isotropic invariants:

$$I_1 = \text{tr}(\sigma), \quad I_2 = \text{tr}(\sigma^2), \quad I_3 = \text{tr}(\sigma^3), \quad I_4 = \text{tr}(\sigma \cdot \mathbf{a}) = \mathbf{n} \cdot \sigma \cdot \mathbf{n}, \quad I_5 = \text{tr}(\sigma^2 \cdot \mathbf{a}) = \mathbf{n} \cdot \sigma^2 \cdot \mathbf{n}. \quad (9)$$

We assume next that the creep strain rate $\dot{\epsilon}^{\text{cr}}$ is derived from a creep potential $\Psi = \Psi(\sigma, t)$, i.e.

$$\dot{\epsilon}^{\text{cr}} = \frac{\partial \Psi}{\partial \sigma}. \quad (10)$$

The creep potential must be a transversely isotropic function, i.e. a function of the form

$$\Psi = \Psi(I_1, I_2, I_3, I_4, I_5, t). \quad (11)$$

Using the chain rule, we can readily show that

$$\dot{\epsilon}^{\text{cr}} = \frac{\partial \Psi}{\partial \sigma} = \sum_{i=1}^5 \frac{\partial \Psi}{\partial I_i} \frac{\partial I_i}{\partial \sigma} = a_1 \mathbf{I} + 2a_2 \sigma + 3a_3 \sigma^2 + a_4 \mathbf{a} + a_5 (\sigma \cdot \mathbf{a} + \mathbf{a} \cdot \sigma), \quad (12)$$

where

$$a_i = \frac{\partial \Psi}{\partial I_i}. \quad (13)$$

Note that equation (13) is a special case of the more general form (8) with $a_6 = 0$.

If the creep response of the material is incompressible, then the following equation must be satisfied

$$3a_1 + 2a_2 \sigma_{kk} + a_4 + 2a_5 \sigma_{nn} = 0 \quad (\text{no sum over } n) \quad (14)$$

for all values of σ , where $\sigma_{nn} = \mathbf{n} \cdot \sigma \cdot \mathbf{n}$.

For comparison purposes, we also consider the corresponding creep constitutive equations of an *isotropic* material. The most general form of the constitutive equation now is

$$\dot{\epsilon}^{\text{cr}} = c_1 \mathbf{I} + 2c_2 \sigma + 3c_3 \sigma^2 \quad (15)$$

where the c_i 's are functions of the isotropic stress invariants I_1 , I_2 and I_3 . The three-dimensional form of the standard 'power-law-creep' constitutive equations is

$$\dot{\epsilon}^{\text{cr}} = \frac{3}{2} \dot{\epsilon}_0 \left(\frac{\sigma_e}{\sigma_0} \right)^{n-1} \frac{\sigma'}{\sigma_0} \quad \text{corresponding to} \quad \Psi(I_1, I_2) = \frac{\sigma_0 \dot{\epsilon}_0}{n+1} \left(\frac{\sigma_e}{\sigma_0} \right)^{n+1} \quad (16)$$

where σ' is the stress deviator, $\sigma_e^2 = 1.5 \sigma'_{ij} \sigma'_{ij} = 0.5 (3I_2 - I_1^2)$ is the von Mises equivalent stress, n is the creep exponent, and $(\sigma_0, \dot{\epsilon}_0)$ are material constants. Equation (16a) is a special case of (15) with

$$c_1 = -\frac{1}{2} \frac{\dot{\epsilon}_0}{\sigma_0} \left(\frac{\sigma_e}{\sigma_0} \right)^{n-1}, \quad c_2 = -3c_1, \quad c_3 = 0. \quad (17)$$

The matrix material of the fiber-reinforced composite is assumed to obey a power-law creep equation of the form (16). Therefore, we require that (13) reduce to (16) when $\mathbf{a} = 0$, i.e. $a_3 = 0$.

Summarizing, we mention that the assumed constitutive equation for the creep strain rate of the fiber-reinforced material is

$$\dot{\epsilon}^{\text{cr}} = a_1 \mathbf{I} + 2a_2 \sigma + a_4 \mathbf{a} + a_5 (\sigma \cdot \mathbf{a} + \mathbf{a} \cdot \sigma) \equiv \mathbf{f}(\sigma, t). \quad (18)$$

3 Identification of material functions a_i

Let the coordinate axis x_3 be along the direction of the fibers, so that $\mathbf{n} = \mathbf{e}_3$, where \mathbf{e}_3 is the unit base vector along the x_3 -axis. Then the constitutive equation (18) can be written as

$$\epsilon_{ij}^{\sigma} = a_1 \delta_{ij} + 2a_2 \sigma_{ij} + a_4 \delta_{i3} \delta_{j3} + a_5 (\sigma_{i3} \delta_{j3} + \delta_{i3} \sigma_{j3}), \quad (19)$$

or, equivalently,

$$\begin{aligned} \epsilon_{11}^{\sigma} &= a_1 + 2a_2 \sigma_{11}, \\ \epsilon_{22}^{\sigma} &= a_1 + 2a_2 \sigma_{22}, \\ \epsilon_{33}^{\sigma} &= a_1 + a_4 + 2(a_2 + a_5) \sigma_{33}, \\ \epsilon_{12}^{\sigma} &= 2a_2 \sigma_{12}, \\ \epsilon_{23}^{\sigma} &= (2a_2 + a_5) \sigma_{23}, \\ \epsilon_{31}^{\sigma} &= (2a_2 + a_5) \sigma_{31}. \end{aligned} \quad (20)$$

The transversely isotropic invariants I_i now take the form

$$I_1 = \text{tr}(\boldsymbol{\sigma}), \quad I_2 = \text{tr}(\boldsymbol{\sigma}^2), \quad I_3 = \text{tr}(\boldsymbol{\sigma}^3), \quad I_4 = \sigma_{33}, \quad I_5 = \sigma_{31}^2 + \sigma_{32}^2 + \sigma_{33}^2. \quad (21)$$

An alternative set of invariants that is commonly used is (Green and Adkins, 1960)

$$J_1 = \sigma_{11} + \sigma_{22}, \quad J_2 = \sigma_{33}, \quad J_3 = \det(\boldsymbol{\sigma}), \quad J_4 = (\sigma_{11} - \sigma_{22})^2 + 4\sigma_{12}^2, \quad J_5 = \sigma_{31}^2 + \sigma_{32}^2. \quad (22)$$

Note that, if $a_5 = \partial W / \partial I_5 \equiv 0$, then the response of the material is identical under longitudinal (σ_{23}, σ_{31}) or transverse shear (σ_{12}). Equations (20) make it clear that a_2 and a_5 relate to the response of the composite under shear, whereas a_1 and a_4 refer to longitudinal and transverse tension.

4 Finite element implementation of the constitutive model

The constitutive model described in section 2 is implemented in a finite element program. In a finite element environment, the solution of the creep problem is developed incrementally and the constitutive equations are integrated at the element Gauss points. In a displacement based finite element formulation the solution is deformation driven. At a material point, the solution $(\boldsymbol{\sigma}_n, \boldsymbol{\epsilon}_n)$ at time t_n as well as the strain $\boldsymbol{\epsilon}_{n+1}$ at time $t_{n+1} = t_n + \Delta t$ are supposed to be known and one has to determine the solution $\boldsymbol{\sigma}_{n+1}$.

4.1 Numerical integration of the constitutive equations

We start with the elasticity equation (2)

$$\boldsymbol{\sigma}_{n+1} = \mathbf{C} : \boldsymbol{\epsilon}_{n+1}^e = \mathbf{C} : (\boldsymbol{\epsilon}_n^e + \Delta \boldsymbol{\epsilon} - \Delta \boldsymbol{\epsilon}^{\sigma}) = \boldsymbol{\sigma}^e - \mathbf{C} : \Delta \boldsymbol{\epsilon}^{\sigma}, \quad (23)$$

where $\Delta \epsilon = \epsilon_{n+1} - \epsilon_n$ and $\Delta \epsilon^c = \epsilon_{n+1}^c - \epsilon_n^c$ are the total- and creep-strain increments, and $\sigma^e = \sigma_n + \mathbf{C} : \Delta \epsilon$ is the (known) elastic predictor.

The creep constitutive equation (18) is integrated using a backward Euler technique, i.e.

$$\Delta \epsilon^c = \mathbf{f}(\sigma_{n+1}, t_{n+1}) \Delta t. \quad (24)$$

Combining the last two equations, we find

$$\Delta \epsilon^c = \mathbf{f}(\sigma^e - \mathbf{C} : \Delta \epsilon^c, t_{n+1}) \Delta t = 0, \quad (25)$$

which is a non-linear equation for $\Delta \epsilon^c$.

The above equation is solved for $\Delta \epsilon^c$ using Newton's method. The first estimate for $\Delta \epsilon^c$ used to start the Newton loop is obtained using a forward Euler scheme, i.e. $(\Delta \epsilon^c)_{\text{est}} = \mathbf{f}(\sigma_n, t_n) \Delta t$. The Jacobian associated with the aforementioned Newton method is given in Appendix A. Once $\Delta \epsilon^c$ is found, equation (23) defines the stress σ_{n+1} , and this completes the integration procedure.

4.2 Linearization moduli

In an implicit finite element code, the overall discretized equilibrium equations are written at the end of the increment, resulting in set of non-linear equations for the nodal unknowns. If a full Newton scheme is used to solve the global non-linear equations, one needs to calculate the so-called 'linearization moduli' \mathcal{J}

$$\mathcal{J} = \frac{\partial \sigma_{n+1}}{\partial \epsilon_{n+1}}. \quad (26)$$

For simplicity, we drop the subscript $(n+1)$, with the understanding that all quantities are evaluated at the end of the increment, unless otherwise indicated. Starting with the elasticity equation (23), we find

$$\mathcal{J} = \mathbf{C} - \mathbf{C} : \frac{\partial \Delta \epsilon^c}{\partial \epsilon}. \quad (27)$$

The derivative $\partial \Delta \epsilon^c / \partial \epsilon$ is evaluated from equation (24) as follows

$$\frac{\partial \Delta \epsilon^c}{\partial \epsilon} = \frac{\partial \Delta \epsilon^c}{\partial \sigma} : \frac{\partial \sigma}{\partial \epsilon} = \Delta t \frac{\partial \mathbf{f}}{\partial \sigma} : \mathcal{J}. \quad (28)$$

Substituting the last equation into (27) and solving for \mathcal{J} , we find

$$\mathcal{J} = \left(\mathbf{J} + \Delta t \mathbf{C} : \frac{\partial \mathbf{f}}{\partial \sigma} \right)^{-1} : \mathbf{C}. \quad (29)$$

It can be readily shown that the derivative $\partial \mathbf{f} / \partial \sigma$ is given by

$$\frac{\partial \mathbf{f}}{\partial \sigma} = \mathbf{I} \mathbf{I} + 2(2b_2 \sigma \sigma + a_2 \mathbf{J}) + 3(3b_3 \sigma^2 \sigma^2 + a_3 \mathbf{B}) + b_4 \mathbf{a} \mathbf{a} + b_5 (\sigma \cdot \mathbf{a} + \mathbf{a} \cdot \sigma)(\sigma \cdot \mathbf{a} + \mathbf{a} \cdot \sigma) + a_5 \mathbf{D}, \quad (30)$$

where

$$b_i = \frac{\partial a_i}{\partial I_i} \quad (\text{no sum over } i), \quad B_{ijkl} = \delta_{ik} \sigma_{jl} + \sigma_{ik} \delta_{jl}, \quad \text{and} \quad D_{ijkl} = a_{ik} \sigma_{jl} + \sigma_{ik} a_{jl}. \quad (31)$$

Equations (30) and (31) show that $\partial f_{ij}/\partial \sigma_{kl}$ is symmetric with respect to the pair of indices (i, j) and (k, l) . Therefore, in view of (30) and the usual symmetries of the elasticity tensor \mathbf{C} , one can readily show that the Jacobian \mathcal{J}_{ijkl} is also symmetric with respect to (i, j) and (k, l) , which leads to a symmetric 'stiffness matrix' in the finite element computations.

5 An analytical model for creeping fiber-reinforced materials

De Botton and Perte Castañeda (1992) have presented recently a constitutive model for non-linear fiber-reinforced composite materials. They developed their model in the context of infinitesimal non-linear elasticity, but their results can be used to describe steady-state creep as well. For the special case in which both the matrix and the fibers creep according to a 'power-law' relationship of the form of equation (16), their model can be summarized as follows.

Let the creep potentials for the matrix and the fibers be of the form

$$\Psi^{(k)}(\sigma_e) = \frac{\sigma_{0k} \dot{\epsilon}_{0k}}{n_k + 1} \left(\frac{\sigma_e}{\sigma_{0k}} \right)^{n_k + 1}, \quad k = 1, 2, \quad (32)$$

where $k = 1$ refers to the matrix and $k = 2$ to the fibers. For the case where $n_1 > n_2$, the creep potential of the composite is estimated to be

$$\Psi(I_1, I_2, I_4) = \min_{\omega, \eta} \left[c_1 \Psi^{(1)}(\sigma_e^{(1)}) + c_2 \Psi^{(2)}(\sigma_e^{(2)}) \right], \quad (33)$$

where

$$\begin{aligned} \sigma_e^{(1)}(\boldsymbol{\sigma}, \omega, \eta) &= \left[(1 + c_2 \omega)^2 \sigma_s^2 + (1 + c_2 \eta)^2 \sigma_d^2 \right]^{1/2}, \\ \sigma_e^{(2)}(\boldsymbol{\sigma}, \omega, \eta) &= \left[(1 - c_1 \omega)^2 \sigma_s^2 + (1 - c_1 \eta)^2 \sigma_d^2 \right]^{1/2}, \\ \sigma_s^2(\boldsymbol{\sigma}) &= \frac{1}{2} (3 I_2 - I_1^2) - \frac{1}{4} (I_1 - 3 I_4)^2, \\ \sigma_d^2(\boldsymbol{\sigma}) &= \frac{1}{4} (I_1 - 3 I_4)^2, \end{aligned} \quad (34)$$

c_1 and c_2 being the volume fractions of the matrix and the fibers respectively ($c_1 + c_2 = 1$).

Note that Ψ is independent of I_5 , which implies that the predicted response of the composite will be the same under longitudinal and transverse shear.

6 Comparison with results of homogenization theory

The predictions of the constitutive model described in the previous section are compared here with the results of the homogenization theory (Sanchez-Palencia, 1980). The homogenization techniques were developed originally in the context of linear elasticity, but they can be easily extended to infinitesimal non-linear elasticity (Jansson, 1992).

The comparisons are carried out for non-linear elastic materials, for which the model of De Botton and Ponte Castañeda (1992) has been developed.

6.1 Homogenization theory

In the following, we briefly summarize some of the results of homogenization theory as developed by Sanchez Palencia (1980) (see also Lene and Leguillon, 1982; Lene, 1986; Jansson, 1992).

Consider an inhomogeneous body which is made of two different non-linear elastic constituents. The composite material is assumed to have *periodic* structure, i.e. its constituents are arranged in such a way that the composite can be constructed by the periodic repetition of self-similar elements. We define the 'unit cell' as the smallest such repeatable element. The characteristic length l of the unit cell is assumed to be small compared to any characteristic dimension L of the body, i.e.

$$\delta = \frac{l}{L} \ll 1. \quad (35)$$

Let \mathbf{x} denote the position vector with respect to a fixed global cartesian coordinate system. A local variable \mathbf{y} is introduced for the unit cell by

$$\mathbf{y} = \frac{\mathbf{x}}{\delta} \quad \text{or} \quad \mathbf{x} = \delta \mathbf{y}. \quad (36)$$

Note that a change of $O(1)$ in \mathbf{y} corresponds to a $O(\delta)$ change in \mathbf{x} .

The constitutive equation of the material can be now written at any point \mathbf{y} within the unit cell as

$$\boldsymbol{\sigma} = \mathbf{f}(\boldsymbol{\epsilon}, \mathbf{y}). \quad (37)$$

Next we search for an asymptotic expansion of the displacement field \mathbf{u} as $\delta \rightarrow 0$. A two-scale expansion of the form (Sanchez Palencia, 1980)

$$\mathbf{u}(\mathbf{x}, \mathbf{y}) = \mathbf{u}^{(0)}(\mathbf{x}) + \delta \mathbf{u}^{(1)}(\mathbf{x}, \mathbf{y}) + O(\delta^2) \quad (38)$$

is attempted. The functions $\mathbf{u}^{(1)}$, $\mathbf{u}^{(2)}$ etc., are assumed to be periodic functions, consistent with the periodicity of the microstructure, i.e.

$$\mathbf{u}^{(k)}(\mathbf{x}, \mathbf{y} + \mathbf{l}_i) = \mathbf{u}^{(k)}(\mathbf{x}, \mathbf{y}), \quad k = 1, 2, \dots, \quad \text{and} \quad i = 1, 2, 3 \quad (39)$$

where \mathbf{l}_i is the characteristic length-vector of the unit cell in the i -th coordinate direction. Functions of the type of equation (39) will be referred to in the following as \mathbf{Y} -periodic.

The corresponding strain and stress expansions are of the form

$$\begin{aligned}\epsilon(\mathbf{x}, \mathbf{y}) &= \epsilon^{(0)}(\mathbf{x}, \mathbf{y}) + O(\delta), \\ \sigma(\mathbf{x}, \mathbf{y}) &= \sigma^{(0)}(\mathbf{x}, \mathbf{y}) + O(\delta).\end{aligned}\quad (40)$$

where

$$\begin{aligned}\epsilon^{(0)}(\mathbf{x}, \mathbf{y}) &= \mathbf{E}^{x(0)}(\mathbf{x}) + \mathbf{E}^{y(1)}(\mathbf{x}, \mathbf{y}), \\ \sigma^{(0)}(\mathbf{x}, \mathbf{y}) &= \mathbf{f}(\epsilon^{(0)}, \mathbf{y}),\end{aligned}\quad (41)$$

with

$$E_{ij}^{x(k)} = \frac{1}{2} \left(\frac{\partial u_i^{(k)}}{\partial x_j} + \frac{\partial u_j^{(k)}}{\partial x_i} \right) \quad \text{and} \quad E_{ij}^{y(k)} = \frac{1}{2} \left(\frac{\partial u_i^{(k)}}{\partial y_j} + \frac{\partial u_j^{(k)}}{\partial y_i} \right). \quad (42)$$

The equilibrium equations can be written, to leading order, as

$$\frac{\partial \sigma_{ji}^{(0)}}{\partial y_j} = 0. \quad (43)$$

Note that the coordinate \mathbf{x} is *constant* at the unit cell level, where positions are described in terms of \mathbf{y} . The above equations can be used to define a boundary value problem over the unit cell as follows. Let $\hat{\mathbf{u}}(\mathbf{y})$, $\hat{\epsilon}(\mathbf{y})$ and $\hat{\sigma}(\mathbf{y})$ be the displacements, strains, and stresses of the unit cell. Then, the above equations can be recasted in the following form

$$\begin{aligned}\hat{\mathbf{u}}(\mathbf{y}) &= \mathbf{E}^{x(0)}(\mathbf{x}) \cdot \mathbf{y} + \mathbf{u}^{(1)}(\mathbf{x}, \mathbf{y}), \\ \hat{\epsilon}_{ij}(\mathbf{y}) &\equiv \epsilon_{ij}^{(0)} = \frac{1}{2} \left(\frac{\partial \hat{u}_i}{\partial y_j} + \frac{\partial \hat{u}_j}{\partial y_i} \right), \\ \hat{\sigma}(\mathbf{y}) &\equiv \sigma^{(0)} = \mathbf{f}(\hat{\epsilon}, \mathbf{y}), \\ \frac{\partial \hat{\sigma}_{ji}}{\partial y_j} &= 0,\end{aligned}\quad (44)$$

where the macroscopic strain field $\mathbf{E}^{x(0)}(\mathbf{x})$ is *constant* at the unit cell level, and $\mathbf{u}^{(1)}$ is Y-periodic.

For any function $\phi(\mathbf{x}, \mathbf{y})$, we define

$$\langle \phi \rangle = \frac{1}{|Y|} \int_Y \phi(\mathbf{x}, \mathbf{y}) dV_y, \quad (45)$$

where Y denotes the unit cell, and note that, in view of the Y-periodicity of $\mathbf{u}^{(1)}$,

$$\langle \hat{\epsilon} \rangle = \mathbf{E}^{x(0)}(\mathbf{x}). \quad (46)$$

Next, we consider the Y-averages of the global strain and stress fields

$$\begin{aligned}\langle \epsilon \rangle &= \mathbf{E}^{x(0)} + O(\delta), \\ \langle \sigma \rangle &= \langle \sigma^{(0)} \rangle + O(\delta).\end{aligned}\quad (47)$$

Let $\langle \epsilon \rangle^{(0)}$ and $\langle \sigma \rangle^{(0)}$ be the leading terms in the above expansions. We would like to determine the relationship between $\langle \epsilon \rangle^{(0)}$ and $\langle \sigma \rangle^{(0)}$, i.e. an equation of the form

$$\langle \sigma \rangle^{(0)} = g(\langle \epsilon \rangle^{(0)}) \quad (48)$$

in which the desired function g would define the constitutive equation of the composite, to leading order. We note next that

$$\langle \sigma \rangle^{(0)} = \langle \sigma^{(0)} \rangle = \langle \dot{\sigma} \rangle \quad (49)$$

and, in view of equation (46),

$$\langle \epsilon \rangle^{(0)} = \mathbf{E}^{r(0)} = \langle \dot{\epsilon} \rangle. \quad (50)$$

The desired equation (48) can be now written as

$$\langle \dot{\sigma} \rangle = g(\langle \dot{\epsilon} \rangle). \quad (51)$$

The last equation shows that the unknown function g can be determined from the solution of the unit cell problem defined by equations (44).

6.2 Numerical solution of the unit cell problem

We consider a composite material made of a non-linear elastic matrix reinforced by continuous aligned fibers, which are also assumed to be non-linear elastic. The constitutive equations for the matrix and the fibers are of the form

$$\epsilon = \frac{3}{2} \epsilon_{0k} \left(\frac{\sigma_e}{\sigma_{0k}} \right)^{n_k-1} \frac{\sigma'}{\sigma_{0k}}, \quad \Psi^{(k)}(\sigma_e) = \frac{\sigma_{0k} \epsilon_{0k}}{n_k + 1} \left(\frac{\sigma_e}{\sigma_{0k}} \right)^{n_k+1}, \quad k = 1, 2. \quad (52)$$

The distribution of the fibers is assumed to be periodic, with the fibers arranged in a hexagonal array as shown in Fig. 1; the dash lines in Fig. 1 indicate the corresponding unit cell.

The loadings considered coincide with the principal material directions; therefore, in view of the resulting symmetries, only one quarter of the unit cell needs to be analyzed. Let the y_3 -coordinate-axis be aligned with the fibers. The following four types of loading are considered:

1. Longitudinal tension: $\sigma_{33} \neq 0$, all other $\sigma_{ij} = 0$,
2. Transverse tension: $\sigma_{11} \neq 0$, all other $\sigma_{ij} = 0$,
3. Transverse shear: $\sigma_{12} = \sigma_{21} \neq 0$, all other $\sigma_{ij} = 0$,
4. Longitudinal shear: $\sigma_{31} = \sigma_{13} \neq 0$, all other $\sigma_{ij} = 0$,

where all stress components are meant to represent the *macroscopic* loading $\langle \sigma^{(0)} \rangle$. The exact form of the boundary conditions used in the unit cell formulation are presented in Appendix B.

The unit cell problem defined by equations (44) is solved using the ABAQUS general purpose finite element program (Hibbitt, 1984). The calculations are carried out for $n_1 = 10$, $n_2 = 3$, $\sigma_{01} = \sigma_{02} = \sigma_0$ and $\epsilon_{01} = \epsilon_{02} = \epsilon_0 = 10^{-5}$. The 'deformation plasticity' model in ABAQUS has an additional 'linear-elastic' term on the right hand side of equation (52a); the elastic moduli used in the finite element computations are four orders of magnitude larger than σ_0 , so that the role of linear elasticity becomes secondary. For the solution of problems 1, 2 and 3 listed above, four-node isoparametric generalized plane strain elements with 2×2 Gauss integration and an independent interpolation for the dilatation rate are used in order to avoid artificial constraints on incompressible modes (Nagtegaal et al., 1974). Problem 4 is solved using three-dimensional eight-node finite elements with $2 \times 2 \times 2$ Gauss integration and an independent interpolation for the dilatation rate.

The volume fraction of the fibers is 39.5%, i.e. $c_2 = 0.395$, $c_1 = 0.605$. Figure 2 shows the finite element mesh used for problems 1, 2 and 3; the dark and white regions in Fig. 2 represent the fibers and the matrix respectively. The layout shown in Fig. 2 is repeated in the third direction to produce the layer of three-dimensional elements used for the solution of problem 4.

Figure 3 shows the calculated longitudinal stress-strain curve. In Figure 3, and in all subsequent figures, the circles correspond to the prediction of the model of De Botton and Castañeda, whereas the dash line is the result of the finite element calculations. The predictions of the analytical model agree well with the finite element solution.

Figure 4 shows the calculated transverse stress-strain curve. At a transverse strain $\epsilon_{11} = 0.01$, there is a 7% difference between the prediction of the analytical model and the finite element solution.

Figure 5 shows the transverse shear stress-strain response. At a transverse shear strain $\epsilon_{11} = \gamma_{12}/2 = 0.01$, there is a 13% difference between the prediction of the analytical model and the finite element solution.

The finite element solution of problem 4 (longitudinal shear) produces a shear stress-strain curve identical to that shown in Fig. 5 for the transverse shear. This is consistent with the structure of the analytical model which also predicts identical response to longitudinal and transverse shear.

Figures 3-5 show that, at a given strain level, the stress predicted by the analytical model is always higher than that of the finite element solution. This is consistent with the fact that the complementary elastic energy function Ψ developed by De Botton and Ponte Castañeda is an upper bound to the actual complementary energy of the composite. It should be also noted that the model of De Botton and Ponte Castañeda is developed for a transversely isotropic composite with a *random* distribution of fibers, whereas the unit cell calculations refer to a composite with a certain *periodic* microstructure (hexagonal array).

Acknowledgments

Fruitful discussions with Profs. De Botton and P. Ponte Castañeda are gratefully acknowledged. This study was supported by the Office of Naval Research contract N00014-92-J-1808 through sub-agreement KK3006 from the University of California, Santa Barbara. The ABAQUS finite element code was made available under academic license from Hibbitt, Karlsson and Sorensen, Inc., Providence, RI.

References

- [1] Aravas, N., 'Finite elastoplastic transformations of transversely isotropic metals', *Int. J. Solids Struct.*, **29**, 2137-2157 (1992).
- [2] De Botton, G. and Ponte Castañeda, P., 'Elastoplastic constitutive relations for fiber-reinforced solids', to appear (1992).
- [3] Christensen, R. M., *Mechanics of Composite Materials*. Wiley, New York (1979).
- [4] Green, A. H. and Adkins, J. E., *Large Elastic Deformations*. Clarendon Press, Oxford (1960).
- [5] Hibbitt, H. D., 'ABAQUS/EPGEN — A general purpose finite element code with emphasis on nonlinear applications', *Nucl. Eng. Des.*, **77**, 271-297 (1984).
- [6] Jansson, S., 'Mechanical characterization and modeling of non-linear deformation and fracture of a fiber reinforced metal matrix composite', *Mech. Mater.*, **12**, 47-62 (1991).
- [7] Jansson, S., 'Homogenized nonlinear constitutive properties and local stress concentrations for composites with periodic internal structure', *Int. J. Solids Struct.*, **29**, 2181-2200 (1992).
- [8] Johnson, A. F., 'Creep characterization of transversely-isotropic metallic materials', *J. Mech. Phys. Solids*, **25**, 117-126 (1977).
- [9] Lene, F., 'Damage constitutive relations for composite materials', *Engng Fract. Mech.*, **25**, 713-728 (1986).
- [10] Lene, F. and Leguillon, D., 'Homogenized constitutive law for a partially cohesive composite', *Int. J. Solids Struct.*, **18**, 443-458 (1982).
- [11] Liu, I.-S., 'On representations of anisotropic invariants', *Int. J. Engng Sci.*, **20**, 1099-1109 (1982).
- [12] McMeeking, R. M., 'Models for the creep of ceramic matrix composite materials', to appear (1992).

- [13] Nagtegaal, J. D., Parks, D. M. and Rice, J. R., 'On numerically accurate finite element solutions in the fully plastic range', *Comp. Methods Appl. Mech. Eng.*, **4**, 153-177 (1974).
- [14] Sanchez Palencia, E., *Non-homogeneous media and vibration theory. Lecture Notes in Physics*, Vol. 127, Springer-Verlag, Berlin (1980).
- [15] Smith, G. F., 'On isotropic functions of symmetric tensors, skew-symmetric tensors and vectors', *Int. J. Engng Sci.*, **9**, 899-1916 (1971).
- [16] Wang, C.-C., 'A new representation theorem for isotropic functions: an answer to Professor G. F. Smith's criticism of my papers on representations of isotropic functions. Part 1. Scalar-valued isotropic functions', *Archs Ration. Mech. Anal.*, **36**, 166-197 (1970a).
- [17] Wang, C.-C., 'A new representation theorem for isotropic functions: an answer to Professor G. F. Smith's criticism of my papers on representations of isotropic functions. Part 2. Vector-valued isotropic functions, symmetric tensor-valued isotropic functions, and skew-symmetric tensor-valued isotropic functions', *Archs Ration. Mech. Anal.*, **36**, 198-223 (1970b).
- [18] Weber, C. H., Löfvander, J. P. A. and Evans, A. G., 'The creep behavior of CAS/Nicalon continuous-fiber composites', to appear (1992).
- [19] Weber, C. H., Yang, J. Y., Löfvander, J. P. A., Levi, C. G. and Evans, A. G., 'The creep and fracture resistance of γ -TiAl reinforced with Al_2O_3 fibers', to appear (1992).

Appendix A

Let $\mathbf{F}(\Delta\epsilon^{\sigma}) = \mathbf{0}$ be the non-linear equation (25) to be solved for $\Delta\epsilon^{\sigma}$, i.e.

$$\mathbf{F}(\Delta\epsilon^{\sigma}) = \Delta\epsilon^{\sigma} - \mathbf{f}(\boldsymbol{\sigma}(\Delta\epsilon^{\sigma}), t) \Delta t = \mathbf{0}, \quad (53)$$

where $\boldsymbol{\sigma}(\Delta\epsilon^{\sigma}) = \boldsymbol{\sigma}^e - \mathbf{C} : \Delta\epsilon^{\sigma}$. The above equation is solved for $\Delta\epsilon^{\sigma}$ using Newton's method. The corresponding Jacobian is

$$\frac{\partial \mathbf{F}}{\partial \Delta\epsilon^{\sigma}} = \mathbf{J} - \Delta t \frac{\partial \mathbf{f}}{\partial \boldsymbol{\sigma}} : \frac{\partial \boldsymbol{\sigma}}{\partial \Delta\epsilon^{\sigma}} = \mathbf{J} + \Delta t \frac{\partial \mathbf{f}}{\partial \boldsymbol{\sigma}} : \mathbf{C}. \quad (54)$$

Appendix B

The boundary conditions used in the four unit cell problems listed in section 6.2 are described in the following. We mention again that the macroscopic strain $\mathbf{E}^{x(0)}$ is constant at the unit cell level. We refer to the coordinate axes (y_1, y_2) shown in Fig. 2, and let h be the thickness of the unit cell in the y_3 -direction.

1. Longitudinal shear.

$$\begin{aligned} y_1 = 0 : \quad \hat{u}_1 &= 0, \\ y_2 = 0 : \quad \hat{u}_2 &= 0, \\ y_3 = 0 : \quad \hat{u}_3 &= 0, \\ y_1 = b\sqrt{3} : \quad \hat{u}_1 &= E_{11}^{x(0)} b\sqrt{3} \quad \text{and} \quad \int_0^b \hat{\sigma}_{11} dy_2 = 0, \\ y_2 = b : \quad \hat{u}_2 &= E_{22}^{x(0)} b \quad \text{and} \quad \int_0^{b\sqrt{3}} \hat{\sigma}_{22} dy_1 = 0, \\ y_3 = h : \quad \hat{u}_3 &= E_{33}^{x(0)} h \quad \text{and} \quad \frac{1}{A} \int_A \hat{\sigma}_{33} dA = \langle \sigma_{33}^{(0)} \rangle, \end{aligned} \quad (55)$$

where A is the area of the finite element mesh on the $y_1 - y_2$ plane shown in Fig. 2.

The macroscopic strain component $E_{33}^{x(0)}$ is applied, and the corresponding $\langle \sigma_{33}^{(0)} \rangle$, $E_{11}^{x(0)}$ and $E_{22}^{x(0)}$ are determined.

2. Transverse tension

$$\begin{aligned} y_1 = 0 : \quad \hat{u}_1 &= 0, \\ y_2 = 0 : \quad \hat{u}_2 &= 0, \end{aligned}$$

$$\begin{aligned}
y_3 = 0 : \quad \dot{u}_3 &= 0, \\
y_1 = b\sqrt{3} : \quad \dot{u}_1 &= E_{11}^{x(0)} b\sqrt{3} \quad \text{and} \quad \frac{1}{b} \int_0^b \dot{\sigma}_{11} dy_2 = \langle \sigma_{11}^{(0)} \rangle, \\
y_2 = b : \quad \dot{u}_2 &= E_{22}^{x(0)} b \quad \text{and} \quad \int_0^{b\sqrt{3}} \dot{\sigma}_{22} dy_1 = 0, \\
y_3 = h : \quad \dot{u}_3 &= E_{33}^{x(0)} h \quad \text{and} \quad \int_A \dot{\sigma}_{33} dA = 0.
\end{aligned} \tag{56}$$

The macroscopic strain component $E_{11}^{x(0)}$ is applied, and the corresponding $\langle \sigma_{11}^{(0)} \rangle$, $E_{22}^{x(0)}$ and $E_{33}^{x(0)}$ are determined.

3. Transverse shear.

$$\begin{aligned}
y_1 = 0 : \quad \dot{u}_2 &= 0, \\
y_2 = 0 : \quad \dot{u}_1 &= 0, \\
y_3 = 0 : \quad \dot{u}_3 &= 0, \\
y_1 = b\sqrt{3} : \quad \dot{u}_2 &= E_{21}^{x(0)} b\sqrt{3} \quad \text{and} \quad \frac{1}{b} \int_0^b \dot{\sigma}_{12} dy_2 = \langle \sigma_{12}^{(0)} \rangle, \\
y_2 = b : \quad \dot{u}_1 &= E_{12}^{x(0)} b \quad \text{and} \quad \frac{1}{b\sqrt{3}} \int_0^{b\sqrt{3}} \dot{\sigma}_{21} dy_1 = \langle \sigma_{21}^{(0)} \rangle, \\
y_3 = h : \quad \int_A \dot{\sigma}_{33} dA &= 0.
\end{aligned} \tag{57}$$

4. Longitudinal shear.

$$\begin{aligned}
y_1 = 0 : \quad \dot{u}_2 &= \dot{u}_3 = 0, \\
y_2 = 0 : \quad \dot{u}_2 &= 0, \\
y_3 = 0 : \quad \dot{u}_1 &= \dot{u}_3 = 0, \\
y_1 = b\sqrt{3} : \quad \dot{u}_2 &= 0, \quad \dot{u}_3 = E_{31}^{x(0)} b\sqrt{3} \quad \text{and} \quad \frac{1}{b} \int_0^b \dot{\sigma}_{13} dy_2 = \langle \sigma_{13}^{(0)} \rangle, \\
y_2 = b : \quad \dot{u}_2 &= 0, \\
y_3 = h : \quad \dot{u}_1 &= E_{13}^{x(0)} h, \quad \dot{u}_2 = 0 \quad \text{and} \quad \frac{1}{A} \int_A \dot{\sigma}_{31} dA = \langle \sigma_{31}^{(0)} \rangle.
\end{aligned} \tag{58}$$

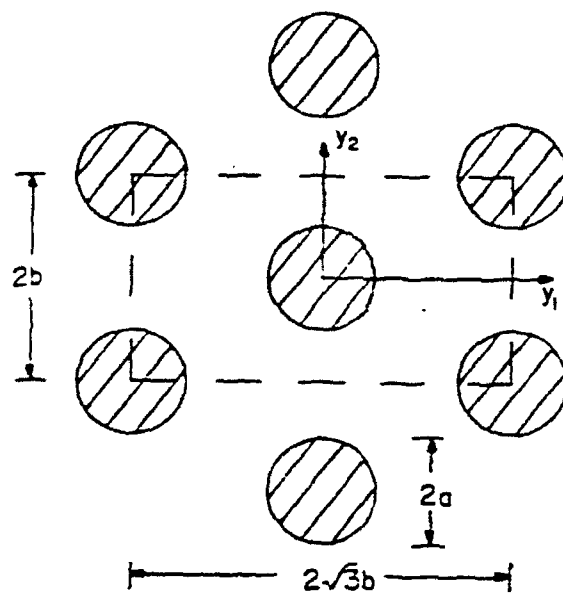


Fig. 1

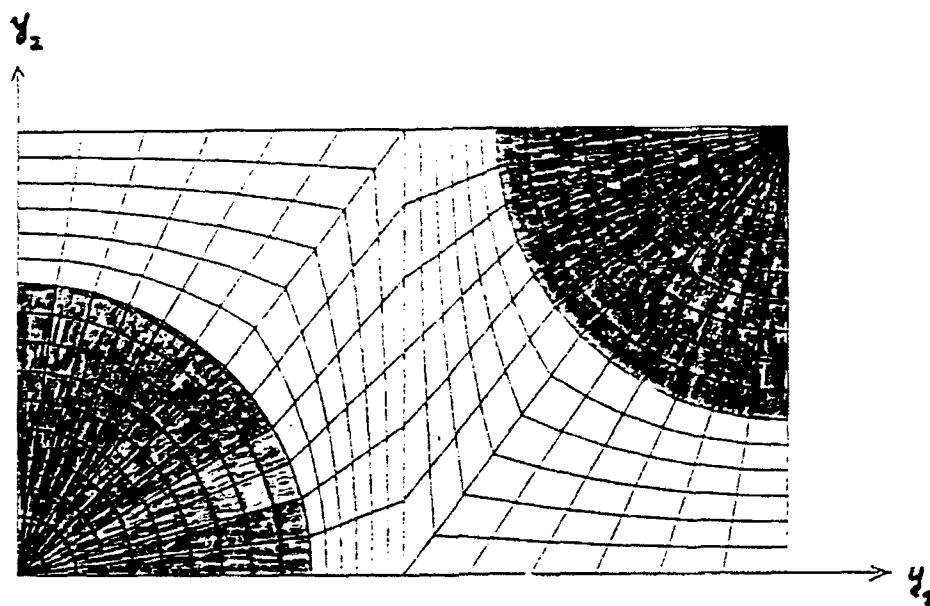


Fig. 2

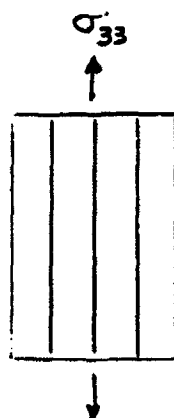
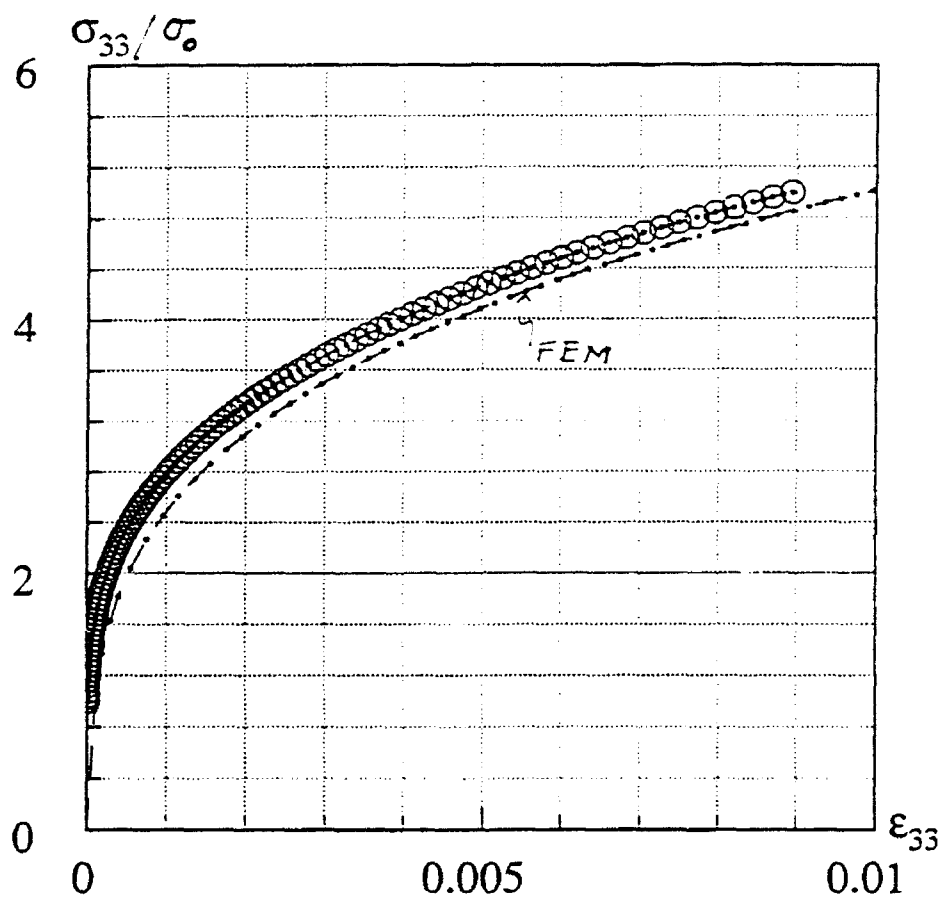


Fig. 3

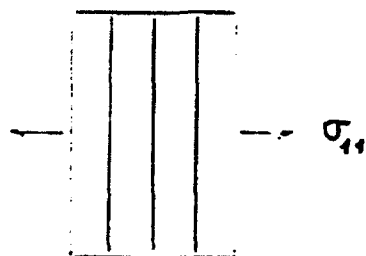
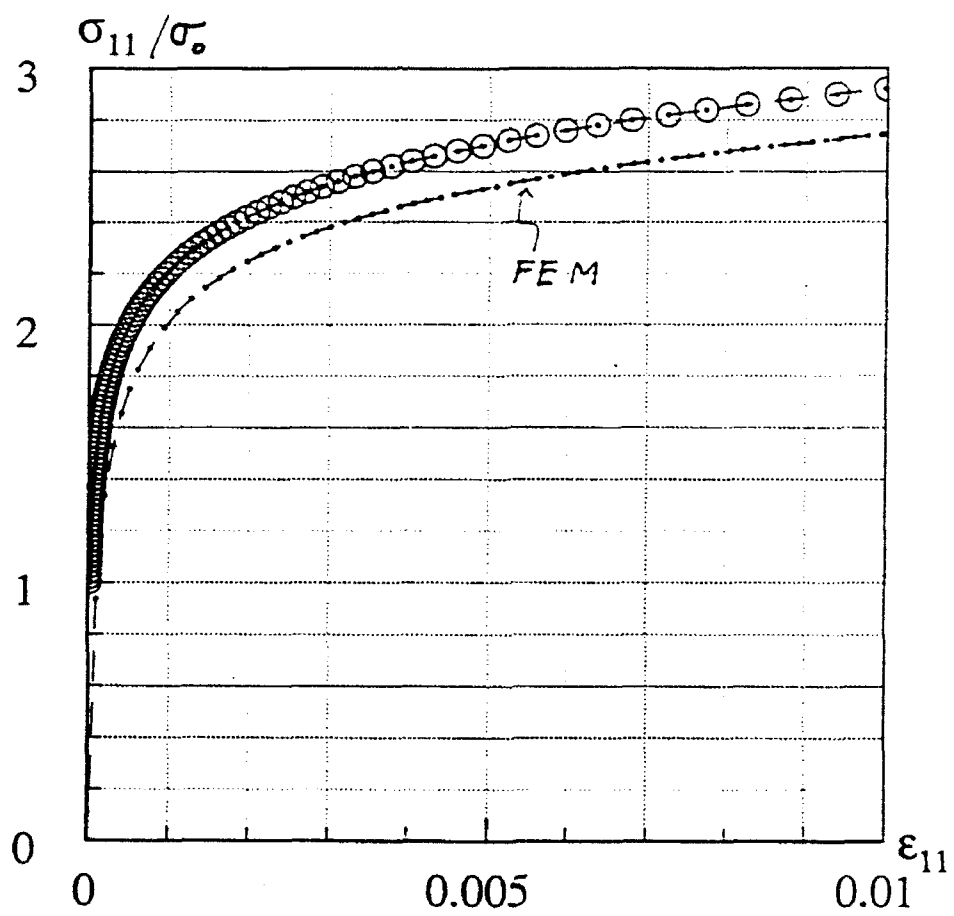


Fig 4

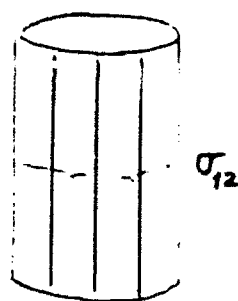
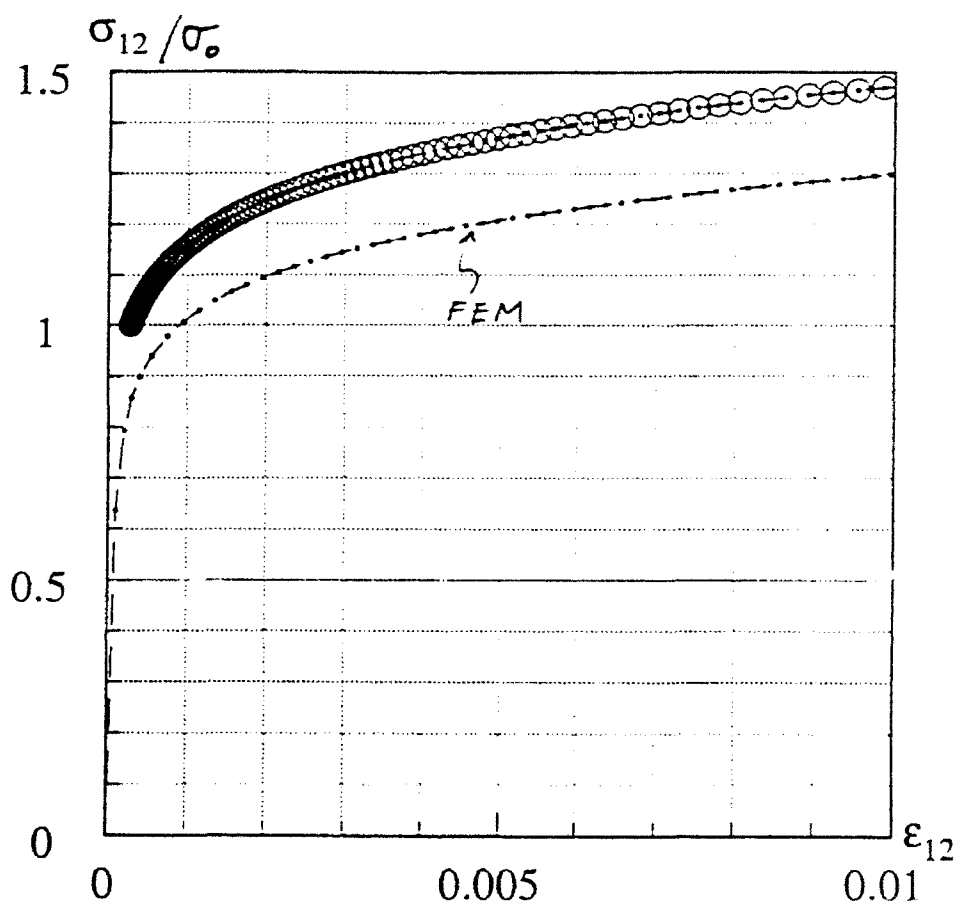


Fig. 5



ON NEUTRAL HOLES IN TAILORED, LAYERED SHEETS

B. Budiansky, J. W. Hutchinson and A G. Evans

Division of Applied Sciences
HARVARD UNIVERSITY
Cambridge, Massachusetts 02138

August 1992

On Neutral Holes in Tailored, Layered Sheets

by

B. Budiansky*, J. W. Hutchinson*, and A. G. Evans**

*Division of Applied Sciences, Harvard University, Cambridge, MA 02138

**Materials Department, University of California, Santa Barbara, CA 93106

It has been suggested that multilayered sheets, in which alternating layers have different elastic moduli, might lend themselves to *tailoring* to reduce, or even eliminate, harmful stress concentrations at holes or other stress raisers. Such tailoring could be implemented by making the sheet thickness spatially nonuniform, varying the *number* of layers, but keeping the layering pattern unchanged; or, keeping the total thickness unchanged, by varying the pattern of layer locations and thicknesses; or by a combination of these two approaches. We will call the first method "thickness tailoring", and the second "modulus tailoring". Tailored fabrication of such nonuniform layered sheets seems particularly well suited to masked deposition techniques.

This note provides a preliminary analytical assessment of the theoretical feasibility of designing a tailored, layered sheet that would alleviate the stress concentration induced by a circular hole in a field of balanced biaxial tension (see Fig. 1). If the stress concentration is actually eliminated, the result is a so-called "neutral" hole. It should be emphasized at the outset that reducing the *average* circumferential stress at the boundary of the hole is definitely not necessarily the desired goal. As we shall see, if modulus tailoring with constant overall thickness is exploited, and only the relative volumes of the layer constituents are changed, the stresses within the individual layers can be reduced while the average stress goes up! (This seemingly paradoxical result takes a little getting used to; the reason it's right is that while the stress in the stiffer material drops, there is more of it, so the average rises.) Conversely, a misguided reduction of the average hole-boundary stress by means of modulus tailoring can lead to higher stress concentrations within the layers.

We consider a two-constituent layered sheet, with Young's moduli E_α ($\alpha=1,2$) in the alternating layers, and for simplicity, we assume the same Poisson's ratio ν in each layer. The effective sheet modulus is $E=f_1E_1 + f_2E_2$, where the f 's are volume fractions. At each r , denote the average radial and circumferential stresses by σ_r and σ_θ , and let $\sigma_r^{(\alpha)}$, $\sigma_\theta^{(\alpha)}$ ($\alpha=1,2$) be the stresses in the layers. The stress-strain relations are

$$\begin{aligned}\epsilon_r &= \frac{\sigma_r^{(\alpha)} - \nu\sigma_\theta^{(\alpha)}}{E_\alpha} = \frac{\sigma_r - \nu\sigma_\theta}{E(r)} \\ \epsilon_\theta &= \frac{\sigma_\theta^{(\alpha)} - \nu\sigma_r^{(\alpha)}}{E_\alpha} = \frac{\sigma_\theta - \nu\sigma_r}{E(r)}\end{aligned}\tag{1}$$

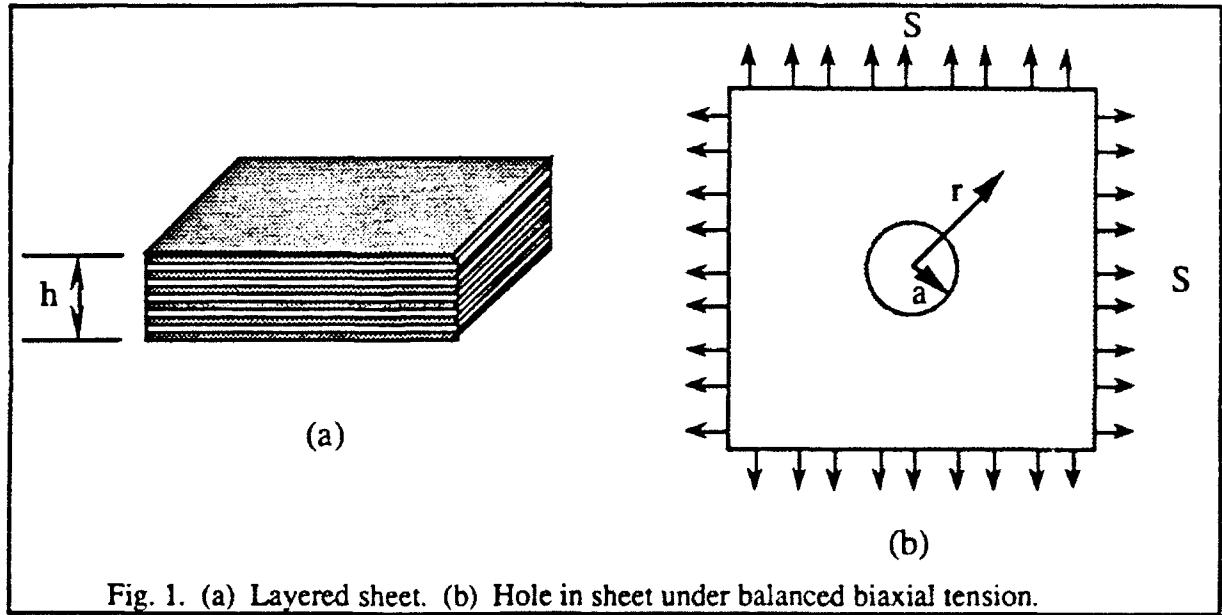


Fig. 1. (a) Layered sheet. (b) Hole in sheet under balanced biaxial tension.

Let

$$\sigma_r = \frac{E(r)}{E(\infty)} s_r, \quad \sigma_\theta = \frac{E(r)}{E(\infty)} s_\theta \quad (2)$$

where $E(\infty)$ is the untailored sheet modulus far from the hole. Then

$$\sigma_r^{(\alpha)} = \frac{E_\alpha}{E(\infty)} s_r, \quad \sigma_\theta^{(\alpha)} = \frac{E_\alpha}{E(\infty)} s_\theta \quad (3)$$

and so the layer stresses are proportional to s_r and s_θ . Hence, it is the value of s_θ at $r=a$ that we must seek to lower by tailoring $E(r)$, or the sheet thickness $h(r)$, or both. Note that while the stress concentration factor (SCF) for the *average* sheet stress σ_θ is $\sigma_\theta(a)/S$, the *layer* concentration factors are

$$\frac{\sigma_\theta^{(\alpha)}(a)}{\sigma_\theta^{(\alpha)}(\infty)} = \frac{s_\theta(a)}{s_\theta(\infty)} = \frac{s_\theta(a)}{S} \quad (4)$$

For a *uniform* layered sheet, these layer concentration factors are equal to the classical stress concentration factor $\sigma_\theta(a)/S = 2$.

The equations of equilibrium and compatibility are

$$\frac{d(rh\sigma_r)}{dr} = h\sigma_\theta \quad (5)$$

and

$$\frac{d(r\epsilon_\theta)}{dr} = \epsilon_r \quad (6)$$

respectively. These may be rewritten as

$$[\lambda \rho s_r]' = \lambda s_\theta \quad (7)$$

$$[\rho(s_\theta - \nu s_r)]' = s_r - \nu s_\theta \quad (8)$$

in terms of $\rho \equiv r/a$, and the *tailoring function* defined by

$$\lambda(r) \equiv \frac{E(r) h(r)}{E(\infty) h(\infty)} \quad (9)$$

Primes denote derivatives with respect to ρ .

We proceed in a semi-inverse fashion by asserting the spatial distribution

$$s_r = S(1 - \rho^{-n}) \quad (10)$$

and solving the compatibility equation (8) for s_θ to get

$$s_\theta = S \left[1 + \frac{1 - v(n-1)}{(n-1-v)\rho^n} - \frac{C}{\rho^{(1+v)}} \right] \quad (11)$$

where C is a constant. The only value of C that leads to a bounded tailoring function is

$$C = \frac{2n - n^2}{n - 1 - v} \quad (12)$$

and this gives the layer stress concentration factor $s_\theta/S = n$ at $\rho=1$. The tailoring formula

$$\lambda(r) = \exp \left[\frac{n(2-n)}{n-1-v} \int_0^{a/r} \frac{x^v - x^{n-1}}{1-x^n} dx \right] \quad (13)$$

follows from the equilibrium equation (7). In all cases the peak value of $\lambda(r)$, as expected, occurs at $r=a$, and is given by

$$\begin{aligned} \lambda(a) &= \exp \left[\frac{n(2-n)}{n-1-v} \int_0^1 \frac{x^v - x^{n-1}}{1-x^n} dx \right] \quad (n \neq 1+v) \\ &= \exp \left[-(1-v^2) \int_0^1 \frac{x^v \log x}{1-x^n} dx \right] \quad (n = 1+v) \end{aligned} \quad (14)$$

For $v=0$ this last result equals $\exp(\pi^2/6)$.

Fig. 2 shows how the peak tailoring magnitude varies with the layer stress concentration factor n , for several values of v . We remark that if only thickness tailoring is used, the SCF for average stress is the same as that for the layers, and so is also reduced below 2. But for pure modulus tailoring, the SCF for the average stress is given by $n\lambda(a)$, and this always exceeds 2 for $n < 2$.

To get a neutral hole, we set $n=1$ in the formula for $\lambda(r)$, and find

$$\lambda_{\text{neutral}}(r) = \exp \left[\frac{1}{v} \int_0^{a/r} \frac{1-x^v}{1-x} dx \right] \quad (15)$$

For $v=0$, this result becomes

$$\lambda_{\text{neutral}}(r) = \exp \left[- \int_0^{a/r} \frac{\log x}{1-x} dx \right] \quad (v=0) \quad (16)$$

Fig. 3 shows how λ_{neutral} varies with r/a for $v=0, 1/4$, and $1/2$.

We should check the values of $\sigma_\theta^{(\alpha)}(r)/\sigma_\theta^{(\alpha)}(\infty) = s_\theta(r)/S$ away from the hole. In the case of the neutral hole, we find

$$\begin{aligned}
 s_{\theta} / S &= 1 - (\rho^{-1} - \rho^{-(1+\nu)}) / \nu \quad (\nu \neq 0) \\
 &= 1 - \rho^{-1} \log \rho \quad (\nu = 0)
 \end{aligned}
 \tag{17}$$

and so the peak layer stress does indeed occur at the hole.

Acknowledgements

This work was supported by DARPA's Defense Sciences Research Council, under contract to the University of Michigan, by a DARPA URI grant to the University of California at Santa Barbara, and by the Division of Applied Sciences, Harvard University.

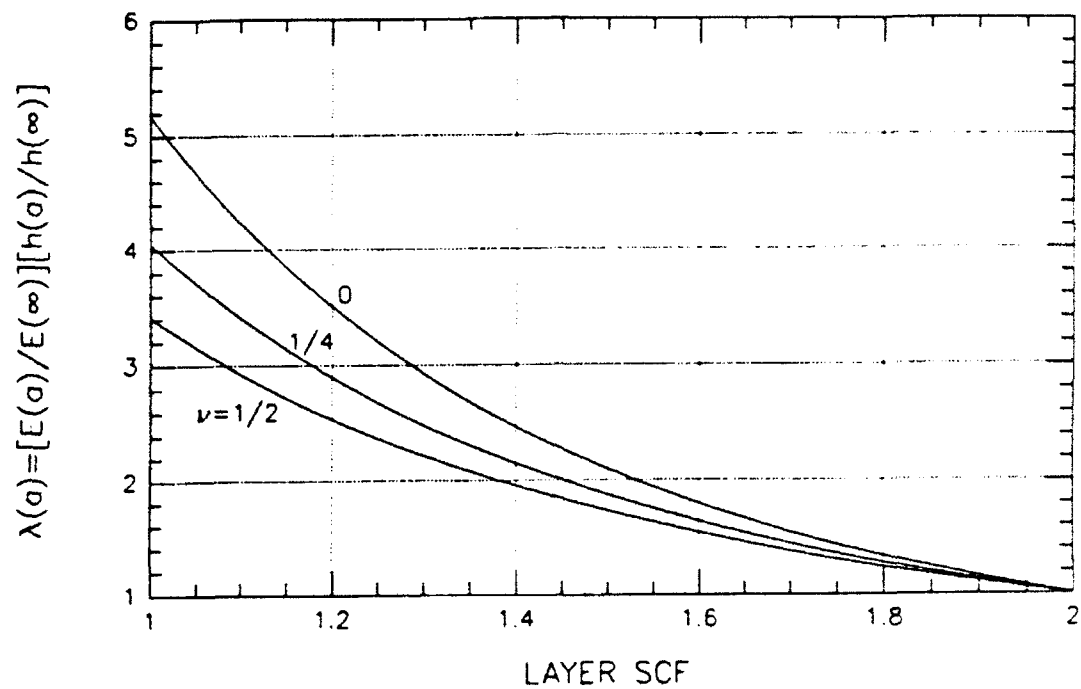


Fig. 2. Tailoring function at hole boundary vs. layer stress concentration factor.

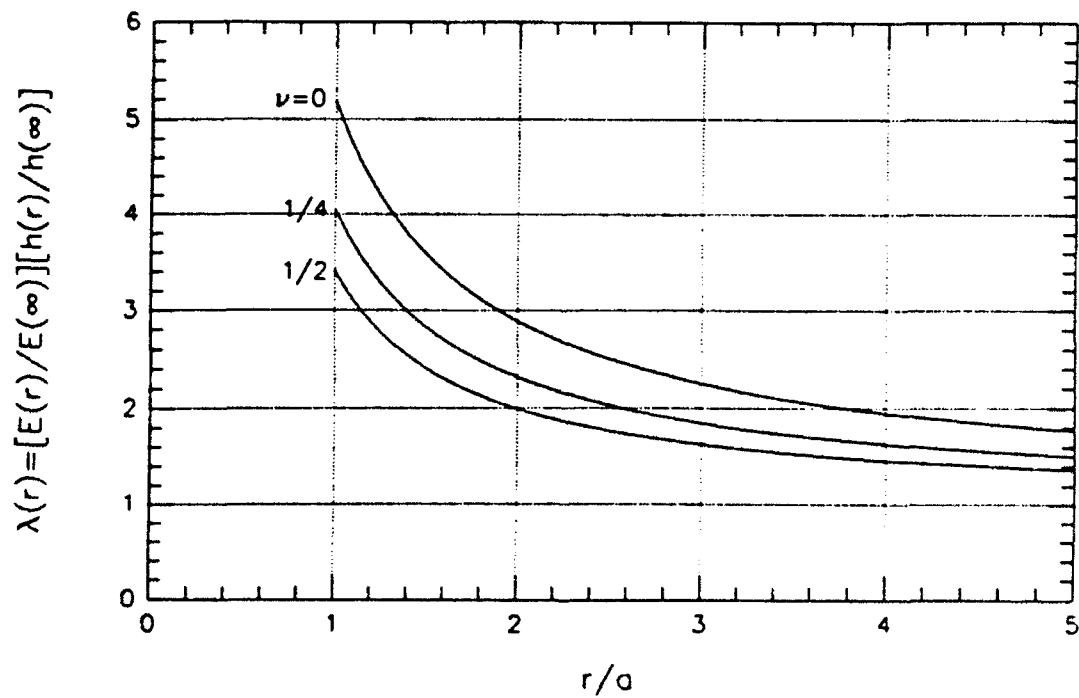
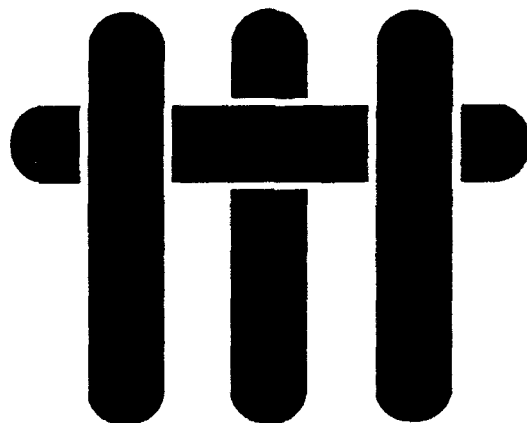


Fig. 3. Spatial variation of tailoring function for a neutral hole.

M A T E R I A L S



THE IN-PLANE SHEAR PROPERTIES OF 2-D CERAMIC MATRIX COMPOSITES

by

Povl Brøndsted
Risø National Laboratory
Roskilde, Denmark

Fernando E. Heredia and Anthony G. Evans
Materials Department
College of Engineering
University of California
Santa Barbara, California 93106-5050

Supported by the Defense Advance Research Projects Agency through the University
Research Initiative under ONR contract N-00014086-K-0753.

Submitted to the Journal of the American Ceramic Society, February 1993

ABSTRACT

The in-plane shear properties of a range of 2-D ceramic matrix composites have been measured using the Iosipescu configuration. The non-linear deformation is found to be associated primarily with matrix cracks. Consequently, the shear modulus decreases as strain proceeds. The flow strength in shear is found to be compatible with the stress at which multiple matrix cracking is expected to occur, without interface slip. Consequently, the shear strength scales with the shear modulus. The shear ductility is found to diminish as the matrix modulus increases. This effect is attributed to the influence of matrix modulus on the bending deformation of fibers between matrix cracks. The experimental observations are used to suggest a mechanism map that identifies (class III) materials which redistribute stress around notches by means of shear bands.

1. INTRODUCTION

The in-plane shear properties of 2-D ceramic matrix composites (CMCs) become important in the vicinity of holes, notches and attachments. In such regions, substantial shear stresses exist, even when the applied loading is either tensile or compressive. The performance of the composite is then influenced by the non-linear shear response of the material. In some cases, a relatively low shear strength is preferred, because shear deformation can redistribute stresses and diminish the notch sensitivity of the material (Fig. 1a).¹⁻⁴ In other cases, a low shear strength may encourage shear localization, leading to inferior structural performance. This latter response is often manifest at pin loaded holes (Fig. 1b). Consequently, the versatile structural application of CMCs requires that the shear responses of the material be predictable and adjustable. A contribution toward this objective is made by measuring the shear properties of a range of CMCs, and making observations of the mechanisms that cause non-linearity.

2. MATERIALS

A range of 2-D materials having differing matrix, fiber and interface properties has been selected for this study⁵ (Table I). Two C/C materials have been chosen, because they are known to be susceptible to shear deformation and damage in the presence of holes and notches.³ Two C matrix materials reinforced with Nicalon (SiC) fibers have also been used, because one exhibits shear damage around notches, whereas the other is subject to tensile failure without detectable damage.² The final material consists of a SiC matrix reinforced with Nicalon fibers.⁶ A summary of the constituent and interface properties (Table I) establishes that a wide range of these properties is encompassed by the choice of materials. All but the latter material have an 8-harness satin weave. The SiC/SiC material has a plain weave.

3. TEST PROCEDURES

The shear tests are conducted using the Iosipescu test specimen⁷⁻⁹ (Fig. 2a). The height of the specimen was chosen to be 25 mm and the V-notch angle was selected to be 110° in order to provide the most uniform shear zone.⁹ The specimens were cut from plates by electro-discharge-machining (EDM). Two strain gauges* were mounted (one on each face), oriented 45° with respect to the loading axis, in order to provide a direct readout of the shear strain.

Tests were carried out using a shear fixture (Fig. 2b) attached to a Servo-Electrical-Mechanical load frame. The load was applied at a crosshead displacement rate of $\sim 2 \mu\text{m s}^{-1}$. In a preliminary study, specimens were monotonically strained beyond the *peak stress*, in order to explore overall behavior. Tests were then conducted with periodic unloading and reloading in order to monitor the influence of the accumulated damage on the stiffness. Data were collected using a PC-based acquisition program, which also controlled the test machine. The sampling was recorded as *time*, *load* and *position* (displacement), as well as *strain* from each of the specimen faces. All tests were performed in air and at room temperature.

To reveal the failure mode, one specimen of each material was deformed beyond the peak stress, immersed in a solution of ZnI_2 and subsequently X-rayed.^{1,2} The gauge region was then sectioned, carefully polished through several layers and inspected by Scanning Electron Microscopy (SEM).

* Micro Measurement type EA-06-031DE-120
Measurements Group Inc., Raleigh, NC 27611.

4. MEASUREMENTS AND OBSERVATIONS

Typical shear stress/strain curves, $T(\gamma)$, for each of the materials and a literature result for SiC/CAS¹⁰ are summarized in Fig. 3. Also shown for comparison (Fig. 4) are the corresponding tensile stress/strain curves, described elsewhere.^{2,3,5} It is evident that, in all cases, substantially larger strains are possible in shear, compared with tensile loading. Furthermore, the spectrum of differing shear behaviors encompassed by this group of CMCs, contrasts with the tensile characteristics. Changes in the unloading shear modulus \bar{G} with strain (Fig. 5) indicate that \bar{G} decreases as non-linearity develops.

The X-ray die penetrant observations made after loading beyond the peak stress (Fig. 6) establish that the non-linear deformation is confined to a band between the notches and that the damage density within the zone is relatively uniform. Such observations are compatible with the state of uniform shear expected between the notches in the Iosipescu geometry.⁷⁻⁹

Observations of damage conducted in the SEM (Fig. 7) establish that matrix cracks form in all of the plies plus the matrix rich regions. These cracks are always inclined at about 45° to the loading plane (Fig. 7). The crack density increases with strain and saturates at strains of order 1%. The crack spacing at saturation is smaller in the plies than in the matrix-dominated regions of the microstructure.

5. ANALYSIS

The non-linearity in the shear stress/strain curve appears to be dominated by matrix cracking, as in the case of tensile loading.^{5,10-14} However, the experimental results suggest a different influence of matrix cracks on the shear properties than on the tensile properties. A matrix cracking model that represents the shear stress/strain curve is expected to have the basic features illustrated in Fig. 8. The cracks are normal to the

tensile stress. Consequently, the non-linear deformations are constrained to occur along the tensile axis, normal to the crack plane, unless the plies delaminate. Without delamination, interface sliding is inhibited. This situation arises because the sliding displacements in adjacent $+45^\circ$ and -45° plies have opposing components parallel to the cracks. A major contribution to the strain should thus be provided by the increase in *elastic compliance* caused by the matrix cracks. An implication is that, by normalizing the stress with the shear modulus (Table II) convergence of the stress/strain curves should be achieved. This expectation is broadly consistent with the present data (Fig. 9). With this normalization, the C matrix materials have the greatest flow strength and ductility. Moreover, similar behavior is exhibited by both SiC and C fiber reinforcements with C matrices. It is also apparent that composites with matrices having larger elastic moduli ($C \rightarrow CAS \rightarrow SiC$) exhibit reduced flow strength and ductility.

When matrix cracking occurs without fiber failure and with no interface debonding/sliding, the tensile matrix cracking stress, σ_{mc} , for a material with homogeneous elastic properties is given by,¹³

$$\sigma_{mc} = \sqrt[3]{B \left[(1+\nu)f^2/(1-f)^2 \right]^{3/2} (G\Gamma_m/R)^{3/2}} \quad (1)$$

where f is the fiber volume fraction, R is the fiber radius, Γ_m is the matrix fracture energy, G is the shear modulus, ν is Poisson's ratio and $B = 1.8$. A similar result should apply in shear, when resolved into the orientation indicated on Fig. 8. Consequently, Eqn. (1) should represent an *upper bound* on the shear strength associated with multiple matrix cracking. (The occurrence of fiber failure and interface sliding must result in diminished flow strength) The upper bound values, estimated from Eqn. (1) using the properties summarized on Tables I and II, are indicated on Fig. 9. It is evident that these

are of the same order as the experimental measurements and also appear to rank the materials correctly.

The decrease in ductility in the order, C \rightarrow CAS \rightarrow SiC, is considered to reflect the effects of the matrix on fiber failure in shear. It is evident from Fig. 8 that the fibers experience bending deflections between the matrix cracks. The bending radius is expected to become smaller as the matrix modulus increases, because the elastic deformation of the matrix needed to accommodate this bending must diminish. Consequently, fiber failures are expected to be more prevalent when the matrix has higher modulus. Such fiber failures would result in composite failure and limit the shear ductility of the material.

The relatively low shear strength of the C matrix materials and their high shear ductility are considered to be responsible for the shear mode of stress redistribution found in notched materials^{3,5} (Fig. 1a). Furthermore, this mechanism is absent in the SiC and CAS matrix materials,⁵ consistent with their greater resistance to shear deformation and reduced shear ductility. This contrast in behavior, dependent upon matrix properties, suggests a mechanism map^{5,15} (Fig. 10). The ordinate of the map is chosen to reflect the competition between shear and tensile failure. The latter is governed by the ultimate tensile strength (UTS), designated S , which has been evaluated in detail.^{5,16} The results of this study suggest that a major scaling function for the shear strength is the shear modulus, G . Consequently, G/S , is used as the ordinate. The corresponding choice for the abscissa is not crucial at the present level of analysis. Hence, it is chosen to be the same as that previously used to distinguish other damage mechanisms in CMCs:^{5,15,16} notably the ratio of the 'yield' strength σ_{mc} to ultimate strength, S . Superposition of experimental data onto the map (Fig. 10) suggests that materials with $G/S \lesssim 80$ exhibit a shear mechanism of stress redistribution (class III). Conversely, materials with $G/S \gtrsim 100$ redistribute stresses by mode I matrix cracks combined with fiber pull-out^{4,5,15} (classes I and II).

6. CONCLUDING REMARKS

A preliminary attempt has been made to measure and correlate the shear properties of 2-D ceramic matrix composites. The shear deformation appears to be dominated by the incidence and evolution of matrix cracks. A solution for matrix cracking in tension has been shown to rank the shear flow strength of the materials tested. However, the approach is simplistic and neglects potentially important effects of the interface and elastic mismatch between fiber and matrix, as well as residual stress. A model that incorporates these factors requires development.

The wide range of shear ductility found in this group of CMCs has important implications for the stress redistribution capacity of the material. It has been noted that the ductility diminishes as the matrix modulus increases. This trend has been attributed to the effect of the matrix on the bending deformation experienced by the fibers between the matrix cracks. A model that relates the bending deformation and stresses to matrix properties is needed to develop an understanding of this behavior.

Finally, a mechanism map has been proposed that attempts to identify CMCs that are capable of redistributing stress by shear band formation. The concept used is elementary. It needs improvements and extensions based on models of shear deformation and failure caused by matrix cracks.

8. ACKNOWLEDGMENTS

This work was supported by the Defense Advance Research Projects Agency through the University Research Initiative under ONR contract N-00014086-K-0753.

TABLE I

Constituent Properties of CMCs⁵

Fibers	Matrix		Fiber Coating	Elastic Moduli (GPa)			Sliding Stress, τ (MPa)	Matrix Fracture Energy, Γ_m (Jm ⁻²)
				E _m	E _f	G _f		
Carbon	Carbon	X	None	37 ± 5	230	~ 5		1-5
		Y						
Nicalon		B	Carbon	330 ± 40	200	84	90 ± 20	
		C					10 ± 5	
	SiC (CVI)						100 ± 20	5-10
	CAS						15 ± 5	15-25

TABLE II

Shear Properties of CMCs

MATERIAL	SHEAR MODULUS G (GPa)	TENSILE STRENGTH, S (MPa)	G/S
C/C	7	320	21
SiC/C _B	19	240	79
SiC/C _C	13	330	38
SiC/SiC	160	175	900
SiC/CAS	50	230	220

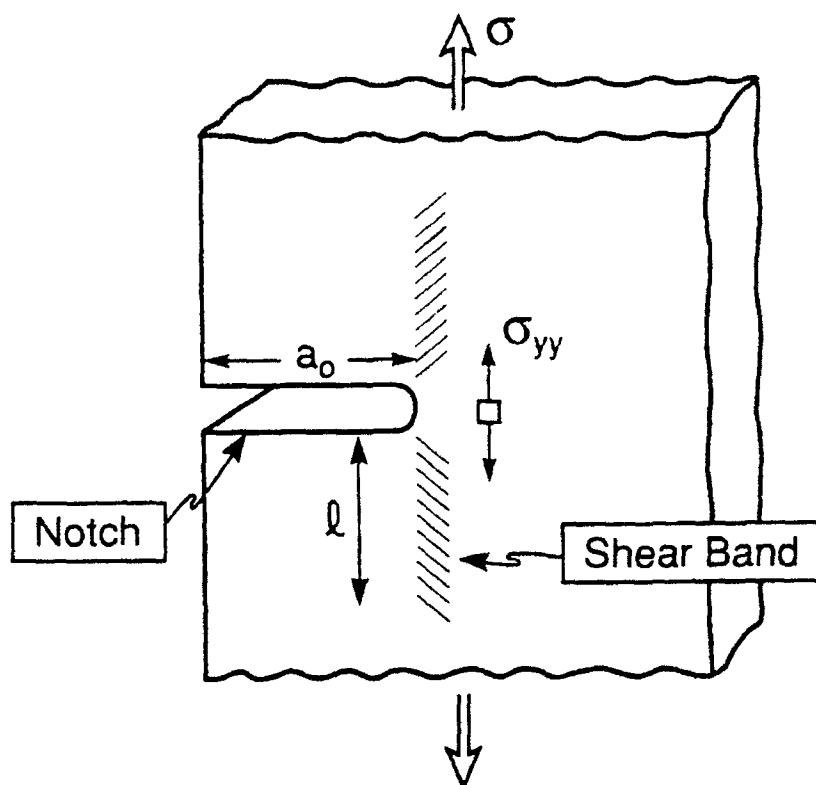
REFERENCES

- [1] M. Spearing, P.W.R. Beaumont and M.F. Ashby, "Fatigue Damage Mechanics of Notched Graphite-Epoxy Laminates," in *Composite Materials: Fatigue and Fracture*, ASTM STP 1110, edited by T.K. O'Brien, pp. 596-616 (1991).
- [2] F.E. Heredia, S.M. Spearing, A.G. Evans, P. Mosher and W.A. Curtin, "Mechanical Properties of Continuous Fiber-Reinforced Carbon Matrix Composites and Relationships to Constituent Properties," *J. Am. Ceram. Soc.*, 75[11], 3017-25 (1992).
- [3] F.E. Heredia, S.M. Spearing, M.Y. He, T.J. Mackin, A.G. Evans, P. Mosher and P.A. Brøndsted, "Notch Effects in Carbon Matrix Composites," *J. Am. Ceram. Soc.*, to be published.
- [4] G. Bao and Z. Suo, "Remarks on Crack Bridging Concepts," *Appl. Mech. Rev.*, 45, 355 (1992).
- [5] A.G. Evans, J.M. Domergue and E. Vagaggini, "A Methodology for Relating Macroscopic Behavior of Ceramic Matrix Composites to Constitutive Properties," *J. Am. Ceram. Soc.*, to be published.
- [6] R. Naslain, "Fiber-Matrix Interphases and Interfaces in Ceramic Matrix Composites Processed by CVI," *Composite Interfaces*, to be published.
- [7] N. Iosipescu, "New Accurate Procedure for Single Shear Testing of Metals," *Jnl. Materials*, 2[3], 537-66 (1967).
- [8] D.E. Walrath and D.F. Adams, "The Iosipescu Shear Test as Applied to Composite Materials," *Exptl. Mech.*, 23 [10], 105-10 (1983).

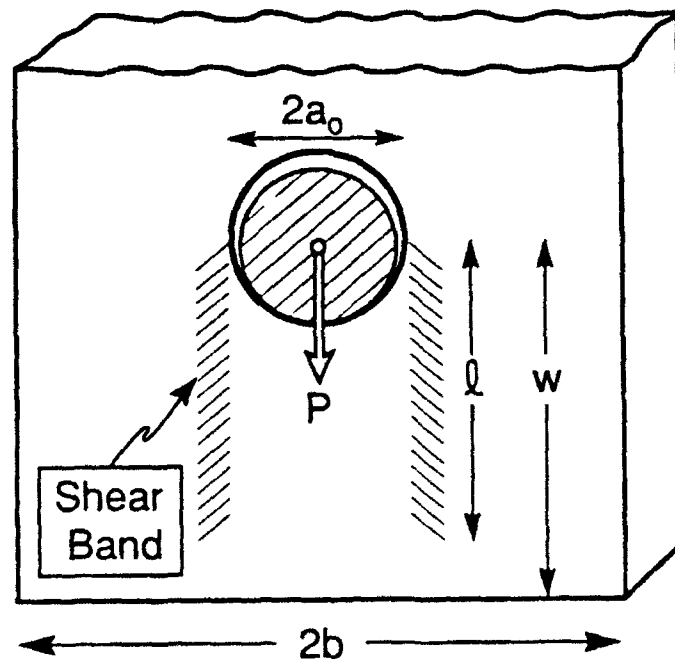
- [9] S.S. Wang and A. Dasgupta, "Development of Iosipescu-Type Test for Determining In-Plane Shear Properties of Fiber Composite Materials: Critical Analysis and Experiment," T & AM Report, *Department of Theoretical and Applied Mechanics, University of Illinois at Urbana-Champaign*, UILLU-ENG-86-5021 (1986).
- [10] B. Harris, F.A. Habib and R.G. Cooke, "Matrix Cracking and the Mechanical Behavior of SiC-CAS Composites," *Proc. Roy. Soc.*, **A43**, 109-131 (1992).
- [11] A.W. Pryce and P. Smith, "Modelling the Stress/Strain Behaviour of Unidirectional Ceramic Matrix Composite Laminates," *J. Mater. Sci.*, **27**[10], 2695-2704 (1992).
- [12] D. Beyerle, S.M. Spearing and A.G. Evans, "Damage Mechanisms and the Mechanical Properties of a Laminated 0/90 Ceramic/Matrix Composite," *J. Am. Ceram. Soc.*, **75**[12], 3321-30 (1992).
- [13] B. Budiansky, J.W. Hutchinson and A.G. Evans, "Matrix Fracture in Fiber-Reinforced Ceramics," *J. Mech. Phys. Solids*, **34**[2], 167-89 (1986).
- [14] D. Beyerle, S.M. Spearing, F.W. Zok and A.G. Evans, "Damage and Failure in a Unidirectional Ceramic-Matrix Composite," *J. Am. Ceram. Soc.*, **75**[10], 2719-25 (1992).
- [15] A.G. Evans and F.W. Zok, "Cracking and Fatigue in Fiber-Reinforced Metal and Ceramic Matrix Composites"; pp. 271-308 in *Topics in Fracture and Fatigue*. Edited by A. S. Argon. Springer-Verlag, New York (1991).
- [16] W.A. Curtin, "Theory of Mechanical Properties of Ceramic Matrix Composites," *J. Am. Ceram. Soc.*, **74**[11], 2837-45 (1991).

FIGURE CAPTIONS

- Fig. 1. The contrasting role of shear deformation on the behavior around holes:
a) open hole, b) pin loaded hole.
- Fig. 2. a) A schematic of the Iosipescu test specimen. The dimensions are in mm.
b) A photograph of a specimen within the test fixture.
- Fig. 3. Shear stress/strain curves measured for each CMC. Also shown is a literature result for SiC/CAS.¹⁰
- Fig. 4. Tensile stress/strain curves for the same CMCs used to obtain the shear data (Fig. 3).
- Fig. 5. Change in unloading shear modulus \bar{G} as a function of shear strain superposed above the stress/strain curves.
- Fig. 6. Die penetrant X-ray image of specimens after testing a) C/C, b) SiC/C.
- Fig. 7. SEM views of matrix cracks formed after the onset of non-linearity a) global view of area between the notches in SiC/C, b) detail showing a matrix rich zone. The contrast is from the ZnI_2 die penetrant.
- Fig. 8. Schematic of matrix cracks in two 0/90 contiguous plies, with the loads indicated.
- Fig. 9. Shear strength normalized by the shear modulus as a function of shear strain for each material.
- Fig. 10. A proposed mechanism range identifying materials that exhibit class III behavior, wherein shear bands redistribute the stress around notches.

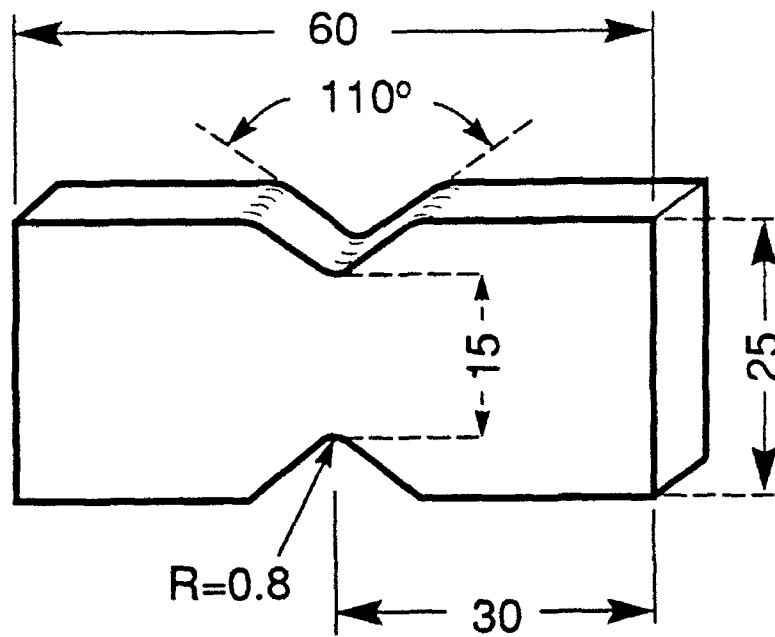


a) Shear Band
Reduces Stress
Concentration, σ_{yy}



b) Shear Band
Reduces Bearing
Strength

Fig. 1



Iosipescu Shear Specimen

Figure 2a

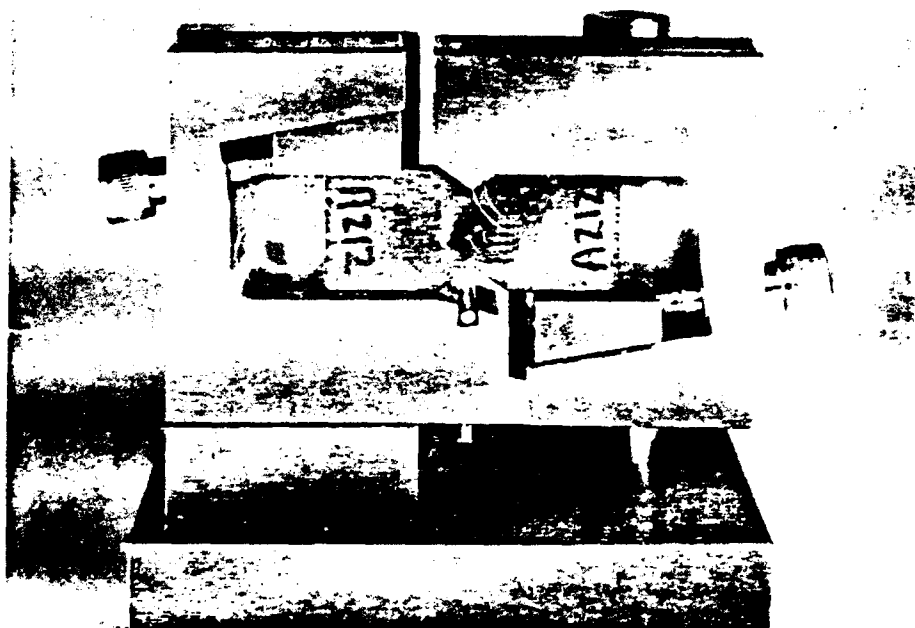


Figure 2b

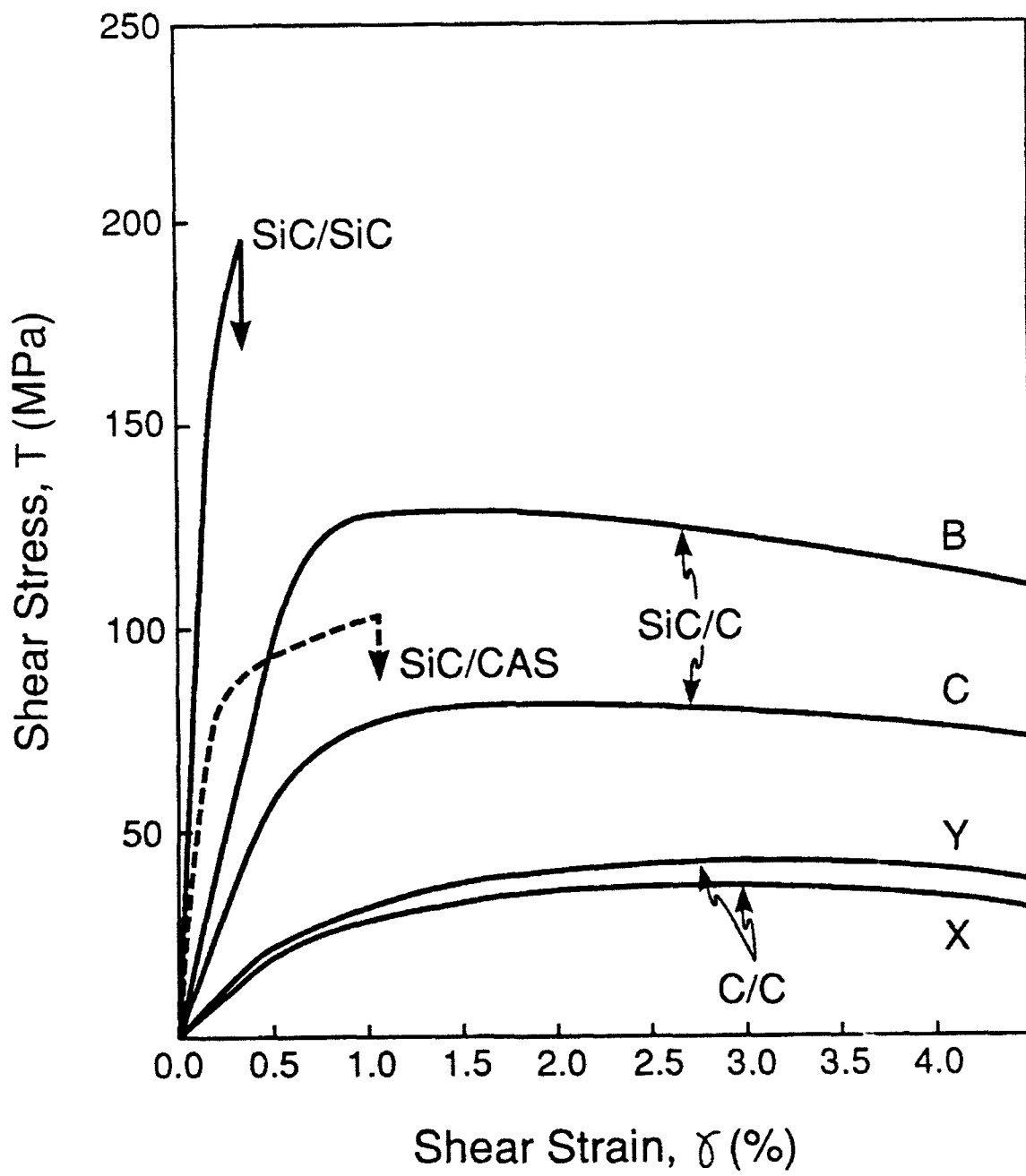


Figure 3

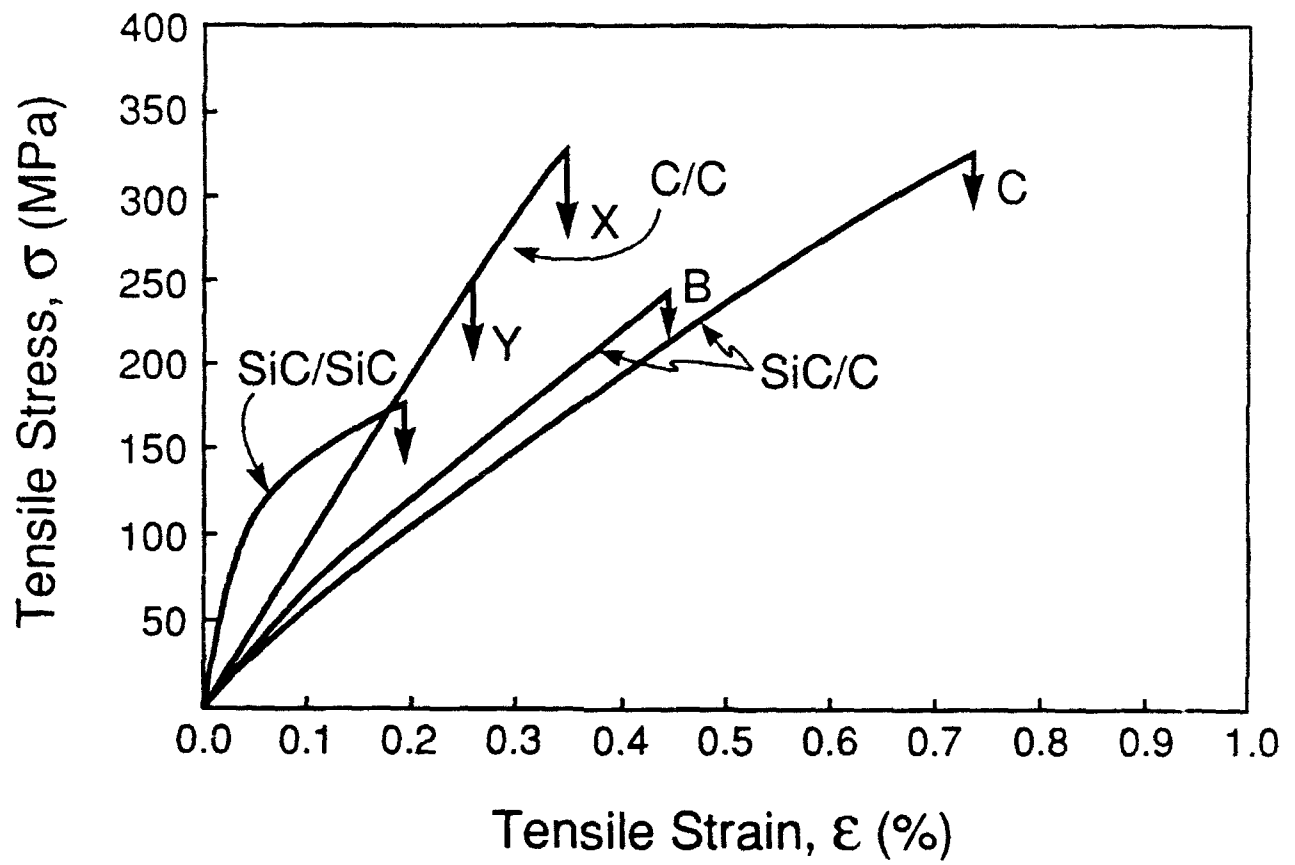


Figure 4

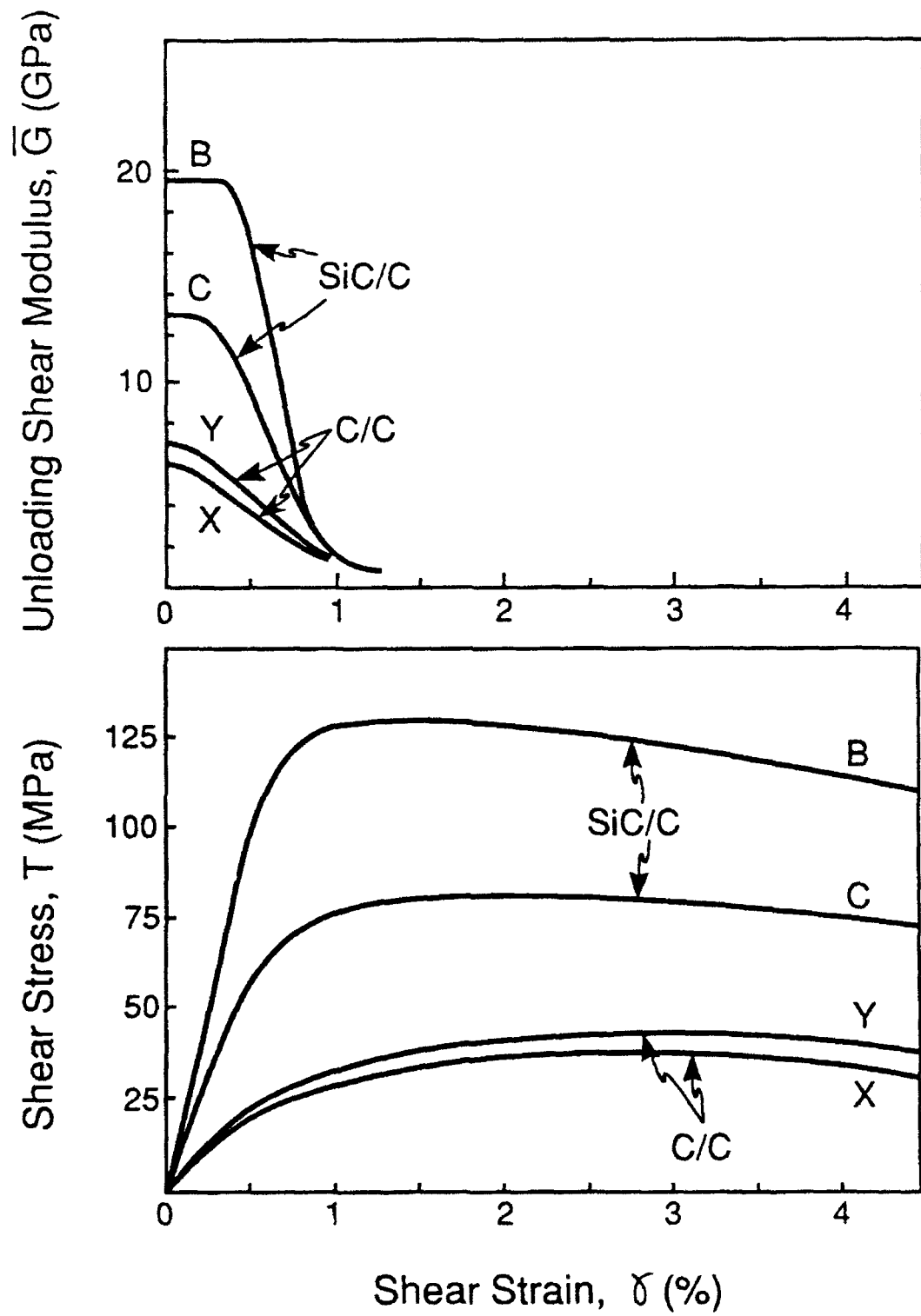
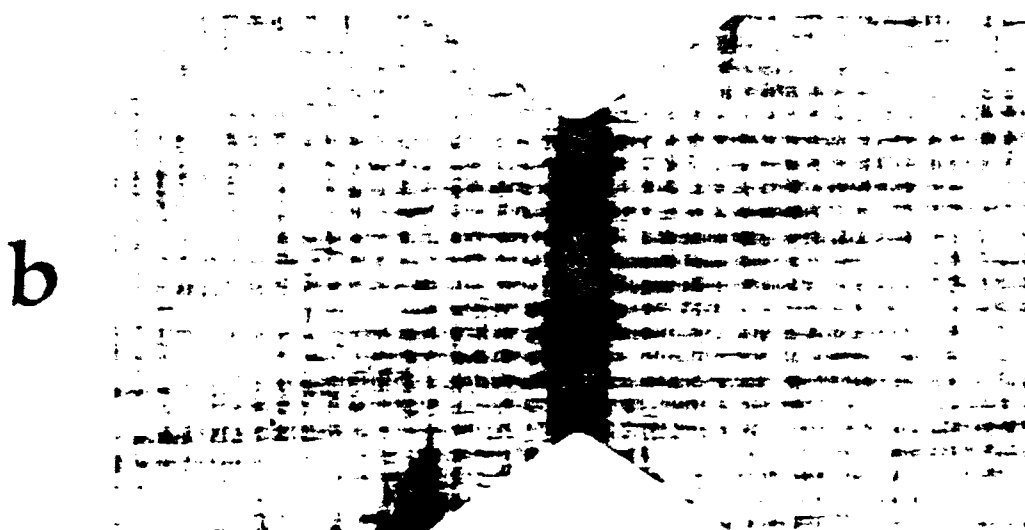


Figure 5



10 mm

Figure 6

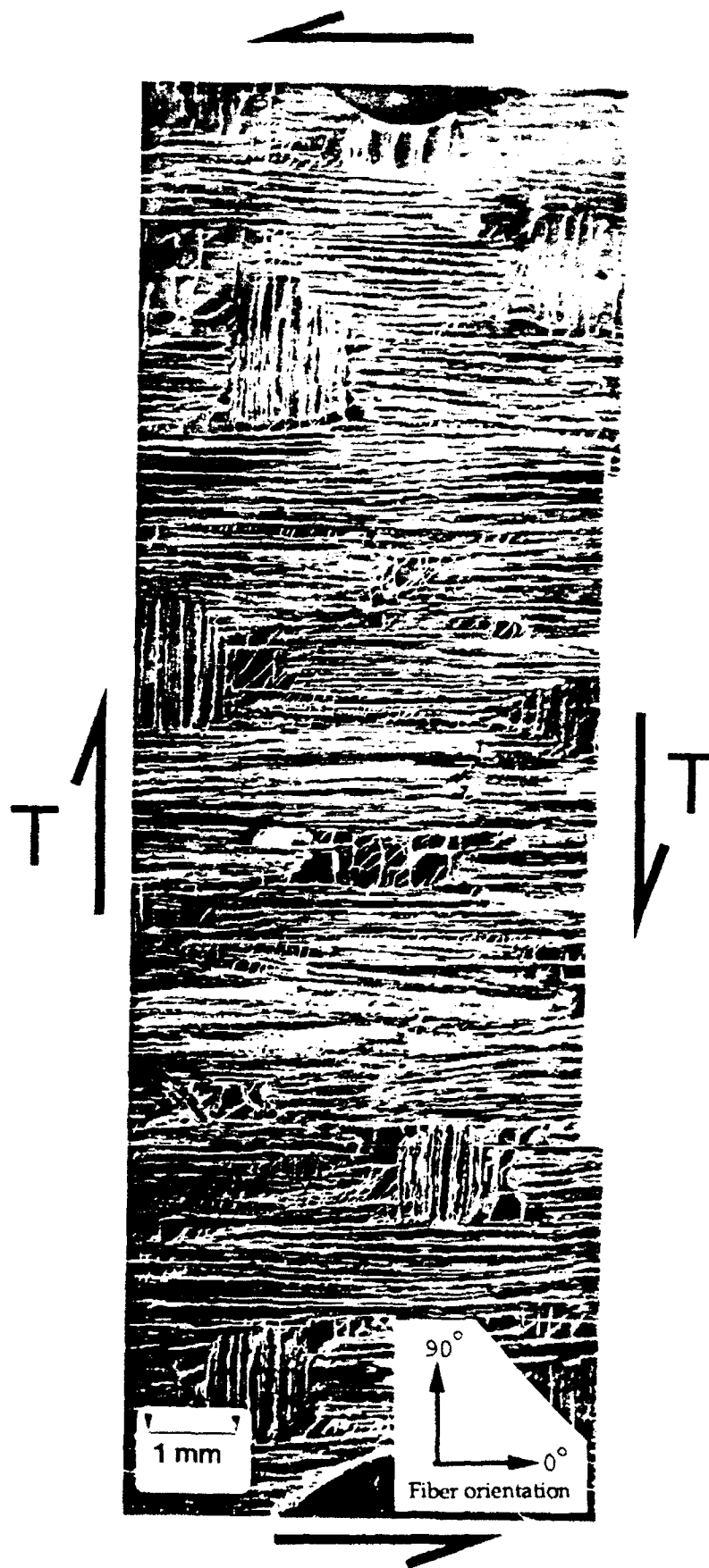


Figure 7a

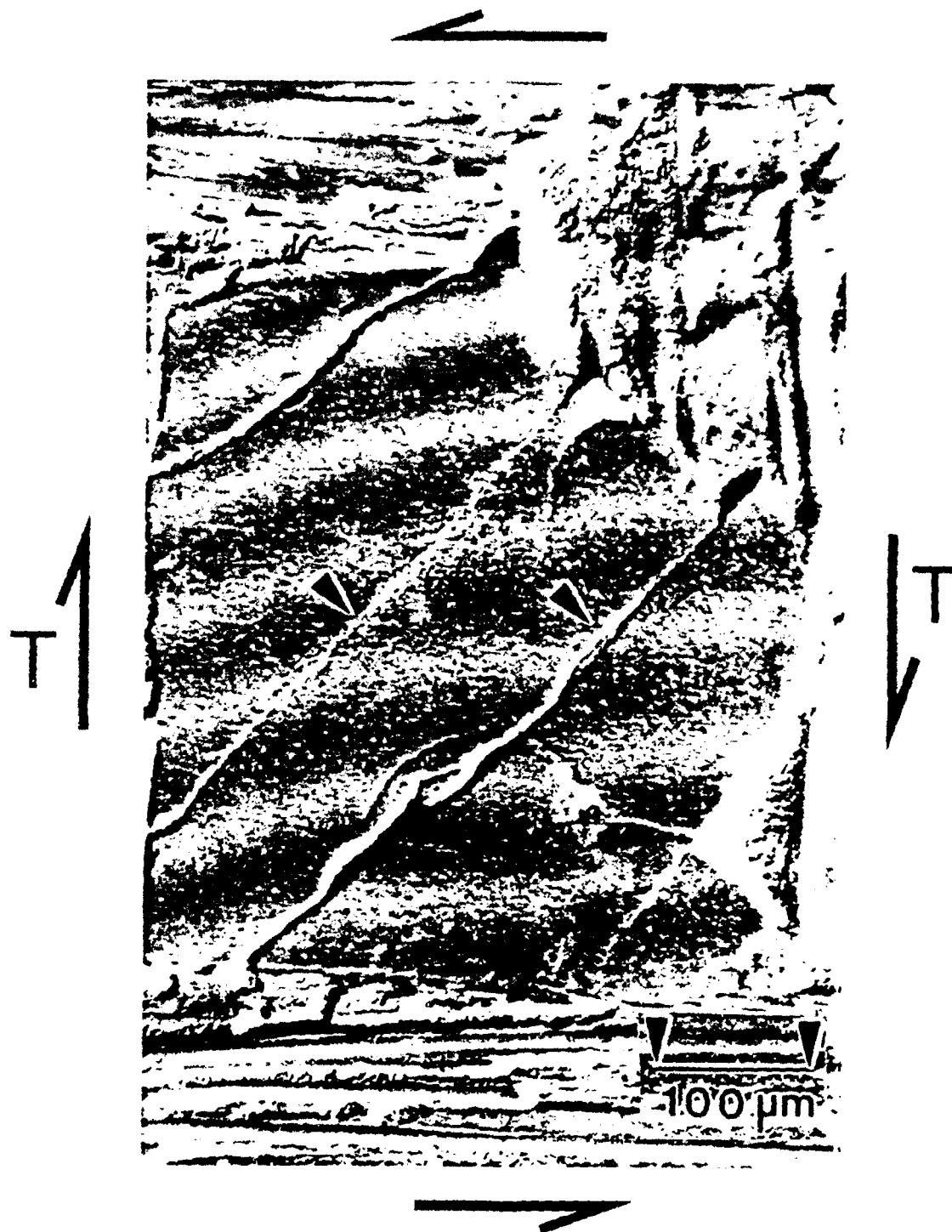


Figure 7b

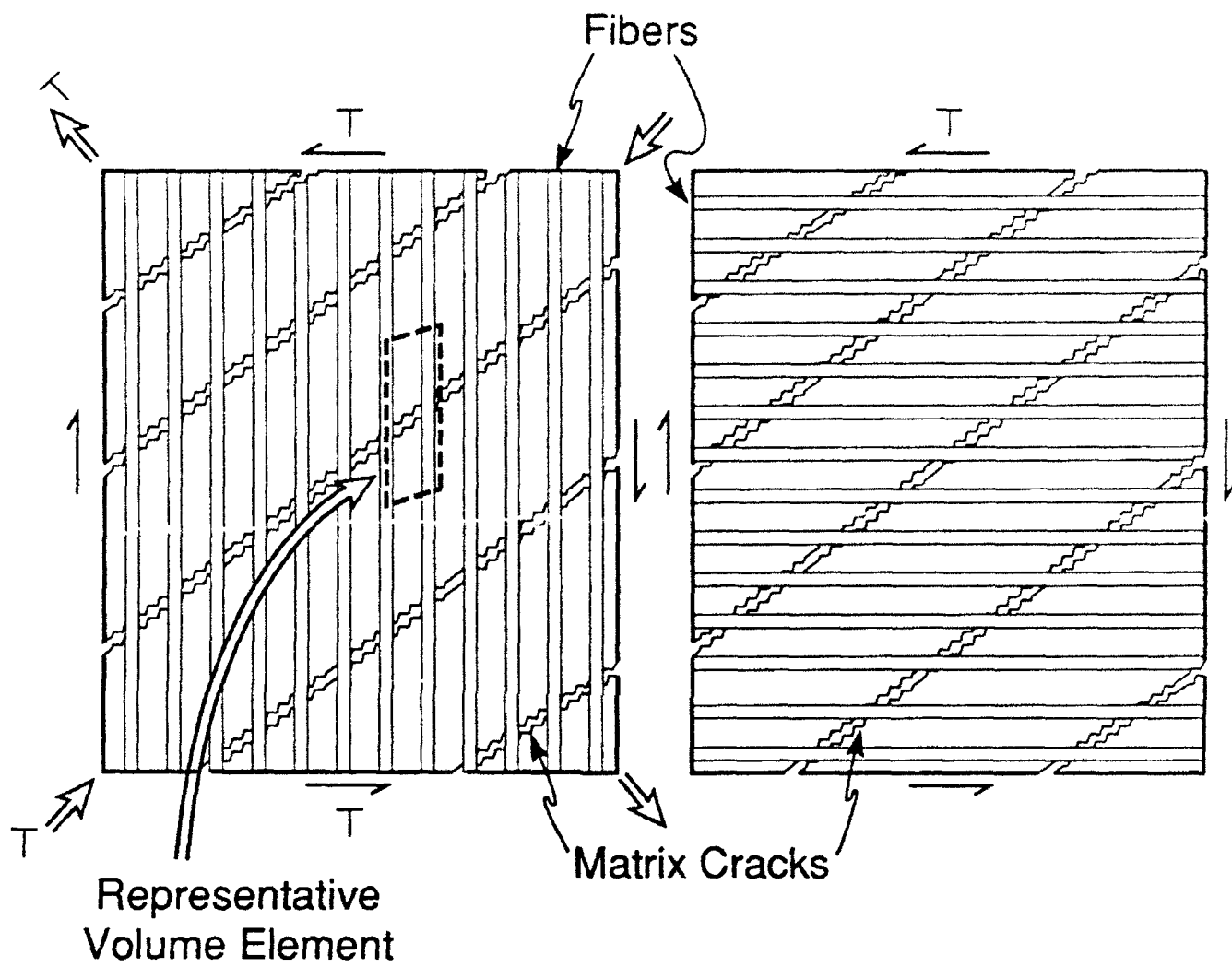


Figure 8

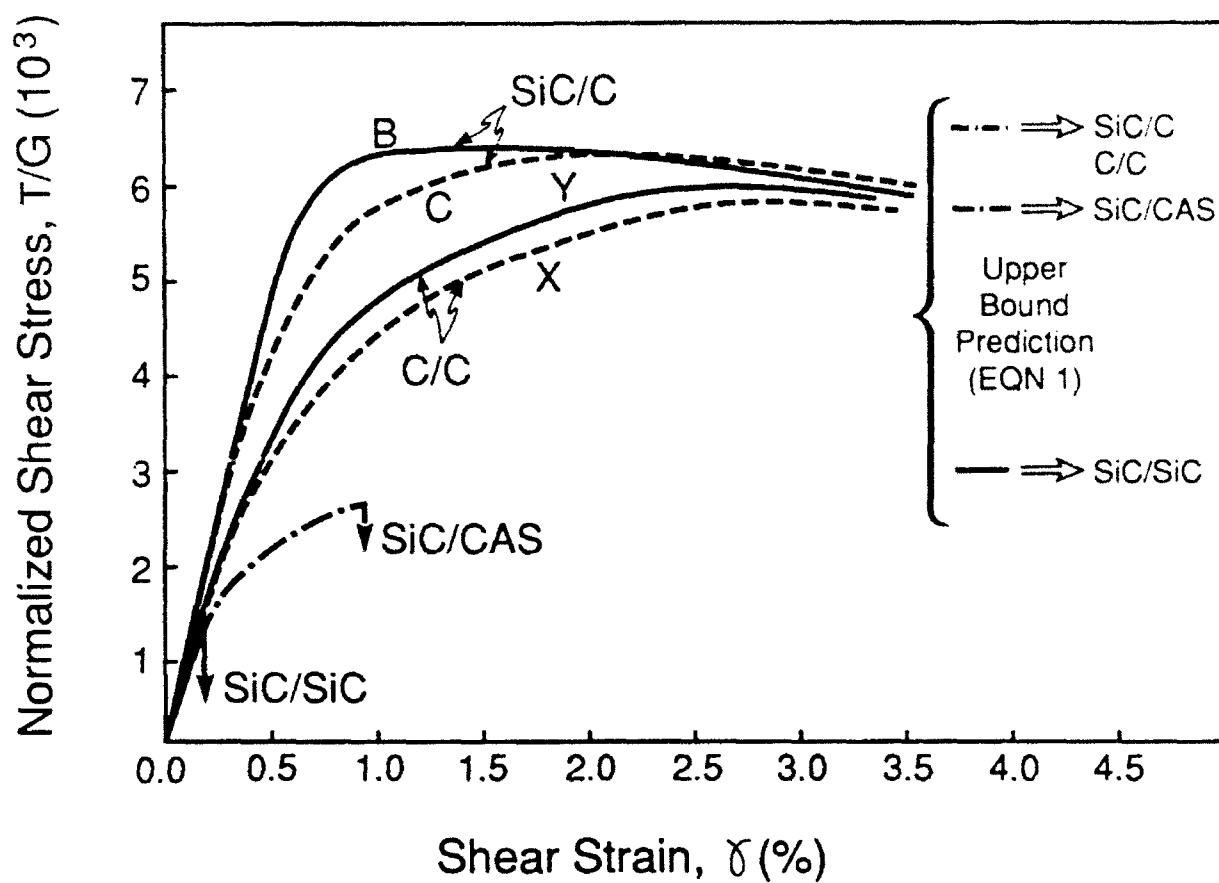


Figure 9

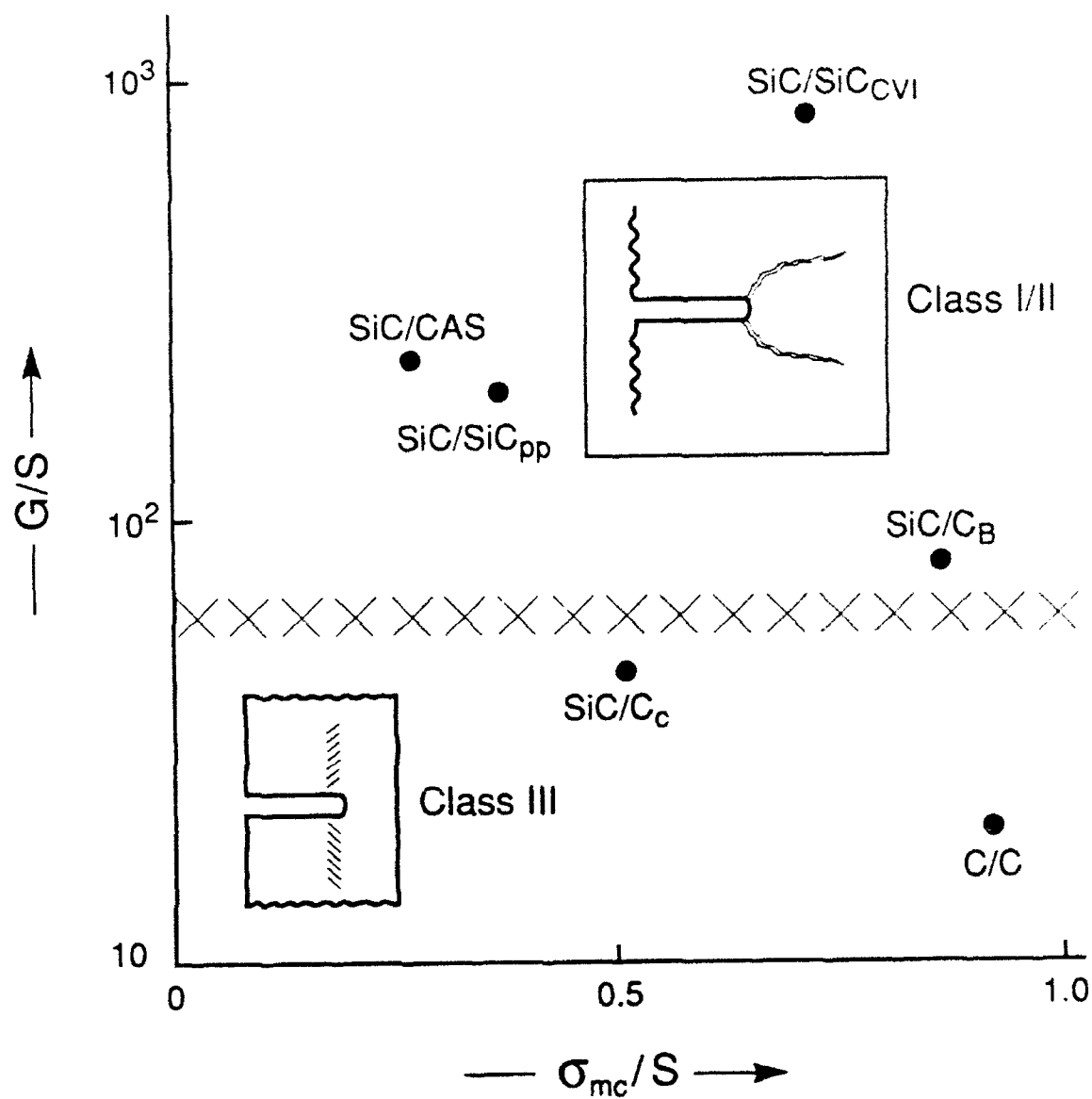


Figure 10



MECH-202

TRANSVERSE CRACKING IN FIBER-REINFORCED BRITTLE
MATRIX, CROSS-PLY LAMINATES

Z. Cedric Xia, Richard R. Carr and John W. Hutchinson

Division of Applied Sciences
HARVARD UNIVERSITY
Cambridge, Massachusetts 02138

December 1992

TRANSVERSE CRACKING IN FIBER-REINFORCED BRITTLE MATRIX, CROSS-PLY LAMINATES

Z.Cedric Xia, Richard R. Carr and John W. Hutchinson

Division of Applied Sciences

Harvard University

Cambridge, MA. U.S.A.

ABSTRACT

The topic addressed in this paper is transverse cracking in the matrix of the 90° layers of a cross-ply laminate loaded in tension. Several aspects of the problem are considered, including conditions for the onset of matrix cracking, the evolution of crack spacing, the compliance of the cracked laminate, and the overall strain contributed by release of residual stress when matrix cracking occurs. The heart of the analysis is the plane strain problem for a doubly periodic array of cracks in the 90° layers. A fairly complete solution to this problem is presented based on finite element calculations. In addition, a useful, accurate closed form representation is also included. This solution permits the estimation of compliance change and strain due to release of residual stress. It can also be used to predict the energy release rate of cracks tunneling through the matrix. In turn, this energy release rate can be used to predict both the onset of matrix cracking and the evolution of crack spacing in the 90° layers as a function of applied stress. All these results are used to construct overall stress-strain behavior of a laminate undergoing matrix cracking in the presence of initial residual stress.

1. INTRODUCTION

The macroscopic tensile properties of uni-directional fiber-reinforced brittle composites have been studied extensively since the 70's, where matrix cracking with intact fibers plays an important role in longitudinal strength. The transverse and shear strengths of such composites are invariably lower than the longitudinal strength. Consequently, in applications where multiaxial stress states are encountered, cross-ply laminates are commonly used. While there has been considerable attention to the elastic properties of cross-ply laminates, relatively less has been done to establish their fracture performance in terms of the properties of the constituent phases. This is the topic of the present paper where emphasis is on brittle matrix composites and explicit results for the effect of matrix cracking on overall stress-strain behavior are developed and presented. Studies of the topic have been carried out within a framework of damage mechanics where the effects of cracks are not explicitly predicted as represented by [1, 2]. More closely related to the present work are studies in [3, 4] where explicit results for the effect of cracks are given for general laminates. These four papers provide additional references to the general problem area.

Recently, a comprehensive experimental study was conducted on a laminated $0^\circ/90^\circ$ ceramic/matrix composite [5]. When the tensile stress was applied along one of the fiber directions, cracks were first observed in the 90° layer and always spanned the entire ply, but arrested at the interfaces between layers, as sketched in Fig. 1. With further increase of the applied stress, additional matrix cracks developed in the 90° layers in the same way as previous cracks. These cracks spread as 3D tunneling cracks from small flaws located in the matrix of the 90° layers in the direction transverse to the applied stress, as depicted in Fig. 1. At even higher applied stress, it was observed that the pre-existing cracks began to extend into the adjacent 0° layers stably and without any fiber failure, until these transverse cracks began overlapping in the 0° layers.

The work in this paper deals with conditions for the onset and subsequent multiplication of tunnel cracks in the 90° layers of cross-ply laminates. In addition, the effect of the tunnel cracks on the overall stress-strain relation of the composite will be determined, including the contribution from the release of residual stress. Such constitutive relations are required if progress is to be made in the effort to understand the role of micro-cracking in altering stress concentration at holes and notches in these materials. The paper is organized as follows. We begin by posing the problem for the energy release rate of steady-state tunnel cracks. This problem can be solved using information from a 2D plane strain problem, which also provides the results needed for the desired constitutive changes. Extensive finite element calculations are then reported, providing conditions for the onset of tunnel cracking and for subsequent multiple crack formation. The results permit one to predict the spacing expected between the 90° layer matrix cracks as a function of the applied stress. Given crack spacing in terms of applied stress, one can then predict the overall stress-strain behavior. This point is illustrated by giving examples of stress-strain behavior as a function of the basic geometry of the composite, the toughness of the matrix, and the residual stress in the next section. An approximate analysis is carried out in the final section leading to closed form expressions for the overall compliance change and the tunneling energy release rate as a function of crack density. These results, which are quite accurate, will be very useful for practical applications.

2. BASIC MECHANICS

2.1. Basic equations for laminates

The elastic properties of an undamaged uni-directional fiber reinforced ply are accurately taken to be transversely isotropic about the fiber direction. With the fibers aligned with the 1-axis, the constitutive relation for the undamaged ply is

$$\begin{aligned}
 \epsilon_{11} &= \frac{1}{E_L} \sigma_{11} - \frac{\nu_L}{E_L} (\sigma_{22} + \sigma_{33}) \\
 \epsilon_{22} &= -\frac{\nu_L}{E_L} \sigma_{11} + \frac{1}{E_T} \sigma_{22} - \frac{\nu_T}{E_T} \sigma_{33} \\
 \epsilon_{33} &= -\frac{\nu_L}{E_L} \sigma_{11} - \frac{\nu_T}{E_T} \sigma_{22} + \frac{1}{E_T} \sigma_{33} \\
 \epsilon_{23} &= \frac{1}{2\mu_L} \sigma_{23} \quad \epsilon_{13} = \frac{1}{2\mu_T} \sigma_{13} \quad \epsilon_{12} = \frac{1}{2\mu_T} \sigma_{12}
 \end{aligned} \tag{1}$$

where the subscript L stands for longitudinal properties and the subscript T stands for transverse properties. Notice that $\mu_T = \frac{E_T}{2(1+\nu_T)}$ but generally $\mu_L \neq \frac{E_L}{2(1+\nu_L)}$.

To limit the number of material parameters in the subsequent development, the difference between the fiber and matrix Poisson's ratios will be neglected (*i.e.*, $\nu_m = \nu_f = \nu$). This approximation is known to involve little error. The moduli of the ply are related to the constituent properties by

$$E_L = cE_f + (1-c)E_m \tag{2}$$

$$\mu_L = \frac{\mu_f(1+c) + \mu_m(1-c)}{\mu_f(1-c) + \mu_m(1+c)} \mu_m \tag{3}$$

and $\nu_L = \nu_T = \nu \tag{4}$

where c is fiber volume fraction. Formula (2) is the rule of mixtures for the longitudinal stiffness, and (3) was given in [6] using the composite cylinders model. The remaining modulus, E_T , has a somewhat greater dependence on the spatial arrangement of the fibers. The approximation used here is taken from [6]

$$E_T \approx \frac{1+2\eta c}{1-\eta c} E_m \tag{5}$$

where $\eta = \frac{\frac{E_f}{E_m} - 1}{\frac{E_f}{E_m} + 2} \tag{6}$

The above formulas apply under the condition that no debonding occurs between the fiber and matrix in the plies. To obtain some insight into the role of fiber/matrix debonding, results will be computed in addition for the limiting case where it is assumed that the complete debonding has occurred. To model this, we have followed the suggestion in [5] and have taken $E_f=0$ in (6), thereby reducing the transverse modulus. The effect of debonding on the longitudinal shear modulus is ignored since this effect is relatively unimportant.

Now consider a cross-ply laminate with equal thicknesses of 0° and 90° plies subject to in-plane loading only, as illustrated in Fig. 2. A standard derivation based on the assumption that the in-plane strains are identical in every ply and that there are an equal number of 0° and 90° plies, gives the overall relation for the laminate to be

$$\begin{aligned}\epsilon_{11} &= \frac{1}{E_0} \sigma_{11} - \frac{\nu_0}{E_0} \sigma_{22} \\ \epsilon_{22} &= -\frac{\nu_0}{E_0} \sigma_{11} + \frac{1}{E_0} \sigma_{22} \\ \epsilon_{12} &= \frac{1}{2\mu_0} \sigma_{12}\end{aligned}\tag{7}$$

where

$$\begin{aligned}E_0 &= \frac{\frac{1}{4}(1 + \frac{E_L}{E_T})^2 - \nu_L^2}{\frac{1}{2}(1 + \frac{E_L}{E_T})(\frac{1}{E_T} - \frac{\nu_L^2}{E_L})} \\ \nu_0 &= \frac{2\nu_L}{1 + \frac{E_L}{E_T}} \\ \mu_0 &= \mu_L\end{aligned}\tag{8}$$

are Young's modulus, Poisson's ratio and shear modulus of the laminate, respectively, in the defined coordinates.

The plane strain Young's modulus defined as

$$\bar{E}_0 = \frac{E_0}{1 - \nu_0^2} = \frac{\frac{1}{2} E_L (1 + \frac{E_L}{E_T})}{\frac{E_L}{E_T} - \nu_L^2} \quad (9)$$

will appear frequently in the sequel. Since the transverse modulus E_T depends on whether the fiber/matrix interfaces are bonded or not, \bar{E}_0 also differs for these two cases.

2.2 Concept of steady-state tunneling cracks

Cracking in layered materials often occurs in the tunneling mode within individual layers, as illustrated in Fig. 1. The energy release rate at the tunnel front can be computed in principle by a three dimensional analysis. However, as the length of the tunnel becomes long compared with layer thickness, a steady-state is reached in which the same mode I energy release rate G_{ss} is attained at every point on the front and is independent of tunnel length [7]. From an energy argument, the steady-state energy release rate G_{ss} can be computed using quantities from the two-dimensional plane strain solution to the crack problem depicted in Fig. 3. The result is

$$G_{ss} = \frac{1}{2} \left\{ \frac{1}{2t} \int_{-t}^t \sigma_0(x) \delta(x) dx \right\} \quad (10)$$

where $2t$ is the layer thickness, σ_0 is the stress normal to the crack surface prior to cracking, and δ is the crack opening displacement. This is applicable to linear elastic anisotropic materials and can be used when residual stress is present.

3. FINITE ELEMENT ANALYSIS

3.1. Isolated cracks and the onset of tunnel cracking

A complete analysis of the isolated crack problem depicted in Fig. 3, is performed by finite element analysis for all practical ranges of fiber volume fraction c and the ratio of Young's modulus of fiber to matrix, for both bonded and separated fiber/matrix interfaces. The results for propagation of an isolated tunneling crack will be used to generate the conditions under which extensive matrix cracking first occurs.

Figure 3 shows the cross section of a laminate with a single transverse crack spanning the entire central 90° layer. The stress-strain behavior of each of the plies is taken to be elastically orthotropic obeying (1), with due regard for the two orientations. The interfaces between the layers are assumed to be perfectly bonded. Plane strain conditions are assumed in the z-direction and $\nu_m = \nu_f = 0.2$. The average tensile stress applied at infinity is σ , and the tensile stress in the 90° layer, prior to cracking, is $\frac{2E_T}{E_L + E_T} \sigma$. One can readily show that the normalized steady-state, tunneling energy release rate, $\frac{G_{ss}\bar{E}_0}{\sigma^2 t}$, defined from (10) is a function only of fiber volume fraction c and the modulus ratio E_f/E_m , assuming the Poisson's ratios have been assigned, i.e.,

$$\frac{G_{ss}\bar{E}_0}{\sigma^2 t} = f\left(\frac{E_f}{E_m}, c\right) \quad (11)$$

where \bar{E}_0 is defined in (9) for the two cases, bonded and unbonded fibers mentioned in connection with (6). Results displaying the dependence are shown in Fig. 4 for the two cases. These results were computed using a 7-layer laminate model with the crack in the central layer, but they should apply for an arbitrary large number of layers with high accuracy. In fact, results computed using a 3-layer model and normalized in exactly the same way differ only very slightly from those shown in Fig. 4.

Denote the toughness of the layers in the tunneling cracking mode by Γ , measured in units of energy per unit area. For a crack propagating entirely in the matrix, this would be the mode I toughness of the matrix, Γ_m . For a tunnel crack front encompassing the unbonded interfaces between the fiber and matrix, Γ would be some fraction of Γ_m . The minimum stress σ_{onset} required for propagation of tunneling cracks in the 90° layers is obtained from (11) as

$$\sigma_{onset} = \sqrt{\frac{\Gamma \bar{E}_0}{t f\left(\frac{E_f}{E_m}, c\right)}} \quad (12)$$

This sets the condition for the *onset* of extensive cracking in 90° layers. Note that this first cracking stress is inversely proportional to the square root of the ply thickness. If an initial

residual tensile stress, σ_R , exists in the 90° layers acting parallel to the applied stress, then the sum of $\sigma_R(E_L+E_T)/(2E_T)$ and σ_{onset} should appear on the left hand side of (12). In other words, residual tension in the layer, modified by the factor $(E_L+E_T)/(2E_T)$, is equivalent to an overall applied stress contribution as far as tunnel cracking is concerned.

3.2. Multiple Cracking

Multiple cracking in 90° layers occurs when the applied stress exceeds the critical level given by (12). Results will be presented in this subsection for the doubly periodic, plane strain crack problem depicted in Fig. 5a. Specifically, results will be presented which allow one to predict: (1) the evolution of crack density in the 90° layers, (2) the increase in overall compliance as a function of crack density, and (3) the extra overall strain released by the cracks in the presence of residual stress. The cracks are taken to be equally spaced within all 90° layers, with spacing $2L$ and with the doubly periodic pattern shown in Fig. 5a. Plane strain conditions are again invoked and no traction is applied in the x-direction. Because of symmetry, only one quarter of a periodic cell needs to be considered in setting up the finite element model, which is shown in Fig. 5b. Standard symmetry boundary conditions are applied on all the edges of the quarter cell in Fig. 5b except along the crack face where traction-free conditions are imposed. The average traction on the vertical faces is required to vanish, consistent with the assumption that no stress is applied in the x-direction.

The finite element results for G_{ss} , expressed in non-dimensional form as

$$\frac{G_{ss}\bar{E}_0}{\sigma_t^2} = g\left(\frac{E_f}{E_m}, c, \frac{t}{L}\right) \quad (13)$$

are shown in Figs. 6a and 6b, respectively, for bonded and separated fiber/matrix interfaces. In Section 4, it will be shown how to use this result for steady-state cracking to predict crack spacing as a function of applied stress. The corresponding results for the effective plane strain Young's modulus for the periodically cracked composite, defined as $\bar{E}_c = \sigma/\epsilon$ where ϵ is the average strain in the y-direction, are shown in Figs. 7a and 7b as

$$\frac{\bar{E}_c}{\bar{E}_0} = h\left(\frac{E_f}{E_m}, c, \frac{t}{L}\right) \quad (14)$$

As the crack density t/L becomes larger than about 2, the results have asymptoted to the limit in which only the 0° layers carry the load, which are simply

$$\frac{\bar{E}_c}{\bar{E}_0} = \frac{E_L}{E_L + E_T} \quad (15)$$

It can be shown, by the reciprocal theorem of elasticity, that (13) and (14) are related by

$$\frac{1}{h\left(\frac{E_f}{E_m}, c, \frac{t}{L}\right)} = 1 + \frac{t}{2L} g\left(\frac{E_f}{E_m}, c, \frac{t}{L}\right) \quad (16)$$

Residual stresses and strains are generally introduced during the process when the plies are bonded together to form the layered composite. As discussed earlier, if an initial, uniform residual stress σ_R exists in the 90° layers acting parallel to the applied stress σ , the effect on the tunneling energy release rate is taken into account by replacing σ on the left side of (13) by the sum of $\sigma_R(E_L + E_T)/(2E_T)$ and σ . An additional overall strain, ϵ_A , occurs due to the release of residual stress by the formation of the cracks in the 90° layers. By a simple process of superposition (see Appendix), one can show that

$$\epsilon_A = \left(\frac{1}{\bar{E}_c} - \frac{1}{\bar{E}_0}\right) \frac{E_L + E_T}{2E_T} \sigma_R = (h^{-1} - 1) \frac{E_L + E_T}{2E_T} \frac{\sigma_R}{\bar{E}_0} \quad (17)$$

In the limit where the crack spacing becomes small (*i.e.*, t/L becomes larger than about 2), the stress in the 0° layers due to the residual stress is reduced to zero. Consequently, in this limit, ϵ_A is just the negative of the initial strain in the 0° layers in the uncracked composite, *i.e.*,

$$\epsilon_A = \frac{E_L + E_T}{2E_L} \frac{\sigma_R}{\bar{E}_0} = \left(1 - \frac{E_T}{E_L} \nu_L^2\right) \frac{\sigma_R}{E_L} \quad (18)$$

4. APPLICATION TO PREDICT CRACK SPACING AND OVERALL STRESS-STRAIN BEHAVIOR

4.1. Prediction of crack spacing

Results obtained in the last section will be used here to predict the tunneling crack spacing in 90° layers as a function of applied stress. The method employed here is identical to that of Hutchinson and Suo [7] used to predict the crack spacing in thin films under residual tension. It considers the effect of a sequential cracking process where a new set of cracks tunnels between an existing set of cracks as the stress is increased, rather than a process where all the cracks tunnel together.

The calculation of the energy release rate for the cracks tunneling in the sequential process makes use of the basic solution (13) for simultaneous steady-state cracking. That solution is for simultaneous tunneling of all the cracks, periodically spaced a distance $2L$ apart, in the 90° layers, as in Fig. 5. For any such laminate, the steady-state tunneling energy release rate for each crack is given by (13),

$$\frac{G_{ss}\bar{E}_0}{\sigma^2 t} = g\left(\frac{t}{L}\right) \quad (19)$$

where here the dependence of g on E_f/E_m and c is left implicit. As noted before, when a residual stress σ_R exists in the 90° layers acting parallel to the overall applied stress σ , then σ in the above formula should be replaced by $\sigma + (E_L + E_T)\sigma_R/(2E_T)$.

Now consider the sequential cracking situation depicted in Fig. 8, where one set of cracks spaced a distance $4L$ apart has already tunneled across all 90° layers, and where a second set bisecting the first set is in the process of tunneling across the layers. We depicted in Fig. 8 only an isolated 90° layer for better viewing. The steady-state energy release rate for the cracks in the process of tunneling can be obtained exactly from the strain energy difference far behind and far ahead of the tunneling fronts as

$$\frac{G_{ss}\bar{E}_0}{\sigma^2 t} = 2g\left(\frac{t}{L}\right) - g\left(\frac{t}{2L}\right) \quad (20)$$

Under the assumption that new cracks will always be nucleated half-way between cracks that have already formed and tunneled, and with G_{ss} identified with the mode I toughness Γ along fiber direction of 90° layers, (20) predicts the relationship between σ and the crack spacing t/L . This relation is plotted in Fig. 9 for bonded fiber/matrix interfaces. There are two features worth noting. For spacing larger than L/t of about 2, there is essentially no interaction between the cracks and the spacing is indeterminate by the present analysis. For smaller spacings the ratio t/L increases approximately linearly with stress σ , and the dependence on the parameters c and E_f/E_m is largely captured in the non-dimensional stress variable $\sigma/\sqrt{(\bar{E}_0\Gamma/t)}$. Implicit in the spacing relationship in Fig. 9 is the assumption that initial flaws exist in the 90° layers of sufficient size and density such that the tunnel cracks *will* initiate when the steady-state condition is met. In this sense, the relation between spacing and stress may predict somewhat smaller spacings at a given stress than actually occurs.

4.2. Prediction of overall stress-strain relation accounting for progressive cracking

Let σ be the overall stress applied to the composite and suppose that a residual stress σ_R exists in the uncracked 90° layers acting parallel to the applied stress. With σ replaced by $\sigma + (E_L + E_T)\sigma_R/(2E_T)$ in the non-dimensional stress variable on the ordinate in Fig. 9, the appropriate curve in this figure can be used to predict t/L as a function of σ . Next, combine (14) and (17) to give the overall strain ϵ as

$$\epsilon = \frac{1}{E_c}\sigma + \epsilon_A = \frac{1}{h}\frac{\sigma}{\bar{E}_0} + \left(\frac{1}{h} - 1\right)\frac{E_L + E_T}{2E_T}\frac{\sigma_R}{\bar{E}_0} \quad (21)$$

Here $h(E_f/E_m, c, t/L)$ can be obtained from Fig. 7 once one has obtained the relation between t/L and σ as just described.

The calculations described above are now illustrated. In Fig. 10 plots are displayed of the normalized overall applied stress against the normalized overall strain for cases in which there is no residual stress. As noted earlier, the stress remains essentially unchanged until the crack spacing reaches an L/t of about 2. This corresponds to the flat portion of the stress-strain curves in Fig. 10. As L/t diminishes to small values (below about $1/2$), the 0° layers carry most of the load, leading to the linear response evident in the figure, with (15) providing the asymptotic slope of these curves. A remarkable feature of these curves is the fact that the non-dimensional overall stress and strain variables used in Fig. 10 nearly collapse all the curves for a wide range of E_f/E_m and c .

Fig. 11 shows the effect of a residual stress σ_R in the 90° layers, a positive value representing a residual tension and a negative value representing a residual compression. The critical stress σ_{cr} used to normalize the residual stress in Fig. 11 is the stress at which cracks begin to tunnel in all the layers in the absence of any residual stress. From (13), this stress is

$$\sigma_{cr} = \sqrt{\frac{\bar{E}_0 \Gamma}{t g(E_f/E_m, c, 0)}} \quad (22)$$

This critical stress is between 5 and 10 % higher than the onset stress for tunneling of an isolated crack given by (12). In Fig. 11, σ is the applied stress. Depending on its sign, the residual stress increases or decreases the applied stress at which matrix cracking occurs and makes a contribution to the overall strain due to its partial release.

5. AN APPROXIMATE THEORETICAL SOLUTION

5.1. The theoretical development

In this section we shall develop an approximate analytical solution to the doubly periodic plane strain crack problem posed in Fig. 5b. Except for a modification suggested at the end of this section, the approximation follows fairly closely a similar solution in [8], where it was

developed to predict the stress transfer between 0° and 90° plies of a cracked laminate. The solution in [8] applies to periodic cracks in a single layer sandwiched between 0° layers on both sides. The following equilibrium equations must be satisfied in both 90° (denoted as material I) and 0° (denoted as material II) plies.

$$\frac{\partial \sigma_x}{\partial x} + \frac{\partial \tau_{xy}}{\partial y} = 0 \quad (23)$$

$$\frac{\partial \tau_{xy}}{\partial x} + \frac{\partial \sigma_y}{\partial y} = 0 \quad (24)$$

The stress-strain relations for plane strain conditions can be easily derived from (1). They are, for 90° plies,

$$\epsilon_x \equiv \frac{\partial u}{\partial x} = \left(\frac{1}{E_T} - \frac{\nu_L^2}{E_L} \right) \sigma_x - \left(\frac{\nu_T}{E_T} + \frac{\nu_L^2}{E_L} \right) \sigma_y \quad (25)$$

$$\epsilon_y \equiv \frac{\partial v}{\partial y} = - \left(\frac{\nu_T}{E_T} + \frac{\nu_L^2}{E_L} \right) \sigma_x + \left(\frac{1}{E_T} - \frac{\nu_L^2}{E_L} \right) \sigma_y \quad (26)$$

$$\epsilon_{xy} \equiv \frac{1}{2} \left(\frac{\partial u}{\partial y} + \frac{\partial v}{\partial x} \right) = \frac{1}{2\mu_T} \tau_{xy} \quad (27)$$

and for 0° plies,

$$\epsilon_x \equiv \frac{\partial u}{\partial x} = \left(\frac{1 - \nu_T^2}{E_T} \right) \sigma_x - \frac{\nu_L(1 + \nu_T)}{E_L} \sigma_y \quad (28)$$

$$\epsilon_y \equiv \frac{\partial v}{\partial y} = - \frac{\nu_L(1 + \nu_T)}{E_L} \sigma_x + \frac{1 - \frac{E_T}{E_L} \nu_L^2}{E_L} \sigma_y \quad (29)$$

$$\epsilon_{xy} \equiv \frac{1}{2} \left(\frac{\partial u}{\partial y} + \frac{\partial v}{\partial x} \right) = \frac{1}{2\mu_L} \tau_{xy} \quad (30)$$

The boundary conditions for a typical cell of the doubly periodic problem are the standard ones reflecting symmetry and the relations between the overall quantities and the averages of local quantities over the cell boundaries.

To proceed, we assume that the stress component σ_y in both plies is independent of x . In other words, we look for an approximate solution of the form

$$\sigma_y^I = -F(y) + \sigma^I \quad (31)$$

$$\sigma_y^{II} = F(y) + \sigma^{II} \quad (32)$$

where σ^I and σ^{II} are the stresses in the 90° and 0° plies, respectively, that would result in a damage-free laminate subject to average remote tensile stress σ . They are given by

$$\sigma^I = \frac{2E_T}{E_T + E_L} \sigma \quad (33)$$

$$\sigma^{II} = \frac{2E_L}{E_T + E_L} \sigma \quad (34)$$

We shall omit a detailed derivation for brevity; most of the details are similar to those given in [8]. After satisfying Eqs. (23-25), (27), (28), (30) exactly, Eqs. (26) and (29) in an average sense with respect to the x -direction, and satisfying all the boundary conditions except those listed below in (36) and (37), we obtain the following linear integral-differential equation for $F(y)$:

$$t^4 F''''(y) - 2a_2 t^2 F''(y) + a_1^2 F(y) + a_0 \frac{1}{L} \int_0^L F(y) dy = 0 \quad (35)$$

where

$$a_2 = \frac{15}{2\Lambda} \left\{ \left(\frac{1}{E_T} - \frac{\nu_L^2}{E_L} + \frac{1 - \nu_T^2}{E_T} \right) \left(\frac{1}{\mu_T} + \frac{1}{\mu_L} \right) - 4 \left[\left(\frac{1}{E_T} - \frac{\nu_L^2}{E_L} \right) \left(\frac{\nu_L(1 + \nu_T)}{E_L} \right) + \left(\frac{\nu_T}{E_T} + \frac{\nu_L^2}{E_L} \right) \left(\frac{1 - \nu_T^2}{E_T} \right) \right] \right\}$$

$$a_1^2 = \frac{45}{\Lambda} \left\{ \left(\frac{1}{E_T} - \frac{v_L^2}{E_L} + \frac{1-v_T^2}{E_T} \right) \left(\frac{1}{E_T} - \frac{v_L^2}{E_L} + \frac{1-\frac{E_T}{E_L}v_L^2}{E_L} \right) - \left[\left(\frac{v_T}{E_T} + \frac{v_L^2}{E_L} \right) - \left(\frac{v_L(1+v_T)}{E_L} \right) \right]^2 \right\}$$

$$a_0 = \frac{45}{\Lambda} \left[\left(\frac{v_T}{E_T} + \frac{v_L^2}{E_L} \right) - \left(\frac{v_L(1+v_T)}{E_L} \right) \right]^2$$

$$\Lambda = \left(\frac{1}{E_T} - \frac{v_L^2}{E_L} + \frac{1-v_T^2}{E_T} \right)^2 + 20 \left(\frac{1}{E_T} - \frac{v_L^2}{E_L} \right) \left(\frac{1-v_T^2}{E_T} \right)$$

The remaining boundary conditions to be satisfied are given by

$$F(0) = 0, \quad F(L) = \sigma^I, \quad \text{and} \quad F'(L) = 0 \quad (36)$$

In addition, it is required that $F(y)$ be an even function in y :

$$F(y) = F(-y) \quad (37)$$

The solution to (35) can be used to express the integral of $F(y)$ as

$$\int_0^L F(y) dy = \tau \Phi\left(\frac{t}{L}\right) \sigma^I \quad (38)$$

where Φ (which is also a function of a_0 , a_1 and a_2) will be given below. The Young's modulus of the cracked composite, \bar{E}_c , is then approximately

$$\bar{E}_c = \frac{\sigma}{\bar{v}^{II}(L)/L} = \frac{\bar{E}_0}{1 + \frac{\tau}{L} \frac{E_T}{E_L} \Phi} \quad (39)$$

and the tunneling energy release rate G_{ss} , calculated from

$$G_{ss} = \sigma^I [\bar{v}^{II}(L) - \bar{v}^I(L)] \quad (40)$$

is given by the approximation

$$\frac{G_{ss}\bar{E}_0}{\sigma^2 t} = \frac{2E_T}{E_L} \Phi \quad (41)$$

In Eqs. (39) and (40), terms such as $\bar{v}(L)$ stand for the average y -displacement along $y=L$.

For the case a_2/a_1 is less than 1, Φ is given by

$$\Phi\left(\frac{t}{L}\right) = \frac{\frac{2(1-h)mn}{m^2+n^2} \left(\cosh \frac{2mL}{t} - \cos \frac{2nL}{t} \right)}{m \sin \frac{2nL}{t} + n \sinh \frac{2mL}{t} - \frac{2hmn}{m^2+n^2} \frac{t}{L} \left(\cosh \frac{2mL}{t} - \cos \frac{2nL}{t} \right)} \quad (42)$$

where

$$m = \sqrt{(a_1 + a_2)/2}$$

$$n = \sqrt{|a_1 - a_2|/2}$$

$$h = \frac{a_0}{a_0 + a_1^2}$$

For cases where a_2/a_1 is equal to or greater than 1, similar solutions can be obtained. However, for most practical fiber-reinforced composites, a_2/a_1 is either less than 1 or sufficiently close to 1 such that (42) is a good approximation.

5.2. Modification using the FEM results

The analytical approximation given by Eqs. (39), (41) and (42) can be further enhanced by a slight modification of Φ in (42), which was suggested by the comparison of the approximate predictions with the more accurate FEM results obtained in Section 3. We found that the accuracy of the above approximation was improved when we replaced m and n in (42) by $1.1m$ and $1.1n$, respectively, and then multiplied Φ by the numerical factor 0.82. Thus the modified Φ is given by

$$\Phi\left(\frac{t}{L}\right) = \frac{0.82 \frac{2(1-h)mn}{m^2+n^2} \left(\cosh \frac{2.2mL}{t} - \cos \frac{2.2nL}{t} \right)}{1.1m \sin \frac{2.2nL}{t} + 1.1n \sinh \frac{2.2mL}{t} - \frac{2hmn}{m^2+n^2} \frac{t}{L} \left(\cosh \frac{2.2mL}{t} - \cos \frac{2.2nL}{t} \right)} \quad (43)$$

Several comparisons of the results given by FEM analysis and the explicit formulas of Eqs. (39) and (41) are demonstrated in Figs. 12a. and 12b. The differences for all practical ranges of E_f/E_m and c are within 5%, and thus we believe the formulas given above are well suited for practical applications.

Acknowledgment

This work was supported in part by the DARPA URI (Subagreement P.O.#KK3007 with the University of California, Santa Barbara, ONR Prime Contract N00014-92-J-1808) and by the Division of Applied Sciences, Harvard University. Finite element analyses are carried using ABAQUS (Hibbitt, Karlsson & Sorensen Inc., Providence, Rhode Island, U.S.A.).

References

1. D. H. Allen, C. E. Harris and S. E. Groves, *Int. J. Solids Structures*. **23**, 1301 (1987).
2. D. H. Allen, C. E. Harris and S. E. Groves, *Int. J. Solids Structures*. **23**, 1319 (1987).
3. P. Gudmundson and S. Ostlund, *J. Composite Materials*. **26**, 1009 (1992).
4. P. Gudmundson and W. Zang, SICOMP Tech. Report 92-007 (1992).
5. D. S. Beyerle, S. M. Spearing and A. G. Evans. To be published.
6. R. M. Christensen, *Mechanics of Composite Materials*. Wiley, New York (1979).
7. J. W. Hutchinson and Z. Suo, in *Advances in Applied Mechanics* (edited by J. W. Hutchinson and T. Y. Wu), Vol. 29, p. 64. Academic Press, New York (1991).
8. L. N. McCartney, *J. Mech. Phys. Solids*. **40**, 27 (1992).

APPENDIX

When an initial residual stress σ_R exists in the 90° layers acting parallel to the applied stress, an additional overall strain ϵ_A occurs due to the release of residual stress by the formation of the cracks in the 90° layers. This additional strain can be calculated by applying a normal stress of $(-\sigma_R)$ to the crack surface. Fig. A1(a) depicts a quarter of such a periodic cell, with standard symmetry boundary conditions applied. By a linear superposition argument, one can

easily verify that the displacement and stress fields of Fig. A1(a) can be obtained by subtracting that in Fig. A1(c) from Fig. A1(b), where (b) has the same crack configuration as (a), and (c) depicts the crack-free laminate. The elements in (b) and (c) are both subject to an average stress $(E_L + E_T)\sigma_R / (2E_T)$. The overall strain ϵ_b associated with (b) is given by (14)

$$\epsilon_b = \frac{1}{\bar{E}_c} \frac{E_L + E_T}{2E_T} \sigma_R = h^{-1} \frac{E_L + E_T}{2E_T} \frac{\sigma_R}{\bar{E}_0} \quad (A1)$$

and the overall strain ϵ_c in (c) is given by a uniform plane strain tension

$$\epsilon_c = \frac{1}{\bar{E}_0} \frac{E_L + E_T}{2E_T} \sigma_R \quad (A2)$$

The overall strain ϵ_A in (a) is then

$$\epsilon_A = \epsilon_b - \epsilon_c = (h^{-1} - 1) \frac{E_L + E_T}{2E_T} \frac{\sigma_R}{\bar{E}_0} \quad (A3)$$

which is (16) given in Section 3.

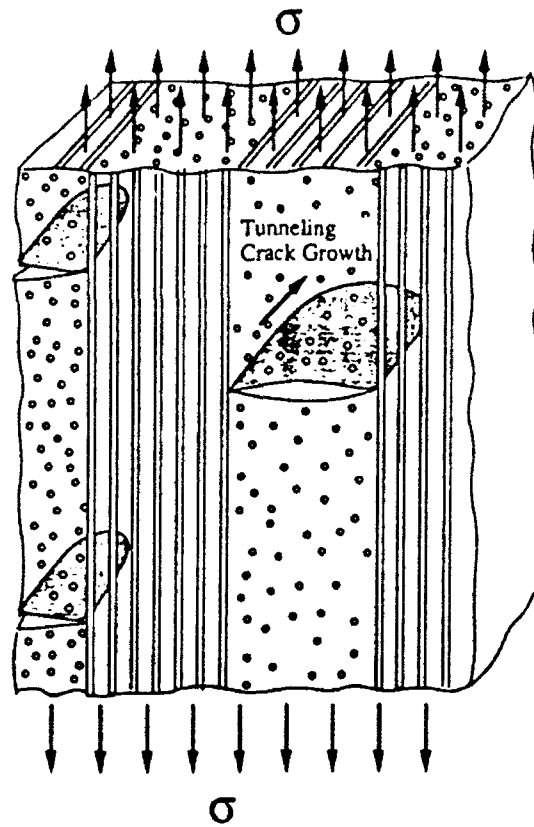


Fig. 1. A schematic of the 3D tunneling cracks in the 90° layers.

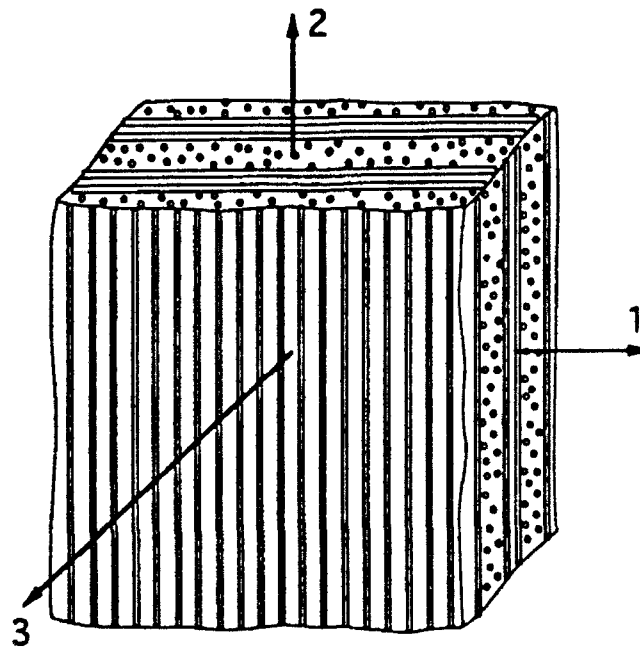


Fig. 2. Conventions for the 3D cross-ply laminate.

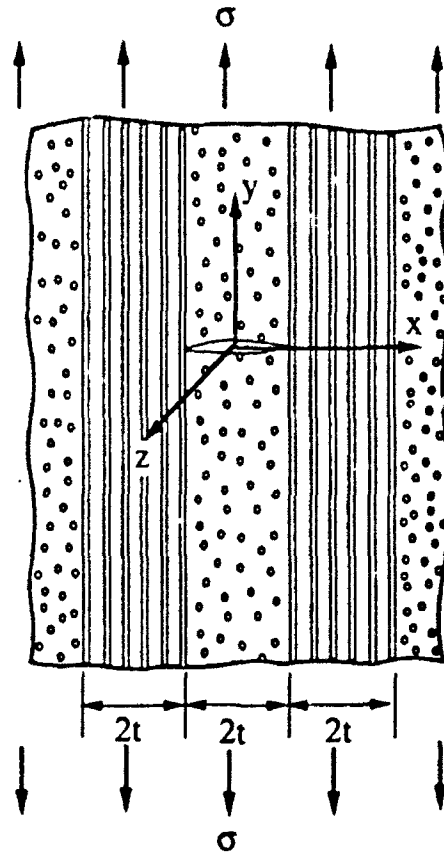


Fig. 3. An isolated crack in a 90° layer.

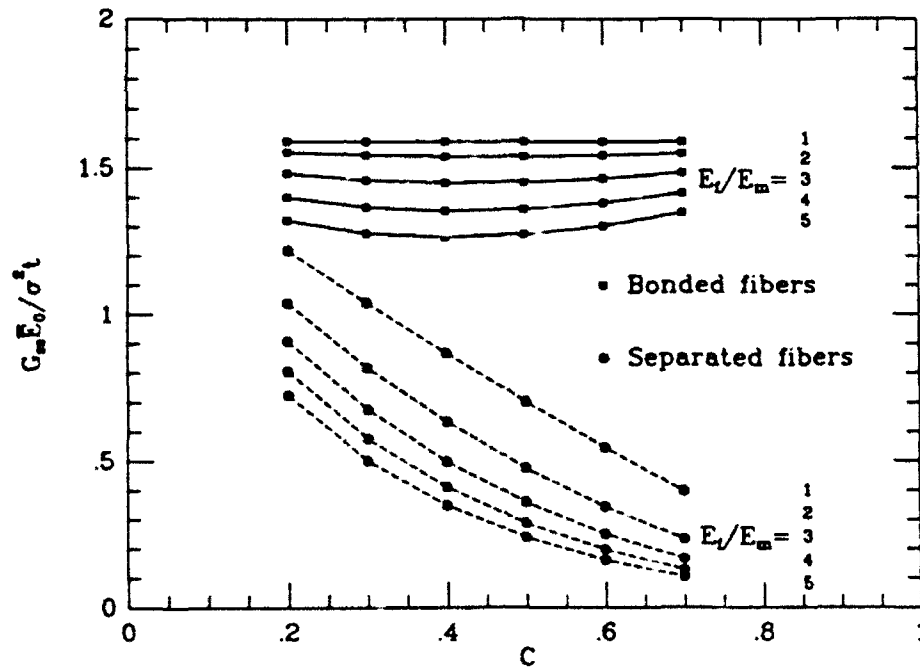


Fig. 4. The function, $f(E_f/E_m, c)$, providing the tunneling energy release rate in (11) for an isolated crack.

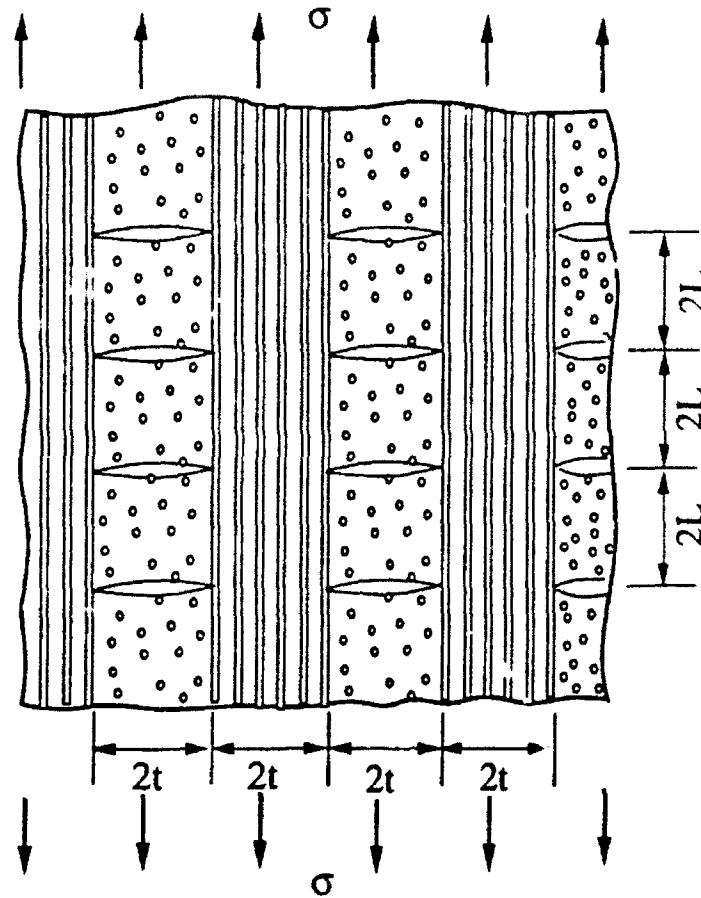


Fig. 5a. The doubly periodic crack pattern analysed in this paper.

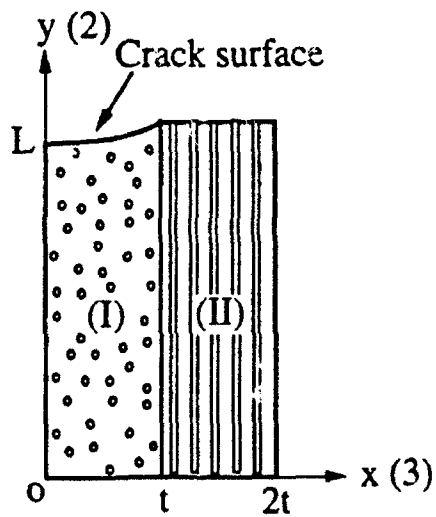


Fig. 5b. A quarter of a periodic cell used for the finite element model.

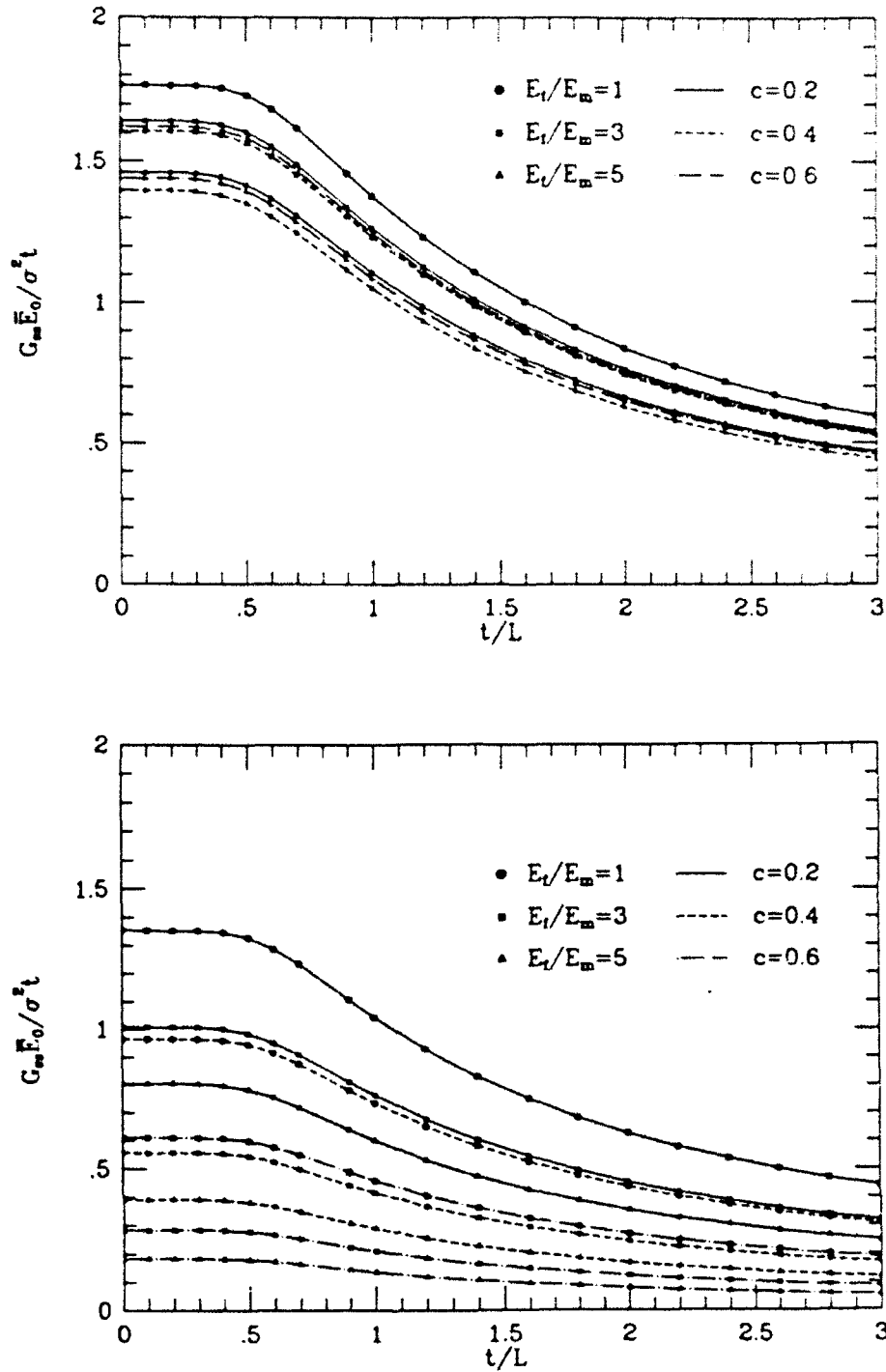


Fig. 6.

The function, $g(E_f/E_m, c, t/L)$, providing the energy release rate for a doubly periodic array of tunneling cracks in (13). (a) Bonded fiber/matrix interfaces, (b) Separated fiber/matrix interfaces.

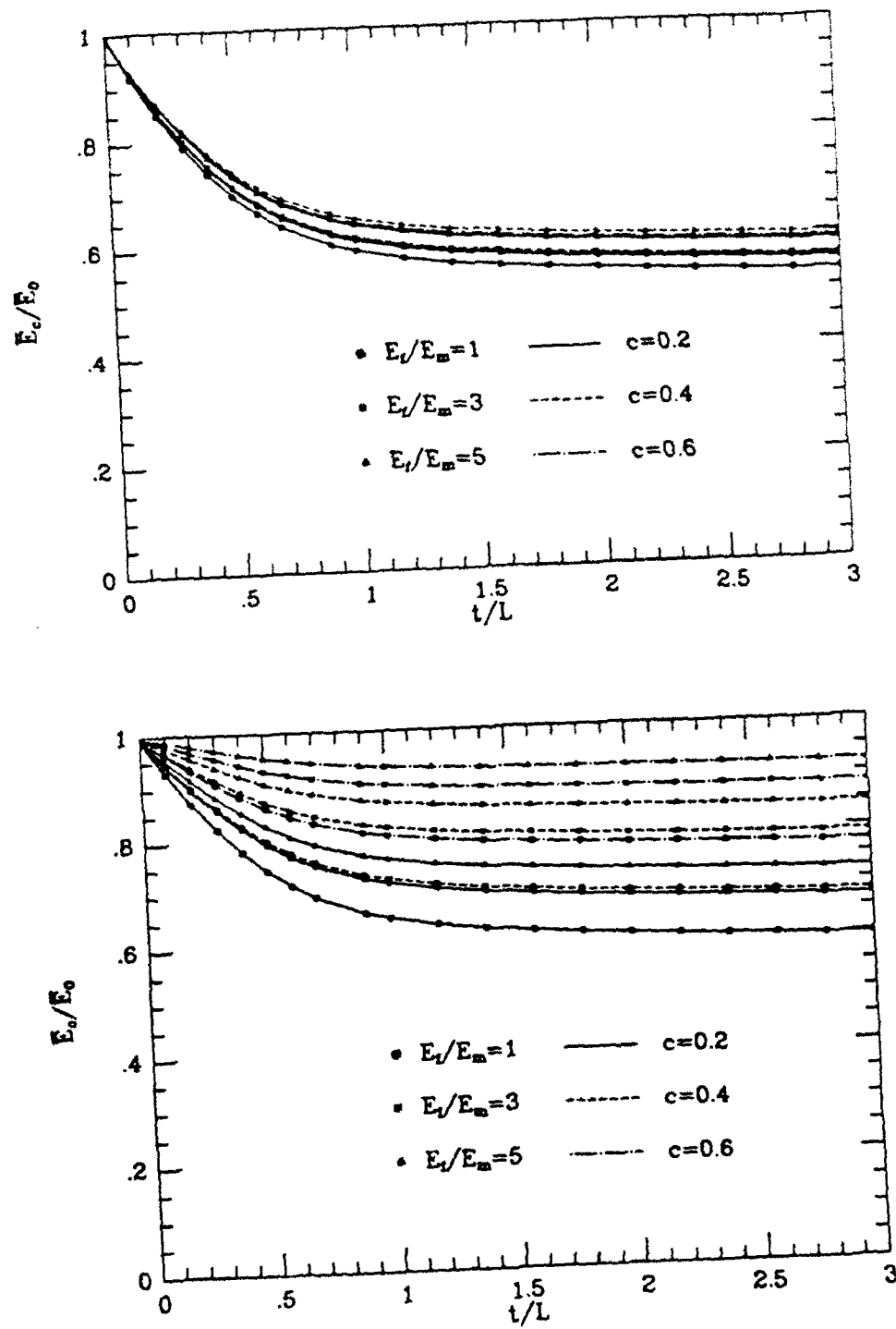


Fig. 7. The function, $h(E_f/E_m, c, t/L)$, providing the effective Young's modulus for the cracked laminate in (14). (a) Bonded fiber/matrix interfaces. (b) Separated fiber/matrix interfaces.

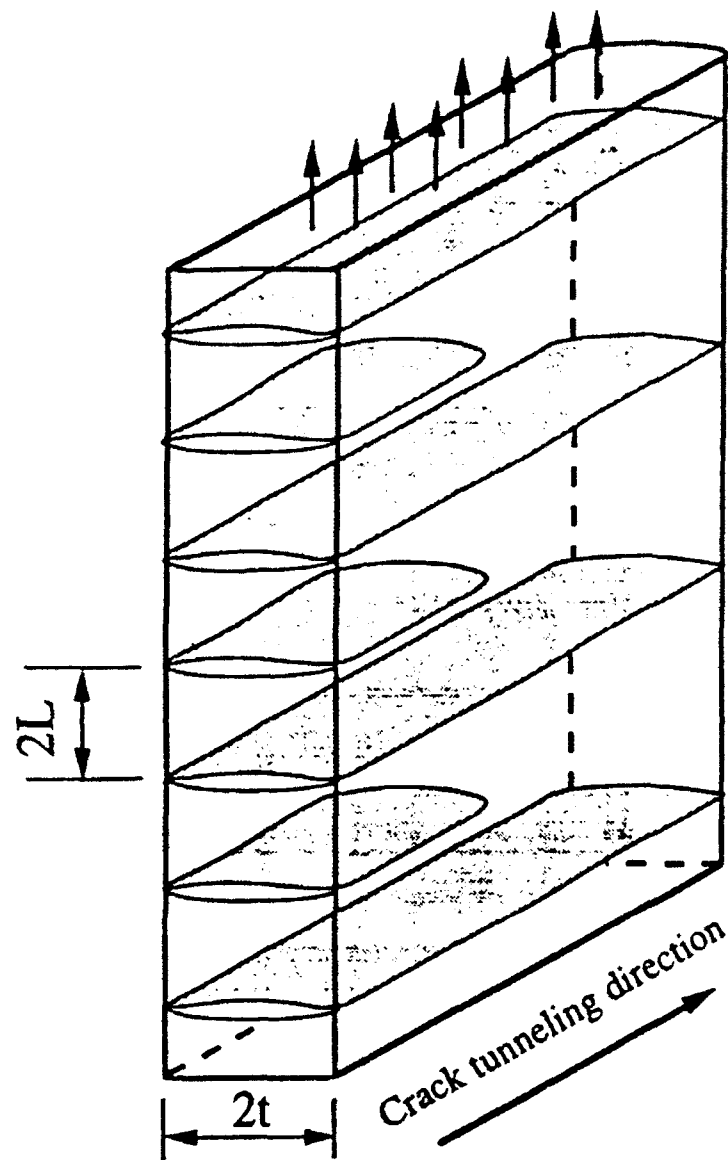


Fig. 8. A new set of tunneling cracks bisecting an existing set of cracks in a given layer.

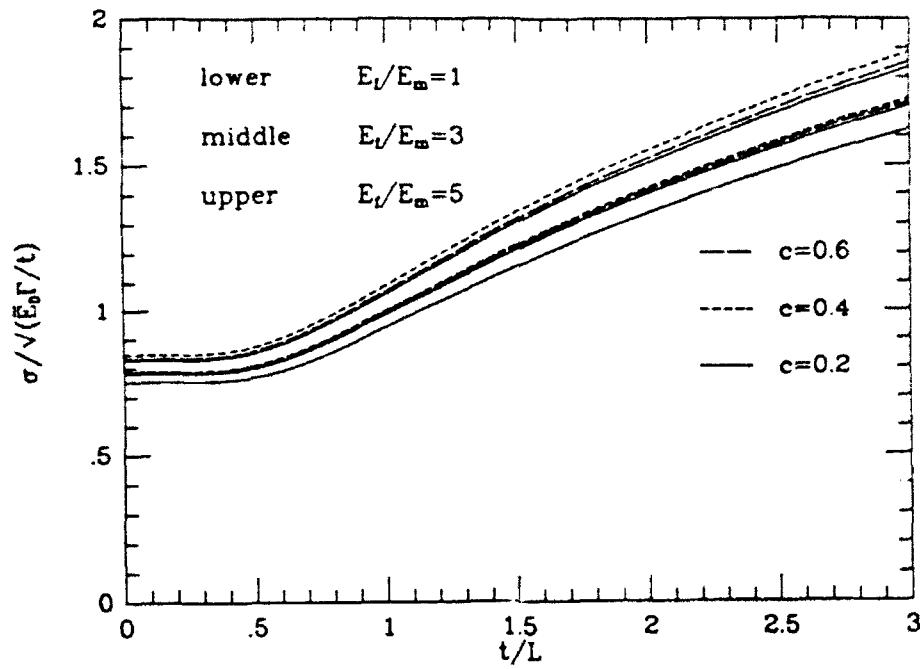


Fig. 9. Relationship between applied stress and crack spacing.

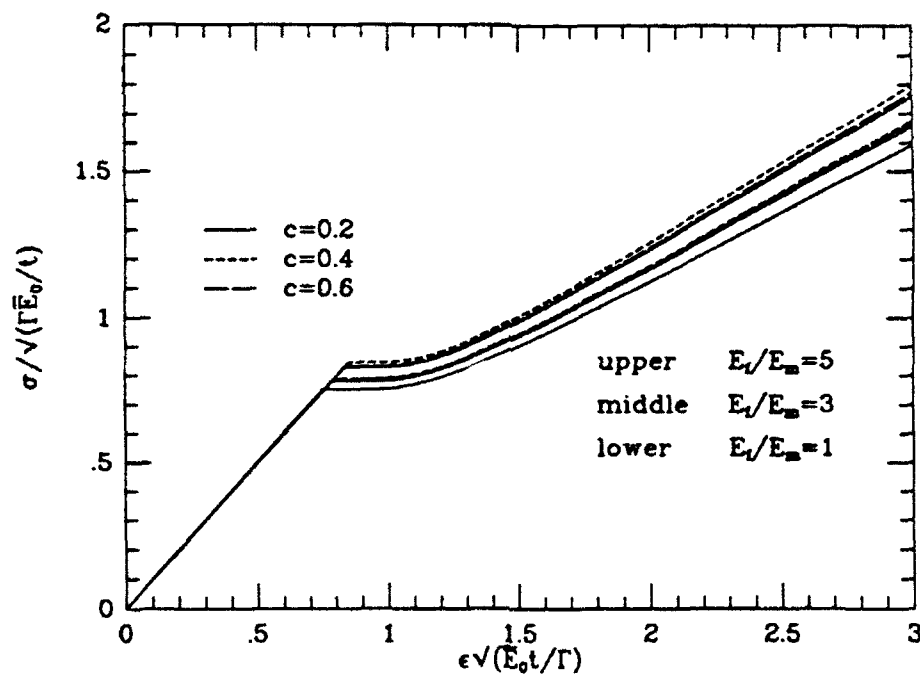


Fig. 10. Overall stress-strain behavior in the absence of residual stress.

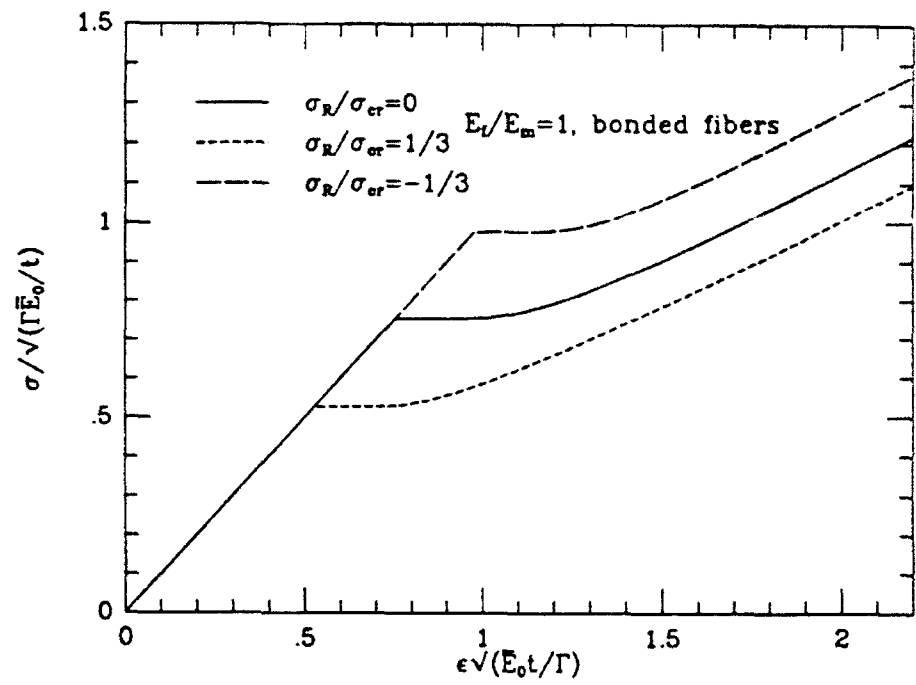


Fig. 11. An illustration of the effect of residual stress on overall stress-strain behavior

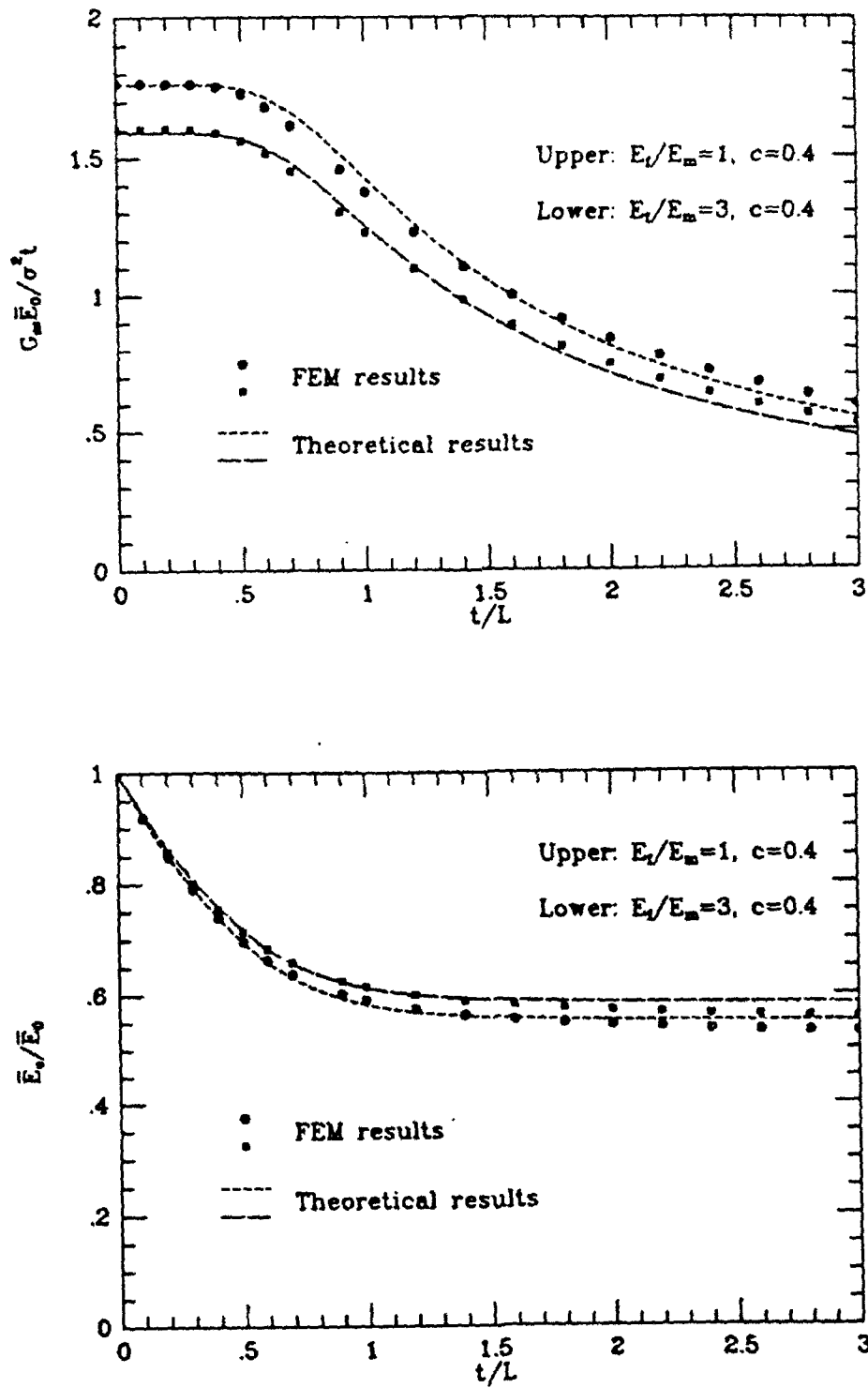


Fig. 12 (a) Demonstration of the accuracy of explicit formula (39). (b) Demonstration of the accuracy of explicit formula (41).

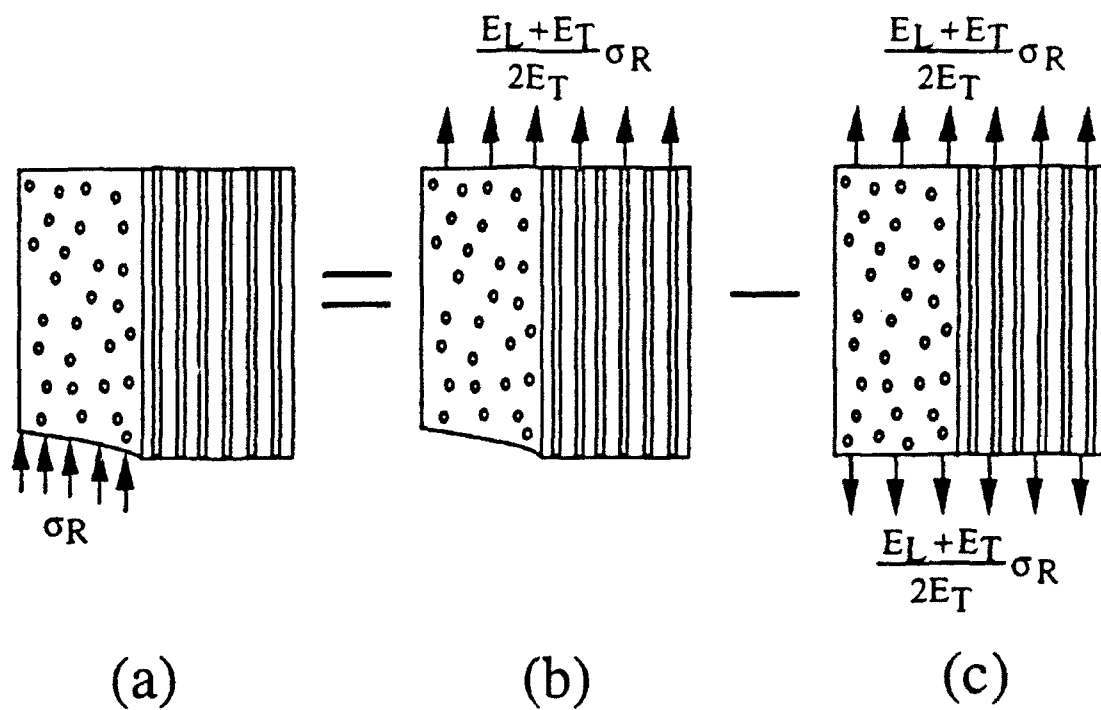


Fig. A1. Superposition scheme for obtaining ϵ_A due to the release of residual stress.



Plane strain delamination growth in composite panels

P.-L. Larsson

Department of Solid Mechanics, The Royal Institute of Technology, S-10044, Stockholm, Sweden

&

F. A. Leckie

Department of Mechanical Engineering, University of California, Santa Barbara, CA 93106, USA

Composite panels with straight-through cracks are analyzed with respect to energy release rates using an asymptotic method. Various combinations of geometry and material parameters are considered and predictions are made about the initiation and stability of crack growth.

1 INTRODUCTION

With the increasing use of composite panels in design, such problems as inter-layer cracks or delaminations have received much attention in recent years. This type of damage may be present already at fabrication but may also develop for example if a structure is exposed to impact. Since the presence of delaminations can severely reduce the stiffness and strength of a load-carrying member they are a common cause of failure in laminates. Perhaps the first investigators to study the problem of delaminated plates in a systematic manner were Chai *et al.*¹ and after that numerous articles have been published dealing with delamination problems in flat panels. However, as pointed out in a survey article by Storåkers² delamination problems for more complex geometries, such as composite shells or curved panels, have been treated very sparsely and in the latter case the analyses have been restricted to determine the buckling load for compressed members containing longitudinal delaminations.^{3,4}

The present study is concerned with a single delamination growth in a curved composite panel. Damage of this type has been reported in a recent experimental study by Lin and Lee⁵ and its practical significance should be substantial, particularly in aircraft structures. The material properties for the individual layers are considered to be linear orthotropic and the calculations are per-

formed under plane strain conditions, with the panels loaded in prescribed displacement. Linear fracture mechanics is relied upon as regards initiation and propagation of crack growth and such events are assumed to occur at a constant value of the critical energy release rate. However, such features as a decomposition of the energy release rate into tearing and shearing modes, as discussed by Suo and Hutchinson⁶ and Suo⁷ could without any difficulties be incorporated into the analysis. The more simple criterion involving the total energy release rate is, however, adopted in the present case due to its solid physical background.

As mentioned earlier the problem of delaminations in curved panels has been treated very sparsely in the literature and, to the authors' knowledge, no attention has been given to, for example, crack growth stability. The aim of the present contribution is therefore not only to examine such features as the effect of geometry and material parameters on the mechanical behaviour but also to provide some general insight as regards crack growth initiation and propagation in curved panels.

2 BASIC EQUATIONS

The problem concerned involves a composite panel loaded in prescribed displacement as depicted in Fig. 1. Plane strain conditions are

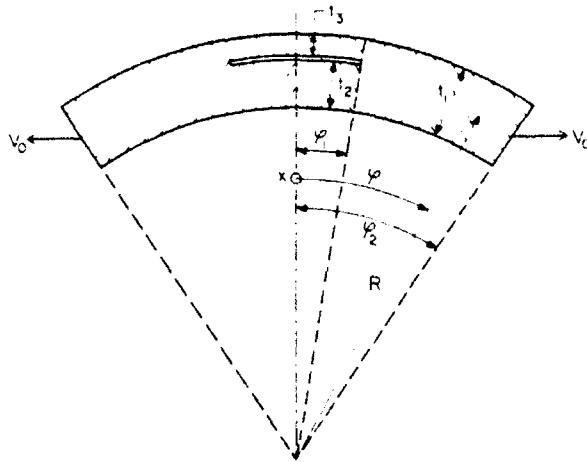


Fig. 1. Panel and delamination geometry.

assumed to prevail which leads to

$$\left. \begin{aligned} u &= 0 \\ \frac{\partial}{\partial x} &= 0 \end{aligned} \right\} \quad (1)$$

u being the displacement in the x -direction. With eqns (1) in mind the only remaining strain component in the Kirchhoff-Love approximation for kinematics then reads

$$\epsilon_\varphi = \frac{1}{R} \frac{dv}{d\varphi} + \frac{w}{R} - \frac{z}{R^2} \frac{d^2 w}{d\varphi^2} \quad (2)$$

where v is the displacement in the φ -direction and w is the transversal displacement. In the present analysis the thickness of the panel is considered to be very small compared to the radius of curvature, R , and the well known Donnell approximations, as utilized in eqn (2), are assumed to give sufficient information as regards kinematics.

For a composite panel, with individual layers assumed to be linear orthotropic with principal axes of orthotropy coinciding with the coordinate directions x and φ , the constitutive equations for relevant quantities reads

$$\left. \begin{aligned} N_\varphi &= \frac{A}{R} \left(\frac{dv}{d\varphi} + w + \frac{1}{2R} \left(\frac{dw}{d\varphi} \right)^2 \right) - \frac{B}{R^2} \frac{d^2 w}{d\varphi^2} \\ M_\varphi &= \frac{B}{R} \left(\frac{dv}{d\varphi} + w + \frac{1}{2R} \left(\frac{dw}{d\varphi} \right)^2 \right) - \frac{D}{R^2} \frac{d^2 w}{d\varphi^2} \end{aligned} \right\} \quad (3)$$

where A , B and D are given by

$$[A, B, D] = \int_{-h/2}^{h/2} Q_p [1, z, z^2] dz \quad (4)$$

In eqn (4), h is the total panel thickness and $Q_p = E_{\varphi p} / (1 - E_{\varphi p} \nu_{\varphi p}^2 / E_{x p})$ is the reduced modulus of the p th layer with moduli $E_{\varphi p}$ and $E_{x p}$, and contraction ratio $\nu_{\varphi p}$, in obvious notation. The non-linear equilibrium equations, with the contribution from the shearing force T_φ retained, is for the present problem

$$\left. \begin{aligned} (i) \quad & \frac{1}{R} \frac{dT_\varphi}{d\varphi} - \frac{N_\varphi}{R} = - \frac{N_\varphi}{R^2} \frac{d^2 w}{d\varphi^2} \\ (ii) \quad & \frac{T_\varphi}{R} + \frac{1}{R} \frac{dN_\varphi}{d\varphi} = \frac{T_\varphi}{R^2} \frac{d^2 w}{d\varphi^2} \\ (iii) \quad & T_\varphi - \frac{1}{R} \frac{dM_\varphi}{d\varphi} = 0 \end{aligned} \right\} \quad (5)$$

In order to completely describe the problem depicted in Fig. 1, presently modelled as composed of three composite panels, it now remains to establish boundary and continuity conditions. With symmetry prevailing around $\varphi = 0$ this requires that

$$\left. \begin{aligned} v &= 0 \\ \frac{dw}{d\varphi} &= 0 \end{aligned} \right\} \quad (6)$$

and

$$T_\varphi = 0 \quad (7)$$

at this point.

With a prescribed displacement v_0 , applied to the free edge of the panel the kinematic conditions at $\varphi = \varphi_0$ are

$$\left. \begin{aligned} v &= v_0 \cos \varphi_2 \\ w &= v_0 \sin \varphi_2 \end{aligned} \right\} \quad (8)$$

and the dynamic boundary condition is

$$M_\varphi = 0 \quad (9)$$

There remains then the need to establish equations of compatibility and continuity of dynamic variables at the crack front, $\varphi = \varphi_2$. Figure 2 shows the details of the geometry of the three panels 1, 2, 3 at the delamination boundary. As regards kinematics continuity of transverse displacement and slope requires

$$w_1 = w_2 = w_3 \quad (10)$$

$$\frac{dw_1}{d\varphi} = \frac{dw_2}{d\varphi} = \frac{dw_3}{d\varphi} \quad (11)$$

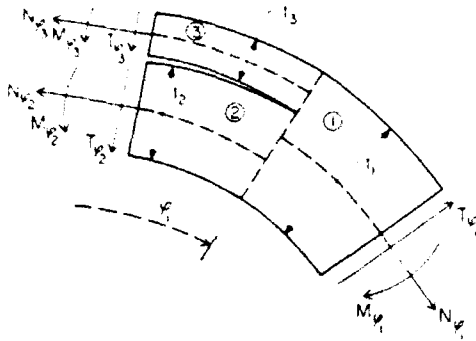


Fig. 2. Load resultants at the delamination front.

while continuity of in-plane displacements requires

$$v_2 - v_1 = -\frac{t_3}{2R} \frac{dw_1}{d\varphi} \quad (12)$$

$$v_3 - v_2 = -\frac{t_1}{2R} \frac{dw_1}{d\varphi} \quad (13)$$

Continuity of membrane forces, shearing forces and bending moments requires

$$N_{q1} = N_{q2} + N_{q3} \quad (14)$$

$$T_{q1} = T_{q2} + T_{q3} \quad (15)$$

$$M_{q1} = M_{q2} + M_{q3} + \frac{1}{2} (N_{q1} t_2 - N_{q2} t_3) \quad (16)$$

respectively.

With the formulation of the boundary value problem completed it is appropriate to introduce dimensionless variables according to

$$\left. \begin{aligned} \bar{v}_i &= v_i/t_1 \\ \bar{w}_i &= w_i/t_1 \\ \bar{R} &= R/t_1 \\ \bar{v}_0 &= v_0/t_1 \end{aligned} \right\} \quad (17)$$

with $i = 1, 2, 3$ for the individual panels.

By using the relations (3) and (5) together with (17) the governing eqns (5) (i) and (ii) can now be written in dimensionless form as

$$\begin{aligned} \bar{D}_i \frac{d^2 \bar{w}}{d\bar{q}^2} - 2\bar{B}_i \frac{d^2 \bar{w}}{d\bar{q}^2} + \bar{A}_i \bar{w} - \bar{B}_i \frac{d^2 \bar{r}}{d\bar{q}^2} + \bar{A}_i \frac{d\bar{r}}{d\bar{q}} \\ = \bar{A}_i \left[\left(\frac{d\bar{r}}{d\bar{q}} + \bar{w} + \frac{1}{2\bar{R}} \left(\frac{d\bar{w}}{d\bar{q}} \right)^2 \right) \frac{d^2 \bar{w}}{d\bar{q}^2} - \frac{1}{2} \left(\frac{d\bar{w}}{d\bar{q}} \right)^2 \right] \\ + \bar{B}_i \left(\frac{d\bar{w}}{d\bar{q}} \right) \left(\frac{d^2 \bar{w}}{d\bar{q}^2} \right) \end{aligned} \quad (18)$$

$$\begin{aligned} (\bar{B}_i + \bar{D}_i) \frac{d^2 \bar{w}}{d\bar{q}^2} - (\bar{A}_i + \bar{B}_i) \left(\frac{d^2 \bar{r}}{d\bar{q}^2} + \frac{d\bar{w}}{d\bar{q}} \right) \\ = (\bar{A}_i + \bar{B}_i) \left(\frac{d\bar{w}}{d\bar{q}} \right) \left(\frac{d^2 \bar{w}}{d\bar{q}^2} \right) \\ - \bar{B}_i \left(\frac{d^2 \bar{r}}{d\bar{q}^2} + \frac{d\bar{w}}{d\bar{q}} + \frac{1}{\bar{R}} \left(\frac{d\bar{w}}{d\bar{q}} \right) \left(\frac{d^2 \bar{w}}{d\bar{q}^2} \right) \right) \frac{d^2 \bar{w}}{d\bar{q}^2} \\ + \bar{D}_i \left(\frac{d^2 \bar{w}}{d\bar{q}^2} \right) \left(\frac{d^3 \bar{w}}{d\bar{q}^3} \right) \end{aligned} \quad (19)$$

where

$$\left. \begin{aligned} \bar{A}_i &= A_i R^2 / \bar{R} D_i \\ \bar{B}_i &= B_i R / \bar{R} D_i \\ \bar{D}_i &= D_i / \bar{R} D_i \end{aligned} \right\} \quad (20)$$

with A_i , B_i and D_i defined in eqn (4).

The dimensionless variables may finally be introduced into the boundary, compatibility and continuity conditions (6)–(16). The resulting explicit expressions, however, are suppressed for brevity.

3 SOLUTION PROCEDURE

In order to solve the problem as given in eqns (18) and (19) an asymptotic method was applied. For this purpose the kinematical variables \bar{r}_i and \bar{w}_i were expressed with the aid of series expansion as

$$\left. \begin{aligned} \bar{r}_i &= s\bar{r}_i^1 + s^2\bar{r}_i^2 + s^3\bar{r}_i^3 + \dots + s^j\bar{r}_i^j + \dots \\ \bar{w}_i &= s\bar{w}_i^1 + s^2\bar{w}_i^2 + s^3\bar{w}_i^3 + \dots + s^j\bar{w}_i^j + \dots \end{aligned} \right\} \quad (21)$$

where s can be any monotonically increasing parameter, in this case chosen to be the non-dimensionalized loading parameter \bar{v}_0 . As regards the displacements \bar{r} and \bar{w} in eqn (21), and in the sequel, lower index $i = 1, 2, 3$ still represents the individual panels while upper index j refers to the order of approximation.

By introducing eqn (21) into the non-linear governing equations (18) and (19) the solution to the problem is now given by solving a number of systems of linear equations reading

$$\begin{aligned}
 s: & \left\{ \begin{aligned} \bar{D}_i \frac{d^4 \bar{w}_i^1}{d\varphi^4} - 2\bar{B}_i \frac{d^2 \bar{w}_i^1}{d\varphi^2} + \bar{A}_i \bar{w}_i^1 - \bar{B}_i \frac{d^3 \bar{r}_i^1}{d\varphi^3} + \bar{A}_i \frac{d\bar{r}_i^1}{d\varphi} &= 0 \\ \bar{B}_i + \bar{D}_i \frac{d^3 \bar{w}_i^1}{d\varphi^3} - (\bar{A}_i + \bar{B}_i) \left(\frac{d^2 \bar{r}_i^1}{d\varphi^2} + \frac{d\bar{w}_i^1}{d\varphi} \right) &= 0 \end{aligned} \right. \\
 s^2: & \left\{ \begin{aligned} \bar{D}_i \frac{d^4 \bar{w}_i^2}{d\varphi^4} - 2\bar{B}_i \frac{d^2 \bar{w}_i^2}{d\varphi^2} + \bar{A}_i \bar{w}_i^2 - \bar{B}_i \frac{d^3 \bar{r}_i^2}{d\varphi^3} + \bar{A}_i \frac{d\bar{r}_i^2}{d\varphi} \\ &= \bar{A}_i \left[\left(\frac{d\bar{r}_i^1}{d\varphi} + \bar{w}_i^1 \right) \frac{d^2 \bar{w}_i^1}{d\varphi^2} - \frac{1}{2} \left(\frac{d\bar{w}_i^1}{d\varphi} \right)^2 \right] + \bar{B}_i \left(\frac{d\bar{w}_i^1}{d\varphi} \right) \left(\frac{d^3 \bar{w}_i^1}{d\varphi^3} \right) \\ (\bar{B}_i + \bar{D}_i) \frac{d^3 \bar{w}_i^2}{d\varphi^3} - (\bar{A}_i + \bar{B}_i) \left(\frac{d^2 \bar{r}_i^2}{d\varphi^2} + \frac{d\bar{w}_i^2}{d\varphi} \right) \\ &= (\bar{A}_i + \bar{B}_i) \left(\frac{d\bar{w}_i^1}{d\varphi} \right) \left(\frac{d^2 \bar{w}_i^1}{d\varphi^2} \right) - \bar{B}_i \left(\frac{d^2 \bar{r}_i^1}{d\varphi^2} + \frac{d\bar{w}_i^1}{d\varphi} \right) \frac{d^2 \bar{w}_i^1}{d\varphi^2} + \bar{D}_i \left(\frac{d^2 \bar{w}_i^1}{d\varphi^2} \right) \left(\frac{d^3 \bar{w}_i^1}{d\varphi^3} \right) \\ &\vdots \end{aligned} \right. \quad (22)
 \end{aligned}$$

The form of the general solution to eqn (22) is the same for all degrees of approximations and reads

$$\begin{aligned}
 \bar{r}_i^j &= (C'_i)_1 \cos \varphi + (C'_i)_2 \sin \varphi + (C'_i)_3 \varphi^3 + (C'_i)_4 \varphi^2 + (C'_i)_5 \varphi + (C'_i)_6 + (f'_i)_1 \\
 \bar{w}_i^j &= \frac{(\bar{A}_i + \bar{B}_i)}{(\bar{A}_i + 2\bar{B}_i + \bar{D}_i)} ((C'_i)_1 \sin \varphi - (C'_i)_2 \cos \varphi) - 3(C'_i)_3 \varphi^2 - 2(C'_i)_4 \varphi - \frac{(\bar{A}_i(C'_i)_5 + 6\bar{B}_i(C'_i)_3)}{\bar{A}_i} + (f'_i)_2 \quad (23)
 \end{aligned}$$

where $(C'_i)_k$, $k=1, \dots, 6$ are unknown constants and $(f'_i)_1$ and $(f'_i)_2$ are functions of φ given by the right-hand side of eqn (22). By introducing eqn (23) into the boundary and continuity conditions (6)–(16) the problem is reduced to solve a system of linear equations with 18 unknowns for each degree of approximation (each value of j). Formally the equation system reads

$$[a'] [C'] = [g'] \quad (24)$$

where the matrix a' is a function of geometry and material parameters and the vector g' is given by $(f'_i)_1$ and $(f'_i)_2$ and its derivatives. Note, however, that in the case of $j=1$ the only non-zero terms in g' are due to the boundary condition (8).

The solution for the unknown constants $(C'_i)_k$ in eqn (24) can then be given in closed form for each degree of approximation even though some tedious but otherwise straightforward calculations are required. However, for brevity the final solution to eqn (24) is not given.

In order to gain confidence in the asymptotic solution described above, finite element calculations were performed using the ABAQUS program system⁸ with eight-node plane strain elements. Remembering that symmetry prevails around $\varphi=0$, half of the panel were discretized into a set of 66 elements and the calculated displacements were compared with the ones given by the asymptotic solution for different material and geometry combinations.

4 THE ENERGY RELEASE RATE AT DELAMINATION GROWTH

As mentioned earlier, the criterion adopted for initiation and continuation of delamination growth is that the energy release per unit area of growth will attain a critical and constant value. When crack growth is self-similar it is then a straightforward matter to determine the rate of change of potential energy of the system. In a general situation, however, the resistance of crack propagation may be mode-dependent and inhomogeneity of crack parameters might become quite intricate. This matter will, however, not be considered in the present analysis.

In the case of a composite plate, local values of the energy release rate taking due account of non-linear kinematics in a general situation have recently been derived by Storakers and Andersson⁵ starting from the von Karman plate theory and first principles. Thus, these writers found that the energy released at crack advance $\delta a(x_\alpha)$ at a crack contour Γ_c having the local normal n_α , could be expressed as

$$-\delta U = \int \| P_{\alpha\beta} \| n_\alpha n_\beta \delta a d\Gamma_c \quad (25)$$

where $P_{\alpha\beta}$ is a plate analogue of Eshelby's momentum tensor and $\| \|$ denotes its jump determined from the individual plate members intersecting at the crack front.

For a composite plate, $P_{\alpha\beta}$ explicitly reads

$$P_{\alpha\beta} = W\delta_{\alpha\beta} - N_{\alpha\gamma}\mu_{\gamma,\beta} + M_{\alpha\gamma}\mu_{\gamma,\beta\beta} - Q_\alpha\mu_{3,\beta} \quad (26)$$

where W denotes the plate strain energy density and Q_α is the effective shear force.

As discussed by Storakers² no fundamental difficulties appear when extending eqns (25) and (26) to apply also to non-linear panel problems. In fact, without going into details, when the Donnell approximation for kinematics is relied upon and plane strain conditions prevail only

$$\frac{1}{R} \frac{\partial v}{\partial q} + \frac{w}{R} \quad (27)$$

need to be introduced as a replacement for $\mu_{\gamma,\beta}$ in eqn (26).

With (27) introduced as a replacement in eqn (26) the released energy per unit area can be determined as

$$G = P_1 - P_2 - P_3 \quad (28)$$

in obvious notation.

With the aid of the adopted constitutive equation, derivation of the P -values for the individual panels expressed in the displacements v and w is quite straightforward. If terms that do not contribute to the total energy release rate in eqn (28), due to compatibility and continuity of dynamic variables at the crack front, are neglected then

$$\begin{aligned} P_1 = & -\frac{A}{2R^2} \left(\frac{dv}{dq} + w + \frac{1}{2R} \left(\frac{dw}{dq} \right)^2 \right) \frac{dv}{dq} \\ & + \frac{B}{2R^2} \left(2 \frac{dv}{dq} + w + \frac{1}{2R} \left(\frac{dw}{dq} \right)^2 \right) \frac{d^2 w}{dq^2} \\ & - \frac{D_1}{2R^2} \left(\frac{d^2 w}{dq^2} \right)^2 \end{aligned} \quad (29)$$

Once the solution to v and w is known it is then a routine matter to determine the energy release rate by aid of eqns (24) and (25) even though due account has to be taken of the degree of approximation in the asymptotic solution. When presenting explicit results it proves suitable though to introduce a dimensionless measure defined by

$$\bar{G} = GR^2/D_1 \quad (30)$$

5 RESULTS AND DISCUSSION

Most of the results presented refer to a situation with a panel composed of two individual layers, separated by the delamination, with equal or different material properties. The governing material parameter in this two-layer model is then

$$k_1 = \frac{E_{q_2}(1 - E_{q_2}(\nu_{q_2})^2/E_{q_2})}{E_{q_1}(1 - E_{q_1}(\nu_{q_1})^2/E_{q_1})} \quad (31)$$

with index 2 and 3 referring to the lower and upper layer, respectively, and Young's moduli and contraction ratios in obvious notation. It is believed that the results provided by these calculations give sufficient information as regards energy release rates and displacements for most practical applications. However, in order to examine in more detail the important features at more realistic situations some results are also presented for a composite panel with a (0/90/0/90)₁-layup.

The results derived by the asymptotic method outlined above are, with few exceptions, second-order approximations. For the present purpose

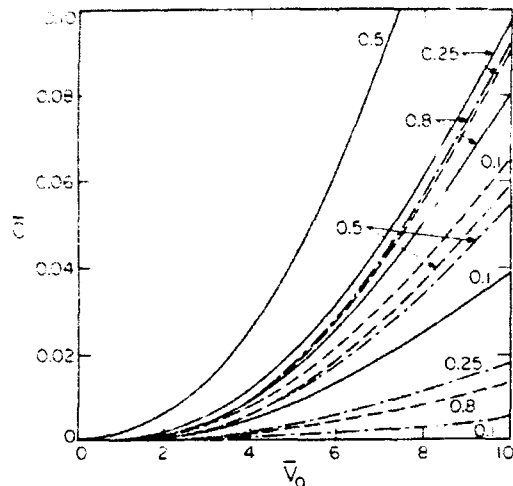


Fig. 3. Energy release rate, $\bar{G} = GR^2/D_1$, as function of prescribed displacement, \bar{v}_0 , for different values of delamination thickness, $\tau = t_3/t_1$, $\varphi_1 = 12^\circ$, $\varphi_2 = 60^\circ$, $\bar{R} = 100$; (---) $k_1 = 0.1$, (—) $k_1 = 1$, (---) $k_1 = 10$.

this order of approximation appears to give adequate information as regards the important features of the problem, a matter that will be discussed in somewhat greater detail below.

The first results shown in Fig. 3 concerns the dependence of the energy release rate on the prescribed displacement for different values on the delamination thickness, here represented by the parameter $\tau = t_3/t_1$, and the material parameter k_1 . Obviously the energy release rate increases, in many cases rapidly, with the external loading and at least when k_1 takes on values close to one the midplane delamination ($\tau = 0.5$) seems to produce the highest values on the energy release rate. This is not, however, the case for relatively large or small k_1 , 10 or 0.1 say. Especially for small values of k_1 the magnitude of the energy release rate increases with increasing τ . The latter observation, though, is due to the fact that in this two-layer model the thickness of the layers is dependent on the delamination thickness. As will be shown below in a more realistic situation with a composite panel with fixed thickness of the layers the midplane delamination always gives the highest value on the energy release rate.

In Fig. 3 k_1 takes on values between 0.1 and 10 and this is believed to be representative of most commercially used composite materials. However, results for more extreme numbers of k_1 will be presented below.

It should be noted that the results in Fig. 3, and in the sequel, are all pertinent to a radius of curvature, \bar{R} , being equal to 100. This value may

perhaps be somewhat low from a practical point of view but was chosen in order to be able to include considerable non-linear effects in the analysis of reasonable values of the prescribed displacement \bar{v}_0 and of the transversal displacement. Remember, though, that with increasing values of \bar{R} the non-linearity of the solution will decrease rapidly, a fact that significantly simplifies the treatment of these types of problems.

In Figs 4-6 the energy release rate is plotted as a function of the crack length, or crack angle, φ_1 for different material and geometry combinations.

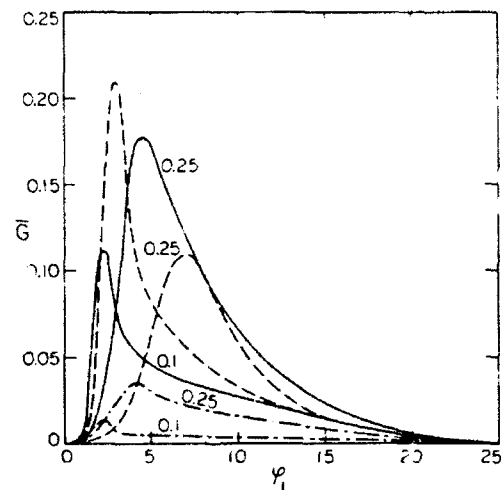


Fig. 4. Energy release rate, $\bar{G} = GR^2/D_1$, as function crack length, φ_1 , for different values of delamination thickness, $\tau = t_3/t_1$, $\varphi_2 = 25^\circ$, $\bar{R} = 100$, $\bar{v}_0 = 1$; (---) $k_1 = 0.1$, (—) $k_1 = 1$, (---) $k_1 = 10$.

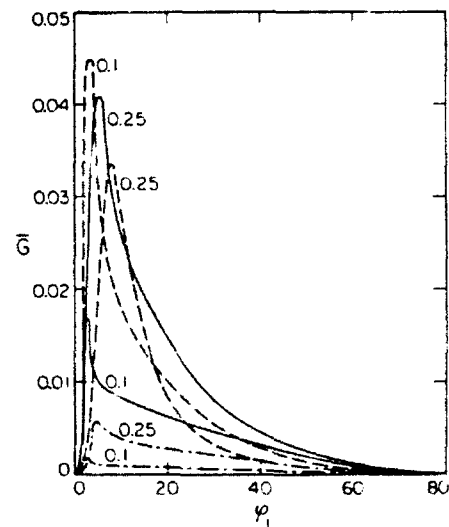


Fig. 5. Energy release rate, $\bar{G} = GR^2/D_1$, as function of crack length, φ_1 , for different values of delamination thickness, $\tau = t_3/t_1$, $\varphi_2 = 80^\circ$, $\bar{R} = 100$, $\bar{v}_0 = 10$; (---) $k_1 = 0.1$, (—) $k_1 = 1$, (---) $k_1 = 10$.

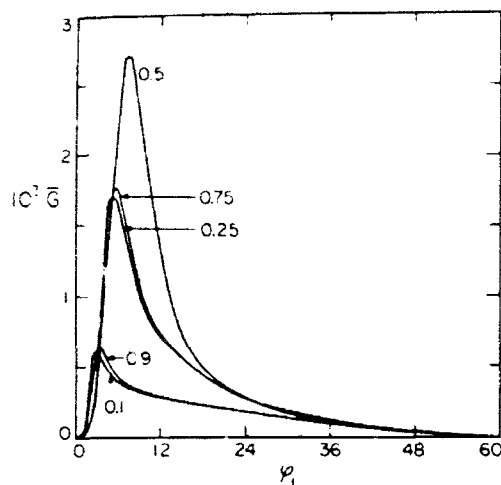


Fig. 6. Energy release rate, $\bar{G} = GR^2/D_1$, as function of crack length, φ_1 , for different values of delamination thickness, $\tau = t_1/t_2$, $\varphi_2 = 60^\circ$, $R = 100$, $k_1 = 1$, $\bar{v}_0 = 1$.

When dealing with flat panels almost with no exception the energy release rate is a monotonically increasing function of the crack length.^{10,11} This is not, however, the case for curved panels. Instead, as may be obvious from Figs 4-6, the energy release rate will attain a maximum value and only at early stages of crack growth is \bar{G} an increasing function of the delamination length. In this sense delaminations in panels, at least for these particular types of problems, grow in a stable manner and crack arrest is a likely event.

It is also interesting to note that the longest period of unstable crack growth apparently occurs when τ takes on values close to 0.5. This further confirms the fact that a midplane delamination from a crack growth point of view is the most dangerous situation, both as regards initiation and stability of growth. Even with this type of delamination present, however, crack growth is essentially a stable process.

In Figs 7 and 8 the energy release rate given by the second-order approximation is compared with results from a linear solution, in this case represented by the linear energy release rate, \bar{G}_L . As may be obvious, the linear results give quite accurate estimates on the energy release rate, except for small values of k_1 , when the delaminated part of the panel is thin, $\tau = 0.1$ and 0.8 say. However, when the delamination is close to the midplane of the panel, or when φ_2 takes on small values, non-linear effects dominate.

Another feature analyzed in the present work is the effect that the bending-stretching coupling, represented by \bar{B}_1 , has on the energy release rate.

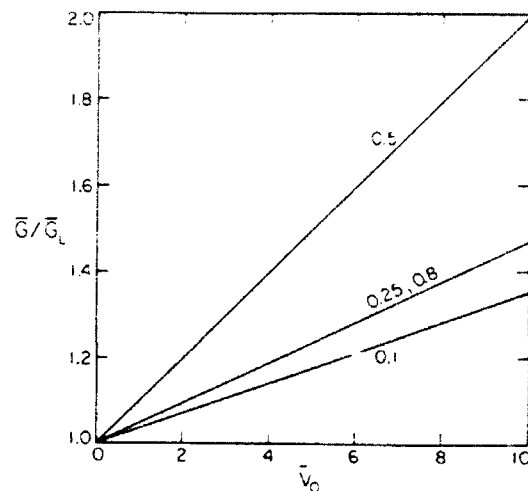


Fig. 7. Normalized energy release rate, \bar{G}/\bar{G}_L , as function of prescribed displacement, \bar{v}_0 , for different values of delamination thickness, $\tau = t_1/t_2$, $\varphi_1 = 12^\circ$, $\varphi_2 = 60^\circ$, $R = 100$, $k_1 = 1$.

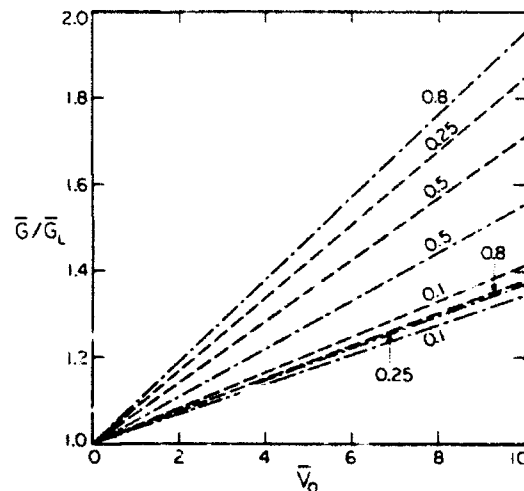


Fig. 8. Normalized energy release rate, \bar{G}/\bar{G}_L , as function of prescribed displacement, \bar{v}_0 , for different values of delamination thickness, $\tau = t_1/t_2$, $\varphi_1 = 12^\circ$, $\varphi_2 = 60^\circ$, $R = 100$; (—) $k_1 = 0.1$, (---) $k_1 = 10$.

This coupling appears notoriously in these types of problems and does, almost without exception, complicate the analysis. In Fig. 9 the ratio between the energy release rate calculated with the bending-stretching coupling neglected, $\bar{G}_{H=0}$, and the one derived by a complete analysis is depicted as a function of the material parameter k_1 . It is obvious that in the present case this coupling has a very significant effect on the results even though, as regards initiation of crack growth, the estimates are almost without exception conservative. It must be remembered, however, that with

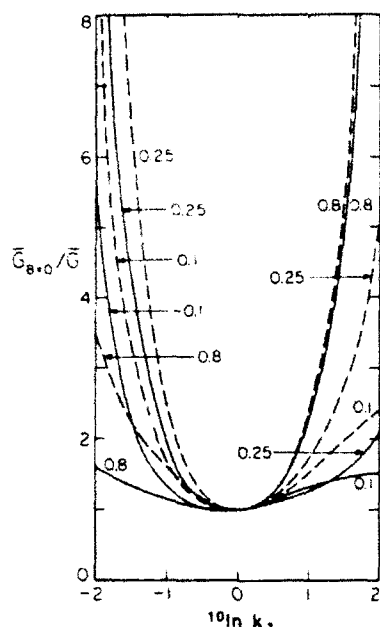


Fig. 9. Normalized energy release rate, \bar{G}_{B+0}/\bar{G} , as function of reduced modulus ratio, k_1 , for different values of delamination thickness, $r = t_3/t_1$, $\varphi_1 = 12^\circ$, $\bar{R} = 100$, $\bar{r}_0 = 1$; (—) $\varphi_2 = 25^\circ$, (---) $\varphi_2 = 60^\circ$.

the layup presently analyzed the bending-stretching coupling is present only in the undamaged part of the panel, which from a practical point of view is perhaps less important than a situation with non-zero \bar{B}_i -values in the panels above and below the crack. This case will, however, be discussed later.

In Figs 10–12 results are shown pertinent to a composite panel with a $(0/90/0/90)_s$ -layup, with the orthotropy angle defined as the angle between the fibre direction and the φ -axis. The ratio between the Young's modulus in the fibre direction and perpendicular to the fibres was in all cases chosen as 10, a value representative of a large number of commercially used composite materials.

In Figs 10 and 11 the energy release rate is plotted as a function of the crack length for different values on the parameter L , which in these calculations is defined as the number of layers below the delamination (ranging from 1 to 7). As may be seen from the figures these results are in obvious agreement with the conclusions drawn above. That is, crack growth in these types of panel problems is essentially a stable process and growth is most likely to occur for a midplane delamination.

Some calculations were also performed on a composite panel with an antisymmetric layup.

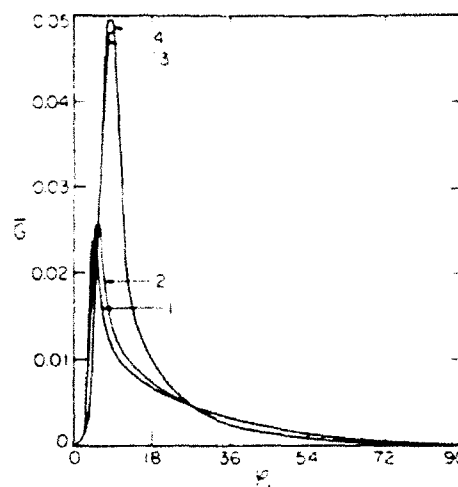


Fig. 10. Energy release rate, $\bar{G} = GR^2/D_1$, as function of crack length, φ_1 , for different values of delamination thickness as defined by the parameter L , $\varphi_2 = 90^\circ$, $R = 100$, $\bar{r}_0 = 10$.

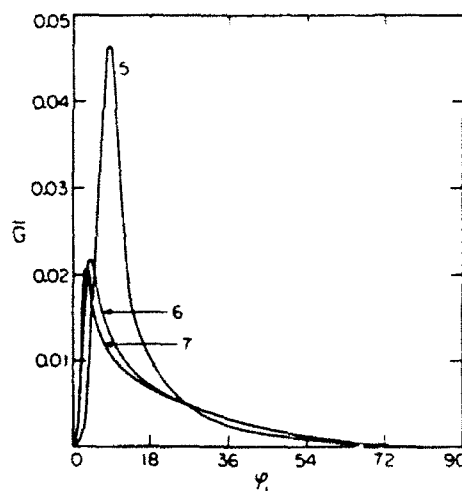


Fig. 11. Energy release rate, $\bar{G} = GR^2/D_1$, as function of crack length, φ_1 , for different values of delamination thickness as defined by the parameter L , $\varphi_2 = 90^\circ$, $R = 100$, $\bar{r}_0 = 10$.

The behaviour of the energy release rate in this case was essentially the same as for a symmetric layup, both as regards initiation and stability of crack growth.

In Fig. 12 the effect of neglecting the bending-stretching coupling mentioned earlier is examined and the values on the energy release rate are compared with results from a complete analysis. It should be noted that in this case the coupling is present only in the part of the panel above and below the crack. As may be seen from the results the effect of neglecting the coupling in the analysis is not particularly dramatic even though slightly

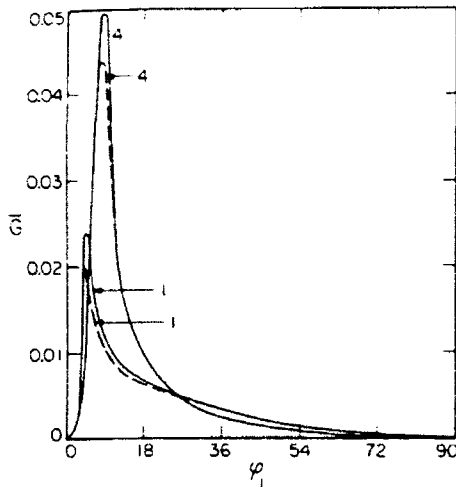


Fig. 12. Energy release rate, $\bar{G} = GR^2/D_1$, as function of crack length, φ_1 , for different values of delamination thickness as defined by the parameter L . $\varphi_2 = 90^\circ$, $\bar{R} = 100$, $\bar{v}_0 = 10$; (—) non-linear asymptotic solution, (---) non-linear asymptotic solution with $\bar{B}_i = 0$, $i = 1, 2, 3$.

non-conservative estimates on the energy release rate is obtained.

No results have been given for the case of negative values on the prescribed displacement \bar{v}_0 . This is due to the finding that for every material and geometry combination analyzed this feature resulted in crack closure and such event will undoubtedly cause very low values on the energy release rate at the crack front, even when contact effects are considered.

The presented results are all pertinent to the boundary conditions as described in Fig. 1 and formulated in eqns (8) and (9). However, a number of calculations were performed with other conditions at $\varphi = \varphi_2$ and these results were essentially in qualitative agreement, as regards energy release rates, with the ones presented above, although in most cases at a significantly lower level.

As regards realistic numbers of the critical energy release rate, certainly a wide scatter of results exists. However, when examining commercially used composite materials and their practical applications the conclusion is that the energy release rates calculated above definitely falls in at least the lower range of the critical values.

Finally in Fig. 13 results given by the asymptotic method is compared with results calculated by using the finite element method. As may be seen, the two methods give almost identical results for the transversal displacement even at high

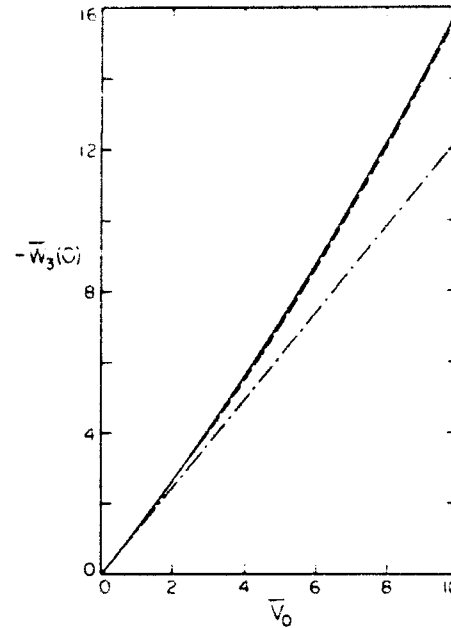


Fig. 13. Transversal displacement, $w_3(0)$, as function of prescribed displacement, \bar{v}_0 . $\varphi_1 = 12^\circ$, $\varphi_2 = 60^\circ$, $\tau = 0.1$, $\bar{R} = 100$, $k_1 = 1$; (—) non-linear asymptotic solution, (---) finite element solution, (-.-) linear solution.

values of the outer loading. This was the case for all analyzed combinations of material and geometry combinations, and at least for values of \bar{v}_0 up to 10 the relative difference in calculated displacements between the two methods never exceeded 5%, a fact that certainly gains confidence in the second-order asymptotic method used in this work as a tool for capturing the important features as regards delamination growth in composite panels.

6 CONCLUSIONS

In contrast to what is known for flat panels the energy release rate for curved panels, at least in the present setting, attains a sharp maximum at early stages of crack growth. This indicates that a progressing delamination is very likely to arrest, especially so when remembering that the resulting energy release rates in most cases were small compared with realistic values on the critical energy release rate.

In many situations, quite satisfactory estimates of the energy release rates could be obtained when neglecting non-linear effects. This was, however, only the case for thin delaminations. Also,

the effect of the bending-stretching coupling could under certain conditions be neglected, essentially though only when this coupling was not present in the undamaged part of the panel.

The boundary conditions proved to be of minor importance as regards the qualitative behaviour of the energy release rate. However, crack closure effects are to be expected at negative values of the prescribed displacement.

REFERENCES

1. Chai, H., Babcock, C. D. & Knauss, W., One dimensional modelling of failure in laminated plates by delamination buckling. *Int. J. Solids Structures*, **17** (1981) 1069-83.
2. Storåkers, B., Nonlinear aspects of delamination in structural members. Proc. XVIIth Int. Congr. Theor. Appl. Mech., North-Holland, 1989, pp. 315-36.
3. Simitses, G. J. & Chen, Z., Delamination buckling of pressure-loaded thin cylinders and panels. In *Composite Structures*, Vol. 1, ed. I. H. Marshall, Elsevier, Barking, 1987, pp. 294-308.
4. Simitses, G. J. & Chen, Z., Buckling of delaminated, long, cylindrical panels under pressure. *Computers & Structures*, **28** (1988) 173-84.
5. Lin, H. J. & Lee, Y. J., Impact-induced fracture in laminated plates and shells. *J. Compos. Mater.*, **24** (1990) 1179-99.
6. Suo, Z. & Hutchinson, J. W., Interface crack between two elastic layers. *Int. J. Fracture*, **43** (1990) 1-18.
7. Suo, Z., Delamination specimens for orthotropic materials. *J. Appl. Mech.*, **57** (1990) 627-34.
8. ABAQUS, Hibbit, Karlson and Sorenson, Inc., USA, version 4.7.
9. Storåkers, B. & Andersson, B., Nonlinear plate theory applied to delamination in composites. *J. Mech. Phys. Solids*, **36** (1988) 689-718.
10. Yin, W. L., Sallam, S. & Simitses, G. J., Ultimate axial load capacity of a delaminated plate. *AIAA J.*, **24** (1986) 1-7.
11. Larsson, P.-L., On delamination buckling and growth in circular and annular orthotropic plates. *Int. J. Solids Structures*, **27** (1991) 15-28.

Mixed mode delamination cracking in brittle matrix composites

G. Bao, B. Fan and A.G. Evans

Materials Department, College of Engineering, University of California, Santa Barbara, CA 93106-5050, USA

Received 30 March 1990; first revision 6 November 1990 and second revision 26 September 1991

The growth of delamination cracks from holes and notches in laminated brittle matrix composites is addressed. It is demonstrated that the behavior is strongly influenced by tractions on the delamination crack faces, caused either by intact matrix ligaments or by bridging fibers. These tractions cause the phase angle of loading ϕ associated with delamination to increase appreciably as the crack extends, causing mode I to be suppressed. This effect can lead to increased resistance to delamination as the crack extends, whenever the fracture mechanism along the delamination plane has a ϕ dependent fracture energy. Trends in resistance curves are predicted.

1. Introduction

Mixed mode cracking is an important damage mechanism in laminated brittle matrix composites, such as ceramic matrix, carbon-carbon, and epoxy matrix systems (Sbaizero et al., 1990; Wang, 1979; Trewetthey et al., 1988; O'Brien, 1982) and in wood (Ashby et al., 1985). Such damage is manifest as delaminations which occur from edges and from either notches (Fig. 1) or holes and as interlaminar cracks which are formed in regions

of high in-plane shear stresses. Many of the important modes are manifest upon the flexural and tensile testing of notched beams and plates. While the damage can have some beneficial influences on performance in special loading situations, generally these mechanisms are detrimental and should be suppressed to achieve acceptable structural performance.

Preliminary studies of delamination crack growth resistance have indicated that cracking is strongly resisted by fibers that cross-over the crack



Fig. 1. A delamination crack propagating from a notch in a laminated ceramic matrix composite.

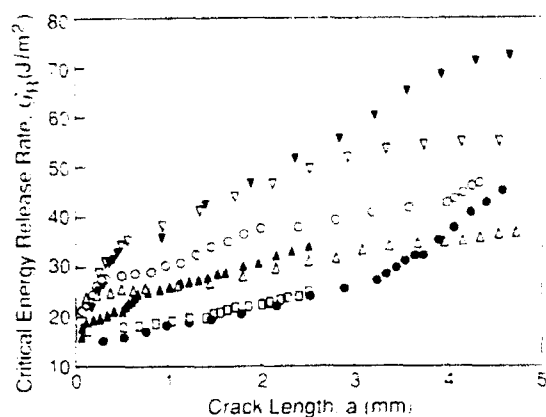


Fig. 2. A series of resistance curves evaluated for delamination crack growth in a laminated ceramic matrix composite when fibers bridge the crack surfaces.

plane leading to a resistance curve (Sbaizero et al., 1990; Bordia et al., 1991) (Fig. 2). An important issue thus appears to be the presence and magnitude of forces normal to the crack, induced either by intact reinforcements or by matrix ligaments. Understanding of this problem also assists in the prediction of effects on mixed mode cracking of a small volume fraction of reinforcements normal to the crack plane, in accordance with 3-D reinforcing schemes. Toward this objective, the present study encompasses calculations of delamination cracks subject to crack surface tractions. Some approximate analytical results are presented first to provide the relevant background. Then, finite element results are generated and used to establish the major trends in the delamination resistance.

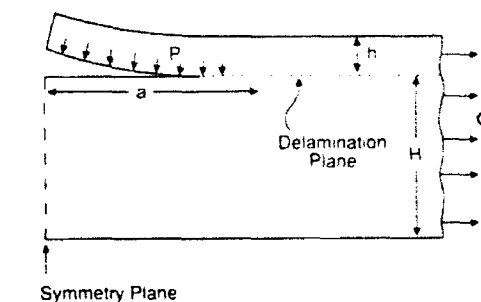
2. Some basic mechanics

An assessment of the effects of normal tractions on delamination cracking is obtained (Fig. 3a) by applying an axial stress σ to the composite causing a delamination crack to extend from an edge notch, depth h . The delamination crack is also subject to surface tractions, magnitude p . For the problem posed in this manner, the body

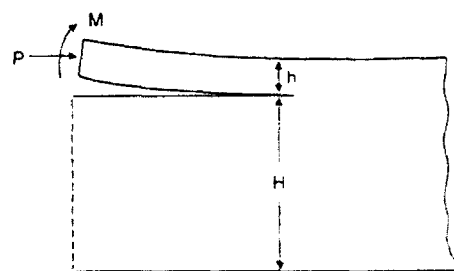
is strictly linear and consequently, the stress intensity factors induced by σ and by p can be added together to give the net magnitudes.

Some important background is provided by solutions for a layer on a substrate with net section width H subjected to an end force P and a moment M (Fig. 3b). Rigorous analytical solutions exist for the steady-state situation wherein the crack length a is long compared with the layer thickness, $h(a/h \geq 3)$. For the elastically homogeneous case, the solution has the form (Suo and Hutchinson, 1989)

$$\begin{aligned} K_I &= \frac{P}{\sqrt{2hA}} \cos \omega + \frac{M}{\sqrt{2hI}} \sin(\omega + \gamma), \\ K_{II} &= \frac{P}{\sqrt{2hA}} \sin \omega - \frac{M}{\sqrt{2hI}} \cos(\omega + \gamma). \end{aligned} \quad (1)$$



a) Specimen Configuration



b) Equivalent Configuration

Fig. 3. (a) A schematic of the delamination crack configuration used for the analysis. (b) A layer subject to an end load P and moment M and the equivalence with the problem posed in (a).

where K_I and K_{II} are the mode I and mode II stress intensity factors, respectively, and A and I are geometric factors given by

$$\frac{1}{A} = 1 + 4\eta + 6\eta^2 + 3\eta^3, \quad \frac{1}{I} = 12(1 + \eta^2),$$

$$\text{with, } \frac{\sin \gamma}{\sqrt{AI}} = 6\eta^2(1 + \eta), \quad \eta = \frac{h}{H}. \quad (2)$$

Note the important effect of the relative notch depth, h/H , on the contribution caused by the end load, P .

The effect of the stress σ in the present problem is directly analogous to that of an end force, with

$$P = \sigma h, \quad (3)$$

because the stress in the body below the notch does not contribute to the stress intensities on the delamination crack. Consequently, the effects of σ are given in steady-state by

$$\frac{K_I}{\sigma\sqrt{h}} = \frac{\cos \omega}{\sqrt{2A}}, \quad \frac{K_{II}}{\sigma\sqrt{h}} = \frac{\sin \omega}{\sqrt{2A}}, \quad (4)$$

An appreciable influence of the relative notch depth, h/H , is apparent. The energy release rate \mathcal{G} and the phase angle of loading ψ can be derived from Eq. (4) using

$$\frac{E\mathcal{G}}{1 - \nu^2} = K_I^2 + K_{II}^2 \quad (5a)$$

and

$$\psi = \tan^{-1}(K_{II}/K_I). \quad (5b)$$

The magnitudes are

$$\frac{E\mathcal{G}}{\sigma^2 h(1 - \nu^2)} = \frac{1}{2A} \quad (6a)$$

and

$$\psi \equiv \omega = 52.1^\circ - 3\eta^\circ. \quad (6b)$$

The stress p on the crack face imposes a moment M per unit length on the layer. When p is uniform and acts over the entire length of the crack (Fig. 3a), M is given by

$$M = -\frac{1}{2}pa^2. \quad (7)$$

In addition to this moment, shear deformations exist in the beam above the crack, which are likely to have an important influence on the stress intensities, except when a/H is large. Inserting Eq. (4) into Eq. (1) thus gives approximate results for the steady-state stress intensities

$$\begin{aligned} \frac{K_I}{p\sqrt{h}} &= -\frac{\sin(\omega + \gamma)}{2\sqrt{2I}} \left(\frac{a}{h}\right)^2, \\ \frac{K_{II}}{p\sqrt{h}} &= \frac{\cos(\omega + \gamma)}{2\sqrt{2I}} \left(\frac{a}{h}\right)^2. \end{aligned} \quad (8)$$

Combining the contributions to K from σ and p , the tip "steady-state" stress intensities are

$$\begin{aligned} \frac{K_I^t}{\sigma\sqrt{h}} &= \frac{\cos \omega}{\sqrt{2A}} - \frac{1}{2} \left(\frac{p}{\sigma}\right) \left(\frac{a}{h}\right)^2 \frac{\sin(\omega + \gamma)}{\sqrt{2I}}, \\ \frac{K_{II}^t}{\sigma\sqrt{h}} &= \frac{\sin \omega}{\sqrt{2A}} + \frac{1}{2} \left(\frac{p}{\sigma}\right) \left(\frac{a}{h}\right)^2 \frac{\cos(\omega + \gamma)}{\sqrt{2I}}. \end{aligned} \quad (9)$$

An important preliminary feature of the solution is the recognition that the mode I tip stress intensity diminishes as the crack extends whereas the mode II component *increases*, because of the dominant effect of the *moment* contribution caused by p . Furthermore K_I^t becomes zero at a *critical crack length* a_c given by

$$\left(\frac{a_c}{h}\right)^2 = 2 \left(\frac{\sigma}{p}\right) \sqrt{\frac{I}{A}} \frac{\cos \omega}{\sin(\omega + \gamma)}. \quad (10)$$

A small stress p relative to σ is thus sufficient to close the delamination crack at lengths of order a few times the notch depth, h .

The interpretation of experimental results is facilitated by obtaining the tip energy release rate \mathcal{G}^t and the phase angle of loading ψ^t as a function of delamination crack length. Hence, from Eq. (9)

$$\begin{aligned} \frac{E\mathcal{G}^t}{\sigma^2 h(1 - \nu^2)} &= \frac{1}{2A} + \frac{1}{8I} \left(\frac{p}{\sigma}\right)^2 \left(\frac{a}{h}\right)^4 \\ &\quad - \frac{\sin \gamma}{2\sqrt{AI}} \frac{p}{\sigma} \left(\frac{a}{h}\right)^2 \end{aligned} \quad (11a)$$

and

$$\psi^I = \omega + \phi, \quad (11b)$$

where

$$\tan \phi = \frac{1}{2} \sqrt{\frac{\bar{A}}{l} \frac{p}{\sigma} \left(\frac{a}{h} \right)^2} \cos \gamma \\ \times \left[1 - \frac{1}{2} \sqrt{\frac{\bar{A}}{l} \frac{p}{\sigma} \left(\frac{a}{h} \right)^2} \sin \gamma \right]^{-1/2}. \quad (11c)$$

Note that in general \mathcal{E}^I is larger than \mathcal{E} in Eq. (6a). When $\eta = h/H \ll 1$, the value of $\mathcal{E}^I/\mathcal{E}$ at $a = a_c$ is

$$\mathcal{E}^I/\mathcal{E} = 1 + \cos^2 \omega \approx 1.6. \quad (12)$$

Consequently, the somewhat unexpected result emerges that the tractions *do not* shield the crack tip. Other features are needed to explain the experimental observation that \mathcal{E}_R increases as the crack extends (Sbaizero et al., 1990; Bordia et al., 1991).

The above behavior is modified when the stress p acts over a definite length l rather than the entire crack length. For that case, a in Eq. (11) is replaced by l , whereupon \mathcal{E}^I and ψ^I are independent of the delamination crack length when a is large compared with h and l . Then, provided that the crack does not arrest before a exceeds l , the delamination will continue to propagate subject to steady-state values of \mathcal{E}^I and ψ^I .

3. Numerical solutions

3.1. The finite element method

Stress intensity factors and energy release rates are determined with the finite element code, ABAQUS. Symmetry about the midsection of the beam, depicted in Fig. 3a, allows the requisite solutions to be obtained by considering one half of the beam. The finite element mesh used in the calculation is shown in Fig. 4. To ensure the accuracy of the "steady-state" result, the beam length L/h is chosen to be 15 (Fig. 4). Since the problem is linear, calculations are carried out separately for the axial loading σ and for the surface tractions p .

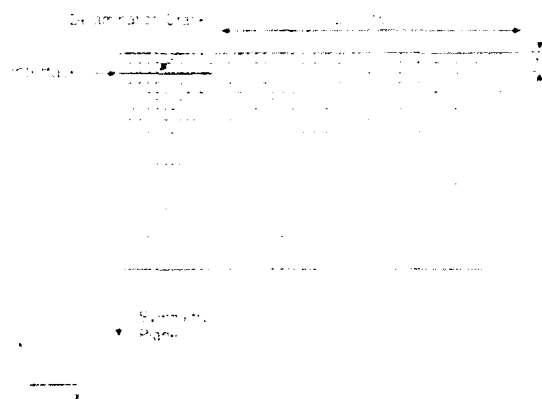


Fig. 4. Finite element mesh used for the calculations.

Stress intensities K_I and K_{II} are calculated from nodal displacement Δu_x and Δu_y in the crack tip region, using (Rice, 1968)

$$\Delta u_x = \frac{\kappa + 1}{2\mu} \sqrt{\frac{r}{2\pi}} K_{II}$$

and

$$\Delta u_y = \frac{\kappa + 1}{2\mu} \sqrt{\frac{r}{2\pi}} K_I. \quad (13)$$

where $\kappa = 3 - 4\nu$ and μ is the shear modulus. The values of K thus computed are then used to obtain \mathcal{E} which, in turn, is compared with the value of the J -integral given in the finite element calculation, to assess consistency.

3.2. Results

Solutions for K and \mathcal{E} have been evaluated separately for the applied stress, σ , and the crack surface traction, p . The effect of σ obtained for $h/H = 0.1$ are plotted in Fig. 5, using the nondimensional parameters $K/\sigma\sqrt{h}$ and $E\mathcal{E}/\sigma^2 h(1 - \nu^2)$. Also indicated on the figure are analytical results for steady-state crack extension. Two aspects of the results are noteworthy. The steady-state values of $K/\sigma\sqrt{h}$ and $E\mathcal{E}/\sigma^2 h(1 - \nu^2)$ are in close agreement with the analytical solutions (Eq. (4)). Furthermore, steady-state conditions for mode I develop even when $a/h < 1$, but only occur for mode II when $a/h \approx 2$. In addition, there is an appreciable decrease in the energy

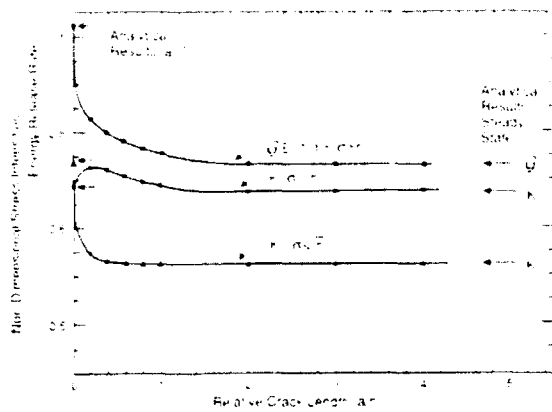


Fig. 5. Nondimensional stress intensities and energy release rate as a function of relative delamination crack length for an applied stress, σ .

release rate between $0 \leq a/h \leq 2$, indicative of a region of stable crack extension.

The stress intensities caused by p acting along the entire crack surface are presented using the normalization suggested by Eq. (8): $K(h/a)^2/p\sqrt{h}$. The results, plotted in Fig. 6, reveal that the nondimensional K_{II} attains "steady-state" at $a/h = 1$ and furthermore, the steady-state value is comparable to the beam theory prediction from Eq. (8). However, the nondimensional K_I does not attain "steady-state," even for $a/h = 5$. In

addition, K_I is larger than the beam theory prediction (Eq. (8)). The difference is attributed to effects of shear deformation. The net influence of this deformation is a stronger effect of the tractions p on γ than anticipated by the analytical results (Eq. (11a)).

4. Resistance curves

The delamination fracture resistance can be ascertained from the preceding results by adopting a *crack extension criterion*. This criterion requires that the tip energy release rate \mathcal{G}^I attains the fracture energy $\Gamma_0(\psi)$ of the material along the delamination plane. The fracture energy typically has the form (Jensen et al., 1991)

$$\Gamma_0(\psi) = \Gamma_0 [1 - (1 - \lambda_2) \sin^2 \psi]^{-1}, \quad (14)$$

where Γ_0 is the fracture energy at $\psi = 0$ and λ_2 is a material dependent coefficient, typically in the range 0.1 to 0.3.

Letting \mathcal{G} in Eq. (6a) become the measured energy release rate \mathcal{G}_R , the following result is obtained

$$\frac{P}{\sigma} = \sqrt{\frac{\Gamma_0}{\mathcal{G}_R}} \sqrt{\frac{\Sigma}{A}}, \quad (15)$$

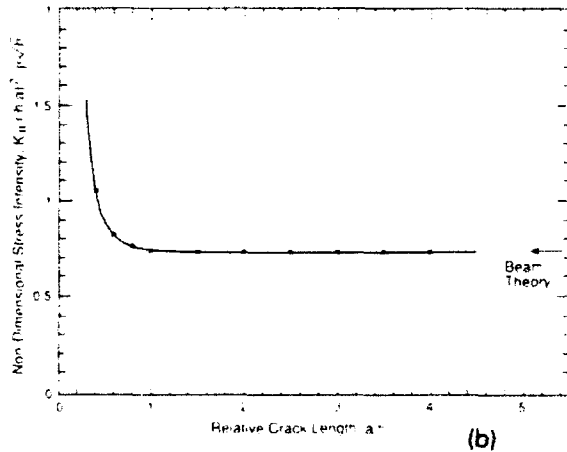
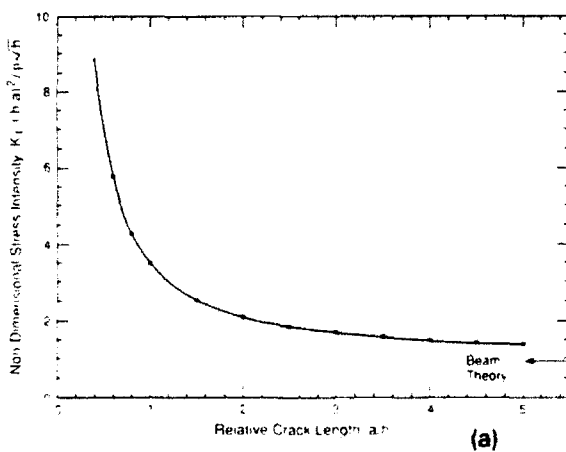


Fig. 6. Nondimensional stress intensity as a function of relative delamination crack length for crack surface tractions, p (a) K_I and (b) K_{II} .

where Σ is a nondimensional parameter representing the effect of p ,

$$\Sigma = \frac{p^2 h (1 - \nu^2)}{2 L E_0} \quad (16)$$

Furthermore, equating \mathcal{E}_R to Γ_0 and using Eq. (15), the normalized energy release rate \mathcal{E}_R / Γ_0 for "steady-state" is determined by the following set of parametric equations

$$\begin{aligned} \frac{\Gamma_0}{\mathcal{E}_R} [1 - (1 - \lambda_2) \sin^2 \psi^t]^{-1} \\ = 1 - \frac{\Gamma_0}{\mathcal{E}_R} (l_d)^4 - 2 \sin \gamma \sqrt{\frac{\Gamma_0}{\mathcal{E}_R}} (l_d)^2 \end{aligned} \quad (17a)$$

and

$$\psi^t = \omega + \phi \quad (17b)$$

and

$$\begin{aligned} \tan \phi = \sqrt{\frac{\Gamma_0}{\mathcal{E}_R}} (l_d)^2 \cos \gamma \\ \times \left[1 - \sqrt{\frac{\Gamma_0}{\mathcal{E}_R}} (l_d)^2 \sin \gamma \right]^{-1}, \end{aligned} \quad (17c)$$

where l_d is a characteristic delamination crack length

$$l_d = \left(\frac{\Sigma}{4I} \right)^{1/4} \left(\frac{a}{h} \right). \quad (18)$$

It is readily apparent from Eqs. (17) and (18) that \mathcal{E}_R / Γ_0 depends on Σ only through l_d . The trends in \mathcal{E}_R / Γ_0 as a function of l_d are plotted in Fig. 7 for different values of λ_2 . Resistance curve behavior is predicted. Each resistance curve in Fig. 7 terminates at a critical value of l_d at which the phase angle ψ^t becomes $\pi/2$. In addition, it is apparent that the value of λ_2 has a strong effect on the predicted resistance behavior. Indeed, when $\lambda_2 = 1$, the resistance \mathcal{E}_R decreases, because, as already noted, the tractions p induce an appreciable K_{II} , having the same sign as the contribution from σ .

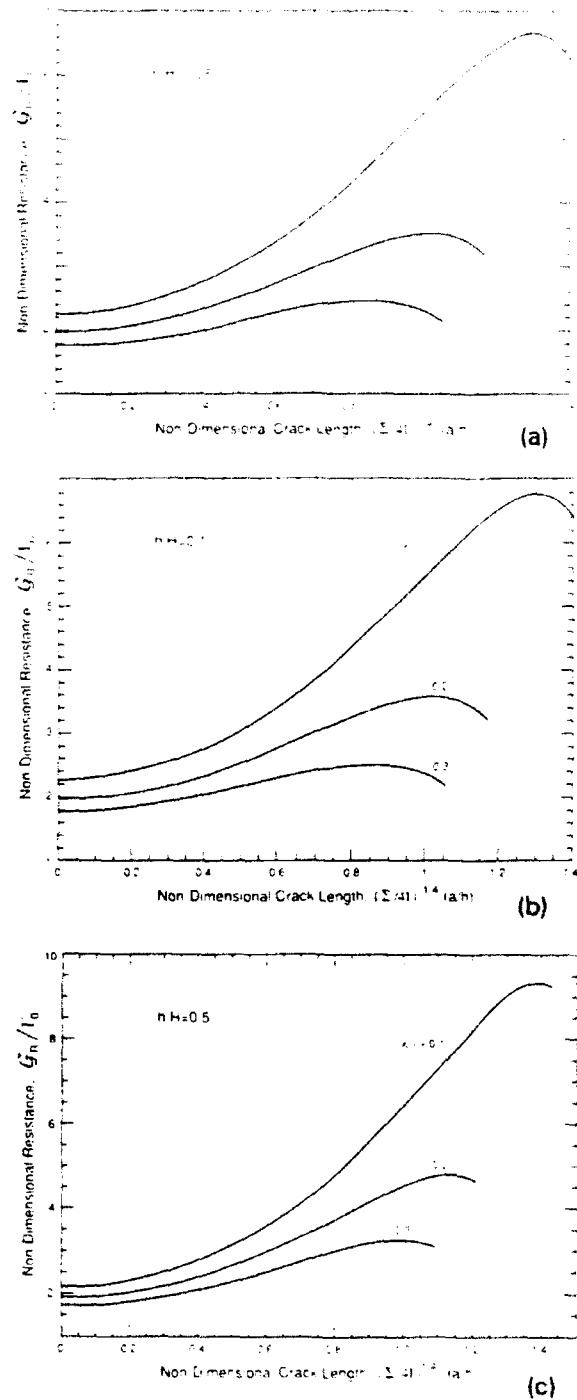


Fig. 7. Analytic prediction of resistance curves for delamination cracking for various λ_2 : (a) $h/H = 0.05$; (b) $h/H = 0.1$ and (c) $h/H = 0.5$.

The preceding results neglect effects of the shear deformation, which provide a contribution to K_I^* . The resistance curve behavior in the transient region at small a/h is also neglected. To assess these effects, the finite element results are used to establish the trends in delamination resistance. For this purpose, it is noted that, for each crack length a/h , the following nondimensional quantities apply,

$$\begin{aligned} E_1 &= \frac{K_{\sigma 1}}{\sigma \sqrt{h}}, & E_2 &= \frac{K_{\sigma 2}}{\sigma \sqrt{h}}, \\ F_1 &= \frac{K_{p1}}{p \sqrt{h}}, & F_2 &= \frac{K_{p2}}{p \sqrt{h}}, \end{aligned} \quad (19)$$

where K_{σ} and K_p are stress intensities caused by σ and p , respectively. Then the normalized delamination energy release rate \mathcal{G}_R/Γ_0 can be determined from the following set of parametric equations

$$\begin{aligned} \frac{\Gamma_0}{\mathcal{G}_R} [1 - (1 - \lambda_2) \sin^2 \psi^1]^{-1} \\ = \left[(E_1 - \zeta F_1)^2 + (E_2 + \zeta F_2)^2 \right] / (E_1^2 + E_2^2) \end{aligned} \quad (20a)$$

and

$$\tan \psi^1 = (E_2 + \zeta F_2) / (E_1 - \zeta F_1), \quad (20b)$$

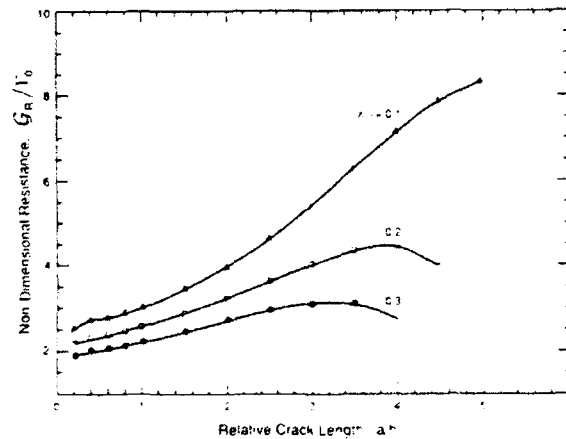


Fig. 8. Numerical prediction of resistance curves for $\Sigma = 10^{-3}$ and $h/H = 0.1$.

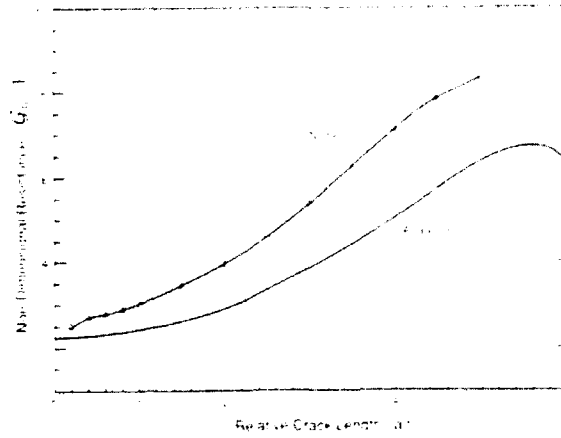


Fig. 9. A comparison of the analytical and numerical resistance curves for the case $\Sigma = 10^{-3}$, $h/H = 0.1$ and $\lambda_2 = 0.1$.

where

$$\zeta = 2\Sigma(E_1^2 + E_2^2) \frac{\Gamma_0}{\mathcal{G}_R}. \quad (21)$$

Trends in \mathcal{G}_R/Γ_0 as a function of a/h are plotted in Fig. 8 for $\Sigma = 0.001$, $h/H = 0.1$ and for different values of λ_2 . The resistance curves obtained from the finite element calculation are similar to those apparent from the steady-state analysis (Fig. 9) except that the \mathcal{G}_R/Γ_0 are slightly higher.

5. Concluding remarks

The predicted resistance curves \mathcal{G}_R (Figs. 7 and 8) have the same features as the curves measured for ceramic matrix composites (Fig. 2). An influence of bridging fibers and/or ligaments thus appears to provide a plausible rationale for resistance curve behavior in delamination cracking, with the tractions p apparently governed by the sliding resistance along the fiber/matrix interface (Bordia et al., 1991). However, one important finding of the calculations is that the slope of the resistance curve is a strong function of the matrix fracture mechanism. Notably, a material with shear insensitive matrix fracture energy would be susceptible to unstable delamination

cracking, because γ_R decreases with crack extension. Conversely, when the matrix fracture energy increases appreciably with increase in phase angle, γ_R rises with crack extension and delamination cracking occurs stably, subject to increasing applied loads. A basic understanding of the matrix fracture process is thus needed to predict and interpret delamination cracking.

Acknowledgements

One of the authors (GB) wishes to thank Professor R.M. McMeeking for his encouragement and comments on the paper. Discussions with Professor Z. Suo were very helpful.

References

- Ashby, M.F., K.E. Easterling, R. Harrison and S.K. Mann (1985), *Proc. Roy. Soc.*, 439S, 23.
- Bordia, R.J., B.J. Dalgleish, P.G. Charalambides and A.G. Evans (1991), *J. Am. Ceram. Soc.*, November, in press.
- Jensen, H., J.W. Hutchinson and K.S. Kim (1990), *Int. J. Solids Struct.*, 26, 1099.
- O'Brien, T.K. (1982), *ASTM STP* 775, 146-167.
- Rice, J.R. (1968), in: H. Liebowitz, ed., *Fracture*, Vol. 2, Academic Press, New York, pp. 191-311.
- Sbaizero, O., P.G. Charalambides and A.G. Evans (1990), *J. Am. Ceram. Soc.*, 73, 1936.
- Suo, Z. and J.W. Hutchinson (1989), *Int. J. Solids Struct.*, 25, 1337.
- Trewetthey, B.R., J.R. Gillespie and L.A. Carlsson (1988), *J. Compos. Mater.*, 22, 459.
- Wang, S.S. (1979), in: S.W. Tsai, ed., *Composite Materials Testing and Design*, ASTM, Philadelphia, ASTM STP 674, pp. 662-663.

Mixed Mode Cracking in Layered Materials

J. W. HUTCHINSON

*Division of Applied Sciences
Harvard University
Cambridge, Massachusetts*

and

Z. SUO

*Mechanical Engineering Department
University of California
Santa Barbara, California*

I. Introduction	64
II. Mixed Mode Fracture: Crack Tip Fields and Propagation Criteria	65
A. Isotropic Elastic Solids	66
B. Homogeneous, Orthotropic Elastic Solids	69
C. Interface Cracks	72
III. Elasticity Solutions for Cracks in Multilayers.....	90
A. Concept of Steady-State Cracking	90
B. Cracks in Layers Loaded along Edges	95
C. A Bilayer Held between Rigid Grips.....	105
D. Small-Scale Features	107
IV. Laminate Fracture Test	112
A. Delamination Beams	112
B. Interfacial Fracture Specimens	116
C. Brazil-Nut Sandwiches	120
D. Delamination <i>R</i> -Curves	122
V. Cracking of Pre-tensioned Films	126
A. Controlling Quantities and Failure Modes	127
B. Cracking in Films.....	131
C. Substrate Cracking	137
D. Interface Debond	143
E. Thermal Shock Spalling.....	146
VI. Buckle-Driven Delamination of Thin Films	147
A. The One-Dimensional Blister	149
B. The Circular Blister	158
C. Conditions for Steady-State Propagation of a Straight-Sided Blister	163

VII. Blister Tests	167
A. Pressure Loading	168
B. Point Loading	171
VIII. Failure Modes of Brittle Adhesive Joints and Sandwich Layers	172
A. Basic Results for Straight Cracks	174
B. Crack Trapping in a Compliant Layer under Non-zero K_{II}^*	175
C. Configurational Stability of a Straight Crack within the Layer	176
D. Interface or In-layer Cracking?	178
E. Alternating Morphology	180
F. Tunneling Cracks	182
Acknowledgments	186
References	187

I. Introduction

The aim of this chapter is to pull together recent work on the fracture of layered materials. Many modern materials and material systems are layered. Interfaces are intrinsic to these materials, as are heterogeneities such as residual stresses and discontinuities in thermal and elastic properties. The structural performance of such materials and systems generally depends on just these features. The potential applications of fracture mechanics of layered materials ranges over a broad spectrum of problem areas. Included are: protective coatings, multilayer capacitors, thin film/substrate systems for electronic packages, layered structural composites of many varieties, reaction product layers, and adhesive joints.

Attention is confined in this chapter to elastic fracture phenomena in which the extent of the inelastic processes is small compared with the relevant geometric length scales, such as layer thickness. For the most part, the separate sections are designed so that they can be read independently. The main exceptions are Section II, which presents the theory of mixed mode interfacial fracture underlying many of the applications, and Section III, which catalogues a number of basic elasticity solutions for layered systems referred to throughout this chapter. Then follow sections on test specimens for determining interfacial toughness, fracture modes in thin films under either tension or compression, blister tests, and, lastly, failure modes of adhesive joints. We believe that most of the important fracture concepts for layered systems emerge in the analysis of these examples. One concept, in particular, that plays a central role is the idea of steady-state cracking. In almost every application considered here, a steady-state analysis provides a simplified solution that is directly relevant to design against fracture.

This chapter builds on earlier work by many researchers, but specifically the contributions to the elasticity theory of cracks in layered materials of Erdogan and coworkers in the 1970s, which comprised most of the available solutions until recently. Special mention must also be made of the article on thin films and coatings by Gille (1985), which gives a comprehensive treatment of fracture modes without the insights from the recent developments in interfacial fracture. It is especially these recent developments that have transformed the subject. We have been fortunate to have been involved with one of the groups (that centered at the University of California, Santa Barbara) that have been concerned with the extension of both experimental and theoretical aspects of fracture mechanics to interfaces. This involvement is reflected in our approach as well as the topics that have been chosen for presentation.

Structural reliability of multilayers is a fast growing field. An article written at this point is most likely transitory work, although we have tried to put various aspects into perspective, and we believe some of them are of permanent nature. Like most review articles of this kind, subject matter with various degrees of novelty that has not been published previously is incorporated. Some fill gaps, others are ready extensions, and still others are simply speculations. The writers sincerely urge the practitioners in the related disciplines to use the article critically, so that the results can be validated, expanded, or modified. A more consolidated version of the article could then emerge on a later occasion.

II. Mixed Mode Fracture: Crack Tip Fields and Propagation Criteria

There is ample experimental evidence that cracks in brittle, isotropic, homogeneous materials propagate such that pure mode I conditions are maintained at the crack tip. This appears to be true for fatigue crack growth and stress corrosion cracking as well as crack advance under monotonic loading. An unloaded crack subsequently subject to a combination of modes I and II will initiate growth by kinking in a direction such that the advancing tip is in mode I. A crack in a material with strongly orthotropic fracture properties, or a crack in an interface with a fracture toughness that is distinct from the materials joined across it, can experience either kinking or straight-ahead propagation under mixed mode loading depending on a number of factors, including the relative toughnesses associated with the competing directions of advance. This section gives results from studies of

crack tip fields for specifying criteria for straight-ahead propagation or kinking under mixed mode loading. An assessment of the competition between different directions of advance can also be made. Homogeneous materials are considered first, starting with the isotropic case and going on to orthotropic symmetry. Cracks on interfaces between dissimilar isotropic elastic solids are dealt with last.

A. ISOTROPIC ELASTIC SOLIDS

The stress fields at the tip of a crack in plane stress or plane strain for a homogeneous, isotropic elastic solid have the well-known general form

$$\sigma_{ij} = K_I(2\pi r)^{-1/2}\sigma_{ij}^I(\theta) + K_{II}(2\pi r)^{-1/2}\sigma_{ij}^{II}(\theta) + T\delta_{ij}, \quad (2.1)$$

where δ_{ij} is the Kronecker delta and r and θ are polar coordinates centered at the tip as shown in Fig. 1. The θ -variations are given in many texts on fracture. They are the same for plane stress and plane strain, except σ_{33} , which vanishes in plane stress and is given by $\nu(\sigma_{11} + \sigma_{22})$ in plane strain, where ν is Poisson's ratio. Mode I fields are symmetric with respect to the crack line with $\sigma_{22}^I = 1$ and $\sigma_{12}^I = 0$ on $\theta = 0$, while the mode II fields are antisymmetric with $\sigma_{12}^{II} = 1$ and $\sigma_{22}^{II} = 0$ on $\theta = 0$. The higher order contributions not included in (2.1) all vanish as $r \rightarrow 0$. The T -stress, $\sigma_{11} = T$, arises in discussions of crack stability and kinking. Thus, the singular tractions on the line ahead of the crack tip ($\theta = 0$) have the mode I and II stress intensity factors as amplitudes according to

$$\sigma_{22} = K_I(2\pi r)^{-1/2}, \quad \sigma_{12} = K_{II}(2\pi r)^{-1/2}. \quad (2.2)$$

The relative displacements of the crack faces behind the tip,

$$\delta_i = u_i(r, \theta = \pi) - u_i(r, \theta = -\pi),$$

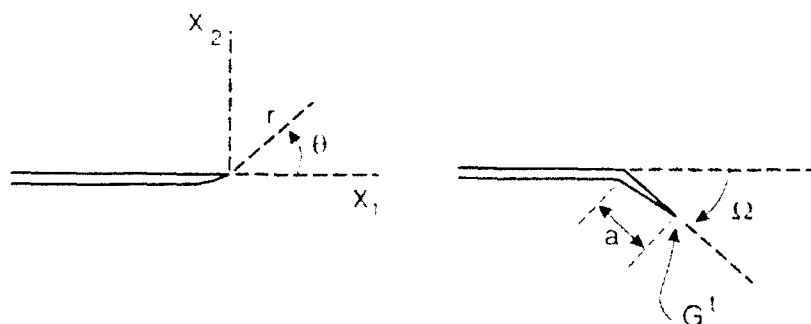


FIG. 1. Conventions at a crack tip and the geometry of a kinked crack.

in the region dominated by the singular fields are given by

$$(\delta_2, \delta_1) = (K_I, K_{II})(8/\bar{E})[r/(2\pi)]^{1/2}, \quad (2.3)$$

where

$$\begin{aligned} \bar{E} &= E/(1 - \nu^2) \quad (\text{plane strain}) \\ &= E \quad (\text{plane stress}) \end{aligned} \quad (2.4)$$

and E is Young's modulus. Irwin's relation between the energy release rate G for straight-ahead quasi-static crack advance and the stress intensity factors is

$$G = (K_I^2 + K_{II}^2)/\bar{E}. \quad (2.5)$$

Next, consider a putative crack segment of length a kinking out the plane of the crack at an angle Ω with the sense shown in Fig. 1. When a is sufficiently small compared with all in-plane geometric lengths, including the crack length itself, there exists a relation between the stress intensity factors K_I^1 and K_{II}^1 at the tip of the putative crack and the stress intensity factors K_I and K_{II} and the T -stress acting on the parent crack tip when $a = 0$. The relation has the form

$$\begin{aligned} K_I^1 &= c_{11}K_I + c_{12}K_{II} + b_1Ta^{1/2}, \\ K_{II}^1 &= c_{21}K_I + c_{22}K_{II} + b_2Ta^{1/2}. \end{aligned} \quad (2.6)$$

The Ω -dependences of the c 's are given by Hayashi and Nemat-Nasser (1981) and by He and Hutchinson (1989b), while the Ω -dependence of the b 's is given by He *et al.* (1991).

The ratio of the energy release rate of the parent crack when it advances straight-ahead to that of the kinked crack, $G^1 = (K_I^{12} + K_{II}^{12})/\bar{E}$, is of the form

$$G/G^1 = F(\Omega, \psi, \eta), \quad (2.7)$$

where F depends on the coefficients in (2.6). In addition, ψ is the measure of mode II to mode I loading acting on the parent crack defined by

$$\psi = \tan^{-1}(K_{II}/K_I) \quad (2.8)$$

and

$$\eta = T[a/(\bar{E}G)]^{1/2}. \quad (2.9)$$

The ratio (2.7) applies to both plane strain and planes stress.

With G_{\max}^1 denoting the value of G^1 maximized with respect to Ω for a given ψ , the ratio G/G_{\max}^1 is plotted as a function of ψ for various values of η in Fig. 2, which was taken from He *et al.* (1991). The kinking angle $\hat{\Omega}$ at

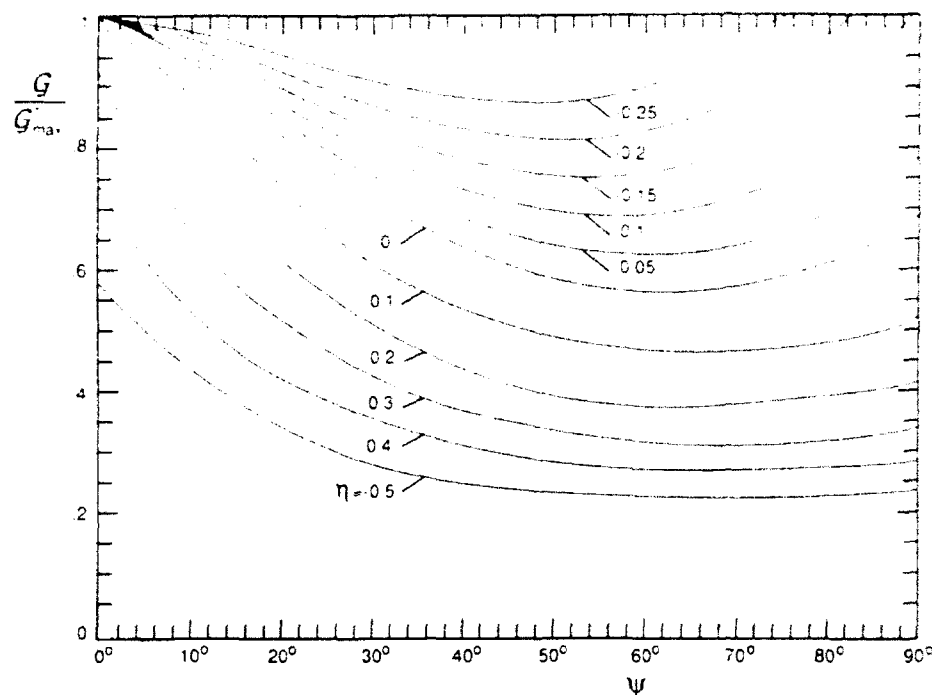


FIG. 2. Ratio of energy release rate for straight-ahead advance to maximum energy release rate for a kinked crack as a function of $\psi = \tan^{-1}(K_{II}/K_I)$. Reproduced from He *et al.* (1991).

which G^I is maximized is plotted as a function of ψ in Fig. 3 for the limit $\eta = 0$. The ratio in Fig. 2 corresponds to $\hat{F}(\psi, \eta) \equiv F(\hat{\Omega}, \psi, \eta)$. The kinking angle that maximizes G^I is nearly coincident with the kinking angle for which $K_{II}^I = 0$, as can be seen in Fig. 3. Only for ψ greater than about 50° is the difference more than one degree, and the difference between the energy release rates for the two directions is numerically insignificant. Thus,

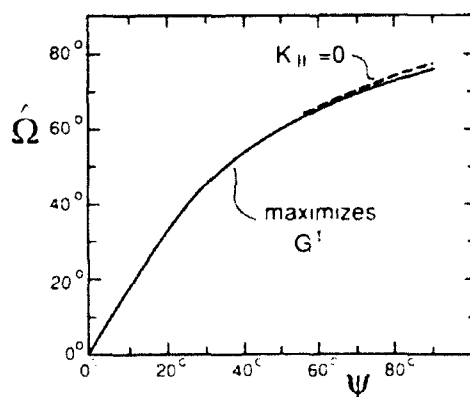


FIG. 3. Kink angle as predicted by two criteria.

for all practical purposes, there is no distinction between a criterion for kinking based on maximizing G' or one based on propagation in the direction in which $K_{II} = 0$. With $\Gamma = K_{IC}^2/\bar{E}$ denoting the mode I toughness, kinking will initiate at a crack tip in a brittle material subject to monotonic mixed mode loading when

$$G = \hat{F}(\psi, \eta = 0)\Gamma, \quad (2.10)$$

where \hat{F} is the ratio in Fig. 2. Once initiated, the advancing tip will be influenced by the T -stress through the η -dependence of \hat{F} .

B. HOMOGENEOUS, ORTHOTROPIC ELASTIC SOLIDS

Consideration will be restricted to plane cracks aligned with the principal axes of orthotropy and crack advance that is either straight-ahead or kinked at 90° parallel to the second in-plane orthotropy axis. With reference to Fig. 1, let the orthotropy axes coincide with the x_i -axes and take the plane of the crack to be $x_2 = 0$ with its edge along the x_3 -axis. Introduce elastic compliances of the solid in a standard way according to

$$\varepsilon_i = \sum_{j=1}^6 s_{ij}\sigma_j, \quad i = 1 \text{ to } 6, \quad (2.11)$$

where

$$\{\varepsilon_i\} = \{\varepsilon_{11}, \varepsilon_{22}, \varepsilon_{33}, 2\varepsilon_{23}, 2\varepsilon_{13}, 2\varepsilon_{12}\},$$

$$\{\sigma_i\} = \{\sigma_{11}, \sigma_{22}, \sigma_{33}, \sigma_{23}, \sigma_{13}, \sigma_{12}\}.$$

For the orthotropy assumed here, deformations in the (1, 2) plane satisfy (Lekhnitskii, 1981)

$$\varepsilon_i = \sum_{j=1,2,6} b_{ij}\sigma_j, \quad i = 1, 2, 6, \quad (2.12)$$

where, for $i, j = 1, 2, 6$,

$$b_{ij} = \begin{cases} s_{ij}, & \text{(plane stress)} \\ s_{ij} - s_{i3}s_{j3}/s_{33}, & \text{(plane strain)} \end{cases} \quad (2.13)$$

with only four independent elastic constants: b_{11} , $b_{12} = b_{21}$, b_{22} , and b_{66} ($b_{16} = b_{26} = 0$).

For simply connected domains with traction boundary conditions, Suo (1990c) has shown that the stresses depend on only the following two

(rather than three) nondimensional elastic parameters:

$$\lambda = b_{11}/b_{22}, \quad \rho = (b_{12} + \frac{1}{2}b_{66})/(b_{11}b_{22})^{1/2}. \quad (2.14)$$

This particular choice of parameters is particularly useful for reasons that will emerge shortly. When $\lambda = \rho = 1$, the in-plane behavior is isotropic (i.e., the material is transversely isotropic with respect to the x_3 -axis), and when just $\lambda = 1$, the material has cubic in-plane symmetry. Positive definiteness of the strain energy density requires $\lambda > 0$ and $-1 < \rho < \infty$.

The singular crack tip fields are contained in the work of Sih *et al.* (1965). Here, mode I and II stress intensity factors are defined such that (2.1) and (2.2) remain in effect, where the functions $\bar{\sigma}_{ij}^I$ and $\bar{\sigma}_{ij}^{II}$ now depend on λ and ρ as well as θ . The displacements of the crack faces behind the tip are

$$(\delta_2, \delta_1) = (\lambda^{-3/4}K_I, \lambda^{-1/4}K_{II})8nb_{11}[r/(2\pi)]^{1/2}, \quad (2.15)$$

where $n = [(1 + \rho)/2]^{1/2}$. The energy release rate for straight-ahead crack advance is

$$G = b_{11}n(\lambda^{-3/4}K_I^2 + \lambda^{-1/4}K_{II}^2) \quad (2.16a)$$

or, equivalently, in a notation used in the composites literature, as $G = G_I + G_{II}$, where

$$G_I = b_{11}n\lambda^{-3/4}K_I^2, \quad G_{II} = b_{11}n\lambda^{-1/4}K_{II}^2. \quad (2.16b)$$

A crack kinking analysis as extensive as that described for the isotropic material has not been performed for orthotropic materials. Many such materials have strongly orthotropic fracture properties, wood and laminated composites being well-known examples. When kinking occurs, it often does so at a right angle to the plane of the crack (ie., $\Omega = 90^\circ$ in Fig. 1) along the plane of the grain or a laminate. Suo *et al.* (1990b) have shown that for $\Omega = 90^\circ$ the generalization of (2.6) is (neglecting T)

$$\begin{aligned} K_{II}^I &= c_{11}\lambda^{-3/8}K_I + c_{12}\lambda^{-1/8}K_{II}, \\ K_{II}^I &= c_{21}\lambda^{-1/8}K_I + c_{22}\lambda^{1/8}K_{II}. \end{aligned} \quad (2.17)$$

The c 's depend on ρ , but this dependence is rather weak.

The energy release rate of the kinked crack tip, G^I , is related to K_I^I and K_{II}^I by an expression similar to (2.16), i.e.,

$$G^I = b_{22}n(\lambda^{3/4}K_I^{I2} + \lambda^{1/4}K_{II}^{I2}), \quad (2.18)$$

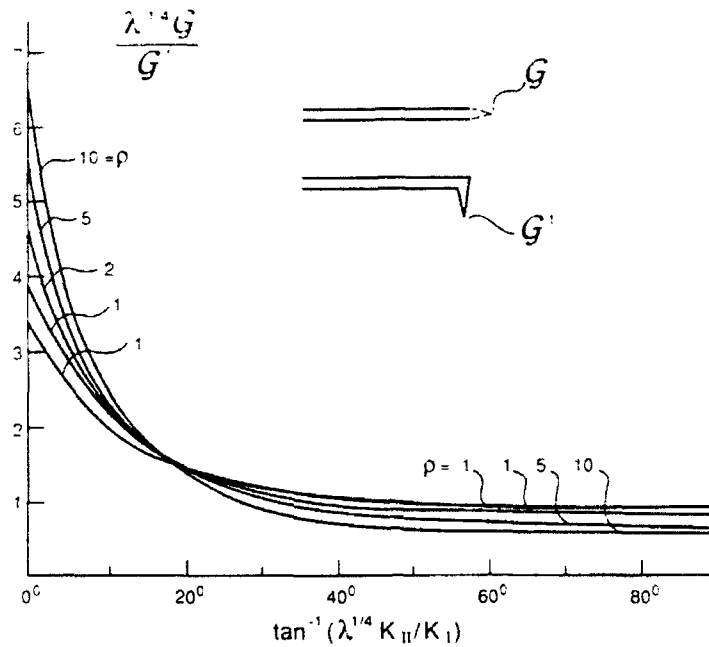


FIG. 4. Normalized ratio of energy release rates for orthotropic material.

where λ , n , and ρ remain defined as before. Thus, the ratio of the energy release rates for the competing trajectories can be obtained from (2.16)–(2.18) as

$$\frac{G}{G'} = \lambda^{1/4} \left[\frac{1 + \zeta^2}{(c_{11}^2 + c_{21}^2) + 2(c_{11}c_{12} + c_{21}c_{22})\zeta + (c_{12}^2 + c_{22}^2)\zeta^2} \right], \quad (2.19)$$

where $\zeta = \lambda^{1/4} K_{II}/K_I$. This ratio is plotted in Fig. 4. Note that it depends on the relative proportion of K_{II} to K_I but not on their magnitudes.

Suppose the main crack tip is subject to a mode I loading ($K_I > 0$, $K_{II} = 0$). Let Γ_0 be the material toughness associated with straight-ahead crack advance, and Γ_{90} be that associated with crack advance by kinking with $\Omega = 90^\circ$. (Note from (2.17) that the tip of the kinked crack is subject to mixed mode with $K'_{II}/K'_I = \lambda^{1/4} c_{21}/c_{11}$. Thus Γ_{90} must represent the mixed mode toughness for cracking parallel to the x_2 -plane.) If

$$\frac{G}{G'} > \frac{\Gamma_0}{\Gamma_{90}},$$

the crack will advance straight ahead since the condition $G = \Gamma_0$ will be reached before $G' = \Gamma_{90}$. The crack will advance by kinking at 90° if the inequality is reversed. From Fig. 4, it can be seen that the condition on the

toughness ratio for kinking is

$$\frac{\Gamma_{90}}{\Gamma_0} < f(\rho)\lambda^{1/4}, \quad (2.20)$$

where $f(1) = 0.26$, $f(1/10) = 0.29$, and $f(10) = 0.16$.

C. INTERFACE CRACKS

The emphasis of much of this chapter is on the mechanics of interfacial fracture and applications. This section introduces some of the basic results on the characterization of crack tip fields and on specification of interface toughness. If an interface is a low-toughness fracture path through joined solids, then one must be concerned with mixed mode crack propagation since the crack is not free to evolve with pure mode I stressing at its tip, as it would in an isotropic brittle solid. The asymmetry in the moduli with respect to the interface, as well as possible nonsymmetric loading and geometry, induces a mode II component. The competition between crack advance within the interface and kinking out of the interface depends on the relative toughness of the interface to that of the adjoining material. This competition will be addressed at the end of this section, but first it is necessary to consider how mixed mode conditions affect crack propagation in the interface. The article will focus on isotropic materials. Extensions to anisotropic materials are reviewed in Suo (1990a) and Wang *et al.* (1990).

1. Crack Tip Fields

Consider two isotropic elastic solids joined along the x_1 -axis as indicated in Fig. 5 with material 1 above the interface and material 2 below. Let μ_i , E_i , and ν_i ($i = 1, 2$) be the shear modulus, Young's modulus, and Poisson's ratio of the respective materials, and let $\kappa_i = 3 - 4\nu_i$ for plane strain and $\kappa_i = (3 - \nu_i)/(1 + \nu_i)$ for plane stress.

Dundurs (1969) has observed that wide class of plane problems of elasticity for bimetals depend on only two (rather than three) nondimensional combinations of the elastic moduli. With the convention set in Fig. 5, the Dundurs' elastic mismatch parameters are

$$\alpha = \frac{\mu_1(\kappa_2 + 1) - \mu_2(\kappa_1 + 1)}{\mu_1(\kappa_2 + 1) + \mu_2(\kappa_1 + 1)} \quad \text{and} \quad \beta = \frac{\mu_1(\kappa_2 - 1) - \mu_2(\kappa_1 - 1)}{\mu_1(\kappa_2 + 1) + \mu_2(\kappa_1 + 1)}. \quad (2.21)$$

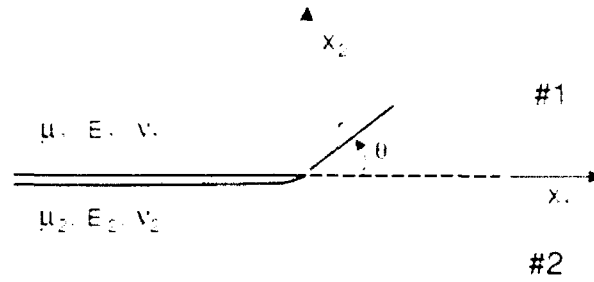


FIG. 5. Geometry and conventions for an interface crack.

A more revealing expression for α is

$$\alpha = (\bar{E}_1 - \bar{E}_2)/(\bar{E}_1 + \bar{E}_2), \quad (2.22)$$

where $\bar{E}_i \equiv E_i/(1 - \nu_i^2)$ in plane strain and $\bar{E}_i \equiv E_i$ in plane stress. Thus, α measures the mismatch in the plane tensile modulus across the interface. It approaches +1 when material 1 is extremely stiff compared to material 2, and approaches -1 when material 1 is extremely compliant. Both α and β vanish when there is no mismatch, and both change signs when the materials are switched.

The parameter β is a measure of the mismatch in the in-plane bulk modulus. In plane strain,

$$\beta = \frac{1}{2} \frac{\mu_1(1 - 2\nu_2) - \mu_2(1 - 2\nu_1)}{\mu_1(1 - \nu_2) + \mu_2(1 - \nu_1)}. \quad (2.23)$$

Thus, in plane strain, β vanishes when both materials are incompressible ($\nu_1 = \nu_2 = 1/2$), and $\beta = \alpha/4$ when $\nu_1 = \nu_2 = 1/3$. In plane stress, $\beta = \alpha/3$ when $\nu_1 = \nu_2 = 1/3$. When $\nu_1 = \nu_2$, α is the same in plane strain and plane stress.

In plane strain, the physical admissible values of α and β are restricted to lie within a parallelogram enclosed by $\alpha = \pm 1$ and $\alpha - 4\beta = \pm 1$ in the (α, β) plane, assuming nonnegative Poisson's ratios. The range of α and β in plane stress is somewhat more restricted. Representative material combinations are plotted for plane strain in Fig. 6, in every case with the stiffer material as material 1 so that α is positive. This plot is similar to one given by Suga *et al.* (1988). Note that most of the (α, β) combinations in Fig. 6 fall between $\beta = 0$ and $\beta = \alpha/4$. Combinations that satisfy $\beta = 0$ give rise to simpler crack tip fields than combinations with $\beta \neq 0$, and special attention will be paid to this restricted family of bimetals in a separate section following this one.

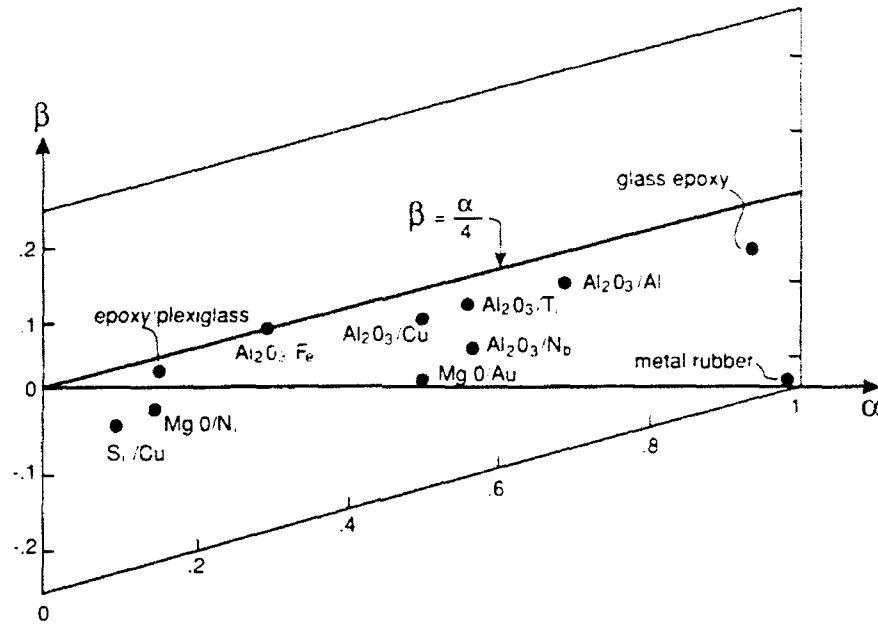


FIG. 6. Values of Dundurs' parameters in plane strain for selected combinations of materials.

Solutions to bimaterial interface crack problems were presented in the earliest papers on the subject by Cherepanov (1962), England (1965), Erdogan (1965), and Rice and Sih (1965). Williams (1959) investigated the singular crack tip fields. Here, the notations and definitions of Rice (1988) for the crack tip fields will be adopted since these reduce to the conventional notation when the mismatch vanishes. Take the origin at the crack tip, as in Fig 5, with the crack flanks lying along the negative x_1 -axis. The dominant stress singularity for any plane problem in which zero tractions are prescribed on a portion of the negative x_1 -axis ending at the origin is of the form

$$\sigma_{\alpha\beta} = \text{Re}[Kr^{i\varepsilon}](2\pi r)^{-1/2}\sigma_{\alpha\beta}^I(\theta, \varepsilon) + \text{Im}[Kr^{i\varepsilon}](2\pi r)^{-1/2}\sigma_{\alpha\beta}^{II}(\theta, \varepsilon), \quad (2.24)$$

where $i = \sqrt{-1}$, r and θ are defined in Fig. 5, and

$$\varepsilon = \frac{1}{2\pi} \ln \left(\frac{1 - \beta}{1 + \beta} \right). \quad (2.25)$$

The complex interface stress intensity factor $K = K_1 + iK_2$ has real and imaginary parts K_1 and K_2 , respectively, which play similar roles to the conventional mode I and Mode II intensity factors. The quantities $\sigma_{\alpha\beta}^I$ and $\sigma_{\alpha\beta}^{II}$ are given by Rice *et al.* (1990); they reduce to the corresponding quantities in (2.1) when $\varepsilon = 0$.

The singular fields are normalized so that the tractions on the interface directly ahead of the tip are given by

$$\sigma_{22} + i\sigma_{12} = (K_1 + iK_2)(2\pi r)^{-1/2} r^{i\epsilon} \quad (2.26a)$$

or

$$\sigma_{22} = \text{Re}[Kr^{i\epsilon}](2\pi r)^{-1/2}, \quad \sigma_{12} = \text{Im}[Kr^{i\epsilon}](2\pi r)^{-1/2} \quad (2.26b)$$

where $r^{i\epsilon} = \cos(\epsilon \ln r) + i \sin(\epsilon \ln r)$. This is a so-called oscillatory singularity, which brings in some complications that are not present in the elastic fracture mechanics of homogeneous solids, as will be discussed in detail later. The associated crack flank displacements a distance r behind the tip, $\delta_i = u_i(r, \theta = \pi) - u_i(r, \theta = -\pi)$, are given by

$$\delta_2 + i\delta_1 = \frac{8}{(1 + 2i\epsilon) \cosh(\pi\epsilon)} \frac{(K_1 + iK_2)}{E_*} \left(\frac{r}{2\pi}\right)^{1/2} r^{i\epsilon}, \quad (2.27)$$

where

$$\frac{1}{E_*} = \frac{1}{2} \left(\frac{1}{\bar{E}_1} + \frac{1}{\bar{E}_2} \right) \quad (2.28)$$

The energy release rate for crack advance in the interface is (Malyshev and Salganik, 1965)

$$G = \frac{(1 - \beta^2)}{E_*} (K_1^2 + K_2^2), \quad (2.29)$$

which reduces to (2.5) in the absence of mismatch. Equations (2.27) and (2.29) can be re-expressed using the connection $1 - \beta^2 = 1/\cosh^2(\pi\epsilon)$.

To help motivate the application of the crack tip fields to characterize interface toughness, it is useful to give two examples of stress intensity factors for solved problems. The problem of the isolated crack of length $2a$ lying on the interface between two remotely stressed semi-infinite blocks (see Fig. 7a) was solved in the early papers cited previously. For the right hand tip of the crack,

$$K_1 + iK_2 = (\sigma_{22}^\infty + i\sigma_{12}^\infty)(1 + 2i\epsilon)(\pi a)^{1/2}(2a)^{-i\epsilon}. \quad (2.30)$$

This particular set of intensity factors depends on the elastic mismatch only through ϵ and, by (2.25), is independent of α . The problem of the infinite double cantilever beam (see Fig 7b) loaded with equal and opposite moments (per unit thickness perpendicular to the (1, 2) plane) was solved by Suo and Hutchinson (1990) as the special case of a more general solution

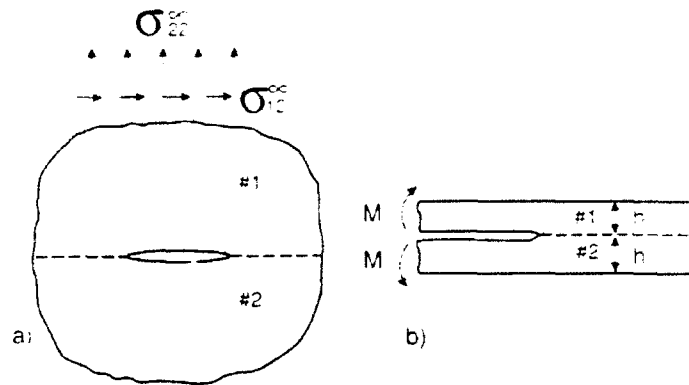


FIG. 7. Two basic interface crack problems.

presented in Section III. The solution is

$$K_1 + iK_2 = 2\sqrt{3} Mh^{-3/2-\epsilon}(1 - \beta^2)^{-1/2} e^{i\omega^*(\alpha, \beta)}, \quad (2.31)$$

where the function $\omega^*(\alpha, \beta)$ is displayed in Fig. 8.

2. Crack Tip Fields and Interface Toughness with $\beta = 0$

When $\beta = 0$ (and thus $\epsilon = 0$ by (2.25)), (2.26) becomes

$$(\sigma_{22}, \sigma_{12}) = (K_1, K_2)(2\pi r)^{-1/2}, \quad (2.32)$$

and (2.27) reduces to

$$(\delta_2, \delta_1) = (8/E_*)(K_1, K_2)[r/(2\pi)]^{1/2}. \quad (2.33)$$

The interface stress intensity factors K_1 and K_2 play precisely the same role as their counterparts in elastic fracture mechanics for homogeneous, isotropic solids. The mode 1 component K_1 is the amplitude of the singularity of the normal stresses ahead of the tip and the associated normal separation of the crack flanks, while the mode 2 component K_2 governs the shear stress on the interface and the relative shearing displacement of the flanks.

When $\beta \neq 0$, the decoupling of the normal and shear components of stress on the interface and associated displacements behind the tip within the zone dominated by the singularity does not occur. When $\beta \neq 0$, the notions of mode 1 and mode 2 require some modification. In addition, the traction-free line crack solution for the displacements (2.27) implies that the crack faces interpenetrate at some point behind the tip. Both of these features have caused conceptual difficulties in the development of a mechanics of interfaces. For this reason, we have chosen to introduce the elastic fracture mechanics for bimaterial systems with $\beta = 0$, either exactly

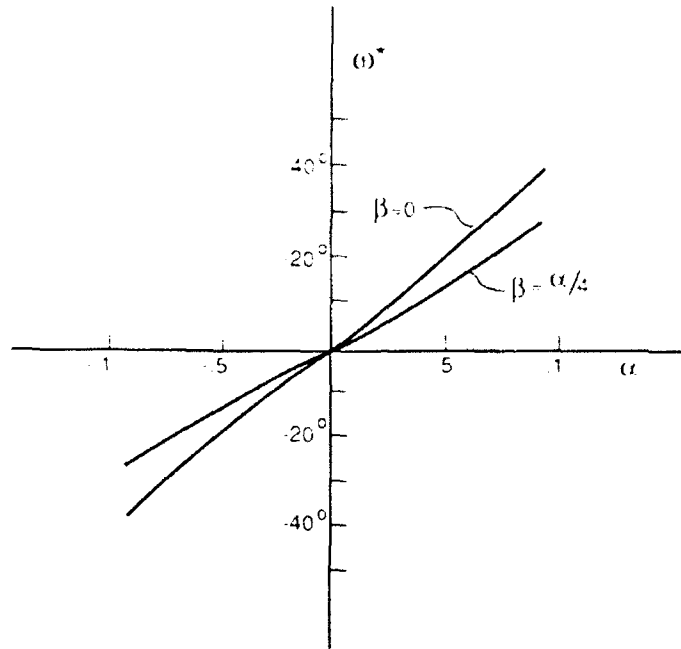


FIG. 8. Phase factor ω^* for the problem of Fig. 7b.

or as an approximation. The extension for systems with $\beta \neq 0$ will be given in the following section, where it will also be argued that the effect of nonzero β is often of secondary consequence.

When $\beta = 0$, take the measure of the relative amount of mode 2 to mode 1 at the crack tip to be

$$\psi = \tan^{-1}(K_2/K_1). \quad (2.34)$$

The finite crack in the infinite plane, (2.30), gives

$$\psi = \tan^{-1}(\sigma_{12}^\infty/\sigma_{22}^\infty), \quad (2.35)$$

while the double cantilever beam loaded by equal and opposite moments, (2.31), has

$$\psi = \omega^*(\alpha, 0). \quad (2.36)$$

The double cantilever has symmetric geometry and loading; the asymmetry is due entirely to the elastic mismatch. Note from Fig. 8 that the specimen is in mode 1 when $\alpha = 0$, as it must by symmetry, but develops a substantial mode 2 component when the elastic mismatch becomes significant.

Efforts to measure interfacial toughness under mixed mode conditions go back some years (e.g., Trantina, 1972, and Anderson *et al.*, 1974), as reviewed by Liechti and Hanson (1988). Parallel efforts have also been

underway to develop mixed mode fracture specimens designed to measure the delamination toughness associated with ply separation in polymer-matrix composites (e.g., Kinloch, 1987). A series of recent experiments (Cao and Evans, 1989; Wang and Suo, 1990; and Liechti and Chai, 1990a) have focussed on the interface between epoxy and glasses, metals and plastics. Thouless (1990b) has carried out mixed mode toughness experiments for crack propagation in the interface between a brittle wax and glass. In all these systems, the interface toughness is not a single material parameter, rather it is a *function* of the relative amount of mode 2 to mode 1 acting on the interface.

The criterion for initiation of crack advance in the interface when the crack tip is loaded in mixed mode characterized by ψ is

$$G = \Gamma(\psi). \quad (2.37)$$

The toughness of the interface, $\Gamma(\psi)$, can be thought of as an effective surface energy that depends on the mode of loading. Condition (2.37) is also assumed to hold for quasi-static crack advance when crack growth resistance effects can be disregarded.

Data from Wang and Suo (1990) for a crack in a plexiglass/epoxy interface is shown in Fig. 9. This data was obtained using a layer of epoxy sandwiched between two halves of a Brazil nut specimen. The specimen, which will be considered later in Section IV.C.2, enables the experimentalist to vary the mix of loading from pure mode 1 to pure mode 2 by varying the

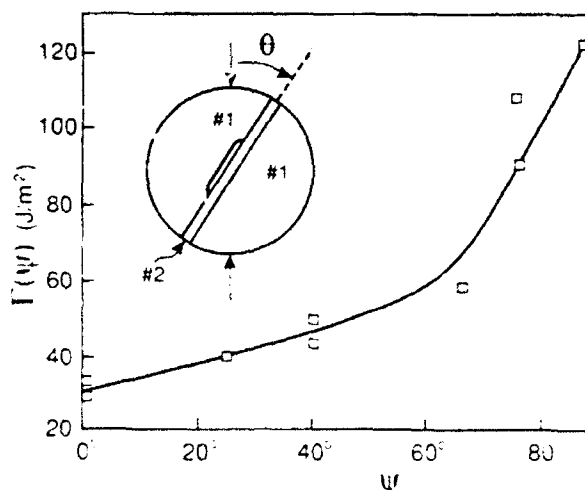


FIG. 9. Interface toughness function for a plexiglass (#1)/epoxy(#2) interface. Obtained using a Brazil nut specimen by Wang and Suo (1990).

angle θ of the compression axis (see the insert in Fig. 9). For the plexiglass (#1)/epoxy(#2) interface in plane strain,

$$\alpha = -0.15, \quad \beta = -0.029, \quad \varepsilon = 0.009. \quad (2.38)$$

The error in taking $\beta = 0$ is negligible for this system as will be clear in the next section. Note, for example, that the error in G in (2.29) from this approximation is less than 0.1%.

3. Phenomenological Characterization of Interface Toughness

A micromechanics of interface toughness is not far advanced. An overview of various mechanisms responsible for the strong dependence of interfaced toughness on mode mixity is given by Evans *et al.* (1990). Two primary mechanisms are asperity contact and plasticity. Asperities on the fracture surfaces will tend to make contact for some distance behind the tip when mode 2 is present along with mode 1. A micromechanics model of shielding of the tip due to asperity interaction was presented by Evans and Hutchinson (1989). That model led to a prediction of $\Gamma(\psi)$ in terms of a nondimensional measure of fracture surface roughness. Crack tip plasticity also depends on ψ , with the plastic zone in plane strain increasing in size as $|\psi|$ increases, with G held fixed (Shih and Asaro, 1988). When an interface between a bimaterial system is actually a very thin layer of a third phase, the details of the cracking morphology in the thin interface layer can also play a role in determining the mixed mode toughness. Some aspects of cracking at the scale of the interface layer itself will be discussed in the final section of this chapter. The approach for the time being is that the interface has zero thickness and is modeled by the toughness function $\Gamma(\psi)$ which, in general, must be determined by experiment.

A simple, one parameter family of mixed mode fraction criteria that captures the trend illustrated by the data in Fig. 9 is

$$E_*^{-1}(K_1^2 + \lambda K_2^2) = G_1^c. \quad (2.39)$$

The parameter λ adjusts the influence of the mode 2 contribution in the criterion. The limit $\lambda = 1$ is the "ideally brittle" interface with initiation occurring when $G = G_1^c$ for all mode combinations. This limit coincides with the classical surface energy criterion. When $\lambda = 0$, crack advance only depends on the mode 1 component. For any value of λ , G_1^c is the pure mode 1 toughness. The criterion can be cast in the form (2.37) where the mixed mode toughness function is

$$\Gamma(\psi) = G_1^c[1 + (\lambda - 1) \sin^2 \psi]^{-1}. \quad (2.40)$$

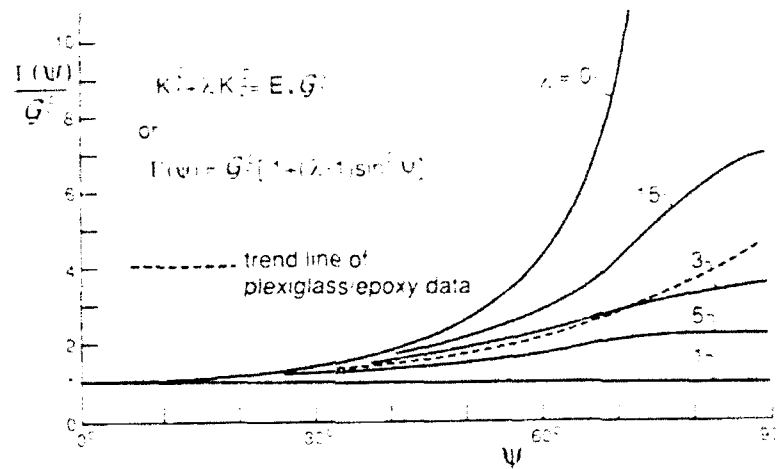


FIG. 10. A family of interface toughness functions and comparison with data for a plexiglass-epoxy interface (represented by the broken line).

The toughness is plotted as a function of ψ in Fig. 10 for various values of λ . Included in this figure is the data for the plexiglass/epoxy interface, which is approximately represented by the choice $\lambda = 0.3$. This particular interface displays a toughness that is far removed from ideally brittle behavior.

The family of criteria (2.39) was extended to include a mode 3 contribution by Jensen *et al.* (1990). In a slightly different form, this family of criteria has been used for some time to characterize interlaminar failure in fiber reinforced composites (*cf.* Kinloch, 1987). When $\beta = 0$, one can introduce "components" of G according to

$$(G_1, G_2) = E_*^{-1}(K_1^2, K_2^2), \quad (2.41)$$

such that $G = G_1 + G_2$.[†] Alternatively, for a crack in a homogeneous orthotropic material, G_1 and G_2 can be defined using (2.16). The criterion (2.39) can be rewritten as

$$(G_1/G_1^c) + (G_2/G_2^c) = 1, \quad (2.42)$$

where $G_2^c \equiv G_1^c/\lambda$ has the interpretation as the pure mode 2 toughness.

Other phenomenological criteria have been proposed to characterize mixed mode toughness data for interlaminar fracture (*e.g.*, Kinloch, 1987). Two alternatives to (2.40) are now given which have qualitative features

[†] The components can be regarded as the work of the normal and shear tractions on the interface through their respective crack face displacements as the crack advances. This decomposition does not exist when $\beta \neq 0$.

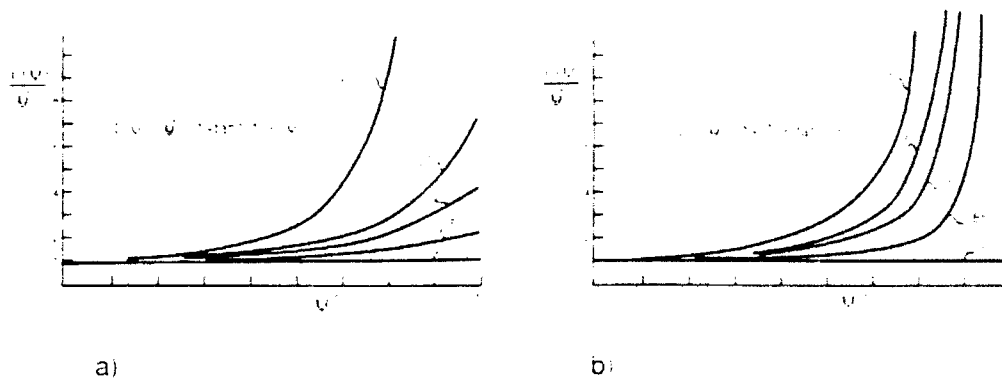


FIG. 11. Alternative families of interface toughness functions.

that may more realistically reproduce data trends for interfacial fracture:

$$\Gamma(\psi) = G_I^c \{1 + \tan^2[(1 - \lambda)\psi]\} \quad (2.43)$$

and

$$\Gamma(\psi) = G_I^c [1 + (1 - \lambda) \tan^2 \psi]. \quad (2.44)$$

These are plotted in Fig. 11. Both coincide with (2.40) in the limit $\lambda = 0$, i.e., they reduce to a criterion based on a critical value of K_I , independent of K_2 . Both are ideally brittle with $\lambda = 1$. According to (2.43), the toughness increases sharply as $\psi \rightarrow 90^\circ$ (mode 2), as opposed to (2.40), which has the toughness leveling off as $\psi \rightarrow 90^\circ$. Equation (2.44) models the toughness as unbounded as $\psi \rightarrow 90^\circ$ for all $\lambda < 1$. While this feature should not be taken literally, it did emerge in the simple model of mixed mode interface toughness due to asperity contact of Evans and Hutchinson (1989). Of the three formulas for $\Gamma(\psi)$, (2.44) most accurately reflects the trends of that model.

All three of the interface toughness functions $\Gamma(\psi)$ are symmetric in ψ . In general, symmetry of interface toughness with respect to ψ should not be expected. Some evidence that $\Gamma(\psi)$ is asymmetric for an epoxy/glass interface will be presented in the next section.

4. Interface Toughness with $\beta \neq 0$

When $\beta \neq 0$, the notion of a mode 1 or a mode 2 crack tip field must be defined precisely, and the possibility of contact of the crack faces within the region dominated by the near tip K -fields must be considered. As noted by Rice (1988), a generalized interpretation of the mode measure is the most important complication raised by the oscillatory singularity, and the

approach recommended here follows largely along the lines of one of his proposals. First, a definition of a measure of the combination of modes is made that generalizes (2.34).

Let l be a reference length whose choice will be discussed later. Noting the stress distribution (2.26b) on the interface from the K -field, define ψ as

$$\psi = \tan^{-1} \left[\frac{\text{Im}(Kl^{\epsilon})}{\text{Re}(Kl^{\epsilon})} \right], \quad (2.45)$$

where $K = K_1 + iK_2$ is the complex stress intensity factor. For a choice of l within the zone of dominance of the K -field, (2.45) is equivalent to (cf. (2.26b))

$$\psi = \tan^{-1} \left[\left(\frac{\sigma_{12}}{\sigma_{22}} \right)_{r=l} \right]. \quad (2.46)$$

Moreover, the definition reduces to (2.34) when $\beta = 0$, since $l^{\epsilon} = 1$ when $\epsilon = 0$. When $\epsilon \neq 0$, a mode 1 crack is one with zero shear traction on the interface a distance l ahead of the tip, and a mode 2 crack has zero normal traction at that point. The measure of the proportion of "mode 2" to "mode 1" in the vicinity of the crack tip requires the specification of *some* length quantity since the ratio of the shear traction to normal traction varies (very slowly) with distance to the tip when $\beta \neq 0$.

The choice of reference length l is somewhat arbitrary, as will be made clear in the following. It is useful to distinguish between a choice based on an in-plane length L of the specimen geometry, such as crack length, and a choice based on a material length scale, such as the size of the fracture process zone or a plastic zone at fracture. The former is useful for discussing the mixed mode character of a bimaterial crack solution, independent of material fracture behavior, while the latter is advantageous in interpreting mixed mode fracture data, as will be discussed. When there is the need to keep the two types of choices clearly distinct, the notation (ψ, l) will be used for a choice based on the specimen geometry and $(\hat{\psi}, \hat{l})$ will be reserved for a material-based choice.

The solution for the complex stress intensity factor to any plane elasticity problem for an interface crack will necessarily have the form

$$K = (\text{applied stress}) \times FL^{1/2-\epsilon}, \quad (2.47)$$

where L is some in-plane length, such as crack length or uncracked ligament length, and F is a complex-valued, dimensionless function of dimensionless

groups of moduli, and in-plane length quantities. Equations (2.30) and (2.31) are two examples. The term Kl'' in the definition of ψ will therefore always involve a dimensionless combination such as $(l/L)'' \equiv \exp[i\epsilon \ln(l/L)]$. For example, the bimaterial double cantilever beam specimen (2.31) has

$$\psi = \omega^*(\alpha, \beta) + \epsilon \ln(l/h), \quad (2.48)$$

which generalizes (2.36).

The freedom in the choice of l in the definition of ψ is a consequence of the simple transformation rule from one choice to another. Let ψ_1 be associated with l_1 , and ψ_2 with l_2 . From the definition in (2.45) one can readily show

$$\psi_2 = \psi_1 + \epsilon \ln(l_2/l_1). \quad (2.49)$$

Thus, as noted by Rice (1988), it is a simple matter to transform from one choice to another. In particular, toughness data can readily be transformed, as will be discussed in the following.

Let \hat{l} denote a length characterizing the size of the fracture process zone or, perhaps, the typical size of the plastic zone at fracture, and let $\hat{\psi}$ be associated through (2.45). Since small-scale yielding or a small-scale fracture process zone is assumed, \hat{l} necessarily lies within the zone of dominance of the K -field. Given the choice \hat{l} , the criterion for interface cracking can again be stated as (2.37), i.e.,

$$G = \Gamma(\hat{\psi}, \hat{l}), \quad (2.50)$$

where the implicit dependence of the toughness function on \hat{l} has been noted. In words, $\Gamma(\hat{\psi}, \hat{l})$ is the critical value of the energy release rate needed to advance the crack in the interface in the presence of a combination of tractions whose relative proportion is measured by $\hat{\psi}$. By (2.49), change in one choice of length in the definition of ψ to another only involves a shift of the ψ -origin of Γ according to

$$\Gamma(\psi_2, l_2) = \Gamma(\psi_1 + \epsilon \ln(l_2/l_1), l_1), \quad (2.51)$$

as depicted in Fig. 12. When ϵ is small, the shift will generally be negligible even for changes of l of several orders of magnitude. This is the case for the plexiglass/epoxy interface (2.38). An illustration for which the ϵ -effect is not negligible in reporting interface toughness is discussed shortly.

In discussing the mixed mode character of a given elasticity solution, it is generally convenient to identify l with an in-plane length of the geometry, such as L in (2.47). For example, if for the double cantilever beam specimen

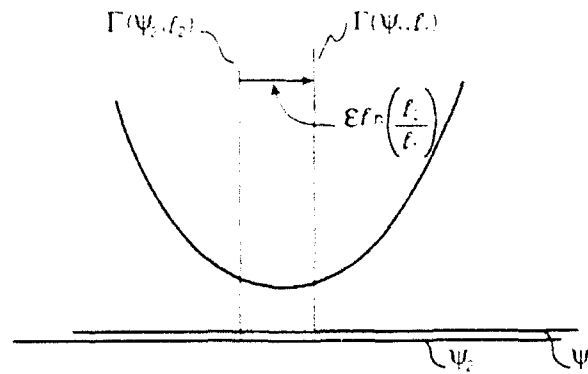


FIG. 12. Procedure for shifting toughness function from one choice of reference length to another.

one picks $l = h$, then by (2.48),

$$\psi = \omega^*(\alpha, \beta), \quad (2.52)$$

which is *independent* of the size of the specimen.[†] This is necessarily a feature of any choice of l that scales with an in-plane length. By contrast, for a choice \hat{l} that is *fixed* at some microstructural length, $\hat{\psi}$ varies with specimen size, e.g., for the double cantilever specimen,

$$\hat{\psi} = \omega^*(\alpha, \beta) + \varepsilon \ln(\hat{l}/h). \quad (2.53)$$

This reflects the fact that the ratio of σ_{12} to σ_{22} at a fixed distance $r = \hat{l}$ ahead of the tip varies as the specimen size changes. Standard arguments underlying the mechanics of fracture, based on Irwin's notion of autonomous crack tip behavior, require that $\Gamma(\hat{\psi}, \hat{l})$ be *independent* of specimen size (assuming, of course, that small scale processes are in effect), while $\Gamma(\psi, l)$ will depend on specimen size if $\varepsilon \neq 0$ when l scales with specimen size. This property, together with the interpretation of mixity in (2.45) in the vicinity of the fracture process zone, favors the choice of a material-based \hat{l} for presenting toughness data.

Liechti and Chai (1990a, b) have developed a bimaterial interfacial fracture specimen that is capable of generating the interface toughness function Γ over essentially the full range of ψ . A schematic of their plane strain specimen is shown in the insert in Fig. 13. The in-plane length of the specimen is long compared to the thickness h of each layer. The bottom

[†] The fact that $l = h$ obviously lies outside the zone of dominance of the K -field is of no consequence. The essential point is that any choice of l is acceptable as long as it is recorded along with the result for ψ , and as long as one is cognizant of the transformation rule.

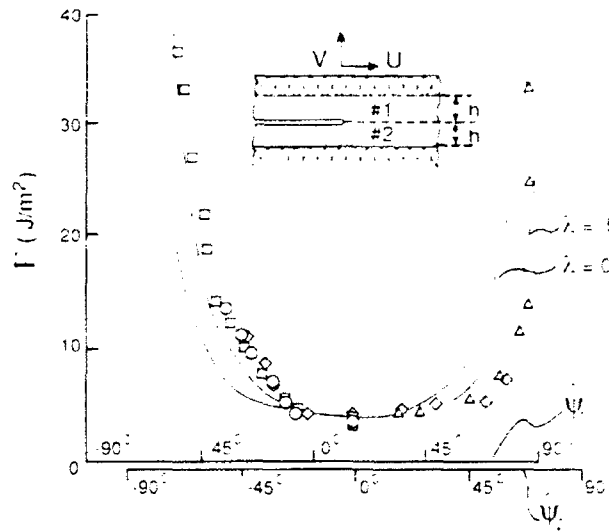


FIG. 13. Data of Liechti and Chai (1990a) for an epoxy (#1) / glass (#2) interface: ψ_1 is based on $\hat{l}_1 = 12.7$ mm and ψ_2 on $\hat{l}_2 = 127$ μ m. The solid curves are $\Gamma(\psi_2)$, where Γ is given by (2.44).

surface is rigidly held and the upper surface is attached to a rigid grip that can impose a horizontal, U , and vertical, V , in-plane displacement. The solution to the problem when the layers are infinitely long and the interface crack is semi-infinite was used by Liechti and Chai to obtain the values of K_1 and K_2 (and G and ψ) associated with the measured combinations of U and V at which the crack propagated in the interface. For plane strain, the solution is (see Section III.C)

$$K_1 + iK_2 = \frac{\sqrt{2}\mu_1\mu_2 h^{-1/2} e^{i\omega}(cV + iU)}{(1 - \beta^2)^{1/2}(\mu_1 + \mu_2)^{1/2}[\mu_1(1 - \nu_2) + \mu_2(1 - \nu_1)]^{1/2}}, \quad (2.54)$$

where ω is a real quantity that depends on μ_1/μ_2 , ν_1 , and ν_2 and

$$c = \left\{ \frac{2(\mu_1 + \mu_2)}{\mu_1[(1 - 2\nu_2)/(1 - \nu_2)] + \mu_2[(1 - 2\nu_1)/(1 - \nu_1)]} \right\}^{1/2}. \quad (2.55)$$

Let γ measure the relative proportion of U to cV applied to the specimen, and define it by

$$\gamma = \tan^{-1}[U/(cV)]. \quad (2.56)$$

Then, with l as the reference length, (2.45) gives

$$\psi = \gamma + \omega + \varepsilon \ln(l/h). \quad (2.57)$$

The data for $\Gamma(\hat{\psi}, \hat{l})$ in Fig. 13 was measured by Liechti and Chai for an epoxy(#1)/glass(#2) interface with the following properties for the system: $E_1 = 2.07$ GPa, $E_2 = 68.9$ GPa, $\nu_1 = 0.37$, $\nu_2 = 0.20$, and $h = 12.7$ mm. The plane strain Dundurs' parameters and the oscillation index are

$$\alpha = -0.935, \quad \beta = -0.188, \quad \text{and} \quad \varepsilon = 0.060. \quad (2.58)$$

For this system $\omega = 16^\circ$ (see Section III.C). Liechti and Chai took $\hat{l} = 12.7$ mm in their definition of ψ , coinciding with the thickness h of the layers.

Liechti and Chai recorded plastic zones in the epoxy to be approximately on the order of $1 \mu\text{m}$ when $\hat{\psi} \cong 0^\circ$ and $140 \mu\text{m}$ when $\hat{\psi} \cong 90^\circ$. If instead of $\hat{l} = 12.7$ mm, \hat{l} is chosen to be two orders of magnitude smaller (i.e., $\hat{l} = 127 \mu\text{m}$), the shift in the $\hat{\psi}$ -origin from (2.49) or (2.51) is -15.8° . This choice seems somewhat more natural in terms of the interpretation given earlier since now \hat{l} lies well within the zone of dominance of the K -field and has a microstructural identity. This choice also places the origin of the $\hat{\psi}$ -axis (i.e., "mode 1" for this choice of l) at the approximate minimum of Γ and roughly centers the data, as can be seen in Fig. 13. Nevertheless, some asymmetry in Γ with respect to $\hat{\psi}$ still persists. Included in this figure is the toughness function $\Gamma(\psi)$ from (2.44) for two choices of λ , with G_I^c chosen to coincide with the measured value at $\hat{\psi}_2 = 0$. Apart from the asymmetry in the data, a λ -value between 0 and 0.5 would seem to give an approximate characterization of the data over the range of $\hat{\psi}$ shown. Other important aspects of the mixed mode fracture behavior of this system have been discussed by Liechti and Chai (1990a). These include possible correlation of the strong increase in toughness with mode 2 with either fracture surface roughness or plasticity, and the role of contact between crack faces when the loading becomes dominantly mode 2.

When interpenetration of the crack faces is predicted on the basis of the formulation for a traction-free line crack, the consequences of contact must be taken into account in any application of the solution to fracture. The bimaterial problem with $\beta \neq 0$ is unusual in that interpenetration of the faces always occurs according to (2.27). This feature of the interface crack problem was noted in the earliest papers on the subject, and solutions to specific problems posed with allowance for contact have been produced (Comninou, 1977, and Comninou and Schmueser, 1979). Fortunately, under most loadings likely to be of concern, the contact zone predicted by the elasticity solution is tiny compared with relevant near tip physical features such as the fracture process zone or the plastic zone. The larger the

proportion of mode 2, the more likely is contact of the crack faces to be an issue.[†]

To see this, a rough estimate of the size of the contact zone is obtained. The estimate is that of Rice (1988), as elaborated on by Wang and Suo (1990). Here, however, emphasis is placed on a definition of $\hat{\psi}$ in (2.45) based on a microstructural scale length \hat{l} . For $r < \hat{l}$, it will be assumed that the fracture process or other inelastic effects supercede linear elasticity. Using the definition of ψ in (2.45), one can readily show that the normal crack face displacement in the near tip region from (2.27) is

$$\delta_2 = |\delta_2 + i\delta_1| \cos[\hat{\psi} + \varepsilon \ln(r/\hat{l}) - \tan^{-1}(2\varepsilon)]. \quad (2.59)$$

Consider the condition for the crack to be open ($\delta_2 > 0$) for $\hat{l} < r < L/10$. The factor 1/10 is arbitrary, but the near tip fields should not be expected to retain accuracy for r larger than some fraction of L . If contact occurs outside the preceding range, it must be assessed using the full solution. If $\varepsilon > 0$, the stated condition is met if

$$-\frac{\pi}{2} + 2\varepsilon < \hat{\psi} < \frac{\pi}{2} + 2\varepsilon - \varepsilon \ln\left(\frac{1}{10} \frac{L}{\hat{l}}\right), \quad (2.60)$$

where $\tan^{-1}(2\varepsilon)$ has been approximated by 2ε since $|\varepsilon| \leq 0.175$. For $\varepsilon < 0$, there will be no contact over the specified region as long as

$$-\frac{\pi}{2} + 2\varepsilon - \varepsilon \ln\left(\frac{1}{10} \frac{L}{\hat{l}}\right) < \hat{\psi} < \frac{\pi}{2} + 2\varepsilon. \quad (2.61)$$

The ε -dependence of the above constraints is inconsequential for many interfacial systems. For the epoxy/glass system (2.58), which has a relatively large ε -value, (2.60) becomes $-83.1^\circ < \hat{\psi} < 89.0^\circ$ for $L/\hat{l} = 100$ and $-83.1^\circ < \hat{\psi} < 73.2^\circ$ for $L/\hat{l} = 10^4$. The difference between the limits obtained above and those derived by Rice (1988) and Wang and Suo (1990) is due mainly to the use in the present work of the material-based definition of $\hat{\psi}$, rather than ψ defined in terms of a length L characterizing the specimen. The combination of the contact due to nonzero ε and the contact arising from fracture surface asperities has not been modeled. The interaction between these two effects acting in concert should be important for mixed mode loadings near the limits listed above.

[†] Now the contact is not due to asperity roughness on the crack faces generated by the fracture process that was discussed earlier. Here, the crack faces are imagined to be smooth and "just touching" in the unloaded state.

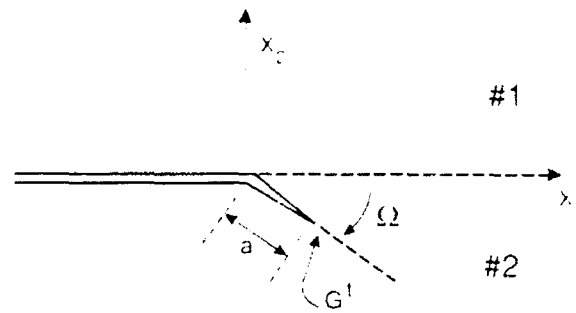


FIG. 14. Conventions for a crack kinking out of an interface.

5. Kinking Out of the Interface

The analysis of kinking parallels that was discussed in Section A for the isotropic elastic solid, and the results presented in what follows are taken from He and Hutchinson (1989a) and He *et al.* (1991). As depicted in Fig. 14, a semi-infinite crack lies along the interface with its tip at the origin. Prior to kinking ($a = 0$), the parent crack is loaded with a complex interface stress intensity factor $K = K_1 + iK_2$ with mixity ψ defined by (2.45) relative to some reference length l . For definiteness, ψ will be taken to be positive with kinking down into material #2 as shown in Fig. 14. Negative ψ -loadings with upward kinking can be analyzed by exchanging the materials, i.e., switching the signs on α and β .

As in the analysis for the isotropic solid, the energy release rate G for straight-ahead advance in the interface is compared with the energy release rate G^1 for a crack with a segment of length a kinking at an angle Ω to the interface. The energy release rate G for advance in the interface is given by (2.29). The conventional mode I and mode II stress intensity factors at the tip of the kinked crack tip are related to K by

$$K_1 + iK_{II} = c(\Omega, \alpha, \beta)Ka^{ie} + \bar{d}(\Omega, \alpha, \beta)\bar{K}a^{-ie} + b(\Omega, \alpha, \beta)Ta^{1/2}, \quad (2.62)$$

where T is the nonsingular contribution to σ_{11} in material #2 at the parent crack tip prior to kinking. The T -stress may arise from remote applied load or it may be present as a residual stress. The functions c , d , and b are complex-valued; c and d are tabulated in He and Hutchinson (1989b), while b is given in He *et al.* (1991).

The energy release rate at the kinked crack tip, G^1 , is given by (2.5), and the ratio of the two release rates has the form

$$G/G^1 = F(\Omega, \bar{\psi}, \eta, \alpha, \beta), \quad (2.63)$$

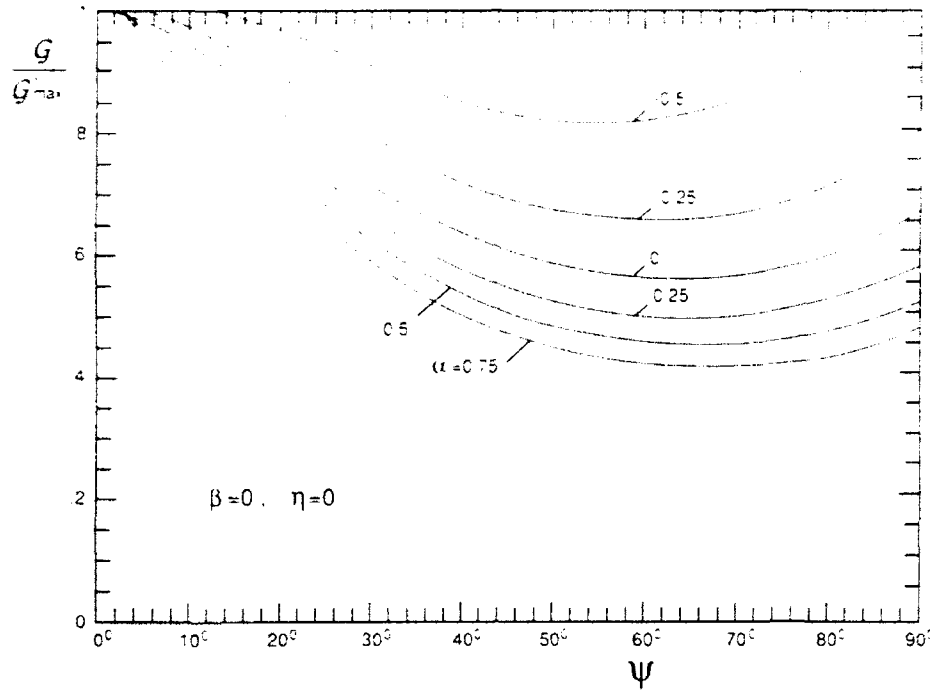


FIG. 15. Ratio of energy release rate for advance in the interface to the maximum energy release rate for the kinked crack for various levels of elastic mismatch, all with $\beta = 0$.

where $\eta = T[a/(E_*G)]^{1/2}$ and

$$\tilde{\psi} = \psi + \varepsilon \ln(a/l). \quad (2.64)$$

The complete expression for F is given by He *et al.* (1991). The a -dependence of this ratio appears through η , and weakly through $\tilde{\psi}$.

The ratio G/G_{\max}^I is plotted against ψ in Fig. 15 for various values of α , in each case for $\beta = 0$ and $\eta = 0$. Here, G_{\max}^I is the maximum of G^I with respect to kink angle Ω for a given ψ . As in the case of the homogeneous isotropic kinking problem, there is very little difference between the kink angle that maximizes G^I and that which is associated with $K_{II} = 0$. The only exception occurs when material 2 is very stiff compared with material 1 ($\alpha < -0.67$). Then, there exists a range of ψ for which the maximum G^I occurs at small kink angles while the kink angle associated with $K_{II} = 0$ is near 45° (He and Hutchinson, 1989a). With $\Gamma(\psi)$ denoting the toughness function of the interface and Γ_c denoting the mode I toughness of material 2, kinking will be favored over continued interface cracking if

$$G/G_{\max}^I < \Gamma(\psi)/\Gamma_c, \quad (2.65)$$

and conversely. Thus, the curves of G/G_{\max}^I in Fig. 15 also give the transition value of interface to substrate toughness, $\Gamma(\psi)/\Gamma_c$, separating the tendency for kinking over interface cracking.

The effect of β on the ratio in (2.63) is relatively weak, as discussed by He and Hutchinson (1989a). The dependence on a through $\tilde{\psi}$ in (2.63) can be interpreted as a shift in the phase of the mode of loading on the interface crack. The influence of η is given by He *et al.* (1991), and is qualitatively similar to that shown in Fig. 2 for the isotropic case.

III. Elasticity Solutions for Cracks in Multilayers

In studying cracks in multilayers, it is found that the crack driving force for many situations is essentially independent of the crack size. This steady-state concept and its implications are elucidated with two examples. Heuristic conclusions thus drawn allow emphasis to be placed on various steady-state problems. Several elasticity solutions for mixed mode cracks in multilayers are gathered in this chapter. The geometries can be found in the figures in this chapter. These solutions were obtained in recent years by analytical and numerical methods, and have been used to calibrate fracture specimens and assess technically representative structures. Details of applications will be given in the subsequent chapters. We will omit several classical exact solutions of interface crack problems obtained in 1965 by Erdogan, England, Rice and Sih. These solutions and some extensions have been reviewed by Suo (1989, 1990a).

A. CONCEPT OF STEADY-STATE CRACKING

For applications to be discussed in the following chapters, the concept of steady-state cracking results in a significant simplification. The purpose of this section is to discuss the concept and its implications using two examples: tunneling in adhesives and delamination in unidirectional composites. We try to convey that the steady-state solutions developed in later sections, although highly idealized, can be used to model real-world phenomena.

1. Tunneling in Adhesives

Consider residual stress cracks in adhesives as illustrated in Fig. 16. A thin, brittle adhesive layer is bonded between two substrates. Biaxial residual stresses usually develop in the adhesive layer during the bonding

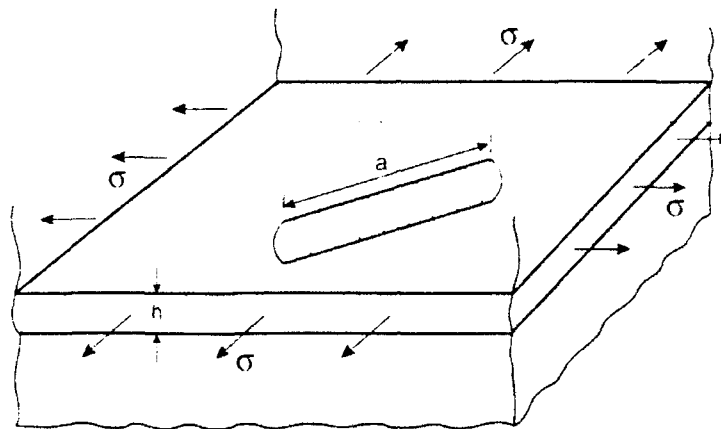


FIG. 16. A thin adhesive layer bonded between two substrates is under biaxial tensile stress. A crack is tunneling through the layer. The substrate on the top is removed for better visualization.

process. In glaze bonding, for example, the ceramic parts are coated with a glass; the parts are placed in contact and heated above the melting temperature of the glass, and then cooled down to the room temperature. For such inorganic adhesives, a major source of the residual stress is thermal expansion mismatch. The residual stress is tensile when the adhesive has larger thermal expansion coefficient than the substrates, which causes cracks to tunnel through the adhesive. Similar cracks are observed in hybrid laminates consisting of alternate tough and brittle sheets, and in coatings or reaction product layers between reinforcements and in matrices in brittle composites. Cracks may penetrate into substrates if the latter are brittle. Debonding is also possible at the intersection of the interfaces and cracks.

Illustrated in Fig. 16 is a crack, nucleated from a flaw, tunneling through the layer. Substrate penetration and interface debonding are assumed not to occur. Crack nucleation is a rather complicated process: A gas bubble would behave differently from a crack-like defect in activating a tunnel. However, as a crack grows long compared with layer thickness, the problem becomes much better defined. A *steady-state* is reached: The tunnel front maintains its shape as it advances, and the energy released per unit advance no longer depends on the tunnel length, nor on the initial flaw geometry. The steady-state problem is still three-dimensional in nature, since the shape of the front should be determined so that the same mode I stress intensity factor is reached at every point along the front. However, this stress intensity factor itself can be calculated without knowing the shape of the front by using a two-dimensional elasticity solution. This attractive possibility

follows from the fact that the energy released per unit length of tunneling equals the energy released to form a plane strain crack traversing the layer, per unit width of crack. For adhesive and substrates with identical elastic constants, the solution (Suo 1990b)

$$K_I = \frac{\sqrt{\pi}}{2} \sigma \sqrt{h} \approx 0.89 \sigma \sqrt{h} \quad (a/h \rightarrow \infty). \quad (3.1)$$

As indicated, the result is valid for the steady-state, that is, when the tunnel is long compared with the thickness of the adhesive layer.

Another limiting case with readily available exact solution is a penny-shaped crack of diameter h . The stress intensity factor along the entire circular front is the same (so it may be thought of as an incipient tunnel), having the value (Tada *et al.* 1985)

$$K_I = \sqrt{2/\pi} \sigma \sqrt{h} \approx 0.80 \sigma \sqrt{h} \quad (a/h = 1). \quad (3.2)$$

Observe that the two results just cited are not very different, suggesting only a mild dependence on a/h . The steady state is practically attained after the tunnel length exceeds a few times adhesive thickness. If the penny-shaped crack is representative of initial flaws, the critical stress needed for the steady-state propagation is only about 10% below the stress to initiate unstable growth from the flaw.

Several implications follow. The tunneling, once activated, would never arrest until it meets another crack or other obstacles. Consequently, under a biaxial stress, a connected tunnel network would emerge, surrounding islands of intact adhesive materials; see Zdaniewski *et al.* (1987) for micrographs. Another implication is that the transient dependence on a/h , which can only be obtained from a complicated three-dimensional analysis, would be unnecessary for most practical purposes. Instead, the steady-state solution provides a conservative, yet still quite tight, design limit. For example, given the substrate and adhesive materials (so the toughness and mismatch stress are fixed), (3.1) would predict the thickest adhesive that can be used with no tunneling cracks. More details of this problem are given in Section VIII.

2. Delamination near a Surface Flaw

As a second example, consider the delamination near a surface notch in a unidirectional composite; see the insert in Fig. 17. The incipient delamination is not well characterized for two reasons. First, the driving force

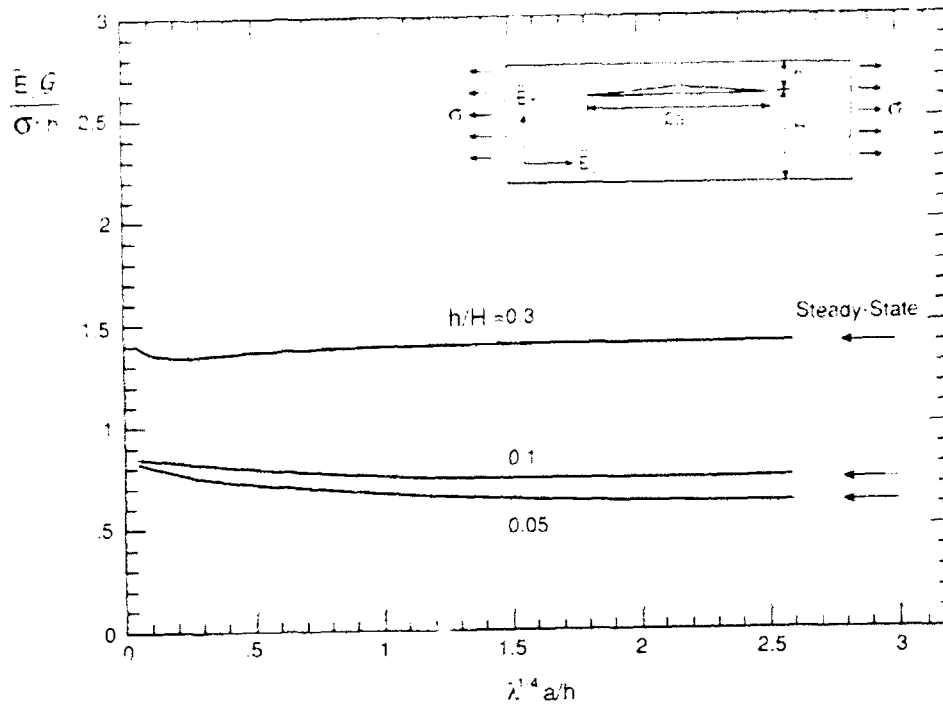


FIG. 17. The insert shows a delamination nucleated from a surface notch and driven by a longitudinal tension. The normalized energy release rate is plotted against the effective delamination length $\lambda^{1/4}a/h$ for several values of notch size h/H . The energy release rate attains the steady-state as soon as $\lambda^{1/4}a/h > 1.5$.

depends on the notch geometry. Secondly, composites usually exhibit *R*-curve behavior: Fracture resistance increases as the crack extends. This can be caused by bridging fibers or matrix ligaments in the wake. However, once the delamination is sufficiently long, a steady state should be reached: Both driving force and toughness become independent of the delamination length and initial flaw geometry. The following example establishes the transient zone size for the driving force. The *R*-curve behavior will be discussed in Section IV.D.

Figure 17 shows a delamination crack nucleated from a sharp notch and driven by an axial tension. Similar problems have been studied by several authors (e.g., O'Brien, 1984, Thouless *et al.*, 1989). The solution that follows is taken from Suo *et al.* (1990b). The delamination is mixed mode. The energy release rate takes the dimensionless form

$$\frac{\bar{E}_1 G}{\sigma^2 h} = f\left(\lambda^{1/4} \frac{a}{h}, \frac{H}{h}, \rho\right) \quad (3.3)$$

where $\bar{E}_1 \equiv 1/b_{11}$ is the effective Young's modulus in the longitudinal direction, λ and ρ are orthotropy parameters, all defined in Section II.B. The dimensionless function g depends on the indicated variables. Notice that λ and a/h affect the final results only through the product $\lambda^{1/4}a/h$, as identified in the original paper using orthotropy rescaling. This detail turns out to be important in understanding the orthotropy effects, as will be seen shortly. Figure 17 plots the solution obtained by finite elements, with $\rho = 1$.

Observe that the energy release rate becomes independent of $\lambda^{1/4}a/h$ when the delamination is sufficiently long. An inspection of Fig. 17 suggests that the *transient-zone* size is given by $\lambda^{1/4}a/h \approx 1.5$, or

$$a/h \approx 1.5(\bar{E}_1/\bar{E}_T)^{1/4}, \quad (3.4)$$

where $\bar{E}_T \equiv 1/b_{22}$ is the effective Young's modulus transverse to the fiber direction. For most polymer composites and woods, $(\bar{E}_1/\bar{E}_T)^{1/4} \approx 2$. Consequently, a split longer than about three times the notch depth is subject to a constant driving force. Equation (3.4) also reveals that elastic orthotropy tends to *prolong* the transient zone by a factor of $(\bar{E}_1/\bar{E}_T)^{1/4}$, as compared with the isotropic counterpart. Finite element calculations (not shown here) also indicate that the size of the transient zone is not significantly affected by ρ within the practical range, so that (3.4) remains valid for general orthotropic materials.

An accurate approximation for the steady-state mixed mode energy release rates at the delamination tip in Fig. 17 is (Suo 1990c)

$$[G_I, G_{II}] = \frac{\sigma^2 h}{2\bar{E}_1} (1 + 4\eta + 6\eta^2 + 3\eta^3)[\cos^2 \omega, \sin^2 \omega], \quad (3.5)$$

$$\omega = 52.1^\circ - 3^\circ \eta, \quad \eta = h/H.$$

This steady-state solution $G = G_I + G_{II}$, is indicated in Fig. 17.

In conclusion, the steady-state condition can usually be easily attained in practice. These steady-state solutions are of unique significance considering the variety of uncertainties associated with the transient state. Mathematically, the steady-state concept allows one to bypass some messy intermediate calculations. Although an accurate estimate of the transient-zone size may not be available for each steady-state solution described in the rest of the section, we feel that, in conjunction with some heuristic judgment, these solutions can be used to assess technical structures.

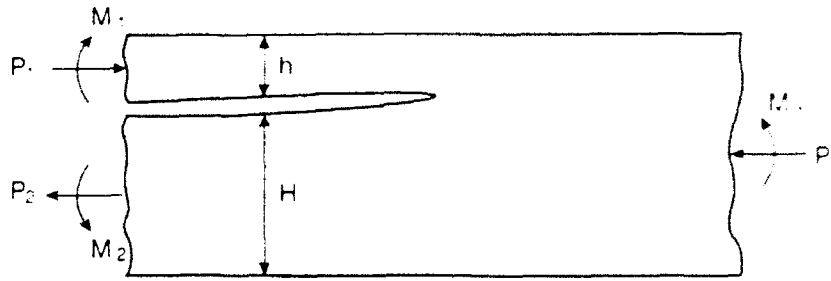


FIG. 18. Cross-section of an infinite layer with a half-plane crack. Axial forces and moments, per unit width, are applied along the three edges.

B. CRACKS IN LAYERS LOADED ALONG EDGES

The problems to be discussed in this section are sketched in Fig. 18. The layer can be of one material or bimaterial, the material isotropic or orthotropic, the crack along the interface or in the substrate. The relation is sought between the applied loads and the mixed mode stress intensity factors.

1. A Homogeneous, Isotropic Layer

Depicted in Fig. 18 is the cross-section of an infinite layer containing a half-plane crack. The geometry is fully specified by h and H , the thicknesses of the two separated arms. The layer is isotropic, homogeneous and linearly elastic, and is subject, uniformly along the three edges, to axial forces and moments per unit width P_i and M_i . The problem at various levels of generality has been considered by several authors (Tada *et al.*, 1985; Williams, 1988; Suo and Hutchinson, 1989b; Schapery and Davidson, 1990). The results in the first two of these references contain conceptual errors. The complete solution presented below is taken from Suo (1990c).

a. General Solution

The near-tip stresses are consistent with the mixed mode crack tip field, with stress intensity factors K_I and K_{II} to be determined. Far from the tip, the three edges are characterized by the linear strain distributions for elementary beams. The energy release rate equals the difference of the strain energy per unit length per unit width stored in the edges far behind and far ahead of the crack tip. Thus,

$$G = \frac{1}{2E} \left[\frac{P_1^2}{h} + 12 \frac{M_1^2}{h^3} + \frac{P_2^2}{H} + 12 \frac{M_2^2}{H^3} - \frac{P_3^2}{h+H} - 12 \frac{M_3^2}{(h+H)^3} \right], \quad (3.6)$$

where \bar{E} is the effective Young's modulus defined in (2.4). This result may be derived alternatively by using the J -integral (Rice, 1968; Cherepanov, 1979).

The preceding energy accounting does not separate the opening and shearing components. The partition is simplified by *linearity* and *dimensionality*, coupled with the Irwin relation (2.5). Consequently, the stress intensity factors take the form

$$\begin{aligned} K_I &= \frac{P}{\sqrt{2hU}} \cos \omega + \frac{M}{\sqrt{2h^3V}} \sin(\omega + \gamma), \\ K_{II} &= \frac{P}{\sqrt{2hU}} \sin \omega - \frac{M}{\sqrt{2h^3V}} \cos(\omega + \gamma). \end{aligned} \quad (3.7)$$

All the preceding quantities except ω are determined by elementary considerations. Specifically, P and M are linear combinations of the applied loads:

$$\begin{aligned} P &= P_1 - C_1 P_3 - C_2 M_3/h, \quad M = M_1 - C_3 M_3, \\ C_1 &= \frac{1}{1/\eta + 1}, \quad C_2 = \frac{6/\eta}{(1/\eta + 1)^3}, \quad C_3 = \frac{1}{(1/\eta + 1)^3} \quad \eta = h/H; \end{aligned} \quad (3.8)$$

and the geometric factors are functions of η :

$$\frac{1}{U} = 1 + 4\eta + 6\eta^2 + 3\eta^3, \quad \frac{1}{V} = 12(1 + \eta^3), \quad \frac{\sin \gamma}{\sqrt{UV}} = 6\eta^2(1 + \eta). \quad (3.9)$$

Accurate determination of ω , which depends only on η , is nontrivial. The elasticity problem was solved rigorously (with the help of numerical solutions of an integral equation). The extracted ω varies slowly with η in the entire range $0 \leq \eta \leq 1$, in accordance with an approximate formula

$$\omega = 52.1^\circ - 3^\circ \eta. \quad (3.10)$$

This is a linear fit of the numerical solution, and the error is believed to be within one percent.

b. A Mixed Mode Double Cantilever Beam

Several special cases are discussed here to illustrate the richness of the solution. First consider a double cantilever beam as in Fig. 19. The specimen is mode I if the crack lies on the mid-plane, but mixed mode if the crack is off the mid-plane. This has been used recently to study mixed mode

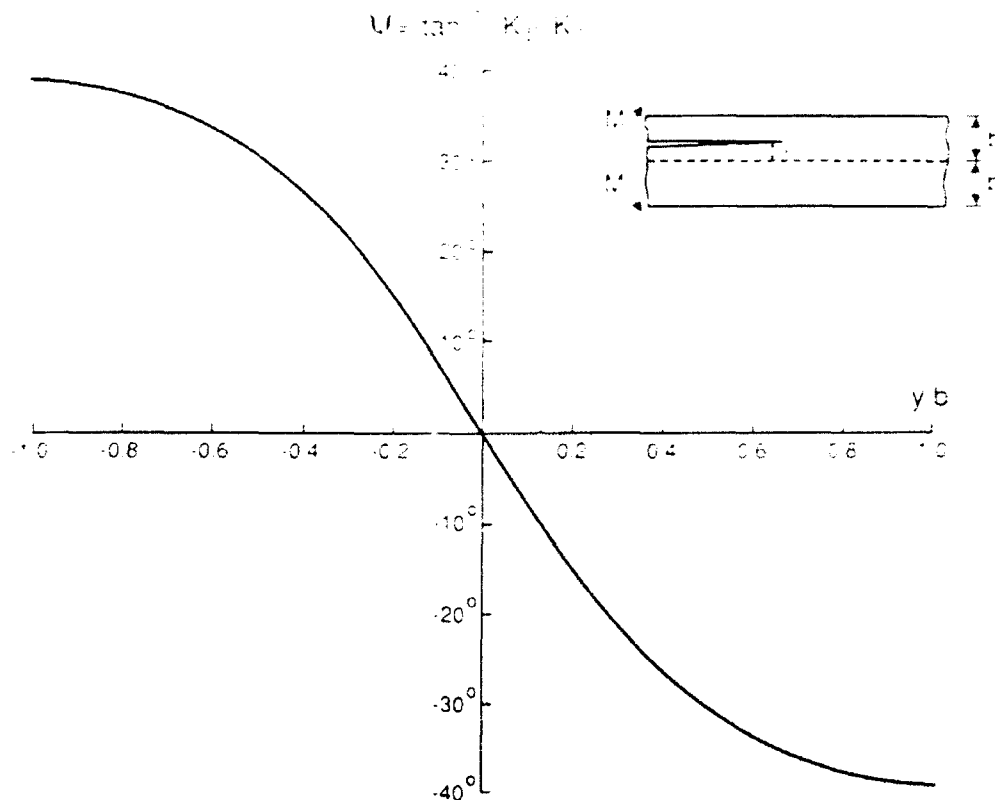


FIG. 19. The insert shows a double cantilever beam with a crack off the mid-plane. The mode mixity $\psi = \tan^{-1}(K_{II}/K_I)$ is plotted against the offset y/b .

fracture of an adhesive layer by Thouless (1990b). On Fig. 19, the mode mixity, $\psi = \tan^{-1}(K_{II}/K_I) = \omega + \gamma - \pi/2$, is plotted against the offset y/b . Focus here is on the configurational stability of an homogeneous specimen when the crack is slightly off the mid-plane as positioned, for example, in the fabrication of the specimen. As indicated by the sign of K_{II} near $y/b = 0$, a crack off the mid-plane will be driven further away from the mid-plane. The mid-plane crack is thus configurationally unstable. Crack path stability will be further discussed in Section VIII.

c. Exact Solutions for the Case $H = h$

Next consider the crack on the mid-plane and subjected to the general edge loads. The crack path selection is seldom an issue in the composite testing since cracks are usually confined to run along the fiber direction. The *exact* solution for ω can be obtained for this case by considering a special loading $M_1 = M_2 = M$ and all others being zero. By symmetry,

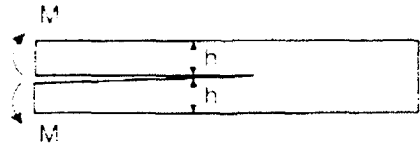
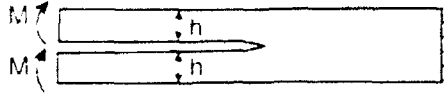
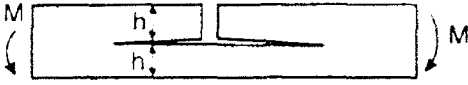
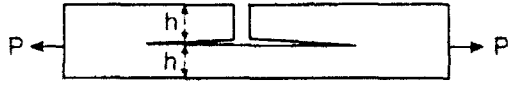
Specimen		\underline{G}_I	\underline{G}_{II}
a		$\frac{12M^2}{E_L h^3}$	0
b		0	$\frac{9M^2}{E_L h^3}$
c		$\frac{3M^2}{E_L h^3}$	$\frac{9M^2}{4E_L h^3}$
d		$\frac{3P^2}{4E_L h}$	$\frac{P^2}{E_L h}$

FIG. 20. Several exact solutions: (a) a pure mode I specimen (double cantilever beam); (b) a pure mode II specimen (end-loaded split); (c) a mixed mode specimen (four-point bend); (d) a mixed mode specimen (crack-lap shear).

$K_{II} = 0$, which, substituted into (3.7), gives $\omega = \cos^{-1}\sqrt{3/7} = 49.1^\circ$. The full solution (3.7) can therefore be specialized to

$$\begin{aligned} K_I &= \sqrt{3}Ph^{-1/2} + 2\sqrt{3}Mh^{-3/2}, & K_{II} &= 2Ph^{-1/2}, \\ P &= P_1 - \frac{1}{2}P_3 - \frac{3}{4}M_1/h, & M &= M_1 - \frac{1}{8}M_3. \end{aligned} \quad (3.11)$$

Several useful edge loads are illustrated in Fig. 20. The mixed mode energy release rates listed are valid for an orthotropic material layer with a principal material axis coincident with the longitudinal direction. Geometries *a* and *b* are pure mode I and pure mode II, respectively. Geometries *c* and *d* are mixed mode.

d. Surface Layer Spalling

As the last example, consider a sub-surface crack in a semi-infinite plate ($\eta = 0$) as illustrated in Fig. 21. The problem was solved by Thouless *et al.*

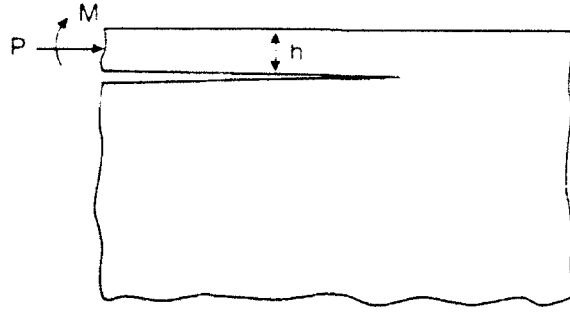


FIG. 21. Spalling of a surface layer due to edge loads.

(1987) in a study of impact spalling of ice sheets. The complete solution is

$$K_I = \frac{1}{\sqrt{2}} [Ph^{-1/2} \cos \omega + 2\sqrt{3} Mh^{-3/2} \sin \omega], \quad (3.12)$$

$$K_{II} = \frac{1}{\sqrt{2}} [Ph^{-1/2} \sin \omega - 2\sqrt{3} Mh^{-3/2} \cos \omega],$$

where $\omega = 52.07^\circ$. Contrary to one's intuition, a significant amount of mode II component is caused by pure bending. The solution will be used in Section V to study decohesion of pre-tensioned films and thermal shock spalling.

2. A Homogeneous, Orthotropic Layer

The same geometry in Fig. 18 was also analyzed for orthotropic solids (Suo, 1990c). The layer lies in a principal material plane and the crack runs in principal axis-1 of the solid. The energy release rate expression (3.6) remains valid but the longitudinal tensile modulus \bar{E}_L should be used, namely,

$$G_I = \frac{1}{2\bar{E}_L} \left[\frac{P}{\sqrt{hU}} \cos \omega + \frac{M}{\sqrt{h^3V}} \sin(\omega + \gamma) \right]^2, \quad (3.13a)$$

$$G_{II} = \frac{1}{2\bar{E}_L} \left[\frac{P}{\sqrt{hU}} \sin \omega - \frac{M}{\sqrt{h^3V}} \cos(\omega + \gamma) \right]^2, \quad (3.13b)$$

where P , M , U , V , and γ are given by (3.8) and (3.9). The quantity ω depends on η and ρ , but *not* λ . An integral equation method was used to determine ω , and the results indicate that the influence of ρ within its entire practical range is below one percent, so that (3.10) is an excellent approximation for orthotropic materials. When the stress intensity factors are

needed, the Irwin-type relation appropriate for orthotropic materials (2.16) must be used.

Notice that all the quantities in the brackets of (3.13) except for ω do not depend on material parameters. Further, ω may be approximated by (3.10), which is also independent of any material parameters. Consequently, the energy release rates of the two modes are essentially the same as their isotropic counterparts, except that the longitudinal tensile modulus should be used.

3. A Symmetric Tilt Strip

Imagine two identical layers cut from an orthotropic solid at an angle ϕ to principal material axis-1 (Fig. 22). The thickness of the two layers are equal, designated as h . The compliances s_{11} , s_{22} , s_{12} , and s_{66} are referred to the principal material axes. The two layers are bonded to form a symmetric tilt boundary, with a semi-infinite crack lying along the interface. The tilt angle is ϕ and the tilt axis, or the crack front, is one of the principal axes of the orthotropic solid. The general edge loads are applied.

The stress field around the crack tip is square root singular. The stress intensity factors are defined such that, asymptotically, traction on the grain boundary varies with the distance r from the crack tip according to

$$\sigma_y = (2\pi r)^{-1/2} K_I, \quad \tau_{xy} = (2\pi r)^{-1/2} K_{II}. \quad (3.14)$$

The Irwin-type relation for a crack on the symmetric tilt grain boundary is (Wang *et al.*, 1990)

$$\begin{aligned} G_I &= [b_{11} b_{22} (1 + \rho)/2]^{1/2} (\lambda^{-1/4} \cos^2 \phi + \lambda^{1/4} \sin^2 \phi) K_I^2, \\ G_{II} &= [b_{11} b_{22} (1 + \rho)/2]^{1/2} (\lambda^{-1/4} \sin^2 \phi + \lambda^{1/4} \cos^2 \phi) K_{II}^2, \end{aligned} \quad (3.15)$$

where the compliances are referred to the principal axes; see Section II.B.

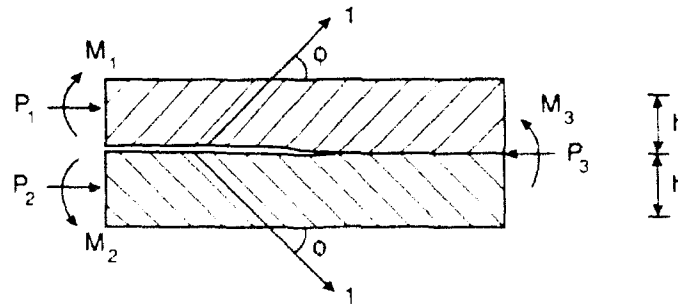


FIG. 22. Two identical grains of an orthotropic crystal form a symmetric tilt boundary, with the principal crystal axis at an angle ϕ from the interface. The sample is under general edge loads.

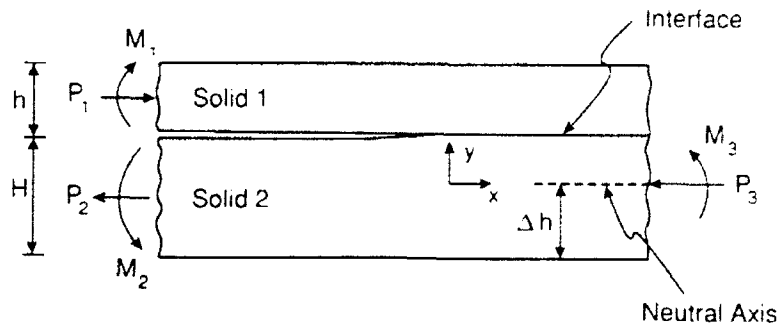


FIG. 23. A bilayer with a half-plane interface crack. The neutral axis of the composite layer is indicated.

The analytical solution is found for the problem. Expressed in energy release rates, it is

$$\begin{aligned} G_I &= 3b_{11}^*(P + 2M/h)^2/h, & G_{II} &= 4b_{11}^*P^2/h, \\ P &= P_1 - \frac{1}{2}P_3 - \frac{3}{4}M_3/h, & M &= M_1 - \frac{1}{8}M_3. \end{aligned} \quad (3.16)$$

Here, b_{11}^* is the compliance in the x direction, which is related to the principal compliances by

$$b_{11}^* = (b_{11}b_{22})^{1/2}(\lambda^{1/2}\cos^4\phi + 2\rho\cos^2\phi\sin^2\phi + \lambda^{-1/2}\sin^4\phi). \quad (3.17)$$

Notice that the energy release rates are identical to the corresponding homogeneous, isotropic results, except that the compliance must be reinterpreted.

4. An Interfacial Crack in a Bilayer

Figure 23 is a cross-section of an infinite bilayer with a half-plane crack on the interface. Each layer is taken to be homogeneous, isotropic, and linearly elastic. The uncracked interface is perfectly bonded with continuous displacements and tractions. The bilayer is loaded uniformly along the three edges with forces and moments per unit width. The problem has been studied by Suo and Hutchinson (1990), and the numerical solution has been presented in the entire parameter range. The generality of the edge loads allows the solution to be used to model a variety of delamination processes. A special loading case (a splitting cantilever bilayer) is discussed in Section II.C.4. The solution will be used to calibrate interfacial fracture specimens in Section IV.B.1, and to assess decohesion of pre-tensioned thin films in Section V.D. Focus here is on the presentation of the elasticity solution.

Far ahead of the crack tip the bilayer may be regarded as a composite beam. The neutral axis lies a distance $h\Delta$ above the bottom of the beam, with Δ being

$$\Delta = \frac{1 + 2\Sigma\eta + \Sigma\eta^2}{2\eta(1 + \Sigma\eta)}, \quad (3.18)$$

where

$$\Sigma \equiv \frac{\bar{E}_1}{\bar{E}_2} = \frac{1 + \alpha}{1 - \alpha}, \quad \eta = \frac{h}{H}. \quad (3.19)$$

The composite layer is in a state of pure stretch combined with pure bending. The only nonzero in-plane stress component is σ_x . The corresponding strain is linear with the distance from the neutral axis, y , according to

$$\varepsilon_x = -\frac{1}{\bar{E}_2} \left(\frac{P_3}{hA} + \frac{M_3}{h^3 I} y \right). \quad (3.20)$$

The dimensionless cross-section A and moment of inertia I are

$$A = \frac{1}{\eta} + \Sigma, \quad I = \Sigma \left[\left(\Delta - \frac{1}{\eta} \right)^2 - \left(\Delta - \frac{1}{\eta} \right) + \frac{1}{3} \right] + \frac{\Delta}{\eta} \left(\Delta - \frac{1}{\eta} \right) + \frac{1}{3\eta^3}. \quad (3.21)$$

The energy release rate can be calculated in close form:

$$G = \frac{1}{2\bar{E}_1} \left(\frac{P_1^2}{h} + 12 \frac{M_1^2}{h^3} \right) + \frac{1}{2\bar{E}_2} \left(\frac{P_2^2}{H} + 12 \frac{M_2^2}{H^3} - \frac{P_3^2}{Ah} - \frac{M_3^2}{Ih^3} \right). \quad (3.22)$$

The energy release rate specifies the magnitude of the near-tip singularity but does not specify the mode mixity. The information is completed by the complex stress intensity factor K , which, to be consistent with linearity, dimensionality and the Irwin-type relation (2.29), takes the form

$$K = h^{-i\epsilon} \left(\frac{1 - a}{1 - \beta^2} \right)^{1/2} \left(\frac{P}{\sqrt{2hU}} - ie^{i\gamma} \frac{M}{\sqrt{2h^3V}} \right) e^{i\omega}, \quad (3.23)$$

where $i = \sqrt{-1}$, and P and M are linear combinations of the edge loads:

$$P = P_1 - C_1 P_3 - C_2 M_3/h, \quad M = M_1 - C_3 M_3. \quad (3.24)$$

The geometric factors are given by

$$C_1 = \frac{\Sigma}{A}, \quad C_2 = \frac{\Sigma}{I} \left(\frac{1}{\eta} + \frac{1}{2} - \Delta \right), \quad C_3 = \frac{\Sigma}{12I}, \quad (3.25)$$

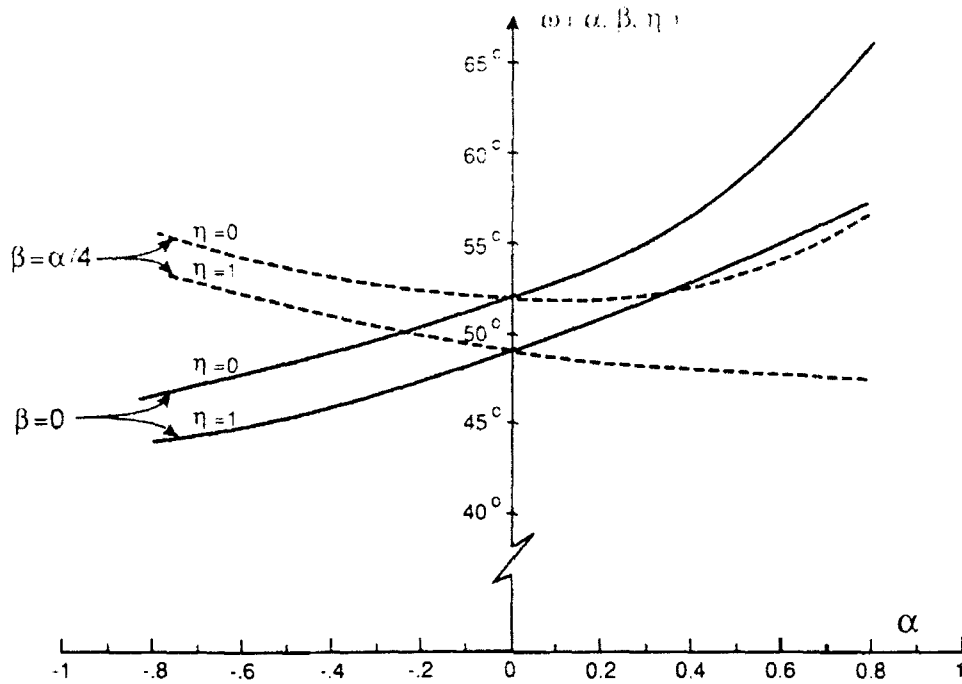


FIG. 24. Calculated values of the function $\omega(\alpha, \beta, \eta)$, which appeared in Eq. (3.23).

and by

$$\frac{1}{U} = 1 + \Sigma \eta(4 + 6\eta + 3\eta^2), \quad \frac{1}{V} = 12(1 + \Sigma \eta^3), \quad \frac{\sin \gamma}{\sqrt{UV}} = 6\Sigma \eta^2(1 + \eta). \quad (3.26)$$

All these formulae are derived from the classical beam theory.

The angle ω is a function of the Dundurs' parameters α , β and relative height η . This function was determined by solving the elasticity problem numerically; the computed values are plotted in Fig. 24, and an extensive tabulation can be found in Suo and Hutchinson (1990).

5. A Substrate Crack in a Bilayer

Depicted in Fig. 25 is an infinite bilayer with a semi-infinite crack parallel to the interface. Each layer is isotropic and homogeneous. There are two length ratios: $\xi_1 = H_1/h$ and $\xi = H/h$. The problem was solved by Suo and Hutchinson (1989b) in the context of substrate spalling of a residual stressed thin film. The details of the application can be found in Section V.C.2, and here we will focus on the solution of the elasticity problem.

Of the three edges, one is a homogeneous beam and the other two are composite beams. The positions of neutral axes for the two composite

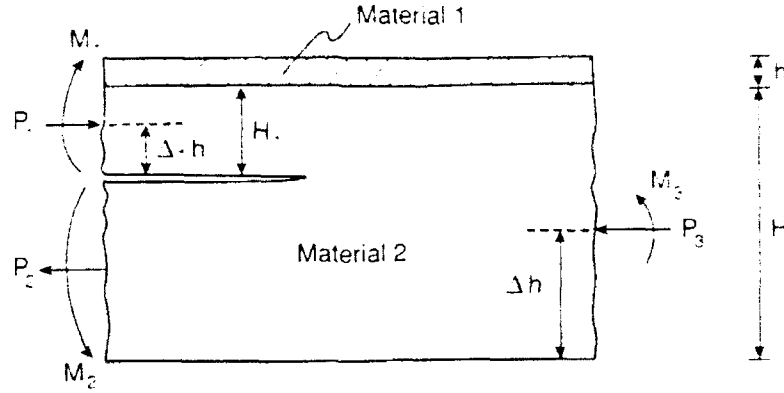


FIG. 25. A bilayer with a crack off the interface. The neutral axes for the two composite layers are indicated.

beams are given by

$$\Delta = \frac{\xi^2 + \Sigma\xi + \Sigma}{2(\xi + \Sigma)}, \quad \Delta_1 = \frac{\xi_1^2 + \Sigma\xi_1 + \Sigma}{2(\xi_1 + \Sigma)}. \quad (3.27)$$

The three beams may be described by a linear variation like (3.20). The effective cross-section and moment of inertia of the two composite beams are given by

$$\begin{aligned} A &= \xi + \Sigma, & I &= \Sigma[(\Delta - \xi)^2 - (\Delta - \xi) + 1/3] \\ & & &+ \Delta\xi(\Delta - \xi) + \xi^3/3, \\ A_1 &= \xi_1 + \Sigma, & I_1 &= \Sigma[(\Delta_1 - \xi_1)^2 - (\Delta_1 - \xi_1) + 1/3] \\ & & &+ \Delta_1\xi_1(\Delta_1 - \xi_1) + \xi_1^3/3. \end{aligned} \quad (3.28)$$

The energy release rate can be calculated in closed form:

$$G = \frac{1}{2E_2} \left[\frac{P_1^2}{hA_1} + \frac{M_1^2}{h^3I_1} + \frac{P_2^2}{h(\xi - \xi_1)} + \frac{12M_2^2}{h^3(\xi - \xi_1)^3} - \frac{P_3^2}{hA} - \frac{M_3^2}{h^3I} \right]. \quad (3.29)$$

The stress intensity factors are

$$\begin{aligned} K_I &= \frac{P}{\sqrt{2hU}} \cos \omega + \frac{M}{\sqrt{2h^3V}} \sin(\omega + \gamma), \\ K_{II} &= \frac{P}{\sqrt{2hU}} \sin \omega - \frac{M}{\sqrt{2h^3V}} \cos(\omega + \gamma), \end{aligned} \quad (3.30)$$

where P and M are linear combinations of edge loads:

$$P = P_1 - C_1 P_3 - C_2 M_3/h, \quad M = M_1 - C_3 M_3, \quad (3.31)$$

$$C_1 = \frac{A_1}{A}, \quad C_2 = \frac{A_1}{I} [(\xi - \Delta) - (\xi_1 - \Delta_1)], \quad C_3 = \frac{I_1}{I}.$$

and the geometric factors are

$$\frac{1}{U} = \frac{1}{A_1} + \frac{1}{\xi - \xi_1} + 12 \frac{[\Delta_1 + (\xi - \xi_1)/2]^2}{(\xi - \xi_1)^3}, \quad \frac{1}{V} = \frac{1}{I_1} + \frac{12}{(\xi - \xi_1)^3},$$

$$\frac{\sin \gamma}{\sqrt{UV}} = 12 \frac{\Delta_1 + (\xi - \xi_1)/2}{(\xi - \xi_1)^3}. \quad (3.32)$$

The angle ω as a function of α , β , ξ , and ξ_1 is extracted from a numerical solution, and is tabulated in Suo and Hutchinson (1989b).

C. A BILAYER HELD BETWEEN RIGID GRIPS

Figure 26 shows a bilayer with thickness h and H constrained between grips. Each layer is taken to be isotropic. The constraint is assumed to be perfectly rigid so that no separation nor sliding take place between the bilayer and grips. Both layers may be subject to residual stress in the layer direction, but it will not affect the singular field, and will therefore be ignored. An interface crack is driven by the relative *translation*, U and V , of the two grips. The problem of a homogeneous layer with a crack running on the mid-plane, i.e., $h = H$, has been solved analytically (Rice, 1968). A gripped epoxy/glass bilayer has recently been used by Liechti and Chai (1990b) to study mixed mode interfacial fracture resistance; see also Section II.C.4. The specimen calibration for a wide range of bimaterials are described in the following.

The debonded layers far behind the crack tip are stress-free, while the bonded layer far ahead is under a *uniform* strain state. An energetic accounting shows that

$$G = \frac{V^2}{2} \left(\frac{h}{\bar{E}_1} + \frac{H}{\bar{E}_2} \right)^{-1} + \frac{U^2}{2} \left(\frac{h}{\mu_1} + \frac{H}{\mu_2} \right)^{-1}, \quad (3.33)$$

where $\bar{E} \equiv 2\mu(1 - \nu)/(1 - 2\nu)$ for plane strain, and $\bar{E} \equiv 2\mu/(1 - \nu)$ for plane stress.

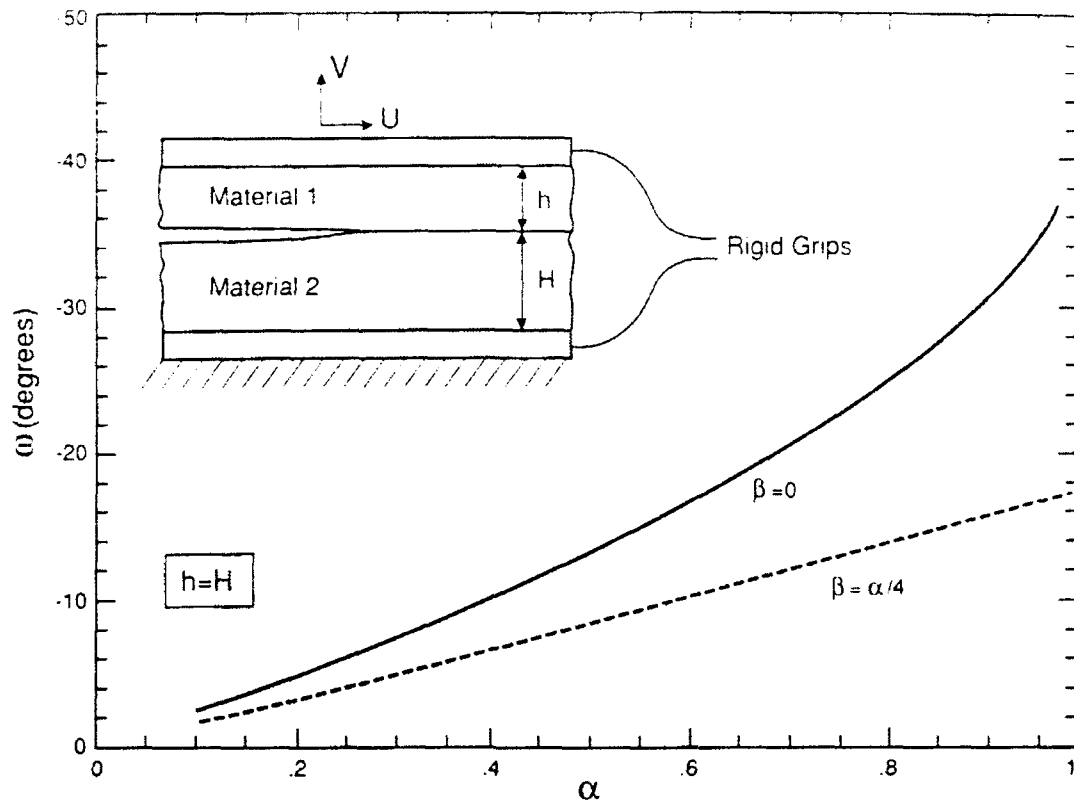


FIG. 26. The insert shows a bilayer held between two rigid grips, and the crack is driven by the relative translation of the two grips. The numerical solution of the angle ω in Eq. (3.34) is plotted.

The mode mixity may be controlled by the relative proportion of the two grip translations. More precisely, the interfacial stress intensity factor is given by

$$K = h^{-i\epsilon} e^{i\omega} \left(\frac{E_*}{1 - \beta^2} \right)^{1/2} \left[\frac{V}{\sqrt{2}} \left(\frac{h}{\bar{E}_1} + \frac{H}{\bar{E}_2} \right)^{-1/2} + i \frac{U}{\sqrt{2}} \left(\frac{h}{\mu_1} + \frac{H}{\mu_2} \right)^{-1/2} \right]. \quad (3.34)$$

This is derived using (3.33) and the Irwin-type relation (2.29). All quantities in the equation have been defined previously except for the angle ω , which is a function of μ_1/μ_2 , ν_1 , ν_2 , and h/H . The problem contains displacement boundary conditions, so that in principle the two Dundurs' parameters are insufficient to characterize the bimaterial. However, it has been confirmed numerically (Beuth, 1991) that, once the Dundurs' parameters are fixed, the solution is almost independent of the third free variable. Finite element calculations are done for the case $H = h$ and the results are plotted in Fig. 26. Linear interpolation is recommended for values between $\beta = 0$ and $\beta = \alpha/4$.

D. SMALL-SCALE FEATURES

Scales play a fundamental role in the development of the fracture mechanics, as in any branch of continuum science. Classical examples are the notions of small-scale yielding, homogenization of composites or damage response. Here, we try to demonstrate, by a concrete example, how interface fracture mechanics may be applied at different scales. Consider two blocks of substrates joined by a thin adhesive layer. One is asked to study the toughness of the assembly. The problem may be tackled at two scales.

At a relatively macroscopic level, one may think of this as an interface fracture process between the two substrates, treating the adhesive as a small scale feature. At such a level, the two substrates explicitly enter the scheme of interface fracture, but the role of the adhesive, as well as damage processes in it, is contained in the macroscopically measured toughness. This evaluation process has been used in the adhesion community for years, except that the two substrates are usually identical, so that only the mixed mode fracture mechanics of homogeneous materials need be invoked. Obviously interface fracture mechanics is ideally suited to study the adhesion of different substrates.

At a more microscopic level, one may study the cracking along the interface between the adhesive and one of the substrates. Interface fracture mechanics can be used provided the crack stays along the interface and other damage processes are confined in a crack tip core region that is small compared with the thickness of the adhesive. These requirements can be realized if the interface is brittle enough. Mathematically, some well-defined small-scale features may be analyzed using a boundary layer approach. A few examples related to multilayers are collected in this section. Applications will be discussed in Section VIII.

1. *A Sub-interface Crack*

Consider a crack running near an interface (Fig. 27). The distance between the interface and crack, h , is small compared to all other in-plane lengths. The overall geometry, viewed at a scale much larger than h , can be regarded as an interface crack, so that the actual load and geometry can be represented by the complex stress intensity factor K appropriate for an interface crack. Near the crack tip, the stress field is that of a mixed mode crack in a homogeneous material, parameterized by K_I and K_{II} . Hutchinson *et al.* (1987) provided a connection between the two sets of the stress

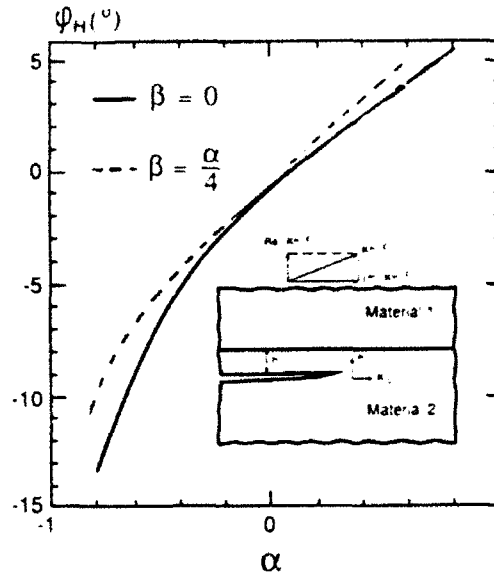


FIG. 27. A sub-interface crack. The spacing h is much smaller than the overall specimen dimension. The remote and local stress intensity factors are connected by Eq. (3.36), and the phase shift ϕ_H is plotted.

intensity factors, and used it to study the existence of mode I trajectory paralleling the interface.

The local and global energy release rates are identical, namely

$$G = \frac{1}{E_2} (K_I^2 + K_{II}^2) = \frac{1 - \beta^2}{E_*} |K|^2. \quad (3.35)$$

This relation gives the energy release rate at the crack tip, provided the remote K is known. Observe that the magnitudes of the two sets of stress intensity factors, $K_I + iK_{II}$ and K , are directly related by (3.35). They can differ only by a phase shift, designated as ϕ_H , so that

$$K_I + iK_{II} = \left(\frac{1 - \beta^2}{1 + \alpha} \right)^{1/2} K h^{1/2} e^{i\phi_H}. \quad (3.36)$$

The phase shift ϕ_H , ranging from -15° to 5° , is a function of the Dundurs' parameters. The numerical solution is plotted in Fig. 27, and a more extensive tabulation can be found in the original paper.

2. An Interfacial Crack in a Sandwich

Any homogeneous fracture specimen may be converted to measure interface toughness by sandwiching a *thin* layer of second material. The

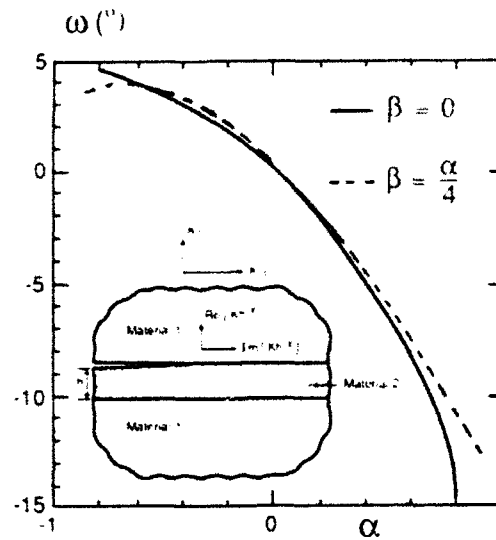


FIG. 28. An interface crack in a sandwich. The remote and local stress intensity factors are connected by Eq. (3.38), and the phase shift ω is plotted.

generic set-up is depicted in Fig. 28. An interlayer of material 2 is embedded in a homogeneous body of material 1, with a pre-existing crack lying along one of the interfaces (upper interface here). Each material is taken to be isotropic and linearly elastic. A solution described in the following, obtained by Suo and Hutchinson (1989a), provides the basis for a variety of sandwich specimens; an example, a Brazil-nut sandwich, will be discussed in Section IV.C.

The problem is asymptotic in that the reference homogeneous specimen is infinite and the crack is semi-infinite, as is appropriate when the layer thickness h is very small compared with all other in-plane length scales. The crack tip field of the homogeneous problem (without the layer) is prescribed as the far field in the asymptotic problem. Thus, the far field is characterized by K_I and K_{II} , induced by the loads on the reference homogeneous specimen. The interface crack tip field is characterized by the (complex) interfacial stress intensity factor K . A relation is developed in what follows that connects these two sets of stress intensity factors, allowing conversion of any homogeneous specimen to a sandwich without further calibration.

The global and local energy release rates are the same:

$$G = \frac{1}{E_1} (K_I^2 + K_{II}^2) = \frac{1 - \beta^2}{E_*} |K|^2. \quad (3.37)$$

Considerations similar to those of the previous subsection give

$$K = h^{-1/2} \left(\frac{1 - \alpha}{1 - \beta^2} \right)^{1/2} (K_I + iK_{II}) e^{i\omega}. \quad (3.38)$$

From numerical calculations, the angle shift ω , which is due exclusively to the moduli dissimilarity, ranges between 5° to -15° , depending on α and β . The solution is plotted in Fig. 28; other cases are tabulated in Suo and Hutchinson (1989a).

3. Parallel Debond

When a sandwich layer is under substantial residual compression, debond may take place along the *two* interfaces. The phenomenon was observed in preparing $\text{Al}_2\text{O}_3\text{—SiC—Al}_2\text{O}_3$ laminate (private communication with A. G. Evans). The laminate was diffusion bonded at an elevated temperature, but debonded into three layers in the cool-down. Parallel cracks under uniaxial loads have been observed in laminates with center notches or matrix cracks. The solution obtained by Suo (1990b) is given in the following.

It can be shown with the Eshelby cut-and-paste technique that, as far as the stress intensity is concerned, the residual compression is equivalent to a mechanical load of layer pull-out. Depicted in Fig. 29 is a slightly generalized situation in which an opening load represented by K_I^∞ is included, in addition to the pull-out stress σ . It is envisioned that the pull-out stress itself

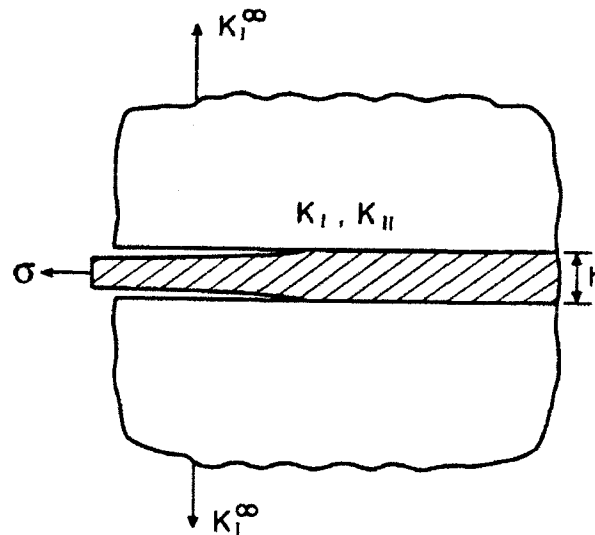


FIG. 29. Parallel debond of a sandwich layer, driven by the pull-out stress σ and the remote opening load K_I^∞ .

may not be high enough to trigger debonding, but the structure debonds with an additional remote mode-I load.

To gain insight into this setup, we ignore the moduli difference in this preliminary treatment. By an energetic argument, one obtains the energy release rate at each tip under combined loads σ and K_I^∞ :

$$G = \frac{1}{E} \left(\frac{K_I^{\infty 2}}{2} + \frac{\sigma^2 h}{4} \right). \quad (3.39)$$

Hence, the interfacial fracture energy can be inferred if one measures σ and the critical K_I^∞ that trigger the debond.

Recall the Irwin formula (2.5) is applicable for each crack tip. Comparing the two energy release-rate expressions, and keeping the linearity of the elasticity problem in mind, one obtains the local stress intensity factors

$$\begin{aligned} K_I &= \frac{1}{\sqrt{2}} K_I^\infty \cos \phi + \frac{1}{2} \sigma \sqrt{h} \sin \phi, \\ K_{II} &= -\frac{1}{\sqrt{2}} K_I^\infty \sin \phi + \frac{1}{2} \sigma \sqrt{h} \cos \phi. \end{aligned} \quad (3.40)$$

The angle ϕ has to be determined by solving the full elasticity problem. An integral equation approach was used and the solution was found to be $\phi \approx 17.5^\circ$.

Consider the case when $K_I^\infty = 0$. The above solution indicates that the pull-out stress induces a significant amount of crack face opening, along with the predominant sliding. By contrast, residual tension (equivalent to a push-in mechanical stress) induces a negative K_I , suggesting that debonding will be a pure mode-II sliding against friction. Therefore, parallel debonding will more likely take place for adhesives in residual compression than in tension, provided other conditions are the the same.

The solution can be generalized to orthotropic materials using the concept of orthotropy rescaling. Suppose the entire material is orthotropic and homogeneous. Two cracks run in the principal axis 1. Using orthotropy rescaling, (3.40) becomes

$$\begin{aligned} K_I &= \frac{1}{\sqrt{2}} K_I^\infty \cos \phi + \frac{\lambda^{3/8}}{2\sqrt{n}} \sigma \sqrt{h} \sin \phi, \\ K_{II} &= -\frac{\lambda^{-1/4}}{\sqrt{2}} K_I^\infty \sin \phi + \frac{\lambda^{1/8}}{2\sqrt{n}} \sigma \sqrt{h} \cos \phi, \end{aligned} \quad (3.41)$$

TABLE 1
 $\phi(\rho)$ (IN DEGREES) FOR PARALLEL DEBOND

ρ	-0.5	-0.3	-0.1	0.1	0.3	0.5	0.7	0.9
ϕ	22.9	21.6	20.6	19.9	19.2	18.7	18.2	17.8
ρ	1	2	3	4	5	6	7	8
ϕ	17.5	15.9	14.9	14.1	13.4	12.9	12.5	12.1

where $n = [(1 + \rho)/2]^{1/2}$. Now the phase shift ϕ depends on ρ . An integral equation is solved numerically, and the results are listed in Table 1.

IV. Laminate Fracture Test

Interlaminar fracture resistance of multilayers is usually measured using beam-type specimens. Fracture mode mixity, ranging from opening, mixed mode, to shearing, can be controlled by the loading configuration. A catalog of such specimens is presented, for application to both orthotropic materials and bimetals. Most of these specimens have been used by the composite community for decades. Yet rigorous, general calibrations are available only recently. Delamination resistance can be enhanced by a variety of bridging mechanisms. A prevailing issue is that the bridging-zone size is usually several times the lamina thickness, so that delamination resistance is no longer a material property independent of specimen size and geometry. The implications will be studied using the Dugdale model.

A. DELAMINATION BEAMS

Beam-type fracture specimens are most frequently used for composites, adhesive joints, and other laminated materials. Small scale features such as fiber/matrix inhomogeneity are typically not explicitly taken into account. For example, homogenized elastic constants are used for composites. The Irwin-Kies compliance calibration is still in use for lack of elasticity solutions. Empirical calibrations obtained this way should be valid only for the materials being tested, since they typically depend on elastic constants. Finite element calibration has been used by many authors, and previous literature on the subject may be found in a volume edited by Friedrich (1989). Guided by an orthotropy rescaling concept, Suo (1990c) and Bao *et al.* (1990)

have analyzed many commonly used specimens, using either integral equations or finite elements. Included were notched bars loaded in various configurations, delamination beams, and hybrid sandwiches. The work of Suo (1990c) has been summarized in Section III.B.2, which is applicable for unidirectional composites under steady-state loading configurations. Several other delamination beams analyzed by Bao *et al.* (1990) will be described in the following.

1. Double Cantilever Beams

Illustrated in Fig. 30 is a double cantilever beam made of a unidirectional composite with fibers along the beam axis. The specimen is pure mode I, and energy release rate is

$$G = 12 \frac{(Pa)^2}{h^3 \bar{E}_L} (1 + Y\lambda^{-1/4}h/a)^2, \quad (4.1)$$

where P is force per unit width, $2h$ beam thickness, a crack length, $\bar{E}_L \equiv 1/b_{11}$ is the effective Young's modulus in fiber direction, and λ and ρ are dimensionless orthotropic parameters. These material constants are defined in Section II.B. The dimensionless factor Y is approximated by

$$Y(\rho) = 0.677 + 0.149(\rho - 1) - 0.013(\rho - 1)^2. \quad (4.2)$$

These formulae are valid for both plane stress and plane strain, for generally orthotropic materials within the entire practical range, $\lambda^{1/4}a/h > 1$ and $0 < \rho < 5$, and the error is within 1%. In particular, the preceding result is valid for isotropic materials when $\rho = \lambda = 1$.

This calibration is obtained using finite elements, together with several analytic considerations. The first term in the bracket in (4.1) reproduces the exact elasticity asymptote as $a/h \rightarrow \infty$, which may be obtained from the

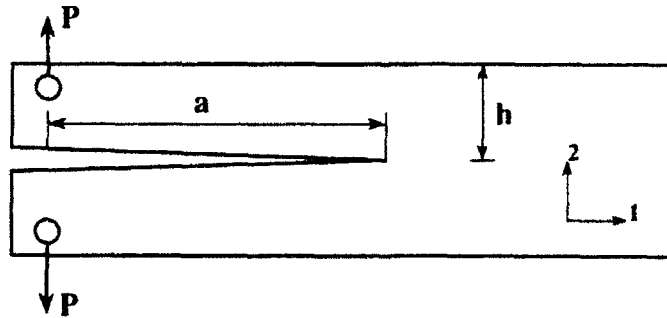


FIG. 30. A mode I delamination specimen (double cantilever beam (DCB)).

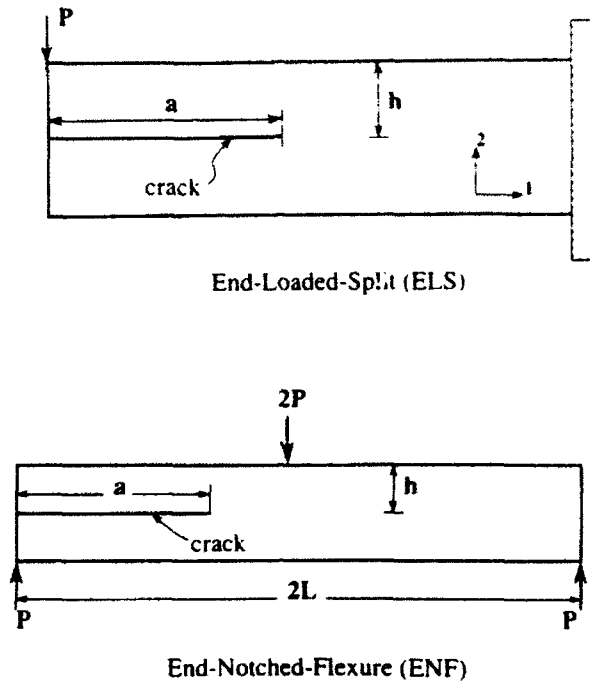


FIG. 31. Two mode II delamination beams: (a) end-loaded split (ELS); (b) end-notched flexure (ENF).

classical beam theory. The second term in the bracket is the first order correction in h/a . As a consequence of the orthotropy rescaling, the consistent correction, including the elastic constants λ and ρ , is of the form (4.1), where Y depends on ρ only; see Suo *et al.* (1990b).

2. End-Loaded Split and End-Notched Flexure

Figure 31 shows two designs of mode II specimens. The calibration for ELS is

$$G = \frac{9(Pa)^2}{4h^3 E_L} (1 + Y\lambda^{-1/4} h/a)^2, \quad (4.3)$$

$$Y(\rho) = 0.206 + 0.078(\rho - 1) - 0.008(\rho - 1)^2. \quad (4.4)$$

All comments in the last subsection are valid here. To a high accuracy, the calibration for ENF is identical to the preceding, as independently confirmed by He and Evans (1990b).

3. Steady-State Mixed Mode Specimens

It is relatively difficult to design a mixed mode fracture specimen having a fixed mode mixity as the crack grows. Two such specimens are depicted in

Fig. 20. As the crack length exceeds about three times the notch depth h , both the driving force and mode mixity become essentially independent of the delamination length. The calibrations are listed in the figure. It is not necessary to measure crack size in a fracture test with such steady-state specimens. Steady-state delamination beams of other edge load combinations and/or of dissimilar arm thicknesses can be specialized from the general solution in Section III.B.2.

4. Other Mixed Mode Delamination Beams

Recall that stress intensity factors are linearly additive. One may use the basic solutions presented in the preceding to obtain calibrations for other specimens. Two examples are illustrated in Figs. 32 and 33. The specimen in Fig. 32a is mixed mode, and can be solved by a superposition of DCB and ELS. Note that both the magnitude of G and the mode mixity change as the crack advances. The three-point bend in Fig. 33 is a superposition of the four-point flexure specimen and the specimen in Fig. 32a.

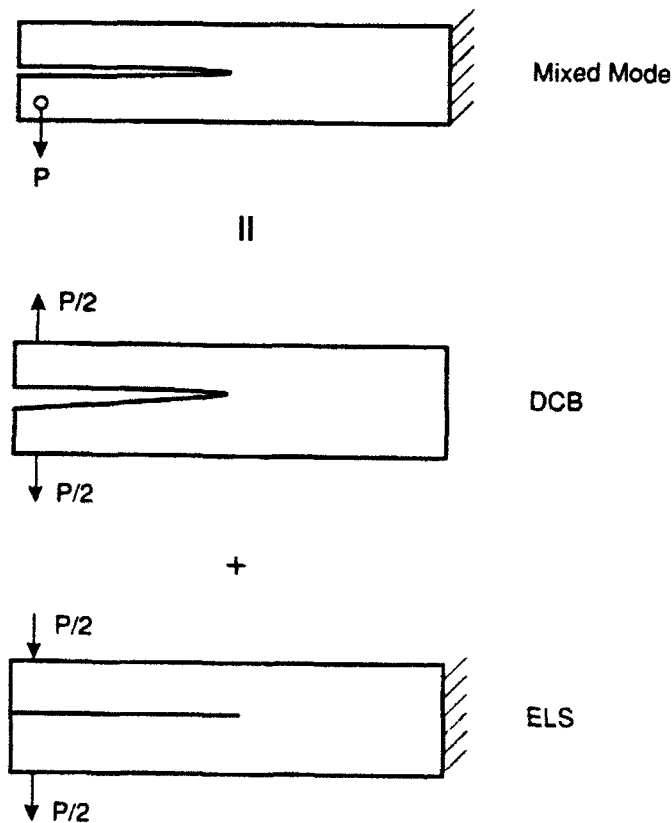


FIG. 32. The mixed mode end-notched split is the superposition of the DCB and ELS.

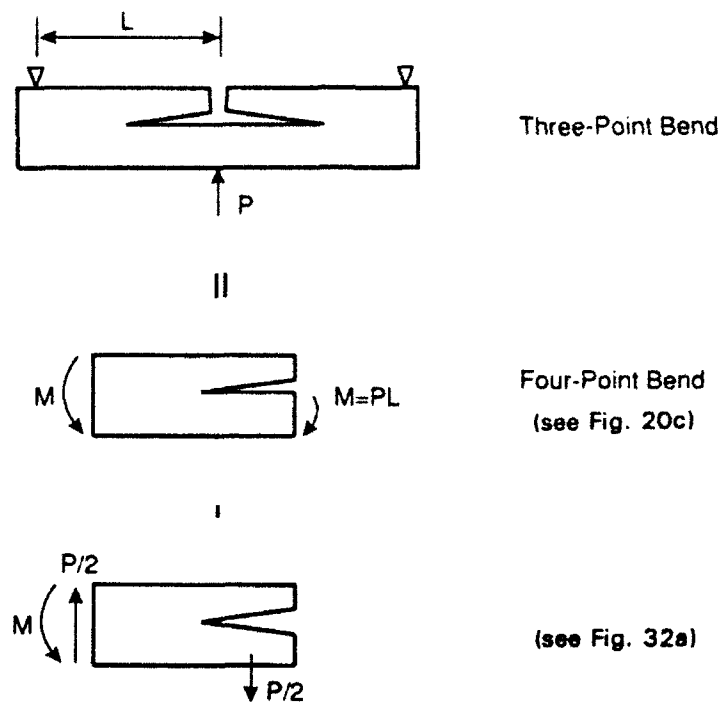


FIG. 33. A superposition scheme for three-point shear.

B. INTERFACIAL FRACTURE SPECIMENS

As discussed in Section II.C, the fracture resistance of an interface generally depends on the mode mixity. Thus, a toughness curve, $\Gamma(\psi)$, must be determined experimentally to fully characterize a given interface. Two strategies have been used in practice to vary the mode mixity: multiloading or multispecimens. The bilayer held between rigid grips discussed in Section III.C.4 and Section III.C is an example of multiloading specimens. In this section, several other specimens are described.

1. Four-Point Flexure of a Bilayer

Figure 34 shows a specimen consisting of roughly the same amount of opening and sliding. The specimen was first analyzed by Charalambides *et al.* (1989), and is a special edge load combination of the general problem in Section III.B.4. Evans and coworkers at the University of California, Santa Barbara have used this configuration to test bimaterial interfaces (Cao and Evans, 1989), ceramic composite laminates (Sbaizero *et al.*, 1990), metallic adhesive joints (Reimanis and Evans, 1990), and thin films (Hu and Evans,

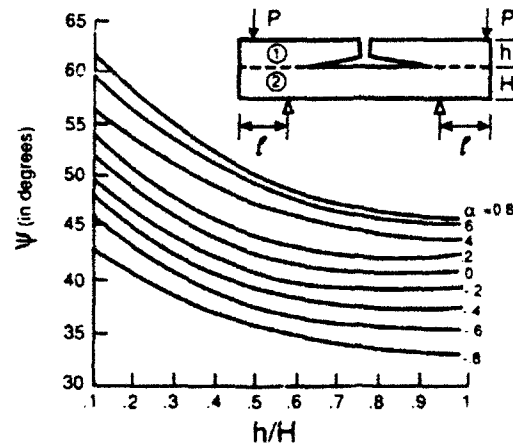


FIG. 34. The insert shows the UCSB four-point flexure of a bilayer. The mode mixity is plotted.

1989). The setups have been collectively referred to as the UCSB four-point flexure specimens.

When the crack exceeds a few times the thickness of the notched layer, h , it can be considered as semi-infinite. The energy release rate is obtained in closed form:

$$G = \frac{M^2}{E_2 h^3} \left(6\eta^3 - \frac{1}{2I} \right), \quad (4.5)$$

where $M = Pl$ is the moment per unit width, and the dimensionless moment of inertia I is given in (3.21). The loading phase ψ is defined by (2.45) with h as the reference length, such that the stress intensity factor is

$$K = |K| h^{-1/2} \exp(i\psi). \quad (4.6)$$

It is plotted in Fig. 34 with $\beta = 0$.

Charalambides *et al.* (1990) carried out a thorough analysis of several complexities of the four-point flexure. One complication concerns the residual stress in bilayers induced in fabrication, which would affect both energy release rate and loading phase. Observe that the complex stress intensity factors due to the bending moment and residual stress can be linearly superimposed, and both are the special cases of the general problem in Section III.B.4. The latter case will also be treated explicitly in Section V.D.

2. Edge-Notched Bend

A predominantly opening specimen is depicted in Fig. 35. Without loss of generality, one can choose material 1 to be relatively rigid, so that the

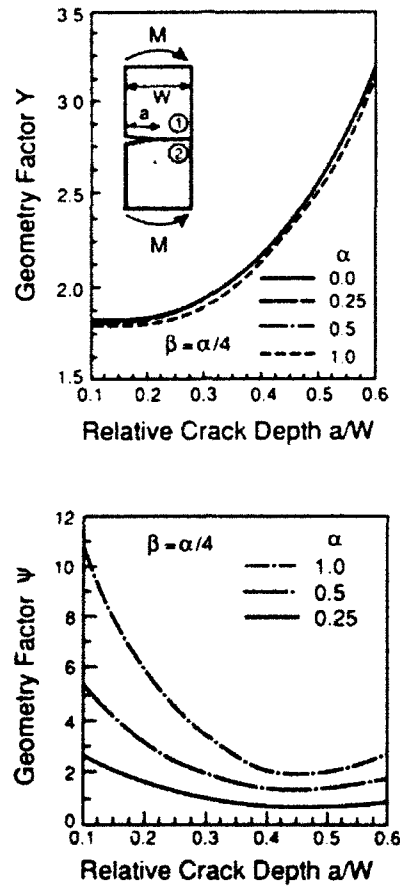


FIG. 35. Calibration of the edge-notched bend of a bimaterial bar.

Dundurs parameter satisfies $\alpha > 0$. With ψ defined by (2.45) with $l = a$, the stress intensity factor is calibrated by

$$K = YT\sqrt{a}a^{-i\epsilon}e^{i\psi}. \quad (4.7)$$

Here, T is the nominal bending stress, related to the moment per unit width M by

$$T = 6M/W^2, \quad (4.8)$$

and Y is the real, positive calibration factor.

Both Y and ψ are dimensionless functions of α , β , and a/W . The finite element results are plotted in Fig. 35 (O'Dowd *et al.*, 1990). Observe that the magnitude factor Y is nearly independent of elastic mismatch. The loading phase ψ varies between 0° to 10° , depending on the elastic mismatch.

3. Edge-Notched Shear

Calibration is also available for the specimen shown in Fig. 36 (O'Dowd *et al.*, 1990). The loading phase is controlled by the offset s/W . The stress intensity factor is

$$K = YT\sqrt{a}a^{-i\epsilon}e^{i\psi}, \quad (4.9)$$

where ψ is again defined by (2.45) with $l = a$, and

$$T = \frac{(A - B)P}{(A + B)W}. \quad (4.10)$$

The dimensionless functions Y and ψ are plotted in Fig. 36.

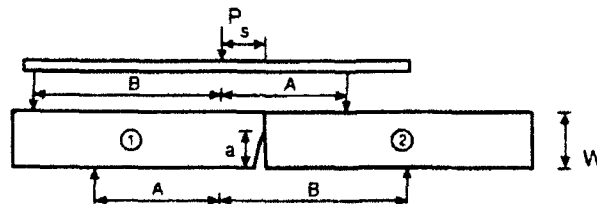
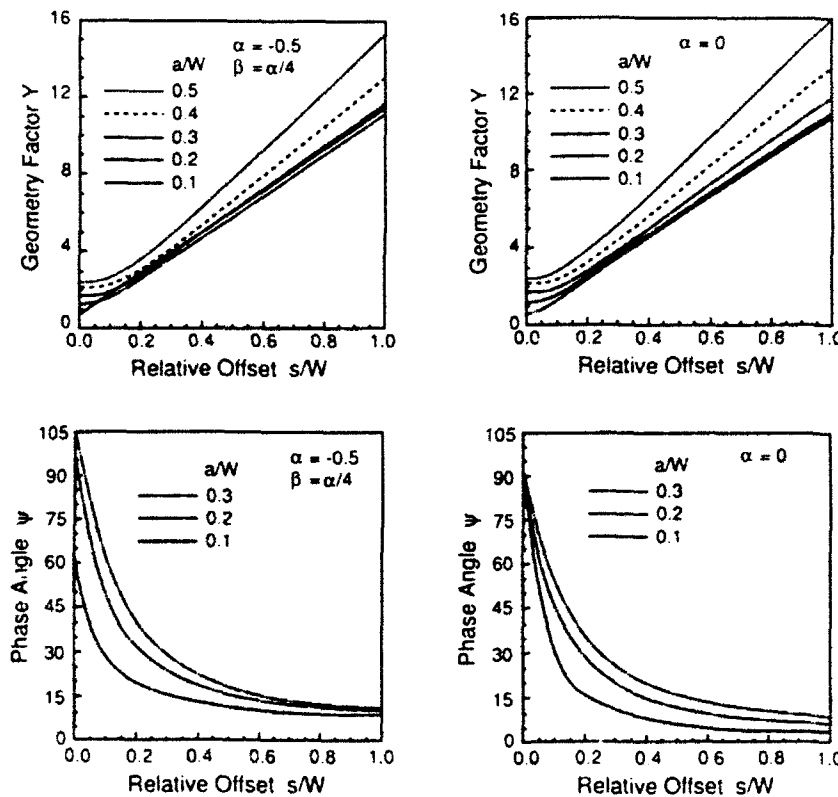


FIG. 36. Calibration of the edge-notched shear of a bimaterial bar.

C. BRAZIL-NUT SANDWICHES

Any homogeneous specimen can be converted to an interfacial specimen by sandwiching a thin layer of a second material between split halves of the specimen. The general setup is analyzed in Section III.D.2. As an example, here we sandwich the Brazil nut with a layer of second material, and a crack is left on one of the interfaces (Fig. 37). The specimen has been developed to determine interfacial toughness by Wang and Suo (1990).

A remarkable feature common to all thin-layer sandwiches is that the residual stress in the layer does *not* drive the crack, because the strain energy stored in the layer due to residual stress is not released in the process of cracking. Thus, one does not have to measure the residual stress to determine toughness. On the other hand, as discussed in Section VIII, excessive

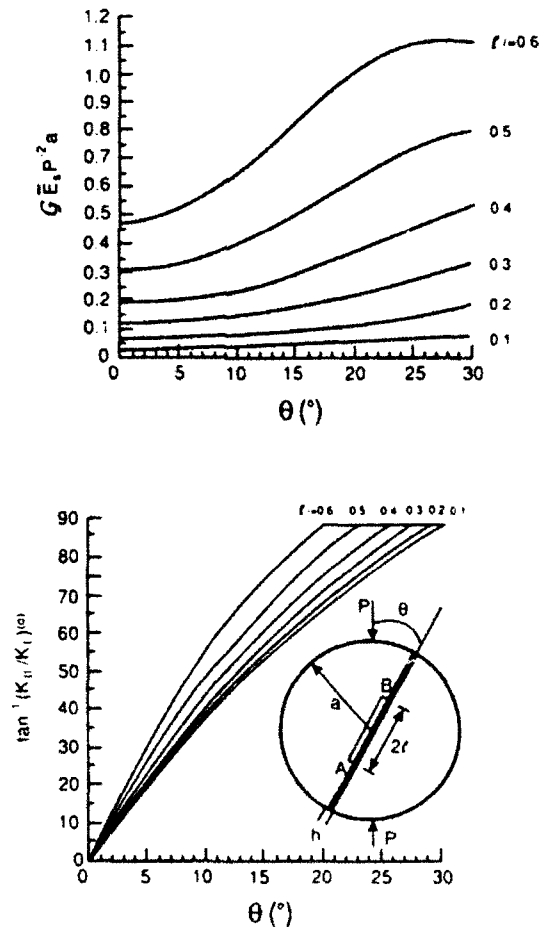


FIG. 37. Driving force and mode mixity of the Brazil-nut sandwich.

residual stress may cause complications such as crack tunneling and kinking, so it should be avoided.

1. Homogeneous Brazil Nuts

A homogeneous Brazil nut is a disk of radius a , with a center crack of length $2l$ (as illustrated in Fig. 37 but without the interlayer), which has been used for mixed mode testing of brittle solids for years. The loading phase is controlled by the compression angle θ : It is mode I when $\theta = 0^\circ$, and mode II when $\theta \approx 25^\circ$. The stress intensity factors are

$$K_I = f_I P a^{-1/2}, \quad K_{II} = \pm f_{II} P a^{-1/2}, \quad (4.11)$$

where the plus sign is for tip A , and minus for B . The nondimensional calibration factors f_I and f_{II} are functions of θ and l/a , and available in fitting polynomial forms in Atkinson *et al.* (1982).

Using the Irwin relation (2.5), the energy release rate is

$$G = (f_I^2 + f_{II}^2) P^2 / a E_S, \quad (4.12)$$

where E_S is plane strain tensile modulus for the substrate. The loading phases at tips A and B are

$$\tan^{-1}(K_{II}/K_I) = \pm \tan^{-1}(f_{II}/f_I), \quad (4.13)$$

respectively. Equations (4.12) and (4.13) are plotted in Fig. 37.

2. Sandwiched Brazil Nuts

A sandwich is made by bonding two halves with a thin layer of a second material. Nonsticking mask is supplied on the prospective crack surface prior to bonding. When the layer thickness h is much smaller than other in-plane macroscopic lengths, the energy release rate can still be calculated from (4.12). This is true because of the conservation of the J -integral, and because the perturbation due to the thin layer is vanishingly small in the far field.

The mode mixity $\hat{\psi}$, defined by (2.45) with \hat{l} as the reference length, is shifted from that for the homogeneous specimen, in accordance with

$$\hat{\psi} = \pm \tan^{-1}(f_{II}/f_I) + \omega + \varepsilon \ln(\hat{l}/h). \quad (4.14)$$

Here, ω , plotted in Fig. 28, is the shift due to elastic mismatch (3.38), and the last term is the shift due to the oscillation index ε , (2.49).

D. DELAMINATION *R*-CURVES

1. Large-Scale Bridging

Over the last decade, it has become increasingly evident that the toughness of brittle materials can be enhanced by a variety of bridging mechanisms. The mechanics language that describes this is resistance curve behavior (*R*-curves): Toughness increases as crack grows. Attention here is focussed on the delamination of unidirectional or laminated composites, where cracks nominally propagate in planes parallel to fibers. A comparative literature study shows that for both polymer and ceramic matrix composites, bridging is usually due to intact fibers left behind the crack front, while the crack switches from one fiber-matrix interface to another as it propagates. Additional resistance for polymer matrix composites comes from damage in the form of voids, craze, or micro-cracks. Three-dimensional architecture of threading fibers may also give rise to substantial fracture resistance.

As the prerequisite for these bridging mechanisms, significant damage must accumulate ahead of the pre-cut tip as an additional energy dissipater. In laminates, for example, the length over which fibers bridge the crack is typically several times lamina thickness. The significance of an *R*-curve as a material property becomes ambiguous, since the *R*-curve now depends on specimen size and geometry. The intent of this section is to describe several generic features unique to delamination *R*-curves, as identified in Suo *et al.* (1990a); references on the subject can be found in the original paper.

2. Essential Features of Delamination *R*-curves

Consider a beam with a pre-cut, loaded at the edges by moments (Fig. 38). The damage zone size L can be comparable to or larger than beam thickness h , but the beam and pre-cut are much longer, so that the geometry is fully

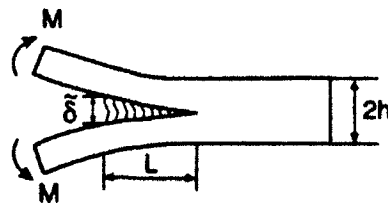


FIG. 38. A mode I delamination beam, with a damage zone as an additional energy dissipater. The geometry is specified by L/h .

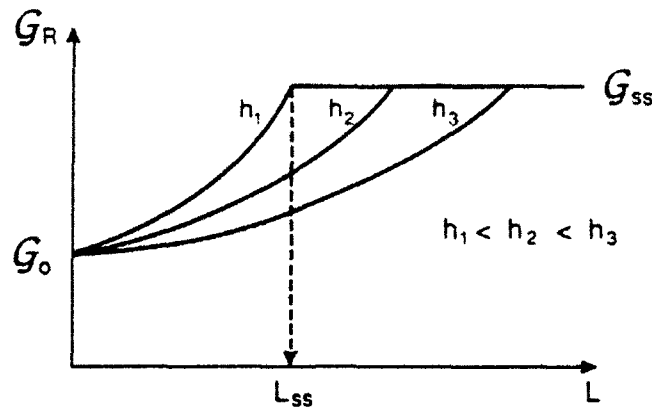


FIG. 39. Two generic features of delamination R -curves. The plateau G_{ss} is independent of the beam thickness h . The steady-state damage zone L_{ss} size increases with h .

characterized by the ratio L/h . The material is assumed to be elastically isotropic and homogeneous, and plane strain conditions prevail. The *nominal*, or *global*, energy release rate is defined as the J -integral over the external boundary as given by Rice (1968):

$$G = CM^2, \quad C = 12(1 - \nu^2)/Eh^3. \quad (4.15)$$

Here, M is the applied moment per unit width, C the beam compliance, $2h$ the thickness, E the Young's modulus, and ν the Poisson's ratio. The specimen has a *steady-state calibration*: The global energy release rate does not depend on crack size, nor does it depend on any information of the damage zone (size, constitutive law, etc.).

Phenomenological delamination R -curve behaviors are shown schematically in Fig. 39. First, focus on a R -curve measured using a beam of a given thickness, say, h_1 in the figure. The specimen can sustain the increasing moment, without appreciable damage at the pre-cut front, up to a critical point corresponding to G_0 . Subsequently, the damage zone size L increases with the applied moment, leading to an increasing curve of resistance G_R . The damage zone may attain a steady-state: It maintains a self-similar opening profile and a constant length L_{ss} , translating in the beam, leaving behind the crack faces free of traction. Correspondingly, a plateau G_{ss} would appear on the R -curve.

To proceed further, the Dugdale (1960) model is invoked, which, in its generalized form, simulates the homogenized damage response with an array of continuously distributed, nonlinear springs. Specifically, at each point in the damage strip, the closure traction σ depends locally on the separation δ

according to

$$\sigma = \sigma(\delta). \quad (4.16)$$

The functional form is related to the nature of damage, but is assumed to be *identical* for every point in the damage strip, and *independent* of the specimen geometry. A maximum separation δ_0 is specified, beyond which the closure traction vanishes. The spring laws may be measured or modeled using simplified systems. They may also be inferred from experimental R -curves, as will be discussed.

For an arbitrary spring law, the following energy balance is due to the J -integral conservation (Rice, 1968):

$$G = G_0 + \int_0^{\bar{\delta}} \sigma(\delta) d\delta, \quad (4.17)$$

where $\bar{\delta}$, referred to as the *end-opening* of the damage zone, is the separation at the pre-cut tip. Here and later, we will not distinguish the driving force G and the resistance G_R , as they can be judged from the context. The two energy release rates G and G_0 will be referred to as *global* and *local*, respectively. The global energy release rate represents the supplied energy, which is related to the applied moment via (4.15); the local one is the energy dissipated at the damage front. The difference given by (4.17) is the energy to create the damage.

The steady-state resistance G_{ss} is attained when the end-opening reaches the critical separation, $\bar{\delta} = \delta_0$. Thus, from (4.17), G_{ss} equals the sum of G_0 and the area under the spring law. The physical significance is that the plateau G_{ss} does not depend on the beam thickness, and is therefore a property for a given composite laminate. However, it is not yet clear how long the damage strip will be before the steady state is attained. The steady-state damage-zone size L_{ss} indicates the "quality" of a bridging mechanism: Toughness gained from too long a damage zone may not be useful in practice. Qualitatively, a thicker, stiffer, beam is more constrained for deflection, and thus exhibits larger L_{ss} . These essential features of the delamination R -curves are indicated in Fig. 39.

Equation (4.17) suggests a way to determine the damage response. By continuously measuring the end-opening $\bar{\delta}$, and by using the experimentally determined R -curve, the spring law can be inferred by differentiating (4.17):

$$\sigma(\bar{\delta}) = \partial G_R / \partial \bar{\delta}. \quad (4.18)$$

The intrinsic resistance G_0 is assumed to be independent of the damage

accumulation. This simple method, which bypasses the complexities of large-scale bridging, is one of the advantages of specimens with steady-state calibrations. Large-scale bridging may be used as an experimental probe to study localized (planar) damage response such as polymer craze and interface separation, as uniform separation over a sample may be difficult to accomplish in reality because of the instabilities triggered by inhomogeneities or edge effects.

3. Rigid Plastic Damage Response

To gain some quantitative feel, consider a two-parameter damage response: The closure traction is σ_0 when $\delta < \delta_0$, and vanishes when $\delta > \delta_0$. The steady-state toughness is

$$G_{ss} = G_0 + \sigma_0 \delta_0. \quad (4.19)$$

The end-opening and crack tip stress intensity factor are given by

$$\bar{\delta} = aL^2\sqrt{CG} - \frac{a^2}{4}L^4C\sigma_0, \quad (4.20a)$$

$$\sqrt{G} = \sqrt{G_0} + \frac{a}{2}\sqrt{C}L^2\sigma_0, \quad (4.20b)$$

where the dimensionless number a depends on L/h only, and the finite element results are listed in Table 2.

The R -curve defined by Eq. (4.20b) is plotted on Fig. 40 in a dimensionless form. The plateau G_{ss} in (4.19) should be a horizontal line independent of h and L (not shown in the figure). From material characterization point of view, an inverse problem is of much more interest: how to infer the model parameters from a given experimental R -curve. The quantities G_0 , G_{ss} , and L_{ss} can usually be read off from the R -curve. Using these, the model parameters σ_0 and δ_0 can be inferred from (4.20).

A family of damage responses including softening and hardening have been analyzed in Suo *et al.* (1990a). The effect of mode mixity has also been discussed. A parallel experimental investigation has been carried out by

TABLE 2

$a(L/h)$

L/h	0.5	1.0	1.5	2.0	3.0	3.5	4.0	10.0	∞
a	4.89	2.60	2.01	1.74	1.58	1.48	1.35	1.14	1.00

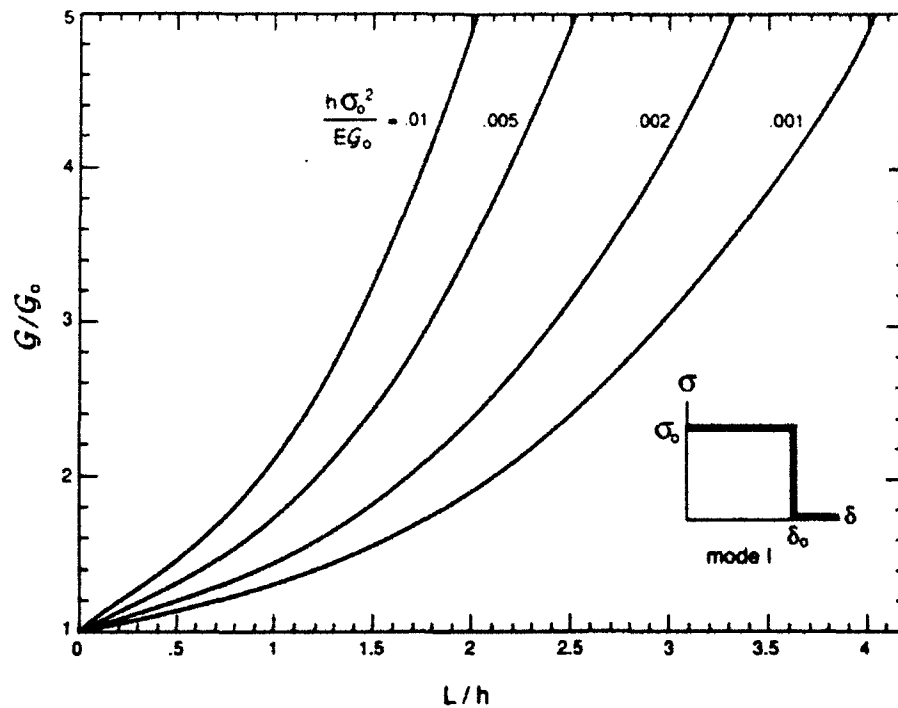


FIG. 40. Dimensionless R -curves predicted using the rigid plastic damage response (mode I).

Spearing and Evans (1990) with a unidirectional ceramic composite. The experimental data and the model show very similar behavior, suggesting that the model incorporates the controlling features of the toughening mechanism.

V. Cracking of Pre-tensioned Films

Thin films of metals, ceramics and polymers, are typically subject to appreciable residual stress, which for ceramic systems can be on the order of a giga-pascal. Such stress can cause cracking of the films. Films under residual tension and compression will be considered in this and the next sections, respectively. In this section, commonly observed fracture patterns in pre-tensioned films are first reviewed, together with a discussion of the governing parameters. These crack patterns are then analyzed in subsequent subsections, with cracking in films, substrates, and along interfaces treated independently. The values of a nondimensional driving force Z will be documented to assist the practitioners of the field. The last subsection presents a speculative analysis of thermal shock spalling.

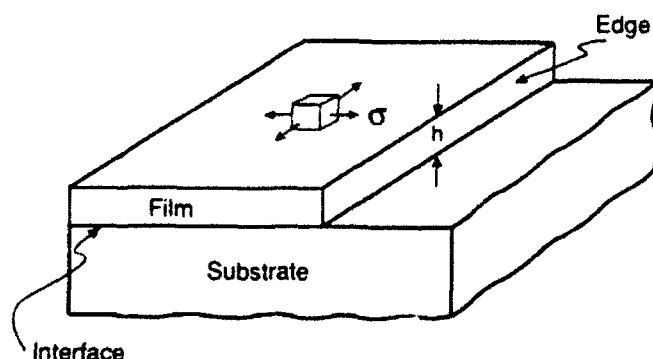


FIG. 41. A pre-tensioned film is deposited on a substrate.

A. CONTROLLING QUANTITIES AND FAILURE MODES

Illustrated in Fig. 41 is a film of thickness h on a substrate. Both materials are taken to be isotropic and linearly elastic, with elastic moduli and thermal expansion coefficients (E_f, ν_f, α_f) and (E_s, ν_s, α_s) , respectively. Elasticity mismatch may be characterized by the two Dundurs parameters α and β defined in (2.21); $\alpha > 0$ when film is stiffer than substrate. A crack will grow as the driving force G attains the fracture resistances $\Gamma_f, \Gamma_s, \Gamma_i$, depending on whether the crack is propagating in the film, substrate, or along the interface. The mode I fracture resistance is usually appropriate for films and substrates, but mixed mode resistance must be used for interfaces.

1. Driving Force Number and Critical Film Thickness

To help visualize the cracking progression, the residual stress is assumed to be due entirely to thermal mismatch. However, with proper interpretation, most of our results would be valid for stress due to other sources. The film-substrate is stress-free at a high temperature T_0 . Upon cooling to the room temperature T_r , the contraction strains in the film and substrate, were they unbonded, would differ by $(\alpha_f - \alpha_s)(T_0 - T_r)$. A biaxial *misfit stress* is defined accordingly:

$$\sigma = (\alpha_f - \alpha_s)(T_0 - T_r)E_f/(1 - \nu_f). \quad (5.1)$$

Notice $\sigma > 0$ when $\alpha_f > \alpha_s$. This stress is large: Typically, $E\alpha \cong 1 \text{ MPa/K}$ for most materials. For example, the stress would be of order 1 GPa if the temperature drops 1000 K (this is common in processing ceramic systems).

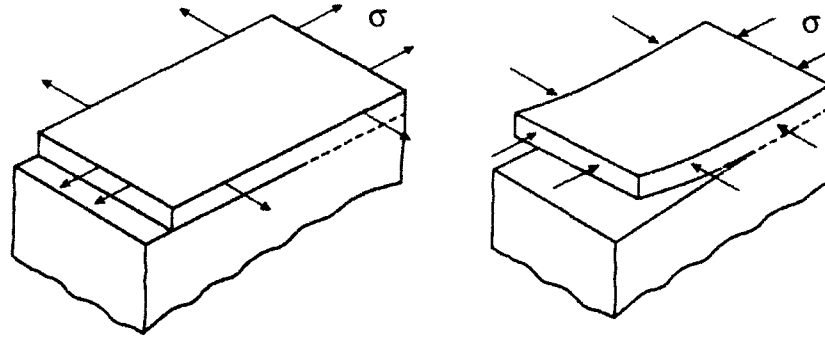


FIG. 42. An Eshelby-type superposition to treat a residually stressed film decohering from a substrate.

The thermal stress field can be evaluated by an Eshelby-type superposition. As an example, consider a thin film decohering from a substrate, driven by a biaxial misfit strain (Fig. 42). Problem (a) is trivial: the misfit strain is negated by a mechanical strain corresponding to the tensile stress σ ; the film is under a uniform biaxial stress, and the substrate is stress-free. In problem (b), a pressure of magnitude σ is applied on the edge of the film, but no misfit strain is present. The superposition recovers the original problem, with misfit strain but without edge load. Since no stress singularity is present in (a), the crack driving force is entirely due to (b). The latter is a standard elasticity problem, which requires numerical analysis.

A unifying dimensionless number Z is defined such that the energy release rate for a crack is

$$G = Z\sigma^2 h/E_f. \quad (5.2)$$

Note that the elastic strain energy stored in a unit area of the film is $(1 - \nu_f)\sigma^2 h/E_f$. The number Z is a dimensionless driving force, or order unity, depending on the cracking pattern and elastic mismatch. The practical significance of this dimensionless number was first documented by Evans *et al.* (1988). Common cracking patterns are sketched in Fig. 43, together with their Z -values, where the film-substrate system is taken to be elastically homogeneous, and the substrate semi-infinite.

Equation (5.2) provides a design limit. Given the mechanical properties and misfit stress, a specific cracking pattern is inhibited if the film is thinner than a *critical thickness*, given by

$$h_c = \Gamma E_f / Z\sigma^2, \quad (5.3)$$

where Γ is the relevant fracture resistance. The following example illustrates a routine application using the information gathered in this section.

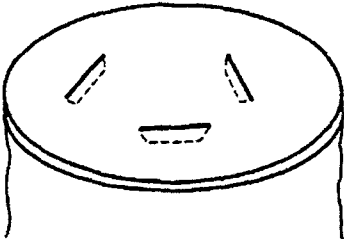
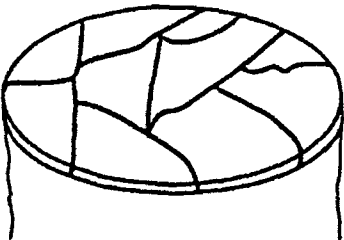
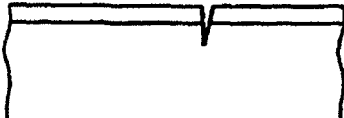


Cracking Patterns	$G = Z \sigma^2 h / \bar{E}_f$
	Surface Crack $Z = 3.951$
	Channeling $Z = 1.976$
	Substrate Damage $Z = 3.951$
	Spalling $Z = 0.343$
	Debond $Z = \begin{cases} 1.028 \text{ (initiation)} \\ 0.5 \text{ (steady - state)} \end{cases}$

FIG. 43. Commonly observed cracking patterns. The dimensionless driving force for each pattern is listed, assuming that the film-substrate is elastically homogeneous, and the substrate is infinitely thick.

Consider channeling cracks in a glass film coated on a thick SiO_2 substrate. Suppose $\Gamma_f = 7 \text{ J/m}^2$, $E_f = 70 \text{ GPa}$, $\sigma = 50 \text{ MPa}$. One reads from Fig. 43 that $Z = 1.976$, which is appropriate since glass and SiO_2 have similar elastic moduli. The critical film thickness computed from (5.3) is $h_c \approx 100 \mu\text{m}$. The channel network is *not* anticipated if the film is thinner than $100 \mu\text{m}$.

2. Cracking Patterns

Let us go through Fig. 43 to define the various cracking modes. A *surface crack* is nucleated from a flaw, and arrested by the interface. Yet the stress is not high enough for the crack to channel through the film. Since flaws are necessarily isolated, one would see stabilized, unconnected slits. The driving force available for surface cracks is high, as indicated by the large value of Z . Isolated cracks are detrimental for some applications, such as corrosion protection coatings, but tolerable for others.

The *channeling* process is unstable: Once activated, it would never arrest until it encounters another channel or an edge. Consequently, a connected channel network would emerge, surrounding islands of the intact film. Such cracking may not be acceptable for most applications, but, for example, is common in glaze on fine pottery, and in pavement of roads.

Cracks in a film can propagate further to cause *substrate damage*. This Z -value is the largest on the list. Such a crack may be stabilized at a certain depth, since the misfit stress is localized in the film. However, the crack may divert to run parallel to the interface, leading to the next cracking pattern.

Substrate spalling is an intriguing phenomenon: The crack selects a path at a certain depth parallel to the interface, governed by $K_{II} = 0$. This is not a localized failure pattern in that extensive flakes can be spalled off. Fortunately, the Z -value for spalling is quite low. If a small amount of substrate damage is acceptable, one gains substantial flexibility in design.

Debonding may initiate from edge defects or channel bottoms. The latter can be stable: The driving force for initiation is higher than that for the long debond. This fact is exploited to introduce pre-cracks for certain types of fracture specimens, such as the UCSB four-point flexure specimen.

In the following sections, these failure modes will be examined in some detail. Emphasis is placed on the relevant elasticity problems that lead to estimates of the driving force number Z . Experimental efforts will be cited in passing. The writers hope this catalog will be used critically by experimentalists in various disciplines, thereby allowing the catalog to be validated or modified.

B. CRACKING IN FILMS

Imagine a process with increasing tensile stress in the film, for example, the cooling process. As illustrated in Fig. 43, a surface flaw is activated by the tensile stress, grows towards the interface, and then arrests if the substrate and interface are tough. With further stress increase, the crack may channel through the film. The two stages will be treated separately in the following.

1. Surface Cracks

We model the situation by a plane strain crack; see the insert in Fig. 45. This is appropriate for an initial surface flaw of length several times h , but may not be valid for an equiaxial flaw. The latter is studied by He and Evans (1990a) but is omitted here. The plane strain problem has been solved by Gecit (1979) and Beuth (1990). The following paragraph is a digression to a few mathematical considerations that capture the main features of the solution, and which may be skipped without discontinuity in the content.

The dimensionless stress intensity factor $K/\sigma\sqrt{h}$ depends only on the relative crack depth a/h and Dundurs' parameters α and β . For small a/h , regardless of the elastic mismatch, the stress intensity factor merges to that of an edge crack in a semi-infinite space, i.e., $K \rightarrow 1.1215\sqrt{\pi a}\sigma$ as $a/h \rightarrow 0$. Asymptotic behavior for another limiting case, $a/h \rightarrow 1$, can be obtained by invoking the Zak-Williams singularity: the stress singularity for a crack perpendicular to, and with the tip on, the interface. Instead of the square root singularity, the stresses near such a crack tip behave like $\sigma_{ij} \sim \bar{K}r^{-s}f_{ij}(\theta)$, where (r, θ) is the polar coordinate centered at the tip, and the f_{ij} are dimensionless angular distributions. The scaling factor \bar{K} plays a part analogous to the regular stress intensity factor, but having different dimensions: [stress][length]^s. The singularity exponent s ($0 < s < 1$) depends on elastic mismatch, and is the root to

$$\cos(s\pi) - 2\frac{\alpha - \beta}{1 - \beta}(1 - s)^2 + \frac{\alpha - \beta^2}{1 - \beta^2} = 0. \quad (5.4)$$

The numerical solution of s is plotted in Fig. 44. For a crack that penetrates the film, $\bar{K} \sim \sigma h^s$, with the pre-factor dependent on α and β only. As $a/h \rightarrow 1$ but with the crack tip still within the film, the stress field away from the small ligament ($h - a$) would not feel such a detail, and behaves as if the crack tip were just on the interface, governed by \bar{K} . Dimensional considerations require the stress intensity factor K to be related to the far

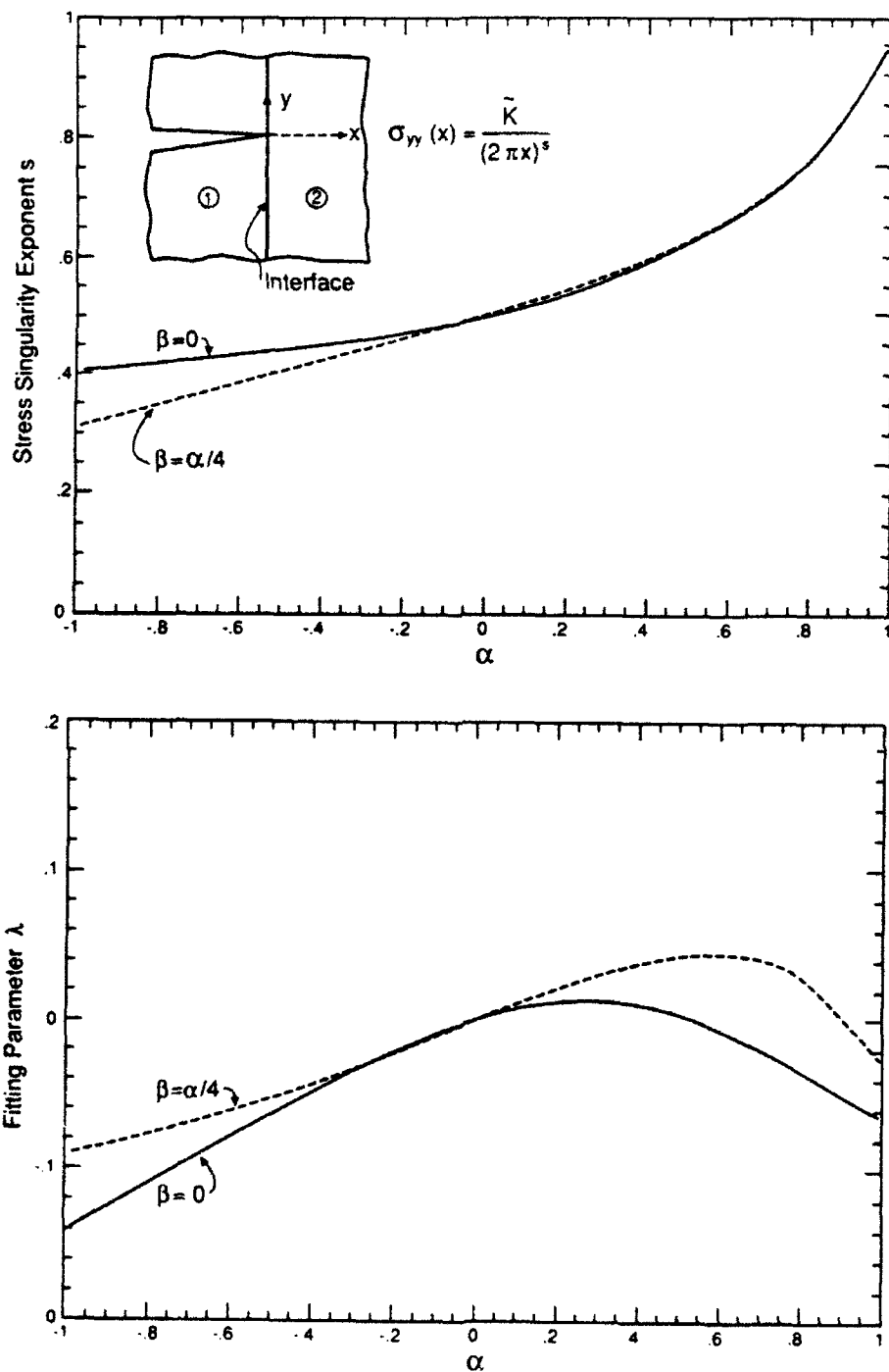


FIG. 44. (a) Zak-Williams singularity. (b) A curve fitting parameter.

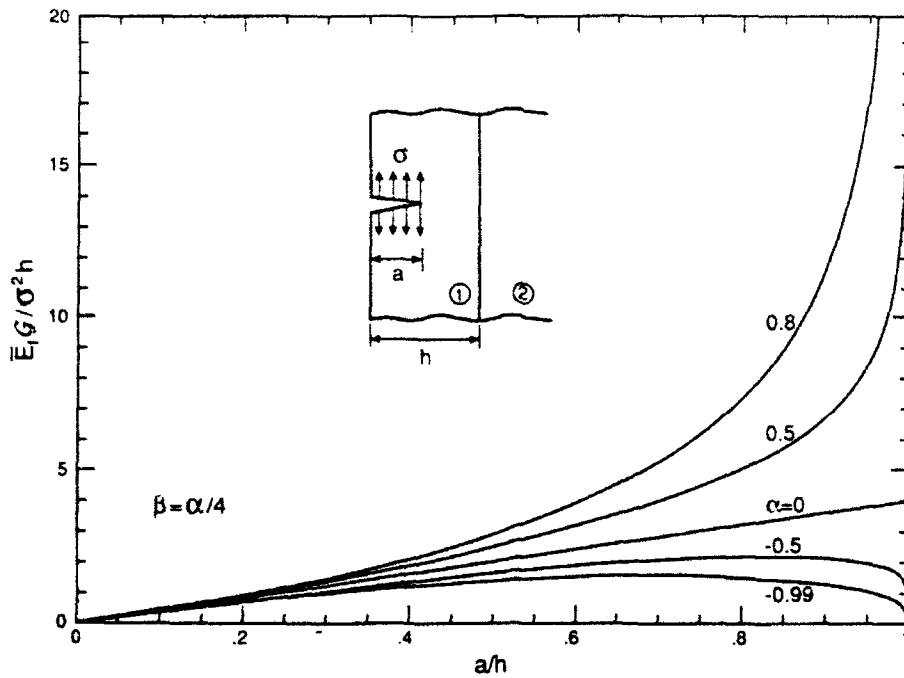


FIG. 45. Driving force available for an edge crack at various depths a/h .

field \tilde{K} according to $K \sim \tilde{K}(h - a)^{1/2-s}$. Combination of the preceding gives $K/\sigma\sqrt{h} \sim (1 - a/h)^{1/2-s}$ as $a \rightarrow h$.

Motivated by these considerations, Beuth fitted his numerical solution with

$$K/\sigma\sqrt{h} = 1.1215\sqrt{\pi}(a/h)^{1/2}(1 - a/h)^{1/2-s}(1 + \lambda a/h), \quad (5.5)$$

where λ is taken to be independent of a/h , and is chosen such that the formula agrees with the full numerical solution at $a/h = 0.98$; the results are plotted in Fig. 44b. The error of (5.5) is within a few percent for intermediate a/h . Equation (5.5) is plotted in Fig. 45 in terms of the dimensionless energy release rate. The energy release rate starts from zero for shallow flaws. As the crack approaches the interface, it drops to zero for relatively compliant films ($\alpha < 0$), but diverges to infinity for stiffer films ($\alpha > 0$).

One needs *a priori* knowledge of flaw size to predict a failure stress or the maximum tolerable film thickness. In practice, a plausible flaw depth may be assumed according to the "quality" of the film. Taking, say, $a/h = 0.8$, one can obtain the nondimensional driving force Z from Fig. 45 for a known elastic mismatch. The flaws will not be activated if the dimensionless fracture resistance satisfies $\Gamma_f E_f / \sigma^2 h > Z$.

Observe that for relatively compliant films, the driving force attains a maximum at an intermediate depth. The practical significance is that no flaws, regardless of initial depth, can be activated, provided the dimensionless resistance $\Gamma_f E_f / \sigma^2 h$ is greater than the maximum. Such a maximum, depending on the elastic mismatch α and β , provides a fail-safe bound for relatively compliant films.

2. Cracks Channeling through a Film

Figure 46 shows a crack channeling through the film. Complications such as substrate penetration, interface debond, and channel interaction are assumed not to occur for the time being. At each instant of the growth, the channel front self-adjusts to a curved shape, such that energy release rate at every point on the front is the same. The elasticity problem is three-dimensional in nature, and an accurate solution would require iteration of the front shape. After the length exceeds a few times the film thickness, the channel asymptotically approaches a steady-state: the entire front maintains its shape as it advances; so does $\delta(z)$, the cross-section profile in the wake, which attains the shape of a plane strain through-crack. The steady-state cracking is analogous to that discussed in Section III.A.1.

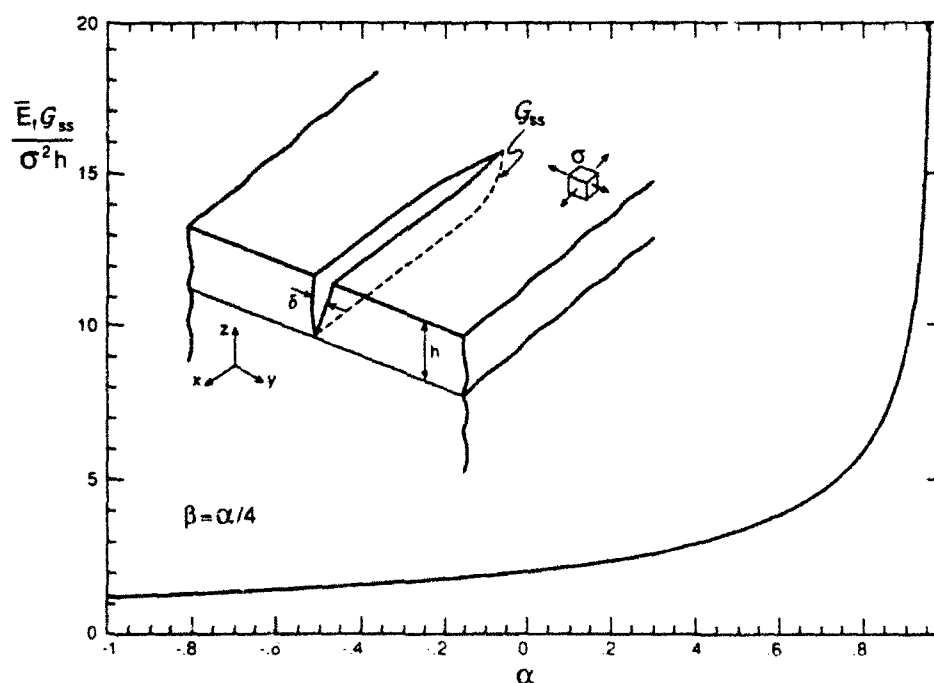


FIG. 46. The insert shows a crack channeling across the film, driven by the tensile stress in the film. The available energy at the channel front is plotted for various elastic mismatch.

In the steady state, the energy release rate at the channel front can be evaluated using two *plane problems*—that is, by subtracting the strain energy stored in a unit slice far behind of the front, from that far ahead. The calculation does not require the knowledge of the front shape. Alternative formulae have been developed with this idea. One is

$$G_{ss} = \frac{1}{2h} \int_0^h \delta(z) \sigma(z) dz. \quad (5.6)$$

Two plane problems are involved: the stress distribution on the prospective crack plane before cracking, $\delta(z)$, which, for the present situation, equals a uniform misfit stress σ , and the displacement profile for a plane strain crack, $\delta(z)$. This is particularly convenient for numerical computation.

A second formula is

$$G_{ss} = \frac{1}{h} \int_0^h G(a) da, \quad (5.7)$$

where $G(a)$ is the energy release rate of a plane strain crack of depth a in Fig. 45. A mathematical interpretation is that G_{ss} is the average of energy release rates for through-cracks at various depths. Both formulae are valid for films and substrates with dissimilar elastic moduli.

As an example, suppose the film-substrate is elastically homogeneous, and the substrate occupies a semi-infinite space. The corresponding plane strain problem is an edge crack in a half plane, with energy release rate $G(a) = 3.952\sigma^2 a/E$ (Tada *et al.*, 1985). The integral (5.7) gives $G_{ss} = 1.976\sigma^2 h/E$. This pre-factor is listed in Fig. 43.

Beuth (1990) carried out an analysis of a thin film on a semi-infinite substrate with dissimilar elastic moduli. The result is reproduced in Fig. 46. If the dimensionless toughness $\Gamma_f E_f / \sigma^2 h$ is below the curve, a channel network is expected. Observe that a compliant substrate ($\alpha > 0$) provides less constraint, inducing higher driving force for channeling.

The channeling cracks were studied analytically by Gille (1985) using the numerical solutions available at that time, and subsequently by Hu and Evans (1988) with a combination of calculations and experiments. The concept has been extended as a fail-safe bound for cracking in multilayers (Suo, 1990b; Ho and Suo, 1990; Ye and Suo, 1990; Beuth, 1990). Applications include thin films, reaction product layers, adhesive joints, and hybrid laminates.

3. Multiple Channeling

The preceding technique can be extended to study interaction among channels. Suppose the biaxial stress is biased so that parallel channels

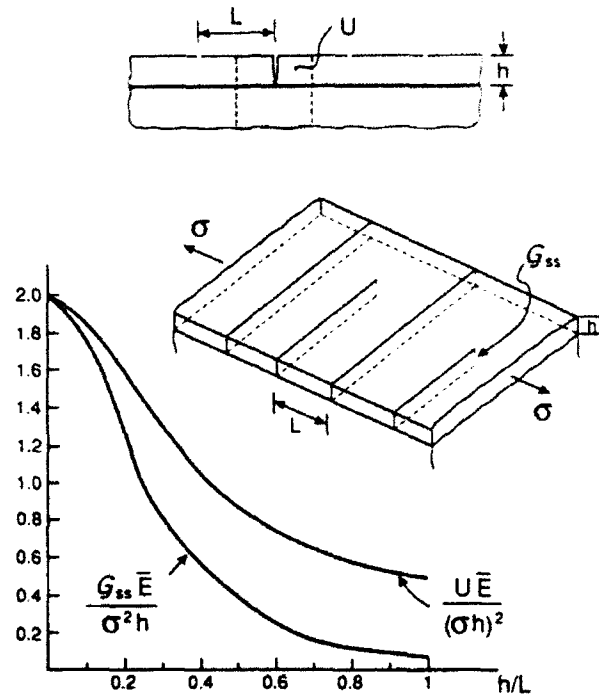


FIG. 47. Interaction of multiple channels.

develop in one direction; see the inserts in Fig. 47. For simplicity, attention is restricted to an elastically homogeneous system with a semi-infinite substrate.

Consider a periodic set of edge cracks of depth a , spacing L , and subject to an opening stress σ . The energy release rate at each crack tip, $G(a)$, is found in Tada *et al.* (1985) in a graphic form, which is then fitted by a polynomial. Based on this information, energetic accounting gives the driving force for cracks channeling in the film.

The strain energy, per crack, gained in creating a set of cracks of depth h is

$$U = \int_0^h G(a) da = f \sigma^2 h^2 / E, \quad (5.8)$$

where the dimensionless factor f depends on the crack density h/L . The results obtained by a numerical integration are plotted in Fig. 47. If these cracks are equally extended in the channeling direction, the energy release rate at each front is $G_{ss} = U/h = f \sigma^2 h / E$. Thus, f is the dimensionless driving force for this situation. Thouless (1990a) has employed this solution in his discussion of crack spacing in thin films.

Next, consider the situation in Fig. 47 where, at a certain stage of loading, the cracks of spacing $2L$ have already channeled across the film, and the

tensile stress in the film has therefore been partially relieved. With further increase of the loading, a new set of cracks are nucleated and grow half-way between the existing channels. The energy release rate at the front of the growing cracks should be computed from

$$G_{ss} = (2U_L - U_{2L})/h = [2f(h/L) - f(h/2L)]\sigma^2 h/E. \quad (5.9)$$

This is derived from the strain energy difference far behind and far ahead of the channeling fronts.

The result is also plotted in Fig. 47. Given the mechanical properties and with the identification $G_{ss} = \Gamma_f$, the plot may be viewed as a relation between the stress level and the channel density. Notice we have assumed that new cracks can always be readily nucleated half-way between existing channels. This might overestimate the crack density for a given stress level. An analysis with aspects similar to the preceding has also been carried out independently by Delannay and Warren (1991).

C. SUBSTRATE CRACKING

Substrate damage may originate from edges or existing channel cracks in the film. The two substrate cracking patterns in Fig. 43 are studied in this section. Observe that the Z -values for the two patterns differ by an order of magnitude.

1. Substrate Damage Caused by Cracks in Films

Suppose the channel cracks in the film have developed at some stage during the cooling but have not yet grown into the substrate, either because the substrate is much tougher or because sufficiently large substrate surface defects are not readily available. The issue is whether these cracks would propagate into the substrate upon further cooling. The problem has been studied by Ye and Suo (1990), and the main results are summarized here.

The driving force for a plane strain crack into a substrate was analyzed using finite elements, and the results are plotted in Fig. 48. Observe that the driving force decays for deep cracks, implying stable propagation. For relative compliant films ($\alpha < 0$), the driving force starts from zero at the interface, and attains a maximum at very small depths. It is difficult for finite elements to resolve these details, so the trend is sketched by dashed lines.

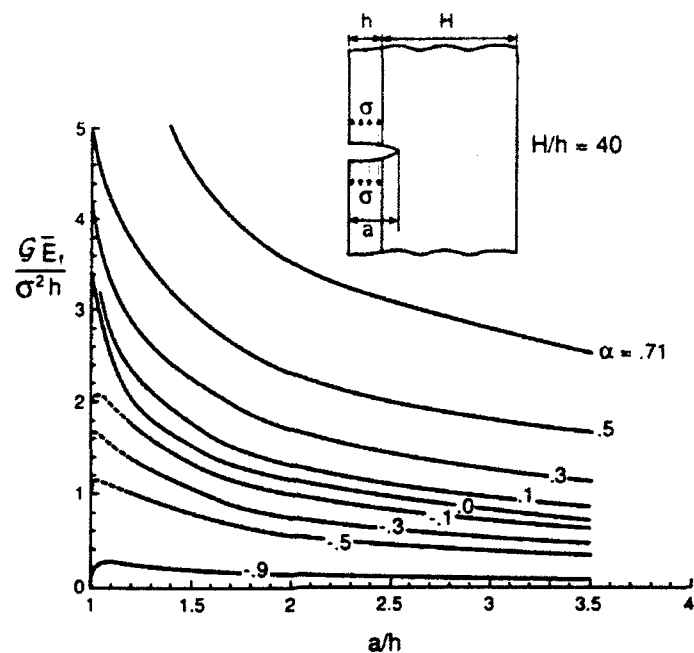


FIG. 48. Energy release rate for a plane strain crack with the tip in the substrate.

The plane strain model is not quite correct, since cracks must be re-nucleated, in a three-dimensional fashion, from a surface flaw on substrate. The insert of Fig. 49 shows a crack growing laterally under an existing channel in the film. The crack arrests at a certain depth because of the decay of the available driving force. The energy release rate at the growing front

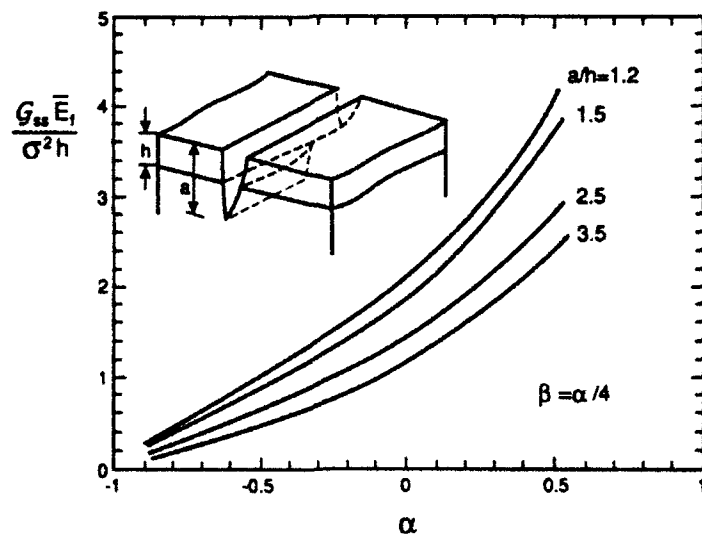


FIG. 49. Energy release rate for a crack propagating under a channel in the film.

may be computed from

$$G_{ss} = \frac{1}{a-h} \int_h^a G(a') da'. \quad (5.10)$$

Again, this is derived from energy accounting. The integral is evaluated using the preceding plane strain results, and the results are summarized in Fig. 49. The plot may be used as a damage tolerance map: Given a damage tolerance a/h , one can read the design number Z . Take the curve for $a/h = 1.2$ as an example. Provided the dimensionless substrate toughness $\Gamma_s \bar{E}_t / h \sigma^2$ is above the curve, no channel with depth $a/h > 1.2$ is anticipated. This holds true even if the initial flaws are deeper than 1.2, as long as they are not channels themselves. Observe that the elastic mismatch plays a significant role. A relatively compliant substrate would provide less constraint, leading to larger driving force.

The so-called T -stress in (2.1) has also been computed by Ye and Suo and is found to be positive, unless the film is much stiffer than the substrate and the crack depth is small. As shown by Cotterell and Rice (1980), a positive T -stress results in a tendency for a straight mode I crack to veer off to one side or the other. Further discussion of crack path stability in a related context is given in Section VIII.C. Here, we simply note that the substrate crack will have a strong tendency to branch into a path parallel to the interface, a cracking pattern to be discussed next.

2. Spalling of Substrates

Cracks, originating from either defects in the film or at the edge, have a strong tendency to divert into the substrate, should the latter be brittle, and follow a trajectory parallel to the interface; see Fig. 43. The key insight was provided by Thouless *et al.* (1987) in a coordinated experimental and theoretical investigation. Their initial intent was to model the impact of ice sheets on offshore structures. The experiments were conducted with PMMA and glass plates, loaded on the edges. Spalling cracks were found to follow a trajectory parallel to the surface, with depth governed by the criterion $K_{II} = 0$. (See also Thouless and Evans, 1990.)

These authors remarked to the effect that this mechanism would operate in the edge spalling of pre-tensioned films, previously observed by Cannon *et al.* (1986). As schematically shown in Fig. 43, the crack initiates at the edge, extends along the interface for typically about two times film thickness, then kinks into the substrate, and finally runs parallel to the

interface at a depth of a few times the film thickness. In this case, the underlying mechanics is the same for giant ice sheets as for micro-electronic films.

Thorough investigations on pre-tensioned films have been conducted, experimentally and analytically, by Hu *et al.* (1988), Hu and Evans (1988), Drory *et al.* (1989), Suo and Hutchinson (1989b), and Chiao and Clarke (1990). Focus here is on the steady-state spalling, with the transient stage ignored, since the former provides a well-defined design limit. In the following, the essential mechanics will be elucidated using a simple system, and results will be cited for more general cases. The analysis is arranged separately for spalling originating from edges or channel cracks (planar geometry), and from holes.

a. Planar Geometry

Inserted in Fig. 50 is a long crack at a depth d in the substrate, driven by the residual tension in the film. Plane strain conditions are assumed. The film is attached to a semi-infinite substrate with the same elastic moduli. Results without these restrictions will be cited later. The equivalent edge force and moment due to σ are

$$P = \sigma h, \quad M = \sigma h(d - h)/2. \quad (5.11)$$

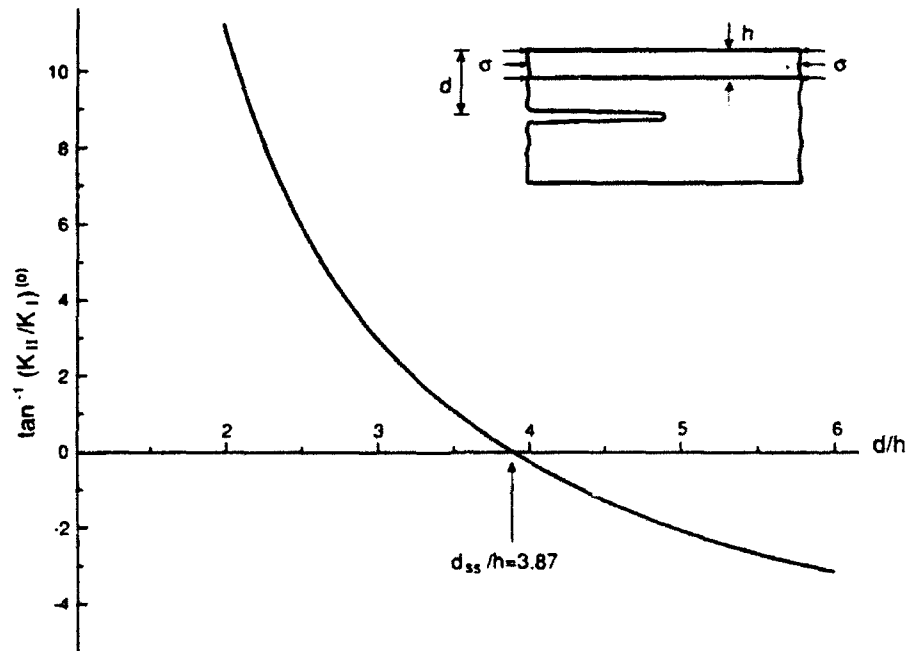


FIG. 50. The insert shows a spalling crack. The plot is the mode mixity for crack at various depths.

Specialized from (3.12), the stress intensity factors are

$$K_I/\sigma\sqrt{h} = (h/2d)^{1/2}[\cos \omega + \sqrt{3}(1 - h/d)\sin \omega], \quad (5.12)$$

$$K_{II}/\sigma\sqrt{h} = (h/2d)^{1/2}[\sin \omega - \sqrt{3}(1 - h/d)\cos \omega]. \quad (5.13)$$

where $\omega = 52.07^\circ$. The mode mixity $\psi = \tan^{-1}(K_{II}/K_I)$ is plotted as a function of crack depth in Fig. 50. Notice $K_{II} > 0$ for small depth, but $K_{II} < 0$ for large depth and, consequently, a pure mode I trajectory exists at an intermediate depth.

This steady-state spalling depth d_{ss} is determined from (5.13) with $K_{II} = 0$. Thus,

$$d_{ss} = 3.86h. \quad (5.14)$$

The steady-state, mode I energy release rate can now be readily evaluated from (5.12), which gives

$$G_{ss} = 0.343\sigma^2 h/E. \quad (5.15)$$

This pre-factor was cited in Fig. 43.

Suo and Hutchinson (1989b) carried out an extensive analysis to include elastic mismatch and finite thickness of the substrate. The general solution for arbitrary edge loads is summarized in Section III.B.5. The results for spalling cracks caused by the residual stress in the film are reproduced in Fig. 51. Observe that the spalling depth depends strongly on both elastic mismatch and substrate thickness. However, the dimensionless stress intensity factor is insensitive to the substrate thickness as long as $H/h > 10$.

There has been no formal proof that the spalling trajectory is configurationally stable. One heuristic explanation, as shown in Fig. 51, is that $K_{II} > 0$ when $d < d_{ss}$, implying that a crack above d_{ss} would be driven down. Analogously, a crack below d_{ss} would be driven up.

b. Spalling from Circular-Cut

Figure 52 shows an axial-section of a spalling crack emanating from the edge of a circular-cut in the film, driven by residual tensile stress in the film. In general, a hole in a pre-tensioned film acts like a stress raiser. However, it differs from an open hole in a plate in that, for the former, cracking is usually confined within a few times hole radius. Other cracking modes around holes include channel cracks in films and decohesion of interfaces. The latter will be treated in the next section.

As indicated in Fig. 52, the hole radius is b_0 , and the crack extends to a radius b . For simplicity, the elastic moduli for the film and substrate are

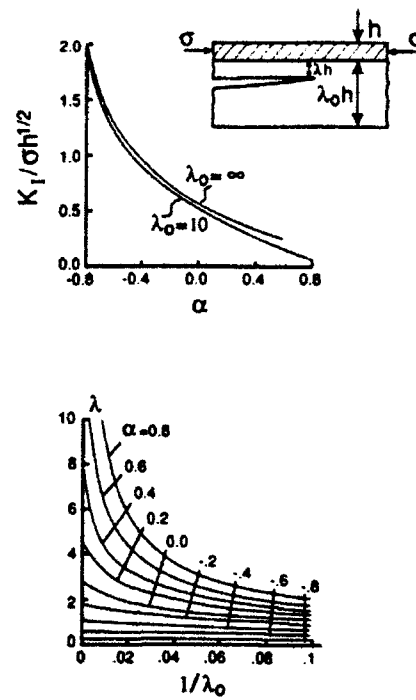


FIG. 51. Spalling results for film-substrate of dissimilar elastic constants and finite substrate. Both mode I stress intensity factor for the steady-state propagation and the depth of the crack path are given.

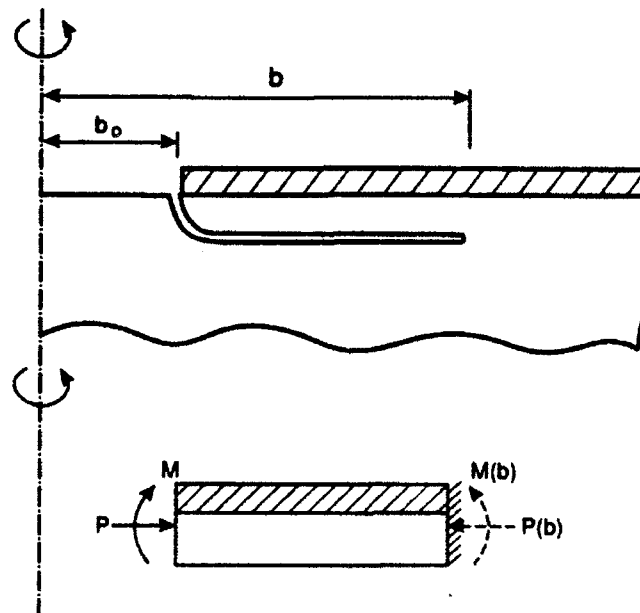


FIG. 52. An axial-section of spalling from the edge of a circular-cut.

taken to be the same, and the substrate semi-infinite. The equivalent edge force P and moment M , per unit length, are still given by (5.11). The stress state in the annulus between b_0 and b can be determined by the classical plate theory, with the outer boundary clamped. The analysis shows that the moment and force at the crack front are modified by a factor:

$$M(b) = M/k, \quad P(b) = P/k, \quad (5.16)$$

where

$$k = \frac{1}{2}[(1 + \nu) + (1 - \nu)(b/b_0)^2]. \quad (5.17)$$

These loads are indicated in Fig. 52.

The results of Section III.B.1.d are applicable with moment and force $M(b)$ and $P(b)$ used. In particular, the energy release rate is modified by factor k^2 , i.e.,

$$G = \frac{1}{2k^2} \left(\frac{M^2}{I} + \frac{P^2}{A} \right), \quad I = \frac{1}{12} E d^3, \quad A = E d. \quad (5.18)$$

This result can also be derived by an energetic accounting, i.e.,

$$G = (2\pi b)^{-1} \partial U / \partial b,$$

where U is the strain energy stored in the clamped circular plate. From this latter approach, it would be clear that the solution is the exact asymptote as $(b - b_0)/h \rightarrow \infty$.

The stress intensity factors (5.12) and (5.13) are modified accordingly by a factor of k . Thus, the steady-state depth d_{ss} is independent of b/b_0 , and is identical to the plane strain result (5.14). The mode I driving force for spalling now becomes

$$G = \frac{0.343 \sigma^2 h}{k^2 E}. \quad (5.19)$$

Since k increases with b/b_0 , the spalling crack from a circular-cut would usually arrest.

D. INTERFACE DEBOND

Pre-tensioned films are susceptible to decohesion or, more precisely, de-adhesion, from substrates. Flaw geometry plays an important role: Debonding emanating from an edge defect, a hole, or a through-cut would behave differently. Analytical results for the first two geometries will be summarized, and the third can be found in Jensen *et al.* (1990).

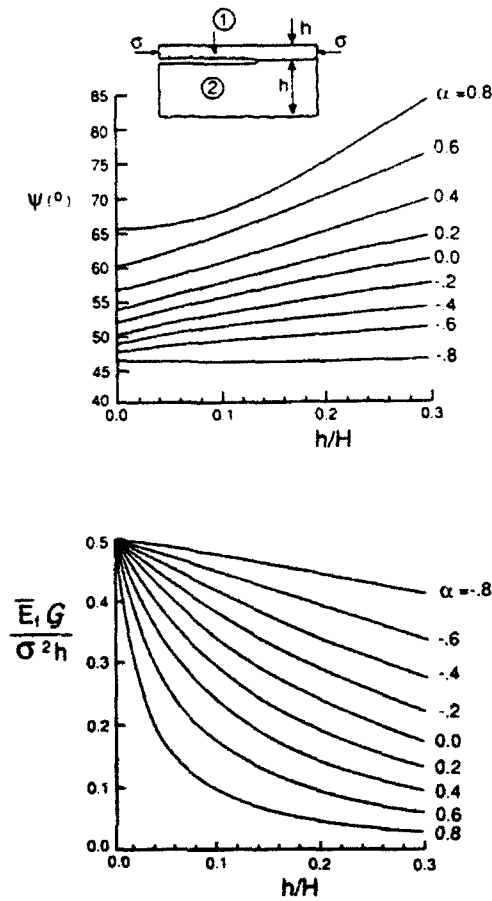


FIG. 53. Mode mixity and energy release rate for a debonding crack.

1. Decohesion from Edges or Channels

Figure 53 illustrates a pre-tensioned film debonding from a substrate. The edge load is a special combination of that studied in Section III.B.4, and the notation there is followed. The misfit stress is equivalent to the mechanical loads (see Fig. 26):

$$P_1 = P_3 = \sigma h, \quad M_3 = (1/2 + 1/\eta - \Delta)\sigma h^2, \quad M_1 = 0. \quad (5.20)$$

Specialized from Eq. (3.22), the energy release rate is

$$G = \frac{\sigma^2 h}{2\bar{E}_f} \left[1 - \frac{\Sigma}{A} - \frac{\Sigma(1/2 + 1/\eta - \Delta)^2}{I} \right]. \quad (5.21)$$

The loading phase ψ is defined by $K = |K|h^{-i\epsilon} \exp(i\psi)$, as is consistent with the convention in (2.45) with $l = h$. Both the driving force and mode mixity are plotted in Fig. 53. Observe that the decohesion process is inherently mixed mode, consisting of somewhat more sliding than opening.

The effect of the substrate thickness on the driving force is significant when the film is stiff.

Argon *et al.* (1989) have used the residual stress as a driving force to measure interface toughness. The result in this section can also be used to calibrate the residual stress effect on some interface fracture specimens, e.g., the UCSB four-point flexure specimen. The complex interfacial stress intensity factor is a superposition of the contribution from residual stress and that from mechanical load.

2. Decohesion from a Hole

Figure 54 illustrates a decohesion crack emanating from the edge of a hole in a pre-tensioned film. Results developed in Section C.2.b for substrate spalling are still valid here. In particular, the energy release rate is given by

$$G = \frac{h\sigma^2}{2E_f k^2}, \quad (5.22)$$

where k is given by Eq. (5.17). The result is now valid for films and substrates with dissimilar elastic constants, but the substrate is still assumed to be much thicker than the film. The mode mixity is independent of b/b_0 when $(b - b_0)/h$ is sufficiently large, and is identical to the plane strain results (Fig. 53, $h/H = 0$).

Decohesion from a circular-cut is stable and has been used to determine interface toughness by Farris and Bauer (1988) and Jensen *et al.* (1990). This is particularly feasible when the film is transparent, so that the decohesion radius b can be readily measured.

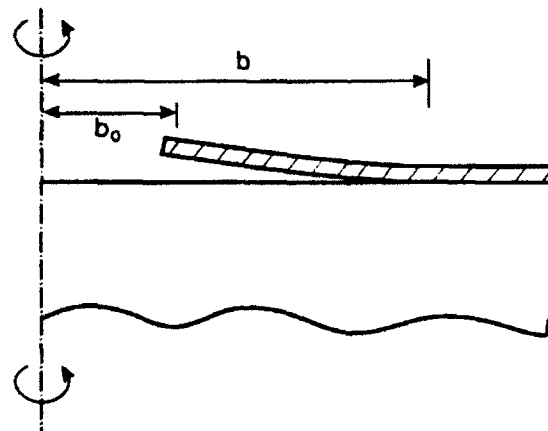


FIG. 54. An axial-section of a decohesion annulus originated from an edge of a circular-cut.

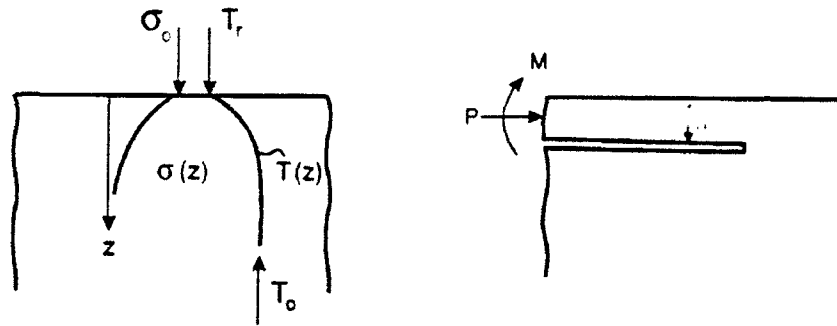


FIG. 55. A model for thermal shock spalling.

E. THERMAL SHOCK SPALLING

1. An Idealized Model

Consider a block of brittle material with a thin, pre-tensioned, surface layer. Spalling is possible if the residual stress has a negative gradient with depth. An example is depicted in Fig. 55. A semi-infinite body is initially immersed in a heat bath of temperature T_0 , so that a uniform temperature is established in the body. Upon the removal of the block from the bath, the surface temperature is assumed to drop instantaneously to the room temperature T_r . A biaxial tensile residual stress thus develops in a surface layer, as shown schematically in Fig. 55. The equivalent edge force and moment are also indicated. The stress profile changes with the time, and so does the ratio M/P .

The problem features a dimensionless number

$$\xi = h/\sqrt{t\alpha_D}, \quad (5.23)$$

where h is the depth of the crack parallel to the surface, α_D the thermal diffusivity, and t the time elapsed after the removal of the heat source. At any given time, a mode I crack path parallel to the surface is available—that is, a number ξ_{ss} exists where $K_{II} = 0$. However, for small t , the depth h is correspondingly small, and therefore the strain energy stored in such a thin layer is insufficient to drive the spalling. Consequently, a certain time elapse is needed before spalling. The following is an attempt to quantify these considerations.

2. Spalling Depth and Time Elapse

Consider first the temperature and stress field prior to cracking. At a given time t after the removal from the heat bath, the temperature at a

depth z is

$$T(z, t) = T_0 + (T_r - T_0) \operatorname{erfc}(z/2\sqrt{t\alpha_D}). \quad (5.24)$$

The biaxial, tensile, thermal stress field varies with the depth and time, in accordance with

$$\sigma_x = \sigma_y = \sigma(z, t) = \sigma_0 \operatorname{erfc}(z/2\sqrt{t\alpha_D}), \quad (5.25)$$

where

$$\sigma_0 = \alpha_E(T_0 - T_r)E/(1 - \nu), \quad (5.26)$$

and α_E is the thermal expansion coefficient. These are classical solutions, which may be extracted from standard textbooks.

Next consider the half space with a spalling crack (Fig. 55). The resultant force and moment can be expressed as

$$P = I\sigma_0 h, \quad M = (\frac{1}{2}I - J)\sigma_0 h^2, \quad (5.27)$$

where

$$I(\xi) = \frac{1}{\xi} \int_0^\xi \operatorname{erfc}(u/2) du, \quad J(\xi) = \frac{1}{\xi^2} \int_0^\xi u \operatorname{erfc}(u/2) du. \quad (5.28)$$

The stress intensity factors can be calculated from Section III.B.1.d.

The number ξ corresponding to a mode I trajectory is determined by enforcing $K_{II} = 0$. The problem involves a nonlinear algebraic equation, and the numerical solution gives

$$h_{ss} = 6.82\sqrt{t\alpha_D}. \quad (5.29)$$

The corresponding mode I stress intensity factor is

$$K_I = 0.190\sigma_0\sqrt{h_{ss}}. \quad (5.30)$$

Given the toughness and stress level, the depth h_{ss} may be predicted from (5.30), and the time elapse for spalling can then be estimated from (5.29). Observe that the spalling depth is independent of the thermal diffusivity, as a feature of this idealized model. As an example, consider a glass with $K_{Ic} = 0.7 \text{ MPa m}^{1/2}$, $\sigma_0 = 100 \text{ MPa}$, $\alpha_D = 0.7 \times 10^{-6} \text{ m}^2/\text{s}$. The predicted crack depth is $h_{ss} = 1.4 \text{ mm}$, and the time to spalling is $t = 6 \times 10^{-2} \text{ s}$. This tiny time elapse is possibly an outcome of the idealized temperature boundary condition that has been adopted.

VI. Buckle-Driven Delamination of Thin Films

In many film/substrate systems, the film is in a state of biaxial compression. Residual compression has been observed in thin films that have been



FIG. 56. The photograph on the left from Argon *et al.* (1989) shows a SiC film on a Si substrate delaminating as a wavy circular blister. On the right is a photograph supplied by M. D. Thouless, which shows examples of the straight-sided blister and the telephone cord blister occurring in a multilayered film delaminating from a glass substrate.

sputtered or vapor deposited and it can arise from thermal expansion mismatch. Some remarkable failure modes of such systems have been observed, examples of which are shown in Fig. 56. These pictures reveal regions where the film has been buckled away from the substrate. Various shapes of the buckled regions evolve, including long straight-sided blisters, circular blisters with and without wavy edges, and the so-called telephone cord blister, which is perhaps the most common morphology. The failure entails the film first buckling away from the substrate in some small region where adhesion was poor or nonexistent. Buckling then loads the edge of the interface crack between the film and the substrate, causing it to spread. The failure phenomenon couples buckling and interfacial crack propagation. The straight-sided blister grows at one of its ends. The telephone cord blister grows at its end as if a worm were tunneling beneath the film.

This section presents an analysis of the straight-sided and circular blisters and concludes with some speculation about the origin of the telephone cord morphology. It will be seen that a key aspect of the phenomena is the mixed mode fracture behavior of the interface, wherein $\Gamma(\psi)$ increases sharply with increasing mode 2.

Formulas relating the energy release rate of the interface crack to the buckling parameters were derived for one-dimensional ply buckles on the surface of laminated composites by Chai *et al.* (1981). Essentially identical results were obtained by Evans and Hutchinson (1984) and Gille (1985) for the thin-film problem. The energy release rate for the circular blister in biaxially compressed films was given by Evans and Hutchinson (1984) and

Yin (1985). The significance of the mixed mode character of the interface crack tip was apparently first appreciated by Whitcomb (1986), who showed that the crack tip becomes predominately mode 2 as a one-dimensional ply buckle spreads. His observation was essential to explain why the buckles do not keep spreading along their edges under constant overall load—that is, why the buckles have a characteristic width. Whitcomb was concerned with compressive failure modes in layered composites. Here, the concern will be with thin films under equi-biaxial compression, but a number of the results and conclusions carry over directly to ply delamination. Storakers (1988) and Rothschilds *et al.* (1988) deal with various aspects of buckling and delamination in composites, and these authors cite relevant literature in the composites arena.

This section starts with a one-dimensional analysis of the infinitely long straight-sided blister, closely paralleling the analysis of Whitcomb (1986). Given the availability in Section III.B.4 of the relationships between the interface stress intensity factors and the moment and resultant force change at the edge of the buckle, the one-dimensional analysis can be carried out in closed form. The analysis of the circular blister, which requires some numerical work, is presented next. The two sets of results are then combined in an analysis of steady-state propagation of a straight-sided blister. The steady-state problem gives perhaps the sharpest insights into design constraints on compressed films.

A. THE ONE-DIMENSIONAL BLISTER

Consider an x -independent segment of the straight-sided blister shown in Fig. 57. The film is taken to be elastic and isotropic with Young's modulus E_1 , Poisson's ratio ν_1 , and thickness h . The substrate is also assumed to be isotropic but with modulus E_2 and Poisson's ratio ν_2 . The substrate is modeled as being infinitely deep. The film is assumed to be unattached to the substrate in the strip region $-b \leq y \leq b$. A plane strain interface crack of width $2b$ exists between the film and the substrate.

The unbuckled film is assumed to be subject to a uniform, equi-biaxial compressive in-plane stress, $\sigma_{xx} = \sigma_{yy} = -\sigma$. In the unbuckled state, the stress intensity factors at the crack tips vanish. Only when the film buckles away from the substrate are nonzero stress intensity factors induced. Under the assumption that $h \ll b$, the film is represented by a wide, clamped Euler column of width $2b$. The complex stress intensity factor K at the right-hand

tip is related to the moment M and to the *change* in resultant stress ΔN at the right-hand end of the column by the relationships given for the 2-layer problem in Section III.B.4. Use of the 2-layer solution to characterize the crack tip field is justified if $h/b \ll 1$, which is, in any case, the condition for the validity of the Euler theory. In what follows, the 2-layer solution is first specialized for the present applications. This solution is also used in the analysis of the blister test discussed in Section VII, and should have fairly wide applicability. Then, the Euler solution is presented and is coupled to the 2-layer solution.

1. General Loading of an Edge Crack on the Interface between a Thin Film and Substrate

Let M and ΔN be defined with the sign convention in Fig. 57. These quantities will be identified with the moment/unit length and the change in resultant stress at the right end of the wide Euler column. Specializing the solution of Section III.B.4 to the limit of the infinitely deep substrate, one finds for the interface crack:

$$G = 6(1 - \nu_1^2)E_1^{-1}h^{-3}(M^2 + h^2 \Delta N^2/12), \quad (6.1)$$

$$Kh^{ie} = -\left[\frac{6(1 - \alpha)}{1 - \beta^2}\right]^{1/2} h^{-3/2} \left[\frac{h \Delta N}{\sqrt{12}} + iM \right] e^{i\omega}, \quad (6.2)$$

$$\tan \psi \equiv \frac{\text{Im}(Kh^{ie})}{\text{Re}(Kh^{ie})} = \frac{\sqrt{12}M \cos \omega + h \Delta N \sin \omega}{-\sqrt{12}M \sin \omega + h \Delta N \cos \omega}. \quad (6.3)$$

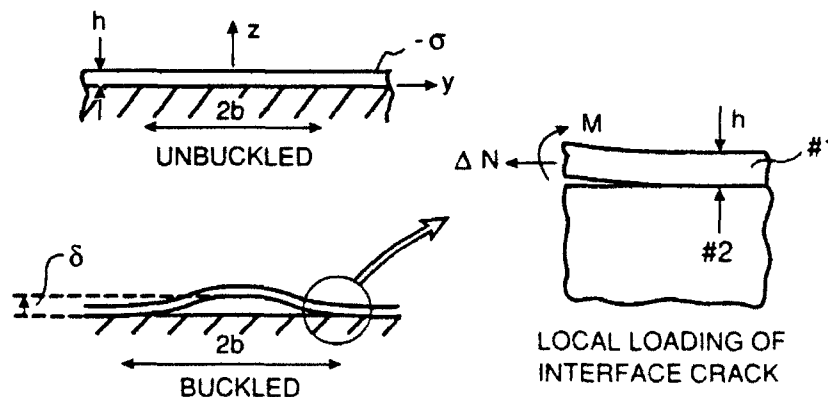
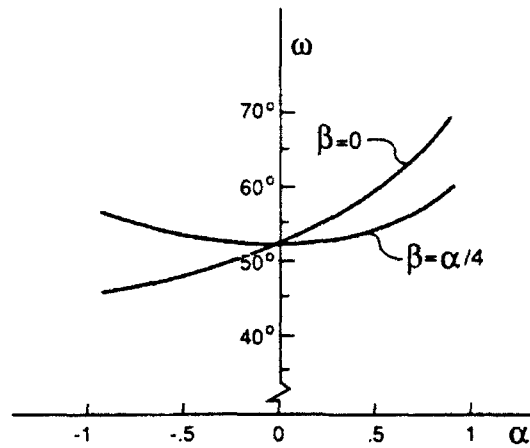


FIG. 57. Geometry of the one-dimensional blister, and conventions for the elasticity solution characterizing conditions near the tip of an interface crack between a thin film and an infinitely thick substrate. Top left: unbuckled; bottom left: buckled; right: local loading of interface crack.

FIG. 58. Phase factor $\omega(\alpha, \beta)$ in (6.2) and (6.3).

Here, $\omega \equiv \omega(\alpha, \beta, h/H = 0)$, which is plotted in Fig. 58 for $\beta = 0$ and $\beta = \alpha/4$. The mode mixity parameter ψ is defined using the film thickness h as the reference length l .

2. Euler Column Solution and Coupling to Interface Edge Crack Solution

The one-dimensional deformation of the wide column in Fig. 57 is characterized by the y - and z -displacements, $V(y)$ and $W(y)$. These are defined to be zero in the unbuckled state with pre-stress $\sigma_{xx} = \sigma_{yy} = -\sigma$. The wide column is taken to be characterized by von Karman nonlinear plate theory with fully clamped conditions at its edges, i.e.,

$$V = W = W, y = 0 \quad \text{at } y = \pm b. \quad (6.4)$$

The change in the y -component of the stretching strain measured from the unbuckled state is

$$\epsilon_y = V, y + \frac{1}{2} W, y^2, \quad (6.5)$$

while the bending strain is W, yy . With N_x and N_y as the resultant stresses and with $\Delta N_x = N_x + \sigma h$ and $\Delta N_y = N_y + \sigma h$ as the changes in the resultant stresses from the unbuckled state, the strain component ϵ_y is related to ΔN_y by

$$\epsilon_y = (1 - \nu_1^2) \Delta N_y / (E_1 h). \quad (6.6)$$

Since $\epsilon_x = 0$, $\Delta N_x = \nu_1 \Delta N_y$. The bending moment is related to the bending strain by $M_y = DW, yy$, where $D = E_1 h^3 / [12(1 - \nu_1^2)]$ is the bending stiffness. In-plane equilibrium requires $\Delta N_y, y = 0$. Therefore, ΔN_y can be

taken to be the value at the end of the beam, ΔN . Moment equilibrium requires

$$DW', yyy - (\Delta N - \sigma h)W', y = 0. \quad (6.7)$$

The solution to the preceding system of equations is given in (6.8)–(6.12):

$$W = \frac{1}{2}\xi h[1 + \cos(\pi y/b)], \quad (6.8)$$

$$M \equiv M_y(b) = \frac{\pi^2}{2} \frac{Dh}{b^2} \xi, \quad (6.9)$$

$$\Delta N = \frac{3\pi^2}{4} \frac{D}{b^2} \xi^2. \quad (6.10)$$

The amplitude of the buckling deflection, ξ , has been defined such that $W(0) = \xi h$. It is related to the residual stress by

$$\xi = \left[\frac{4}{3} \left(\frac{\sigma}{\sigma_c} - 1 \right) \right]^{1/2}, \quad (6.11)$$

where

$$\sigma_c = \frac{\pi^2 D}{b^2 h} = \frac{\pi^2}{12} \frac{E_1}{(1 - \nu_1^2)} \left(\frac{h}{b} \right)^2. \quad (6.12)$$

Here, σ_c is the classical buckling stress of a clamped-clamped wide plate. The residual compression in the film, σ , must exceed σ_c if the film is to buckle away from the substrate for a given interface crack length $2b$. The nondimensional "loading parameter" is σ/σ_c . Since σ_c decreases as b increases, σ/σ_c increases as b increases.

The energy release rate is determined by substituting the expressions for M and ΔN in (6.9) and (6.10) into (6.1), with the result

$$G = [(1 - \nu_1^2)h/(2E_1)](\sigma - \sigma_c)(\sigma + 3\sigma_c). \quad (6.13)$$

This result is in agreement with Chai *et al.* (1981), Evans and Hutchinson (1984), and Gille (1985). Substitution of the same expressions into (6.3) gives

$$\tan \psi = \frac{4 \cos \omega + \sqrt{3} \xi \sin \omega}{-4 \sin \omega + \sqrt{3} \xi \cos \omega}. \quad (6.14)$$

Recall that ψ is defined relative to the reference length $l = h$, and is given here for the crack tip at $y = +b$.

For large σ/σ_c , G asymptotically approaches

$$G_0 \equiv [(1 - \nu_1^2)h/(2E_1)]\sigma^2. \quad (6.15)$$

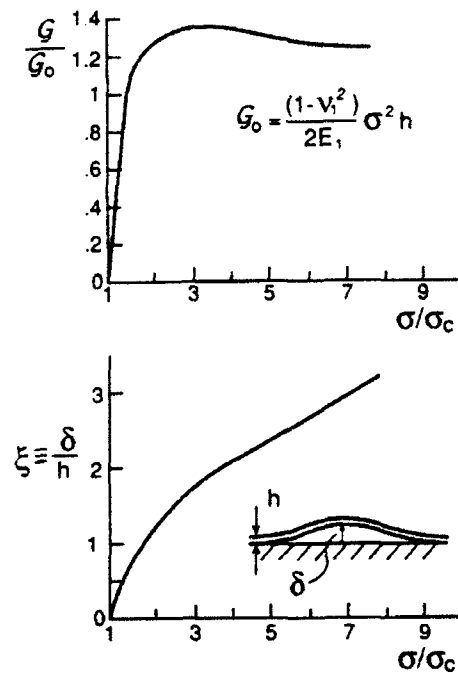


FIG. 59. Energy release rate and buckling deflection for one-dimensional blister.

This is just the strain energy per unit area in the film, which is available when released subject to the plane strain constraint $\epsilon_x = 0$.[†] The normalized energy release rate is

$$\frac{G}{G_0} = \left(1 - \frac{\sigma_c}{\sigma}\right) \left(1 + 3 \frac{\sigma_c}{\sigma}\right), \quad (6.16)$$

which is plotted in Fig. 59 together with the buckling deflection amplitude from (6.11). The interface crack length $2b$ enters the expression for G through σ_c in (6.12). For a given pre-stress σ , G approaches G_0 as $b \rightarrow \infty$; it vanishes when $\sigma_c = \sigma$; and it attains its peak value $4G_0/3$ at $\sigma/\sigma_c = 3$. The fact that G exceeds G_0 is not a violation of energy conservation. The total energy released per unit length of buckle (i.e., the integral of $2G$ with respect to b) is always less than $2G_0b$, and only approaches $2G_0b$ as $b \rightarrow \infty$. The explicit expression is given later in (6.35).

[†] The strain energy per unit area stored in the film is $[(1 - \nu_1)h/E_1]\sigma^2$. Reducing N_y to zero subject to $\epsilon_x = 0$ releases (6.15) when negligible bending energy remains in the film. The results in (6.8)–(6.16) are valid for residual stresses for any σ_x as long as $\sigma_y = -\sigma$. They apply not only to the thin film problem but also to the x -independent mode of delamination for a surface ply on a thick composite plate.

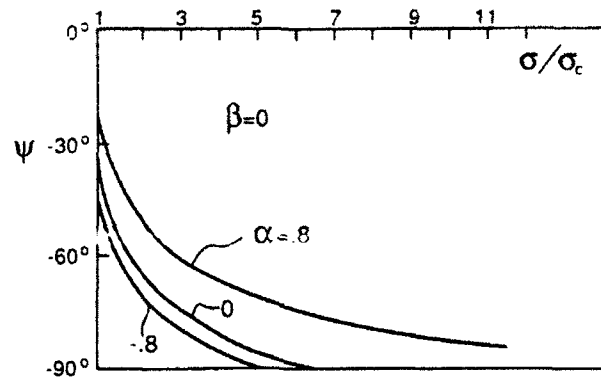


FIG. 60. Phase of loading ψ at the right-hand crack tip for the one-dimensional blister.

Curves of the mode mixity measure ψ at the right-hand crack tip are shown as a function of σ/σ_c in Fig. 60 for several values of α , all with $\beta = 0$. Elastic mismatch affects ψ only through ω in (6.14). Since ω is relatively insensitive to mismatch when $\beta = \alpha/4$ (see Fig. 58), plots of ψ versus σ/σ_c have not been displayed for this case. For σ/σ_c slightly above unity, and thus small ξ , (6.14) gives

$$\tan \psi \cong -\cot \omega, \quad \text{or} \quad \psi \cong -((\pi/2) - \omega). \quad (6.17)$$

In the absence of elastic mismatch, $\omega = 52.1^\circ$ and ψ starts at -37.9° . As σ/σ_c increases and as ξ increases, the relative proportion of mode 2 to mode 1 increases. The value of σ/σ_c at which the crack tip loading becomes pure mode 2 (i.e., $\psi = -90^\circ$) can be obtained from (6.11) and (6.14).

$$\sigma/\sigma_c = 1 + 4 \tan^2 \omega, \quad (6.18)$$

which is attained when $\xi = (4/\sqrt{3}) \tan \omega$. Note that this point where all mode 1 is lost is a fairly strong function of elastic mismatch. For no mismatch, $\sigma/\sigma_c = 7.55$. The strong increase in mode mixity as the buckle spreads has important implications for buckle-driven decohesion, as will be discussed with the aid of several interface toughness functions in the next subsection.

Before applying the results of this section, we note in passing that the von Karman nonlinear plate equations accurately represent the buckling behavior as long as $h/b \ll 1$ and rotations satisfy $(W, y)^2 \ll 1$. Comparison of the predictions from von Karman theory with the more accurate elastica, for example, reveals that the present predictions retain reasonable accuracy for buckling deflections $W(0)$ that do not exceed $b/3$. Note from Fig. 59 or (6.11) that $W(0) = 3.46h$ when $\sigma/\sigma_c = 10$. Thus, for example, if h/b is less than about $1/10$, the above predictions retain accuracy for σ/σ_c as large as 10.

3. Extent of Interface Decohesion: The One-dimensional Blister as a Model

There is often some rate dependence associated with buckling-driven decohesion, due most likely to species in the air gaining access to the interface crack tip, a process akin to corrosion assisted crack growth. The discussion that follows will neglect any rate dependence. It will be assumed that interface crack advance occurs when the condition $G = \Gamma(\psi)$ is reached.

Consider first the consequences of assuming an ideally brittle interface where the critical energy release rate is mode-independent, i.e., $G = G_I^c$. To facilitate the discussion, assume an initial decohered region of width $2b_i$ exists on the interface, and imagine a scenario in which biaxial compressive stress in the film σ is increased, due, for instance, to temperature change when there exists a thermal expansion mismatch between the film and substrate. For a given set of parameters of the system, plot curves of G/G_I^c versus b at various levels of σ using the normalized curve in Fig. 59. Such curves are sketched in Fig. 61a, where the lowest curve corresponds to the value of σ at which the buckling starts with $b = b_i$. Denote by σ_* the value of σ associated with the curve that intersects the fracture criterion, $G/G_I^c = 1$, at $b = b_i$. In the scenario in which σ is increased, one would observe buckling without decohesion for σ between $(\sigma_c)_i$ and σ_* . At σ_* , crack advance would be initiated and would necessarily be unstable since G/G_I^c exceeds 1 as b increases. The blister would spread dynamically without arrest.

Alternatively, suppose a level of σ exists below σ_* , say $\sigma = \sigma_1$ in Fig. 61a, and suppose an external agent forces the decohered region to expand until b reaches the point where $G/G_I^c = 1$. As in the previous scenario, the crack would expand unstably from that point onward. In some previous work (e.g., Gille, 1985), it has been argued that the combination of G_I^c , b , and σ lies on the decreasing portion of the G versus b curve, thereby allowing stable crack growth. Although this is a possibility, this argument seems implausible as a general explanation because the drop from the peak to the asymptote for $b \rightarrow \infty$ is small. In fact, G increases monotonically with increasing blister radius in the case of the circular blister discussed in the next subsection; thus, there is no drop and there would be no arrest for that geometry.

The qualitative influence of the mode dependence of interface toughness on the arrest of blister spreading can be anticipated from the relation between ψ and σ/σ_c in Fig. 60. Neglect for the moment any consideration

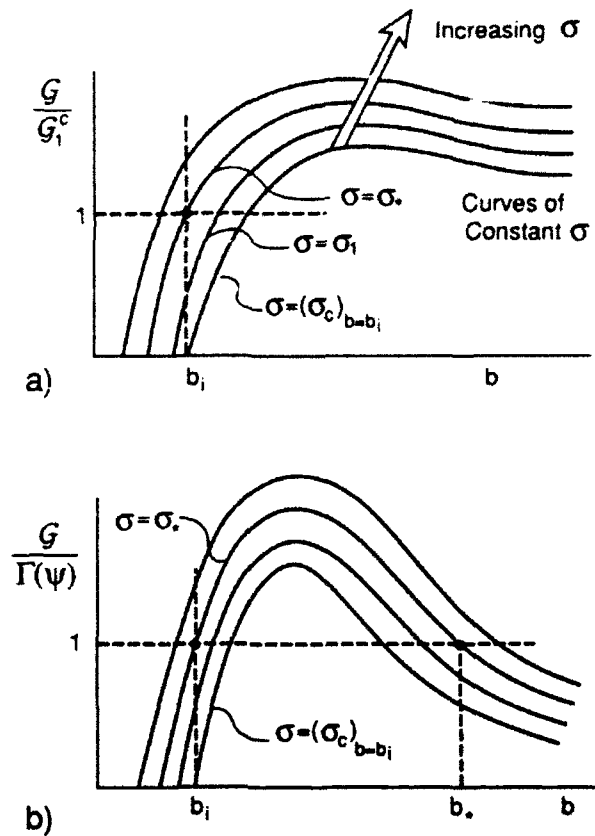


FIG. 61. Schematic of instability analysis of one-dimensional blister. a) based on an ideally brittle interface with propagation condition $G = G_1^c$. b) Based on $G = \Gamma(\psi)$, where Γ increases with increasing $|\psi|$.

of β -effects in the elastic mismatch, and suppose that the toughness function $\Gamma(\psi)$ increases with increasing $|\psi|$ as discussed in Section II. Then, curves of $G/\Gamma(\psi)$ versus b at various levels of σ would display the trends shown in Fig. 61b. Given an initially decohered region of width $2b_i$, the blister would spread dynamically when σ attains σ_* , and would arrest at $b = b_*$. With further increase of σ , the blister would spread stably with the condition $G = \Gamma(\omega)$ maintained. Whether it would spread beyond the point where (6.18) is attained depends on the condition governing pure mode 2 crack growth.

A quantitative prediction requires the specification of a specific functional form for $\Gamma(\psi)$. The discussion that follows will use the forms (2.40) and (2.44), which are plotted in Figs. 10 and 11, for the purpose of illustration. They will be used again in the analyses of the circular blister and the steady-state growth of the straight-sided blister. For either form, let

$$\Gamma(\psi) = G_1^c f(\psi), \quad (6.19)$$

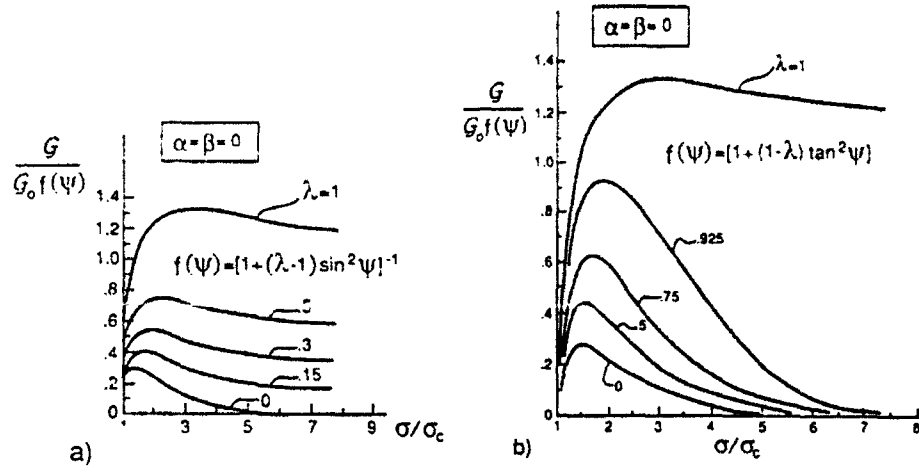


FIG. 62. Mode-adjusted crack driving force for the one-dimensional blister for two families of interface toughness functions. No elastic mismatch.

where

$$f(\psi) = [1 + (\lambda - 1) \sin^2 \psi]^{-1} \quad \text{for (2.40),} \quad (6.20)$$

$$f(\psi) = [1 + (1 - \lambda) \tan^2 \psi] \quad \text{for (2.44).} \quad (6.21)$$

Then, $G/f(\psi)$ can be regarded as a mode-adjusted crack driving force in the sense that the criterion for crack advance is $G/f(\psi) = G_1^c$. Curves of normalized crack driving force are plotted in Fig. 62 for various choices of λ for each of the two families of toughness functions. The curves are obtained directly using (6.16) and (6.14), and are shown for the case of no elastic mismatch ($\alpha = \beta = 0$). Recall that in each case the choice $\lambda = 1$ reduces to the ideally brittle criterion $G = G_1^c$, while $\lambda = 0$ coincides with the criterion $K_1 = K_1^c \equiv (E_* G_1^c)^{1/2}$.

The two families of interface toughness functions (6.20) and (6.21) probably bracket toughness trends for a class of material combinations, such as those discussed in Section II, in the sense that (6.20) most likely underestimates the rate of increase of $\Gamma(\psi)$ with respect to ψ near mode 2 while (6.21) probably overestimates that rate of increase. Depending on λ and the other parameters of the system, either arrest or unarrested spreading of the blister can occur according to (6.20). Arrest will always occur according to (6.21), assuming $\lambda < 1$.

The effect of elastic mismatch on the normalized driving force is shown in Fig. 63 for one choice of λ for each of the two toughness functions, in each case for various α with $\beta = 0$. A stiff film on a compliant substrate ($\alpha > 0$) enhances the peak crack driving force and accentuates its fall-off

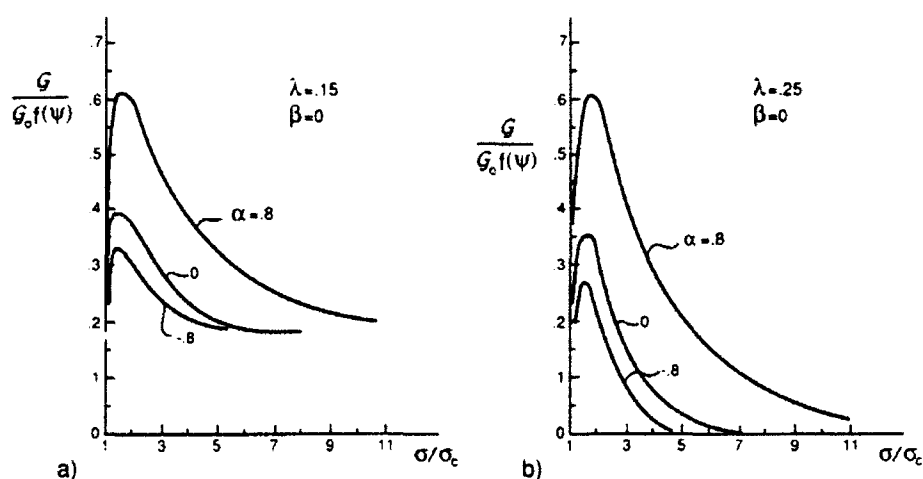


FIG. 63. Effect of elastic mismatch on the mode-adjusted crack driving force for the one-dimensional blister: (a) based on (6.20); and (b) based on (6.21).

with increasing b . When $\beta \neq 0$, the approach is similar to that just described except that now the criterion for advance is $G/f(\hat{\psi}) = G_1^c$, where $\hat{\psi}$ is associated with some material-based length \hat{l} through (2.45). Since ψ in (6.14) is defined for the choice $l = h$, one must take into account the relation (2.49) between ψ and $\hat{\psi}$ in determining the crack driving force.

B. THE CIRCULAR BLISTER

In this section, the axisymmetric counterpart to the one-dimensional blister is considered. An analysis along similar lines to that presented here was given by Chai (1990) for the special case where no elastic mismatch exists between the film and the substrate. The geometry for the circular blister is similar to that in Fig. 57 except that the radius of the buckled region is taken to be R . The analysis again couples a buckled plate representing the circular decohered region of the film with the elastic solution for a semi-infinite edge crack on an interface, as depicted in Fig. 57 and as presented in Section VI.A.1. For the axisymmetric geometry, the nonlinear von Karman plate equations cannot be solved in closed form, except asymptotically for sufficiently small buckling amplitudes. Numerical methods must be used to solve the equations for the buckled plate.

1. Governing Equations

The von Karman nonlinear plate equations for axisymmetric deformations of a completely clamped circular plate of radius R , thickness h , and

subject to an equi-biaxial compressive stress σ in the unbuckled state are as follows. Let r be the distance from the center of the plate normalized by R , $N_r(r)$ the resultant radial in-plane stress, $\Delta N_r(r) \equiv N_r(r) + \sigma h$ the change in this component from its value in the unbuckled state, and let $W(r)$ be the vertical displacement component. With

$$\phi(r) = [6(1 - \nu_1^2)]^{1/2} h^{-1} \frac{dW}{dr} \quad (6.22)$$

as a measure of the rotation, the two equations of equilibrium can be written in nondimensional form as

$$\frac{d}{dr} \left(r \frac{d\phi}{dr} \right) - r^{-1} \phi + r \phi (\bar{\sigma} - \Delta \bar{N}_r) = 0, \quad (6.23)$$

$$\frac{d}{dr} \left(r^3 \frac{d\Delta \bar{N}_r}{dr} \right) + r \phi^2 = 0, \quad (6.24)$$

where $\bar{\sigma} = \sigma h R^2 / D$ and $\Delta \bar{N}_r = \Delta N_r R^2 / D$. As before, $D = E_1 h^3 / [12(1 - \nu_1^2)]$ is the bending stiffness. The conditions at $r = 0$ are $\phi = 0$ and $d\Delta \bar{N}_r / dr = 0$. The fully clamped conditions at $r = 1$ require

$$\phi = 0, \quad \frac{d}{dr} (r \Delta \bar{N}_r) - \nu_1 \Delta \bar{N}_r = 0. \quad (6.25)$$

The energy release rate, interface stress intensity factors, and mode mixity parameter in (6.1)–(6.3) are evaluated using the bending moment and the change in resultant stress at the edge of the plate, which are given by

$$\begin{aligned} M &= DhR^{-2} [6(1 - \nu_1^2)]^{-1/2} (d\phi/dr)_{r=1}, \\ \Delta N &= DR^{-2} (\Delta \bar{N}_r)_{r=1}. \end{aligned} \quad (6.26)$$

2. Asymptotic Solution for Small Buckling Deflections

Evans and Hutchinson (1984) derived a formula for the energy release rate using an asymptotically valid solution to the preceding system of equations for small buckling deflections. That result will be reproduced here without derivation along with a new companion result for the mode mixity parameter ψ .

The classical buckling stress of a clamped circular plate is

$$\sigma_c^* = \frac{\mu^2 D}{R^2 h} = 1.2235 \frac{E_1}{1 - \nu_1^2} \left(\frac{h}{R} \right)^2, \quad (6.27)$$

Where $\mu = 3.8317$ is the first nontrivial zero of $J_1(x)$, the Bessel function of the first kind of order one. The associated axisymmetric mode is

$$W_1(r) = [0.2871 + 0.7129J_0(\mu r)]h, \quad (6.28)$$

where $J_0(x)$ is the Bessel function of the first kind of order zero. The mode is normalized such that $W_1(0) = h$.

The asymptotic solution is obtained by developing an expansion of the buckling deflection (and other quantities) in the form

$$W(r) = \xi W_1 + \xi^2 W_2 + \dots, \quad (6.29)$$

where ξ is the buckling amplitude. To lowest order, $\xi = \delta/h$, where δ is the deflection at the center of the plate. The asymptotic relation between ξ and σ/σ_c^* is

$$\xi = \left[\frac{1}{c_1} \left(\frac{\sigma}{\sigma_c^*} - 1 \right) \right]^{1/2}, \quad (6.30)$$

where $c_1 = 0.2473(1 + \nu_1) + 0.2231(1 - \nu_1^2)$. The asymptotic result for the energy release rate is

$$\frac{G}{G_0^*} = c_2 \left[1 - \left(\frac{\sigma_c^*}{\sigma} \right)^2 \right], \quad (6.31)$$

where $c_2 = [1 + 0.9021(1 - \nu_1)]^{-1}$ and

$$G_0^* = (1 - \nu_1)h\sigma^2/E_1 \quad (6.32)$$

is the strain energy per unit area stored in the unbuckled film.[†] The asymptotic relation between the mode mixity parameter for the interface crack and the buckling deflection is

$$\tan \psi = \frac{\cos \omega + 0.2486(1 + \nu_1)\xi \sin \omega}{-\sin \omega + 0.2486(1 + \nu_1)\xi \cos \omega}. \quad (6.33)$$

For sufficiently small ξ , ψ approaches (6.17), just as in the case of the one-dimensional blister. The asymptotic results are shown in Figs. 64 and 65, where they are compared with the results of an accurate numerical analysis described next.

[†] The expression for c_2 given here corrects the coefficient given by Evans and Hutchinson (1984). Their derivation made use of a result for the initial post-buckling behavior of a clamped circular plate given in the text by Thompson and Hunt (1973), which does not correctly account for the Poisson's ratio dependence. The present result incorporates the corrected solution. The difference between c_2 and the earlier result of Evans and Hutchinson is less than 1% for $\nu_1 = 0.3$.

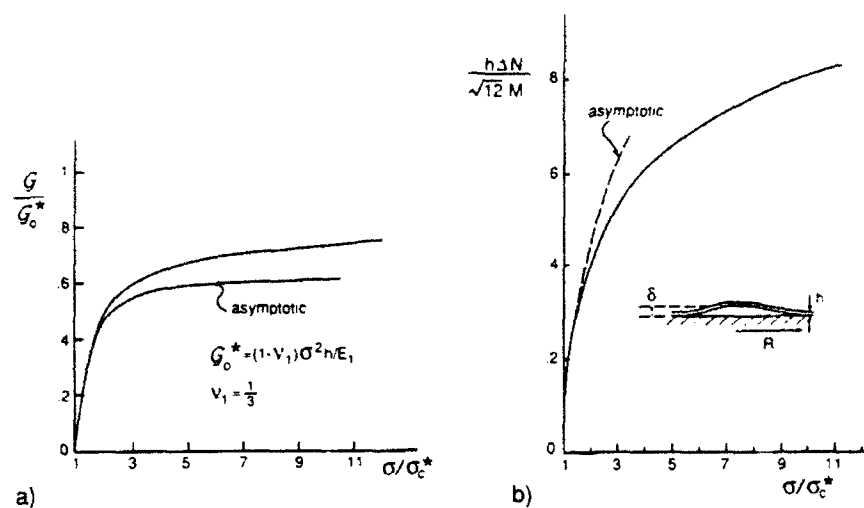


FIG. 64. Energy release rate and edge loading ratio for the circular blister.

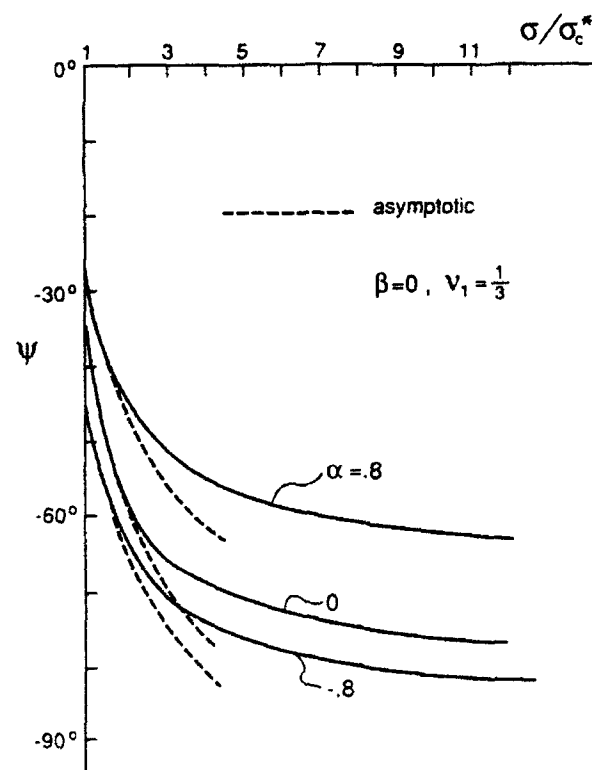


FIG. 65. Phase of loading ψ at interface crack tip for the circular blister for three levels of elastic mismatch.

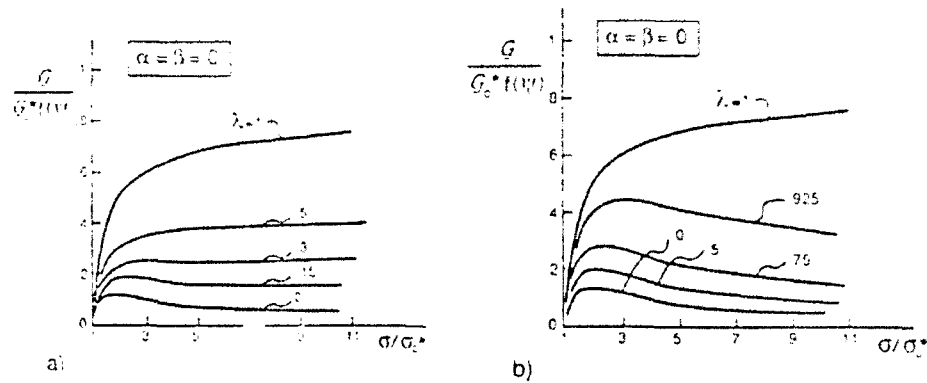


FIG. 66. Mode-adjusted crack driving force for the circular blister: a) based on (6.20); and b) based on (6.21).

3. Numerical Solution for Arbitrarily Large Buckling Deflections

An accurate finite difference method was used to solve the coupled ordinary differential equations (6.23) and (6.24), subject to the stated boundary conditions. Newton iteration was used to obtain a converged solution for each specified value of σ/σ_c^* . All calculations were carried out with $\nu_1 = 1/3$. The results for the quantities of interest are shown in Figs. 64–66. The results for G are in agreement with calculated results of Yin (1985) and Chai (1990), while the present results for ψ for the case of no elastic mismatch are in accord with the trends of G_1 and G_2 presented by Chai. Note that the curve for $h \Delta N/(\sqrt{12}M)$ in Fig. 64 permits ψ to be computed using (6.3) for any elastic mismatch.

The energy release rate of the interface crack increases monotonically with increasing R (decreasing σ_c^*) for the circular blister, as can be seen in Fig. 64. Its approach to G_0^* is very slow. At $\sigma/\sigma_c^* = 50$, $G/G_0^* \cong 0.85$ (not shown in plot). The asymptotic formula (6.31) is reasonably accurate for σ/σ_c^* up to about 3. The asymptotic formula (6.30) for δ/h retains its accuracy to surprisingly large values of σ/σ_c^* . A plot of δ/h is not shown, but, with $\xi \equiv \delta/h$, (6.30) overestimates the accurate numerical result at $\sigma/\sigma_c^* = 10$ by only 7%. As in the case of the one-dimensional blister, buckling deflections that are large compared to the film thickness imply residual stresses that are many times the classical buckling stress σ_c^* of the corresponding plate of film. The asymptotic formula (6.33) for ψ is also valid for values of σ/σ_c^* up to about 2 or 3, as can be seen in Fig. 65. However, ψ does not vary as strongly with σ/σ_c^* for the circular blister as for the one-dimensional blister (*cf.* Fig. 60), a feature also emphasized by Chai (1990). In particular, the interface crack of the circular blister does not

attain pure mode 2 in the range of σ/σ_c^* shown, as its one-dimensional counterpart does. Even for σ/σ_c^* as large as 50, some mode 1 persists with $\psi = -84^\circ$ for $\alpha = \beta = 0$. This feature may be at the heart of why growth of the blisters is favored along a curved front rather than a straight one.

Plots of the normalized crack driving force $G/[G_0^*f(\psi)]$ are shown in Fig. 66 for the same two interface toughness functions, (6.20) and (6.21), used to construct the plots for the one-dimensional blister in Fig. 62. For reasons noted previously, the crack driving force does not fall off nearly as rapidly as the blister spreads as for the one-dimensional blister. The fact that circular blisters have been observed for some systems is indirect evidence for an interface toughness function that increases sharply with increasing mode 2, such as that used in constructing the curves in Fig. 66b.

4. *Tendency toward Spalling as the Blister Spreads*

Circular spalls are observed in some systems where the film is brittle. Evidently, the radius of the blister increases until it reaches a point where the crack kinks out of the interface into the film, spalling out a circular patch of film. The mixed mode conditions at the tip of the interface crack derived in the previous sections contribute to the likelihood of this type of spalling in two ways. First, with reference to the kinking solution in Section II.C.5, one notes that kinking upward into the film is favored energetically as ψ becomes more negative, with the largest value of G_{\max}^I/G attained at $\psi \cong -60^\circ$. Secondly, as the blister spreads and as $|\psi|$ increases, the G needed to advance the interface crack increases, assuming $\Gamma(\psi)$ increases with increasing $|\psi|$. Thus, as the blister spreads, the maximum energy release rate available for a crack kinking into the film, G_{\max}^I , increases. Kinking, and spalling, is to be expected if G_{\max}^I attains the fracture toughness of the film.

C. CONDITIONS FOR STEADY-STATE PROPAGATION OF A STRAIGHT-SIDED BLISTER

An example of the straight-sided blister is shown in Fig. 56 and is sketched in Fig. 67b. Under steady-state conditions, the width of the blister remains fixed and the growth occurs by interface crack advance along the more-or-less circular end of the blister. An approximate analysis of the conditions for steady-state blister propagation is given.

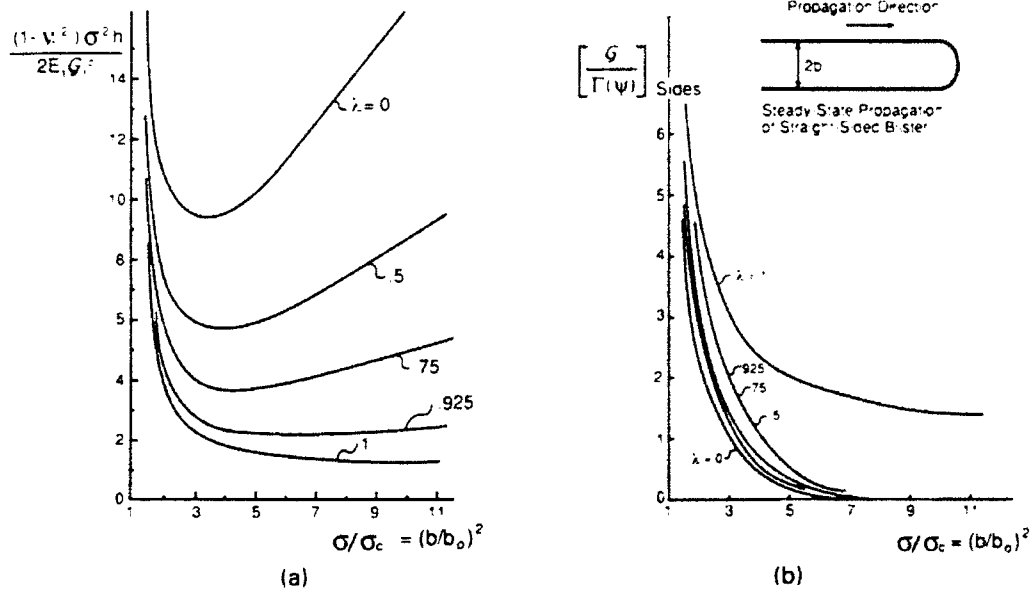


FIG. 67. a) Condition for steady-state propagation of straight-sided blister for the interface toughness function (6.21). b) Mode-adjusted crack driving force on the sides of the straight-sided blister. The condition that the sides are in an arrested state is $G/\Gamma(\psi) < 1$.

Under steady-state conditions, the total energy released per unit advance of the blister is precisely the energy released by a unit length of the one-dimensional blister of Section B.2 in spreading from the smallest width for which the buckle has nonzero amplitude, $2b_0 = 2\pi[D/(\sigma h)]^{1/2}$, to $2b$. Thus, the *average steady-state* energy release rate of the advancing end is

$$G_{ss} = b^{-1} \int_{b_0}^b G db, \quad (6.34)$$

where G is given by (6.16). Noting that σ_c depends on b according to (6.12), one readily obtains

$$G_{ss} = \left(1 - \frac{\sigma_c}{\sigma}\right)^2 G_0. \quad (6.35)$$

It is also useful to note that $b_0/b = (\sigma_c/\sigma)^{1/2}$.

An exact propagation condition would require that G_{ss} be equal to the average of the interface toughness $\Gamma(\psi)$ across the propagating end of the blister. This, in turn, would require knowledge of the precise distribution of ψ across the end of the blister. As an approximation, take

$$G_{ss} = \Gamma(\psi^*), \quad (6.36)$$

where ψ^* is the mode mixity parameter for a full circular blister of radius b subject to the same biaxial stress σ . To see how this generates specific predictions, again represent the interface toughness function as

$$\Gamma(\psi) = G_1^c f(\psi). \quad (6.37)$$

and rewrite the propagation condition (6.36), using (6.35) and (6.15), as

$$\frac{G_0}{G_1^c} \equiv \frac{(1 - \nu_1^2)\sigma^2 h}{2E_1 G_1^c} = \left(1 - \frac{\sigma_c}{\sigma}\right)^{-2} f(\psi^*). \quad (6.38)$$

The right-hand side of this equation is a function of σ/σ_c since ψ^* is a function of σ/σ_c^* (cf. Fig. 65) and $\sigma_c^*/\sigma_c = 1.4876$.

The right-hand side of (6.38) is plotted in Fig. 67a for a choice of $f(\psi)$ used previously, (6.21), for several values of λ . These curves were computed using the solid line curve for ψ^* versus σ/σ_c^* in Fig. 6.10 for the case $\alpha = \beta = 0$ with $\nu_1 = 1/3$. Recall that $\lambda = 0$ corresponds to the interface fracture criterion $K_1 = K_1^c$, while $\lambda = 1$ corresponds to the Griffith criterion $G = G_1^c$. To interpret these curves, it is helpful to present results that display whether or not the parallel sides are in a state consistent with interface crack arrest. For this purpose, the ratio $G/\Gamma(\psi)$ holding on the sides is plotted as a function of σ/σ_c in Fig. 67b, where G is given by (6.16) and ψ is given by (6.14) for the straight-sided blister. The combination of (6.16) and (6.38) gives

$$\frac{G}{\Gamma(\psi)} = \left(1 - \frac{\sigma_c}{\sigma}\right)^{-1} \left(1 + 3 \frac{\sigma_c}{\sigma}\right) \frac{f(\psi^*)}{f(\psi)}, \quad (6.39)$$

which is the expression used in plotting the curves in Fig. 67b. The fact that $G/\Gamma(\psi) \rightarrow 0$ at $\sigma/\sigma_c = 7.55$ for all $\lambda < 1$ is a consequence of unbounded mode 2 toughness assumed in connection with the choice (6.21) for $f(\psi)$.

Consider the curves in Fig 67 for one of the λ -values such that $\lambda < 1$. Note that $[G/\Gamma(\psi)]_{\text{sides}} < 1$ for all values of σ/σ_c greater than or equal to its value at the minimum of $(1 - \nu_1^2)\sigma^2 h/(2E_1 G_1^c)$. Thus, the sides of the blister are in a state consistent with interface crack arrest everywhere to the right of the minimum in Fig. 67a. By contrast, $[G/\Gamma(\psi)]_{\text{sides}}$ exceeds unity for nearly all σ/σ_c to the left of the minimum, implying a lack of consistency with arrest of the sides. One concludes that the relevant branch of each of the curves for $\lambda < 1$ in Fig. 67a is that to the right of the minimum. (The transition $G/\Gamma(\psi)$ so near the minimum may be somewhat fortuitous since the solution is not exact.)

For a particular λ ($\lambda < 1$), the *smallest* value σ consistent with steady-state propagation is given by

$$\frac{(1 - \nu_1^2)\sigma^2 h}{2E_1 G_1^c} = c(\lambda), \quad (6.40)$$

where $c(\lambda)$ denotes the value of the ordinate in Fig. 67a at the minimum. Equivalently, if σ is regarded as prescribed, (6.40) gives the smallest value of film thickness h consistent with steady-state propagation. The half-width of the blister associated with (6.40) is

$$\frac{b}{h} = \frac{\pi}{2\sqrt{3}} \left\{ \frac{d(\lambda)}{[2c(\lambda)]^{1/2}} \right\}^{1/2} \left[\frac{E_1 h}{(1 - \nu_1^2)G_1^c} \right]^{1/4}, \quad (6.41)$$

where $d(\lambda)$ is the value of σ/σ_c at the minimum.

For film stresses σ larger than the minimum in (6.40), or for film thicknesses h larger than the minimum, solutions exist on the branch to the right of the minimum of the curves in Fig. 67a. The associated width of the blister increases with increasing σ . Equation (6.41) continues to apply with (d, c) denoting a point on the curve in Fig. 67a. From a practical standpoint, the minimum is probably of the most interest. For a film stress less than the minimum (or a film thickness less than the minimum), extensive propagation of an initial blister can be avoided.

The behavior associated with the interface fracture criterion $G = G_1^c$ (i.e., $\lambda = 1$) must be discussed separately. From Fig. 67a, one notes that there exists a propagation solution for all values of $(1 - \nu_1^2)\sigma^2 h/(2E_1 G_1^c)$ greater than unity. But, from Fig. 67b, one sees that these solutions are inconsistent with arrest of the interface crack along the sides. Thus, it must be concluded that there exist no steady-state straight-sided blister solutions when the classical criterion $G = G_1^c$ is presumed to hold.

The particular interface toughness function, (6.37) with (6.21), was invoked to illustrate the calculation procedures for steady-state blister propagation and to bring out some of its qualitative features. The example reveals that steady-state blister propagation, as opposed to complete decohesion of the film, is innately tied to the property of the toughness function wherein it increases with increasing proportion of mode 2. Details of the propagation of the straight-sided blister do depend on the specifics of $f(\psi)$. For example, the previous calculations were repeated using (6.20) rather than (6.21). The function $f(\psi)$ in (6.20) levels off as

$|\psi|$ approaches $\pi/2$ as opposed to (6.21), which increases sharply as the mixity approaches pure mode 2. Only for a fairly small range of λ (i.e., $0 \leq \lambda < 0.15$) does there exist a steady-state solution satisfying the conditions discussed in the preceding. For λ in the range $0.15 < \lambda \leq 1$, no solutions exist consistent with interface crack arrest along the straight sides. Whether solutions exist in this range that are characteristic of the telephone cord morphology (*cf.* Fig. 56) is not known. The answer to this question would obviously shed light on the nature of the interface toughness function.

We end this section with some additional speculation on the possible origin of the telephone cord morphology of blister propagation. The approximate solution for the straight-sided blister does not address the issue of the stability of the configuration. For example, is the symmetric configuration (symmetric with respect to the line parallel to, and centered between, the straight sides) stable with respect to nonsymmetric perturbations of the interface crack front? One possibility is that, at sufficiently large values of $(1 - \nu_1^2)\sigma^2 h / (2E_1 G_1^*)$, the steady-state straight-sided configuration becomes unstable. Partial support for this speculation comes from stability results for the circular blister (unpublished work in progress). The circular blister becomes unstable to nonaxisymmetric perturbations of the interface crack front at sufficiently large σ . The value of σ/σ_c^* at which this instability occurs depends on the choice of $\Gamma(\psi)$, but is typically at or above the value associated with the minimum of $(1 - \nu_1^2)\sigma^2 h / (2E_1 G_1^*)$ in the steady-state problem.

VII. Blister Tests

The blister test is used to measure interface toughness for a crack on the interface between a film and a substrate. The test avoids edge effects of various kinds and is highly stable. Although mixed mode conditions prevail at the tip of the interface crack, most approaches to the subject have concentrated on the relation between the energy release rate and the various parameters of the test (Liechti, 1985; and Storakers, 1988). Recent work by Chai (1990) and Jensen (1990) has elucidated the mixed mode character of the test using an approach similar to that described in the previous section. The separated blister is treated by plate theory and is coupled to the 2-layer edge crack solution of Section VI.A.1 to give G and ψ . The results that follow are taken from Jensen (1990).

A. PRESSURE LOADING

A circular blister loaded by a pressure p acting between the film and substrate is depicted in cross-section in the insert in Fig. 68. The film is modeled as a clamped plate of radius R subject to lateral pressure p . At small deflections, within the linear range, the moment at the edge of the plate is

$$M = \frac{1}{8}pR^2, \quad (7.1)$$

and the deflection δ at the center of the plate is

$$\delta = \frac{1}{64}pR^4/D. \quad (7.2)$$

The resultant in-plane stress N is of order p^2 . Thus, for sufficiently small p , by (6.1) and (7.1),

$$G = \frac{3}{32} \frac{(1 - \nu_1^2)}{E_1 h^3} p^2 R^4 = \frac{8}{3} \frac{E_1 h^3 \delta^2}{(1 - \nu_1^2) R^4} \quad (7.3)$$

and, by (6.3),

$$\tan \psi = -\cot \omega \Rightarrow \psi = -((\pi/2) - \omega). \quad (7.4)$$

This is the same combination of mode 1 and 2 that exists for the buckled blisters at small buckling deflections. As in those problems, ψ is defined here with $l = h$. Equation (7.4) is valid for sufficiently small p even in the presence of an initial pre-stress in the film since the change in membrane stress, ΔN , at the edge of the plate is of order p^2 . However, the range of applicability of the formula will depend on the residual stress level.

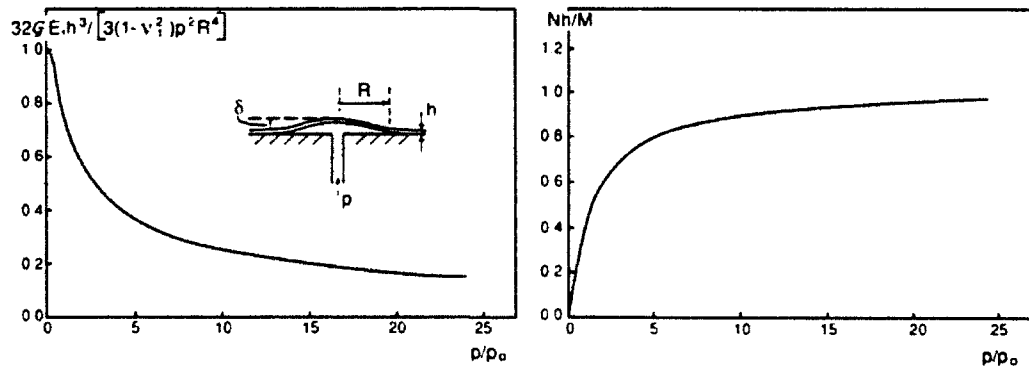


FIG. 68. Energy release rate and ratio of edge loads for a blister under uniform pressure.

There are only a few results in the literature based on rigorous 3-D elasticity solutions that permit a direct assessment of the approximate procedure that couples the plate solution to the 2-layer edge crack solution. Kamada and Higashida (1979) present results for K_1 and K_2 for the case of no elastic mismatch, based on a full elasticity solution to the circular blister loaded by uniform pressure. They find that $\psi = -30^\circ$ for $R/h = 5$ and $\psi = -37^\circ$ for $R/h = 10$. This can be compared with $\psi = -37.9^\circ$ from (7.4) when $\alpha = \beta = 0$. Thus, their results suggest that the approximate procedure is accurate for R/h as small as 10. Erdogan and Arin (1972) have presented results for a penny-shaped blister crack on an interface between materials with the mismatch characteristic of epoxy and aluminum, but a numerical comparison with the present results is not meaningful since the largest value of R/h for which they have reported results is 2.5.

Calculations for G and ψ at large deflections have been carried out by Chai (1990) and Jensen (1990) using the nonlinear von Karman plate equations for the case of no residual pre-stress. Results from Jensen are given in Fig. 68 as plots of a nondimensional G and Nh/M versus p/p_0 , where N is the resultant in-plane radial stress at the edge of the plate and

$$p_0 = \frac{16}{3} \frac{E_1}{(1 - \nu_1^2)} \left(\frac{h}{R} \right)^4. \quad (7.5)$$

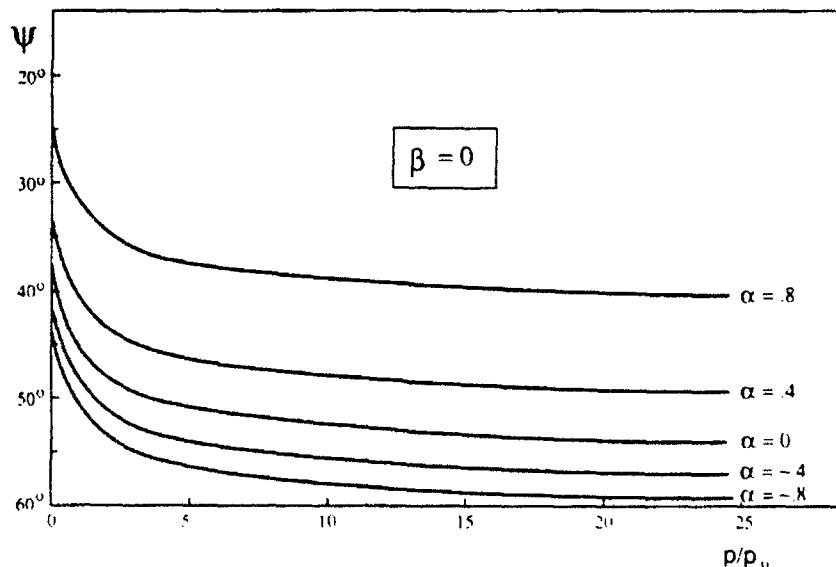


FIG. 69. Phase of loading of interface crack tip for several levels of elastic mismatch for a blister under uniform pressure.

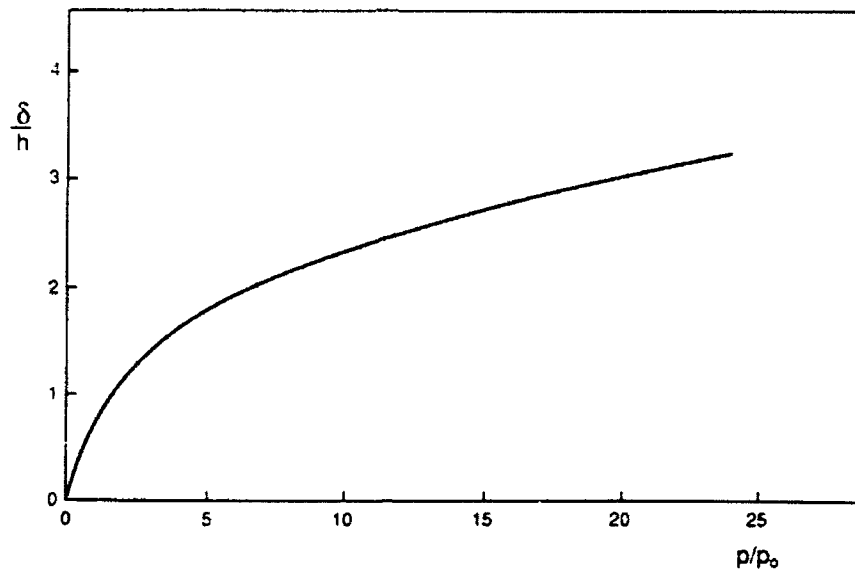


FIG. 70. Deflection-pressure relation for a blister under uniform pressure.

The ratio Nh/M is the basic information needed in (6.3) (with $\Delta N \equiv N$) to generate ψ for any elastic mismatch between the film and substrate. The curves of ψ versus p/p_0 are plotted in Fig. 69 for various α with $\beta = 0$. As p increases, the ratio Nh/M increases giving rise to an increasing proportion of mode 2 to mode 1. The increase only entails a change of ψ of about 15° . For completeness, curves of δ/h versus p/p_0 are shown in Fig. 70. The curves in these figures were computed with $\nu_1 = 1/3$, but they are only weakly dependent on ν_1 .

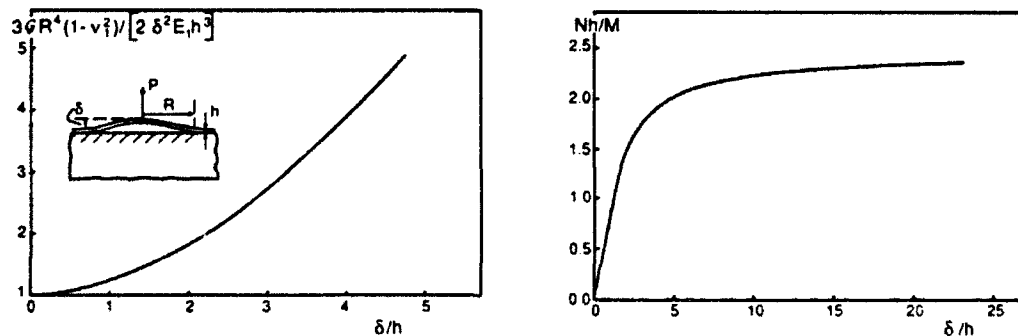


FIG. 71. Energy release rate and ratio of edge loads for a blister under point load.

B. POINT LOADING

The theoretical predictions for a circular blister loaded by a concentrated load P at its center (see insert in Fig. 71) have also been computed by Jensen (1990). In the linear range, the moment at the edge of the clamped plate is

$$M = \frac{1}{4\pi} P, \quad (7.6)$$

and the center deflection is

$$\delta = \frac{3(1 - \nu_1^2)PR^2}{4\pi E_1 h^3}. \quad (7.7)$$

Then, by (6.1),

$$G = \frac{2E_1 h^3 \delta^2}{3(1 - \nu_1^2)R^4}, \quad (7.8)$$

and ψ is again given by (7.4). Curves of a nondimensional G and Nh/M versus δ/h for arbitrarily large δ/h are shown in Fig. 71. Curves of ψ versus δ/h are given in Fig. 72 for various α with $\beta = 0$. The mode dependence is similar to that for the pressurized blister, except with a somewhat larger change in ψ as the deformation becomes nonlinear. The dependence of δ/h on P is plotted in Fig. 73. All these results were computed with $\nu_1 = 1/3$, and initial residual stress is not included.

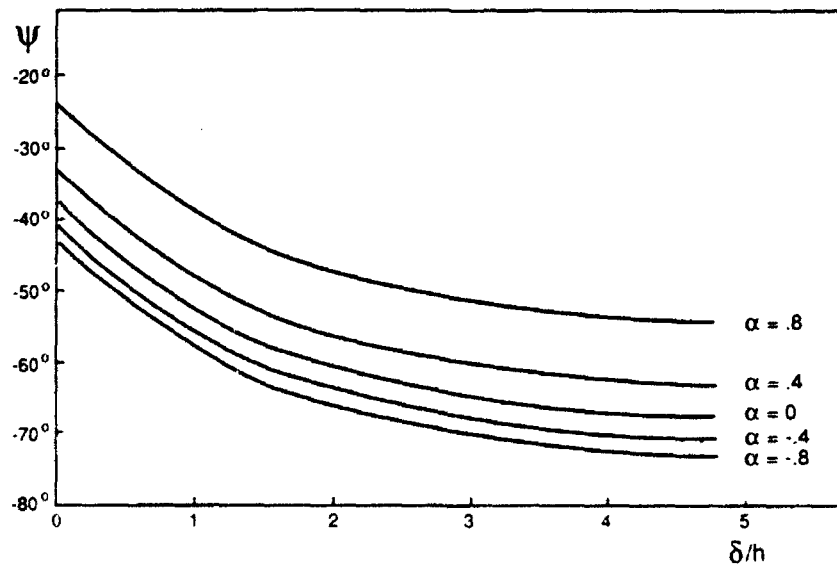


FIG. 72. Phase of loading of interface crack tip for several levels of elastic mismatch for a blister under point load.

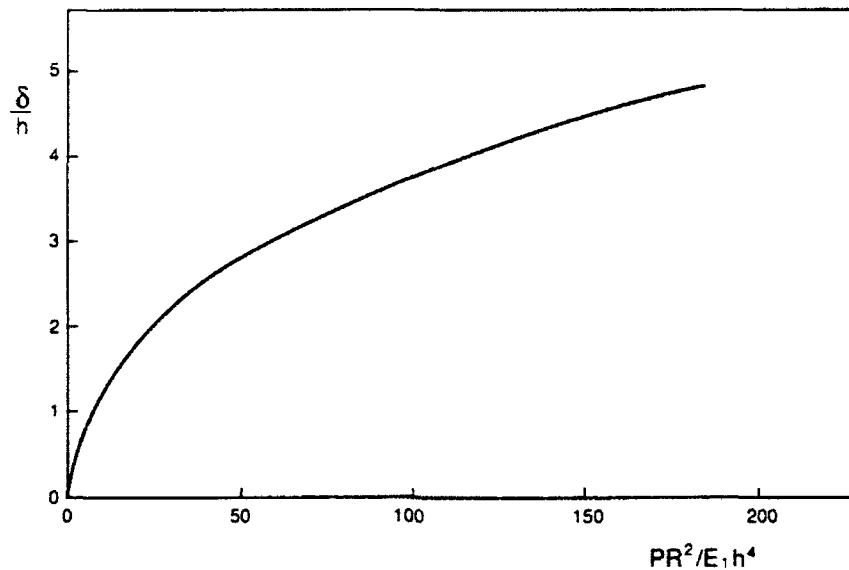


FIG. 73. Deflection-load relation for a blister under point load.

VIII. Failure Modes of Brittle Adhesive Joints and Sandwich Layers

This final section focuses down to a finer scale than has hitherto been addressed in most of this chapter. Attention is directed to modes of cracking of a thin, brittle adhesive layer joining two identical bulk solids. The discussion also has bearing on sandwich specimens, such as those discussed in Section IV.C, which are designed to measure toughness of the interface between the thin layer material and the adjoining material comprising the bulk of the specimen. Figure 74 shows one such sandwich specimen. Below it, at higher magnification, are depicted some of the multitude of cracking morphologies that have been observed in brittle systems. A test series carried out using any such sandwich specimen provides the macroscopic, or effective, interface toughness function $\bar{\Gamma}(\psi)$ characterizing the joint. In assessing the effectiveness of a joint or in making engineering applications, one need not necessarily be concerned with the local cracking morphology. On the other hand, $\bar{\Gamma}(\psi)$ itself may be a strong function of the cracking morphology, and, if so, it is essential to understand what controls the local cracking morphology in any attempt to improve the quality of the joint. Similarly, attempts to measure the interface toughness $\Gamma(\psi)$ between two materials using a sandwich specimen can be defeated by tendencies for an interface crack to misbehave in one of the other modes of cracking.

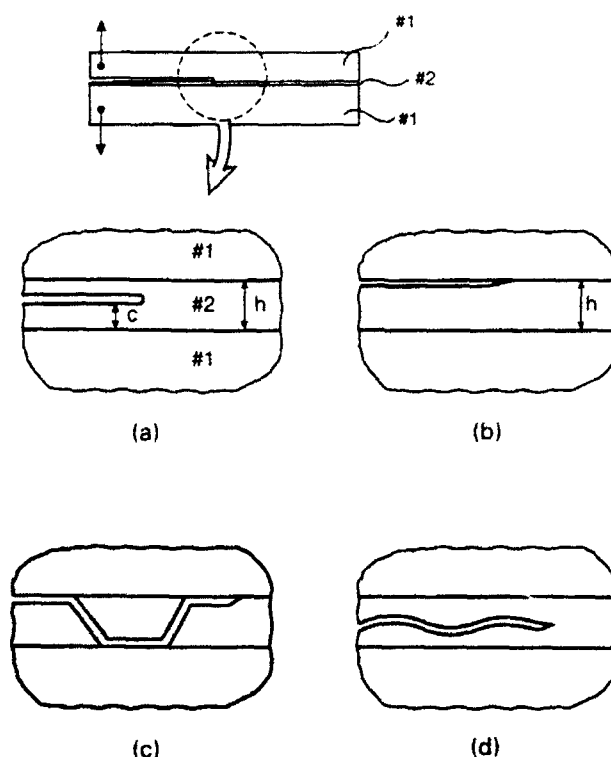


FIG. 74. Modes of cracking in a thin, brittle adhesive layer: (a) straight crack within layer; (b) interface crack; (c) alternating crack; (d) wavy crack.

This section addresses some of the many issues surrounding local cracking morphology. The discussion is restricted to brittle systems for which any inelastic behavior occurs on a scale that is small compared with the layer thickness h . The layer thickness is assumed to be very small compared with the in-plane dimensions of the joint or of the sandwich specimen. At the macroscopic level, the tip of a crack along the joint or layer is characterized by macroscopic, or applied, stress intensity factors K_I^∞ and K_{II}^∞ . As discussed in Section IV, these are determined from a standard analysis that ignores the existence of the thin layer. The macroscopic energy release rate is

$$G^\infty = E_1^{-1}(K_I^{\infty 2} + K_{II}^{\infty 2}), \quad (8.1)$$

where the numbering for the materials is shown in Fig. 74. The effective toughness function of the joint as determined in a test is identified with the critical value of the overall energy release rate at crack advance according to

$$\Gamma(\psi^\infty) = G_c^\infty, \quad (8.2)$$

where $\psi^\infty = \tan^{-1}(K_{II}^\infty/K_I^\infty)$.

A. BASIC RESULTS FOR STRAIGHT CRACKS

1. Straight Crack within the Layer (Fig. 74a)

A simple energy argument or application of the J -integral establishes the equality of G^∞ and the local energy release rate at the tip, G . With K_I and K_{II} as the local stress intensity factors, $G = \bar{E}_2^{-1}(K_I^2 + K_{II}^2)$. The condition $G = G^\infty$, together with (8.1) and linearity in the relation between stresses, allows one to write the connection between the local and applied stress intensity factors such as

$$(K_I + iK_{II}) = \left(\frac{1-\alpha}{1+\alpha}\right)^{1/2} (K_I^\infty + iK_{II}^\infty) e^{i\phi(c/h, \alpha, \beta)}. \quad (8.3)$$

Here, $\phi = \psi - \psi^\infty$ is the shift in the phase angle between the local and applied intensities. Fleck *et al.* (1991) have carried out calculations for ϕ ; they give the approximation

$$\phi = \varepsilon \ln\left(\frac{h}{c} - 1\right) + 2\left(\frac{c}{h} - \frac{1}{2}\right) \tilde{\phi}(\alpha, \beta), \quad (8.4)$$

where $\tilde{\phi}$ is plotted in Fig. 75. This result is unaffected by the presence of a residual stress $\sigma_{11} \equiv \sigma_R$ in the layer.

If the macroscopic specimen is loaded in mode I ($K_{II}^\infty = 0$) and if the crack does propagate down the centerline of the layer (*cf.* discussion in next subsection), then (8.3) gives $K_{II} = 0$ and

$$K_I = \left(\frac{1-\alpha}{1+\alpha}\right)^{1/2} K_I^\infty. \quad (8.5)$$

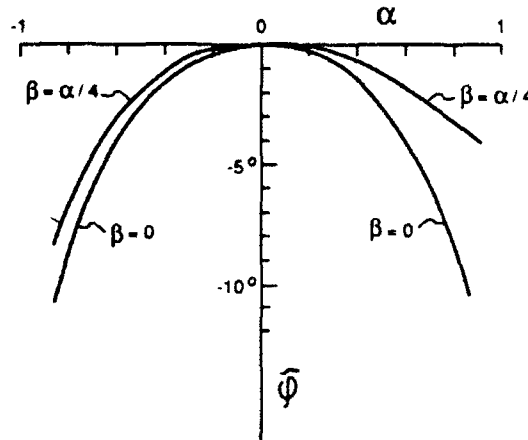


FIG. 75. Phase factor $\tilde{\phi}(\alpha, \beta)$ in (8.4).

This result, which was obtained originally by Wang *et al.* (1978), reveals that a crack within a compliant layer ($\alpha > 0$) is shielded. With K_{Ic} as the intensity toughness of the layer material, the *apparent toughness* measured using the sandwich specimen is

$$K_{Ic}^{\infty} = \left(\frac{1 + \alpha}{1 - \alpha} \right)^{1/2} K_{Ic}. \quad (8.6)$$

An equivalent statement concerning the elastic shielding is that the load needed to fracture the sandwich specimen differs from that needed to fracture a geometrically similar specimen made entirely from the layer material by the factor $[(1 + \alpha)/(1 - \alpha)]^{1/2}$. This factor can be quite large when a stiff material is joined by a compliant adhesive, as is the case when, for example, metal or ceramic parts are joined by a polymer adhesive. If the strength of a joint is controlled by crack-like flaws that are on the order of the adhesive thickness or somewhat larger, then this same magnification factor will apply to the strength of the joint compared to the strength of the bulk adhesive with flaws of similar size. If the controlling flaws are much smaller than the layer thickness, the magnification effect is lost.

3. Crack along the Interface (Fig. 74b)

The relation $G^{\infty} = G$ also holds for this case, where G is related to the interfacial stress intensity factors K_I and K_{II} by (2.29). The equation relating K_I and K_{II} to K_I^{∞} and K_{II}^{∞} is (3.38) with $K_I \equiv K_I^{\infty}$ and $K_{II} \equiv K_{II}^{\infty}$. With ψ for the tip on the interface defined by (2.45) with $l = h$, the ω -quantity in (3.38) is $\psi - \psi^{\infty}$. This shift in phase is generally small and even for the largest elastic mismatches never more than about 15° .

As discussed in Section IV.C, sandwich specimens are attractive for measuring interface toughness. Assuming the crack does advance in the interface, the equation for the interfaces toughness function is simply

$$\Gamma(\psi, l = h) = \bar{\Gamma}(\psi^{\infty}), \quad (8.7)$$

where $\psi = \psi^{\infty} + \omega$. Conversion of $\Gamma(\psi, h)$ to $\Gamma(\hat{\psi}, \hat{l})$ where $\hat{\psi}$ is defined using a material-based length \hat{l} is readily carried out as specified by (2.51).

B. CRACK TRAPPING IN A COMPLIANT LAYER UNDER NONZERO K_{II}^{∞}

Equation (8.3) predicts a strong trapping effect due to elastic mismatch between the layer and the adjoining blocks. When K_{II}^{∞} is not too large

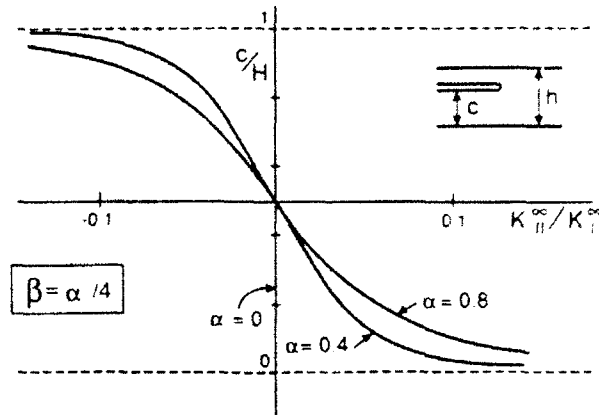


FIG. 76. Location of trapped crack in a compliant sandwich layer.

compared to K_I^∞ , (8.3) reveals the existence of a straight, mode I crack path within the layer. The condition for $K_{II} = 0$ from (8.3) gives the relation between the location of the crack, c/h , and ψ^∞ as

$$\phi(c/h, \alpha, \beta) = -\psi^\infty. \quad (8.8)$$

Since ϕ vanishes when the elastic mismatch vanishes, there can be no straight crack paths within the layer unless $\psi^\infty = 0$ under this circumstance. A plot of the solution to (8.8) is shown in Fig. 76 for several levels of mismatch, all with $\beta = \alpha/4$. When there is significant mismatch, a mode I path well within the layer can exist for $|K_{II}^\infty|$ as large as 10% of K_I^∞ . Such paths exist whether the layer is compliant or stiff, but generally a straight crack in a stiff layer will be configurationally unstable, as will now be discussed.

C. CONFIGURATIONAL STABILITY OF A STRAIGHT CRACK WITHIN THE LAYER

Given the existence of a straight mode I path within the layer, the issue now addressed is whether the path will be insensitive to small perturbations, returning to the straight trajectory, or will be deflected into the interface or possibly into a wavy morphology. Consider a loading with $K_{II}^\infty = 0$ such that the center line through the layer is a mode I crack trajectory. Two results are presented that indicate whether or not the centerline path is configurationally stable.

First, suppose at the start of propagation the crack lies off the centerline (i.e., $c/h \neq 1/2$ in Fig. 74a). From (8.3), with $K_{II}^\infty = 0$,

$$K_{II} = [(1 - \alpha)/(1 + \alpha)]^{1/2} \sin \phi K_I^\infty. \quad (8.9)$$

The offset crack will kink *toward* the centerline if $K_{II} > 0$ when $c/h > 1/2$, and if $K_{II} < 0$ when $c/h < 1/2$. The function ϕ given by (8.4) is odd with respect to the centerline at $c/h = 1/2$. For a compliant layer ($\alpha > 0$) with $\beta = \alpha/4$, ϕ is positive when $c/h > 1/2$, implying by (8.9) that the crack will kink toward the centerline. By contrast, when the layer is stiff ($\alpha < 0$), ϕ is negative when $c/h > 1/2$ and the crack will kink *away* from the centerline. A compliant layer with $\beta = 0$ has a small negative ϕ when $c/h > 1/2$ and would also cause the offset crack to kink away from the centerline. This particular test of configurational stability requires *both* α and β be positive. This same test has been used in Section III.B.1.b for the double cantilever beam, and in Section V.C.2.a for substrate spalling driven by residual tension in the film.

Another insight is provided by the condition for stability of a straight, mode I crack path to small perturbations derived by Cotterell and Rice (1980). Their necessary condition for straight cracking is $T < 0$, where T is the second-order term in the crack tip expansion (2.1). Fleck *et al.* (1991) have solved for T for the crack problem of Fig. 74a. For the centerline crack ($c/h = 1/2$) under $K_{II}^\infty = 0$, they give

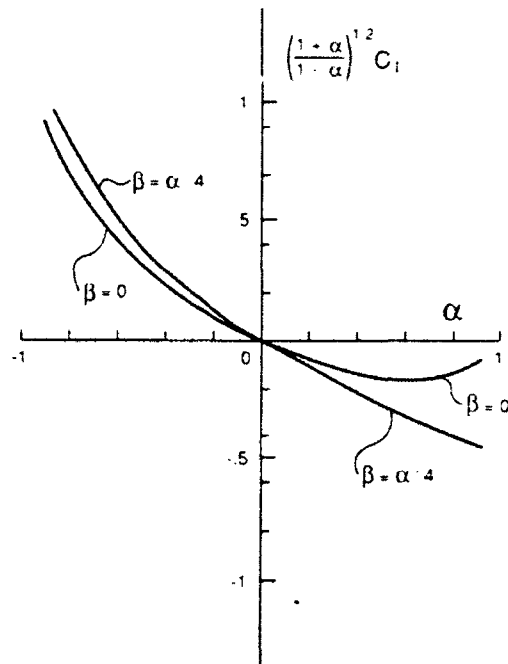
$$T = [(1 - \alpha)/(1 + \alpha)]T^\infty + \sigma_R + c_1(\alpha, \beta)K_I^\infty h^{-1/2}. \quad (8.10)$$

Here, T^∞ is the T -stress for the homogeneous specimen in the absence of the layer, σ_R is the residual stress in the layer acting parallel to the centerline, and c_1 is tabulated by Fleck *et al.* and presented here in Fig. 77. Residual compression parallel to the crack plane contributes to stability, as does a compliant mismatch of the layer relative to the rest of the specimen through the last term in (8.10). The last term in (8.10) is destabilizing when the film is stiff. Note that the residual stress σ_R has no effect on the existence of a mode I path in the layer, just on its stability.

When there is significant elastic mismatch, the first term in (8.10) will usually be insignificant compared to the third term, since T^∞ is typically on the order of $K_I^\infty L^{-1/2}$, where L is a length characterizing an overall dimension of the specimen, which is assumed to be large compared to h . When this is the case, the T -stress at fracture is

$$T \equiv \sigma_R + [(1 + \alpha)/(1 - \alpha)]^{1/2} c_1 K_{Ic} h^{-1/2}, \quad (8.11)$$

where, by (8.6), K_{Ic} is the intensity toughness of the layer material. The requirement $T < 0$ will always be met for a compliant layer supporting a compressive (or zero) residual stress. When the residual stress is tensile, the sign of T depends on which of the preceding terms is larger. Note that the

FIG. 77. Coefficient c_1 in (8.10).

second term in (8.11), which is always negative for a compliant layer, increases in magnitude as the layer thickness diminishes.

A number of examples of sandwich systems that have been reported to exhibit straight in-layer cracking are discussed by Fleck *et al.* (1991), and two of these will be remarked on in what follows. To emphasize the significance of this effect, one can point to the symmetrically loaded, double cantilever beam specimen, which is notoriously unstable in the absence of a layer due to the fact that $T^\infty > 0$. Because of the stabilizing influence of a thin compliant layer, the specimen can be used successfully to measure the toughness of a material in a sandwich layer.

D. INTERFACE OR IN-LAYER CRACKING?

Two sets of toughness data taken using sandwich specimens are shown in Fig. 78. Indicated for each data point is whether the crack propagated along the interface or within the interior of the layer. Thouless's (1990b) data, for a brittle wax layer joining silica glass, is presented as a function of the applied phase angle of loading ψ^∞ . Only for $\psi^\infty = 0$ did the crack propagate within the brittle wax layer. The toughness of the wax was about one half

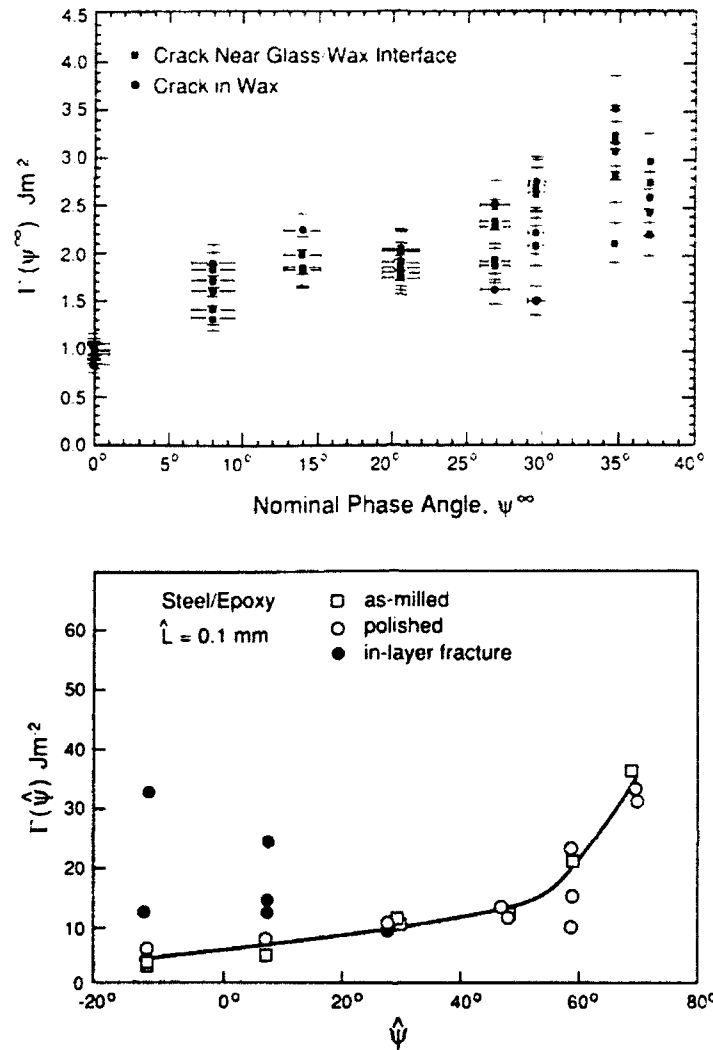


FIG. 78. a) Data of Thouless (1990b) for brittle wax layer sandwiched between glass substrates. b) Data of Wang and Suo (1990) for an epoxy layer between steel substrates.

that of the interface for near-mode-I fracture. The data of Wang and Suo (1990) for an epoxy adhesive layer joining two halves of a steel Brazil nut shows instances of in-layer propagation for $|\hat{\psi}|$ -values as large as about 10° . Moreover, the epoxy is significantly tougher than the interface at low values of $\hat{\psi}$, and the in-layer path involves substantially higher energy dissipation and applied load than the interface path. Nevertheless, a number of specimens did exhibit in-layer propagation. This preference for a high energy path over a low energy path in close proximity highlights the importance of understanding the mechanics of crack path selection. It remains an open question as to why a path down the interface was not selected, especially

since Wang and Suo started their cracks on the interface and observed a small amount of interface crack growth prior to the crack kinking into the interior of the layer. Condition (2.65) for kinking out of the interface, including the influence of the η -contribution, does not appear to be satisfied. This is the feature of the behavior that remains to be explained.

Both sandwich systems in Fig. 78 have a highly compliant layer, and both systems have a tensile residual stress σ_R in the layer. But in each case the second term in (8.11) is at least twice as large in magnitude as σ_R (cf. Fleck *et al.*, 1991, for complete details). Thus, the mode I specimens have a distinctly negative T -stress, and straight cracking within the layer is consistent with the stability theory. By contrast, the plexiglass/epoxy sandwich system of Fig. 9 has relatively small elastic mismatch and a positive T -stress under mode I loading. For this system, the crack always followed one of the two interfaces.

For values of $|\psi^\infty|$ outside the range of possible trapping of the crack within the layer (e.g., $|\psi^\infty|$ greater than 0° to 10° , depending on the mismatch), the crack will be driven toward one interface or the other—toward the lower interface if $\psi^\infty > 0$ and toward the upper if $\psi^\infty < 0$. If material #1 is sufficiently tough to resist any attempts for the interface crack to kink into it, the crack will follow the interface and the test will generate the interface toughness according to (8.7). This is the case for both sets of test data presented in Fig. 78, other than those data points mentioned in the preceding. Various micro-morphologies of interface fracture have been observed, some of which have been discussed by Evans *et al.* (1989). If the interface toughness is low compared with that of both materials #1 and #2, then the crack will tend to follow the interface fairly cleanly. If, however, the interface toughness is comparable to that of the layer material, then the interface crack will interact with flaws in the layer adjacent to the interface, and nucleate microcracks. The effect of the mixed mode loading is to grow these microcracks back towards the interface. The resulting fracture surface will be covered with tiny chunks of the layer material. Additional discussion of the micro-morphology of interface fracture is given by Chai (1988), Wang and Suo (1990), and by several authors in the volume on metal-ceramic interfaces (Rühle *et al.*, 1990).

E. ALTERNATING MORPHOLOGY (Fig. 74c)

In the alternating mode of cracking of Fig. 74c, the crack switches back and forth between interfaces with a fairly regular interval, which is typically

several times the layer thickness. The mode has been reported in matrix layers between plies of a composite when the loading is nominally mode I, and it has been fully documented for mode I loading of an aluminum/epoxy/aluminum sandwich specimen by Chai (1987). Chai used a heat setting epoxy, which gives rise to a relatively high residual tensile stress in the layer ($\sigma_R \approx 60$ MPa), which is more than twice the magnitude of the second term in the T -stress in (8.11) (*cf.* Fleck *et al.*, 1991). Thus, Chai's system has a strongly positive T -stress and is not expected to display straight cracking within the layer.

Akisanya and Fleck (1990) have carried out a quantitative analysis of the alternating mode of cracking with specific attention to the aluminum/epoxy system. Central to the phenomenon is the variation in the proportion of mode 2 to mode 1 of the interface crack as it propagates from the point where it first joins the interface in any given cycle, i.e., at $c = 0$ in Fig. 79. The trends of the variation in ψ found by Akisanya and Fleck are sketched in Fig. 79, where ψ is defined by (2.45) with $l = h$. When $\sigma_R = 0$, ψ rapidly approaches the limiting value given by (3.38) with $K_{II} \equiv K_{II}^\infty = 0$, i.e., $\psi = \omega$. (For the aluminum/epoxy sandwich, $\alpha = 0.93$, $\beta = 0.22$, $\varepsilon = -0.07$ and $\omega \cong -15^\circ$.) However, when $\sigma_R \sqrt{h}/K_I^\infty$ is on the order of unity,

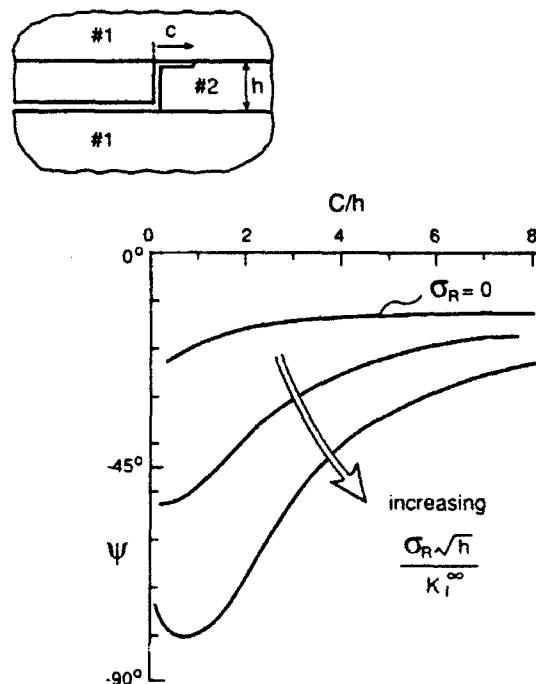


FIG. 79. Sketch of trends of phase of loading at interface crack tip for various levels of residual tension σ_R in the layer. The remote loading is mode I.

which is the case for the Chai specimen, the interface crack starts with a large component of mode 2, which then diminishes to the value $\psi = \omega$ as c/h increases. The large negative mode 2 component forces the crack to remain in the interface, since it cannot penetrate the aluminum. Only when c/h has increased to the point where the magnitude of ψ is sufficiently low does kinking down into the layer become possible. With the aid of the kinking analysis of Section II.C.5, the value of c/h was determined at which a mode I kink crack is possible. For the aluminum/epoxy system of Chai, Akisanya and Fleck found that the kinking condition is met when c/h reaches a value of about 2, in agreement with the intervals observed by Chai.

F. TUNNELING CRACKS

An example illustrating the ability of a crack in a brittle adhesive layer to tunnel through the layer was given in Section III.A.1. If the layer material is sufficiently less tough than the interface and the adjoining material, cracking will be confined to the layer as depicted in Fig. 16. Steady-state tunneling results are useful because they provide fail-safe limits on stress levels (or on layer thicknesses) such that extensive cracking can be avoided. The particular example of Section III.A.1 reveals that an initial crack-like flaw whose greatest dimension is equal to the layer thickness (e.g., a penny-shaped crack) will initiate growth at a stress that is only about 10% higher than the steady-state tunneling stress. For many systems where the flaw size is on the order of the layer thickness, the tunneling results should provide realistic upper limits. When the flaw size is much smaller, the stress to initiate crack growth is much higher than that predicted by the steady-state tunneling limit, and the transient tunneling process is then highly unstable.

Several steady-state tunneling results for layers are presented in this section. The results and their potential applications have a close resemblance to the results for thin-film cracking in Section V.B.

1. *Isolated Tunneling Crack*

As previously emphasized, the energy released, hG_{ss} , per unit length of steady-state propagation of a tunneling crack is precisely the energy released by a plane strain crack extended across the layer. Calculations have been performed for G_{ss} by Ho and Suo (1990) for finite thickness sandwiches, as specified in the insert in Fig. 80. In Fig. 80, σ denotes the uniform tensile

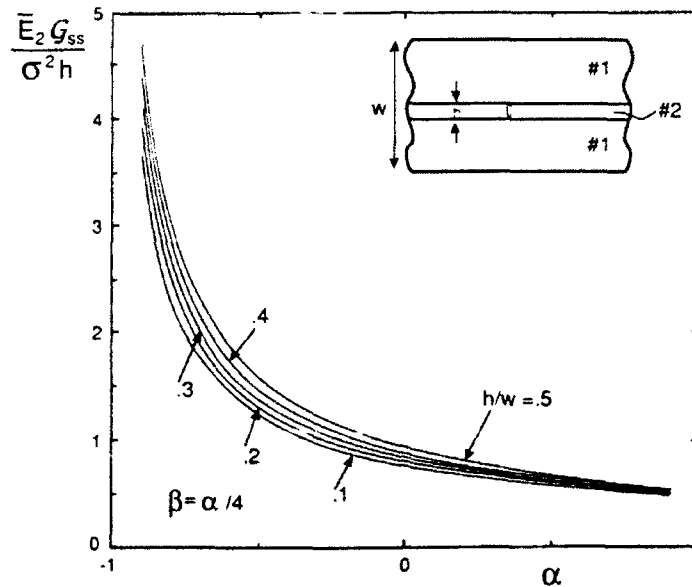


FIG. 80. Steady-state energy release rate for isolated tunneling crack. The crack extends from interface to interface, and is propagating in the direction perpendicular to the cross-section shown.

stress within the central layer prior to introduction of the crack. That stress may be due to a load applied to the sandwich or it may be a self-equilibrated residual stress. Curves of the nondimensional G_{ss} are shown as a function of the elastic mismatch parameter α with $\beta = \alpha/4$ for various values of layer thickness to total thickness, h/w . As long as the central layer is not too stiff compared to the adjoining layers, the results for $h/w = 0.1$ are close to the limiting case $h/w = 0$. For example, for $\alpha = 0$, the normalized G_{ss} is 0.788 for $n/w = 0.1$ and 0.785 for $h/w = 0$. Observe that a relatively compliant substrate (i.e., small E_1 and/or w/h) provides less constraint, inducing higher driving force. It is likely, for the same reason, that higher driving force will be induced by crack-induced plasticity in the substrates, by interface debonding, or by any other source of constraint loss. These effects have been noted in thin film channeling by Hu and Evans (1989).

2. Multiple Tunneling Cracks

The approach to multiple cracking pursued here is identical to that presented in Section V.B.3 for thin films under residual tension. The reader is referred to that section for a more complete discussion of the derivations underlying the results. Here, consideration will be limited to a layer of thickness h sandwiched between two infinitely thick blocks. Elastic mismatch

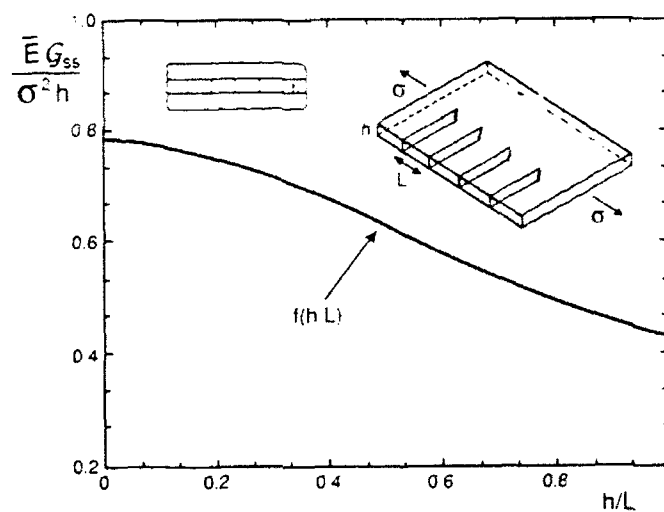


FIG. 81. Steady-state tunneling cracks with uniform spacing, in the absence of elastic mismatch. The cracks extend from interface to interface.

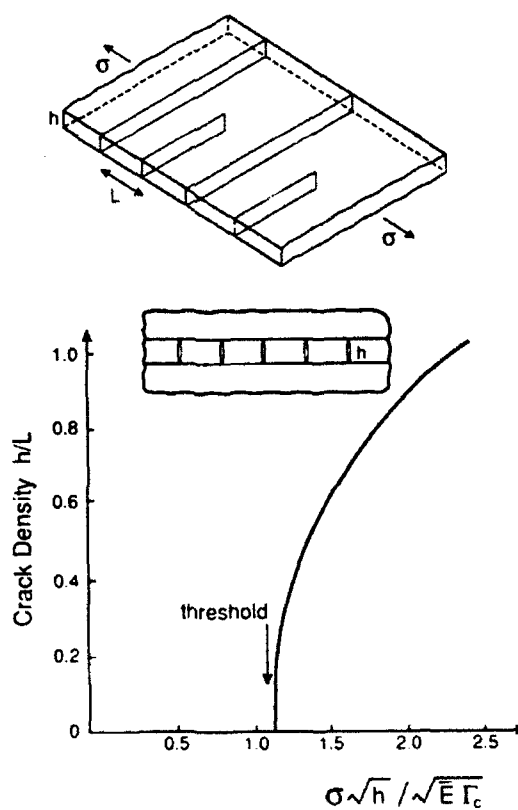


FIG. 82. Relation between tunnel crack density and residual stress in the layer in the absence of elastic mismatch. The curve is obtained from (8.14) with $G_{ss} = \Gamma_c$.

between the layer and the adjoining blocks is neglected ($\alpha = \beta = 0$). The stress in the layer in the absence of the cracks is σ , which may be due to applied load or a residual stress.

First, consider an infinite set of cracks periodically spaced a distance apart as in Fig. 81. If these cracks are equally extended in the tunneling direction,

$$\frac{\bar{E}G_{ss}}{\sigma^2 h} = f(h/L). \quad (8.12)$$

The function $f(x)$, which can be evaluated using results from Tada *et al.* (1985), is plotted in Fig. 81. For $h/L \rightarrow 0$, $f = 0.785$ and (8.12) reduces to (3.1).

Next, consider the situation in Fig. 82 where one set of cracks spaced a distance $2L$ apart has already tunneled across the layer, and where a second set bisecting the first set is in the process of tunneling across the layer. The steady-state energy release rate for the cracks in the process of tunneling is

$$\frac{\bar{E}G_{ss}}{\sigma^2 h} = 2f(h/L) - f(\frac{1}{2}h/L). \quad (8.13)$$

Imagine a process in which σ is monotonically increased, as in application of an overall load or stressing due to temperature change with thermal expansion mismatch. Under the assumption that new cracks will be nucleated half-way between cracks that have already formed and tunneled, the preceding equation gives the relation between σ and the crack spacing h/L . With G_{ss} identified with the mode I toughness of the layer material Γ_c , (8.13) provides the desired relationship, which is plotted in Fig. 82. The threshold corresponds to the lowest stress at which steady-state tunneling can occur, i.e., for $h/L \rightarrow 0$,

$$\sigma[h/(\bar{E}\Gamma_c)]^{1/2} = 1.128. \quad (8.14)$$

The effect of elastic mismatch on this threshold level can be determined using the results for the isolated tunneling crack.

3. Lateral Tunneling of a Kinked Crack

Tunneling appears to be a prevalent mode of cracking in layered materials. When the brittle layer is thin and the flaw size is comparable to the layer thickness, the cracks can be readily nucleated. A variety of applications of these ideas can be found in Ho and Suo (1990) and Ye and Suo (1990). Here, we give one more example to show the versatility.

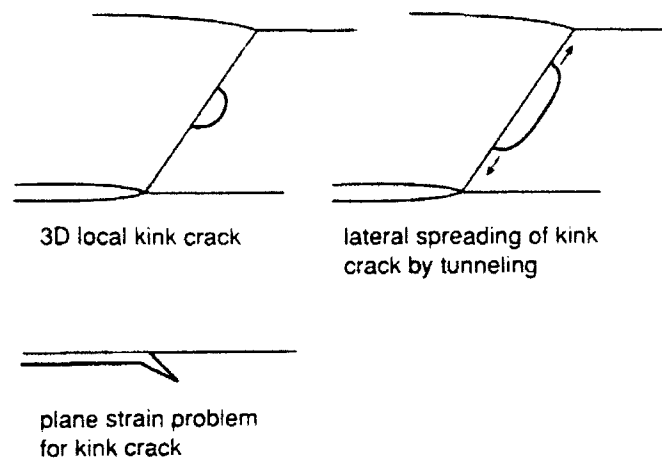


FIG. 83. Spread of a local kink by tunneling. Top left: 3-D local kink crack; top right: lateral spreading of kink crack by tunneling; bottom: plane strain problem for kink crack.

Because it has relevance to the ability of an interface crack to nucleate a kink into the adjoining layer, we mention in passing application of the tunneling concept to crack kinking. Suppose the parent interface crack depicted in Fig. 83 encounters a local, three-dimensional flaw that is capable of nucleating kinking. Consider the process in which the kinked segment of crack "tunnels" laterally along the interface crack front. Formally, this tunneling process can be treated as a steady-state process. The average energy release rate at the laterally spreading crack front can be evaluated using the energy released in the plane strain problem, just as in the previous examples. To simplify the discussion, assume $\beta = 0$ and $\eta = 0$, where η is given by (2.63). Since the energy release rate for the plane strain problem for a small kink is independent of kink crack length (*cf.* Section II.C.5), it follows that the average energy release rate for lateral tunneling along the interface crack front is *equal* to the plane strain energy release rate. Consequently, there is no barrier to the lateral spread of a locally nucleated kink. This observation may help to explain why crack kinking often appears to occur simultaneously along a more-or-less straight segment of crack front.

Acknowledgments

The work of JWH was supported in part by the DARPA University Research Initiative (Subagreement P.O. # VB38639-0 with the University of California, Santa Barbara, ONR Prime Contract N00014-86-K0753), the

Materials Research Laboratory (Grant NSF-DMR-89-20490), and the Division of Applied Sciences, Harvard University. The work of ZS was supported in part by the DARPA University Research Initiative (ONR Prime Contract N00014-86-K0753), the National Science Foundation (Grant MSS-9011571), and the University of California, Santa Barbara.

References

- Akisanya, A. R., and Fleck, N. A. (1990). Analysis of a wavy crack in sandwich specimens. To be published in *Int. J. Fracture*.
- Anderson, G. P., DeVries, K. L., and Williams, M. L. (1974). Mixed mode stress field effect in adhesive fracture. *Int. J. Fracture* **10**, 565-583.
- Argon, A. S., Gupta, V., Landis, H. S., and Cornie, J. A. (1989). Intrinsic toughness of interfaces between SiC coatings and substrates of Si or C fibers. *J. Mater. Sci.* **24**, 1406-1412.
- Atkinson, C., Smelser, R. E., and Sanchez J. (1982). Combined mode fracture via the cracked Brazilian disk test. *Int. J. Fracture* **18**, 279-291.
- Bao, G., Ho, S., Fan, B., and Suo, Z. (1990). The role of material orthotropy in fracture specimens for composites. *Int. J. Solids Structures* (in press).
- Beuth, J. (1990). Cracking of thin bonded films in residual tension. To be published.
- Beuth, J. (1991). Ph.D. thesis research in progress, Harvard University.
- Cannon, R. M., Fisher, R., and Evans, A. G. (1986). Decohesion of thin films from ceramics. In *Proc. Symp. on Thin Films—Interfaces and Phenomena*, Boston, Mass. Mater. Res. Soc. 1986, pp. 799-804.
- Cao, H. C., and Evans, A. G. (1989). An experimental study of the fracture resistance of bimaterial interface, *Mechanics of Materials* **7**, 295-305.
- Chai, H. (1987). A note on crack trajectory in an elastic strip bounded by rigid substrates. *Int. J. Fracture* **32**, 211-213.
- Chai, H. (1988). Shear fracture. *Int. J. Fracture* **37**, 137-159.
- Chai, H. (1990). Three-dimensional fracture analysis of thin film debonding. *Int. J. Fracture* **46**, 237-256.
- Chai, H., Babcock, C. D., and Knauss, W. G. (1981). One dimensional modelling of failure in laminated plates by delamination buckling. *Int. J. Solids Structures* **17**, 1069-1083.
- Charalambides, P. G., Cao, H. C., Lund, J., and Evans, A. G. (1990). Development of test method for measuring the mixed mode fracture resistance of bimaterial interfaces. *Mechanics of Materials* **8**, 269-283.
- Charalambides, P. G., Lund, J., Evans, A. G., and McMeeking, R. M. (1989). A test specimen for determining the fracture resistance of bimaterial interfaces. *J. Appl. Mech.* **56**, 77-82.
- Cherepanov, G. P. (1962). The stress state in a heterogeneous plate with slits (in Russian). *Izvestia AN SSSR, OTN, Mekhan. i Mashin* **1**, 131-137.
- Cherepanov, G. P. (1979). "Mechanics of Brittle Materials." McGraw-Hill, New York.
- Chiao, Y.-H., and Clarke, D. R. (1990). Residual stress induced fracture in glass-sapphire composites: Planar geometry. *Acta Met.* **38**, 251-258.
- Comninou, M. (1977). The interface crack. *J. Appl. Mech.* **44**, 631-636.
- Comninou, M., and Schmueser, D. (1979). The interface crack in a combined tension-compression and shear field. *J. Appl. Mech.* **46**, 345-348.

- Cotterell, B., and Rice, J. R. (1980). Slightly curved or kinked cracks. *Int. J. Fract.* **16**, 155-169.
- Delannay, F., and Warren, P. (1991). On crack interaction and crack density in strain-induced cracking of brittle films on ductile substrates. *Acta Metall. Mater.* **39**, 1061-1072.
- Drory, M. D., Thouless, M. D., and Evans, A. G. (1988). On the decohesion of residually stressed thin films. *Acta Met.* **36**, 2019-2028.
- Dugdale, D. (1960). Yielding of steel sheets containing slits. *J. Mech. Phys. Solids*, **8**, 100-108.
- Dundurs, J. (1969). Edge-bonded dissimilar orthogonal elastic wedges. *J. Appl. Mech.* **36**, 650-652.
- England, A. H. (1965). A crack between dissimilar media. *J. Appl. Mech.* **32**, 400-402.
- Erdogan, F. (1965). Stress distribution in bonded dissimilar materials with cracks. *J. Appl. Mech.* **32**, 403-410.
- Erdogan, F., and Arin, K. (1972). Penny-shaped interface crack between an elastic layer and a half space. *Int. J. Engng. Sci.* **10**, 115-125.
- Evans, A. G., Dalgleish, B. J., He, M., and Hutchinson, J. W. (1989). On crack path selection and the interface fracture energy in bimaterial systems. *Acta Metall.* **37**, 3249-3254.
- Evans, A. G., Drory, M. D., and Hu, M. S. (1988). The cracking and decohesion of thin films. *J. Mater. Res.* **3**, 1043-1049.
- Evans, A. G., and Hutchinson, J. W. (1984). On the mechanics of delamination and spalling in compressed films. *Int. J. Solids Structures* **20**, 455-466.
- Evans, A. G., and Hutchinson, J. W. (1989). Effects of non-planarity on the mixed mode fracture resistance of bimaterial interfaces. *Acta Metall. Mater.* **37**, 909-916.
- Evans, A. G., Rühle, M., Dalgleish, B. J., and Charalambides, P. G. (1990). The fracture energy of bimaterial interfaces. *Mater. Sci. Engng. A* **126**, 53-64.
- Farris, R. J., and Bauer, C. L. (1988). A self-determination method of measuring the surface energy of adhesion of coatings. *J. Adhesion* **26**, 293-300.
- Fleck, N. A., Hutchinson, J. W., and Suo, Z. (1991). Crack path selection in a brittle adhesive layer. *Int. J. Solids and Structures*, **27**, 1683-1703.
- Friedrich, K., ed. (1989). "Application of Fracture Mechanics to Composite Materials." Elsevier, New York.
- Gecit, M. R. (1979). Fracture of a surface layer bonded to a half space. *Int. J. Engng. Sci.* **17**, 287-295.
- Gille, G. (1985). Strength of thin films and coatings. In "Current Topics in Materials Science." Vol. 12 (E. Kaldis, ed.), North-Holland, Chap. 7.
- Hayashi, K. and Nemat-Nasser, S. (1981). Energy-release rate and crack kinking under combined loading. *J. Appl. Mech.* **48**, 520-524.
- He, M.-Y., Bartlett, A., Evans, A. G., and Hutchinson, J. W. (1991). Kinking of a crack out of an interface: role of in-plane stress. *J. Am. Ceram. Soc.* **74**, 767-771.
- He, M.-Y., and Evans, A. G. (1990a). Initial cracking of thin films. Manuscript in preparation.
- He, M.-Y., and Evans, A. G. (1990b). Finite element analysis of beam specimens used to measure delamination resistance of composites. *J. Composites Tech. Res.* (in press).
- He, M.-Y., and Hutchinson, J. W. (1989a). Kinking of crack out of an interface. *J. Appl. Mech.* **56**, 270-278.
- He, M.-Y., and Hutchinson, J. W. (1989b). Kinking of a crack out of an interface: Tabulated solution coefficients. Available for a limited period from Marion Remillard, Pierce Hall 314, Division of Applied Sciences, Harvard University, Cambridge, Massachusetts 02138.
- Ho, S., and Suo, Z. (1990). Tunneling cracks in constrained layers. Manuscript in preparation.
- Hu, M. S., and Evans, A. G. (1989). The cracking and decohesion of thin films on ductile substrate. *Acta Met.* **37**, 917-925.

- Hu, M. S., Thouless, M. D., and Evans, A. G. (1988). The decohesion of thin films from brittle substrates. *Acta Met.* **36**, 1301-1307.
- Hutchinson, J. W. (1990). Mixed mode fracture mechanics of interfaces. In "Metal-Ceramic Interfaces," (M. Rühle, A. G. Evans, M. F. Ashby, and J. P. Hirth, eds.), Pergamon Press, New York, pp. 295-306.
- Hutchinson, J. W., Mear, M. E., and Rice, J. R. (1987). Crack paralleling an interface between dissimilar materials. *J. Appl. Mech.* **54**, 828-832.
- Jensen, H. M. (1990). Mixed mode fracture analysis of the blister test. *Engin. J. Fracture Mech.* (in press).
- Jensen, H. M., Hutchinson, J. W., and Kim, K.-S. (1990). Decohesion of a cut prestressed film on a substrate. *Int. J. Solids Structures* **26**, 1099-1114.
- Kamada, K., and Higashida, Y. (1979). A fracture model of radiation blistering. *J. Appl. Physics* **50**, 4131-4138.
- Kinloch, A. J. (1987). "Adhesion and Adhesives," Chapman and Hall, London.
- Lekhnitskii, S. G. (1981). "Theory of Elasticity of an Anisotropic Body," Mir Publishers, Moscow.
- Liechti, K. M. (1985). Moiré of crack-opening interferometry in adhesive fracture mechanics. *Experimental Mechanics* **25**, 255-261.
- Liechti, K. M., and Chai, Y.-S. (1990a). Asymmetric shielding in interfacial fracture under inplane shear. *J. Appl. Mech.*, in press.
- Liechti, K. M., and Chai, Y.-S. (1990b). Biaxial loading experiments for determining interfacial toughness. *J. Appl. Mech.*, in press.
- Liechti, K. M. and Hanson, E. C. (1988). Nonlinear effects in mixed-mode interfacial delaminations. *Int. J. Fracture* **36**, 199-217.
- Malyshev, B. M., and Salganik, R. L. (1965). The strength of adhesive joints using the theory of cracks. *Int. J. fracture. Mech.* **5**, 114-128.
- O'Brien, T. K. (1984). Mixed-mode strain-energy-release rate effects on edge delamination of composites. In "Effects of Defects in Composite Materials," ASTM STP 836, American Society for Testing and Materials, pp. 125-142.
- O'Dowd, N. P., Shih, C. F., and Stout, M. G. (1990). Test geometries for measuring interfacial toughness. Submitted for publication.
- Reimanis, I. E., and Evans, A. G. (1990). The fracture resistance of a model metal/ceramic interface. *Acta Metall. Mater.* (in press).
- Rice, J. R. (1968). A path independent integral and approximation analysis of strain concentration by notches and cracks. *J. Appl. Mech.* **35**, 379-386.
- Rice, J. R. (1988). Elastic fracture concepts for interfacial cracks. *J. Appl. Mech.* **55**, 98-103.
- Rice, J. R., and Sih, G. C. (1965). Plane problems of cracks in dissimilar media. *J. Appl. Mech.* **32**, 418-423.
- Rice, J. R., Suo Z., and Wang, J.-S. (1990). Mechanics and thermodynamics of brittle interfacial failure in bimaterial systems. In "Metal-Ceramic Interfaces". (M. Rühle, A. G. Evans, M. F. Ashby, and J. P. Hirth, eds.), Pergamon Press, New York, pp. 269-294.
- Rothschilds, R. J., Gillespie, J. W., and Carlsson, L. A. (1988). Instability-related delamination growth in thermoset and thermo-plastic composites. In "Composite Materials: Testing and Design," ASTM STP 972 (J. D. Whitcomb, ed.), pp. 161-179.
- Rühle, M., Evans, A. G., Ashby, M. F., and Hirth, J. P., eds. (1990). "Metal-Ceramic Interfaces," Acta-Scripta Metallurgica Proc. Series 4, Pergamon Press, New York.
- Sbaizero, O., Charalambides, P. G., and Evans, A. G. (1990). Delamination cracking in a laminated ceramic matrix composite. *J. Am. Ceram. Soc.* **73**, 1936-1940.
- Shapery, R. A., and Davidson, B. D. (1990). Prediction of energy release rate for mixed-mode delamination using classical plate theory. *Appl. Mech. Rev.* **43**, S281-S287.

- Shih, C. F., and Asaro, R. J. (1988). Elastic-plastic analysis of cracks on bimaterial interfaces: Part I. Small scale yielding. *J. Appl. Mech.* **55**, 299-316.
- Sih, G. C., Paris, P. C., and Irwin, G. R. (1965). On cracks in rectilinearly anisotropic bodies. *Int. J. Fracture Mech.* **1**, 189-203.
- Spearing, S. M., and Evans, A. G. (1990). The role of fiber bridging in the delamination resistance of fiber-reinforced composites. *Acta Metall. Mater.* (in press).
- Storakers, B. (1988). Nonlinear aspects of delamination in structural members. In "Proc. XVIIth Int. Cong. Theor. Appl. Mech." (P. Germain, *et al.*, eds.), Grenoble, France, Elsevier, 315-336.
- Suga, T., Ellsner, E., and Schmander, S. (1988). Composite parameters and mechanical compatibility of material joints. *J. Composite Materials* **22**, 917-934.
- Suo, Z. (1989). Singularities interacting with interfaces and cracks. *Int. J. Solids Structure* **25**, 1133-1142.
- Suo, Z. (1990a). Singularities, interfaces and cracks in dissimilar anisotropic media. *Proc. R. Soc. Lond. A* **427**, 331-358.
- Suo, Z. (1990b). Failure of brittle adhesive joints. *Appl. Mech. Rev.* **43**, S276-S279.
- Suo, Z. (1990c). Delamination specimens for orthotropic materials. *J. Appl. Mech.* **57**, 627-634.
- Suo, Z., Bao, G., and Fan, B. (1990a). Delamination *R*-curves phenomena due to damage. *J. Mech. Phys. Solids* (in press).
- Suo, Z., Bao, G., Fan, B., and Wang, T. C. (1990b). Orthotropy rescaling and implications for fracture in composites. *Int. J. Solids and Structures*, in press.
- Suo, Z., and Hutchinson, J. W. (1989a). On sandwich test specimen for measuring interface crack toughness. *Mater. Sci. Engng. A* **107**, 135-143.
- Suo, Z., and Hutchinson, J. W. (1989b). Steady-state cracking in brittle substrate beneath adherent films. *Int. J. Solids Structure* **25**, 1337-1353.
- Suo, Z., and Hutchinson, J. W. (1990). Interface crack between two elastic layers. *Int. J. Fracture* **43**, 1-18.
- Tada, H., Paris, P. C., and Irwin, G. R. (1985). "The Stress Analysis of Cracks Handbook," Del Research, St. Louis, Missouri.
- Thompson, J. M. T., and Hunt, G. W. (1973). "A General Theory of Elastic Stability," Wiley, New York.
- Thouless, M. D. (1990a). Crack spacing in brittle films on elastic substrates. *J. Am. Ceram. Soc.* **73**, 2144-2146.
- Thouless, M. D. (1990b). Fracture of a model interface under mixed-mode loading. *Acta Met.* **38**, 1135-1140.
- Thouless, M. D., Cao, H. C., and Mataga, P. A. (1989). Delamination from surface cracks in composite materials. *J. Mater. Sci.* **24**, 1406-1412.
- Thouless, M. D., Evans, A. G., Ashby, M. F., and Hutchinson, J. W. (1987). The edge cracking and spalling of brittle plates. *Acta Met.* **35**, 1333-1341.
- Thouless, M. D., and Evans, A. G. (1990). Comment on the spalling and edge-cracking of plates. *Scripta Met. and Mater.* **24**, 1507-1510.
- Trantina, G. C. (1972). Combined mode crack extension in adhesive joints. *J. Composite Materials* **6**, 271-285.
- Wang, J. S., and Suo, Z. (1990). Experimental determination of interfacial toughness using Brazil-nut-sandwich. *Acta Met.* **38**, 1279-1290.
- Wang, S. S., Mandell, J. F., and McGarry, F. J. (1978). An analysis of the crack tip stress field in DCB adhesive fracture specimens. *Int. J. Fracture* **14**, 39-58.
- Wang, T. C., Shih, C. F., and Suo, Z. (1990). Crack extension and kinking in laminates and bicrystals. *Int. J. Solids Structures* (in press).

- Whitcomb, J. D. (1986). Parametric analytical study of instability-related delamination growth. *Compos. Sci. Technol.* **25**, 19-48.
- Williams, J. G. (1988). On the calculation of energy release rates for cracked laminates. *Int. J. Fracture* **36**, 101-119.
- Williams, M. L. (1959). The stress around a fault or crack in dissimilar media. *Bull. Seismol. Soc. Am.* **49**, 199-204.
- Ye, T., Suo, Z., and Evans, A. G. (1990). Thin film cracking and the roles of substrate and interface. Submitted for publication.
- Yin, W.-L. (1985). Axisymmetric buckling and growth of a circular delamination in a compressed laminate. *Int. J. Solids Structures* **21**, 503-514.
- Zak, A. R., and Williams, M. L. (1963). Crack point singularities at a bi-material interface. *J. Appl. Mech.* **30**, 142-143.
- Zdaniewski, W. A., Conway, J. C., and Kirchner, H. P. (1987). Effect of joint thickness and residual stress on the properties of ceramic adhesive joints: II. Experimental results. *J. Am. Ceram. Soc.* **70**, 104-109.

Crazing of laminates

Jean LEMAITRE **, **Frederick A. LECKIE *** and **Dov SHERMAN ***

ABSTRACT. — The main features of the behavior of a brittle-ductile type of laminates are derived from a one-dimensional study which emphasizes the mechanism of cracking-debonding. The analysis is based upon a shear lag model and the experiments are performed on an alumina-graphite epoxy laminate. The sequence of cracking-debondings giving rise to crazes is pointed out with a limiting value of the crack spacing due to a debonding length found to be of the same order of magnitude as the thickness of the layers. The reduction of stiffness due to crazes is also calculated, measured and used to find the homogenized behavior of the laminate as an elastic damaged material.

1. Introduction

The laminates considered in this study are made of alternative layers of brittle and ductile thin sheets. This system is a compromise which benefits from the high strength of brittle materials such as ceramics but avoids brittle failure by providing toughness [Evans, 1990], [Lange, Marshall & Folsom, 1990]. For high temperature use laminates consisting of alumina and Inconel bonded by a diffusion process could conceivably result in high strength tough materials with good creep resistance properties. It is not difficult to visualize other combinations which would provide the properties dictated by different design requirements. It is likely that a wide range of properties can be predicted by a generic mechanics which describes the underlying mechanisms and the purpose of this study is to understand and model the mechanisms of failure by cracking and debonding as a function of the laminate parameters. As a consequence, several simplified hypotheses are introduced to obtain analytical results which have to be considered as qualitative. In particular, the sequence of debonding and cracking, the length of debonding, the limit of the crack spacing, the reduction of stiffness may be described using the one-dimensional problem described in this study. The crack growth in two dimensions is studied in a later report.

Many investigators have used shear lag models to study the transverse matrix cracking in cross-ply laminates [Garrett & Bailey, 1977], [Parvizi & Bailey, 1978], [Bailey, Curtis

* Department of Mechanical and Environmental Engineering, University of California, Santa Barbara, CA 93106, U.S.A.

** Professor, Université Paris-VI, L.M.T., 61, Avenue du Président-Wilson, 94235 Cachan Cedex, France. Visiting Professor at U.C.S.B.

& Parvizi, 1979] based on the early work of [Cox, 1952] and on a deterministic location of the cracks. Latter on several works appear introducing statistics in the location of the cracks either by a Weibull strength distribution [Manders *et al.*, 1983], [Fukunaga *et al.*, 1984] or by a distribution of initial flaw sizes [Wang & Crossman, 1986] or by a probability density function associated with the transverse cracking [Laws & Dvorak, 1988]. The present work mainly emphasizes the effects of debonding, general order of magnitude of debonding length and limiting crack spacing and some practical considerations helpful in the design of laminates.

2. Basic one-dimensional problem

The debond lengths and cracking spacing are governed by the state of stress in the interface and in the brittle layer. To determine the crack spacing let us consider the one-dimensional case of two layers for which B brittle and D ductile. The portion of the laminate between two adjacent cracks is shown in Figure 1.

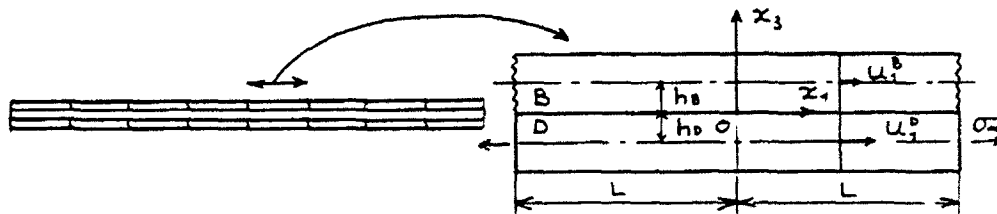


Fig. 1. - Laminate and its basic cell.

The geometrical and material properties used in this work are the following.

	Brittle material	Ductile material	Interface
Thickness.....	$2h_B$	$2h_D$	0
Length.....	$2L$	$2L$	$2L$
Linear elasticity:			
Young's modulus.....	E_B	E_D	G_i shear modulus
Brittle failure or debonding:			
Strain energy density release rate.....	Y_i^B	-	Y_i^D
Perfect plasticity:			
Yield stress.....	-	σ_i^D	

The laminate is supposed to be free of any initial residual stresses.

Three convenient groups of parameters are defined:

$$E_r = \frac{E_B h_B + E_D h_D}{h_B + h_D} \quad \text{such that} \quad \sigma_r = E_r \epsilon_r.$$

$$h = \left(\frac{2 h_B h_D E_B E_D}{G_i E_r} \right)^{1/2} \quad \text{which is of the order of magnitude of the layer thickness } 2h.$$

$$k = \left(\frac{2 G_i h_B E_B}{E_D h_D E_D} \right)^{1/2} \quad \text{which is of the order of unity.}$$

The loading consists of a farfield tensile stress σ_1 . The stresses σ_{11}^B in the brittle material, σ_{11}^D in the ductile material and σ_{13}^i in the interface may be determined as functions of the coordinate x_1 using the so-called Shear Lag Theory developed on the basis of three hypothesis which are now discussed.

H1 KINEMATIC HYPOTHESIS

The displacement u_1 in B and D is linear in x_3 for $-h_D < x_3 < +h_B$. Let us call:

$$\begin{aligned} u_1^B(x_1) &= u_1(x_1, x_3 = h_B), & \epsilon_{11}^B &= \frac{\partial u_1^B}{\partial x_1}, \\ u_1^D(x_1) &= u_1(x_1, x_3 = -h_D), & \epsilon_{11}^D &= \frac{\partial u_1^D}{\partial x_1}, \\ u_1(x_1, x_3) &= \frac{u_1^B(h_D + x_3) + u_1^D(h_B - x_3)}{h_B + h_D}. \end{aligned}$$

H2 APPROXIMATION

The displacement u_3 does not depend upon x_1 . This allows us to calculate the shear strain at the interface

$$\epsilon_{13}^i = \frac{1}{2} \left(\frac{\partial u_1}{\partial x_3} + \frac{\partial u_3}{\partial x_1} \right) = \frac{1}{2} \frac{u_1^B - u_1^D}{h_B + h_D}$$

and the shear stress σ_{13}^i from the law of elasticity $\sigma_{13}^i = 2 G_i \epsilon_{13}^i$ from which $\partial \sigma_{13}^i / \partial x_1 = (G_i / (h_B + h_D)) (\epsilon_{11}^B - \epsilon_{11}^D)$.

H3 ONE DIMENSIONAL PROBLEM

The stresses induced by the mismatch of the contractions of the two layers are neglected so that the only non-stress component is σ_{11}^B or σ_{11}^D .

This allows us to replace the strains by the stresses through the law of elasticity

$$\begin{aligned} \epsilon_{11}^B &= \frac{\sigma_{11}^B}{E_B}, & \epsilon_{11}^D &= \frac{\sigma_{11}^D}{E_D}, \\ \frac{d\sigma_{13}^i}{dx_1} &= \frac{G_i}{h_B + h_D} \left(\frac{\sigma_{11}^B}{E_B} - \frac{\sigma_{11}^D}{E_D} \right). \end{aligned}$$

This is the first stress equation for the three unknowns: σ_{13}^i , σ_{11}^B , σ_{11}^D . The others are calculated using the equilibrium conditions (Fig. 2).

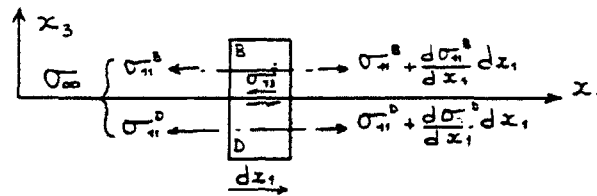


Fig. 2. - Equilibrium of the layers.

They involve integrals of stresses over the thickness but since u_1 is linear with x_3 , ϵ_{11} and σ_{11} are also linear so that

$$\int_0^{2h_B} \sigma_{11}(x_3) dx_3 = 2h_B \sigma_{11}^B, \quad \int_{-2h_D}^0 \sigma_{11}(x_3) dx_3 = 2h_D \sigma_{11}^D.$$

From consideration of equilibrium of each of the layers:

$$2h_B \frac{d\sigma_{11}^B}{dx_1} - \sigma_{13}^i = 0,$$

$$2h_D \frac{d\sigma_{11}^D}{dx_1} + \sigma_{13}^i = 0$$

whilst overall equilibrium of the system in the x direction gives

$$\sigma_{11}^B h_B + \sigma_{11}^D h_D = \sigma_x (h_B + h_D).$$

An equation in σ_{11}^B may be obtained from the differential equation in σ_{13}^i in which expressions for σ_{11}^D and $\partial \sigma_{13}^i / \partial x_1$ are taken from the equilibrium equations to give

$$\frac{d\sigma_{11}^B}{dx_1^2} - \frac{\sigma_{11}^B}{h^2} + \frac{E_B}{E_x} \frac{\sigma_x}{h^2} = 0$$

where the parameters E_x and h were defined earlier.

The solution of the differential equation is:

$$\sigma_{11}^B = A_1 \exp\left(\frac{x_1}{h}\right) + A_2 \exp\left(-\frac{x_1}{h}\right) + \frac{E_B}{E_x} \sigma_x.$$

The boundary conditions:

$$x_1 = L \rightarrow \sigma_{11}^B = 0 \text{ because of the two end cracks,}$$

$$x_1 = 0 \rightarrow \sigma_{13}^i = 0 \text{ from the symmetry condition}$$

give the solution

$$\sigma_{13}^i = \sigma_x k \frac{\sinh x_1 h}{\cosh L h} (-1)$$

$$\sigma_{11}^R = \sigma_x \frac{E_R}{E_x} \left(1 - \frac{\cosh x_1 h}{\cosh L h} \right)$$

$$\sigma_{11}^D = \sigma_x + \frac{h_B}{h_D} (\sigma_x - \sigma_{11}^R)$$

where k is the parameter defined in the matrix. The stress distributions are plotted in the dimensionless form shown in Figure 3.

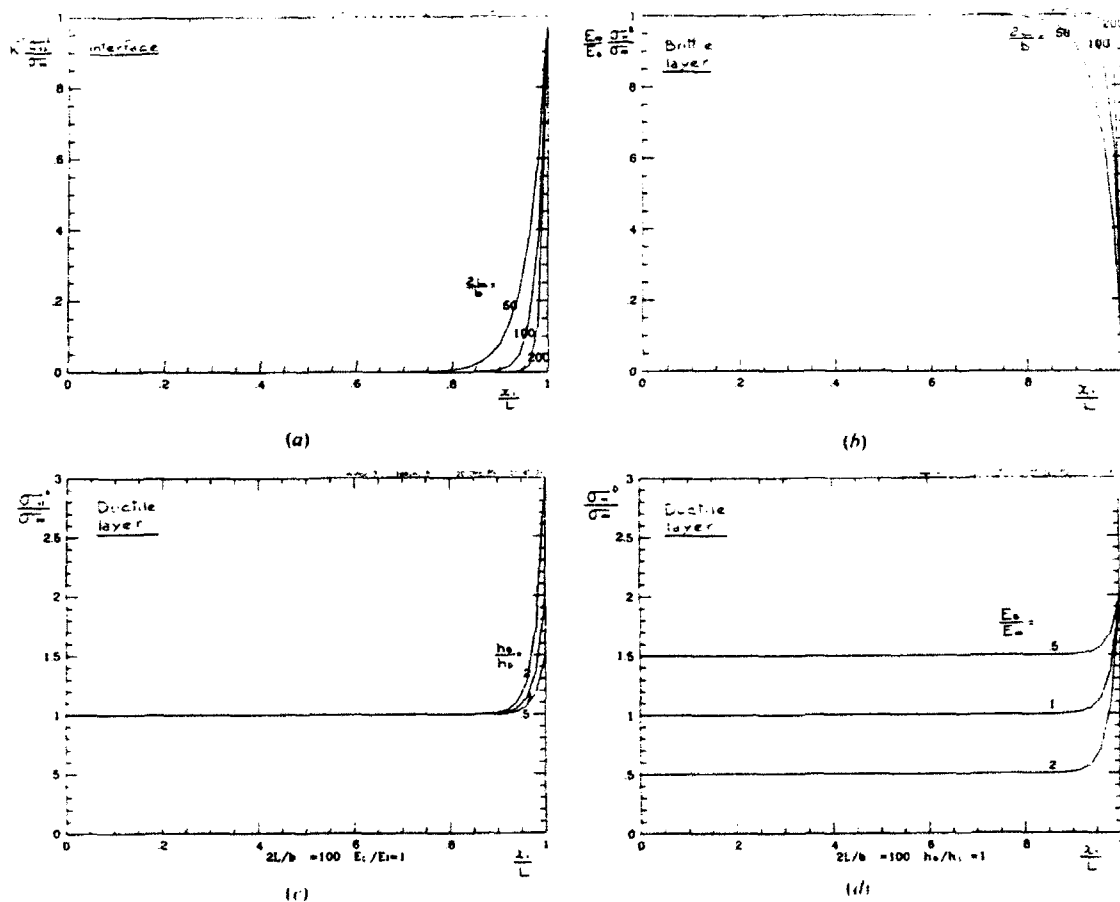


Fig. 3. — Stress distribution in the basic laminate cell.

These curves give the classical results of a shear lag analysis that is the basis of the mechanism of debonding and cracking of the laminate.

It is the length x_1^* of the edge effect in which the stresses strongly increase or decrease is very small $x_1^* L \sim 10^{-6}$.

The stress gradient is very large in that region which models the stress singularity which occur in the exact solution.

3. Mechanism of damage by crazing

3.1. DESCRIPTION OF THE DEBONDING-CRACKING MECHANISM

Consider a monotonic increase of the applied stress σ_x from the curves of Figure 3, and assuming at first that no plastic yielding occurs in the ductile layer, the first event to occur is a debonding of the interface at the two edges in the vicinity of $x_1 = \pm L$. The condition for debonding is $Y^i \geq Y_c^i$.

From damage mechanics, the strain energy release rate density Y is the variable associated with the damage variable D defined as the surface density of debonding. If linear elasticity is coupled to damage then Y is derived from the elastic strain energy density w_e as [Lemaitre & Chaboche, 1990]

$$Y = - \frac{\partial w_e}{\partial D} = \frac{\sigma^2}{2E} \quad \text{in pure tension} \quad \text{and} \quad Y = \frac{\tau^2}{2G} \quad \text{in pure shear.}$$

The length of debonding l_1 is defined by the set of x_1 where

$$\frac{1+\nu_i}{E_i} \sigma_{13(x_1)}^2 \geq Y_c^i \quad \text{or} \quad \sigma_{13(x_1)}^i \geq \left(\frac{E_i}{1+\nu_i} Y_c^i \right)^{1/2} = \tau_c^i \quad \text{for convenience.}$$

This criterion assumes that the length at which the debonding stops is given by a static calculation based upon the elastic stress distribution some what similar to that used to define the process zone size at the front of a crack in small scale yielding. Kinetic and dynamic effects, blunting at the tip of the debonding zone are not taken into account.

Taking the expression of σ_{13}^i as a function of x_1 gives

$$\sinh\left(\frac{L-l_1}{h}\right) = \frac{\tau_c^i}{\sigma_x} \frac{\cosh L}{k} \frac{h}{k}.$$

The approximation for $L/h \gg 1$ then gives $l_1 \cong h \ln(k(\sigma_x/\tau_c^i))$.

Numerical applications to practical cases show that the ratio $\sigma_x / \tau_c^i \geq 2$ to 3. Then, l_1 is of the order of h , which is the order of magnitude of the layer thickness $2h$. This is the first important qualitative result shown in Figure 4. $l_1 \sim 2h$.

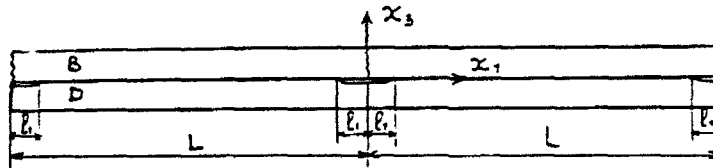


Fig. 4. - Debonding cracking mechanism.

Referring to Figure 4 we may consider that after these two debondings and with zero friction in the debonded zones, the effective length to be considered in the stress equation is no longer L but $L - l_1$. In particular in the brittle layer

$$\sigma_{11}^B = \sigma_x \frac{E_B}{E_T} \left(1 - \frac{\cosh x_1/h}{\cosh((L-l_1)/h)} \right).$$

This result shows that to support the same applied stress σ_x , the magnitude σ_{11}^B should increase due to the decrease of the characteristic length from L to $(L-l_1)$. If so or for an increase of σ_x , its maximum value upon x_1 , that is for $x_1=0$ may reach the condition for brittle failure: $Y^B = Y_c^B$.

In pure tension: $Y^B = (\sigma_{11}^B)^2 / 2 E_B$.

Then the brittle failure occurs when $\sigma_{11}^B = (2 E_B Y_c^B)^{1/2} = \sigma_c^B$ (for convenience) which corresponds to the applied stress derived from the expression of σ_{11}^B with $x_1=0$

$$\sigma_x = \frac{E_T}{E_B} \sigma_c^B \left(1 - \frac{1}{\cosh((L-l_1)/h)} \right)^{-1}.$$

As the crack appears it induces a free edge condition at $x_1=0$ ($\sigma_{11}^B(x_1=0)=0$) which produces the quasi-singularity of the shear stress in the interface and the condition for immediate debonding (Fig. 4)

$$\sigma_{13}^i \geq \tau_c^i \rightarrow \text{debonding for } -l_1 < x < l_1.$$

3.2. SEQUENCE OF DEBONDINGS-CRACKINGS

As the external applied stress σ_x continues to increase, the length of the previous debondings increases until the condition of a new cracking is reached.

This sequence of debonding and cracking mechanisms repeats itself as σ_x increases with a cell length divided by two at each new crack formation and diminished by $2l_1$ at

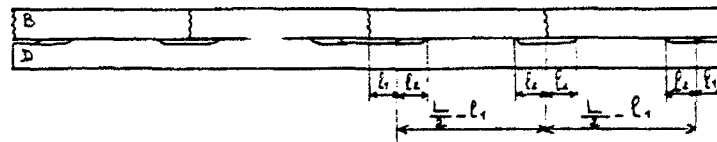


Fig. 5. - Second debonding-cracking mechanism

each debonding (Fig. 5). We now calculate the condition of the second debonding-cracking sequence.

The same formula applied either for debonding or cracking except that the length of half the basic cell is now $(L - 2l_1)/2$.

Then the length l_2 of the four additional debonded regions is defined by

$$\sinh\left(\frac{L - 2l_1}{2h} - \frac{l_2}{h}\right) = \frac{\tau_c^i}{\sigma_x} \frac{\cosh((L - 2l_1)/2h)}{k}$$

which shows that for $(L - 2l_1)/2h \gg 1$

$$l_2 \cong h \ln\left(k \frac{\sigma_x}{\tau_c^i}\right) \cong l_1.$$

Then each new debonding may be considered to have approximately the same length: $l_i \cong l \cong h$.

The external applied stress to cause the second debonding is

$$\sigma_x = \frac{E_x}{E_B} \sigma_c^B \left(1 - \frac{1}{\cosh(((L - 2l_1)/2h) - (l_2/h))}\right)^{-1}.$$

Using this result it is now possible to extrapolate for m successive mechanisms of debondings-cracking inducing n cracks in the following steps where the approximation $l_i = l$ has been made

Several interesting qualitative results may be observed from this sequence of the debonding-cracking damaging process.

- The crack spacing and the crack density are plotted against the applied stress (Figs. 6, 7). The crack spacing and crack density are normalized by the parameter h ($h \cong 2h$) and the stress σ_x by the ratio $E_x/\sigma_c^B E_B$. The results do not depend upon the geometrical aspect ratio $2L/h$. Then these curves can be used as master curves for many applications.

- The number of cracks increases very rapidly with the applied stress σ_x and the crack spacing decreases very rapidly and approaches saturation. These observations have been pointed out in several experimental studies [Crossman *et al.*, 1980]. The practical limit reached in Figure 6 is $2L/(n-1)h \cong 3$ which corresponds to a crack spacing limit of the order of $2h$: $2L/(n-1) \cong 3h$ which is about twice the thickness of the layer when the layers are of the same size. Otherwise $2L/(n-1) \cong 3(2h_B h_D E_B E_D G_i E_x)^{1/2}$ which is

Mechanism number	Applied stress $\sigma_x = \frac{E_B}{E_f \sigma_1^H}$	Cumulative debonding length	Crack density	Crack spacing
0	0	0	$\frac{2}{2L}$	$2L$
1	$\left[1 - \left(\cosh \frac{L-l}{h}\right)^{-1}\right]^{-1}$	$4l$	$\frac{3}{2L}$	L
2	$\left[1 - \left(\cosh \frac{L-4l}{2h}\right)^{-1}\right]^{-1}$	$12l$	$\frac{5}{2L}$	$\frac{L}{2}$
m	$\left[1 - \left(\cosh \frac{2L - (3 \cdot 2^m - 4)l}{2^m h}\right)^{-1}\right]^{-1}$	$4(2^m - 1)l$	$\frac{2^m + 1}{2L}$	$\frac{2L}{2^m}$
or expressed as \rightarrow Function of the number of cracks		$\left[1 - \left(\cosh \frac{2L - (3n-2)l}{(n-1)h}\right)^{-1}\right]^{-1}$	$\frac{n}{2L}$	$\frac{2L}{n-1}$

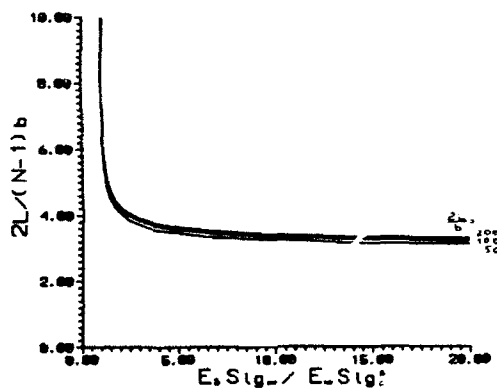


Fig. 6. - Crack spacing.

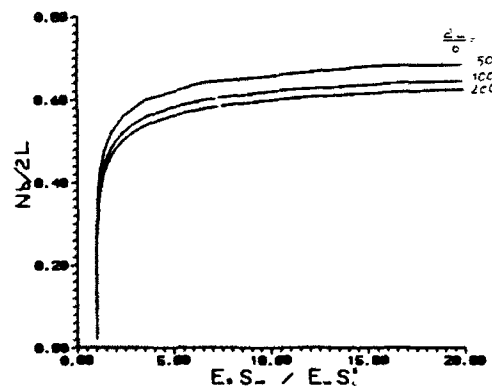


Fig. 7. - Crack density.

in accordance with experimental results of [Highsmith & Reifsnider, 1982] and [Wang, 1984]. Notice that the theories which do not take debonding into account cannot predict this limiting crack spacing.

3.3. EXPERIMENTAL STUDY

Experiments have been performed on a laminate composite made of two brittle layers of Alumina Al_2O_3 bounded by the epoxy of a "ductile" layer of Carbon fiber-epoxy

composite having the fibers in the longitudinal direction of the tensile specimen shown in Figure 8 which also gives the properties of the two materials.

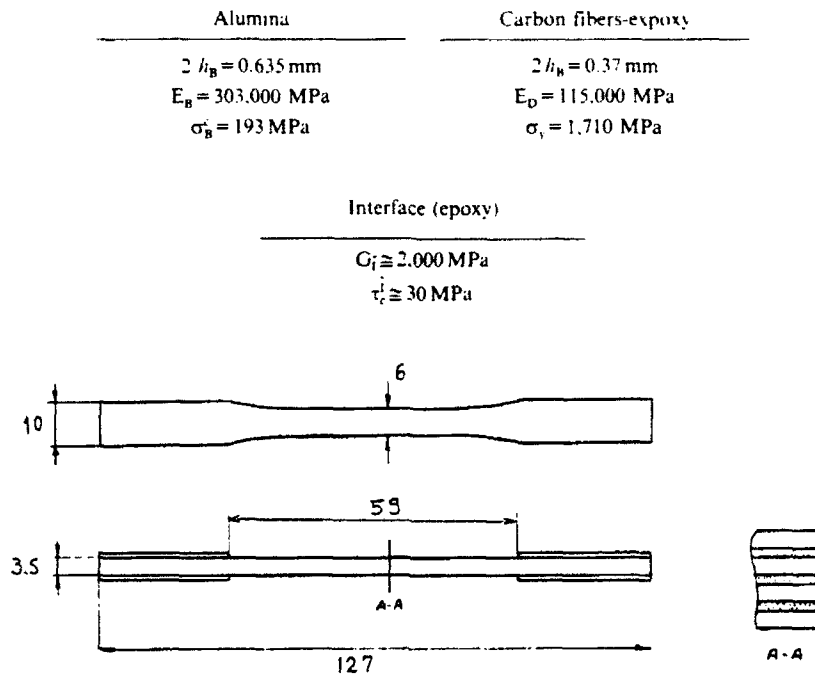


Fig. 8. — One-dimensional laminate specimen.

The processing consists in a hot pressing of the ceramic and carbon fibers epoxy plies at a pressure of 0.350 MPa and a temperature of 135°C for 90 min. Due to the thermal expansion mismatch between the two materials, residual stresses develop during cooling. They have not been taken into consideration in the present study but a method to introduce such initial residual stresses in the analysis is developed in [L & D, 1988].

A monotonic loading is applied and the sequence of cracking is recorded.

The formation of cracks does not occur exactly at mid distance of two existing cracks (nature is not as perfect as the equation!) but appears randomly along the specimen as shown by the sequences of cracking in Figure 9 which shows also the corresponding stress-strain curve and evolution of the number of cracks. However the final pattern is close to the one predicted. Notice that some crack branching occur which are not considered in the theory.

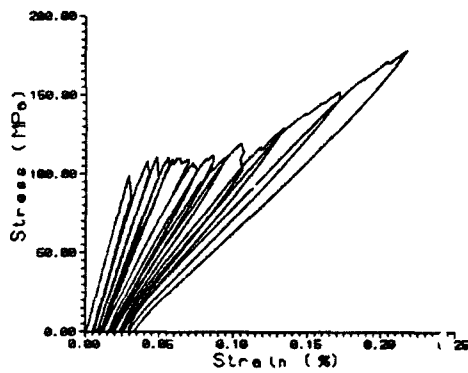
The elementary debonding length when a crack appears is by observation $0.5 < l < 2 \text{ mm}$.

The prediction is

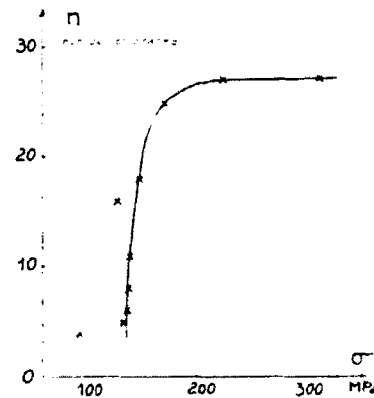
$$l_1 \approx b \approx 2\sqrt{h_p h_n} \approx 1 \text{ mm}.$$



(a)



(b)



(c)

Fig. 9. - Crazes on laminates (a), corresponding stress-strain curve (b) and number of cracks (c).

At saturation, the crack density, the crack spacing and the cumulative debonding estimated as average values of measurements from 3 experiments are:

- crack density: $\approx 0.5 \text{ mm}^{-1}$;
- crack spacing average: $\sim 2 \text{ mm}$.

The corresponding predicted values calculated with $h=1$ are respectively 0.33 mm^{-1} and 3 mm . The correlation is satisfactory enough if we consider that the residual stresses induced by the processing of the Laminate are not taken into account in the theory.

4. Limit load by plasticity in the ductile layer

Crazes continue to develop on the brittle layer until the steady state is reached and the ductile layer may yield when the stress σ_{11}^D is equal to the yield stress σ_y^D . Then from the formulas of Section 2

$$\sigma_{11}^D = \sigma_x + \frac{h_B}{h_D} \sigma_x = \sigma_y^D \quad \text{or} \quad \sigma_x = \sigma_y^D \left(1 + \frac{h_B}{h_D} \right)^{-1}.$$

For that value of the applied stress the laminate behaves as a perfectly plastic material until damage develops in the ductile layer to reach ultimate fracture.

5. Reduction of stiffness

An important effect of crazing is the reduction of the stiffness of the laminate. The stiffness reduction is not due to the cracks but to the debondings which roughly speaking unload the brittle layer over a length $2l$ at each crack (Fig. 10).

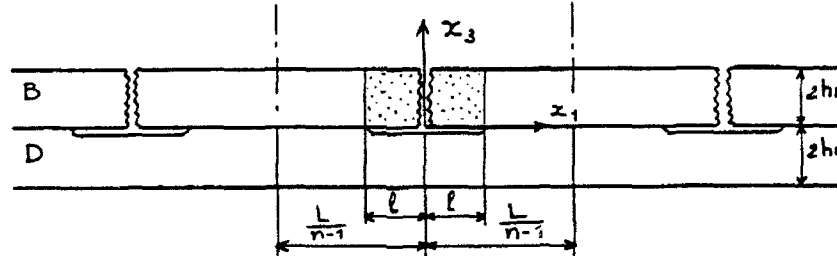


Fig. 10. - Stiffness of a damaged laminate.

Consider one cell whose length is the crack spacing $2L/(n-1)$ (n being the number of cracks in a length $2L$) containing one crack at $x_1=0$. The stiffness of that cell is the stiffness of the ductile layer over a length $2L/(n-1)$ in parallel with two stiffnesses of the brittle layer over the lengths $-(L/(n-1)) < x_1 < -l$ and $l < x_1 < L/(n-1)$.

If \tilde{E} is the elastic modulus of the cell:

$$\left(E_D \frac{2h_D}{(2L/(n-1)) - 2l} + E_B \frac{2h_B}{(2L/(n-1)) - 2l} \right)^{-1} + \left(E_D \frac{2h_D}{2l} \right)^{-1} = \left(\tilde{E} \frac{2(h_B + h_D)}{2L/(n-1)} \right)^{-1},$$

$$\tilde{E} = \frac{E_x}{1 + (l(n-1)/L)(E_B h_B / E_D h_D)}.$$

For many cells in series, \bar{E} is also the elastic modulus of the laminate.

A practical order of magnitude for the modulus is $\bar{E} = E_r/2$ which is reported by [Hashin, 1986] and [Highsmith *et al.*, 1982]. This value is obtained when considering the steady-state limiting case

$$\left. \begin{array}{l} \frac{2L}{(n-1)b} = 2 \quad \text{with } b \cong 2h \cong l \\ \text{together with } \frac{E_R h_R}{E_D h_D} \cong 1 \end{array} \right\} \quad \text{then } \bar{E} = \frac{E_r}{2}$$

The evolution of the damaged elastic modulus \bar{E} as a function of the crack density is compared with experiments of section 3.3 in Figure 11 and comparison is quite good.

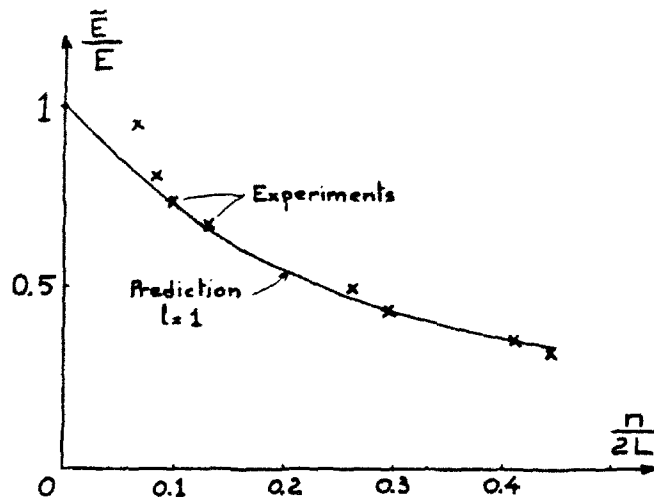


Fig. 11. - Damaged elastic modulus.

6. Homogenization

Having the expression of the elastic modulus of the laminate as a function of the number of cracks (which is a known function of the applied stress σ_r), it is straightforward to derive the constitutive equation of the equivalent continuous material having its elasticity coupled with damage [L & C. 1990].

The one-dimensional continuous damage variable of the laminate is defined by

$$D = 1 - \frac{\bar{E}}{E_r} = \frac{1}{1 + (L/l(n-1))(E_D h_D/E_R h_R)}$$

The same approximations as in Section 5 show that the limiting value of D is of the order of 0.5 which corresponds to the brittle layer fully damaged with a ductile layer undamaged.

The one-dimensional law of elasticity of the homogenized laminate is

$$\varepsilon_x = \sigma E_x (1 - D)$$

This law can be used for structural calculations in engineering applications. The overall behavior resulting from the elasticity, cracking of the brittle layer, debonding of the interface and yielding of the ductile layer is represented in figure 12. It has to be compared with the experimental stress-strain curve depicted in Figure 9 of section 3.3. The main difference is the irreversible strains existing in the experiment that the model does not take into account before the yielding of the ductile layer. They are due to initial residual stresses [L & D, 1988].

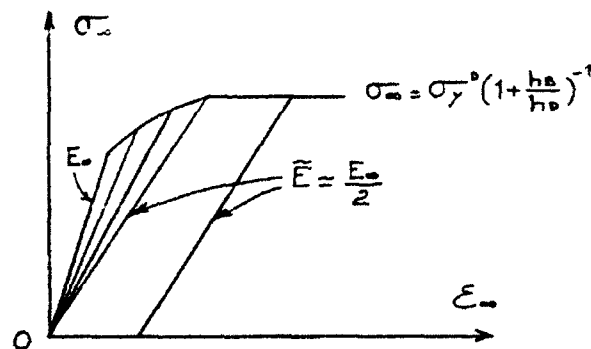


Fig. 12. — Schematic tensile curve as modelled.

APPLICATION TO A PURE BENDING PROBLEM

As an exercise, let us derive the pure bending equation of a damaged beam by a fixed value of the damage D which reduces the elasticity modulus to $E_x (1 - D)$ in tension but does not affect the compression behavior because of the crack closure phenomenon. Then the constitutive equation is

$$\varepsilon = \begin{cases} \frac{\sigma}{E_x (1 - D)} & \text{if } \sigma \geq 0 \\ \frac{\sigma}{E_x} & \text{if } \sigma < 0 \end{cases}$$

This is a classical beam problem solved with Bernoulli's hypothesis. Assuming also a rectangular cross-section with the notations of Figure 1

$$\epsilon_{11} = - \frac{x_3}{R}$$

If R is the curvature and y the beam deflection

$$R = \frac{d^2 y}{dx_1^2}$$

The equilibrium of the forces in the x_1 direction gives the position of the neutral axis in the thickness $2t$ of the beam defined by $-h_1 < x_3 < h_2$ with $h_1 + h_2 = 2t$

$$\int_{-h_1}^{h_2} \sigma_{11}(x_3) dx_3 = 0 \rightarrow \begin{cases} h_1 = 2t \frac{1 - \sqrt{1-D}}{D} \\ h_2 = 2t \left(1 - \frac{1 - \sqrt{1-D}}{D} \right) \end{cases}$$

where the edge h_1 is in tension and h_2 in compression. The equilibrium of moments gives the beam equation: $\int_{-h_1}^{h_2} \sigma_{11}(x_3) x_3 dx_3 + M = 0$, $d^2 y / dx_1^2 = M / E_x I \Delta_{(D)}$, where I is the

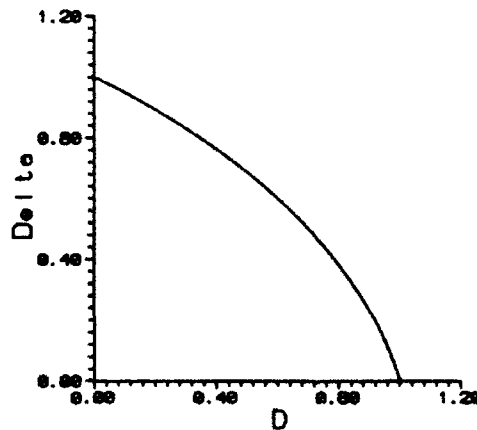


Fig. 13. - Damaging correction function for pure bending of beams.

bending inertia of the beam section and Δ the damage function represented in Figure 13.

$$\Delta_{(D)} = 4 \left[(1-D) \left(\frac{1 - \sqrt{1-D}}{D} \right)^3 + \left(1 - \frac{1 - \sqrt{1-D}}{D} \right)^3 \right]$$

It is also possible to consider the coupled problem of damage induced by the bending but only by means of a numerical analysis. A closed form solution could not be found.

Acknowledgement

This work was partially supported by the Air Force Office of Scientific Research and that support is gratefully acknowledged.

REFERENCES

- BAILEY J. E., CURTIS P. T. and PARVIZI A., 1979, On the transverse cracking and longitudinal splitting behavior of glass and carbon fibre reinforced epoxy cross ply laminates and the effect of Poisson and thermally generated strain, *Proc. R. Soc. Lond. A.*, **366**, 599.
- COX H. L., 1952 The elasticity and strength of paper and other fibrous materials, *Br. J. Appl. Phys.*, **3**, 72-79.
- CROSSMAN F. W., WARREN W. J., WANG A. S. D. and LAW Jr. G. E., 1980, Initiation and growth of transverse cracks and edge delamination in composite laminates. Part 2: Experimental Correlation, *J. Comp. Mater. Suppl.*, **14**, 88.
- EVANS A., 1990, Perspective on the development of high-toughness ceramics, *J. Am. Ceram. Soc.*, **73** [2], 187-206.
- FUKANAGA H., CHOU T. W., PETERS P. W. M. and SCHULTE K., 1984, Probabilistic failure strength analysis of graphite-epoxy cross-ply laminates, *J. Comp. Mater.*, **18**, 339.
- GARRETT K. W. and BAILEY J. E., 1977, Multiple transverse fracture in 90° cross-ply laminates of a glass fibre-reinforced polyester, *J. Mater. Sci.*, **12**, 157.
- HASHIN Z., 1986, Analysis of stiffness reduction of cracked cross-ply laminates, *Engng. Fract. Mech.*, **25**, [5-6], 771-778.
- HIGHSMITH A. L. and REIFSNIDER K. L., 1982, Stiffness reduction mechanisms in composite laminates, *ASTM STP 775*, p. 103.
- LANGE F., MARSHALL D. B. and FOLSOM C., 1990, *U.C.S.B. Patent Application*.
- LAWS N., DVORAK G. J. and HEJAZI M., 1983, Stiffness changes in unidirectional composites caused by crack systems, *Mech. Mater.*, **2**, 123.
- LAWS N. and DVORAK G. J., 1988, Progressive transverse cracking in composite laminates, *J. Comp. Mater.*, **22**, October.
- LEMAITRE J. and CHABOCHE J. L., 1990, *Mechanics of solid materials*, Cambridge University Press.
- MANDERS P. W., CHOU T. W., JONES F. R. and ROCK J. W., 1983, Statistical analysis of multiple fracture in 0°/90°/0° glass fibre-epoxy resin laminates, *J. Mater. Sci.*, **18**, 2876.
- PARVIZI A. and BAILEY J. E., 1978, On multiple transverse cracking in glass fibre epoxy cross-ply laminates, *J. Mater. Sci.*, **13**, 1231.
- WANG A. S. D. and CROSSMAN F. W., 1980, Initiation and growth of transverse cracks and edge delamination in composite laminates. Part 1: An energy method, *J. Comp. Mater. Suppl.*, **14**, 71.
- WANG A. S. D., 1984, Fracture mechanics of sublaminate cracks in composite materials, *Composites Tech. Rev.*, **6**, 45.

(Manuscript received November 27, 1990;
accepted April 24, 1991.)